



Investigation of Low Temperature Cracking in Asphalt Pavements National Pooled Fund Study - Phase II

Minnesota
Department of
Transportation

**RESEARCH
SERVICES**

Office of
Policy Analysis,
Research &
Innovation

Mihai Marasteanu, Principal Investigator
Department of Civil Engineering
University of Minnesota

August 2012

Research Project
Final Report 2012-23



Your Destination... Our Priority



Technical Report Documentation Page

1. Report No. MN/RC 2012-23	2.	3. Recipients Accession No.	
4. Title and Subtitle Investigation of Low Temperature Cracking in Asphalt Pavements, National Pooled Fund Study -Phase II		5. Report Date August 2012	
		6.	
7. Author(s) Mihai Marasteanu, William Buttlar, Hussain Bahia, and Christopher Williams, et al.		8. Performing Organization Report No.	
9. Performing Organization Name and Address Department of Civil Engineering University of Minnesota 500 Pillsbury Drive SE Minneapolis, MN 55455		10. Project/Task/Work Unit No. CTS #2008077	
		11. Contract (C) or Grant (G) No. (C) 89261 (WO) 103	
12. Sponsoring Organization Name and Address Minnesota Department of Transportation Research Services 395 John Ireland Blvd., MS 330 St. Paul, MN 55155		13. Type of Report and Period Covered Final Report	
		14. Sponsoring Agency Code	
15. Supplementary Notes http://www.lrrb.org/pdf/201223.pdf			
16. Abstract (Limit: 250 words) <p>The work detailed in this report represents a continuation of the research performed in phase one of this national pooled fund study. A number of significant contributions were made in phase two of this comprehensive research effort. Two fracture testing methods are proposed and specifications are developed for selecting mixtures based on fracture energy criteria. A draft SCB specification, that received approval by the ETG and has been taken to AASHTO committee of materials, is included in the report.</p> <p>In addition, alternative methods are proposed to obtain mixture creep compliance needed to calculate thermal stresses. Dilatometric measurements performed on asphalt mixtures are used to more accurately predict thermal stresses, and physical hardening effects are evaluated and an improved model is proposed to take these effects into account. In addition, two methods for obtaining asphalt binder fracture properties are summarized and discussed.</p> <p>A new thermal cracking model, called "ILLI-TC," is developed and validated. This model represents a significant step forward in accurately quantifying the cracking mechanism in pavements, compared to the existing TCMODEL. A comprehensive evaluation of the cyclic behavior of asphalt mixtures is presented, that may hold the key to developing cracking resistant mixtures under multiple cycles of temperature.</p>			
17. Document Analysis/Descriptors Low temperature cracking, Asphalt mixtures, Asphalt binders, Fracture properties, Thermal stresses, Temperature fatigue, Fatigue (Mechanics), Strength of materials, Creep properties, Contraction (Thermodynamics), Thermal expansion, Materials at high or low temperatures, Pavement cracking		18. Availability Statement No restrictions. Document available from: National Technical Information Services, Alexandria, Virginia 22312	
19. Security Class (this report) Unclassified	20. Security Class (this page) Unclassified	21. No. of Pages 377	22. Price

Investigation of Low Temperature Cracking in Asphalt Pavements National Pooled Fund Study – Phase II

Final Report

Prepared by:

Mihai Marasteanu
Ki Hoon Moon
Eyoab Zegey Teshale
Augusto Cannone Falchetto
Mugurel Turos

Department of Civil Engineering
University of Minnesota

William Buttlar
Eshan Dave
Glaucio Paulino
Sarfraz Ahmed
Sofie Leon
Andrew Braham
Behzad Behnia

University of Illinois

Hussain Bahia
Hassan Tabatabaee
Raul Velasquez
Amir Arshadi
Sebastian Puchalski
Salvatore Mangiafico

University of Wisconsin

Christopher Williams
Ashley Buss
Jason Bausano
Andrea Kvasnak

Iowa State University

August 2012

Published by:

Minnesota Department of Transportation
Research Services
395 John Ireland Boulevard, Mail Stop 330
St. Paul, Minnesota 55155

This report represents the results of research conducted by the authors and does not necessarily represent the views or policies of the Minnesota Department of Transportation, University of Minnesota, University of Illinois, Iowa State University, or the University of Wisconsin. This report does not contain a standard or specified technique.

The authors, the Minnesota Department of Transportation, the University of Minnesota, the University of Illinois, Iowa State University, and the University of Wisconsin do not endorse products or manufacturers. Any trade or manufacturers' names that may appear herein do so solely because they are considered essential to this report.

Table of Contents

Chapter 1. Introduction.....	1
Background	1
Objectives and Research Approach	1
Chapter 2. Literature Review	3
Introduction	3
Experimental Methods and Analyses.....	3
<i>Binder and Mastic Testing</i>	3
<i>Mixture Testing</i>	6
<i>Fracture Test Methods</i>	11
Low Temperature Cracking Models	18
Other Relevant Studies.....	24
Asphalt Research Consortium.....	27
MNROAD Reconstruction and Low Temperature Research.....	29
<i>Field Performance</i>	30
Conclusion	31
Chapter 3. Expand Phase I Test Matrix	32
<i>Statistical Analysis Summary</i>	33
<i>Subtask on Physical Hardening</i>	33
Experimental Work	34
<i>Preparation of Laboratory Compacted Asphalt Mixture Specimens</i>	34
<i>Preparation of Field Cored Asphalt Mixture Test Samples</i>	35
Testing Methods and Test Results	36
<i>Disc-Shaped Compact Tension (DCT) Test</i>	36
<i>DCT Test Results for Laboratory Compacted and Field Samples</i>	37
<i>DCT Results for Field Specimens</i>	41
<i>DCT Results for Tests Performed at UMN</i>	42
<i>Semi-Circular Bend (SCB) Test</i>	42
<i>SCB Results for Laboratory Compacted and Field Samples</i>	43
<i>SCB Results for Field Specimens</i>	47
<i>SCB Results for Tests Performed at UIUC</i>	48
<i>Indirect Tensile Test IDT Creep Stiffness and Strength Tests</i>	48
<i>IDT Test Results for Laboratory Compacted and Field Samples</i>	49
<i>IDT Results for Field Specimens</i>	53

Summary of Results from Laboratory Compacted Non-Conditioned Specimens	53
<i>Data Analysis of Fracture Energy Results</i>	53
<i>Data Analysis of Fracture Toughness Results</i>	56
<i>Data Analysis of IDT Strength Results</i>	57
<i>Data Analysis of IDT Creep Stiffness</i>	59
<i>Ranking of Mixtures</i>	60
<i>Comparison of DCT and SCB Fracture Energy</i>	65
Analysis of Results from Conditioned Laboratory Specimens and Field Cores.....	67
<i>Data Analysis of Test Results</i>	68
<i>Comparison of Field Cores and Laboratory Compacted Test Results</i>	71
Analysis of Variance (ANOVA) for Conditioned Samples	73
<i>DCT Conditioning Analysis</i>	74
<i>SCB Conditioning Analysis</i>	75
<i>IDT Conditioning Analysis</i>	76
<i>IDT Peak Strength Conditioning Analysis</i>	76
Comparison of Air Voids and Test Temperature	77
<i>DCT Air Void and Temperature Analysis</i>	78
<i>SCB Air Void and Temperature Analysis</i>	78
IDT Air Void and Temperature Analysis.....	80
<i>Stiffness at 500 Seconds</i>	80
Comparison of Experimental Results Obtained at UIUC and UMN	82
<i>Reproducibility of SCB Tests</i>	86
Statistical Analysis Conclusions	89
Summary of Findings	89
Chapter 4. Subtask on Physical Hardening	91
Introduction	91
Literature Review.....	91
Materials and Experimental Methods	93
<i>Asphalt Binders</i>	93
<i>Test Methods</i>	94
Results and Discussion.....	96
<i>Effect of Binder Source and Modification</i>	96
<i>Physical Hardening and Glass Transition</i>	98
<i>Effect of Thermal History</i>	100

<i>Development of Model to Predict Physical Hardening</i>	101
<i>Physical Hardening in MnROAD Binders</i>	107
<i>Effect of Polyphosphoric Acid (PPA) and Warm Mix Additives (WMA)</i>	110
Dimensional Stability of Asphalt Mixtures during Isothermal Storage.....	111
Summary of Findings and Conclusions	114
Chapter 5. Develop Low Temperature Specification for Asphalt Mixtures.....	116
Introduction	116
<i>Subtask 1 – Develop Test Method</i>	116
<i>Subtask 2 – Develop Specification</i>	116
<i>Subtask 3 – Propose Simplified Method to Obtain Mixture Creep Compliance</i>	116
Chapter 6. Subtask 1: Develop Test Method	117
Summary of Fracture Testing Methods	117
<i>Disc-Shaped Compact Tension DC(T)Test</i>	117
<i>Semi Circular Bend (SCB) Test</i>	118
Proposed Standard Fracture Test Method	118
Chapter 7. Subtask 2: Develop Specification.....	123
Revisit Performance Grade (PG) Specification for Asphalt Binders.....	123
<i>Development of PG Low Temperature Cracking Criteria</i>	123
Develop Asphalt Mixture Low Temperature Specification	124
<i>Asphalt Mixture Low Temperature Specification Based on DC(T) Fracture Energy</i>	125
<i>Alternative Asphalt Mixture Low Temperature Specification Based on SCB Fracture Energy</i>	126
Chapter 8. Subtask 3: Proposed Simplified Method to Obtain Mixture Creep Compliance – Part 1	129
Obtaining Creep Compliance from DC(T) Test.....	129
<i>Finite Element Simulations</i>	131
Obtaining Creep Compliance from SCB Test.....	136
<i>Linear Viscoelastic Conditions</i>	136
<i>Analysis of Stress State in SCB Specimen</i>	137
<i>Analysis of the Effect of Time on the Stresses in SCB Specimen</i>	142
<i>Stress Equations</i>	144
<i>Equation for SCB Creep Compliance</i>	145
<i>Verification of the Proposed SCB Creep Model</i>	147
<i>Numerical Validation</i>	147

<i>Determination of Creep Compliance from Numerical Simulations</i>	148
<i>Experimental Validation</i>	149
<i>Conclusions</i>	153
Chapter 9. Subtask 3 Proposed Simplified Method to Obtain Mixture Creep Compliance	
– Part 2	154
Obtaining Creep Compliance from BBR Tests on Mixture Beams.....	154
<i>Experimental Work</i>	155
Evaluate the Feasibility of Using Hirsch Model to Obtain Mixture Creep Stiffness from Binder Creep Stiffness	160
<i>Hirsch Model</i>	160
<i>Analogical Models</i>	162
<i>Huet Model</i>	163
<i>Huet-Sayegh Model</i>	164
<i>2S2PID Model</i>	165
<i>ENTPE Transformation</i>	166
<i>Material and Testing</i>	167
<i>Data Analysis</i>	168
<i>Forward Problem: Mixtures from Binders</i>	173
<i>Inverse Problem: Binders from Mixtures</i>	176
<i>Hirsch Model</i>	177
<i>ENTPE Transformation</i>	179
<i>Conclusions</i>	181
Using Binder Creep Stiffness to Obtain Mixture Creep Stiffness Threshold Value	181
<i>Binder PAV to Binder RTFOT</i>	182
<i>Binder RTFOT to Mixture</i>	183
Obtaining Strength from BBR Tests on Mixture Beams	184
<i>Experimental Work</i>	184
<i>Effect of Cooling Medium on BBR Strength</i>	189
Chapter 10. Subtask 3: Proposed Simplified Method to Obtain Mixture Creep Compliance – Part 3	191
Introduction.....	191
The Single Edged Notched Beam Test	192
<i>Proposed SENB Geometry</i>	192
<i>Finite Element Simulations</i>	193
<i>Single-Edge Notched Bending (SENB) Test Procedure</i>	194

<i>Sources of Variability in SENB</i>	195
<i>Materials</i>	196
Results and Discussion.....	197
<i>SENB vs. BBR</i>	197
<i>SENB vs. Tg</i>	198
<i>SENB vs. ABCD</i>	199
<i>Effect of Physical Hardening on SENB Fracture Properties</i>	201
<i>SENB as a Low Temperature Performance Specification</i>	202
Validation of SENB Measurements.....	207
<i>Comparison of SENB Results to Mixture Fracture Tests</i>	207
<i>Comparison of SENB Results to LTPP Field Data</i>	208
Chapter 11. Develop Improved TC Model	211
Background	211
Model Components	211
Visual LTC.....	212
<i>Running Visual LTC</i>	212
<i>Communication with Analysis Modules</i>	213
<i>User Types</i>	213
<i>Visual LTC User Inputs</i>	214
<i>Data Storage</i>	216
Preprocessor	216
Input File Generator	217
Preanalyzer.....	218
Finite Element Analysis Engine.....	220
<i>Viscoelastic Finite Element Analysis</i>	220
<i>Fracture Modeling of Asphalt Concrete</i>	223
Probabilistic Crack Distribution Model	224
Calibration of ILLI-TC Model.....	225
Pre-Analyzer Runs	226
Finite Element Runs.....	228
Model Calibration Discussion.....	230
Summary	232
Chapter 12. Modeling of Asphalt Mixtures Contraction and Expansion Due to Thermal Cycling	234

Introduction	234
Objectives.....	235
Background	235
Materials and Experimental Methods	236
<i>Asphalt Binders and Mixtures</i>	236
Test Methods.....	237
<i>Glass Transition (T_g) Test Procedure for Asphalt Binders</i>	237
<i>Asphalt Thermal Cracking Analyzer (ATCA)</i>	238
Experimental Evaluation of Thermal Response of Asphalt Binders and Mixtures during Cooling and Heating (Objective 1)	241
<i>Thermo-Volumetric Response of Asphalt Binders and Mixtures during Thermal Cycles</i>	241
Thermal Stress Response of Asphalt Binders and Mixtures during Thermal Cycles	245
Thermal Stress Buildup and Relaxation.....	248
Micromechanical Simulation of Thermo-Volumetric Properties in Asphalt Mixtures – Objective 2	253
<i>Introduction</i>	253
<i>Background</i>	253
Thermal Expansion/Contraction Coefficient of Composites	254
General Description of FEM Simulation	255
Importance of Aggregate Structure on Thermal Properties of the Mixture	256
Finite Element Modeling of Asphalt Mixture Binary Images	258
Models for Estimation of α_l and α_g of Asphalt Mixtures	262
Sensitivity Analysis of Thermo-Volumetric Parameters through Modeling (Objective 3) ...	265
Model Input and Assumptions	266
<i>Thermo-Volumetric Behavior and Glass Transition of Asphalt Mixtures</i>	266
Physical Hardening in Asphalt Binders and Mixtures	266
Prediction of Thermal Stress Buildup and Relaxation.....	269
Sensitivity Analysis.....	271
Summary of Findings and Conclusions	275
<i>Conclusions</i>	275
Recommendations and Potential Applications for DOTs	276
Chapter 13. Validation of New Specification	278
Introduction	278
Test results	279

<i>Effect of Aggregate Size</i>	288
<i>Effect of RAP</i>	289
Field Validation.....	289
Predicting Mixture Creep Stiffness from Binder Creep Stiffness.....	295
Hirsch Model.....	297
Huet Model and ENTPE Transformation	298
Predicting Mixture Creep Stiffness from Binder Experimental Data	300
Chapter 14. Summary and Conclusions	306
References	309
Appendix A: Air Void and Temperature Analysis	
Appendix B: User’s Manual for ILLI-TC using Visual-LTC GUI	

List of Tables

Table 2.1: HMA field testing data (62).....	30
Table 3.1: Asphalt mixtures used in Task 2.....	32
Table 3.2: Laboratory experimental layout.....	33
Table 3.3: Air void content for field cores.....	36
Table 3.4: DCT test results for specimens with 4% air void content	38
Table 3.5: DCT test results for specimens with 7% air void content	39
Table 3.6: DCT test results for conditioned specimens	40
Table 3.7: DCT test results for field specimens.....	41
Table 3.8: DCT test results for mixtures tested at the UMN	42
Table 3.9: SCB test results for specimens with 4% air void content.....	44
Table 3.10: SCB test results for specimens with 7% air void content.....	45
Table 3.11: SCB test results for conditioned specimens.....	46
Table 3.12: SCB test results for field cored samples	47
Table 3.13: SCB test results for mixtures tested at the UIUC	48
Table 3.14: IDT strength and creep stiffness (500s) for specimens with 4% air void content.....	50
Table 3.15: IDT strength and creep stiffness (500s) for specimens with 7% air void content.....	51
Table 3.16: IDT strength and creep stiffness (500s) for conditioned specimens.....	52
Table 3.17: IDT strength and creep stiffness (500s) for field specimens	53
Table 3.18: Range of fracture energy test results	54
Table 3.19: Range of fracture toughness test results	56
Table 3.20: Range of IDT strength test results	59
Table 3.21: Range of IDT creep stiffness (500s) test results.....	60
Table 3.22: Summary of results for 4% void mixtures tested at PGLT+10°C	61
Table 3.23: Summary of results for 4% void mixtures tested at PGLT.....	61
Table 3.24: Summary of results for 7% void mixtures tested at PGLT+10°C	62
Table 3.25: Summary of results for 7% void mixtures tested at PGLT.....	62
Table 3.26: Average rank for 4% void mixtures 4% void tested at PGLT+10°C	63
Table 3.27: Overall ranking of mixtures with 4% void content	64
Table 3.28: Overall ranking of mixtures with 7% void content	64
Table 3.29: Effects test for DCT Gf comparing conditioning	74
Table 3.30: Effects test for SCB KIC conditioning comparison	75
Table 3.31: ANOVA for SCB conditioning	75

Table 3.32: ANOVA for IDT conditioning comparison.....	76
Table 3.33: IDT peak strength conditioning analysis	77
Table 3.34: IDT peak strength conditioning Tukey’s comparison	77
Table 3.35: DCT ANOVA and random effects for temperature and air voids.....	78
Table 3.36: Tukey HSD multiple comparison for DCT	78
Table 3.37: SCB ANOVA and random effects.....	79
Table 3.38: Tukey HSD for SCB KIC analysis for air void and temperature	79
Table 3.39: SCB Gf ANOVA and random effects analysis for air voids and temperature	80
Table 3.40: SCB Gf Tukey analysis for air voids and temperature	80
Table 3.41: IDT Stiffness ANOVA and random effects analysis for air voids and temperature .	81
Table 3.42: IDT Stiffness Tukey analysis for air voids and temperature	81
Table 3.43: IDT Strength ANOVA and random effects analysis for air voids and temperature..	82
Table 3.44: IDT Strength Tukey analysis for air voids and temperature.....	82
Table 3.45: ANOVA and random effects comparisons of DCT testing.....	85
Table 3.46: DCT testing Tukey HSD comparison of laboratories and mixes	85
Table 4.1: SHRP asphalt binders	94
Table 4.2: Asphalt binders selected for Task 2.....	94
Table 6.1: Estimated costs for DC(T) and SCB tests.....	121
Table 7.1: Recommended low-temperature cracking specification for loose mix	126
Table 7.2: LTPP low pavement temperature at 50% reliability level.....	127
Table 7.3: Mixture parameter and total length of transverse cracking in the field.....	127
Table 8.1: Fracture energy for creep + fracture versus fracture only testing.....	131
Table 8.2: Input parameters for GMM model in ABAQUS	143
Table 8.3: Stress function fitting coefficients	145
Table 8.4: Geometry of model beams.....	148
Table 9.1: Description of asphalt mixtures	156
Table 9.2: Statistical summary for dimensions of 3x, 2x, and 1x beams	156
Table 9.3: Variables definition for statistical analysis.....	159
Table 9.4: Correlation factors for all temperatures	159
Table 9.5: ANOVA for all temperatures.....	160
Table 9.6: Asphalt binders and mixtures	168
Table 9.7: Mixture volumetric properties	168
Table 9.8: Aggregate modulus.....	168
Table 9.9: Huet Model parameters for binders and granite mixtures	170

Table 9.10: α values for the four binders mixtures groups	172
Table 9.11: Parameters used in Hirsch Model	173
Table 9.12: Binder PAV Tcr and corresponding S(60)RTFOT	183
Table 9.13: Predicted mixture S(60) at PAV binder critical temperature.....	183
Table 9.14: BBR asphalt binder test results.....	186
Table 9.15: DTT asphalt binder experimental design and test results	187
Table 9.16: Comparison between DTT vs. BBR asphalt binder strength.....	188
Table 9.17: BBR and DTT results and comparison for different cooling media.....	189
Table 9.18: Effect of cooling medium on BBR strength	190
Table 10.1: Prony series coefficients for FE simulations	193
Table 10.2: Description of the asphalt binders tested in BBR-SENB	197
Table 10.3: SENB results at -12°C for LTPP binders.	208
Table 11.1: Visual LTC steps	213
Table 11.2: Climatic locations available to user in Visual LTC.....	214
Table 11.3: Summary of pavement materials user inputs.....	215
Table 11.4: Material properties required by the analysis model.....	218
Table 11.5: Preanalyzer results (number of critical events) compared to field cracking	228
Table 11.6: ILLI-TC model calibration results.....	232
Table 12.1: Asphalt binders selected for Task 2.....	236
Table 12.2: Asphalt binder and mixture thermal strain model parameters during cooling	241
Table 12.3: Asphalt binder and mixture thermal strain model parameters during heating.....	242
Table 12.4: Microstructural analysis of mixtures	258
Table 12.5: Analysis matrix used for the sensitivity analysis.....	272
Table 12.6: Parameter values used for the sensitivity analysis.....	272
Table 13.1: Asphalt mixtures used in Task 6.....	278
Table 13.2: DC(T) fracture energy for mixtures tested at PGLT+10°C	279
Table 13.3: DC(T) fracture energy for mixtures tested at PGLT	280
Table 13.4: SCB fracture energy for mixtures tested at PGLT+10°C	281
Table 13.5: SCB fracture energy for mixtures tested at PGLT.....	282
Table 13.6: SCB fracture toughness for mixtures tested at PGLT+10°C.....	283
Table 13.7: SCB fracture toughness for mixtures tested at PGLT	284
Table 13.8: Summary of results for mixtures tested at PGLT+10°C.....	286
Table 13.9: Summary of results for mixtures tested at PGLT	287
Table 13.10: Fracture energy and field cracking for validation sections.....	290

Table 13.11: Preanalyzer results and field cracking for validation sections.....	293
Table 13.12: ILLI-TC predictions and field cracking for validation sections using calibrations from Task 4.....	294
Table 13.13: Summary of RTFOT binder S(60s) and m(60s) from BBR creep testing.....	295
Table 13.14: Summary of S(60s) and S(500s) from IDT mixture creep testing.....	296
Table 13.15: Huet Model parameters for tested binders.....	302
Table 13.16: α parameter values for mixtures for ENTPE transformation	303

List of Figures

Figure 2.1: Creep stiffness measurement for sealant NN (13).....	5
Figure 2.2: 1x, 2x, and 3x asphalt mixture beam specimens. (17)	7
Figure 2.3: a) Uniaxial tension test device, b) Tensile strength reserve plot. (25)	10
Figure 2.4: Dog-bone direct tension test prototype (27).....	10
Figure 2.5: Single edge notched beam test (28).....	11
Figure 2.6: 3-Point bend experimental setup (29)	12
Figure 2.7: Comparison table (29).....	12
Figure 2.8: Variation of fracture energy with diameter and thickness (31).....	14
Figure 2.9: Bilinear cohesive fracture model (37).....	15
Figure 2.10: Fracture process zone according to Hu and Wittmann (31).....	16
Figure 2.11: Fenix test and typical load vs. displacement output curve. (43)	18
Figure 2.12: Thermal cracking prediction using MEPDG (44)	18
Figure 2.13: Measured versus predicted total fracture energy (44)	20
Figure 2.14: Comparison between analytical and FEM solution (at -30°C) (49)	22
Figure 2.15: Crack-profile superposition (53)	24
Figure 2.16: Lattice simulation vs. experimental stress - strain curves (56)	25
Figure 2.17: Aggregate and air voids comparison (57)	27
Figure 2.18: Temperature distribution (60)	28
Figure 2.19: Modeled thermal temperature and strain (60)	29
Figure 2.20: Dynamic modulus master curves (62).....	31
Figure 3.1: Non-conditioned specimens used at UMN.....	34
Figure 3.2: Non-conditioned specimens used at UIUC	34
Figure 3.3: Conditioned specimens.....	35
Figure 3.4: Sample preparation for field cores	35
Figure 3.5: DCT test scheme	37
Figure 3.6: Typical load-CMOD plots from DCT tests of three replicates	37
Figure 3.7: SCB test scheme.....	42
Figure 3.8: Typical load-LLD plots from SCB tests of three replicates.....	43
Figure 3.9: DCT fracture energy results for 4% void specimens	54
Figure 3.10: DCT fracture energy results for 7% void specimens	55
Figure 3.11: SCB fracture energy results for 4% void specimens.....	55
Figure 3.12: SCB fracture energy results for 7% void specimens.....	56
Figure 3.13: SCB fracture toughness results for 4% void specimens.....	57

Figure 3.14: SCB fracture toughness results for 7% void specimens.....	57
Figure 3.15: IDT strength results for 4% void specimens	58
Figure 3.16: IDT strength results for 7% void specimens	58
Figure 3.17: IDT stiffness for 4% void specimens	59
Figure 3.18: IDT stiffness for 7% void specimens	60
Figure 3.19: DCT vs. SCB correlation plots.....	65
Figure 3.20: DCT and SCB load-displacement curves.....	66
Figure 3.21: Correlation DCT and SCB fracture energy – 4%	67
Figure 3.22: Correlation DCT and SCB fracture energy – 7%	67
Figure 3.23: DCT fracture energy test results for conditioned and field samples	68
Figure 3.24: SCB fracture energy test results for conditioned and field samples.....	69
Figure 3.25: SCB fracture toughness test results for conditioned and field samples	69
Figure 3.26: IDT tensile strength test results for conditioned and field samples	70
Figure 3.27: IDT stiffness test results for conditioned and field samples	71
Figure 3.28: Results comparison field to laboratory compacted, DCT fracture energy	71
Figure 3.29: Results comparison field to laboratory compacted, SCB fracture energy	72
Figure 3.30: Results comparison field to laboratory compacted, SCB fracture toughness	72
Figure 3.31: Results comparison field to laboratory compacted, IDT tensile strength	73
Figure 3.32: Results comparison field to laboratory compacted, IDT stiffness	73
Figure 3.33: RCBD statistical factors for comparison of conditioning	74
Figure 3.34: Variables and treatment combinations for each mix in the split plot analysis	77
Figure 3.35: IDT stiffness data trends with 95% confidence interval	81
Figure 3.36: IDT strength data trends with 95% confidence interval.....	82
Figure 3.37: Comparison DCT test result from UMN and UIUC	83
Figure 3.38: Load vs. CMOD and time vs. CMOD plots.....	84
Figure 3.39: Split plot design for comparing DCT results between laboratories	84
Figure 3.40: DCT comparison of residual plots.....	86
Figure 3.41: Comparison SCB test result from UMN and UIUC – fracture energy	87
Figure 3.42: Load vs. CMOD and time vs. CMOD plots.....	87
Figure 3.43: Comparison SCB test result from UMN and UIUC – fracture toughness	88
Figure 3.44: Comparison of SCB test data	88
Figure 4.1: Physical hardening and its relation to free volume	92
Figure 4.2: Dilatometric system used to measure glass transition temperature (T_g) of asphalt binders.....	95

Figure 4.3: Typical results from glass transition temperature (T_g) test of asphalt binders	96
Figure 4.4: Thermal cycle	96
Figure 4.5: Hardening index after 24hrs (relative to one hour) of isothermal conditioning at different temperatures for SHRP binders.....	97
Figure 4.6: Hardening index after 24 hr of isothermal conditioning at different temperatures using data from Lu and Isacsson (5)	98
Figure 4.7: Schematic of proposed material behavior in glass transition region.....	100
Figure 4.8: PG 58-34+ PPA binder from MnROAD 33- creep stiffness as function of conditioning time	100
Figure 4.9: Effect of thermal history on physical hardening by measuring changes in creep stiffness and m-values of binders in Table 4.2	101
Figure 4.10: Empirical function used to account for glass transition temperature in prediction model. ($2*x$ is the length of the glass transition region).....	103
Figure 4.11: Comparison of model described by [4.4] with experimental data (hardening rate= $\Delta S/S_0$).....	104
Figure 4.12: Goodness of fit between the predictions using Equation [4.4] using T_g for T_0 and the experimental data. (hardening rate= $\Delta S/S_0$).....	104
Figure 4.13: Goodness of fit between model described by [4.4] with fitted T_0 and experimental data (hardening rate= $\Delta S/S_0$).....	105
Figure 4.14: $S(60)$ after 1hr conditioning for one of the SHRP binders plotted against test temperature	106
Figure 4.15: Correlation between G and η and B for the SHRP binders.....	106
Figure 4.16: Goodness of fit between model described by [4.6] using T_g for T_0 and experimental data.....	107
Figure 4.17: Goodness of fit of the physical hardening model for the MnROAD binders (a) using measured glass transition temperature values, (b) using values fitted by model.....	108
Figure 4.18: Comparison of the G parameter derived from the fitted physical hardening model	108
Figure 4.19: Comparison of the η parameter derived from the fitted physical hardening model.....	109
Figure 4.20: Comparison of the average hardening for each binder over all tested conditioning times and temperatures	109
Figure 4.21: Comparison of the average hardening for each binder over all tested conditioning times and temperatures	110
Figure 4.22: Comparison of G parameter derived from the fitted physical hardening model....	111
Figure 4.23: Comparison of the η parameter derived from the fitted physical hardening model.....	111
Figure 4.24: T_g mixture results for unglued and glued specimen	112

Figure 4.25: Comparison of T_g results from samples with $\phi = 1"$ and $2.5"$	113
Figure 4.26: Prismatic beams made from gluing blocks cut out of gyratory samples	113
Figure 4.27: Test setup used for the glass transition temperature of beams made from gyratory compacted samples	113
Figure 6.1: DC(T) testing scheme.....	117
Figure 6.2: Typical load-CMOD plots from DCT tests of three replicates	117
Figure 6.3: SCB testing scheme.....	118
Figure 6.4: Typical load-LLD plots from SCB tests of three replicates	118
Figure 6.5: a) DC(T) test and b) CMOD gage attached to gage points	119
Figure 6.6: DC(T) marking template	119
Figure 6.7: The SCB test.....	121
Figure 7.1: Field data suggesting a minimum fracture energy of 400 J/m^2 at PGLT + 10°C to prevent thermal cracking.....	125
Figure 7.2: Field data suggesting a minimum SCB fracture energy of 350 J/m^2 at PGLT + 10°C to prevent thermal cracking	128
Figure 7.3: Field data suggesting a minimum fracture toughness of $800\text{kPa}\times\text{m}^{0.5}$ at PGLT + 10°C to prevent thermal cracking.....	128
Figure 8.1: Comparison of disk-shaped compact tension [DC(T)] test, indirect tension test (IDT) and combined DC(T)-IDT test geometries.	130
Figure 8.2: Typical creep deformation results in DC(T) - IDT test obtained from extensometers mounted on both sides of the specimen near the crack tip	130
Figure 8.3: Finite element mesh of DCTIDT sample	132
Figure 8.4: (a) DCTIDT sample with notch (b) DCTIDT sample without notch.....	132
Figure 8.5: DCTIDT sample with notch elastic model simulation results	133
Figure 8.6: DCTIDT sample with notch elastic simulation results	133
Figure 8.7: DCTIDT sample with notch elastic simulation results	134
Figure 8.8: DCTIDT sample without notch elastic model simulation results	134
Figure 8.9: DCTIDT sample without notch elastic simulation results	135
Figure 8.10: DCTIDT sample without notch elastic simulation results	135
Figure 8.11: Verification of FE model.....	137
Figure 8.12: SCB stress state for a load of 1kN	138
Figure 8.13: SCB stress state for a load of 2kN	138
Figure 8.14: SCB stress state – plot of principal stress.....	138
Figure 8.15: Stress distribution along several horizontal trajectories in SCB specimen	140
Figure 8.16: Potential SCB profiles for displacement measurements	141

Figure 8.17: Variation of transversal stresses along the thickness of the measurement strip.....	141
Figure 8.18: Variation of vertical stresses along the thickness of the measurement strip	142
Figure 8.19: Generalized Maxwell Model (GMM)	142
Figure 8.20: Variation of transversal stresses in time.....	143
Figure 8.21: Variation of vertical stresses in time	144
Figure 8.22: Segments selected for displacement measurements	144
Figure 8.23: Validation of SCB creep model.....	147
Figure 8.24: 3D model representations of 3-point bending and notched semi-circular beams ..	147
Figure 8.25: Schematization of 3-point bending beam.....	148
Figure 8.26: Calibration of the 3-point bending beam FE model	149
Figure 8.27: IDT and SCB experimental testing setup	150
Figure 8.28: Results from numerical simulation.....	151
Figure 8.29: Results from experimental testing.....	152
Figure 9.1: Bending beam rheometer with beam of asphalt mixture.....	154
Figure 9.2: IDT and BBR test specimens	154
Figure 9.3: Gradation curves for granite and limestone aggregate.....	155
Figure 9.4: 1x, 2x, and 3x asphalt mixture beam specimens	156
Figure 9.5: Test results for PG 58-34 mixtures.....	158
Figure 9.6: Semi-empirical model proposed by Christensen et al. (5)	161
Figure 9.7: Maxwell Model (a) and Kelvin-Voigt Model (b).....	162
Figure 9.8: Huet Model.....	163
Figure 9.9: Huet-Sayegh Model (29).....	165
Figure 9.10: 2S2P1D Model	165
Figure 9.11: Binder to mixture transformation scheme	167
Figure 9.12: Huet Model for PG 58-34 M2 binder and granite mixture, T=-24°C.....	169
Figure 9.13: Huet Model for PG 58-34 M2 binder and limestone mixture, T=-24°C	170
Figure 9.14: τ relationship for PG-34 binders and corresponding mixtures.....	171
Figure 9.15: τ relationship for PG-28 binders and corresponding mixtures.....	171
Figure 9.16: Hirsch Model predictions for PG 58-34 M2 mixture, T=-24°C	173
Figure 9.17: Hirsch Model predictions for PG 58-28 U2 mixtures, T=-18°C	174
Figure 9.18: Hirsch Model predictions for PG 64-34 M2 mixture, T=-24°C	174
Figure 9.19: Hirsch Model predictions for PG 64-28 M1 mixtures, T=-18°C	174
Figure 9.20: ENTPE transformation for PG 58-34 M2 mixtures, T=-24°C	175
Figure 9.21: ENTPE transformation for PG 58-28 U2 mixtures, T=-18°C	175

Figure 9.22: ENTPE transformation for PG 64-34 M2 mixture, T=-24°C	176
Figure 9.23: ENTPE transformation for PG 64-28 M1 mixtures, T=-18°C	176
Figure 9.24: Simplified mixture function for granite mixture	177
Figure 9.25: Simplified mixture function for limestone mixture.....	178
Figure 9.26: Predicted (Hirsch) binder creep stiffness for PG 58-34 M2 mixtures, T=-24°C....	178
Figure 9.27: Predicted (Hirsch) binder creep stiffness for PG 58-28 U2 mixtures, T=-18°C	178
Figure 9.28: Predicted (Hirsch) binder creep stiffness for PG 64-34 M2 mixtures, T=-24°C....	179
Figure 9.29: Predicted (Hirsch) binder creep stiffness for PG 64-28 M1 mixtures, T=-18°C....	179
Figure 9.30: ENTPE transformation for PG 58-34 M2 mixtures, T=-24°C	180
Figure 9.31: ENTPE transformation for PG 58-28 U2 mixtures, T=-18°C	180
Figure 9.32: ENTPE transformation for PG 64-34 M2 mixtures, T=-24°C	180
Figure 9.33: ENTPE transformation for PG 64-28 M1 mixtures, T=-18°C	181
Figure 9.34: Predicting S(60)RTFOT corresponding to S(60)PAV = 300MPa	182
Figure 9.35: Predicted mixture S(60s) at PAV binder critical temperature.....	184
Figure 9.36: TE-BBR pro device	185
Figure 9.37: BBR (a) and DTT (b) strength tests	186
Figure 9.38: Cooling medium effect on BBR stress strain curves for binder PG64-22	189
Figure 10.1: SENB test schematic	191
Figure 10.2: Adhesion problems observed in current SENB geometry.....	192
Figure 10.3: SENB specimen mold	193
Figure 10.4: Stress distribution for (a) proposed and (b) current SENB geometry from finite element simulations	194
Figure 10.5: SENB system.....	194
Figure 10.6: Temperature (X in °C) vs. deflection at maximum load curve (Y in mm) (9).....	195
Figure 10.7: Modified SENB mold system with alignment pins.....	196
Figure 10.8: Results of SENB replicates after procedure improvement.....	196
Figure 10.9: SENB Gf and KIC plotted against BBR m-value at different temperatures (hatched line show Superpave BBR criteria limit; green arrow shows side passing this criterion).....	197
Figure 10.10: SENB Gf and KIC plotted against BBR creep stiffness at different temperatures (hatched line show Superpave BBR criteria limit; green arrow shows side passing this criterion)	198
Figure 10.11: Glass transition temperature plotted against the BBR-SENB fracture energy and fracture deformation at -12°C	199
Figure 10.12: Tg plotted against BBR parameters at -12°C	199
Figure 10.13: ABCD critical cracking temperature plotted against TFT and Tg	200

Figure 10.14: ABCD critical cracking temperature plotted against SENB fracture load and deformation	200
Figure 10.15: ABCD critical cracking temperature plotted against BBR parameters	200
Figure 10.16: (a) Slope of P-u curve before and after isothermal conditioning at T _g (b) schematic of general trend observed after conditioning	201
Figure 10.17: Normalized SENB parameters (a) G _f , (b) K _{IC} , and (c) slope of P-u curve, after 0.5 and 72hrs of conditioning	202
Figure 10.18: Difference in performance as measured by the SENB G _f for binders of the same PG, tested at (a) -12°C, and (b) -24°C	203
Figure 10.19: Brittle-ductile transition behavior using SENB parameters (a) fracture deflection, (b) fracture energy, and (c) fracture toughness	204
Figure 10.20: Comparison of SENB fracture deflection with BBR stiffness of modified and unmodified binders tested at -12, -18 and -24°C (orange line indicates BBR S(60) limit criteria and green line shows SENB deflection of 0.35mm).....	205
Figure 10.21: (a) Exponential curve fitting to fracture deflection at three test temperatures to use for calculation of TFT, and (b) the glass transition temperature (°C) plotted against the TFT (°C) parameter from the SENB.....	206
Figure 10.22: (a) Exponential curve fitting to fracture energy at three test temperatures to use for calculation of TFT, and (b) the glass transition temperature (°C) plotted against the TFT (°C) parameter from the SENB.....	206
Figure 10.23: (a) SENB and SCB G _f compared (b) SENB and SCB K _{IC} compared	207
Figure 10.24: G _f vs. normalized number of transverse cracks at -12°C and -24°C	209
Figure 10.25: Comparison of SENB load-deflection curves for LTPP binders. Lower performance index shows better performance [Labels: LTPP code (performance index)] summary of findings	209
Figure 11.1: Flowchart of stand-alone low temperature cracking model, called ILLI-TC.....	212
Figure 11.2: Locations in the library of pavement temperature profiles available to the user ...	215
Figure 11.3: Finite element model from input file generator (a) model geometry and boundary conditions (domain size: 0.18 m by 6 m, four asphalt layers) (b) close-up of the mesh in vicinity of potential crack path.....	217
Figure 11.4: Verification of preanalyzer (a) comparison of stresses obtained with the preanalyzer (VE1D) and the analytical solution (b) thermal loading.....	219
Figure 11.5: Results from preanalyzer (a) surface temperatures for five-year analysis period (b) resulting surface stresses where four critical events were identified.....	219
Figure 11.6: Comparisons for thermo-viscoelastic analysis conducted using recursive-incremental viscoelastic finite element formulations and commercial software ABAQUS (from Dave et al., 2010)	223

Figure 11.7: Bi-linear cohesive zone model	224
Figure 11.8: Finite element (FE) engine results of the cohesive zone model with recursive incremental viscoelastic finite element formulations. Temperature linearly decreases from 0°C to -10°C during 600 sec.....	224
Figure 11.9: Pavement surface temperature using default climatic files in ILLI-TC for MnROAD site (in the category of moderate climate within the state of Minnesota).....	226
Figure 11.10: Thermal stress on pavement surface for MnROAD03 from pre-analyzer (red line indicated 80% of IDT tensile strength).....	227
Figure 11.11: Thermal stress on pavement surface for MnROAD19 from pre-analyzer (red line indicated 80% of IDT tensile strength).....	227
Figure 11.12: Thermal stress on pavement surface for MnROAD33 from pre-analyzer (red line indicated 80% of IDT tensile strength).....	227
Figure 11.13: Thermal stress on pavement surface for MnROAD34 from pre-analyzer (red line indicated 80% of IDT tensile strength).....	228
Figure 11.14: Thermal stress built-up along longitudinal direction for MnROAD19 (tensile strength = 4.22 MPa, surface temperature = -23.3°C)	229
Figure 11.15: Partial depth softening damage for MnROAD19 (tensile strength = 4.22 MPa, surface temperature = -24.3°C).....	229
Figure 11.16: Partial crack for MnROAD19 (tensile strength = 4.22 MPa, surface temperature = -25.4°C)	230
Figure 11.17: Fully-formed crack for MnROAD19 (tensile strength = 4.22 MPa, surface temperature = -29.6°C).....	230
Figure 12.1: Dilatometric system used to measure glass transition temperature (T _g) of asphalt binders.....	237
Figure 12.2: Typical results from glass transition temperature (T _g) test of asphalt binders	238
Figure 12.3: (a) Illustration of the Asphalt Thermal Cracking Analyzer (ATCA) system; (b) restrained beam setup, (c) unrestrained beam setup, and (d) restrained beam after failure.....	239
Figure 12.4: (a) Typical T _g result for asphalt mixtures, (b) typical result of the stress buildup	239
Figure 12.5: (a) Cutting of SGC sample for thermal cycling testing of mixtures in ATCA (b) sample gluing setup.....	240
Figure 12.6: ATCA results and calculated relaxation modulus curve.....	241
Figure 12.7: Glass transition temperature of binders and mixtures	242
Figure 12.8: Change in glass transition temperature of base binder FH PG 64-22 with volume fraction (ϕ) for different fillers (LS2-limestone, DS2-dolomite, GS2-granite) (24)	243
Figure 12.9: Change in glass transition temperature with volume fraction, PG 64-22 mixed with granite filler at (ϕ)=0, 10, 40% (24).....	243

Figure 12.10: Stress buildup vs. temperature for full thermal cycle (a) Experimental, and (b) modeled.....	244
Figure 12.11: Thermal strain in MnROAD Cell 20 in the cooling cycles	244
Figure 12.12: Thermal strain for MnROAD Cell 20 sample during one cooling and heating cycle	245
Figure 12.13: Thermal strain in asphalt mixture beam (WI) in 3 consecutive cycles	245
Figure 12.14: Stress buildup curves under thermal cycling for MnROAD Cell 20	246
Figure 12.15: Stress buildup curves under thermal cycling and isothermal conditioning for MnROAD Cell 33	247
Figure 12.16: Stress buildup in restrained MnROAD Cell 33 beam using the ATCA, with and without the isothermal conditioning step.....	248
Figure 12.17: Thermal stress in asphalt mixtures after 5 and 10hrs of isothermal conditioning	249
Figure 12.18: Comparison of thermal stress and strain during cooling and isothermal conditions at 0.1 and 1°C/min cooling rates.....	250
Figure 12.19: ATCA restrained beam fracture during isothermal conditions (MN County Road 112-Valero).....	251
Figure 12.20: ATCA restrained beam fracture under isothermal conditions (MN County Road 112-CITGO).....	252
Figure 12.21: Comparison of physical hardening susceptibility of two asphalt binders of identical Superpave performance grades. The field section using mixture of source “A” cracked two times more than mixture of source “B”	252
Figure 12.22: Composite under temperature shrinkage in x-direction (Case 1).....	254
Figure 12.23: Composite under temperature shrinkage in x-direction (Case 2).....	254
Figure 12.24: 2D asphalt mixture model showing the boundary conditions	256
Figure 12.25: (a) Random structure (b) first structure (c) second structure	257
Figure 12.26: CTE versus temperature	257
Figure 12.27: Gradation of mixtures for FEM.....	258
Figure 12.28: Binary representation of asphalt mixtures (a) lowest number of contact zones (b) highest number of contact zones.....	259
Figure 12.29: CTE of three different mastics	260
Figure 12.30: Stiffness of three different mastics	260
Figure 12.31: CTE vs. number of contact zones/points for mixtures with Mastic 1	261
Figure 12.32: CTE vs. number of contact zones/points for mixtures with Mastic 2	261
Figure 12.33: CTE vs. number of contact zones/points for mixtures with Mastic 3	262
Figure 12.34: α_l from FEM vs. prediction using proposed model.....	263
Figure 12.35: α_g from FEM vs. prediction using proposed model.....	264

Figure 12.36: Comparison of αl from FE simulations and using proposed model.....	264
Figure 12.37: Comparison of αg from FE simulations and using proposed model.....	265
Figure 12.38: 3-D representation of the physical hardening model for a glass transition temperature of -20°C	268
Figure 12.39: (a) Isothermal strain rate in asphalt mixture beam plotted against conditioning time, and (b) strain in the same asphalt mixture beam plotted against specimen temperature...	269
Figure 12.40: Concept of incremental stress buildup and relaxation in viscoelastic material....	269
Figure 12.41: Thermal stress calculation with and without using time-dependent strain and accounting for physical hardening (PH) as a function of time (a), and temperature (b)	270
Figure 12.42: Calculated and measured thermal stress buildup plotted against time and temperature at cooling rates of $0.1^{\circ}\text{C}/\text{min}$ (a, b) and $1^{\circ}\text{C}/\text{min}$ (c, d).....	271
Figure 12.43: Sensitivity analysis of calculated mixture stress buildup with and without accounting for physical hardening, by changing (a) T_g , (b) R , (c) αl , and (d) αg	273
Figure 12.44: Variation of thermal stress at -20°C , by changing thermal parameters by $\pm 20\%$ (X_{\pm} shown in the chart indicates that parameter X has been changed by $\pm 20\%$)	274
Figure 12.45: Comparison of effect of different assumptions for CTE on (a) thermal stress curves, and (b) stress at -30°C normalized to stress at when both αl and αg are considered	274
Figure 12.46: Sensitivity analysis of calculated mixture stress reduction during heating with and without accounting for physical hardening, by changing (a) T_g , (b) R , (c) αl , and (d) αg	275
Figure 13.1: Final validation: SCB fracture energy.....	285
Figure 13.2: Final validation: DC(T) fracture energy.....	285
Figure 13.3: Final validation: SCB fracture toughness.....	286
Figure 13.4: Ranking of mixtures tested at PGLT+ 10°C	287
Figure 13.5: Ranking of mixtures tested at PGLT	288
Figure 13.6: Example of SCB test data.....	289
Figure 13.7: Example of linear extrapolation to obtain DC(T) G_f at PGLT+ 10°C (MIF_RAP_12.5mm).....	291
Figure 13.8: Preanalyzer results for WRI1-1 section (MIF_RAP_12.5mm).....	292
Figure 13.9: Preanalyzer results for WRI1-2 section (MIF_12.5mm).....	292
Figure 13.10: Preanalyzer results for WRI1-3 section (Marathon_12.5mm)	292
Figure 13.11: Preanalyzer results for WRI1-4 section (Valero_12.5mm).....	293
Figure 13.12: Preanalyzer results for WRI1-5 section (Citgo_12.5mm).....	293
Figure 13.13: Thermal stresses at the end of the critical event for WRI1-4 section (Valero 12.5mm)	294
Figure 13.14: RTFOT binder S(60s) and m(60s) results from BBR creep testing.....	296
Figure 13.15: Results of S(60s) and S(500s) from IDT mixture creep testing	297

Figure 13.16: Semi-empirical model proposed by (<i>Christensen et al., 2003</i>).....	297
Figure 13.17: Huet Model (Huet, 1963)	298
Figure 13.18: Hirsch Model predictions for Citgo mixtures.....	300
Figure 13.19: Hirsch Model predictions for Marathon mixtures	301
Figure 13.20: Hirsch Model predictions for MIF 12.5mm mixtures	301
Figure 13.21: Hirsch Model predictions for MIF 19.0mm mixtures	301
Figure 13.22: Hirsch Model predictions for Valero mixtures.....	302
Figure 13.23: Huet Model predictions for binders Citgo (PG 58-28) and Marathon (PG 58-28)	303
Figure 13.24: Huet Model predictions for binders MIF (PG 58-28) and Valero (PG 58-28).....	303
Figure 13.25: ENTPE transformation predictions for Citgo mixtures.....	304
Figure 13.26: ENTPE transformation predictions for Marathon mixtures	304
Figure 13.27: ENTPE transformation predictions for MIF 12.5mm mixtures	304
Figure 13.28: ENTPE transformation predictions for MIF 19.0mm mixtures	305
Figure 13.29: ENTPE transformation predictions for Valero mixtures.....	305

Executive Summary

Good fracture properties of asphalt materials are critical for building long lasting asphalt pavements in cold climates. Currently, there is no agreement with respect to what experimental methods and analyses to use to investigate the fracture resistance of asphalt materials and the fracture performance of asphalt pavements. The work performed in this research effort builds upon the findings and recommendations of the previous research effort in phase I. The main thrust is the development of test methods and specification criteria for selecting fracture resistant asphalt mixtures and binders at low temperatures.

First, a literature review is performed, as detailed in Chapter 2 of the report, which includes research in asphalt materials characterization, experimental results analysis and modeling, pavement system analysis and modeling, and pavement performance related to low temperature behavior of asphalt pavements.

In Chapter 3 a set of asphalt mixtures prepared with Recycled Asphalt Pavement (RAP), Poly-Phosphoric Acid (PPA), and with SBS, and Elvaloy polymers, are evaluated using Indirect Tensile (IDT), Semi-Circular Bend (SCB), and Disc-Shaped Compact Tension (DCT) tests. Field specimens cored from MnROAD test cells are also tested and compared to the laboratory asphalt mixtures. The experimental results were analyzed using a range of statistical tools. In Chapter 4, research is performed to understand how physical hardening is affected by parameters such as temperature, conditioning time, modification, thermal history, and glass transition temperature, and a comprehensive model in which the physical hardening of asphalt binders can be predicted is proposed.

At the beginning of Chapter 6, a thermal cracking specification for asphalt mixtures is proposed based on DC(T) procedure. In later chapters, an alternative specification, based on SCB fracture energy, is also proposed. Then, testing procedures to obtain mixture creep compliance from DC(T) and SCB testing configurations are proposed and validated. In addition, a method to obtain mixture creep compliance from BBR tests on thin mixture beams and extrapolation from binder data are presented. The feasibility of developing a stiffness limiting value for asphalt mixture creep, equivalent to the current binder creep stiffness criterion, is discussed. Summaries of two research efforts to develop new test methods for asphalt binder fracture and strength properties at low temperatures are also presented.

In Chapter 11, the development of a new thermal cracking model, called "ILLI-TC," is detailed. ILLI-TC improves the manner in which fracture is handled in the simulation scheme, compared to the TCMODEL currently used. The cohesive zone approach considers both material strength and fracture energy in computing crack initiation and propagation using fundamental fracture mechanics principles. This model represents a significant step forward in accurately quantifying the cracking mechanism in pavements.

Chapter 12 contains a comprehensive experimental and modeling investigation on the contraction and expansion of asphalt mixtures due to thermal cycles. A model is developed for thermal stress analysis during cooling/heating cycles using different cooling rates and isothermal conditioning periods. The model accounts for the asphalt mixture glass transition and physical

hardening, and it can be used to investigate which thermo-volumetric parameters significantly affect the asphalt mixture response during cooling and heating cycles. This work provides the foundation to developing cracking resistant mixtures under multiple cycles of temperature.

In Chapter 13, the proposed DC(T) specification is validated using eleven mixtures used in pavement sections constructed in Olmsted County (Minnesota) during the 2006 construction season. It is found that the proposed method and the new thermal cracking program do a reasonable job predicting the initial field performance data available at the conclusion of the project. Validation of the method to predict mixture creep stiffness from binder experimental data is also performed in this chapter.

Chapter 14 summarizes the work and the findings of this comprehensive research effort and provides recommendations for future work.

Chapter 1. Introduction

Background

Low temperature cracking represents the dominant distress in asphalt pavements built in cold climates. In phase I, a comprehensive research effort was performed, using both traditional and new experimental protocols and analyses, on a statistically designed set of laboratory prepared specimens and on field samples from pavements with well documented performance. At the end of phase I, four major conclusions were drawn:

1. Field performance correlates best with fracture parameters for both asphalt mixtures and binders. While the current properties such as creep and strength are needed for stress calculations and pavement design, the selection of fracture resistant binders and mixtures should be based on simple fracture tests.
2. The PG specification for asphalt binders provides a good start; however, other factors such as aggregate type, air voids, and in particular the addition of recycled materials affect fracture resistance. Therefore, asphalt mixture specification criteria similar to the current PG system for binders need to be developed
3. At low temperature, asphalt mixtures are complex viscoelastic composite materials that are significantly temperature and loading rate dependent. Any new specification should be based on test results at multiple temperatures and loading rates similar to the rates experienced by real pavements.
4. The selection of materials with good fracture properties significantly improves pavement performance. However, it is critical to understand the role of all components of the pavement system. Therefore, the pavement mechanics models developed in phase I need to be further refined.

Objectives and Research Approach

The work in phase II builds upon the findings and recommendations of phase I. Each of the four main recommendations are addressed, however, the main thrust is the development of test methods and specification criteria that will allow the selection of fracture resistant asphalt mixtures and binders at low temperatures. In order to accomplish these objectives, the following major tasks are pursued in phase II:

- Expand the work performed in Phase I with additional field samples that include new materials compared to the previous study, such as warm mix asphalt, polyphosphoric acid, reclaimed asphalt pavement
- Investigate physical hardening effects for modified asphalt binders
- Develop and recommend a fracture testing method for asphalt mixtures at low temperatures and, based on it, develop a specification for selecting asphalt mixtures with good fracture resistance
- Investigate and propose other potential test methods that can be used to determine low temperature properties of asphalt binders and mixtures
- Develop an improved TC model that uses fracture mechanics properties obtained with the new test methods

- Model asphalt mixture behavior during expansion and contraction temperature cycles to address the issue of thermal fatigue at low temperatures.
- Develop a final report and provide a new computer program.

The research performed in each task of the phase II of the low temperature pooled fund study is presented in detail in the next chapters.

Chapter 2. Literature Review

Introduction

This literature review summarizes the research done in the area of low temperature cracking in the last three years (2006-2009). The purpose was to identify new developments in terms of test procedures, material selection, and data analysis that can be used in the follow up research effort part of Phase II. For each review, the main ideas of the research performed are briefly described and the benefits of the new reference to the current project and what was learned from it are presented. To better match the review with the various tasks of the current project, the summaries were divided into different sections.

Experimental Methods and Analyses

In this section, research efforts focused on laboratory experimental methods for both asphalt binders and mixtures are presented. Presently, thermal cracking specifications are based on strength and creep tests performed on asphalt binders and asphalt mixtures. For asphalt binders the Bending Beam Rheometer test (1) and the Direct Tension test (2) are used to determine the performance grade (3) based on tests performed on PAV binders (4). For asphalt mixtures, the Indirect Tension Tester (IDT) is used to perform creep and strength tests on cylindrical specimens loaded in compression along the diameter (5). A critical cracking temperature can be obtained at the intersection of the tensile strength-temperature master curve and the thermal stress-temperature master curve. This approach is also used in the TCMODEL subroutine of the new Mechanistic Empirical Pavement Design Guide (MEPDG) (6).

Binder and Mastic Testing

In the US, the PG system has been used for more than a decade to select and characterize asphalt binders. In Europe, only recently certain tests were adopted to specify asphalt binders or bitumens. For example Hase and Oelkers (7) used the BBR to investigate the influence of polymer type on low temperature properties. Twelve binders were tested according to DIN EN 14771 (8) at three different temperatures: -10°C , -16°C and -25°C . The results indicated, as expected, that the type of modification can influence both the stiffness and the relaxation properties of binders at low temperature, and that using the BBR can provide useful information for selecting an appropriate polymer modifier.

Khedoe et al. (9) conducted an investigation in which a stiff binder (C-fix) with a penetration of 9 at 25°C was compared to a conventional 70/100 pen grade bitumen. Direct Tension (DTT), which is not part of the European specifications, was used to perform tests on the two binders as well as mastic samples prepared with these binders. Tensile strength and strain at failure, as well as relaxation properties of the different materials, were determined. The results indicated that C-fix binder and mastics relaxed significantly less than the 70/100 binder and mastic. Additional experiments indicated that increasing the quantity of filler in the binder made the mastic stiffer and less relaxing; however, it increased stiffness and toughness. Two useful conclusions were drawn from this research: it is possible to use DTT to investigate the relaxation

properties of asphalt binders and mastics; the addition of filler has both negative (less relaxation) and positive (increased strength and toughness) effects on binder low temperature properties.

In Canada, Yee et.al (10) developed an extended Bending Beam Rheometer test (BBR) protocol to take into account the effect of storage time on low temperature properties based on the “reversible aging” theory first introduced by Struik (11) and later applied to binders by Bahia(12) during SHRP research effort. Based on extensive experimental work, it was found that the double logarithmic shift rate μ , given by equation 2.1, is constant for a vast range of conditioning and loading times, with only minor deviations at short loading times and high stiffness.

$$\mu = \frac{-d(\log a)}{d(\log t_e)} \quad [2.1]$$

Where:

a = shift factor used to overlap creep compliance curves,

t_e = time for the sample is equilibrated at cold temperature.

This finding can be used to reasonably predict the creep stiffness and m -value without performing time consuming experiments. Although pavements cool over periods of weeks, obtaining long-term creep data as part of a binder grading protocol is not practical. For each binder, eight BBR beams were prepared, and were divided between two conditioning baths, which were set at -24°C ($T+10$) and -14°C ($T+20$). The samples were labeled $B1, B2, B1, B2, C1, C2, D1, \text{ and } D2$. After 1 hour of conditioning at -24°C , samples A were tested at -24°C and Samples B were tested at -14°C . Samples B were conditioned at -14°C for 10 minutes before the data were collected. The average creep stiffness and m -values obtained after 60 seconds of loading were used to determine continuous grade temperatures at which $S = 300$ MPa or $m = 0.3$, for a conditioning time of 1 hour at -24°C . The same procedure was repeated for Samples C and D after 1 hour of conditioning at -14°C , but now Samples D were conditioned for 10 minutes before testing at -24°C . Immediately after testing, all samples were returned to their respective storage baths to be tested again after 1, 3, and 7 days of conditioning. (The 7-day conditioning period is not required in the MTO LS-308 test method but was considered useful in this particular investigation). From this study it can be concluded that the extended BBR protocol can be used effectively to identify better performing binders. In some instances, this approach may lead to a more economical solution than lowering the grade requirement, which requires more expensive polymer modified binders.

Due to its simplicity and repeatability, it is not surprising that the BBR procedure was targeted as a candidate test for specifying other types of asphalt based materials. A prime example is the work performed by Al-Qadi et al. (13), who developed a modified BBR test called Crack Sealant Bending Beam Rheometer test (CSBBR) to investigate the behavior of crack sealant at low temperature. Based on previous work performed by Zanzotto (14) and Zofka et al. (15), the authors proposed a modification of the machine and of the specimen size (thickness was doubled to reduce mid span deflection due to the soft characteristic of sealants). Good repeatability was obtained by preparing a homogenized sample. In their study, the authors used nine sealants (BB the softest, QQ the stiffest) that were expected to perform in a temperature range from -4 to -40°C . The sealant was also placed into a vacuum-pressure oven for 16 hours at 115°C to age. For

the CSBBR a load of $980 \pm 10 \text{ mN}$ was applied for 240 seconds, followed by a seating load of $35 \pm 10 \text{ mN}$ for 480 seconds. To identify nonlinear effects, additional creep test were performed using 250, 490 and 980mN load levels. The results showed that the stiffness was independent of the applied stress level and that nonlinear effects were not present (see Figure 2.1). Further verification of the validity of the superposition principle in loading and unloading cycles was obtained using FEM simulations.

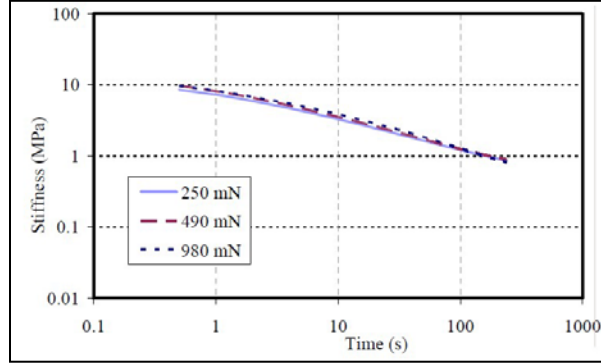


Figure 2.1: Creep stiffness measurement for sealant NN (13)

The authors also investigated the ability of the sealants to dissipate energy and maintain flexibility for a longer period time. The measured stiffness at 240 seconds was used to estimate stiffness after 5 hours of loading (5 hours is considered to be a proper time to dissipate the internal stresses due to relaxation phenomena) using the time temperature superposition principle. Three different temperatures were used to test stiff sealants ($-40, -34, -28^\circ\text{C}$) and three for the soft ones ($-16, -10, -4^\circ\text{C}$). The calculations indicated that after 5 hours, the materials “relaxed” 70-80% of the stiffness measured at 240 seconds.

In the analysis, the authors used a two-term Prony series model for creep compliance:

$$D(t) = \frac{1}{E_0} + \frac{1}{E_1} (1 - e^{-t/\tau_1}) + \frac{1}{E_2} (1 - e^{-t/\tau_2}) \quad [2.2]$$

Where:

$D(t)$ = the tensile creep compliance at time t ,

E_i = material constants,

τ_i = retardation time.

The Prony series parameters were used to calculate the dissipated and stored energy for each sealant.

$$W_{stored} = \sigma_0^2 \left[\frac{1}{2E_0} + \frac{1}{2E_1} (1 - 2e^{-(t/\tau_1)} + e^{-(2t/\tau_1)}) + \frac{1}{2E_2} (1 - 2e^{-(t/\tau_2)} + e^{-(2t/\tau_2)}) \right]$$

$$W_{dissipated} = \sigma_0^2 \left[\frac{1}{2E_1} (1 - e^{-(2t/\tau_1)}) + \frac{1}{2E_2} (1 - e^{-(2t/\tau_2)}) \right]$$
[2.3]

Where:

W = is energy per volume,

t = maximum loading time (240s),

σ_0 = stress in the outer fiber in the mid span.

The energy dissipation ratio is calculated by the following expression:

$$ER = W_{dissipated} / W_{stored}$$
[2.4]

In this study, the aging effect on sealant was also investigated. The results showed that aged sealant became stiffer, and the stiffness increment depends on the chemical compositions. Moreover in checking constitutive modeling of crack sealant behavior, the model developed by Elseifi (16) was used where the crack sealants behave as a viscoelastic material. The stiffness $E(t)$ of a linearly viscoelastic material was expressed as a normalized Prony series as:

$$\frac{E(t)}{E_0} = 1 - \sum_{i=1}^K \zeta_i (1 - e^{-t/\tau_i})$$
[2.5]

Where:

E_0 = initial modulus

ζ_i = normalized parameter defined as the ratio between relaxation strength and E_0

τ_i = relaxation time.

In addition to the experimental investigation a finite element model was used to validate the sealant constitutive model. The deflection at the mid-span of the beam obtained from the FE model was compared to the experimental results showing that the Prony series satisfactorily simulates the results of bituminous crack sealant deformation for 240 seconds and 480 seconds of loading and unloading, respectively, at low temperatures.

Mixture Testing

Research performed at the University of Minnesota indicated that the Bending Beam Rheometer (BBR) could also be used to test thin asphalt mixture beams to obtain reliable measurements of creep compliance (15). However, small size specimens that contain a limited volume of material may not be representative of larger size specimens and real pavement conditions. Velásquez et al. (17) investigated this critical aspect by performing three point bending creep tests on beams

of different sizes. A total of 10 laboratory mixtures were tested. Low temperature three point bending creep tests were performed on specimens with three different sizes: 6.25×12.5×100 mm (1x), 12.5×25×200 mm (2x), and 18.75×37.5×300 mm (3x) (Figure 2.2). The temperature effect on the representative volume element was studied by performing bending creep tests at three temperatures: high temperature (HT) level (PG low limit +22°C), intermediate temperature (IT) level (PG low limit + 10°C), and low temperature (LT) level (PG low limit -2°C).



Figure 2.2: 1x, 2x, and 3x asphalt mixture beam specimens. (17)

Statistical analyses were performed in order to evaluate the influence of various parameters like the size of the specimen, PG of the binder, aggregate type, loading time and temperature on the creep stiffness of asphalt mixtures. It was found that as the temperatures decreases, the mismatch between the stiffness of aggregates and of the binder (mastic) diminishes and the creep stiffness of asphalt mixture becomes less dependent on the size and distribution of aggregate particles. The effect of the beam size on the creep stiffness was negligible at intermediate temperature. At high temperature, the difference between the stiffness of the aggregates and the asphalt binder (mastic) started to increase and the mechanical response of the mixture became dependent on the size of the aggregates. At the lowest test temperature, other factors, such as the difficulty of measuring very small deflection and the formation of layers of ice on the supports and around the extensometers, influenced the results and made the comparison difficult.

The current Indirect Tension Tester (IDT) (5) was used by Apeageyi et.al (18) to investigate the cracking resistance of antioxidant modified asphalt (AOX) mixtures; a common cause of increased asphalt stiffness is the oxidative hardening that occurs during asphalt mixture production and service life. Asphalt mixtures prepared with one AOX-modified asphalt binder, one un-modified asphalt binder, and typical limestone aggregates from Illinois quarries were prepared in the laboratory. Two levels of mixture aging at 135°C were considered: short-term oven aging (STOA) of loose mix in a forced-draft oven for two hours and long-term oven aging (LTOA) for eight hours. E* tests were performed at -10°C, 4°C, and 20°C using frequency sweeps of 0.01 Hz, 0.1 Hz, 0.5 Hz, 1 Hz, 5 Hz, 10 Hz, and 25Hz in the indirect tension mode using procedures recommended by Kim et al.(19). Standard AASHTO creep compliance tests were performed at temperatures of -20°C, -10°C and 0°C, and indirect tensile strength tests were performed after creep testing -10°C using the standard loading rate of 12.5 mm/min. Two models, Voight-Kelvin and a power-law model were fit to the creep compliance data to obtain the master curve for each mixture. Creep compliance decreased with increasing levels of aging and this effect was less pronounced in the antioxidant modified mixtures. It could be seen that

aging resulted in a slight increase in tensile strength for both the modified and unmodified mixtures. The average tensile strength was higher in the modified mixtures in comparison with the unmodified. The study concluded that there is benefit to using antioxidant modifiers with respect to low temperature properties.

Katicha and Flintsch (19) used IDT testing and analyses to show that a linear elastic approach is not adequate to account for possible differences between tensile and compressive HMA properties. The stress distribution in a bimodular IDT specimen was investigated based on the Ambartsumyan model, (21), (22) for different compressive to tensile modulus ratios. The distribution was obtained through an iterative procedure since, in the constitutive equations of the Ambartsumyan material, the stress-strain constitutive relationship is a function of the principal stresses values and directions. The analysis showed that: as the compressive to tensile modulus increases, the tensile stresses throughout the specimen decrease; as the compressive to tensile modulus increases, the compressive stresses near the vertical diameter (loading diameter) increase; as the compressive to tensile modulus increases the compressive stresses away from the vertical diameter decrease.

Other authors (23) used IDT test data and Displacement Discontinuity Method (DDM) to predict asphalt mixtures fracture energy density in a Bending Beam Test. Voronoi tessellation theory and 2-D simulation method were also used. The experimental tests were performed at 10°C on nine Bending Beam test specimens (three replicates for each mixture) The strain value at failure were estimated at the point of first fracture and the fracture energy densities were computed as the resulting area under the stress-strain curve up to the fracture point. The simulation showed there is a considerable damage prior to reaching the peak of the stress-strain curves in all the tests and that prior to peak load the first fracture takes place. The results showed that DDM is able to characterize the fracture behavior of asphalt concrete at low temperature and provides acceptable predictions of fracture energy density.

Although the Thermal Stress Restraint Specimen Test (TSRST) is not part of the current AASHTO specifications, many researchers, in particular in Europe, have used it to study low temperature cracking of asphalt pavements. Sauzéat et.al (23) analyzed thermo-mechanical effects, in particular the characterization of cracking and propagation of cracks at low temperature, based on results from TSRST and direct tension tests performed on mixture specimens instrumented with Acoustic Emission sensors. The loading system had a capacity of 50kN both in traction and compression, and allowed for a minimal speed of 6.4×10^{-6} mm/min. Three non-contact transducers located on two rings in the central part of the specimen were used to measure displacements. The initial distance between these rings was 9 cm for a 12 cm high specimen. The device for measuring the Acoustic Emission used three piezoelectric sensors with a contact surface of 15 mm diameter and a bandwidth range from 50 to 200 kHz. Using the measured wave parameters, the energy could be estimated in two ways: the envelop energy, computed from the area of the signal (mV. μ s), and the true energy calculated from the integral of the square signal (10^{-18} J). The localization of the micro-cracks, which creates the acoustic emission, was performed by specific software. The TSRST was started at 5°C and at a cooling rate of 10°C/h. Some issues related to failure location prompted the authors to use specimen thinned in the central region. However, preparing such specimens may result in specimen damage before tests were conducted. Uniaxial tension tests (UTT) were also performed at different temperatures using a strain rate equal to 300×10^{-6} /h. From the TSRST test, it was

shown that the thinned specimen yielded almost the same results as the cylindrical shape. The direct tension test showed that at low temperatures the mixtures tested were brittle, while at high temperatures they were ductile, with no clear transition phase. The stress-strain behavior was significantly affected by strain rate at high temperatures; at low temperature, the strain rate effect was not significant, suggesting that the behavior under very small strain rates, similar to those observed in pavements under low temperature, can be predicted from tests performed at higher strain rates.

Uniaxial tension test were also performed by Khedoe et al.(9). Three types of tests were performed on Porous Asphalt Concrete (PAC) gyratory compacted mixtures specimens: relaxation in displacement-controlled tests, relaxation in temperature controlled tests, and tensile strength tests. The research team concluded that adding filler to the C-fix binder material has both a stiffening effect as well as toughening effect, which matches the Direct Tension Test results on binders and mastics and that mastic behavior appears to be the driving force in terms of relaxation properties.

Hase and Oelkers (25) used uniaxial tension test, performed on prismatic asphalt mixture specimens, to investigate the influence of polymer modified bitumen (PMB) on life cycle analysis at low temperature. Stone mastic asphalt 0/8S (SMA) and binder course asphalt 0/16S (BCA) were evaluated at low temperatures based on uniaxial tension tests and cooling tests (Figure 2.3) using a standardized testing procedures (26). The parameters investigated from the uniaxial tension test were the maximum stress (tensile strength) $\beta_t(T)$ and the corresponding tensile failure strain $\varepsilon_{failure}(T)$ at the test temperature T. From the cooling test, the progression of the “cryogenic” stress over the temperature $\sigma_{cry}(T)$ and the failure stress $\sigma_{cry, failure}$ at the failure temperature $T_{failure}$ were obtained. Figure 2.3 shows the results of uniaxial tension tests in terms of tensile strength reserve. The tensile strength reserve was computed as the difference between the tensile strength and the cryogenic stress at the same temperature T:

$$\Delta\beta_t(T) = \beta_t(T) - \sigma_{cry}(t) \quad [2.6]$$

From further statistical analyses and taking into consideration traffic effects, it was shown that cryogenic tensile stress is an important factor in the predicted pavement life and cannot be disregarded.

It should be mentioned that the UTT test, similar to TSRST, is not widely used due to specimen alignment problems in direct tension tests in general. A small deviation from vertical alignment of the sample leads to uneven stress distribution in the specimen and to bending effect that can affect the reliability of the results.

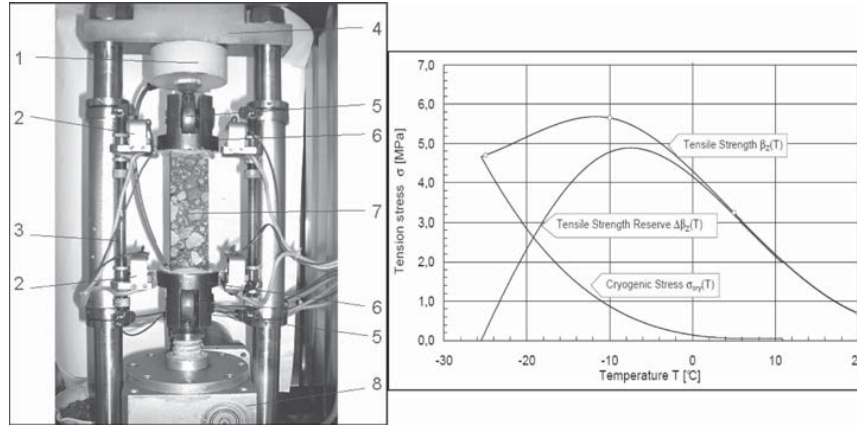


Figure 2.3: a) Uniaxial tension test device, b) Tensile strength reserve plot. (25)

Koh et al. (27) proposed an alternative type of test to determine the asphalt mixture properties. This test method, according to the authors, can reduce the disadvantages of IDT and UTT tests, and allows direct tension testing of gyratory compacted specimens or field cores of various types of mixtures (dense-graded, open-graded) of different thicknesses (thin or thick). The Dog-Bone Direct Tension test (DBDT) also has the advantage of having the failure plane known a priori, which allows measuring failure limits directly on the failure plane. Because of the specimen geometry, stress concentrations near the ends of specimen are less critical, and the location where failure is likely to occur is maximized. The DBDT specimens can be produced by simply coring opposing sides from slices or disks obtained from cylindrical laboratory samples or field cores. To optimize the specimen geometry, two-dimensional finite element analysis was conducted and, based on predicted stress distributions for two-inch wide specimens, a coring radius of 75.9 mm and a coring overlap of 50.8 mm were selected. The DBDT system is composed of several pieces, including a specimen coring jig, a dual cylinder tensile load equalizer, specimen loading heads, strain gage sensors and attachment kits, and a PC controlled servo-hydraulic load frame with an integrally mounted environmental chamber (Figure 2.4).



Figure 2.4: Dog-bone direct tension test prototype (27)

Finite element analysis was used to develop correction factors to accurately determine stress and strain based on simple equations from extensometers measurements obtained on the faces and edges of the DBDT specimens. The accuracy of the DBDT was verified with a Delrin specimen

of known modulus. Tests on Open Graded Friction Course (OGFC) mixtures have shown promising results and the authors concluded that the effect of open graded friction course on top-down cracking performance may be evaluated based on tensile properties obtained from the DBDT procedure.

Fracture Test Methods

The test methods previously presented do not allow using fracture mechanics concepts since the test specimens are considered homogeneous with no crack present and therefore, no possibility to monitor crack propagation with loading. This type of analysis requires testing notched specimens and controlling the load based on crack growth to obtain post peak behavior related to crack propagation.

The Single Edge Notched Beam SE(B) Test (Figure 2.5) is the most documented method to determine fracture properties based on linear elastic fracture mechanics (LEFM) conditions (28).

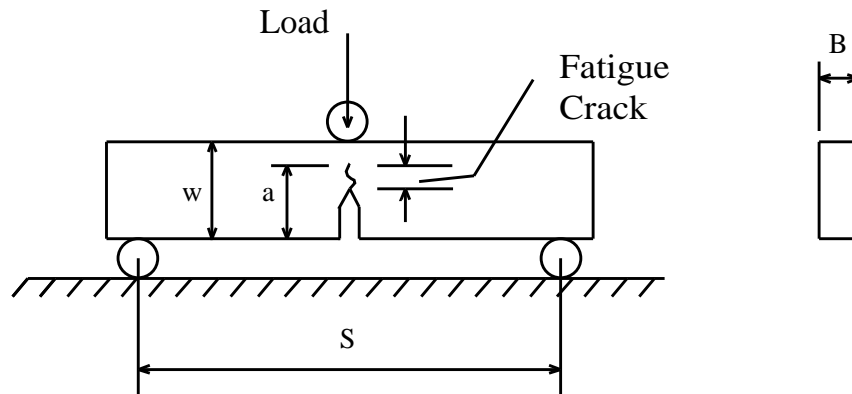


Figure 2.5: Single edge notched beam test (28)

Portillo and Cebon (29) used a three-point bending test for bitumen and idealized asphalt mix specimens to study the fracture behavior over a wide range of temperatures and loading rates, in order to develop a failure mechanism map to characterize the response of these materials similar to the failure mechanism pattern for bitumen films previously reported by Harvey and Cebon (30). The idealized mixture consisted of pure bitumen and 64% volume fraction of sub spherical sand particles between 150 and 300 μm in size. The experimental data was used to calculate key fracture parameters, such as stress intensity factor K_{IC} , fracture energy G_{IC} , and J-Integral J_{IC} . A 3-point bending fixture was designed to carry out fracture tests on pure bitumen and bituminous mixtures, see Figure 2.6.

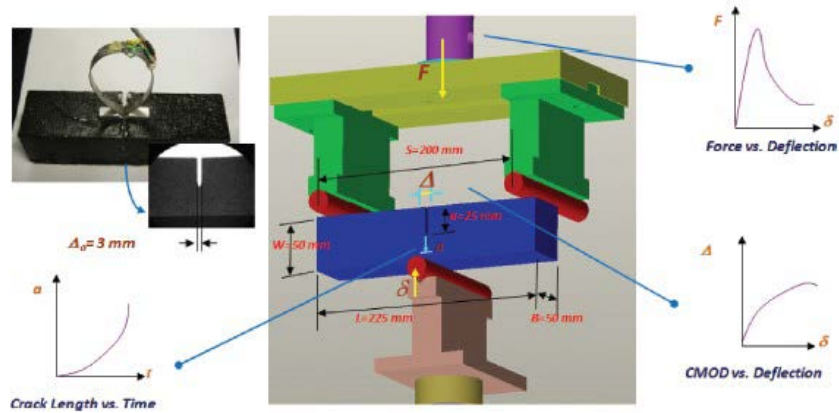


Figure 2.6: 3-Point bend experimental setup (29)

All tests were conducted under constant axial displacement rate control and a spring steel chip gauge was used to measure the crack mouth opening displacement. Crack length analysis was conducted using an optical system. The system comprised of an analog video camera located outside the environmental chamber which photographed the test specimen through a window. A flashing LED light signal was used to synchronize the time signals recorded on the video and the servo-hydraulic testing machine.

Fracture 3-point bending tests on pure bitumen specimens were conducted at temperatures ranging from -30°C to 0°C ; the values of stress intensity factor K_{IC} , fracture energy G_{IC} showed to be similar to the results of Genin and Cebon (31) (Figure 2.7).

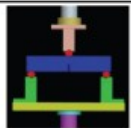
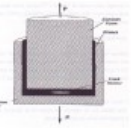
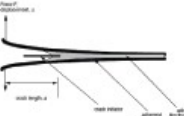
Author	Test	Test Temperature	K_{IC} (MPa m ^{1/2})	G_{IC} (J/m ²)
<i>Portillo and Cebon</i>	3Point Bend SE(B) 	-20 °C	0.01 - 0.04	2 - 13
		-30 °C	0.06 - 0.1	5 - 11
<i>Genin and Cebon (2000)</i>	Plug Pull-Out 	-20 °C	0.02 - 0.05	
<i>Harvey and Cebon (2005)</i>	DCB 	-30 °C		5 - 10

Figure 2.7: Comparison table (29)

Temperature-compensated crack mouth opening strain rate \dot{E}_T was defined to compare experimental results from tests at different temperatures and load rates as:

$$\dot{E}_T = \frac{\dot{\Delta}}{\Delta_0} \exp\left[\frac{-Q}{R} \left(\frac{1}{T_0} - \frac{1}{T_1}\right)\right] \quad [2.7]$$

Where:

$\dot{\Delta}$ = the crack mouth opening displacement rate,

Δ_0 = the initial notch width,

Q = the thermal activation energy,

R = the universal gas constant,

T_0, T_1 = the reference temperature and test temperatures, respectively.

Similar results to the fracture mechanism map of Harvey and Cebon (32) were found: in the brittle region, the fracture energy is significantly lower than in the ductile region, indicating that the energy needed to initiate fracture is less at lower temperatures and high displacement rates. Idealized asphalt mixtures were tested on 3-point bending configuration over a temperature range from -30°C to 30°C . K_{IC} and fracture energy G_{IC} increased with an increase in temperature; this indicates that less potential fracture energy is needed for crack propagation at lower temperatures. Failure mechanism maps showed ductile, brittle and transition failure regimes; moreover in the brittle regime when temperature decreased from -10°C to -30°C J-integral decreases showing that at lower temperatures resistance to crack growth is lower.

The beam geometry limits the use of SE(B) method on asphalt mixture gyratory specimens and field cores. An alternative geometry is used in the Disk Compact Tension DC(T) test, which was extensively investigated in the first phase of the current project.

The size effect on fracture property of asphalt concrete was investigated by Wagoner and Buttlar (31) using the Disk Shaped compact tension test DC(T), the size effect law (SEL) proposed by Bazant (34) and the boundary effect model. Testing was conducted with a single temperature of -10°C . Two sensitivity sets of test were performed: in the first four different diameters (100, 150, 300, 450 mm) with a constant 50 mm thickness were tested and in the second five thicknesses (from 25 to 150mm) and two diameters (150 and 300 mm) were selected. The crack mouth opening displacement was used as control parameter. CMOD was scaled accordingly to the specimen dimension.

Experimental and statistical results showed that diameter influenced the fracture energy and as it increases also the fracture energy increases. Also the specimen thickness affects the fracture energy especially in the range of 25-50 mm. As the thickness increased an increase in the fracture energy was experienced (Figure 2.8). It was concluded that fracture properties are affected by specimen size and this effect should be taken into account in modeling the pavement.

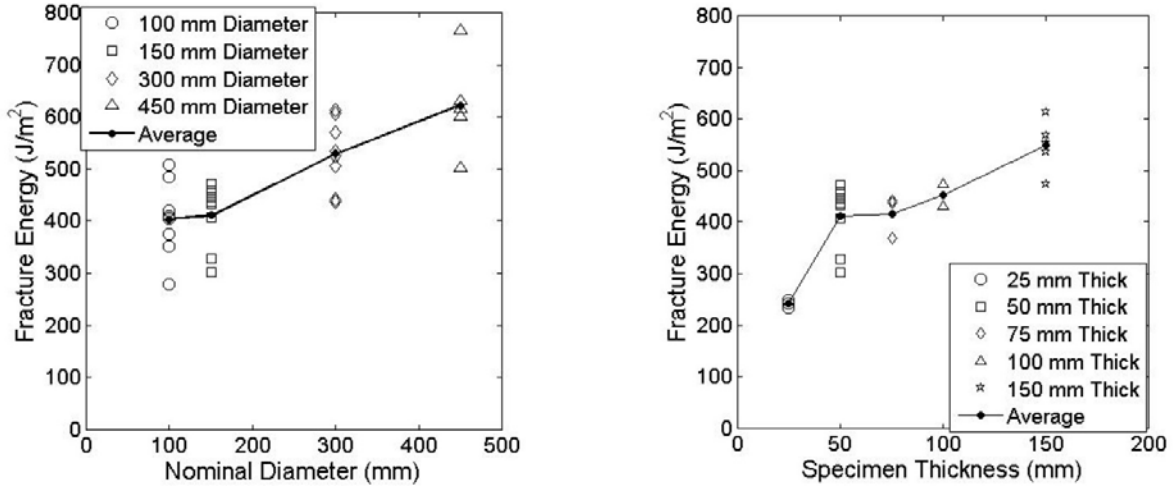


Figure 2.8: Variation of fracture energy with diameter and thickness (31)

In the size effect law analysis it was found that the selected size ranges were adequate to investigate the size effect. On the other hand the computed specific fracture energy, $G_f = 87.5 \text{ J/m}^2$ is only a portion of the total fracture energy; however it is able to capture the initial portion of the load displacement curve that is independent of the specimen size. The fracture process zone FPZ was estimated as 42.8mm and this value is in agreement with the 40mm length obtained in a previous study of Marasteanu et al. (35).

The size effect on fracturing of asphalt concrete based on DC(T) test was also investigated by Kim et al. (36) using Discrete Element Method (DEM). Cohesive softening model was employed to analyze asphalt fracture behaviors and DC(T) fracture tests were conducted for different sizes of asphalt concrete varying from 100 mm to 450 mm diameter. The different size specimens were modeled and simulated using homogeneous DEM fracture models with bulk viscoelastic properties. The experimental and numerical specimen size dependency of asphalt concrete was compared with the size effect law, which was proposed by Bazant (34). The size effect law may be expressed as:

$$\sigma_n = \frac{Bf_t}{\sqrt{1 + \beta}} \quad [2.8]$$

Where:

σ_n = nominal strength;

f_t = tensile strength;

β = brittleness number equal to d/d_0 ;

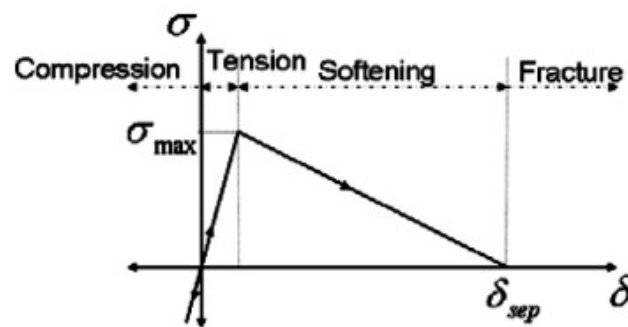
d = depth of the beam;

B and d_0 = empirical constants.

It was found that the bulk viscoelastic DEM fracture model with the same material properties could predict the size effect on the nominal strength of asphalt concrete based on two sets of material properties. By comparing elastic and viscoelastic homogeneous DEM fracture models, it

was shown that viscoelastic properties of asphalt concrete play an important role on the fracture behavior as the specimen size becomes larger. Heterogeneous fracture model for different specimen size was also implemented and applied for the investigation of size effects; however the calibration procedure of material parameters was necessary based on experimental test data. The global fracture responses obtained from the heterogeneous DEM models were matched well with experimental fracture behaviors in the force versus CMOD curves and a 3-D fracture analysis investigation was recommended.

In a previous study, Kim et.al (37) investigated the effects of material microstructure on fracture mechanics and the rate dependency of asphalt concrete using a cohesive zone model with bulk viscoelastic properties combined with bi-linear post-peak softening (Figure 2.9). Other aspects like material heterogeneity have been taken into account and a Discrete Element Method (DEM) model was implemented.



(c) Bilinear Cohesive Fracture Model

Figure 2.9: Bilinear cohesive fracture model (37)

Two types of tests were performed on asphalt concrete mixture with PG 64-22. The fracture energy was obtained from DC(T) tests and viscoelastic properties were obtained from IDT tests. The creep compliance was measured at three temperatures (-20, -10 and 0°C). The indirect tension test was also used to measure the tensile strength at the intermediate temperature. The relaxation model parameters were used in the DEM fracture model. The elastic DEM fracture model simulation resulted in an over-prediction of the pre-peak load-CMOD behavior and under-predicts the global softening tail while viscoelastic DEM model was in better agreement with experimental results, even if the softening tail resulted in a slightly under-prediction. Different loading rates was also investigated in the case of the viscoelastic model showing that loading rate affects the softening tail and peak load as well as the initial slope of the global load-time curve. Overall the DEM fracture model seemed to be able to represent the rate-dependency of the asphalt mixture tested in the DCT: mixtures tested at higher loading rates showed more brittle behavior while post-peak softening behavior at lower loading rates was more evident. The shape of the predicted softening curve was improved including heterogeneity into the DEM model even though only the elastic simulation was performed. Micro-cracks, crack tortuosity, and bridging were better simulated by the heterogeneous microstructure underlining the importance of heterogeneity compared to the material viscoelasticity at the low temperatures.

Note that, in the case of the Boundary effect model, the energy consumed by the FPZ is considered as a material constant. Boundary limit can prevent the FPZ to fully develop. Hu and

Wittmann (38) proposed a fracture process zone (FPZ) formed of an inner region W_{sf} and an outer region W_f (Figure 2.10).

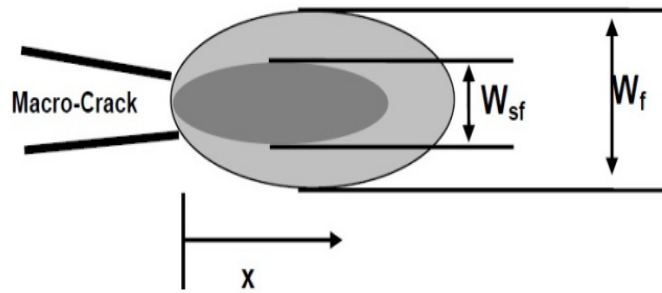


Figure 2.10: Fracture process zone according to Hu and Wittmann (31)

The size dependent fracture energy is then expressed as:

$$G_f = \frac{1}{W-a} \int_0^{W-a} g_f(x) dx \quad [2.9]$$

Where:

$W-a$ = initial ligament length

g_f = local fracture energy

G_f = size dependent fracture energy

A bilinear assumption is adopted by the boundary effect model for the variation of the local fracture energy as the crack approaches the boundary of the specimen. The total fracture energy should increase until a critical specimen size is reached. Beyond that threshold the fracture energy becomes a constant since the FPZ is no more influenced by the specimen boundary. The results obtained by the authors showed that the model fit was acceptable and a size independent fracture energy of $G_f = 605 \text{ J/m}^2$ with $a_l/W = 0.45$ was obtained.

Another simpler alternative to SE(B) is the Semi Circular Bend SCB test originally proposed by Chong and Kuruppu (39); this test was also investigated extensively in the first phase of the current project. Recently, Van Rooijen and de Bondt (40) used a draft procedure developed in the Netherlands, which was based on Paris' law, to study the crack propagation during cyclic SCB tests performed at relatively low temperature on one type of asphalt mixture prepared with five different binders. The proposed procedure is also based on Paris' law:

$$\frac{dc}{dN} = A \cdot K_I^n \quad [2.10]$$

Where:

c = length of crack [mm];

K_I = stress intensity factor [$\text{MPa} \times \text{mm}^{0.5}$];

N = number of load cycles;

A, n = material parameters determined from the experimental results.

The test method consists of four steps. In the first step, the maximum load F_{\max} , the maximum load at failure F_{failure} , and the fracture strength K_{IC} , are predicted from a monotonic Semi-Circular Bending (SCB) test for each specimen. The crack opening displacement amplitude (COD) is then defined as the difference between maximum and minimum displacement during one load cycle. The crack length calculation is performed during the second step of the procedure based on finite element analysis. In the third part of this method the calculation of stress intensity factor, K_I , and stress level (σ_{SCB}) is carried out. Finally the material parameters A and n are determined.

Monotonic SCB test and cyclic SCB test were carried out on an asphalt binder/base course with a maximum nominal aggregate size of 11.2mm and 5.2% bitumen (of the total mixture) prepared with two types of standard penetration grade bitumen (i.e. Pen 40/60 and Pen 160/220) and three types of polymer modified binder (PMB). The load at failure obtained from the monotonic SCB test was used to determine the maximum load, F_{\max} , for the cyclic SCB test. Tensile properties of the binders such as yield strain, strain at failure, and the deformation energy to failure, were determined with the force-ductility test (EN 13589 (41) and EN 13703 (42)). After the test the following relationship between n and $\log(A)$ was obtained:

$$\log(A) = -1.4397 \cdot n - 2.5273 \quad [2.11]$$

From the calculation of the stress intensity factor K_{IC} , the authors concluded that the duration of the crack propagation phase was relatively short for all binders, which is in disagreement with field experience that suggests that the effect of healing and creep should be taken into account.

An alternative tensile test, called Fenix, was developed by Perez et al.(43). The authors objective was to develop a procedure with a low cost set up to determine crack resistance through calculation of dissipated energy that would eliminate the difficulties associated with SE(B) specimen preparation and SCB loading head compression testing issues. Fenix test is a traction test applied to a half cylindrical sample with a 6 mm depth notch, placed in the middle of the flat side of the specimen (Figure 2.11). The sample is fabricated with a gyratory-compactor and/or Marshall device. Two steel plates are fixed on the flat side separated by the notch. Steel plates are attached to the loading platen, allowing plates to rotate around fixed points once test has begun. Test is carried out under controlled displacement conditions. Displacement velocity is established at 1 mm/min. Temperature is chosen according to the environmental conditions that have to be reproduced.

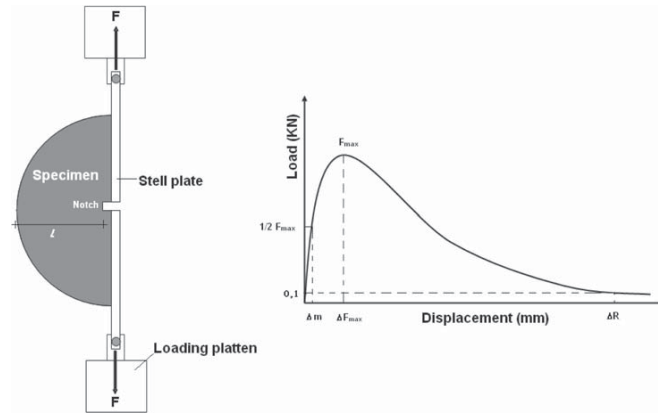


Figure 2.11: Fenix test and typical load vs. displacement output curve. (43)

The test calibration, obtained by sensitivity analysis, showed that Fenix test can be used over a wide range of test temperatures. It was found that it was possible to obtain and analyze mixture behavior in the post peak (softening) region.

Low Temperature Cracking Models

The experimental results and the analyses performed on the experimental results, obtained using the test methods previously described, provide the critical parameters required to develop models of the cracking phenomenon that can be incorporated in pavement performance prediction models.

Zbrowski and Kaloush (44) evaluated the capability of the TCMODEL in characterizing thermal cracking resistance of asphalt rubber mixture. Since this model doesn't properly estimate the asphalt rubber behavior, they developed a new method based on fracture energy parameter rather than on tensile strength at -10°C of the material and slope of creep compliance. Comparison of a traditional mixture and a gap graded asphalt rubber mixture showed that the latter mix behaves better than the traditional (Figure 2.12):

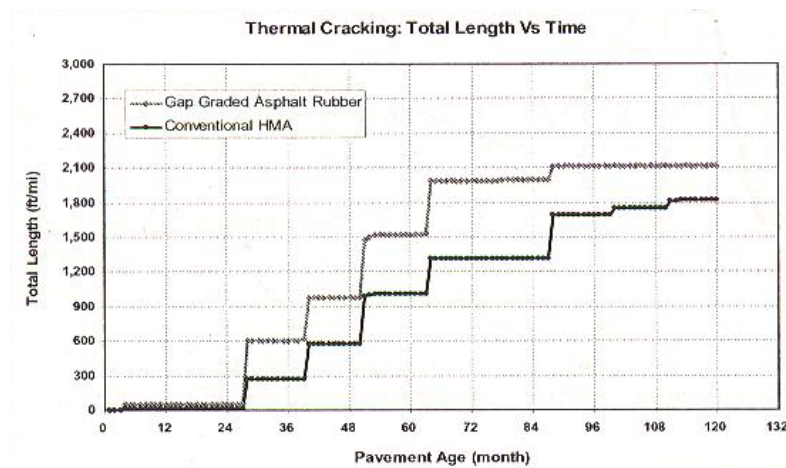


Figure 2.12: Thermal cracking prediction using MEPDG (44)

From fracture energy tests it was found that the asphalt rubber mixture had a two times higher fracture energy compared to a traditional mixture. A new method to calculate the crack propagation based on the total fracture energy, the creep compliance, D_1 , in combination with the tensile strength maximum limit and the slope of creep compliance was developed based on the Superpave TCMODEL. The experimental part was based on eighteen conventional and twenty-one asphalt rubber mixtures. Based on the test results, thermal cracking prediction equations were obtained. The following modified creep compliance prediction equation was proposed:

$$\log(D_1^*) = 0.145 \cdot (-8.5246 + 0.0104T + 0.7956 \log(V_a) + 2.0093 \log(VFA) - 1.92231 \log(A_{RTFO})) \quad [2.12]$$

Where:

D_1^* (1/kPa) and m^* = the fracture coefficients obtained from the creep compliance of the mixture;

T = Test temperature (°C);

V_a = Air Voids (%);

VFA = Void filled with asphalt (%);

Pen_{25} = Penetration (0.1 mm) at 25°C;

A_{RTFO} = Intercept of binder Viscosity – Temperature relationship for the RTFO condition.

An additional variable was included, the rubber percentage, to take into account the modification due to a crumb rubber and the following fracture energy expression was proposed:

$$\begin{aligned} \Gamma_{fr} = & 0.1129792 * (4497.832 - 439.057 * AC + 46.284 * AC^2 - 2057.821 * AV \\ & + 40.009 * AV^2 + 12612 * \log(V_{beff}) + 13571.050 * \log(VMA) - 345.948 * VFA \quad [2.13] \\ & + 8.056 * Pen_{25} - 0.052 * Pen_{25}^2 + 1.044 * AC * Rubber(\%) \end{aligned}$$

Where:

Γ_{fr} = fracture energy (see Figure 2.13):

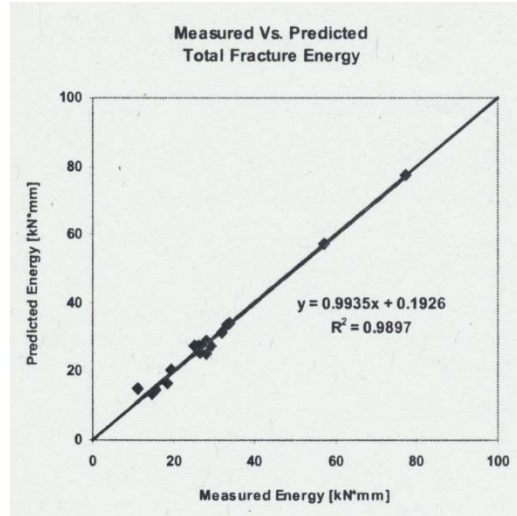


Figure 2.13: Measured versus predicted total fracture energy (44)

Based on previous research performed at University of Florida (45, 46), Kim et.al (45) developed an analytical model to evaluate the effect of thermal loading and mixture properties on cracking and dissipated creep strain energy (DCSE). TCMODEL and Prony series were used for the representation of the Creep compliance and irreversible creep strain. Knowing the thermal stress and the dissipated creep strain, the dissipated creep energy may be computed at each increment of time, Δt . On the other hand, $DCSE_f$ varies with temperature. Since DCSE is related to $DCSE_f$, the energy transfer can be obtained from a transformation of DCSE at a given temperature into DCSE at a reference temperature. Finally, the accumulated DCSE at any given time, t , is expressed by the following equation:

$$DSCE(t) = \sum DSCE(\Delta t) \quad [2.14]$$

The model used was represented by a thin plane with a central crack 10 mm length and a process zone of 5 mm. Four steps were implemented to compute the HMA thermal fracture: first the process zones are defined; second the thermal stresses are predicted; then the mean stresses in each process zone is calculated, and finally DCSE is evaluated. The following method is based on time increments and a 100 mm crack length was used as limit to stop the computation. The master curve and the energy transfer were obtained by setting the reference temperature as the lowest temperature (0°C).

A series of experimental tests, performed on a total of 99 specimens from eleven sections in Florida, were used to evaluate the model with a constant mixture thermal coefficient 2.0×10^{-5} 1/C. The model expresses the amount of cracks in function of time increments: a longer cracking time of mixture implies a good resistance to thermal damage.

Top-down cracking is not only related to the thermal cracking; the traffic load plays a fundamental role in the induced damage. The cracked and uncracked pavements were discriminated by the single failure time named Minimum Time Requirement (MTR) obtained from field data. This parameter was used to define the Modified Energy Ratio (MER) in such a way that it can take into account traffic load and thermal effects. The MER was expressed as:

$$\text{Modify Energy Ratio (MER)} = \text{IFT/MTR} \quad [2.15]$$

Where:

IFT = Integrated Failure Time;

MTR = Minimum Time Requirement.

Good correlation between observed field performance and predicted top-down cracking was obtained.

Based on the IDT and E* results described in the previous section, Apeageyi et al. (18) used TCMODEL to predict transverse cracking, expressed as length of cracks in meters per 500 meters of pavement. A theoretical pavement, approximately 300 mm (12 in.) thick, located in Minnesota, was simulated. It was determined that aging resulted in significant reduction in pavement life for all the mixtures. This analysis provided a useful quantitative measure of the benefit of antioxidant modified asphalt (AOX) in terms of thermal cracking pavement performance.

The authors also applied fracture energy concept and the method proposed by Zhang (48) to further investigate the effect of antioxidant modified asphalt (AOX) on cracking behavior. The Zhang method involves five steps in which Fracture Energy (FE) and Elastic Energy (EE) are first computed in order to obtain the Dissipated Creep strain energy threshold (DCSE_f) as the difference between FE and EE. The Dissipated Creep Strain Energy per cycle (DCSE/cycle) for load duration of 0.1 sec, the average stress σ_{AVE} , and maximum strain rate at 100 sec ϵ_{pmax} are then computed according to the following expressions:

$$\frac{DSCE}{cycle} = \int_0^{0.1} \sigma_{AVE} \sin(10\pi) \epsilon_{pmax} \sin(10\pi) dt \quad [2.16]$$

$$\frac{DSCE}{cycle} = \frac{1}{20} \sigma_{AVE}^2 D_1 m (100)^{m-1}$$

Finally, creep compliance parameter, D_1 , and the m-value are obtained during creep testing. Once the stress levels in the mixture and the DCSE/cycle are known the number of cycles required to reach the DCSE threshold at a given crack length are determined. The results showed that the number of cycles to DCSE_f varies with stress level and that aging reduces the number of cycles (N) needed to reach DCSE_f. Comparison of the number of cycles for long term oven aging (LTOA) to short term oven aging (STOA) for a single stress level of 100 psi indicated that the use of antioxidants provided benefits against thermal cracking expressed by a decreased binder stiffness at lower temperatures and increased binder stiffness at high temperatures relative to the untreated control binder.

In a different research effort, the authors (49) investigated the effect of cooling rates on accumulation of thermal stresses in asphalt pavements. The experimental part was carried out on five mixtures from the SHRP General Pavement Study (GPS). Using a generalized Maxwell model the relaxation modulus master curves were obtained at a reference temperature of -20°C and thermal stresses were computed for different cooling rates (1, 2, 3, 5, 10°C/h). Thermal

stresses were positively correlated with cooling rates up to 5°C/h; for higher values, the effect of cooling rate is less evident.

The cooling rate effects on asphalt pavement were also investigated using FEM simulations. The pavement structure of five MnROAD test cells were selected, and six cooling cycles, during which the pavement surface temperature drops from 0 to -30°C at different rates, were simulated. As expected, stress accumulation was found dependent on cooling rate, and peak tensile stresses were found at -30°C.

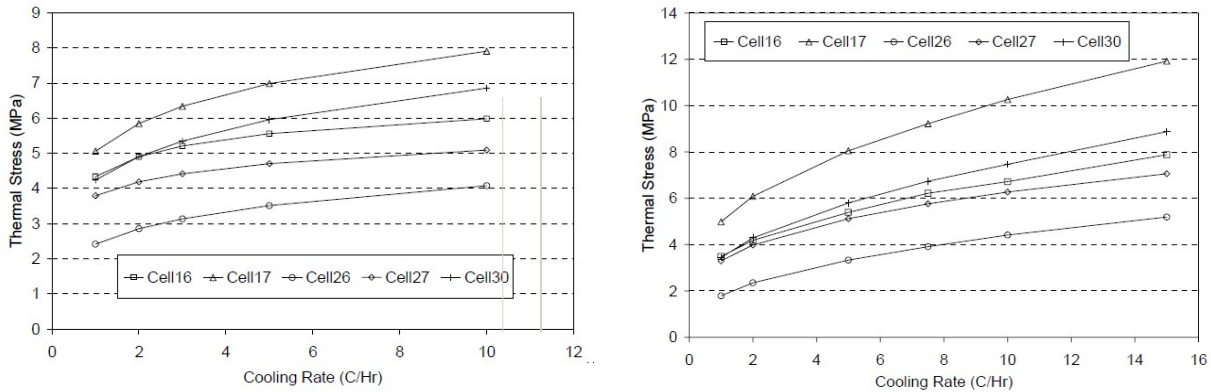


Figure 2.14: Comparison between analytical and FEM solution (at -30°C) (49)

The TCMODEL was used to obtain pavement life predictions. A 45% reduction of service life was evaluated when the cooling rate increased from 2 to 3°C/h, and an additional average reduction of 32% was estimated for a cooling rate increase from 3 to 4°C/h. For the coolest single event, FE simulation and field data were in agreement, although the test sections were subjected to traffic loading and not only to thermal stresses. The model results were finally compared to AASHTO MEPDG performance predictions (50). Some differences were found between TCMODEL and FE and analytical solutions since the former is related to pavement serviceability level while FE and analytical solutions are related to the thermal stresses that develop at various cooling rates, but overall, the predictions compared well with the field performance.

Five MnROAD test cells, two from high volume traffic sections, and three from low traffic volume test loop) were used to perform an integrated laboratory study coupled with finite element simulation by Dave et.al (51). Creep compliance and the tensile stresses of each of the five specimens were obtained from Indirect Tension (IDT) while the fracture energy was measured using the Semi-Circular Bend (SC[B]), the Disk-Shaped Compact Tension (DC[T]), and the Single-Edge Notch Beam (SE[B]). Because of the different tests' configurations size effects and differences in fracture energy values were experienced. For this reason only the fracture energy obtained from the DCT was used in the numerical simulations. The FE simulation was performed in 5 steps. The FE models domain for low-temperature cracking simulations were constructed using graded meshes in order to reduce the computational requirements. Asphalt concrete was modeled using the generalized Maxwell model where model parameters were determined using the creep compliance data from laboratory testing. A cohesive zone model was adopted and the material parameters material strength (σ_t) and fracture energy (G_f) estimated through laboratory testing were input in the model. Thermal and traffic tire load

was applied, moreover a critical condition approach in which the coolest pavement temperatures reached were identified was selected for the model simulation. In general, the simulation results were found to comply with field observations.

Traffic induced stresses and temperature-related stresses were addressed by Wistuba et al. (52) in correlation with the analysis of surface-initiated longitudinal cracking in asphalt pavements. Cracking resistance is investigated both with numerical analysis tools and laboratory experimentation. The pavement was modeled as a multilayer system with an axle load acting on a circular area. The equation of energy balance and Fourier's linear heat condition law were used to obtain the pavement surface temperature and its variation in the pavement structure. The asphalt material was modeled with the power law model (linear spring and non-linear dashpot in series) while material parameters were obtained by uniaxial creep test and dynamic stiffness test. The numerical analysis provided evidence that the maximum horizontal tensile stresses are concentrated between the wheel paths and along the road axis and moreover allows seeing the separate effects of the temperature associated and traffic associated stresses. The experimental evaluation of cracking resistance was assessed by a Cyclic Tensile Stress Test (in order to simulate the traffic load). Furthermore thermal induced stress was simulated by applying a constant tensile stress to the asphalt specimen. Healing effects on the material was also addressed and then different loading conditions were selected from a real traffic spectrum and then separated in several groups. Each load groups was characterized by constant force amplitude, a specific number of load cycles and a uniform frequency. The rest period between two consecutive load pulse-groups was related to the time gaps between trucks. Based on traffic data rest periods of 3 seconds and 6 seconds were selected. The loading frequency was computed based on the time gaps between individual axles. Considering the different multiple axle configuration of HGVs, a time gap between the axles of 0.066 seconds was found and a 15Hz frequency was selected to perform laboratory testing for multiple axle configuration. For single axle configuration 5Hz frequency was adopted and four load modes were applied during testing. From the data obtained on the test it was evident that more load cycles are needed as test better approximate the real loading. Furthermore it was noted that stiffness modulus E^* decreases with increasing number of load cycles in the case of fatigue. Relaxation effects were observed in the asphalt material during the rest time: thus a healing effect was experienced even at -15°C .

International Roughness Index (IRI) was used as a discriminating parameter in the investigation of thermal cracks on pavement by Bae et al. (53). An Automated Laser Profile System (ALPS) was used to measure the thermal cracks data form 14 cells from the mainline test roadway (at the MnROAD and for each cells three randomly selected crack were superimposed to a free crack pavement profile with different initial IRI (Figure 2.15).

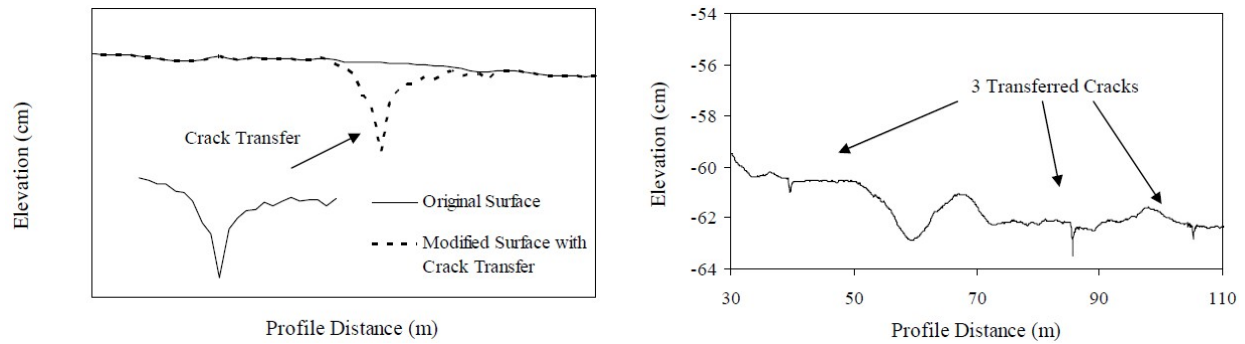


Figure 2.15: Crack-profile superposition (53)

From the computation of the final IRI it was found that the range of increment was of 0.06 to 0.2 m/km for a 1.20 m/km profile and of 0.01 to 0.1 m/km for the 4.33 m/km profile. Higher IRI profiles were found to be less sensitive to the cracks superposition compared to those with low IRI, but overall a significant IRI increment was experienced for all the profiles showing that cracks with amplitudes larger than 0.5 cm sensibly influence roughness. The IRIs for real pavement profiles with the actual number of cracks were also evaluated showing a considerable increase in the IRI value. The annual increase in vehicle operating costs due to thermal cracks was estimated at 14,000 to 97,000\$/km.

Other Relevant Studies

The Discrete Element Method (DEM), developed by Cundall and Strack (54) was used by Wu et.al (55) to simulate the monotonic compressive behavior of an idealized asphalt mixture in the elastic regime (low temperature, high strain rate). The effect of random variations in internal sample geometry, the distribution of bond strengths between adjacent particles and the coefficient of friction between particles were investigated with the use of the ITASCA software PFC-3D. A numerical sample containing 6,000 particles, 1.77mm in diameter was simulated with a particles density of 63.5% of the total volume and an average 5.8 contacts per particle. The post-peak (softening) behavior was modeled by allowing bond breakage when either normal or shear stress between contacting particles exceeds the normal or shear bond strength. Different friction coefficient, μ , ranging from 0 to 0.9 were evaluated showing that the compressive strength increases as the friction coefficient increases up to a value of 0.5 after which it remains approximately constant. In general it was found that 6,000 particles are required for reasonably accurate estimates of bulk material properties in the case of compressive strength. Moreover the random effect of particle position on predicted compressive strength is not significant in comparison to the variability in bond strength and the friction coefficient. The overall shape of the predicted stress-strain curve from the DEM approach showed a good agreement with the experimental results.

A micromechanics-based virtual testing procedure was presented and developed by Feng et al (56) to study the HMA cracking dependence on the interaction of the aggregate and asphalt binder. A lattice modeling methodology that incorporates a fracture energy based criterion is used to predict the mechanical behavior of HMA is coupled with a stand-alone virtual micro structure fabrication technique. A multi-scale modeling method that considers the effect of different aggregate sizes at different scales was used to reduce the computational cost while

capturing the mechanical phenomena at various scale length. The method was validated comparing the simulation results of uniaxial tension test to those obtained from the physical tests (Figure 2.16). An aggregate gradation four-scale approach method (1 corresponding to coarse aggregate and 4 to fine aggregate) was applied.

In the comparison between simulated and experimental data a mismatch was found for lower strain rates. These results pointed out the two important phenomena need to be carefully studied: the stiffening of the binder in thin-films due to the complex behavior of asphalt and the scale dependency of fracture energy.

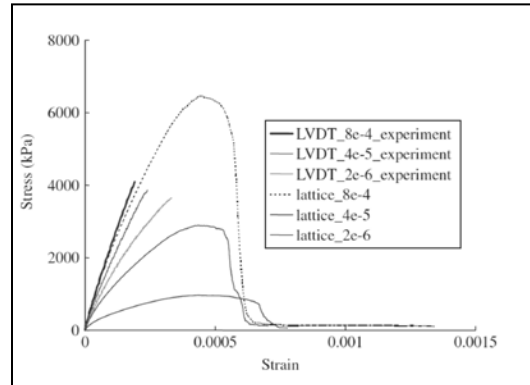


Figure 2.16: Lattice simulation vs. experimental stress - strain curves (56)

Marasteanu et al. (35, 57) used Acoustic Emission (AE) test to estimate the micro-structural phenomenon and the corresponding macroscopic behavior in the asphalt mixtures at low temperature conditions. IDT creep and strength tests were performed and different load levels were applied in the creep configuration to investigate its effect on the development of the micro damage. Three test temperatures, -12°C , -24°C , and -36°C were selected based on the PG lower limit of the asphalt binder.

An AE device with eight-channel recording systems was used to monitor the asphalt mixture specimens during creep and strength tests. The AE events were estimated for the three different temperature conditions showing very few AE events at the beginning of the test until a constant AE rate of 7 to 8 events per second is reached. Overall, before the loading level applied in the creep test was reached, more than 100 AE events were recorded.

For different loading condition and constant temperature, more events were counted during the creep test with higher load level. By using different transducers placed at various locations on the specimen the source location of the AE events was determined on the basis of the differences in time of signals arrival. Since only 143 events were located with 10 mm error for the creep test under the lower loading level at -24°C , this value was selected and a 90% confidence region for AE signals was investigated to evaluate the effect of temperature. The different shape and skewness of the region indicated that, due to its heterogeneity, asphalt mixture properties can be affected by air voids and aggregate distribution. Also the area with micro cracking inside the region (damage zone) showed a shape change with temperature in the case of strength test.

In general it was found that at higher load levels during creep test more events were recorded than at lower load levels for all test temperatures suggesting that micro damage occurs during creep phase.

Marasteanu et.al (57) also applied Acoustic emission (AE) and AE energy to the study of the FPZ (fracture process zone) under a Semi-Circular Bending test (SCB) configuration. The stress intensity factor K and the critical stress intensity factor was evaluated according to Lim et al. (59) procedure and the fracture work was evaluated as the area under the loading-deflection curve. The fracture energy, G_f , was computed by dividing the fracture work by the ligament area (ligament length \times specimen thickness) as:

$$G_f = \frac{W_f}{A_{lig}} \quad \text{and} \quad W_f = \int p du \quad [2.17]$$

Where:

W_f = fracture work;

A_{lig} = area of a ligament.

The occurrence of the AE events, the cumulative number, and the rate of occurrence, amplitude distribution, energy and frequency distribution were also evaluated. The AE energy was related to the fracture resistant of the material and to the square of the voltage of the electric signals as:

$$E_i = \int_0^{t_{ae}} V_i^2(t) dt \quad [2.18]$$

Where:

E_i = AE energy for channel i ;

V_i = recorded voltage transient for channel i ;

t_{ae} = duration of the event for channel i .

The volume affected by micro cracks accumulations was detected as the location in the specimen where more than the 95% of the total AE energy is reached before the peak load. Three specimens were tested for 8 different mixtures with two voids content (4% and 7%) at three different temperatures correlated to the binder performance grade: binder PG -2°C (-30°C), PG + 10°C (-18°C) and PG + 22°C (-6°C). The results showed that temperature has a significant effect on fracture properties: fracture energy increased and fracture toughness decreased as the test temperature increased. Moreover more AE events were detected at low temperature than at high temperature. The ANOVA statistical analysis performed to evaluate the three parameters aggregate, asphalt content and air voids showed that aggregate type is an important factor both for fracture energy and toughness and also that the FPZ is highly affected by air voids level and aggregate type, but is less sensitive to asphalt content (Figure 2.17).

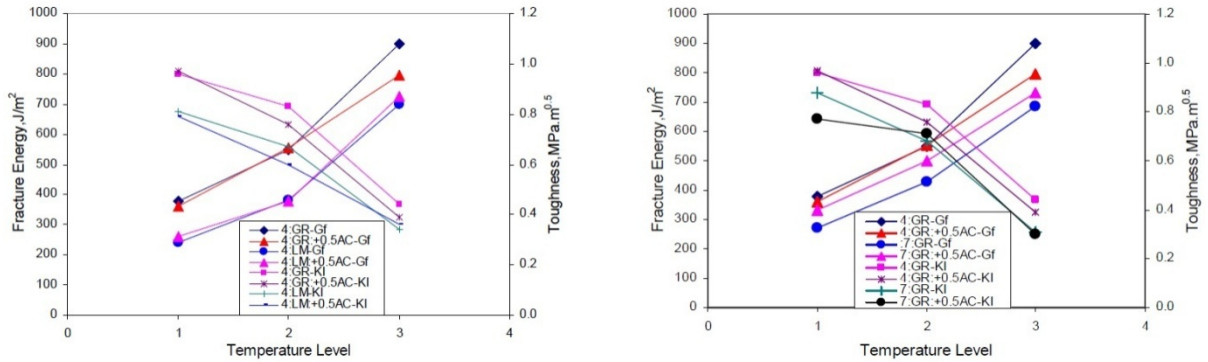


Figure 2.17: Aggregate and air voids comparison (57)

Asphalt Research Consortium

The Asphalt Research Consortium (ARC) (60) is composed by several research groups and it is coordinated by Western Research Institute with partners Texas A&M University, the University of Wisconsin-Madison, the University of Nevada Reno, and Advanced Asphalt Technologies. The research plans were grouped into seven areas, Moisture Damage, Fatigue, Engineered Paving Materials, Vehicle-Pavement Interaction, Validation, Technology Development, and Technology Transfer.

The work element E2d: Thermal Cracking Resistant Mixes for Intermountain States (in the Engineered Paving Materials area) is the part of ARC research project that is related to the topic of the Pooled Fund Study Phase II. The objective of ARC research is to develop a binder/mix evaluation and testing system that could effectively simulate the long term properties of HMA mixtures in the intermountain region and to assess the impact of such properties on the resistance of HMA mixtures to thermal cracking. More specifically the objective of the experimental work element E2d is a system that can simulate the field aging and the thermal cracking process of HMA mixtures. It comprises several sub-tasks:

- E2d-1: Identify Field Sections
- Subtask E2d-2: Identify the Causes of the Thermal Cracking
- Subtask E2d-3: Identify an Evaluation and Testing System
- Subtask E2d-4: Modeling and Validation of the Developed System
- Subtask E2d-5: Develop a Standard

During the first year of activity, the experimental plan was developed and the materials for the various experiments were identified and obtained; moreover, the field sections were selected. The criteria used for the selection of sites included the availability of hourly temperature profiles throughout the depth of the HMA layer, availability of materials properties, and availability of long-term performance data. The relationship between pavement's thermal cracking and the glass transition behavior of asphalt binders and mixtures was considered.

In order to study the glass transition of ten binders, a dilatometric system for measuring binder properties was used. From the results it was noticed that there was a variation in the glass transition behavior as function of the binder grade and modification. Moreover, it was found that

binder glass transition properties do not correlate with the glass transition temperature, T_g , of the mixtures. This fact was indication of the importance of aggregate characteristics and mixture compaction data for mixture thermo-volumetric properties. Furthermore, the contraction and dilation behavior of mixtures showed a hysteretic response.

In order to simulate the temperature gradient and strain distribution in 2.5-in by 2.5-in cross-section mix specimen during thermal cycling, a finite difference model was developed. The heat diffusion equation considered was:

$$\frac{\partial T(x, z, t)}{\partial t} = k \cdot \left(\frac{\partial^2 T(x, z, t)}{\partial x^2} + \frac{\partial^2 T(x, z, t)}{\partial z^2} \right) \quad [2.19]$$

Where:

k = thermal diffusivity;

$T(x, z, t)$ = specimen temperature as function of space and time.

Distribution of the temperature was computed for heating and cooling cycle (Figure 2.18).

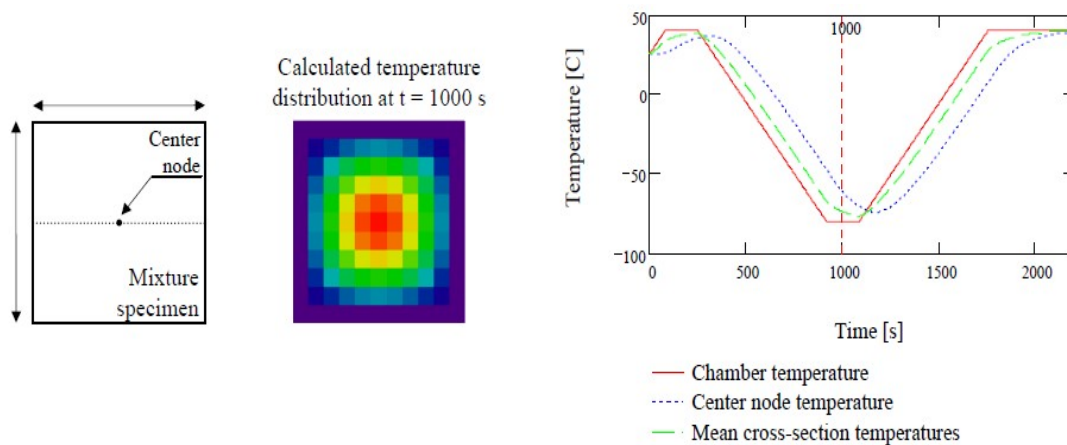


Figure 2.18: Temperature distribution (60)

It was shown that a single thermocouple could not be reliable to explain the true response of the asphalt mixture. Figure 2.19 shows the calculated thermal strain of specimen where a looping response was detected.

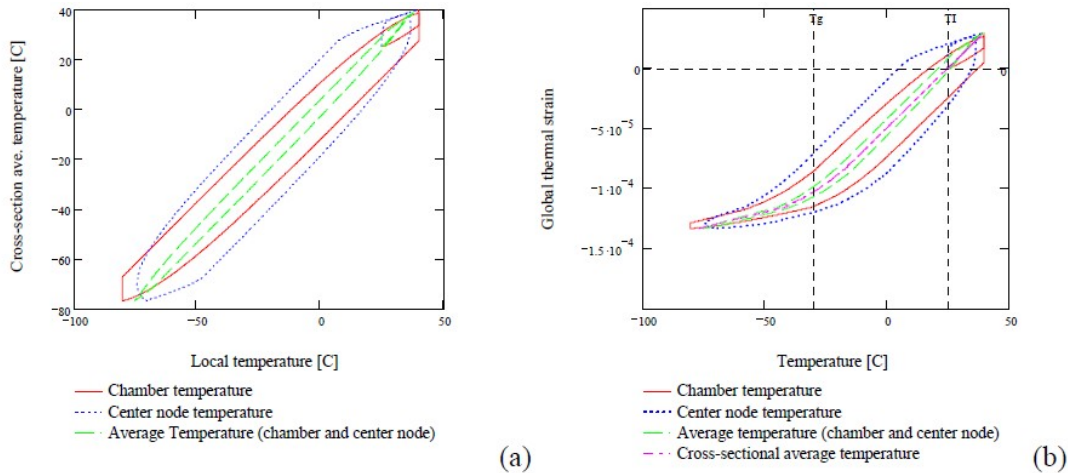


Figure 2.19: Modeled thermal temperature and strain (60)

The objectives of the second year of investigation include the analysis of the available data on the long-term aging of binders, the evaluation of the impact of aggregate properties on the aging of binders, and the development of an effective testing system for HMA.

MNROAD Reconstruction and Low Temperature Research

Most of the asphalt mixtures and binders used in this study were used in test cells built as part of MnROAD Phase II Construction, which began in 2007. A comprehensive report, documenting the construction effort was recently published (61). Apart from the current study, a few other studies were performed related to the test cells used in the present study or to low temperature behavior.

In one recent study (62), the use of Polyphosphoric acid (PPA) to improve the performance of binders was investigated. A 12.5 mm Superpave mix with 4% air voids and no RAP was used during the investigation. Two sets of cell were dedicated to this research:

- Cells 33-35, specifically dedicated to the acid study
- Cells 77-79, dedicated to a fly ash study, that have the wearing course made with PPA+Elvaloy modified binder. For these cells, the base was reclaimed up to 10" to the subgrade plane. Stabilization with fly ash was performed for cell 79. Cell 78 was selected as reference, since the same base used in cells 33-35 was applied. This allowed for a comparison between the acid study and the fly ash study.

Table 2.1 presents the volumetric data of the mixture used. It may be noticed that a larger amount of air voids is present in the PPA+Elvaloy mixture.

Table 2.1: HMA field testing data (62)

Mix type	Test	Cell 33	Cell 34	Cell 35	Cell 77	Cell 79
Loose Mix	Ig Oven AC%	5.4	5.5	5.4	5.2	5.3
	%Fine Agg Angularity	46	46		46	45
	% Coarse Agg Angularity	100/-	100/-	100/-	100/-	100/-
	Gmm	2.478	2.474	2.471	2.484	2.478
	Gmb @ N-design	2.378	2.389	2.379	2.403	2.355
	%Air Voids @ N-design	4.0	3.4	3.7	3.3	5.0
	VMA	16.4	16.2	16.5	15.6	17.2
	VFA	75.4	78.8	77.4	78.8	71.1
Field Cores	% Max Density	94.2	93.5	93.6	92.2	92.1
	% Air Voids	5.8	6.5	6.4	7.8	7.9

Field Performance

The field performance of the test sections was evaluated by means of the falling weight deflectometer, rutting measurements, and IRI evaluation. Laboratory tests were also performed both on binders and mixtures. Three testing condition were applied to binder: tank binder, RTFOT (Rolling thin film oven test) aged, and recovered from field cores (field aging). The recovered binder was also subjected to PAV aging showing in two cases a significant increasing in stiffness at low temperature. Field mixtures were used to perform APA ruts tests and Wet Hamburg tests. Dynamic modulus tests at different temperatures and frequencies were run showing a good behavior of PPA+Elvaloy mixture (Figure 2.20). The investigators concluded that almost no cracking and rutting were observed in the new cells. The laboratory tests, however, indicated that the combination of PPA + polymer will perform better than the PPA alone.

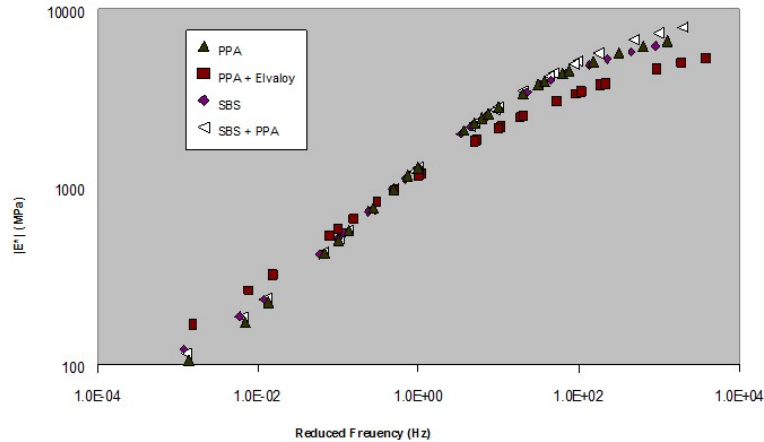


Figure 2.20: Dynamic modulus master curves (62)

In another study, very recently completed (63), low temperature testing was performed for an additional set of fourteen asphalt mixtures used in the 2008 MnROAD reconstruction project. Limited data analysis was performed in this effort since the focus was on obtaining experimental results.

Conclusion

In the past four years researchers have performed extensive research to better understand the mechanism of low temperature cracking and to develop new test procedures and better pavement models to improve asphalt pavements performance. Some of the most notable findings are:

- More and more researchers are using fracture tests to evaluate low temperature cracking resistance and to model pavement performance
- Physical hardening effects made a come-back and are considered in a new specification in Canada
- Size effects in fracture testing were experimentally evaluated and the effects are being incorporated in pavement prediction models
- New tools, such as acoustic emission, are being used to understand the crack propagation phenomenon.
- Low temperature testing of small beams of asphalt mixture and asphalt sealants has been shown to provide critical information on the low temperature properties of these materials and new specifications are being proposed.

Chapter 3. Expand Phase I Test Matrix

Introduction

In this task, the research team tested and analyzed nine asphalt mixtures used in field studies with respect to their low temperature cracking resistance. The tests consisted of Indirect Tensile (IDT) creep and strength tests, as well as Semi-Circular Bend (SCB) and Disc-Shaped Compact Tension (DCT) tests. The set of mixtures included Recycled Asphalt Pavement (RAP) mixtures, Poly-Phosphoric Acid (PPA) modified mixtures, and polymer modified mixtures (SBS, and Elvaloy). The mixtures are described in Table 3.1.

Table 3.1: Asphalt mixtures used in Task 2

Location	Construction date	Binder Grade	Asphalt modifiers	RAP
MnRoad 33	September 2007	PG 58-34	PPA	-
MnRoad 34	September 2007	PG 58-34	SBS+PPA	-
MnRoad 35	September 2007	PG 58-34	SBS	-
MnRoad 77	September 2007	PG 58-34	Elvaloy+PPA	-
MnRoad 20	August 2008	PG 58-28	-	30% Non-Fractioned
MnRoad 21	August 2008	PG 58-28	-	30% Fractioned
MnRoad 22	August 2008	PG 58-34	-	30% Fractioned
WIS Superpave E-30 WisDOT mix	2008	PG 64-22	-	-
NY Typical Mix	2008	PG 64-22	-	-

The experimental variables considered in the experimental work and analyses were test temperature, air voids content and asphalt mixture conditioning. Two test temperatures were selected based on the asphalt binder used, as follow:

- PGLT
- PGLT+ 10°C

*PGLT is the binder PG low temperature limit.

Two levels of air voids were considered in the preparation of laboratory cylinders from the loose mix collected at the job sites: 4% and 7%, which represent the design air voids and typical field compaction levels, respectively. The asphalt mixture samples with 7% air voids were also long term aged according to AASHTO R30-02. Note that for the NY's mixture, it was not possible to compact specimens to achieve 4% air voids.

In summer of 2010, cores were also obtained from the MnRoad sites described in Table 3.1, and tested following the same methods used for the loose mix laboratory prepared specimens.

Table 3.2 describes the experimental plan pursued in Task 2, and the shadowed cells indicate the data missing from the experimental layout.

Table 3.2: Laboratory experimental layout

Test Device	Temp	Mix Conditioning	MnRoad Test Section				WIS		Mixture NY	
			33, 34, 35,77		20, 21, 22					
			Air Voids, %							
			4	7	4	7	4	7	4	7
SCB	PG	None	xxx	xxx	xxx	xxx	xxx	xxx	xxx	xxx
	PG+10°C	None	xxx	xxx	xxx	xxx	xxx	xxx	xxx	xxx
	PG	5 days@85°C		xxx		xxx		xxx		xxx
	PG	cores		xxx		xxx		xxx		xxx
DC(T)	PG	None	xxx	xxx	xxx	xxx	xxx	xxx	xxx	xxx
	PG+10°C	None	xxx	xxx	xxx	xxx	xxx	xxx	xxx	xxx
	PG	5 days@85°C		xxx		xxx		xxx		xxx
	PG	cores		xxx		xxx		xxx		xxx
IDT	PG	None	xxx	xxx	xxx	xxx	xxx	xxx	xxx	xxx
	PG+10°C	None	xxx	xxx	xxx	xxx	xxx	xxx	xxx	xxx
	PG	5 days@85°C		xxx		xxx		xxx		xxx
	PG	cores		xxx		xxx		xxx		xxx

Statistical Analysis Summary

The statistical analysis using data from Indirect Tensile Strength testing (IDT), Semi-Circular Bend (SCB) test and the Disc-Shaped Compact Tension (DCT) test. The analysis compares the conditioning of the samples, the air voids and testing temperature as well as a comparison between the testing results between two different laboratories. The thicknesses of the NY specimens were less than 50 mm however the results were used in the analysis. The significance level for each analysis is set to $\alpha=0.05$. Multiple comparison testing was performed using Tukey HSD or student's t-test where appropriate.

Subtask on Physical Hardening

This task also includes a subtask dealing with physical hardening effects in the asphalt binders used to prepare the mixtures in Table 3.1. A protocol to simplify the measurements of physical hardening and to adjust S and m values based on such protocol based on climatic condition is proposed in this subtask. In addition, glass transition measuring techniques were used to quantify the effect of isothermal storage on dimensional stability of asphalt mixtures. A separate report is provided for this work.

Experimental Work

As stated in the introduction, two sets of material were investigated. The first set consists of laboratory prepared specimens following a statistically designed test matrix and using asphalt mixtures obtained from nine different test sections, as described in Table 3.1. The second set consists of field cores taken from the field sections.

Preparation of Laboratory Compacted Asphalt Mixture Specimens

Approximately 200 kg of loose asphalt mixture from each source, described in Table 3.1, were delivered to University of Minnesota (UMN) research team. All gyratory specimens were compacted in the UMN pavement laboratory and then distributed to Illinois (UIUC) and Wisconsin (UWM) research teams. Half of the 7% air voids cylinders were conditioned for 5 days at 85°C, according to AASHTO R30-02 protocol. The IDT, SCB and DCT specimens were obtained by cutting the gyratory cylinders as shown in Figures 3.1, 3.2, and 3.3.

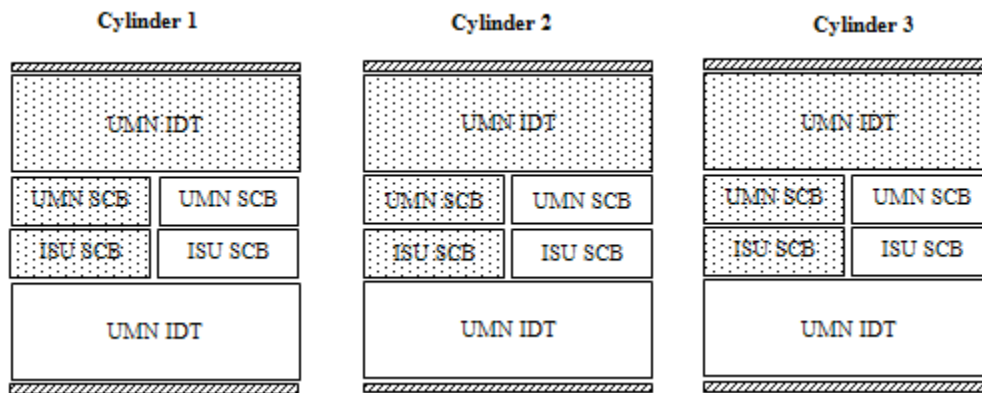


Figure 3.1: Non-conditioned specimens used at UMN

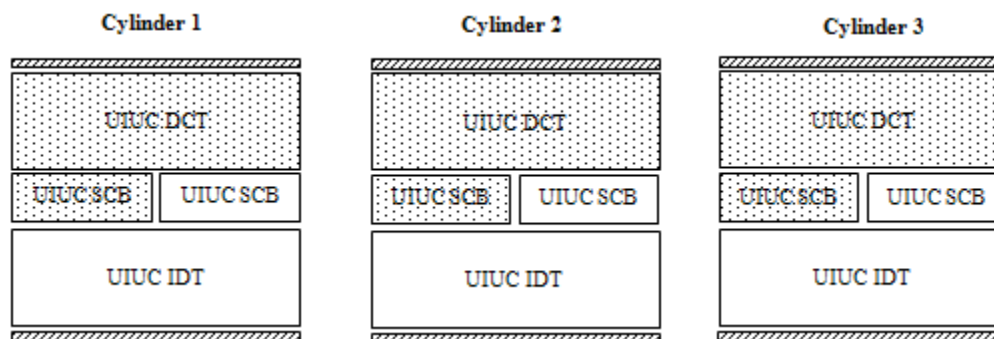


Figure 3.2: Non-conditioned specimens used at UIUC

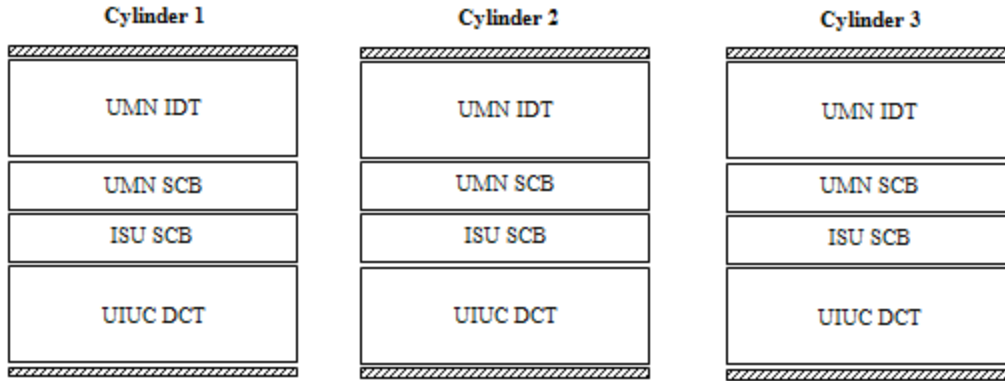


Figure 3.3: Conditioned specimens

The dotted surfaces in Figure 3.1 and Figure 3.2 represent the specimens tested at PGLT, while the blank surfaces represent the specimens tested at PGLT+10°C. All conditioned specimens were tested at PGLT temperature.

In addition, the reproducibility of the newly developed fracture tests was evaluated by comparing results from different laboratories. For this purpose, for three randomly selected mixtures, a fourth cylinder was gyratory compacted and utilized to prepare DCT specimens to be tested at UMN. Similarly, three mixtures were randomly selected and utilized to prepare SCB specimens to be tested at UIUC.

Preparation of Field Cored Asphalt Mixture Test Samples

Field cores were taken from cells 20, 21, 22, 33, 34, 35, and 77 at the MnROAD facility. The cores were taken from MnROAD in June 2010, approximately 2 and 3 years after the constructions of the cells 33, 34, 35, 77 and cells 20, 21, and 22, respectively. Eleven cylindrical field cores, for each mixture, sampled from between wheel paths, approximate offset 6 ft. of the pavement test sections, were delivered to UMN. The thickness of the cores ranged from 100 mm to 150 mm (4" to 6").



Figure 3.4: Sample preparation for field cores

The cells from which the samples were collected had several layers, but only the top layers were made of the mixtures of interest to this research study. Therefore the bottom layers were cut and discarded (see Figure 3.4). In addition, the upper 5 mm (0.20") was also cut and discarded (see

Figure 3.4). The cylindrical cores were then cut into IDT, SCB, and DCT test specimens and distributed to the research teams.

The air voids for the field cores were obtained in a previous study carried out at UMN; the air void content of 145 field cores, extracted from various cells at MnROAD, were determined according AASHTO T166. The air void content values for the mixtures in Task 2 are presented in Table 3.3.

Table 3.3: Air void content for field cores

Field cores air void content		
Cell	Mean	CV
20	6.0	0%
21	5.1	2%
22	5.7	2%
33	5.3	1%
34	5.9	2%
35	6.4	2%
77	5.1	13%

Testing Methods and Test Results

The test methods used to determine the low temperature fracture properties of the asphalt mixtures and the test results are presented in the next section. As indicated in Table 3.2, each test parameter is determined from the average of three test replicates. The repeatability was assessed by the coefficient of variation (COV). In some cases, due to fabrication or testing errors, only two replicates were considered to be valid. The shaded cells represent test results which were discarded from the analysis.

Disc-Shaped Compact Tension (DCT) Test

The Disc-Shaped Compact Tension test (DCT) was developed as a practical method for the determination of low-temperature fracture properties of cylindrically-shaped asphalt concrete test specimens. The DCT's advantages include easy specimen fabrication, from both field and gyratory samples, and it is a standard fracture test configuration (3 and 4). The specimen configuration is shown in Figure 3.5. The DCT specimen are placed in a controlled chamber and conditioned for a minimum of 2 hours at the desired temperature. The test is performed under tensile loading and the crack mouth opening displacement (CMOD) is measured with a clip-on gage at the face of the crack mouth. After temperature conditioning, the specimens are inserted in loading fixtures, subjected to a preload, no greater than 0.2 kN, and then tested with a constant

CMOD of 1mm/min (0.017 mm/s or 0.00067 in/s). The test is completed when the post peak level has reduced to 0.1 kN.

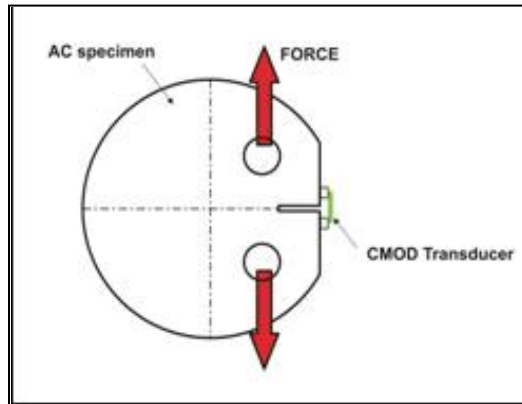


Figure 3.5: DCT test scheme

Typical plots of Load vs. CMOD are shown in Figure 3.6. The fracture energy is calculated by determining the area under the Load-CMOD curve normalized by the initial ligament length and thickness.

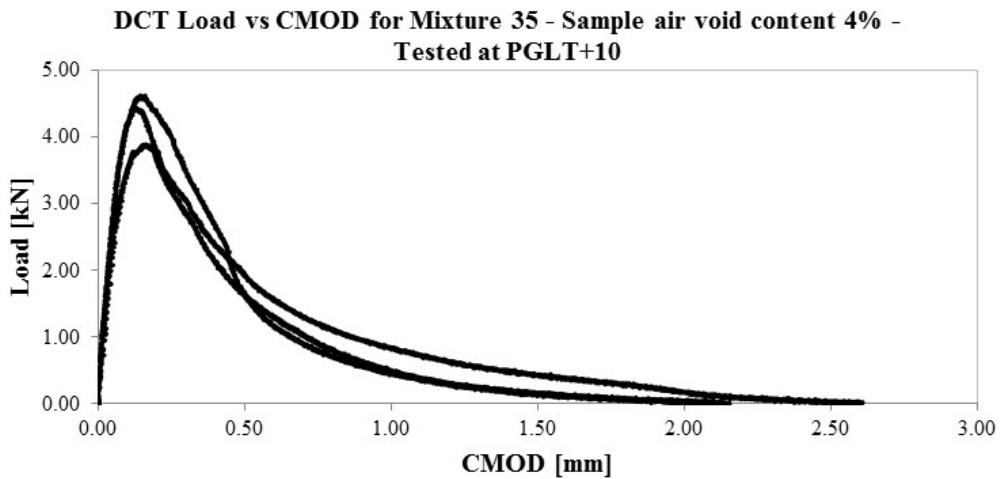


Figure 3.6: Typical load-CMOD plots from DCT tests of three replicates

DCT Test Results for Laboratory Compacted and Field Samples

Table 3.4 to Table 3.6, show DCT data obtained at UIUC for the laboratory compacted specimens.

Table 3.4: DCT test results for specimens with 4% air void content

Mixture	Type	Binder PG	Void [%]	Temp [°C]	G _f [J/m ²]		
					rep.	mean	COV
20	30% Non Fractioned RAP	58-28	4	-18	543.93	483.14	12%
					480.74		
					424.74		
				-28	371.93	363.66	10%
					323.64		
					395.41		
21	30% Fractioned RAP	58-28	4	-18	612.15	575.22	18%
					656.97		
					456.53		
				-28	431.69	379.23	13%
					370.88		
					335.11		
22	30% Fractioned RAP	58-34	4	-24	582.65	594.85	10%
					656.49		
					545.42		
				-34	382.09	346.20	10%
					315.35		
					341.16		
33	PPA	58-34	4	-24	624.01	544.37	13%
					490.42		
					518.69		
				-34	516.45	474.26	13%
					N/A		
					432.07		
34	SBS + PPA	58-34	4	-24	760.42	747.07	10%
					811.81		
					668.98		
				-34	396.59	440.35	13%
					417.56		
					506.89		
35	SBS	58-34	4	-24	636.47	645.41	9%
					706.73		
					593.02		
				-34	443.15	436.22	2%
					725.83*		
					429.30		
77	Elvaloy + PPA	58-34	4	-24	446.09	547.32	16%
					592.37		
					603.51		
				-34	468.27	465.48	15%
					533.07		
					395.12		
WIS	Superpave E-30 WisDOT mix	64-22	4	-12	414	12%	
				-22	273.7	32%	

*: because of outlier, the following value(s) were (was) not selected in computation.

Table 3.5: DCT test results for specimens with 7% air void content

Mixture	Type	Binder PG	Void [%]	Temp [°C]	G _f [J/m ²]		
					rep.	mean	COV
20	30% Non Fractioned RAP	58-28	7	-18	550.53	504.72	16%
					412.48		
					551.16		
				-28	345.04	341.99	1%
					338.93		
					341.99		
21	30% Fractioned RAP	58-28	7	-18	633.40	559.01	12%
					530.33		
					513.30		
				-28	396.34	377.70	7%
					347.99		
					388.76		
22	30% Fractioned RAP	58-34	7	-24	415.71	440.76	5%
					460.63		
					445.94		
				-34	352.68	322.47	10%
					285.88		
					328.85		
33	PPA	58-34	7	-24	626.75	594.38	12%
					512.20		
					644.21		
				-34	365.93	340.81	8%
					344.63		
					311.87		
34	SBS + PPA	58-34	7	-24	618.27	670.92	16%
					795.78		
					598.71		
				-34	406.62	476.18	13%
					527.71		
					494.20		
35	SBS	58-34	7	-24	718.58	647.36	13%
					556.99		
					666.50		
				-34	489.96	473.02	3%
					464.24		
					464.86		
77	Elvaloy + PPA	58-34	7	-24	517.18	526.62	5%
					505.12		
					557.54		
				-34	500.86	428.05	24%
					355.23		
					N/A		
WIS	Superpave E-30 WisDOT mix	64-22	7	-12	400	10%	
				-22	237	10%	
NY	"Typical Mix"	64-22	7	-12	523.06	435.99	17%
					402.47		
					382.45		
				-22	N/A	302.70	2%
					299.16		
					306.24		

Table 3.6: DCT test results for conditioned specimens

Mixture	Type	Binder PG	Void [%]	Temp [°C]	G _f [J/m ²]		
					rep.	mean	COV
20	30% Non Fractioned RAP	58-28	7	-28	247.42	269.83	12%
					N/A		
					292.25		
21	30% Fractioned RAP	58-28	7	-28	N/A	307.35	7%
					322.04		
					292.66		
22	30% Fractioned RAP	58-34	7	-34	348.17	365.99	16%
					317.16		
					432.64		
33	PPA	58-34	7	-34	272.17	355.06	21%
					380.93		
					412.07		
34	SBS + PPA	58-34	7	-34	286.07	350.13	18%
					408.68		
					355.63		
35	SBS	58-34	7	-34	499.38	451.73	11%
					459.36		
					396.46		
77	Elvaloy + PPA	58-34	7	-34	403.20	399.83	8%
					366.60		
					429.68		
WIS	Superpave E-30 WisDOT mix	64-22	7	-22		341.5	9%
NY	"Typical Mix"	64-22	7	-22	299.31	275.44	8%
					268.97		
					258.04		

DCT Results for Field Specimens

The DCT test results for field cores are reported in Table 3.7.

Table 3.7: DCT test results for field specimens

Mixture	Type	Binder PG	Void [%]	Temp [°C]	G _f [J/m ²]		
					rep.	mean	COV
20	30% Non Fractioned RAP	58-28	7	-28	283.0	277.67	3%
					283.0		
					267.0		
21	30% Fractioned RAP	58-28	7	-28	282.0	326.67	13%
					331.0		
					367.0		
22	30% Fractioned RAP	58-34	7	-34	282.0	246.67	13%
					235.0		
					223.0		
33	PPA	58-34	7	-34	317.0	334.00	5%
					339.0		
					346.0		
34	SBS + PPA	58-34	7	-34	278.0	295.50	8%
					313.0		
					525.0		
35	SBS	58-34	7	-34	344.0	312.00	9%
					297.0		
					295.0		
77	Elvaloy + PPA	58-34	7	-34	373.0	395.00	30%
					290.0		
					522.0		
WIS	Superpave E-30 WisDOT mix	64-22	7	-22		294	11%
NY	"Typical Mix"	64-22	7	-22		287.5	20%

DCT Results for Tests Performed at UMN

Three randomly selected mixtures were also DCT tested at the UMN. The fracture energy was computed from the Load-CMOD curve as described above. The results are shown in Table 3.8.

Table 3.8: DCT test results for mixtures tested at the UMN

Mixture	Binder/ Mix Type	Binder PG	Void [%]	Temp [°C]	G _f [J/m ²]		
					rep.	mean	COV
20	30% Non Fractioned RAP	58-28	7	-18	574.8	552.00	22%
					660.7		
					420.5		
21	30% Fractioned RAP	58-28	4	-18	566.7	571.98	1%
					577.5		
					571.7		
21	30% Fractioned RAP	58-28	4	-28	490.7	439.51	16%
					388.3		
					700.82*		
22	30% Fractioned RAP	58-34	7	-24	552.0	593.85	7%
					597.6		
					632.0		

*: because of outlier, the following value(s) were (was) not selected in computation.

Semi-Circular Bend (SCB) Test

The Semi-Circular Bend (SCB) test method takes advantage of the simple specimen preparation from Super-pave Gyrotory compacted cylinders and the simple loading setup. A schematic of the test set-up is shown in Figure 3.7.

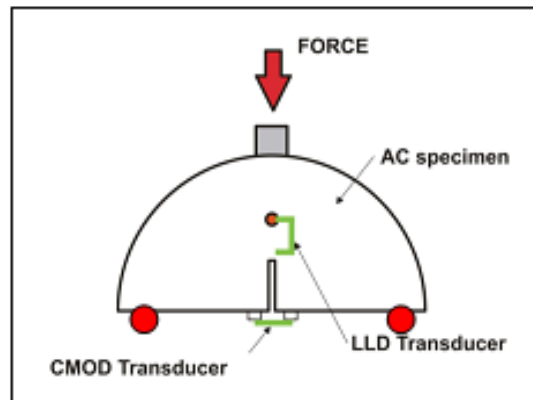


Figure 3.7: SCB test scheme

An MTS servo-hydraulic testing system equipped with an environmental chamber was used to perform the SCB test. The load line displacement (LLD) was measured using a vertically mounted Epsilon extensometer with 38 mm gage length and ±1 mm range; one end was mounted on a button that was permanently fixed on a specially made frame, and the other end was attached to a metal button glued to the sample. The crack mouth opening displacement (CMOD) was recorded by an Epsilon clip gage with 10 mm gage length and a +2.5 and -1 mm range. The

clip gage was attached at the bottom of the specimen. A constant CMOD rate of 0.0005mm/s was used and the load and load line displacement (P-u), as well as the load versus LLD curves were plotted. A contact load with maximum load of 0.3 kN was applied before the actual loading to ensure uniform contact between the loading plate and the specimen. The testing was stopped when the load dropped to 0.5 kN in the post peak region. All tests were performed inside an environmental chamber. Liquid nitrogen was used to obtain the required low temperature. The temperature was controlled by the environmental chamber temperature controller and verified using an independent platinum RTD thermometer. Typical Load versus LLD plots obtained from SCB tests are shown in Figure 3.8.

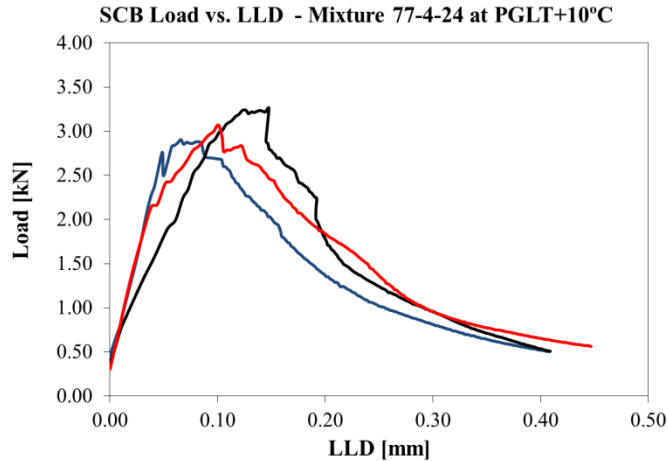


Figure 3.8: Typical load-LLD plots from SCB tests of three replicates

The tail part of the Load-LLD curve can be reasonably obtained by fitting the data curve in post peak region following a method described elsewhere (5). The load and load line displacement data were used to calculate the fracture toughness and fracture energy as described in the National Pooled Fund Study 776 (6).

SCB Results for Laboratory Compacted and Field Samples

The fracture energy and fracture parameters were computed from the SCB test results. Table 3.9 through Table 3.11, report the results obtained at UMN.

Table 3.9: SCB test results for specimens with 4% air void content

Mixture	Type	Binder PG	Void [%]	Temp [°C]	K _{IC} [MPa*m ^{0.5}]			G _f [J/m ²]		
					rep.	mean	COV	rep.	mean	COV
20	30% Non Fractioned RAP	58-28	4	-18	0.96	0.98	4%	789.46	544.41	64%
					1.01			299.37		
					N/A			N/A		
				-28	0.86	0.99	19%	327.21	381.10	20%
					1.13			434.98		
					N/A			N/A		
21	30% Fractioned RAP	58-28	4	-18	0.85	0.82	8%	414.53	400.41	5%
					0.74			376.06		
					0.86			410.65		
				-28	0.95	0.96	7%	210.83*	379.15	20%
					1.03			432.00		
					0.90			326.31		
22	30% Fractioned RAP	58-34	4	-24	0.80	0.88	7%	405.18	368.90	14%
					0.93			392.35		
					0.90			309.16		
				-34	1.00	0.98	14%	235.26	238.69	2%
					0.83			242.11		
					1.10			572.10*		
33	PPA	58-34	4	-24	0.91	0.86	10%	517.81	397.80	27%
					0.76			307.35		
					0.91			368.26		
				-34	0.94	0.90	5%	351.21	336.22	12%
					0.85			289.21		
					0.91			368.26		
34	SBS + PPA	58-34	4	-24	0.91	0.91	11%	456.74	600.12	22%
					1.01			632.98		
					0.81			710.64		
				-34	1.09	1.06	4%	416.09	406.31	10%
					1.08			361.06		
					1.00			441.77		
35	SBS	58-34	4	-24	0.90	0.95	7%	494.39	685.60	39%
					1.00			876.82		
					N/A			N/A		
				-34	0.96	1.00	4%	289.12	296.11	16%
					1.03			347.54		
					1.01			251.65		
77	Elvaloy + PPA	58-34	4	-24	0.80	0.85	6%	482.33	540.56	10%
					0.90			556.45		
					0.84			582.89		
				-34	0.85	0.91	9%	286.73	378.41	34%
					0.97			470.08		
					N/A			N/A		
WIS	Superpave E-30 WisDOT mix	64-22	4	-12	0.83	0.84	3%	231.33	246.20	9%
					0.81			261.07		
					0.87			461.22*		
				-22	0.92	0.91	2%	187.26	208.46	20%
					0.92			181.35		
					0.89			256.78		

*: because of outlier, the following value(s) were (was) not selected in computation.

Table 3.10: SCB test results for specimens with 7% air void content

Mixture	Type	Binder PG	Void [%]	Temp [°C]	K _{IC} [MPa*m ^{0.5}]			G _f [J/m ²]		
					rep.	mean	COV	rep.	mean	COV
20	30% Non Fractioned	58-28	7	-18	0.70	0.73	6%	337.34	388.65	26%
					0.78			504.70		
					0.72			323.92		
				-28	0.77	0.81	4%	314.39	268.34	16%
					0.84			226.38		
					0.81			264.25		
21	30% Fractioned	58-28	7	-18	0.68	0.71	10%	265.60	389.59	28%
					0.66			429.72		
					0.80			473.44		
				-28	0.44	0.66	29%	N/A	336.51	1%
					0.79			335.17		
					0.74			337.85		
22	30% Fractioned	58-34	7	-24	0.86	0.81	6%	588.58	441.73	29%
					0.78			351.70		
					0.77			384.90		
				-34	0.81	0.75	13%	291.80	228.46	24%
					0.64			197.70		
					0.80			195.88		
33	PPA	58-34	7	-24	0.69	0.71	7%	361.59	343.17	5%
					0.77			336.64		
					0.68			331.29		
				-34	0.75	0.74	10%	224.59	246.22	28%
					0.81			322.64		
					0.67			191.43		
34	SBS+PPA	58-34	7	-24	0.85	0.82	7%	492.32	452.35	9%
					0.76			413.02		
					0.87			451.69		
				-34	0.80	0.77	5%	248.54	285.26	11%
					0.79			297.16		
					0.73			310.08		
35	SBS	58-34	7	-24	0.85	1.00	22%	524.98	632.74	24%
					1.16			740.51		
					0.53			276.39		
				-34	0.74	0.88	17%	203.62	217.61	9%
					1.03			364.64		
					0.88			231.60		
77	Elvaloy+ PPA	58-34	7	-24	0.74	0.74	12%	649.95	380.87	22%
					0.83			440.46		
					0.66			321.29		
				-34	0.67	0.76	16%	263.26	278.50	15%
					0.71			326.81		
					0.89			245.42		
WIS	Superpave E-30 WisDOT mix	64-22	7	-12	0.94	0.77	20%	300.55	233.89	26%
					0.74			182.12		
					0.64			219.01		
				-22	0.83	0.78	8%	219.14	190.86	14%
					0.80			186.45		
					0.71			166.99		
NY	"Typical Mix"	64-22	7	-12	0.89	0.81	9%	485.64	414.96	20%
					0.75			436.68		
					0.78			322.56		
				-22	0.91	0.86	8%	266.17	301.34	10%
					0.89			323.40		
					0.78			314.44		

Table 3.11: SCB test results for conditioned specimens

Mixture	Type	Binder PG	Void [%]	Temp [°C]	K _{IC} [MPa*m ^{0.5}]			G _f [J/m ²]		
					rep.	mean	COV	rep.	mean	COV
20	30% Non Fractioned RAP	58-28	7	-28	0.88	0.84	5%	267.47	229.98	23%
					0.80			399.18*		
					0.85			192.49		
21	30% Fractioned RAP	58-28	7	-28	0.77	0.88	12%	266.66	289.69	9%
					0.88			319.32		
					0.99			283.08		
22	30% Fractioned RAP	58-34	7	-34	0.94	1.01	6%	216.02*	405.71	7%
					1.03			385.88		
					1.06			425.54		
33	PPA	58-34	7	-34	0.69	0.73	6%	175.48	230.48	22%
					0.78			272.88		
					0.71			243.07		
34	SBS + PPA	58-34	7	-34	0.84	0.85	6%	N/A	305.70	18%
					0.80			265.98		
					0.91			345.43		
35	SBS	58-34	7	-34	0.80	0.85	5%	357.55	331.90	12%
					0.88			351.90		
					0.87			286.26		
77	Elvaloy + PPA	58-34	7	-34	0.85	0.82	11%	308.68	293.35	18%
					0.88			335.98		
					0.72			235.40		
WIS	Superpave E-30 WisDOT mix	64-22	7	-22	0.84	0.81	4%	210.57	214.85	3%
					0.78			N/A		
					0.82			219.12		
NY	"Typical Mix"	64-22	7	-22	0.83	0.87	8%	170.09	215.98	25%
					0.83			275.27		
					0.94			202.57		

*: because of outlier, the following value(s) were (was) not selected in computation.

SCB Results for Field Specimens

The SCB specimens, obtained from field cored samples, were also subjected to the SCB test in order to evaluate their fracture parameters. Table 3.12 reports the results.

Table 3.12: SCB test results for field cored samples

Mixture	Type	Binder PG	Void [%]	Temp [°C]	K _{IC} [MPa*m ^{0.5}]			G _f [J/m ²]		
					rep.	mean	COV	rep.	mean	COV
20	30% Non Fractioned RAP	58-28	7	-28	0.67	0.68	5%	259.45	238.46	8%
					0.66			224.29		
					0.72			231.65		
21	30% Fractioned RAP	58-28	7	-28	0.72	0.79	15%	200.50	200.06	0%
					0.72			199.62		
					0.93			366.74*		
22	30% Fractioned RAP	58-34	7	-34	0.73	0.77	4%	276.44	306.49	15%
					0.80			282.45		
					0.78			360.58		
33	PPA	58-34	7	-34	0.85	0.80	8%	278.16	246.34	12%
					0.74			220.88		
					0.82			239.99		
34	SBS + PPA	58-34	7	-34	0.73	0.81	10%	245.97	288.36	16%
					0.79			280.30		
					0.89			338.82		
35	SBS	58-34	7	-34	0.86	0.85	7%	454.87	421.29	19%
					0.90			329.39		
					0.78			479.62		
77	Elvaloy + PPA	58-34	7	-34	0.96	0.87	12%	316.51	329.03	24%
					0.89			413.53		
					0.76			257.04		
WI	Superpave E-30 WisDOT mix	64-22	7	-22	0.75	0.70	9%	194.10	218.83	16%
					0.66			243.55		
					N/A			N/A		
NY	"Typical Mix"	64-22	7	-22	0.68	0.62	8%	233	212.5	14%
					0.58			143		
					0.61			192		

*: because of outlier, the following value(s) were (was) not selected in computation.

SCB Results for Tests Performed at UIUC

As for the DCT, three randomly selected mixtures were also SCB tested at the UIUC in order to evaluate the reproducibility of the test. Results are reported in Table 3.13.

Table 3.13: SCB test results for mixtures tested at the UIUC

Mixture	Type	Binder PG	Void [%]	Temp [°C]	K _{IC} [MPa*m ^{0.5}]			G _f [J/m ²]		
					rep.	mean	COV	rep.	mean	COV
35	SBS	58-34	4	-24	0.86	0.97	12%	412.0	435.67	7%
					1.09			425.0		
					0.96			470.0		
35	SBS	58-34	7	-24	0.86	0.86	2%	515.0	512.00	2%
					0.84			501.0		
					0.87			520.0		
NY	"Typical Mix"	64-22	7	-12	0.79	0.80	1%	341.0	348.67	15%
					0.81			405.0		
					0.80			300.0		

It must be noted however, that the above reported fracture energy were not computed using LLD measurements. Instead, the displacement of the loading piston, recorded through its LVDT, was used.

Indirect Tensile Test IDT Creep Stiffness and Strength Tests

Two parameters, creep compliance and strength were determined using the current AASHTO specification T 322-03(7). Each mixture was tested at two different temperatures determined based on the PG grade of the binder. At each temperature, three replicates were tested. First, all IDT specimens were tested for the creep stiffness and later for the strength. Both procedures are specified in AASHTO T 322-03 and the resultant parameters are calculated as follows:

- *Creep stiffness:*

$$D(t) = \frac{\Delta X \cdot D_{avg} \cdot b_{avg}}{P_{avg} \cdot GL} \cdot C_{cpl} \quad [3.1]$$

Where:

D(t) – creep compliance,

ΔX – trimmed mean of the horizontal deformations,

D_{avg} – average specimen diameter,

B_{avg} - average specimen thickness,

P_{avg} – average force during the test,

GL – gage length (38mm)

C_{cpl} – creep compliance parameter at any given time, computed as

$$C_{cmtl} = 0.6354 \cdot \left(\frac{X}{Y} \right)^{-1} - 0.332 \quad [3.2]$$

Where:

X – horizontal deformation,

Y – vertical deformation.

Creep stiffness $S(t)$ at the time t was calculated as the inverse of the creep compliance $D(t)$, i.e. $S(t)=1/D(t)$.

- *Tensile strength:*

$$S = \frac{2 \cdot P_{fail}}{\pi \cdot b \cdot D} \quad [3.3]$$

Where:

P_{fail} – failure (peak) load,

b, D – specimen thickness and diameter, respectively.

IDT Test Results for Laboratory Compacted and Field Samples

Table 3.14 through Table 3.19 report the IDT test results obtained at UMN.

Table 3.14: IDT strength and creep stiffness (500s) for specimens with 4% air void content

Mixture	Type	Binder PG	Void [%]	Temp [°C]	IDT Strength [MPa]			Creep Stiffness [GPa]		
					rep.	mean	COV	rep.	mean	COV
20	30% Non Fractioned RAP	58-28	4	-18	5.65	5.54	3%	8.41	8.41	0%
					5.42			8.41		
					NA			NA		
				-28	5.08	4.90	3%	18.54	17.19	7%
					4.85			16.78		
					4.77			16.26		
21	30% Fractioned RAP	58-28	4	-18	5.41	5.24	5%	18.60*	7.63	32%
					5.06			5.92		
					NA			9.34		
				-28	4.86	4.89	2%	14.94	17.02	11%
					4.80			18.38		
					5.01			17.73		
22	30% Fractioned RAP	58-34	4	-24	NA	5.20	7%	N/A	7.83	14%
					4.96			8.59		
					5.44			7.06		
				-34	5.23	5.26	2%	22.66	23.64	8%
					5.38			25.89		
					5.18			22.36		
33	PPA	58-34	4	-24	4.96	4.65	10%	9.43	10.75	11%
					4.91			11.45		
					4.10			11.38		
				-34	4.83	4.45	8%	18.25	15.81	16%
					4.16			15.88		
					4.37			13.30		
34	SBS + PPA	58-34	4	-24	5.64	5.26	7%	12.67	11.12	12%
					4.86			10.26		
					5.30			10.44		
				-34	5.14	4.88	6%	15.69	18.75	17%
					4.91			22.04		
					4.59			18.52		
35	SBS	58-34	4	-24	5.58	5.67	1%	11.46	11.11	3%
					5.70			11.13		
					5.71			10.73		
				-34	5.13	5.43	7%	21.21	20.61	6%
					5.87			21.44		
					5.28			19.17		
77	Elvaloy + PPA	58-34	4	-24	4.45	4.73	5%	9.21	8.86	4%
					4.88			8.48		
					4.85			8.89		
				-34	4.74	4.32	12%	20.20	21.65	11%
					3.72			20.32		
					4.50			24.44		
WIS	Superpave E-30 WisDOT mix	64-22	4	-12	7.90	7.56	4%	18.37	15.96	21%
					7.35			13.56		
					7.44			8.93*		
				-22	6.41	7.06	26%	25.58	22.38	17%
					5.61			23.28		
					9.15			18.27		

*: because of outlier, the following value(s) were (was) not selected in computation.

Table 3.15: IDT strength and creep stiffness (500s) for specimens with 7% air void content

Mixture	Type	Binder PG	Void [%]	Temp [°C]	IDT Strength [MPa]			Creep Stiffness [GPa]		
					rep.	mean	COV	rep.	mean	COV
20	30% Non Fractioned RAP	58-28	7	-18	4.36	4.27	4%	8.67	7.32	16%
					4.36			6.88		
					4.08			6.40		
				-28	N/A	4.31	3%	15.09	15.09	2%
					4.39			15.45		
					4.22			14.73		
21	30% Fractioned RAP	58-28	7	-18	4.45	4.72	5%	8.65	7.51	29%
					4.90			5.03		
					4.82			8.85		
				-28	4.30	4.27	4%	10.30	12.19	18%
					4.44			11.73		
					4.07			14.54		
22	30% Fractioned RAP	58-34	7	-24	4.78	5.00	6%	14.47	13.52	16%
					4.88			11.08		
					5.34			15.03		
				-34	4.30	4.36	8%	21.94	22.93	7%
					4.72			21.93		
					4.07			24.90		
33	PPA	58-34	7	-24	3.56	3.80	7%	5.03	5.24	6%
					4.06			5.44		
					3.78			8.74*		
				-34	3.74	3.14	24%	13.73	15.37	18%
					3.37			13.88		
					2.30			18.48		
34	SBS + PPA	58-34	7	-24	4.25	4.51	5%	9.31	7.62	19%
					4.70			6.74		
					4.58			6.82		
				-34	3.32	3.61	7%	13.11	13.55	5%
					3.82			30.32*		
					3.70			13.99		
35	SBS	58-34	7	-24	4.60	4.50	4%	7.59	7.86	15%
					4.63			9.15		
					4.28			6.85		
				-34	4.65	4.54	3%	21.07	16.24	26%
					4.39			13.89		
					4.59			13.76		
77	Elvaloy + PPA	58-34	7	-24	3.97	3.72	10%	9.47	8.91	11%
					3.46			9.46		
					NA			7.80		
				-34	3.71	3.75	1%	16.81	17.41	5%
					3.77			16.94		
					3.78			18.47		
WIS	Superpave E-30 WisDOT mix	64-22	7	-12	5.20	6.14	15%	10.22	11.26	19%
					6.13			13.68		
					7.08			9.89		
				-22	5.95	6.60	13%	20.64	21.39	22%
					7.54			17.02		
					6.33			26.51		
NY	"Typical Mix"	64-22	7	-12	7.06	6.74	5%	14.55*	6.94	7%
					6.40			6.61		
					6.77			7.28		
				-22	6.35	6.67	8%	7.83	7.12	9%
					7.26			6.82		
					6.39			6.71		

*: because of outlier, the following value(s) were (was) not selected in computation.

Table 3.16: IDT strength and creep stiffness (500s) for conditioned specimens

Mixture	Type	Binder PG	Void [%]	Temp [°C]	IDT Strength [MPa]			Creep Stiffness [GPa]		
					rep.	mean	COV	rep.	mean	COV
20	30% Non Fractioned RAP	58-28	7	-28	3.96	3.88	4%	10.50	13.34	20%
					3.97			15.76		
					3.70			13.76		
21	30% Fractioned RAP	58-28	7	-28	4.30	4.12	5%	10.58	12.47	13%
					4.17			13.22		
					3.91			13.61		
22	30% Fractioned RAP	58-34	7	-34	4.60	4.53	4%	19.40	20.87	7%
					4.66			21.09		
					4.34			22.12		
33	PPA	58-34	7	-34	3.19	3.57	10%	21.14	17.69	18%
					3.63			15.09		
					3.88			16.82		
34	SBS + PPA	58-34	7	-34	NA	3.93	3%	19.74	19.91	1%
					3.85			20.14		
					4.02			19.85		
35	SBS	58-34	7	-34	4.59	4.72	5%	14.38	14.62	3%
					4.56			15.06		
					5.02			14.43		
77	Elvaloy + PPA	58-34	7	-34	3.48	3.31	6%	21.07	20.81	3%
					3.11			20.14		
					3.34			21.21		
WIS	Superpave E- 30 WisDOT mix	64-22	7	-22	7.60	6.59	15%	18.61	20.03	19%
					5.65			24.24		
					6.52			17.25		
NY	"Typical Mix"	64-22	7	-22	6.77	6.88	1%	6.78	6.86	7%
					6.94			6.46		
					6.94			7.34		

IDT Results for Field Specimens

IDT strength and creep stiffness were also obtained for field cored specimens. The results are presented in Table 3.17.

Table 3.17: IDT strength and creep stiffness (500s) for field specimens

Mixture	Type	Binder PG	Void [%]	Temp [°C]	IDT Strength [MPa]			Creep Stiffness [GPa]		
					rep.	mean	COV	rep.	mean	COV
20	30% Non Fractioned RAP	58-28	7	-28	3.76	3.75	1%	18.32	17.56	4%
					3.79			17.53		
					3.69			16.84		
21	30% Fractioned RAP	58-28	7	-28	3.40	3.78	9%	18.65	17.78	7%
					3.84			18.22		
					4.10			16.46		
22	30% Fractioned RAP	58-34	7	-34	3.43	3.51	5%	20.73	20.57	5%
					3.72			19.54		
					3.37			21.44		
33	PPA	58-34	7	-34	3.47	3.60	4%	19.71	18.43	8%
					3.58			16.84		
					3.76			18.74		
34	SBS + PPA	58-34	7	-34	3.83	3.72	4%	18.24	18.45	15%
					3.53			15.88		
					3.79			21.22		
35	SBS	58-34	7	-34	4.13	3.84	8%	19.75	17.13	14%
					3.90			16.52		
					3.49			15.13		
77	Elvaloy + PPA	58-34	7	-34	3.91	4.12	4%	19.48	18.55	12%
					4.23			16.06		
					4.23			20.12		
WIS	Superpave E-30 WisDOT mix	64-22	7	-22	4.70	5.54	14%	11.87	13.28	13%
					6.19			12.84		
					5.72			15.14		
NY	"Typical Mix"	64-22	7	-22	2.63	2.64	9%	10.62	11.67	13%
					2.88			13.48		
					2.43			10.93		

Summary of Results from Laboratory Compacted Non-Conditioned Specimens

In this chapter the laboratory test results are analyzed to evaluate the effect of the various test factors on the fracture parameters.

Data Analysis of Fracture Energy Results

The range values of the DCT and SCB fracture energy test results are reported in Table 3.18. As temperature drops, the mixtures behave in an increasingly brittle manner and absorb relatively little energy prior to fracture. This important aspect, ductile-to-brittle transition, is well captured by the fracture energy parameter of both DCT and SCB tests. Although the effect of void content is less pronounced, it is not negligible.

Table 3.18: Range of fracture energy test results

Void [%]	Cond.	PGLT +10°C		PGLT	
		Min [J/m ²]	Max [J/m ²]	Min [J/m ²]	Max [J/m ²]
DCT					
4	N.C.	414	750	274	474
7	N.C.	400	671	237	476
7	C.	-	-	270	451
7	Field	-	-	365	395
SCB					
4	N.C.	246	685	208	406
7	N.C.	234	632	190	337
7	C.	-	-	214	405
7	Field	-	-	200	422

The DCT fracture energy mean values, computed from three replicates, are summarized in Figure 3.9 and Figure 3.10. Specimens tested at the highest temperature level, PGLT+10°C, have considerably larger fracture energy than specimens tested at the lowest level of test temperature, PGLT.

The SCB fracture energy test results are presented in Figure 3.11 and Figure 3.12. As for DCT, the SCB fracture energy values obtained at PGLT+10°C are always higher than those obtained at PGLT, regardless of the air void content level.

The fracture energy results also indicate that at PGLT+10°C, the SBS+PPA and only SBS modified mixtures possess superior fracture resistance than the remaining mixtures. However, when temperature drops to PGLT the difference among the mixtures is diminished.

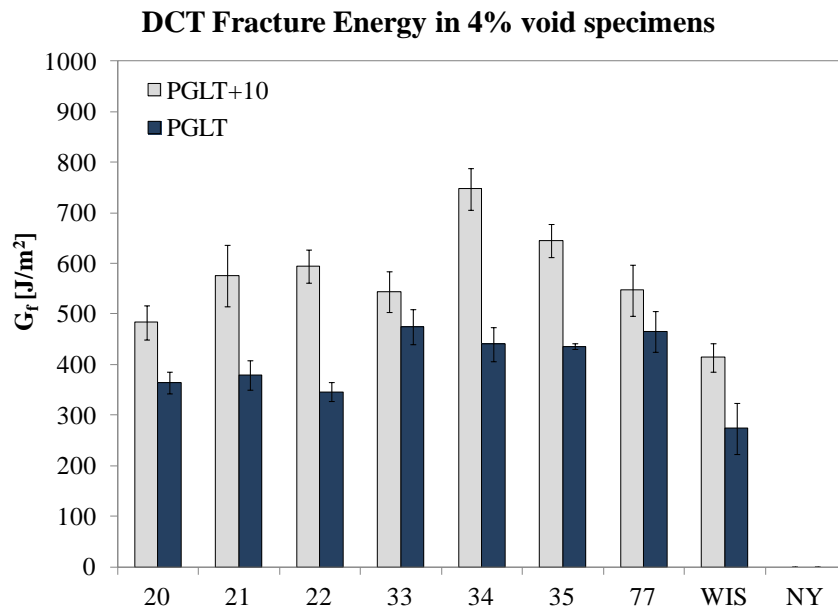


Figure 3.9: DCT fracture energy results for 4% void specimens

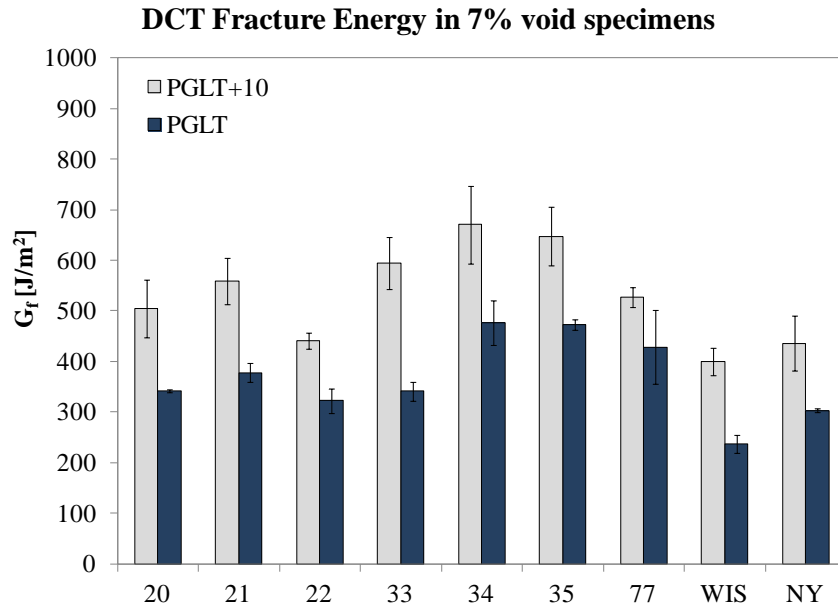


Figure 3.10: DCT fracture energy results for 7% void specimens

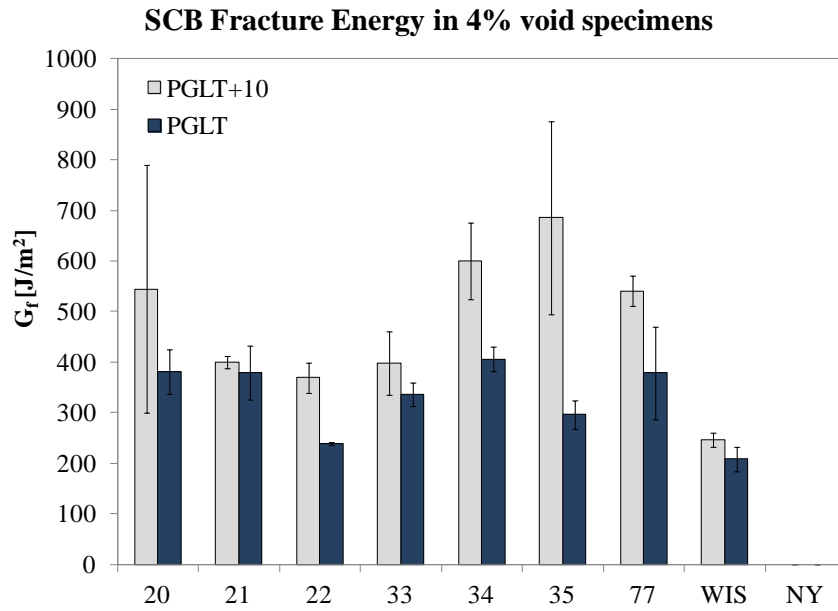


Figure 3.11: SCB fracture energy results for 4% void specimens

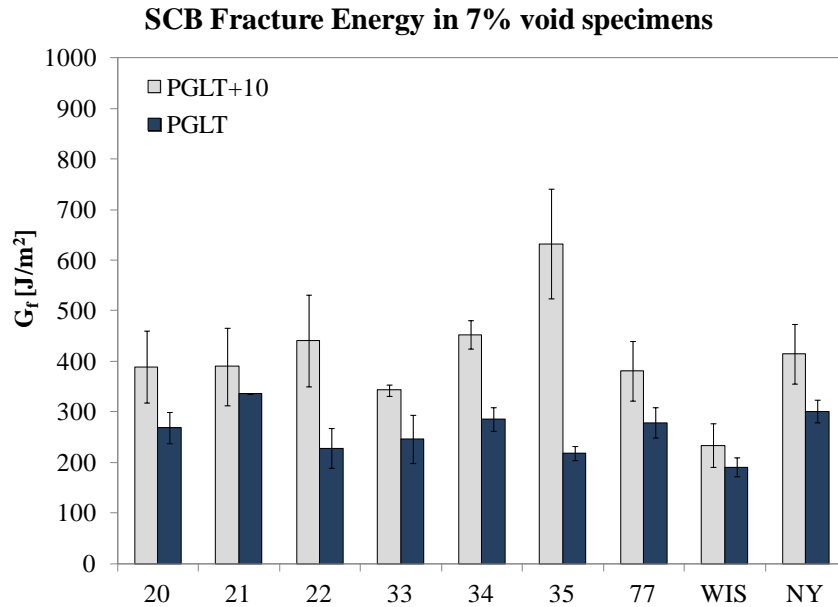


Figure 3.12: SCB fracture energy results for 7% void specimens

Data Analysis of Fracture Toughness Results

The fracture toughness of the mixtures computed from SCB test results are discussed below. The range values of the SCB fracture toughness test results are reported Table 3.19.

Table 3.19: Range of fracture toughness test results

Void [%]	Cond.	PGLT +10°C		PGLT	
		Min [MPa*m ^{0.5}]	Max [MPa*m ^{0.5}]	Min [MPa*m ^{0.5}]	Max [MPa*m ^{0.5}]
SCB					
4	N.C.	0.82	0.98	0.90	1.06
7	N.C.	0.71	1.00	0.66	0.88
7	C.	-	-	0.73	1.01
7	Field	-	-	0.62	0.87

The SCB fracture toughness mean values, computed from three replicates, are summarized in Figure 3.13 and Figure 3.14. The results obtained from specimens with 4% air voids content, indicate that the fracture toughness is higher at the lowest test temperature. For specimens with 7% air void content level, a mixed behavior is observed: mixtures 20, 33, 77, Wisconsin, and NY have slightly higher toughness values at the lowest testing temperature, while the others have higher fracture toughness at the highest testing temperature. In general, the difference in fracture toughness between the mixtures is small.

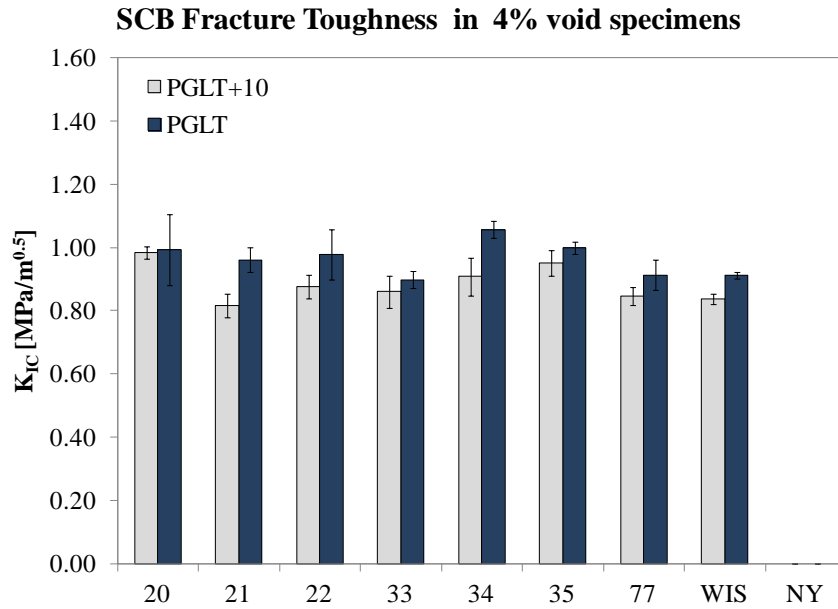


Figure 3.13: SCB fracture toughness results for 4% void specimens

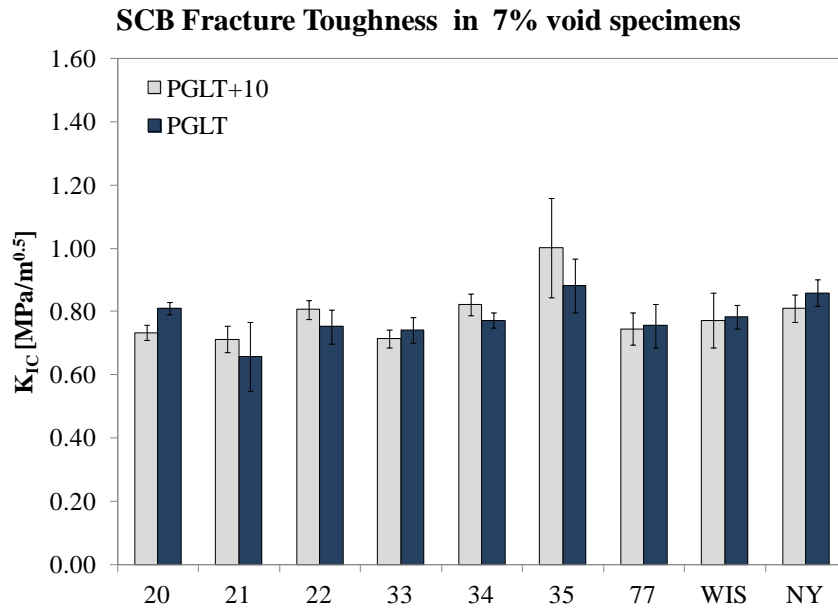


Figure 3.14: SCB fracture toughness results for 7% void specimens

Data Analysis of IDT Strength Results

A summary of the strength results obtained from IDT tensile test is shown in Figure 3.15 Figure 3.16. The range values of the IDT strength test results are reported Table 3.20.

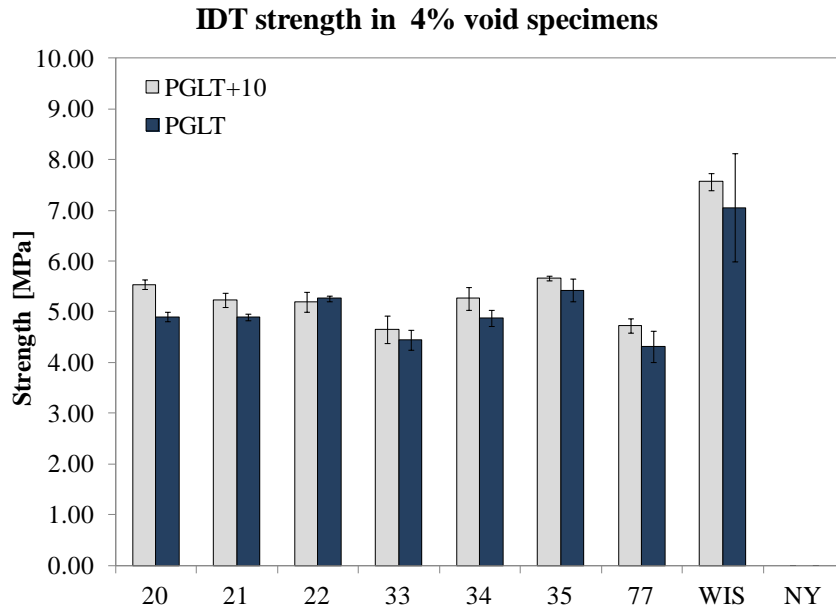


Figure 3.15: IDT strength results for 4% void specimens

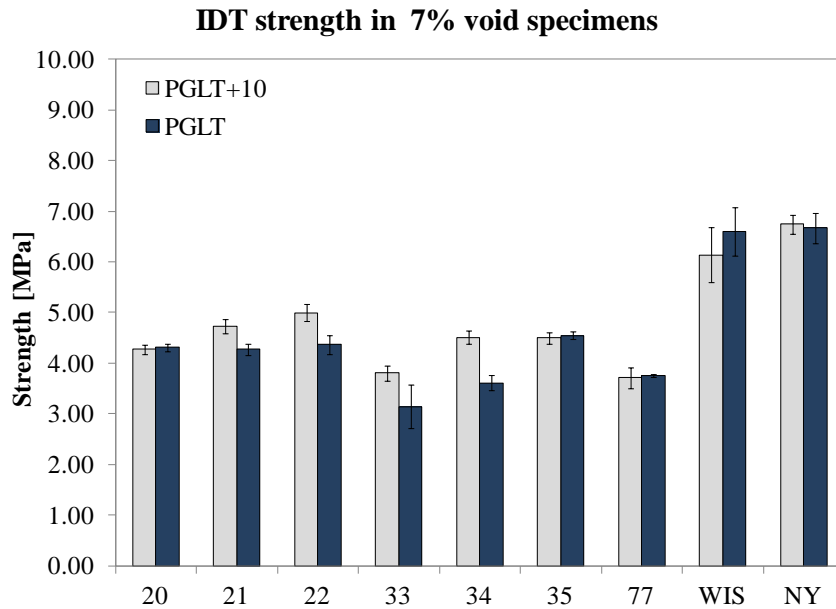


Figure 3.16: IDT strength results for 7% void specimens

For specimens with 4% air voids content, the strength decreases with decreasing temperature for all mixtures except mixture 22. For specimens with 7% air void content a mixed behavior is observed. The graphs also show relatively high strength values for the New York and Wisconsin mixtures. In addition, the RAP containing mixtures appear to be comparable to the polymer and/or acid modified mixtures.

Table 3.20: Range of IDT strength test results

Void [%]	Cond.	PGLT +10°C		PGLT	
		Min [MPa]	Max [MPa]	Min [MPa]	Max [MPa]
SCB					
4	N.C.	4.65	7.56	4.32	7.06
7	N.C.	3.72	6.74	3.14	6.67
7	C.	-	-	3.31	6.88
7	Field	-	-	2.64	5.54

Data Analysis of IDT Creep Stiffness

The results for the creep stiffness, computed from the IDT creep test data, are reported next. Figure 3.17 and Figure 3.18 summarize the result for creep stiffness at 500 obtained from 4% and 7% air voids content, respectively. It can be noticed that at the lowest test temperature, the stiffness increases considerably for all mixtures except NY. The effect of test temperature is less pronounced in the New York mixture.

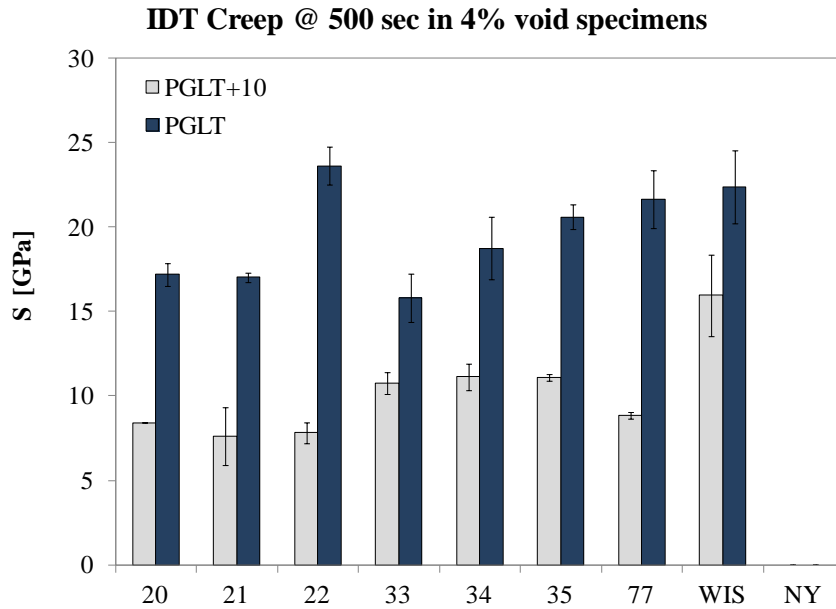


Figure 3.17: IDT stiffness for 4% void specimens

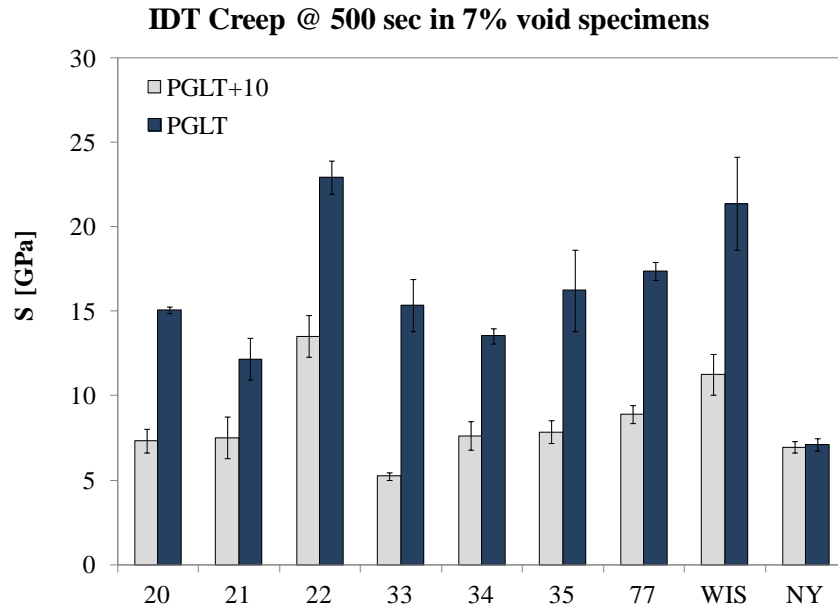


Figure 3.18: IDT stiffness for 7% void specimens

The range values of the IDT creep test results are reported Table 3.21.

Table 3.21: Range of IDT creep stiffness (500s) test results

Void [%]	Cond.	PGLT +10°C		PGLT	
		Min [GPa]	Max [GPa]	Min [GPa]	Max [GPa]
SCB					
4	N.C.	7.63	15.96	15.81	23.64
7	N.C.	5.24	13.52	7.12	22.93
7	C.	-	-	6.86	20.87
7	Field	-	-	11.61	20.57

Ranking of Mixtures

Summary tables of all the laboratory test results (non-conditioned mixtures) are presented in Table 3.22 and Table 3.25. In the tables, the mixtures are ranked from the largest response to the smallest, according to each test parameter. A reasonably good agreement between the DCT and SCB fracture energy ranking is observed. It is also interesting to notice that the mixture Wisconsin has relatively poor fracture properties but high IDT strength and stiffness. On the contrary, the SBS alone and SBS+PPA modified mixtures (34 and 35) have generally high fracture properties associated with high strength and stiffness.

Table 3.22: Summary of results for 4% void mixtures tested at PGLT+10°C

DCT		SCB		SCB		IDT		IDT	
Mixture Rank	G _f [J/m ²]	Mixture Rank	G _f [J/m ²]	Mixture Rank	K _{IC} [MPa*m ^{0.5}]	Mixture Rank	Strength [MPa]	Mixture Rank	Stiffness [GPa]
34	747.07	35	685.60	20	0.98	WIS	7.56	WIS	15.96
35	645.41	34	600.12	35	0.95	35	5.67	34	11.12
22	594.85	20	544.41	34	0.91	20	5.54	35	11.11
21	575.22	77	540.56	22	0.88	34	5.26	33	10.75
77	547.32	21	400.41	33	0.86	21	5.24	77	8.86
33	544.37	33	397.80	77	0.85	22	5.20	20	8.41
20	483.14	22	368.90	WIS	0.84	77	4.73	22	7.83
WIS	414.00	WIS	246.20	21	0.82	33	4.65	21	7.63

Table 3.23: Summary of results for 4% void mixtures tested at PGLT

DCT		SCB		SCB		IDT		IDT	
Mixture Rank	G _f [J/m ²]	Mixture Rank	G _f [J/m ²]	Mixture Rank	K _{IC} [MPa*m ^{0.5}]	Mixture Rank	Strength [MPa]	Mixture Rank	Stiffness [GPa]
33	474.26	34	406.31	34	1.06	WIS	7.06	22	23.64
77	465.48	20	381.10	35	1.00	35	5.43	WIS	22.38
34	440.35	21	379.15	20	0.99	22	5.26	77	21.65
35	436.22	77	378.41	22	0.98	20	4.90	35	20.61
21	379.23	33	336.22	21	0.96	21	4.89	34	18.75
20	363.66	35	296.11	WIS	0.91	34	4.88	20	17.19
22	346.20	22	238.69	77	0.91	33	4.45	21	17.02
WIS	273.70	WIS	208.46	33	0.90	77	4.32	33	15.81

Table 3.24: Summary of results for 7% void mixtures tested at PGLT+10°C

DCT		SCB		SCB		IDT		IDT	
Mixture Rank	G_f [J/m ²]	Mixture Rank	G_f [J/m ²]	Mixture Rank	K_{IC} [MPa*m ^{0.5}]	Mixture Rank	Strength [MPa]	Mixture Rank	Stiffness [GPa]
34	670.92	35	632.74	35	1.00	NY	6.74	22	13.52
35	647.36	34	452.35	34	0.82	WIS	6.14	WIS	11.26
33	594.38	22	441.73	NY	0.81	22	5.00	77	8.91
21	559.01	NY	414.96	22	0.81	21	4.72	35	7.86
77	526.62	21	389.59	WIS	0.77	34	4.51	34	7.62
20	504.72	20	388.65	77	0.74	35	4.50	21	7.51
22	440.76	77	380.87	20	0.73	20	4.27	20	7.32
NY	435.99	33	343.17	33	0.71	33	3.80	NY	6.94
WIS	400.00	WIS	233.89	21	0.71	77	3.72	33	5.24

Table 3.25: Summary of results for 7% void mixtures tested at PGLT

DCT		SCB		SCB		IDT		IDT	
Mixture Rank	G_f [J/m ²]	Mixture Rank	G_f [J/m ²]	Mixture Rank	K_{IC} [MPa*m ^{0.5}]	Mixture Rank	Strength [MPa]	Mixture Rank	Stiffness [GPa]
34	476.18	21	336.51	35	0.88	NY	6.67	22	13.52
35	473.02	NY	301.34	NY	0.86	WIS	6.60	WIS	11.26
77	428.05	34	285.26	20	0.81	35	4.54	77	8.91
21	377.70	77	278.50	WIS	0.78	22	4.36	35	7.86
20	341.99	20	268.34	34	0.77	20	4.31	33	5.24
33	340.81	33	246.22	77	0.76	21	4.27	20	7.32
22	322.47	22	228.46	22	0.75	77	3.75	34	7.62
NY	302.70	35	217.61	33	0.74	34	3.61	21	7.51
WIS	237.00	WIS	190.86	21	0.66	33	3.14	NY	6.94

A better reading of the above tables is achieved through the overall ranking of each mixture. For this purpose, the average of the mixture's ranking (sum of all the mixture's rankings divided by the number of test parameters used for its characterization) was first computed. For example, the ranking test results shown in Table 3.22 can be reorganized as shown in Table 3.26. The numbers in the non-shaded cells represent the ranking of the mixtures indicated in the first

column of the table, according to the different test parameters. The second last column contains the average of the rankings. The lowest average rank value corresponds to the mixture which ranked the highest in the individual test rankings.

Table 3.26: Average rank for 4% void mixtures 4% void tested at PGLT+10°C

Mixture	DCT	SCB	SCB	IDT	IDT	Sum	Testing	Average	Overall
	G _f	G _f	K _{IC}	Strength	Stiffness	rank	parameters	rank	rank
20	7	3	1	3	6	20	5	4.00	3
21	4	5	8	5	5	27	5	5.40	6
22	3	7	4	6	6	26	5	5.20	5
33	6	6	5	8	8	33	5	6.60	8
34	1	2	3	4	4	14	5	2.80	2
35	2	1	2	2	2	9	5	1.80	1
77	5	4	6	7	7	29	5	5.80	7
WIS	8	8	7	1	1	25	5	5.00	4

The overall mixture rankings, corresponding to test results of the two test temperatures, were then summed up to produce a final ranking. Accordingly, the smallest value is associated with the mixture that ranked highest (performed best) in all individual test methods and test temperatures. The rankings according to this final overall rank of the mixtures are shown in Table 3.27 and Table 3.28. According to the overall ranking some mixtures, 35 and 34, at low temperature possess relatively high fracture resistance, strength and stiffness, without becoming brittle. This is particularly interesting finding suggests the following: when PPA is used to substitute part of the SBS, a mixture comparable to the SBS-only modified one with respect to fracture resistance is produced. Mixture denoted Wisconsin, exhibits reasonably high strength and toughness, but its relatively high stiffness leads to a relatively brittle type of fracture and thus small fracture energy. The PPA modified mixture has the least favorable response. The remaining mixtures exhibit intermediate behaviors.

Table 3.27: Overall ranking of mixtures with 4% void content

Mixture	Binder / Mix Type	Overall Rank
35	SBS	1
34	SBS + PPA	2
20	30% Non Fractioned, PG 58-28	3
WIS	Superpave E-30, WisDOT mix	4
21	30% Fractioned, PG 58-28	5
77	Elvaloy + PPA	6
22	30% Fractioned, PG 58-34	7
33	PPA	8

Table 3.28: Overall ranking of mixtures with 7% void content

Mixture	Binder / Mix Type	Overall Rank
35	SBS	1
34	SBS + PPA	2
22	30% Fractioned, PG 58-34	3
WIS	Superpave E-30, WisDOT mix	4
NY	"Typical Mix"	5
21	30% Fractioned, PG 58-28	6
77	Elvaloy + PPA	7
20	30% Non Fractioned, PG 58-28	8
33	PPA	9

Comparison of DCT and SCB Fracture Energy

As shown above, the ranking of the mixtures according to the DCT and SCB fracture energy showed fairly good agreement. The fracture energy results also appeared to be within similar range of values. A closer look at the relationship between DCT and SCB fracture energy is given through the correlation plots shown in Figure 3.19. The average DCT fracture energy of each mixture (in the x-axis) is plotted against the average SCB fracture energy (in y-axis). The inclined line represents identity line. For some of the mixtures the results correlated well, but in general the DCT test method predicted slightly higher fracture energy than SCB.

Notice, that for 4% void mixtures tested at PGLT+10°C, mixture 20 and 35 have higher SCB fracture energy than that of DCT. However, the accuracy of the SCB fracture energy result for these two mixtures, at the highest test temperature, is compromised by a high standard error obtained from only two valid test replicates. Therefore, the results from mixtures 20 and 35 were removed from the correlation analysis. Similarly, for the lowest test temperature (PGLT) analysis, mixture 77 is not considered. The Pearson correlation coefficients are indicated in the figures. Relatively good correlation is observed for mixtures compacted with 4% air voids content.

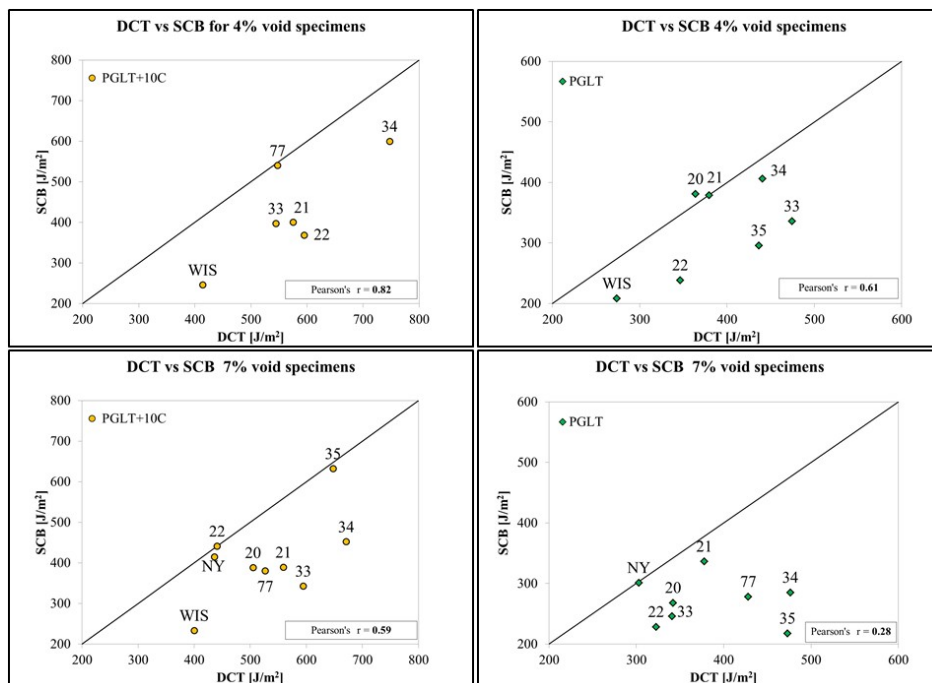


Figure 3.19: DCT vs. SCB correlation plots

Consider mixtures NY, 35, 34 and 77 at test temperature PGLT+10°C and air void content level 7%. The correlation points for the first two mixtures fall close to the identity line. The latter two, are located far from the identity line. Averaged load-CMOD and load-LLD curves for these mixtures are plotted below.

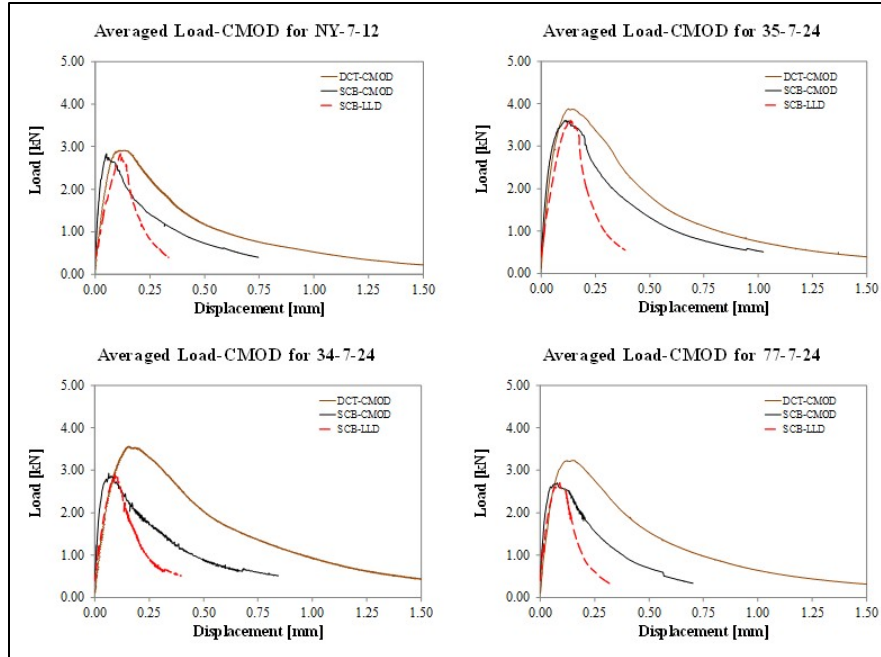


Figure 3.20: DCT and SCB load-displacement curves

By observing the plots, the following considerations can be drawn:

- The slope of the initial linear part of DCT load-CMOD curve is considerably similar to the slope observed in SCB load-CMOD and load-LLD curves.
- The post-peak softening described by DCT load-CMOD curves is strongly similar to the one described by the SCB load-CMOD curves.
- The similarity in the softening curves indicates that the tested materials undergo the same type of failure in both SCB and DCT. This in turn suggests that the lengths of fracture ligament of both test configurations induce similar post-peak behavior.
- The mixtures which showed high DCT to SCB correlation, NY and 35, have also similar peak loads in both DCT and SCB test results. On the contrary, in mixture 34 and 77 the SCB peak load is considerably lower than that of DCT. Therefore, it can be said that the discrepancy between DCT and SCB fracture energy is mainly related to the reduced peak load in SCB test method. The geometry, loading configuration, and significantly faster loading rate in DCT may be plausible reasons for higher peak load values. Other factors that may have affected the outcome are the value of the initial seating load and the reasonableness of fitting the tail of the softening curve. The initial seating load for DCT tests was set to be approximately 0.1kN. Whereas, for SCB was set at 0.5kN. In addition, for DCT was possible to run the tests until the initial seating load value of 0.1 kN was reached. Therefore, the tail of the curve was obtained without the need of fitting.

Finally, the DCT and SCB valid test results are plotted in Figure 3.21 and Figure 3.22, respectively, for specimens with 4% and 7% air voids content. In these plots, the effect of temperature was not considered. Equations that describe the reasonably linear relationship between the DCT and SCB fracture energy test results are also included in the plots.

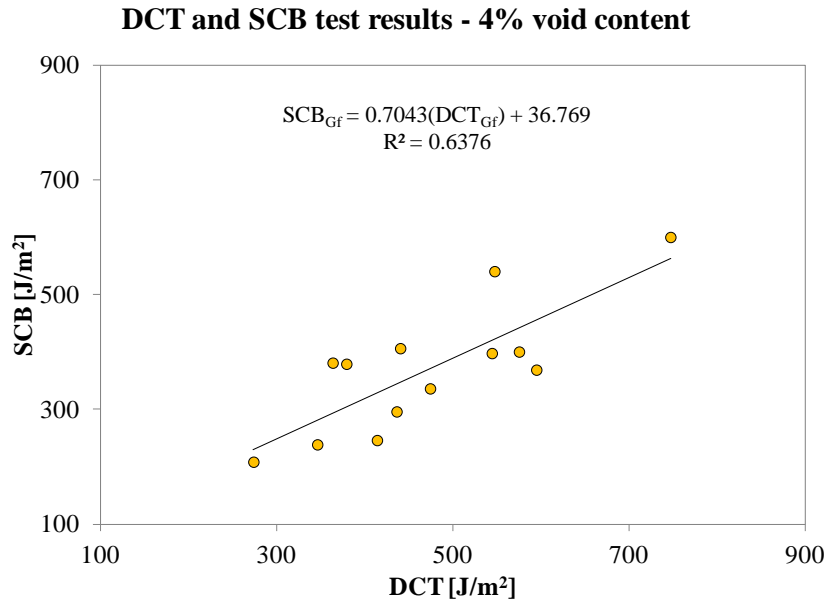


Figure 3.21: Correlation DCT and SCB fracture energy – 4%

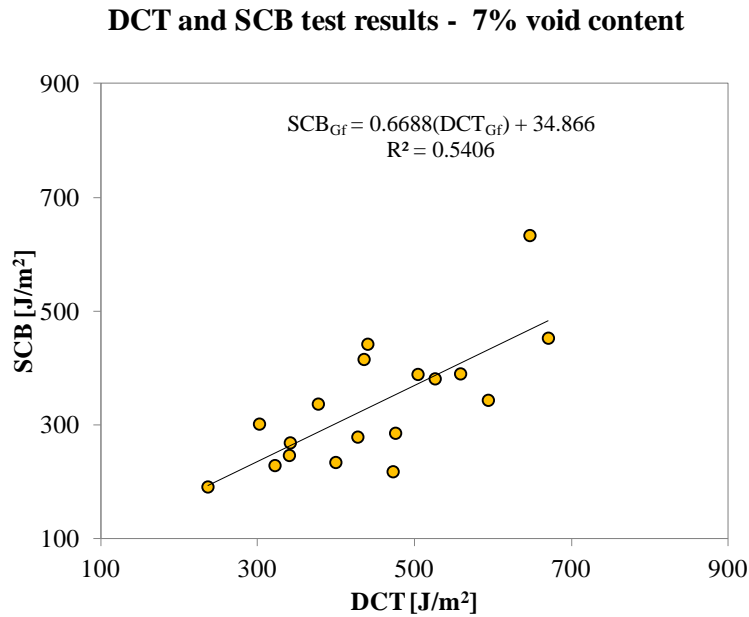


Figure 3.22: Correlation DCT and SCB fracture energy – 7%

Analysis of Results from Conditioned Laboratory Specimens and Field Cores

In this section the effect of aging on the fracture properties of the mixtures is investigated in both laboratory conditioned and field cored specimens. The laboratory conditioned specimens were held in oven for 5 days at 85°C prior to testing. The specimens considered for this investigation, were all compacted to 7% void content, and were tested at the lowest test temperature, PGLT. The field cores were also tested at the lowest test temperature.

Data Analysis of Test Results

The results are presented in Figure 3.23 to Figure 3.26. For comparison purposes, the laboratory compacted mixture results are also included in the figures.

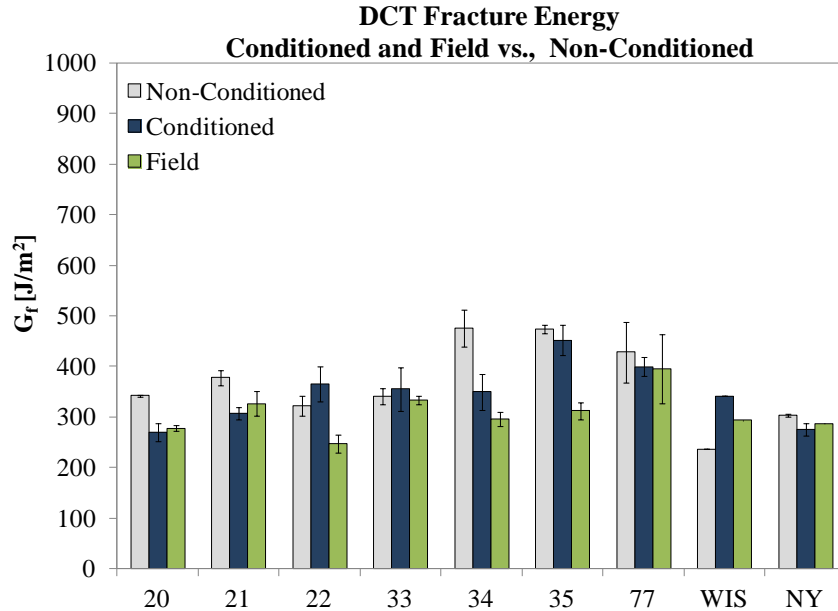


Figure 3.23: DCT fracture energy test results for conditioned and field samples

In Figure 3.23, the DCT fracture energy values for the field cores resulted are generally lower than the fracture energy values of non-conditioned laboratory specimens. On the other hand, when compared to the laboratory conditioned specimens, the field core results are comparable for mixtures 20, 21, 33, 77, and NY. While for mixtures 22, 34, 35, and WI the laboratory conditioned results are higher than the field ones.

By taking into account only the field results, it can be noticed that the Elvaloy + PPA modified mixture (mixture 77) has considerably higher fracture energy. The remaining mixtures are fairly similar. The SCB fracture energy results in Figure 3.24, indicates that the responses of field specimens are generally comparable to results of laboratory specimens (see mixture 20, 33, 34, 77, WIS, and NY). For mixture 35 the field fracture energy is unexpectedly higher than the laboratory ones. The results obtained from mixtures 20, 21, 33, and NY, appear to suggest that laboratory conditioning decreases the fracture energy. The opposite is observed for the remaining mixtures.

When only the field results are considered, the SBS and Elvaloy + PPA modified mixtures (mixtures 35 and 77) have the highest fracture energy.

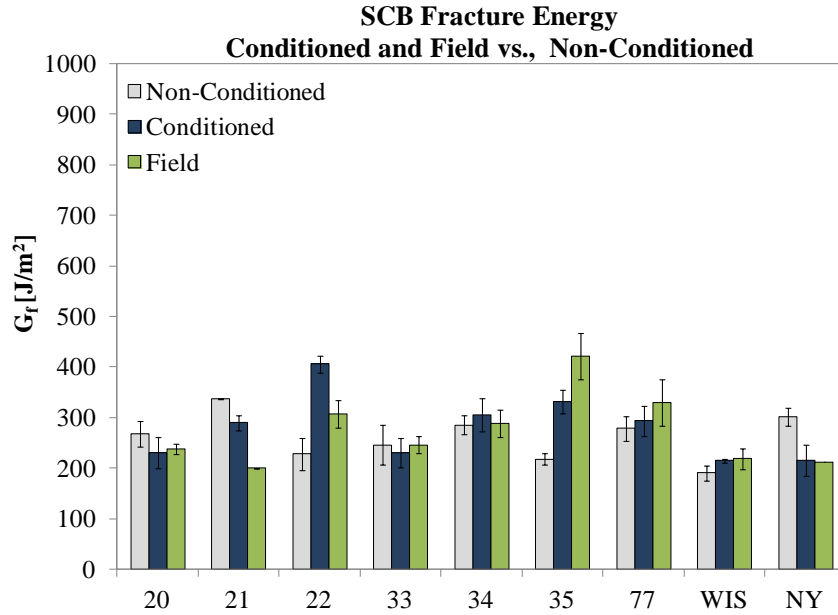


Figure 3.24: SCB fracture energy test results for conditioned and field samples

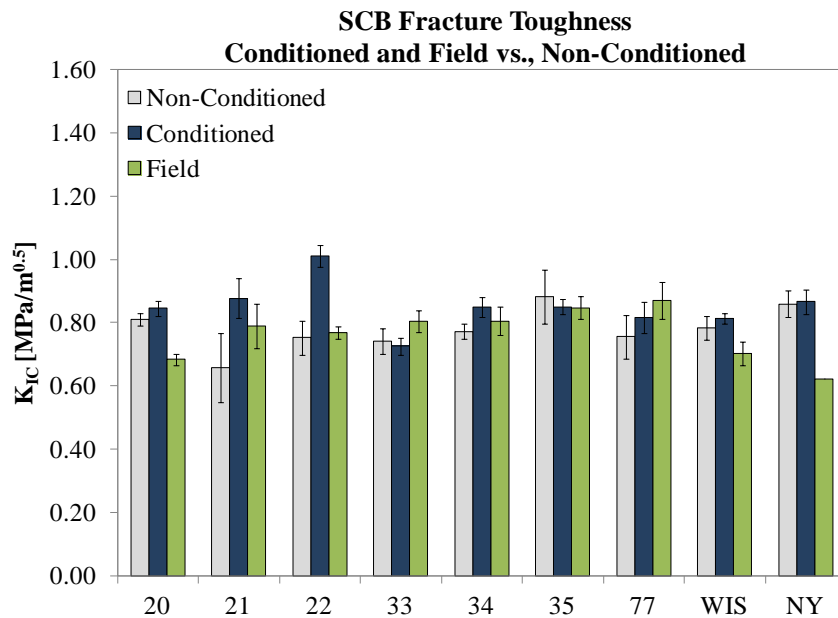


Figure 3.25: SCB fracture toughness test results for conditioned and field samples

In Figure 3.25, the fracture toughness of the field cores is compared to the fracture toughness of laboratory compacted specimens. The fracture toughness of field cores appears to be comparable to the fracture toughness of the non-conditioned laboratory samples of mixtures 22, 33, 34, and 35. The field toughness of mixtures 21 and 77 are higher than those of non-conditioned, while the contrary is observed for mixtures 20, WIS, and NY. The effect of laboratory conditioning is noticeable mainly in mixtures 21 and 22.

According to the fracture toughness of field cored specimens, although results are very similar, mixtures 35 and 77 distinguish with higher values.

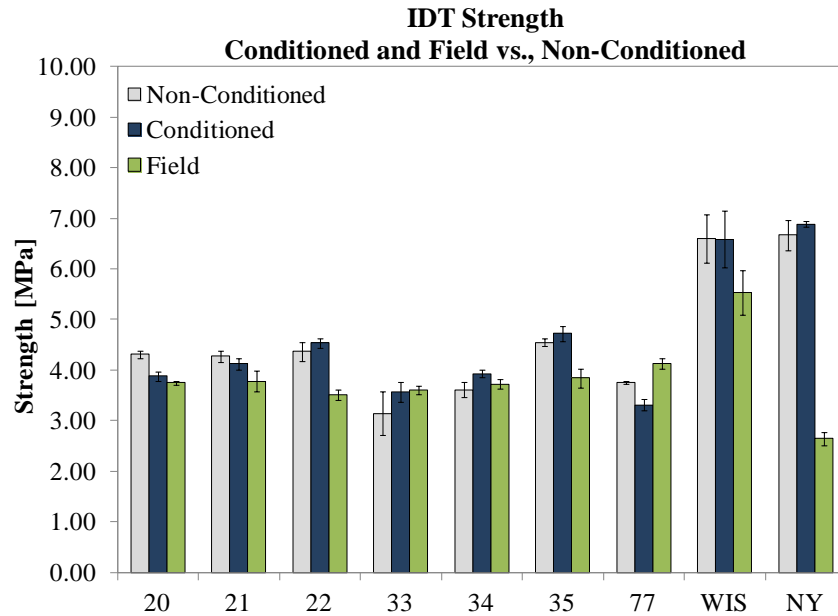


Figure 3.26: IDT tensile strength test results for conditioned and field samples

In Figure 3.26, the IDT strength responses of field and laboratory specimens are plotted and compared. Field strength results of mixtures 20, 21, 22, 33, 34, 35, and 77 appear to be similar. While mixtures WIS and NY have, respectively, the highest and the lowest IDT strength results. In addition, the plot shows that mixtures 22, 35, WIS, and NY from field have considerably softer smaller strength results compared to the laboratory compacted specimens.

Figure 3.27 reports the creep stiffness results. The field stiffness results for all mixtures, except 22 and WIS, are considerably higher than those obtained from non-conditioned laboratory specimens. Laboratory conditioning, on the other hand, produced mixed behavior: mixture 21, 33, 34, and 77 have become relatively stiffer due to conditioning, while in mixtures 20, 22, 35, WIS and NY occurred the inverse.

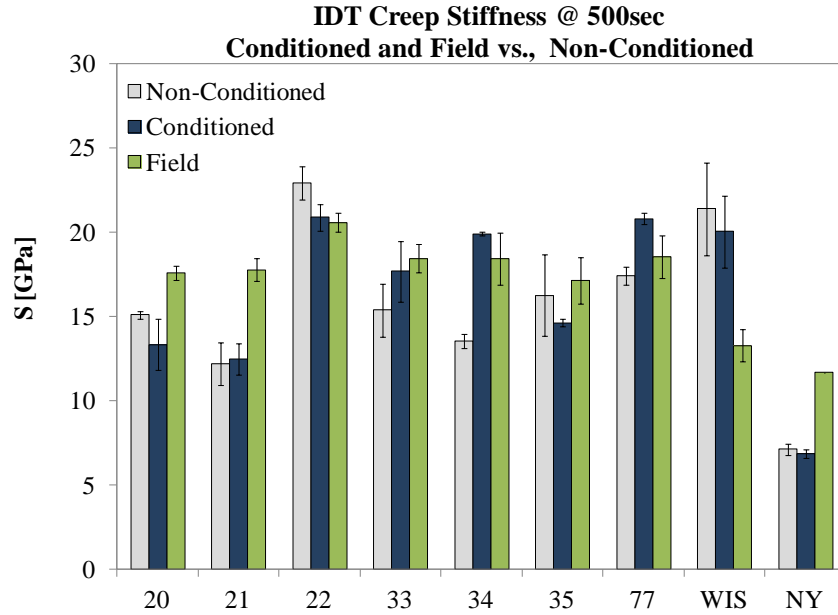


Figure 3.27: IDT stiffness test results for conditioned and field samples

Comparison of Field Cores and Laboratory Compacted Test Results

In Figure 3.28 to Figure 3.30 the results for the field specimens are plotted against the results for the laboratory specimens tested at PGLT. For comparison reason, the results of all 7% void content laboratory specimens are included.

For DCT and SCB the fracture energy results of conditioned laboratory specimens show good correlation to field results.

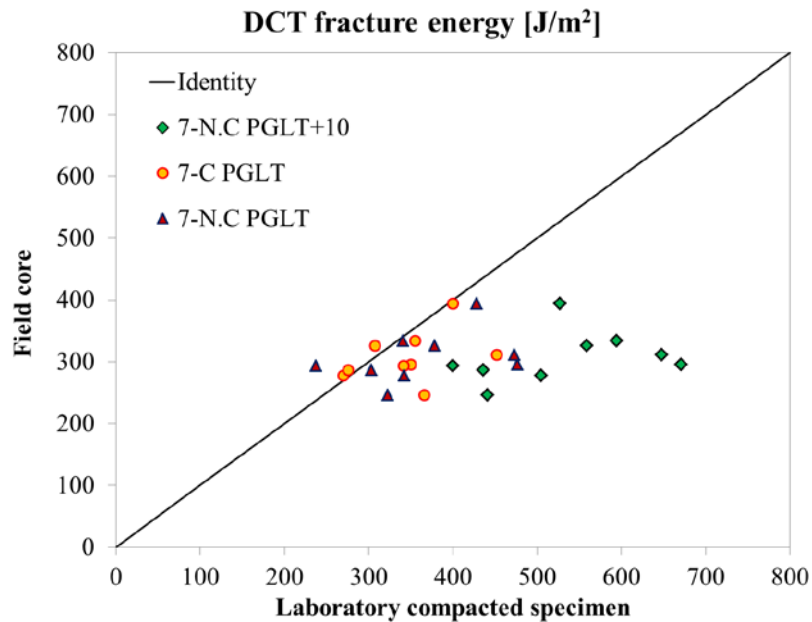


Figure 3.28: Results comparison field to laboratory compacted, DCT fracture energy

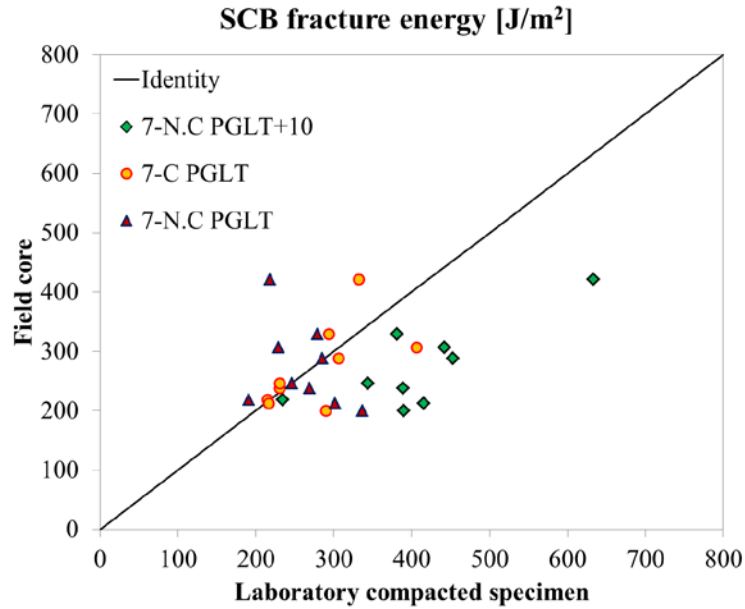


Figure 3.29: Results comparison field to laboratory compacted, SCB fracture energy

The SCB fracture toughness correlation points are dispersed and do not indicate any reasonable correlation.

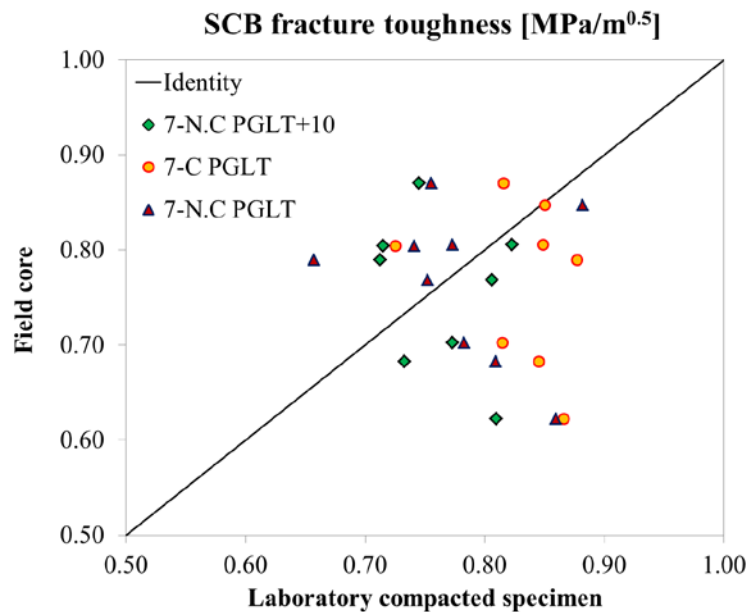


Figure 3.30: Results comparison field to laboratory compacted, SCB fracture toughness

IDT strength results, plotted in Figure 3.31, suggest relatively poor correlations between field and laboratory specimens. The correlation points are more dispersed and far from the identity line.

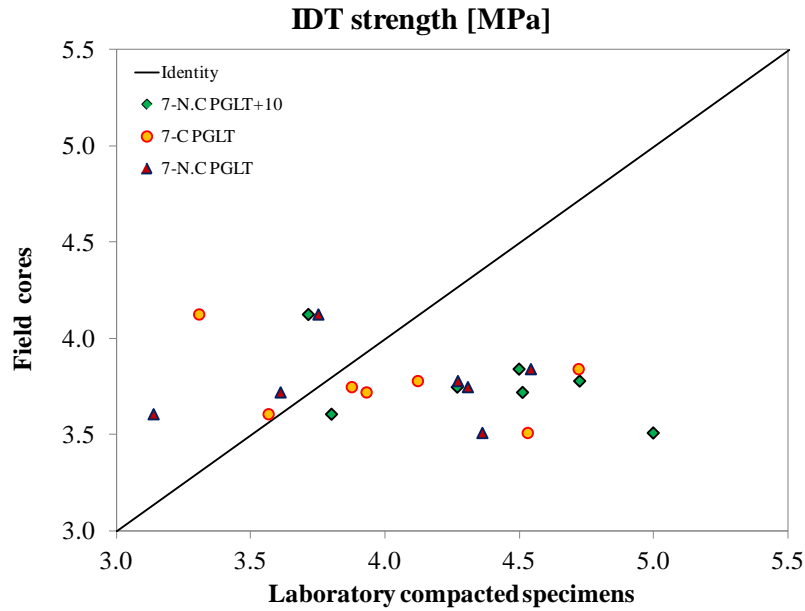


Figure 3.31: Results comparison field to laboratory compacted, IDT tensile strength

IDT stiffness results, plotted in Figure 3.32, indicated a reasonably linear correlation between the field and laboratory specimens tested at the lowest test temperature.

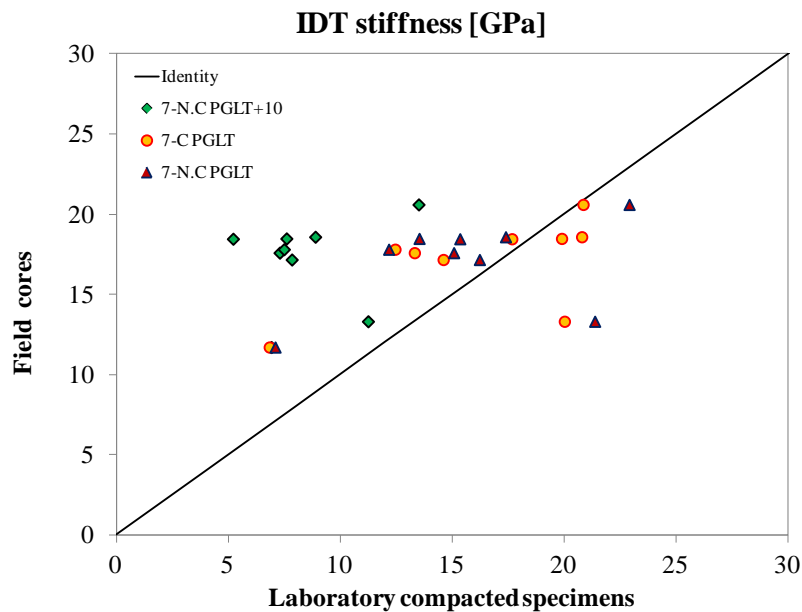


Figure 3.32: Results comparison field to laboratory compacted, IDT stiffness

Analysis of Variance (ANOVA) for Conditioned Samples

This ANOVA analysis compares conditioned samples at 7% air voids. The air voids are similar to field specimens. The conditioning duration is 5 days at 85°C, according to AASHTO R30-02 protocol. The samples are compared for DCT, SCB and IDT testing. The analysis is a

randomized complete block design. The blocking factor is the mix type. Each mix is different and test results cannot be compared without considering the differences for each mix. The factor of interest is the conditioning and how the conditioning treatment effects will impact the results of the test.

Blocking Factor	Treatment Condition
Mix	YES (Conditioned)
	NONE
	FIELD (Core)

Figure 3.33: RCBD statistical factors for comparison of conditioning

The air voids for this analysis is 7% in order for the conditioned samples and the control samples to appropriately match the air voids of the field cores. All testing was performed at the low temperature performance grade (LTPG). This is designated as “PG” in the raw data tables. The analysis in this section used data from only one laboratory in order to ensure that there were no confounding effects between the different laboratories for the test results. It was assumed that each category contains three test observations. The analysis also assumes that the results are independent and identically distributed, that the data follows a normal distribution and that the variances are equal.

DCT Conditioning Analysis

The DCT tests were performed at UIUC. The response variable for the DCT test is the fracture energy, G_f [J/m^2]. The analysis includes samples with 7% air voids and test temperatures of LTPG. The blocking factor is the mix and the conditioning is the factor of interest. The analysis shows that the differences in the mixes are statistically significant. This confirms the necessity of having an analysis that incorporates mix as a blocking factor. The conditioning is also statistically significant. The interaction of mix and conditioning has a p-value of greater than 0.05 but shows there may be some possible interaction. The interaction plots show no typical trend for each mix and conditioning combination and a clear visual interpretation of the interaction plot is not evident. The plot of residuals shows there may be a trend of higher variability as the G_f value increases. The Tukey HSD was performed for the mix and the condition variables. The Tukey HSD shows that no variable is statistically significant from all other treatments.

Table 3.29: Effects test for DCT G_f comparing conditioning

Effect Tests					
Source	Nparm	DF	Sum of Squares	F Ratio	Prob > F
Mix	8	8	165145.94	6.9792	<.0001*
Condition	2	2	30691.46	5.1882	0.0093*
Mix*Condition	16	16	84998.62	1.7961	0.0617

SCB Conditioning Analysis

The SCB tests for this analysis were performed at UMN. The samples were 7% air voids and tested at the PG of the binder. The response variables are K_{IC} [$MPa \cdot m^{0.5}$] and G_f [J/m^2]. Both response variables were analyzed. The blocking factor is the mix and the conditioning is the factor of interest.

KIC Response Variable

The analysis shows no statistical differences between the mixes and shows a statistical difference between the conditioning levels with conditioned samples having statistically significant higher K_{IC} values. The not-conditioned samples and field cores were not statistically different. The interaction of mix*conditioning has a statistically significant p-value but the interaction plots show no distinct trend.

Table 3.30: Effects test for SCB KIC conditioning comparison

Effect Tests					
Source	Nparm	DF	Sum of		
			Squares	F Ratio	Prob > F
Mix	8	8	0.08905108	1.6511	0.1327
Condition	2	2	0.11086832	8.2224	0.0008
Mix*Condition	16	16	0.30437418	2.8217	0.0024

SCB Fracture Energy Response Variable

The analysis for the fracture energy, G_f shows that there are statistical differences in the mix but shows no statistical differences in the conditioning. Table 3.31 shows the ANOVA table with effects tests. The conditioned samples have the highest average fracture energy but not conditioning treatment is statistically different. Mix number 35 has the highest average fracture energy when tested at 7% and at the low temperature PG.

Table 3.31: ANOVA for SCB conditioning

Analysis of Variance					
Source	DF	Sum of		F Ratio	Prob > F
		Squares	Mean Square		
Model	26	203890.11	7841.93	2.2509	
Error	50	174198.63	3483.97		Prob > F
C. Total	76	378088.74			0.0069

Effect Tests					
Source	Nparm	DF	Sum of		
			Squares	F Ratio	Prob >
Mix	8	8	107283.52	3.8492	0.0014
Condition	2	2	2130.49	0.3058	0.7379
Mix*Condition	16	16	91864.68	1.6480	0.0904

IDT Conditioning Analysis

The IDT tests were performed at UMN at 7% air voids at the low PG temperature. The blocking factor is the mix and the conditioning is the factor of interest. The IDT procedures recorded measurements of stiffness and strength. The stiffness at 500 seconds is used in the analysis and the peak tensile strength.

Stiffness at 500 Seconds Conditioning Analysis

The creep stiffness at 500 seconds shows that the mix is a statistically significant factor and the interaction of mix and conditioning is statistically significant. Table 3.32 shows the ANOVA table for the IDT which displays which factors are statistically impacting the results. The conditioning is not impacting the values statistically. On average, the field mixes show the highest average stiffness. The interaction plot of mix and conditioning show that conditioning will impact the tested mixes in different ways and a single trend applicable to all mixes is not present. The NY mix showed the lowest stiffness and was statistically lower than all other mixes. The plot of residuals indicated that as creep stiffness increased, the variability in the values increased.

Table 3.32: ANOVA for IDT conditioning comparison

Analysis of Variance					
Source	DF	Sum of Squares	Mean Square	F Ratio	
Model	26	1301.1090	50.0427	6.3077	
Error	54	428.4157	7.9336		Prob > F
C. Total	80	1729.5247			≤.0001

Effect Tests					
Source	Nparm	DF	Sum of Squares	F Ratio	Prob >
Mix	8	8	1001.4226	15.7781	≤.0001
Conditioning	2	2	9.9973	0.6301	0.5364
Mix*Conditioning	16	16	289.6890	2.2821	0.0125

IDT Peak Strength Conditioning Analysis

The peak strength analysis shows that the mix, conditioning and the interaction of mix and conditioning are statistically significant. The interaction plot shows the laboratory conditioned and non-conditioned samples follow similar patterns and the field is different. The interaction is significant because the effects of conditioning on the samples are not the same for all mixes. The field cores show statistically significant lower peak strength values. The ANOVA table, Table 3.33, gives a summary of the important factors. Table 3.34 gives the Tukey multiple comparison test which rank the treatment effects and shows whether there are statistical differences.

Table 3.33: IDT peak strength conditioning analysis

Analysis of Variance					
Source	DF	Sum of Squares	Mean Square	F Ratio	Prob > F
Model	26	100.64316	3.87089	25.0405	
Error	52	8.03843	0.15459		
C. Total	78	108.68159			≤.0001

Effect Tests					
Source	Nparm	DF	Sum of Squares	F Ratio	Prob > F
Mix	8	8	58.184953	47.0492	≤.0001
Conditioning	2	2	10.405631	33.6566	≤.0001
Mix*Conditioning	16	16	31.371292	12.6837	≤.0001

Table 3.34: IDT peak strength conditioning Tukey’s comparison

LSMeans Differences Tukey HSD		
α=	0.050	2.4126
		Least
Level		Sq Mean
YES A		4.6161111
NONE A		4.5842593
FIELD B		3.8333333

Levels not connected by same letter are significantly different.

Comparison of Air Voids and Test Temperature

This is a split plot analysis meaning that there are “whole plots” and “sub plots” considered in the design of the experiment. There are also “whole plot factors” and “sub plot factors”. The whole plots are the different mixes. The whole plot factor for this experiment is the air void levels of 4% and 7%. The subplots are the mix at a particular air void content. The sub plot factor is the testing temperature of the mix, which occurs at either the low temperature performance grade, designated PG, or 10°C warmer than the low temperature grade, designated PG+10. The alpha level of significance was taken as $\alpha=0.05$.

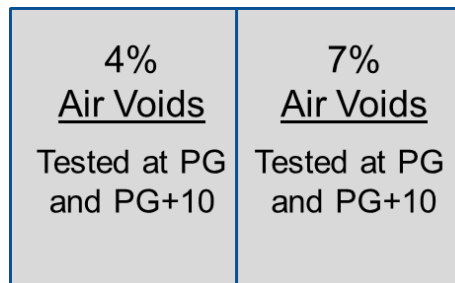


Figure 3.34: Variables and treatment combinations for each mix in the split plot analysis

This analysis is conducted for the DCT, SCB and IDT testing results.

DCT Air Void and Temperature Analysis

The ANOVA analysis shows that the mixes and the temperatures are statistically different while the difference between 4% and 7% were not significant. The differences between mixes with samples treated the same is statistically significant and the interaction of test temperature and air voids is significant. The mixes of NY and WI appear to have a larger decrease in fracture energy between 4 and 7% air voids compared to the other mixes and this is the reason the interaction of air voids and temperatures is significant. The ANOVA table is shown in Table 3.35. The Tukey HSD multiple comparison test, Table 3.36, showed that no statistical difference was found between air voids at the lower testing temperature but a difference between 4% and 7% air voids was distinguished for a test temperature 10 degrees above the low temperature PG grade. The full JMP output is provided in Appendix A.

Table 3.35: DCT ANOVA and random effects for temperature and air voids

Analysis of Variance					
Source	DF	Sum of Squares	Mean Square	F Ratio	Prob >
Model	18	1409592.3	78310.7	14.53	
Error	79	425778.0	5389.6		Prob >
C. Total	97	1835370.4			≤.0001

Tests wrt Random Effects					
Source	SS	MS Num	DF Num	F Ratio	Prob >
Air Voids (%)	66430	66430	1	1.2346	0.2840
Mix[Air Voids (%)]&Random	810437	54029.1	15	10.0247	≤.0001
Relative Temp	585141	585141	1	108.5685	≤.0001
Relative Temp*Air Voids (%)	1018.81	1018.81	1	0.1890	0.6649

Table 3.36: Tukey HSD multiple comparison for DCT

LSMeans Differences Tukey HSD			
α=	0.050	2.62457	
Level		Least Sq Mean	
PG+10,4	A	568.92250	
PG+10,7	B	510.12185	
PG,4	C	407.15959	
PG,7	C	361.31796	

Levels not connected by same letter are significantly different.

SCB Air Void and Temperature Analysis

Data from the testing at UMN was used in this portion of the analysis. The asphalt modifiers and RAP are considered in the blocking of the mixes. The K_{IC} values and SCB fracture energy, G_f , are analyzed for SCB testing that was performed at 4% and 7% air voids at the LTPG and LTPG+10.

SCB K_{IC} Analysis

The ANOVA analysis, Table 3.37, shows that air voids, temperature and the interaction of temperature and air voids are significant. The Tukey analysis, Table 3.38, shows that the samples are more sensitive to temperature change at a lower air void content and overall, 7% K_{IC} is statistically smaller than 4%.

Table 3.37: SCB ANOVA and random effects

Analysis of Variance					
Source	DF	Sum of Squares	Mean Square	F Ratio	P-Value
Model	18	0.8252002	0.045844	5.0	<0.0001
Error	79	0.7132528	0.009029		
C. Total	97	1.5384531			

Tests wrt Random Effects					
Source	SS	MS Num	DF Num	F Ratio	P-Value
Air Voids	0.52602	0.52602	1	34.2528	<0.0001
Mix[Air Voids]&Random	0.23195	0.01546	15	1.7127	0.06
Relative Temp	0.04693	0.04693	1	5.1982	0.02
Relative Temp*Air Voids	0.03585	0.03585	1	3.9712	0.04

Table 3.38: Tukey HSD for SCB K_{IC} analysis for air void and temperature

LSMeans Differences Tukey HSD		
$\alpha =$	0.0500	2.62457
Least Sq Mean		
Level		
PG,4	A	0.96553861
PG+10,4	B	0.88287806
PG,7	C	0.77888889
PG+10,7	C	0.77333333

Levels not connected by same letter are significantly different.

SCB G_f Analysis

The ANOVA analysis for the fracture energy, Table 3.39, shows statistical differences between the various mixes and test temperatures. The air voids also have a low p-value, just above 0.05. The interaction of air voids and temperature is not significant. No single test temperature and air void combination is statistically different from all other combinations but there is a clear trend in the multiple comparison testing, Table 3.40. The full JMP output is shown in Appendix A.

Table 3.39: SCB Gf ANOVA and random effects analysis for air voids and temperature

Analysis of Variance					
Source	DF	Sum of Squares	Mean Square	F R	Prc
Model	18	973561.7	54086.8	4.6	
Error	78	915083.4	11731.8		Prc
C. Total	96	1888645.1			≈.00

Tests wrt Random Effects					
Source	SS	MS Num	DF Num	F Ratio	Prc
Air Voids	117712	117712	1	4.4778	0.05
Mix[Air Voids]&Random	397823	26521.5	15	2.2606	0.01
Relative Temp	466915	466915	1	39.7990	≈.00

Table 3.40: SCB Gf Tukey analysis for air voids and temperature

LSMeans Differences Tukey HSD		
α=	0.050	2.62529
Level		Least Sq Mean
PG+10,4	A	475.19770
PG+10,7	A B	405.42926
PG,4	B C	336.01063
PG,7	C	264.95827

Levels not connected by same letter are significantly different.

IDT Air Void and Temperature Analysis

UMN performed the testing on the data for the IDT analysis. The split plot experimental design was used to perform the analysis for the stiffness and the peak strength.

Stiffness at 500 Seconds

The ANOVA analysis shows that the mixes and testing temperatures are statistically significant. The air voids show some differences with a p-value of 0.0552. The average stiffness at PG was significantly higher than at the testing temperature of PG+10. There was a larger distinction between air voids at the lower PG testing temperature than at PG+10. The interaction of temperature and air voids is not statistically significant. The ANOVA summary, Table 3.41, and Tukey HSD multiple comparisons, Table 3.42 are shown and the full JMP analysis is provided in Appendix A.

Table 3.41: IDT Stiffness ANOVA and random effects analysis for air voids and temperature

Analysis of Variance					
Source	DF	Sum of Squares	Mean Square	F Ratio	Prob > F
Model	18	2450.6983	136.150	11.7111	
Error	81	941.6860	11.626		
C. Total	99	3392.3843			≤.0001

Tests wrt Random Effects					
Source	SS	MS Num	DF Num	F Ratio	Pr
Air Voids	152.546	152.546	1	3.9566	0.04
Mix(Air Voids)&Random	581.186	38.7457	15	3.3327	0.00
Relative Temp	1690.47	1690.47	1	145.4070	≤.0
Relative Temp*Air Voids	16.9607	16.9607	1	1.4589	0.23

Table 3.42: IDT Stiffness Tukey analysis for air voids and temperature

LSMeans Differences Tukey HSD		
α=	0.0500	2.62318
		Least Sq Mean
PG,4	A	19.630417
PG,7	B	16.318148
PG+10,4	C	10.533136
PG+10,7	C	8.877407

Levels not connected by same letter are significantly different.

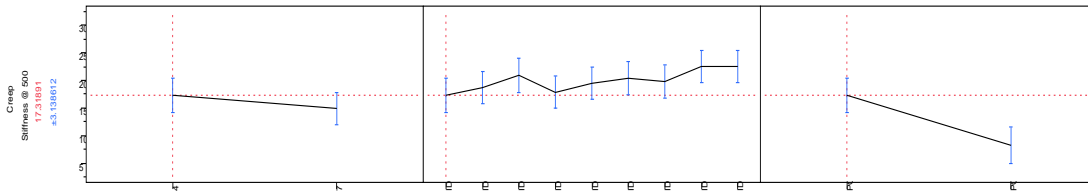


Figure 3.35: IDT stiffness data trends with 95% confidence interval

Peak Strength

The peak strength analysis shows that mix and relative temperature are statistically significant but there is not a distinguishable difference between 4 and 7% air voids. The averages show the PG+10 having a slightly higher strength than the LTPG. The ANOVA table, Table 3.43, and Tukey HDS multiple comparisons, Table 3.44, are shown as well as a graph, Figure 3.36, showing the trends in peak strength among variables.

Table 3.43: IDT strength ANOVA and random effects analysis for air voids and temperature

Analysis of Variance					
Source	DF	Sum of Squares	Mean Square	F Ratio	Prob
Model	18	101.03312	5.61295	23	
Error	78	18.47766	0.23689		
C. Total	96	119.51078			

Tests wrt Random Effects					
Source	SS	MS Num	DF Num	F Ratio	Prob
Air Voids	8.96788	8.96788	1	1.5016	0.239
Mix[Air Voids]&Random	90.4405	6.02937	15	25.4518	<.000
Relative Temp	2.04034	2.04034	1	8.6129	0.004
Relative Temp*Air Voids	0.04088	0.04088	1	0.1726	0.679

Table 3.44: IDT Strength Tukey analysis for air voids and temperature

LSMeans Differences Tukey HSD		
$\alpha =$	0.0500	2.62529
Level		Least Sq Mean
PG+10,4	A	5.4829505
PG,4	A B	5.1491667
PG+10,7	B C	4.8288372
PG,7	C	4.5778295

Levels not connected by same letter are significantly different.

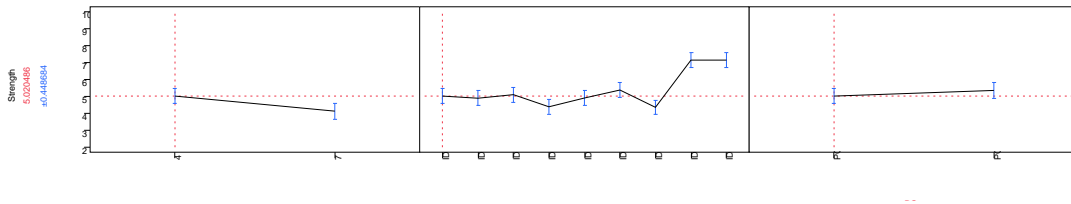


Figure 3.36: IDT Strength data trends with 95% confidence interval

Comparison of Experimental Results Obtained at UIUC and UMN

As mentioned in the introduction, DCT test were performed at UMN for three randomly selected mixtures. Likewise, SCB tests were performed at UIUC for three randomly selected mixtures. The results are discussed next.

Reproducibility of DCT tests

Three mixtures were randomly selected and DCT tested at UMN using the same procedures and specification used by the UIUC research team. The mixtures tested at UMN were 20, 21, and 22. Comparison of the results is shown in Figure 3.37.

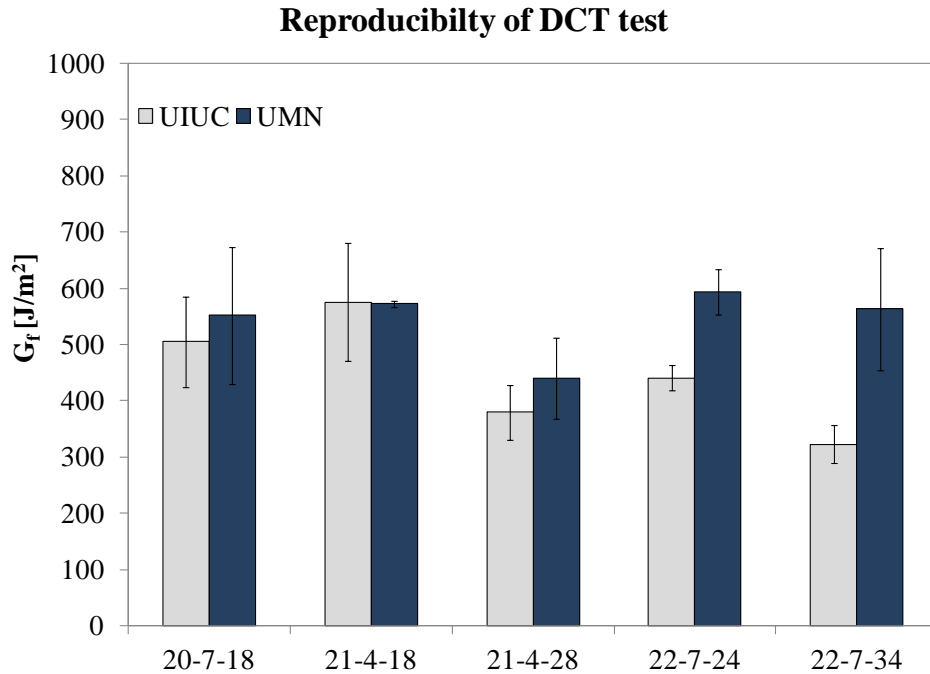


Figure 3.37: Comparison DCT test result from UMN and UIUC

Overall, the results appear to be in good agreement, except for mixture 22. To understand the reason for the considerable discrepancies in mixture 22, the test results were investigated further. The Load vs. CMOD and the CMOD vs. Time plots for the three replicates of mixture 22, that has the highest difference, are shown in Figure 3.38.

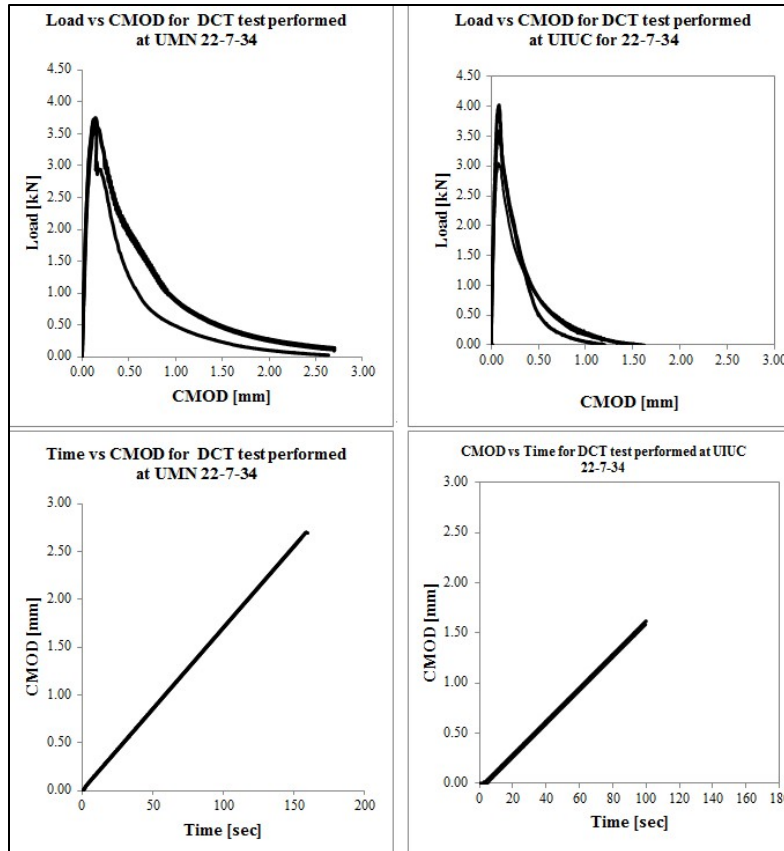


Figure 3.38: Load vs. CMOD and time vs. CMOD plots

The Load-CMOD curves presented in the Figure 3.39 show that post-peak curve from UMN test data decreases slower than the post-peak curves from UIUC. The registered peak loads are also slightly higher for UIUC performed tests. The CMOD vs. Time plots were also produced to check for a possible cause of the discrepancy. For the tests performed at UMN, time was recorded for each test. In the test data obtained from UIUC, time was not provided. Thus, a time column were calculated based on sampling rate of 50Hz, as indicated by UIUC researches.

The analysis of the DCT laboratory comparison is a split plot experimental design but there are different factors considered compared with the other split plot analyses. Since each mix that was tested had the same air void content within that mix, the variability of the air voids is already considered in the error term of the mix. For this experiment the whole plots are the different university laboratories. The whole plot factor is the various mixes that each laboratory tested. The sub plot is the mixes tested at each of the university laboratories and the subplot factor is the test temperature of PG or PG+10°C. The factors are shown in Figure 3.39.

UIUC		UMN	
MIX 20, 21, 22		MIX 20, 21, 22	
PG	PG+10°C	PG	PG+10°C

Figure 3.39: Split plot design for comparing DCT results between laboratories

The analysis for the DCT testing showed that there are statistical differences between the two laboratories. The full ANOVA table is shown below in Table 3.45. The Tukey HSD comparison, Table 3.46, shows the combination of laboratory and mix gives the most information. This shows where the differences are and which mixes were the most different. DCT 22 gave the largest difference between the two laboratories and DCT 21 showed the least difference. Mix 21 was tested at 4% air voids and showed less difference than the other mixes which had 7% air voids. It may be beneficial to do a multiple laboratory comparison changing the air voids of the same mix and testing at various laboratories. On average, UMN had higher DCT G_f values than samples tested at UIUC laboratories. The variability of test results within each lab should be evaluated. Figure 3.40 gives a graphical comparison of the residuals for each set of data. The residuals help to display variability from the mean value as a measure of data variability. Since only two laboratories were evaluated, it may be useful in the future to perform a set of round robin testing among additional laboratories as a further measure of multi-lab variability for the DCT test.

Table 3.45: ANOVA and random effects comparisons of DCT testing

Analysis of Variance						
Source	DF	Sum of Squares	Mean Square	F Ratio		
Model	8	269019.40	33627.4	4.3282		
Error	27	209774.91	7769.4		Prob > F	
C. Total	35	478794.31			0.0019	

Tests wrt Random Effects						
Source	SS	MS Num	DF Num	F Ratio	Prob >	
Mix-AV	7244.42	3622.21	2	0.0598	0.9431	
University[Mix-AV]&Random	181828	60609.4	3	7.8010	0.0007	
Relative Temp	76196.2	76196.2	1	9.8072	0.0042	
Mix-AV*Relative Temp	3750.57	1875.29	2	0.2414	0.7872	

Table 3.46: DCT testing Tukey HSD comparison of laboratories and mixes

LSMeans Differences Tukey HSD		
$\alpha =$	0.050	3.06385
Level		Least Sq Mean
[DCT-22-7%AV]UMN	A	578.28000
[DCT-20-7%AV]UMN	A	552.72833
[DCT-21-4%AV]UMN	A	549.29667
[DCT-21-4%AV]UIUC	A B	477.22167
[DCT-20-7%AV]UIUC	A B	423.35500
[DCT-22-7%AV]UIUC	B	381.61500

Levels not connected by same letter are significantly different.

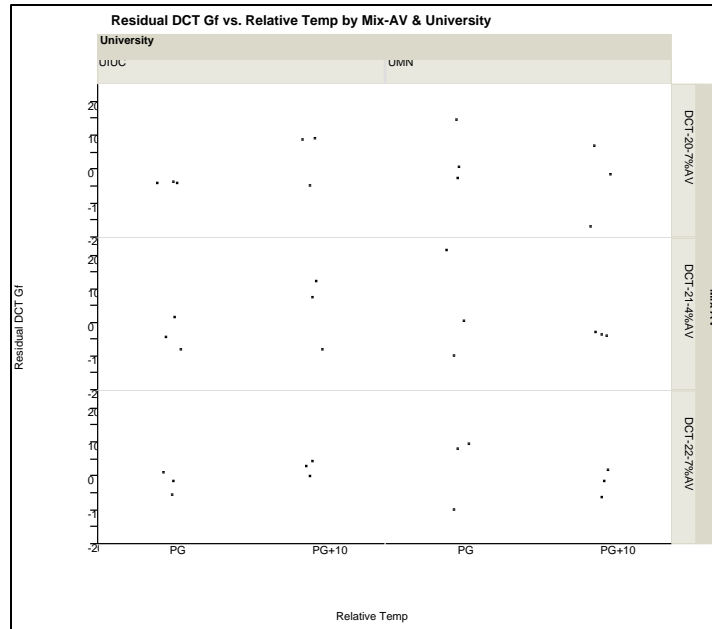


Figure 3.40: DCT comparison of residual plots

Reproducibility of SCB Tests

Three randomly selected mixtures were SCB tested at UIUC. The mixtures tested were mixture 35 at two different void contents, and mixture ‘NY’. The fracture energy results shown in Figure 3.41 indicate relatively small differences between UIUC and UMN results. However, it must be noted that the SCB test performed at UIUC did not use LLD measurements. Instead, the displacement of the loading piston, recorded through its LVDT, was used.

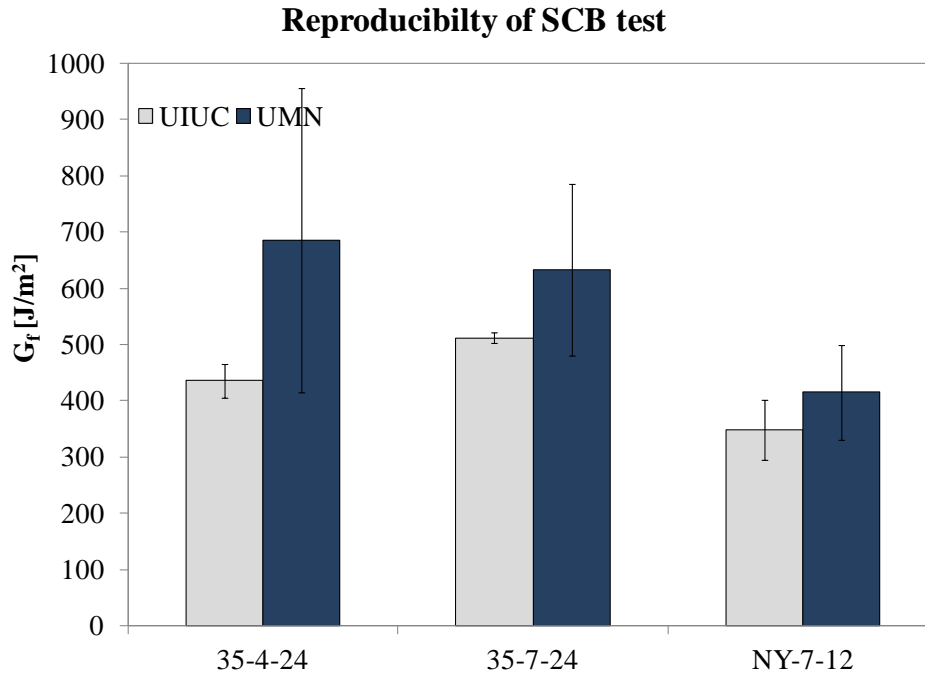


Figure 3.41: Comparison SCB test result from UMN and UIUC – fracture energy

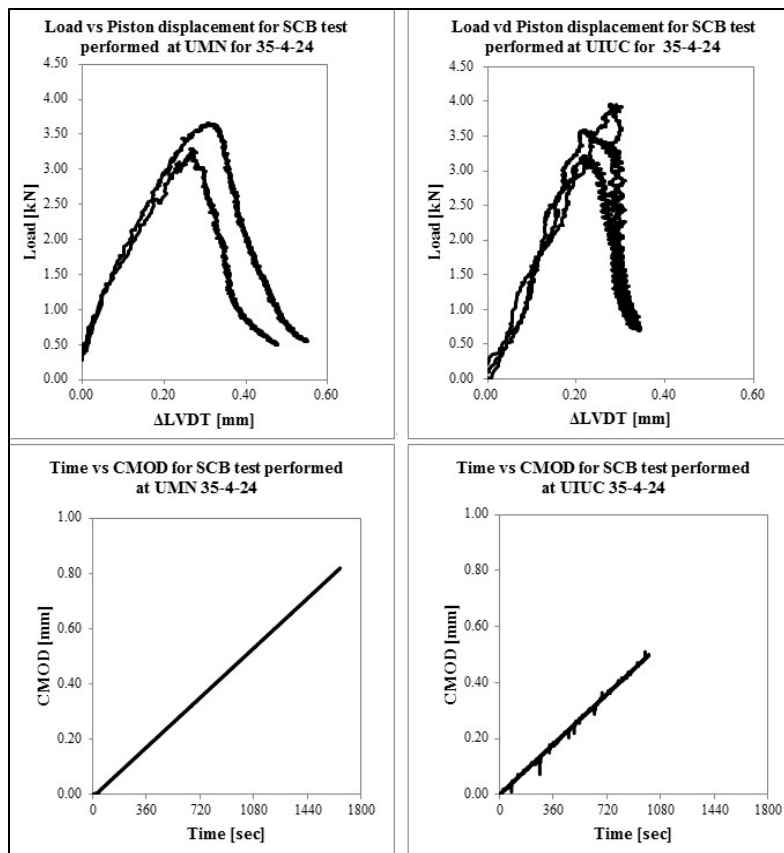


Figure 3.42: Load vs. CMOD and time vs. CMOD plots

The fracture toughness values of the mixtures were also computed from the test data obtained from UIUC and compared to the test performed at UMN. The results are reported in Figure 3.43. For fracture toughness the results are in good agreement.

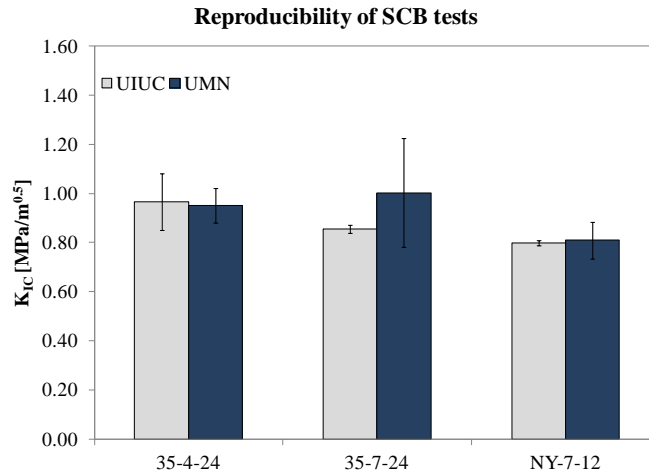


Figure 3.43: Comparison SCB test result from UMN and UIUC – fracture toughness

A full factorial experimental analysis was not performed because the NY could not be compacted to 4% and the split plot analysis could not be used. A graph of the data was created to show the variability and differences between the data within each category. The SCB-NY mix was the most comparable of the mixes between the two laboratories. The UMN laboratory has more variability with the SCB-35 mix at 4 and 7% air voids as shown in Figure 3.44.

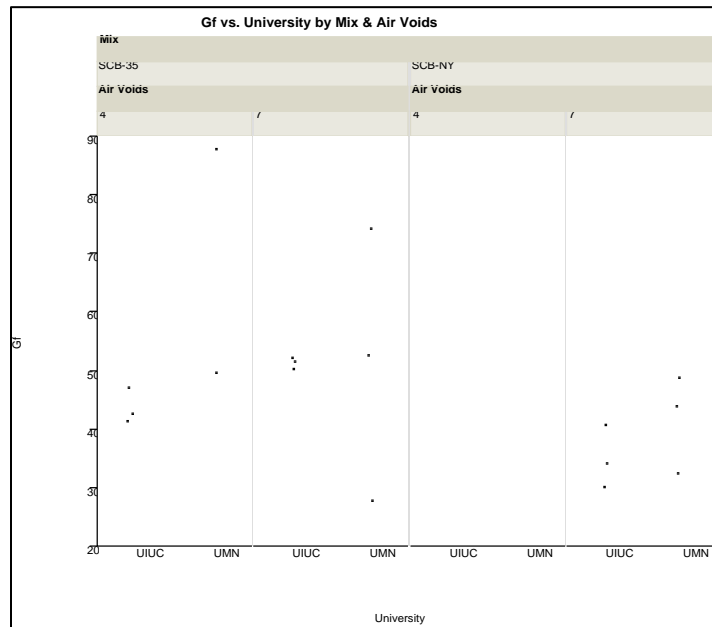


Figure 3.44: Comparison of SCB test data

Statistical Analysis Conclusions

The conditioning blocked by mix showed there is not an overall trend to predict exactly how the conditioning will impact a mix. The various tests showed some statistical differences were found. Four of the five tests ranked the averages, from highest to lowest, as “conditioned”, “no conditioning” and “field cores”. The DCT ranked the conditioning in the order of “no conditioning”, “conditioned” and “field”; however, no treatment effect was different from all of the rest. The IDT strength and SCB KIC designated statistical differences between conditioning treatment effects. The mixes used in the analysis were ranked by their average test results and compared. The DCT and SCB results correlate the best but no mix is statistically different from all other mixes. The test that appears to show the ability to best distinguish statistical rankings between mixes is the IDT but the stiffness and strength results are not well correlated and the IDT shows different trends from the DCT and SCB mix rankings.

The purpose of the air void-temperature analysis is to show how the test temperature and air voids impact the results for each mix in the various tests performed. The DCT results are more sensitive to temperature than to air voids. The data shows the air void levels of 4 and 7% are statistically different when tested at PG+10°C but are not statistically different when tested at LTPG. This trend is also documented in the IDT stiffness testing results. Temperature had the largest impact on the testing data overall.

The laboratory comparison showed that UMN had higher DCT values on average. The mix with 4% air voids showed a good comparison between the laboratories. The SCB comparison showed a good correlation with SCB-NY but mix 35 showed high variability in testing at UMN. Further testing and comparisons are needed in order to make a complete comparison between the laboratories.

Summary of Findings

The main objective of the research investigation was to characterize the low-temperature fracture properties of modified asphalt mixtures by means of traditional and newly developed experimental procedures. The set of mixtures included Recycled Asphalt Pavement (RAP) mixtures, Poly-Phosphoric Acid (PPA) modified mixtures, and polymer modified mixtures (SBS, and Elvaloy). Nine laboratory compacted asphalt mixtures were tested at low temperatures using Indirect Tensile (IDT), Semi-Circular Bend (SCB), and Disc-Shaped Compact Tension (DCT) test protocols. The effect of aging was also investigated by conditioning the mixtures for 5 days at 85°C. In addition, field specimens cored from MnROAD test cells, were tested and compared to the laboratory asphalt mixtures.

A summary of the findings from the research performed in this task are presented next.

- The DCT and SCB fracture energy predictions showed reasonably good agreement. Nevertheless, the DCT results are generally slightly higher. Analysis of the load-displacement curve suggests that such scatter can be attributed to slightly higher peak load observed in DCT tests.
- The fracture energy results for non-conditioned laboratory compacted mixtures ranged from approximately 190 J/m² to 800 J/m². The values obtained at PGLT+10°C were

always larger than those obtained at PGLT. Overall, the effect of the air void content on fracture energy appeared to be minimal.

- The SCB fracture toughness values varied from 0.45 to 1.20 MPa*m^{0.5}. For specimens with 4% air void content, the fracture toughness value increased when temperature decreases. Contrarily to fracture energy, the KIC results suggest testing temperature has a minimal effect.
- The IDT tensile strength ranged from 2.30 to 7 MPa. The strength was higher for mixtures with lower air void content. In addition, except for a few mixtures, the strength values obtained at PGLT+10°C were higher than the values obtained at PGLT. The NY and Wisconsin mixtures had significantly higher strength than all the other mixtures tested at the same conditions. Please note that this is the mixture that could not be compacted to 4% air voids.
- A simple overall ranking of the mixtures is also proposed. According to the ranking the PPA+ SBS and SBS modified mixtures (34 and 35) possess relatively high fracture resistance, strength and stiffness. These mixtures demonstrated relatively high ductility associated with considerable strength and stiffness. On the other hand, mixture Wisconsin, exhibited reasonably high strength and toughness, but failed in a relatively brittle manner for small fracture energy values. The PPA modified mixture had the least favorable response. The remaining mixtures exhibited intermediate behaviors.
- For field cores, the SBS and Elavoloy+PPA modified mixtures exhibited higher fracture properties. When strength was instead considered, mixture Wisconsin has the highest response. The difference among the other mixtures can be considered minimal.
- A comparison between laboratory mixtures and field cores was performed by means of correlation plots. Generally, the laboratory conditioned specimens best correlated to the field results.
- The reproducibility of both SCB and DCT test, evaluated from limited comparison of test performed at UMN and UIUC, indicated highly favorable outcome.

Chapter 4. Subtask on Physical Hardening

Introduction

Physical hardening in asphalt binders was first observed during the Strategic Highway Research Program (SHRP) contract A002-A (1, 2). The phenomenon was called physical hardening by the SHRP researchers (2) to avoid confusion with oxidative aging and to emphasize the reversibility of the phenomenon. It was shown that this phenomenon causes an increase in the asphalt binder stiffness when stored at a constant low temperature. Such isothermal age-hardening has been known for plastics, polymers, and other amorphous solids, but it has been neglected in standard protocols and specification for asphalt binders.

The discovery of physical hardening during the SHRP program resulted in a requirement in the M320 specification (3) of testing in the Bending Beam Rheometer (BBR) after 1 and 24 hours. Although this requirement was not implemented, recent work by Hesp and Subramani (4) has shown that better correlations with field performance are observed if physical hardening is taken into account. One of the main reasons physical hardening has been neglected is the absence of a reliable and simple procedure to estimate the changes in properties (e.g., creep stiffness and m -value) of binders caused by this phenomenon from relatively short and simple laboratory tests.

This section summarizes a comprehensive investigation on the effect of binder source, modification (e.g., Polyphosphoric Acid, Warm Mix Additives, etc), glass transition behavior, and thermal history on physical hardening. The asphalt binders studied included materials used in MnROAD sections, the 8-core SHRP binders, and 40 binders from a study conducted by Lu and Isacson (5).

The details of the development and implementation of a prediction model for physical hardening of asphalt binders is also included in this section. The prediction model was formulated based on a modification of a typical viscoelastic creep model. The model was developed based on experimental data from the 8-core SHRP binders and used to predict physical hardening of MnROAD binders.

Also, this section includes a proposed method to prepare asphalt mixtures samples to be used in measuring dimensional stability of mixtures due to isothermal storage and for glass transition (T_g) temperature testing.

Literature Review

Physical hardening in polymers was first reported by Struik (6). However, the first comprehensive study on physical hardening in asphalt binders was reported during SHRP (1, 2). In asphalt binders as well as many amorphous polymers, physical hardening is a reversible process that occurs at low temperatures. This phenomenon causes time dependent isothermal changes in specific volume and consequently changes in mechanical properties. The effect of physical hardening is completely removed when the material is heated up to room temperatures (2, 6). Physical hardening can be explained by the free volume theory proposed by Struik (6) and Ferry (7).

This phenomenon occurs as a consequence of isothermal reduction of free volume at temperatures close to the glass transition temperature as indicated in Figure 4.1. The effect of physical hardening is an increase in stiffness and a reduction of the stress relaxation capacity of the asphalt binder.

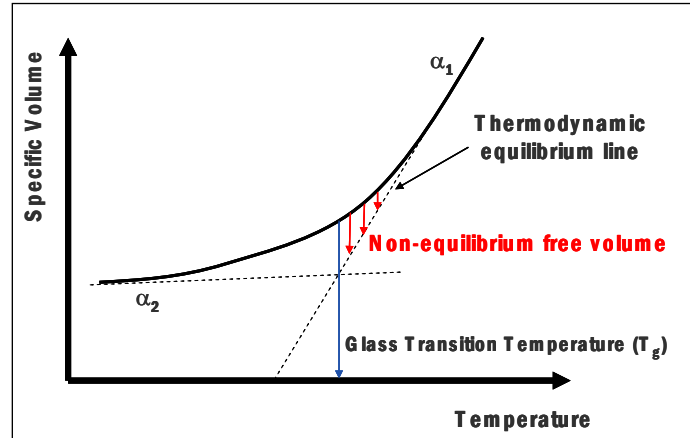


Figure 4.1: Physical hardening and its relation to free volume

The total volume of the material is constituted by a fraction of occupied volume, which is the volume of molecules and their vibrational motion, and a fraction of free volume due to packing irregularities. Previous studies by Doolittle (8), Doolittle and Doolittle (9), and Williams et al. (10) showed how the internal mobility of amorphous materials is better related to the free volume rather than temperature.

When asphalt binders are cooled down from high temperatures, volume changes due to molecular adjustments are significantly larger than volume changes due to vibrational motion. Therefore, collapse of free volume follows a linear trend with temperature. However, when reaching the glass transition region, the speed of the molecular adjustment becomes slower and the reduction of free volume cannot be accomplished in the experimental time. Thus, further collapse of free volume is due to the reduction of the vibrational motion of molecules. However, if the material is kept in isothermal condition for an extended period of time then the molecular adjustments can take place. These molecular adjustments at isothermal conditions generate significant changes in the free volume and as a consequence changes in the mechanical properties (6). This phenomenon was called physical hardening as reported by Bahia and Anderson (2). Note that in the glass transition region (Figure 4.1), the asphalt binder is in a metastable state (i.e., not in thermodynamic equilibrium) (2, 7) and that first order properties, such as entropy, remain continuous but second order properties, such as coefficients of thermal expansion/contraction and heat capacity, are discontinuous (11).

Bahia and Anderson found that the approach used to account for the effect of changing temperature in viscoelastic materials (i.e., time-temperature superposition principle) can be applied to the stiffening effect of physical hardening with conditioning time by using a shift factor on the time scale. They reported that creep curves obtained at the same temperature but at different conditioning times can be superimposed into a hardening master curve (2). They conducted an extensive study about the relationship between physical hardening and glass

transition of asphalt binders and concluded that the concepts used by Struik (6) for amorphous materials can be applied to asphalt binders.

Recent studies have reported that the hardening rate depends on the chemical composition of the asphalt binder (e.g., length of molecular chains and wax content) (12). Moreover, Kriz et al. (13) showed that physical hardening may still occur at temperatures well above T_g due to partial crystallization of some components of the asphalt binder.

Lu and Isacson (5) investigated the rate of physical hardening for five unmodified and 35 polymer modified binders. They noticed that the hardening index did not always increase with decreasing storage temperature. They also concluded that the kinetics of physical hardening in modified binders seems to be largely dependent on the base binders.

Anderson and Marasteanu (14) showed that physical hardening in asphalt binders occurs both above and below the glass transition temperature, in contrast to amorphous polymers, for which physical hardening occurs only below T_g . The data presented in this paper supported the hypothesis that physical hardening is caused in addition to free volume collapse by the formation of crystalline fractions (1, 15). The authors showed that asphalt binders with higher wax content show stronger physical hardening effects both above and below their T_g .

Romero et al. (16) investigated the effect of different mineral fillers and different volumetric properties on the physical hardening of asphalt mixtures. The authors concluded that fracture rather than strength properties are affected by physical hardening.

Hesp and Subramani (4) investigated low temperature Performance Grade (PG) losses due to reversible aging. They raised the question of whether it is necessary to test in the BBR for 1, 3, and 72 hours, or even longer. The authors observed better correlations with field performance when samples were conditioned for 72 hours. The results from this study indicated that a better measurement of the asphalt binder performance was obtained when physical hardening is considered. Furthermore, the authors showed how physical hardening can affect the reliability of the current method used to classify and select asphalt binders for paving applications.

Materials and Experimental Methods

A total of 55 modified and unmodified asphalt binders were used to investigate the effect of binder source, modification, and thermal history on physical hardening and in the development of the prediction model. A set of 40 binders from a study conducted by Lu and Isacson (5) were used to develop the concepts behind the model. The results collected for the eight-core SHRP binders were used in the development and verification of the prediction model. Finally, the prediction model was used with physical hardening data obtained from the seven binders proposed in the experimental program of Task 2.

Asphalt Binders

Table 4.1 shows the materials reference library (MRL) code, PG grade, crude oil source, and glass transition temperature (T_g) of the eight-core SHRP binders. Note that the SHRP binders were aged with the thin film oven (TFO).

Table 4.2 presents a description of the proposed Task 2 asphalt binders. Note that these binders were subjected to short term aging using the rotating thin film oven (RTFO). Also, a PG 64-22 binder modified with 1% of polyphosphoric acid (PPA) and with 2% of Sasobit®, a warm mix asphalt additive, were tested to assess the effect of these modifiers on physical hardening.

Table 4.1: SHRP asphalt binders

MRL Code	PG Grade	Crude Oil Source	T_g (°C)*
AAA-1	PG 58-28	Lloydminster	-28.2
AAB-1	PG-58-22	WY Sour	-13.9
AAC-1	PG 58-16	Redwater	-9.9
AAD-1	PG 58-28	CA Valley	-24.3
AAF-1	PG 64-10	W TX Sour	-6.1
AAG-1	PG 58-10	CA Valley	-9.9
AAM-1	PG 64-16	WTX Inter	-4.1

*From Bahia (2)

Table 4.2: Asphalt binders selected for Task 2

Binder	Location	Description
PG58-34 PPA	MnROAD 33	Modified with Polyphosphoric Acid (PPA)
PG58-34 SBS+Acid	MnROAD 34	Modified with Styrene-Butadiene Styrene (SBS) +PPA
PG58-34 SBS	MnROAD 35	Modified with SBS
PG58-34 Elvaloy +Acid	MnROAD 77	Modified with PPA + Elvaloy
PG58-28	MnROAD 20	Neat
PG58-34	MnROAD 22	Unknown Modification
Wisconsin	Wisconsin	Binder used in construction of SMA pavement
PG 64-22 – New York	New York	Typical binder used in New York

Test Methods

The measurements of physical hardening were obtained by measuring the change in creep stiffness (S) of asphalt binder beams with isothermal age at different temperatures. All measurements were collected using the Bending Beam Rheometer (BBR) and following AASHTO T 313-05 (17). The asphalt binder beams from the MnROAD cells (Table 4.2) were tested after 1, 4, 24 and 72 hours of isothermal conditioning time at -12, -18 and -24°C. The

SHRP binders were tested after 2, 6, 24 and 96 hours at -10, -15, -25 and -35°C and the binders studied by Lu and Isacson (5) were tested at 1, 4 and 24 hours at -15, -25 and -35°C.

The glass transition temperature (T_g) of the asphalt binders in Table 4.2 was measured with a dilatometric system developed at the University of Wisconsin-Madison. Note that no standard for this equipment is available and therefore the test was performed following procedure developed by Bahia and Anderson (18) and later modified by Nam and Bahia (19). The concept behind the procedure is based on precise measurements of volume change in time of an asphalt binder specimen when the temperature decreases at a constant rate. For T_g test, the sample is prepared by pouring 10 g of hot asphalt into a circular silicone rubber mold with a diameter of 40 mm and a height of 8.0 mm.

The dilatometric cell is connected to a vertical capillary tube (i.e., $\phi=1$ mm) with its top end open. The volume changes in the sample are calculated by estimating the change in the height of the ethyl alcohol column inside the capillary tube. For this study, the system was further modified by using very precise pressure transducers (Figure 4.2) to measure the changes in alcohol column height.

Calculation of the glass transition temperature (T_g) is based on a non-linear model proposed originally by Bahia (2) and later successfully used by Nam and Bahia (19). Figures 4.2 and 4.3 shows the dilatometric system and typical results for T_g measurements, respectively.

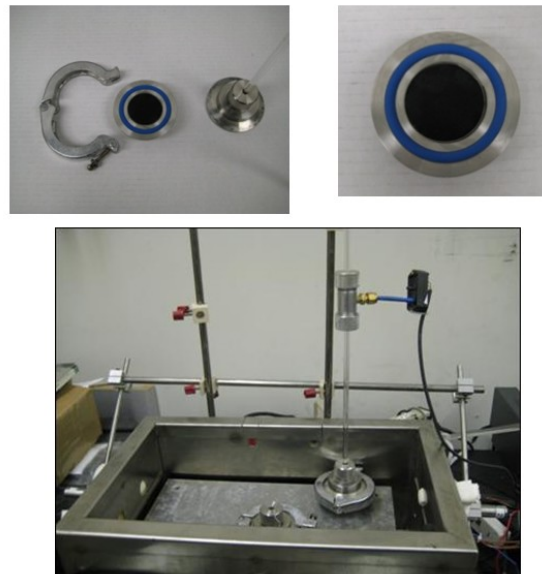


Figure 4.2: Dilatometric system used to measure glass transition temperature (T_g) of asphalt binders

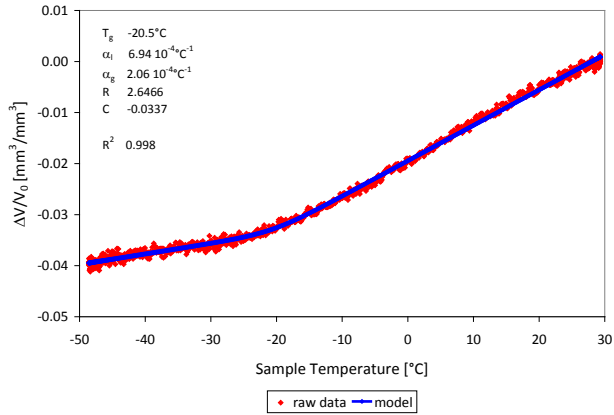


Figure 4.3: Typical results from glass transition temperature (T_g) test of asphalt binders

To investigate the effects of thermal history on physical hardening, the asphalt binders in Table 4.2 were subjected to a thermal cycle consisting of successive isothermal conditioning periods at different temperatures as shown in Figure 4.4. The thermal cycle included a cooling and heating phase. The selected conditioning times and temperatures were 1, 4 and 24 hours, and -12°C, -18°C and -24°C, respectively. Creep tests were performed during the cycle to measure low temperature rheological properties.

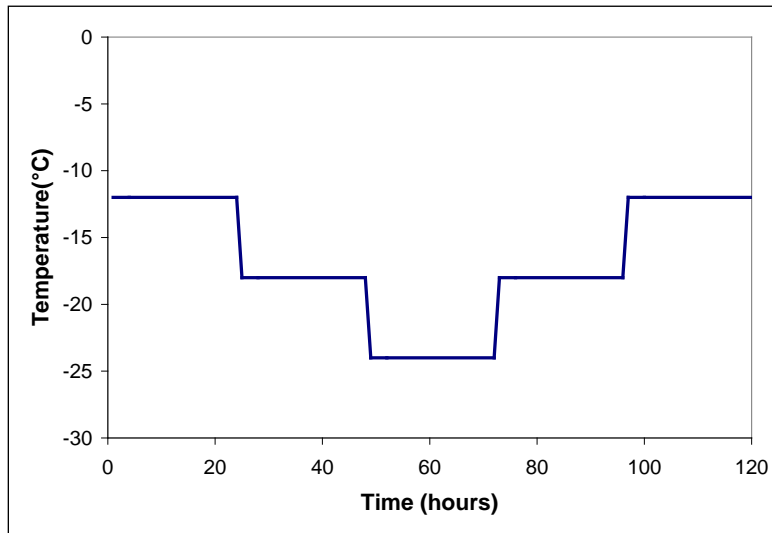


Figure 4.4: Thermal cycle

Results and Discussion

Effect of Binder Source and Modification

A hardening index, S_i/S_0 , defined as the ratio of the creep stiffness, $S(60)$, after time t_i of isothermal storage to the initial stiffness measurement after time t_0 of isothermal storage (t_0 is always equal to one hour in this report), is generally used to show the rate at which physical hardening occurs at different isothermal conditions (5, 13, and 20).

Although generally assumed that at lower isothermal condition temperatures the rate of physical hardening increases, some studies suggest otherwise. Figure 4.5 shows that for all SHRP binders, the hardening rate at -35°C was in fact less than the rate at -25°C . Lu and Isacson (5) tested a wide array of modified and unmodified binders and observed that although for three of the five tested base binders the maximum hardening index was achieved at the lowest experimental temperature (i.e., -35°C), for the other two base binders and their corresponding modified binders, the maximum rate was observed at higher temperatures (5).

These observations indicate that the concept of ever increasing hardening rates as the temperature decreases is not valid as a general rule and that a lower temperature limit to physical hardening occurrence may exist.

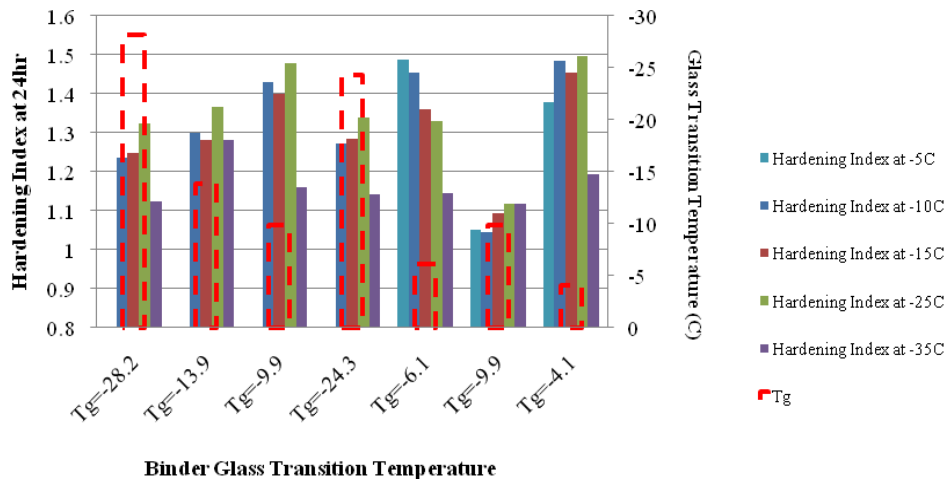


Figure 4.5: Hardening index after 24hrs (relative to one hour) of isothermal conditioning at different temperatures for SHRP binders

Figure 4.6 shows the hardening index and glass transition temperature from tests conducted by Lu and Isacson (5). As it was observed with the SHRP binders, the rate of hardening at -35°C is less than the rate at -25°C for many of the binders.

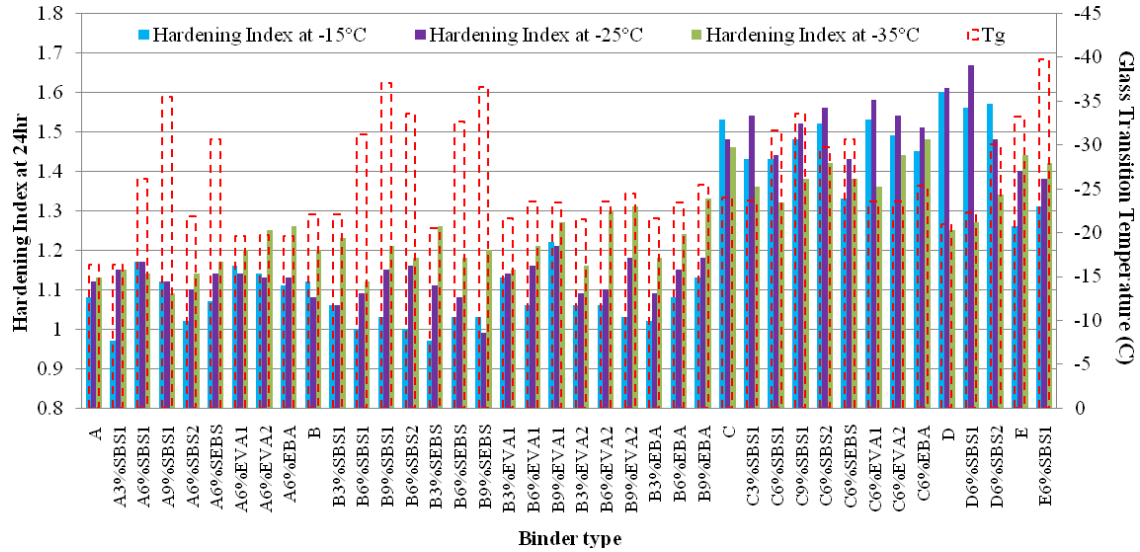


Figure 4.6: Hardening index after 24 hr of isothermal conditioning at different temperatures using data from Lu and Isacson (5)

To investigate the effect of modification on the rate of physical hardening, the data collected by Lu and Isacson (5) was used to conduct ANOVA test at 95% significance level. Three of the base binders modified with five types of modifiers (i.e., three elastomers and two plastomers at a 6% concentration) were selected for this analysis. The results showed that the base binder source is a very significant factor, while polymer modification is insignificant. Furthermore, it was observed that the temperature corresponding to the maximum hardening rate is more or less constant for all modifications of each base binder.

A similar analysis was done on the actual hardening index at -25°C and using the maximum hardening index at the three testing temperatures. The ANOVA results for both cases showed that the base binder is very significant in the prediction of hardening rate, while the type of modification was insignificant at a 95% significance level.

The results analyzed indicate that the base binder properties are the controlling factor for the rate of hardening and that the physical hardening behavior of the base binder phase will dominate the modified binder's hardening rate.

Physical Hardening and Glass Transition

According to the free volume concept as described by Struik (6), as the amorphous material is cooled, the molecular transport mobility, M , and the molecular free volume, v_f , decrease simultaneously. Since molecules attract each other and free volume consists of voids within the molecules, the existence of free volume represents an increase in internal energy, ΔU , with respect to the zero-free volume state. The existence of free volume is accompanied by an increase in entropy, ΔS . Thus, the increase in internal energy due to free volume, ΔU , must be balanced with $T\Delta S$, where T is temperature. The rate of this process is determined by the segmental mobility, M , which itself is a function of the free volume, v_f . This implies a non-linear trend to the volume relaxation phenomena (6).

The free volume cannot decrease indefinitely as temperature decreases, and at a certain temperature, M becomes so small that the decrease in v_f becomes insignificant. This temperature is referred to as the glass transition temperature, T_g . The small values of M at temperatures below T_g indicates that the volume continues to decrease very slowly over time. The reduction in mobility M in temperatures close to T_g will significantly affect the rate in which the free volume collapses to the equilibrium state (6).

Although many researchers agree upon the effects of physical hardening, there is some disagreement about the temperature range in which physical hardening occurs (14). Generally, it is claimed that physical hardening occurs below the glass transition temperature (5, 6). Experimental data in this study shows that the occurrence of physical hardening begins well before reaching the glass transition temperature.

Glass transition temperature is determined as the temperature at which the two asymptotes to the linear regions before and after the glass transition on the volume-temperature curve intersect. However, the glassy transition begins well before this point (i.e., where the material starts to deviate from thermodynamic equilibrium), thus according to the free volume concept physical hardening will occur as the material enters this transition region.

The existence of a “peak” in the hardening rate as the temperature is decreased, and the subsequent decrease in the rate of hardening observed in the experimental data as temperature falls below the peak temperature in many of the tested binders, suggests the existence of a lower temperature limit to the occurrence of physical hardening. This is schematically shown in Figure 4.7.

The decrease in rate implies that there is a limiting temperature for which the material no longer tends toward the original equilibrium line, but toward a state with a higher energy level than the thermodynamic equilibrium state, shown with the red arrows in Figure 4.7. This is hypothesized to be the extension of the linear region occurring below the glass transition region. Thus, as the temperature is further decreased, the rate of physical hardening will continue to decrease, ultimately reaching a negligible level at the end of the glass transition region.

Figure 4.7 and the experimental results indicate the potential importance of the glass transition region in the occurrence of physical hardening, suggesting that any accurate prediction model for physical hardening should include the position of the target temperature relative to the glass transition region of the binder.

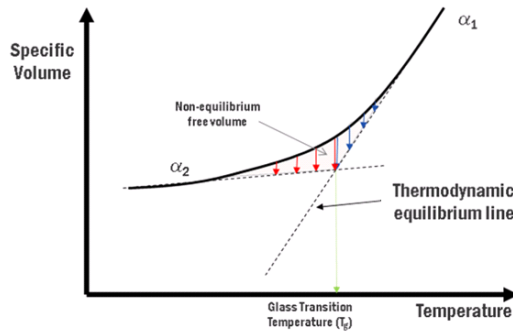


Figure 4.7: Schematic of proposed material behavior in glass transition region

Effect of Thermal History

The asphalt binders described in Table 4.2 were used to investigate the influence of thermal history on the development of physical hardening. Figure 4.8 shows typical results of the effect of thermal history on the creep stiffness (S) of binders. The thermal cycle applied to the PG 58-34 +PPA binder from MnROAD 33 is depicted as the solid blue line in Figure 4.8.

Although absolute values represent an indication of how stiffness and m -value (i.e., relaxation property) change during the thermal cycle, a better indication of the development of physical hardening is obtained when relative changes are used. Therefore, both properties, stiffness and m -value at 60 seconds, were normalized with respect to their value at the beginning of each isothermal period (i.e., $S(60)$ and $m(60)$ at 1 hour of conditioning). Figure 4.9 shows the normalized values for creep stiffness (S) and m -value at 60 seconds during the thermal cycle for all binders.

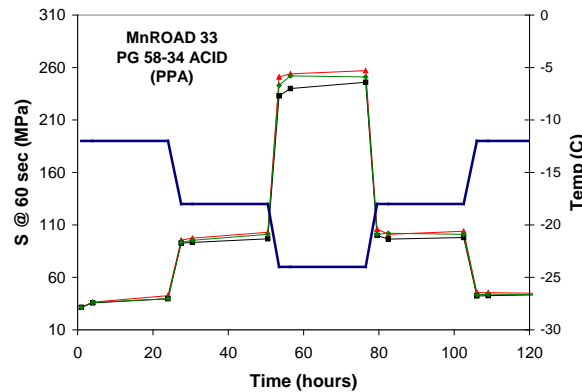


Figure 4.8: PG 58-34+ PPA binder from MnROAD 33- creep stiffness as function of conditioning time

Figure 4.9 indicates that significant physical hardening was observed during the first conditioning period after reducing the temperature from 25°C (i.e., room temperature) to -12°C. During the subsequent conditioning periods (i.e. further cooling), the asphalt binders showed a significant reduction on the magnitude and rate of hardening, confirming the influence of previous conditioning periods or thermal history on physical hardening. During the heating component of the thermal cycle, mechanical properties of the asphalt binders remained

approximately unchanged regardless of the isothermal conditioning time. During the heating phase of the thermal cycle, the asphalt binder is very close to the thermodynamic equilibrium line. Therefore, when heated from a lower to a higher temperature, the amount of free volume available for isothermal contraction is minimal and thus any molecular adjustment will be extremely slow. Then, as it can be seen in Figure 4.9, no physical hardening is observed in terms of stiffness and m-value within the experimental time of the isothermal conditioning periods at -18°C and -12°C in the heating phase. Note that New York binder was not available to the research team when performing these tests.

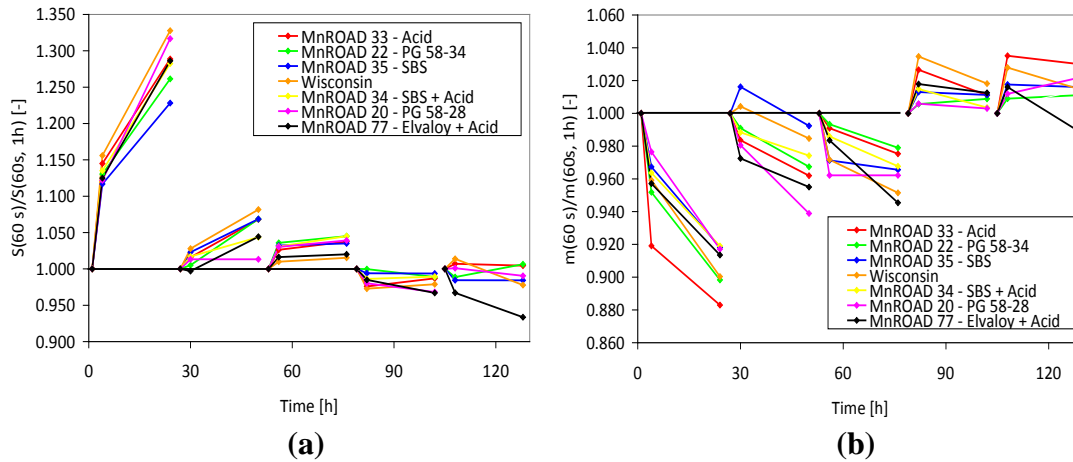


Figure 4.9: Effect of thermal history on physical hardening by measuring changes in creep stiffness and m-values of binders in Table 4.2

Further evidence of this effect can be found by observing the creep curves from the single BBR tests performed during the thermal cycle. The creep curves for different conditioning times are well distinguishable during the isothermal period immediately following the initial quench at -12 °C. However, they become closer and closer for the two isothermal periods at -18 °C and -24 °C, proving that physical hardening occurrence is reduced. Finally, during the isothermal periods in the heating ramp, creep curves are practically superimposed on each other, revealing the absence of remarkable physical hardening within the experimental time scale.

Development of Model to Predict Physical Hardening

The proposed model is built upon concepts of rheological response of viscoelastic materials. In rheology creep is defined as the progressive deformation under a constant stress. Creep in a linear material is a function of time only (21). One may describe creep as the gradual redistribution of the molecules, resulting in a change in free volume and a decrease in the creep stiffness (increase in creep compliance). Similarly in hydrostatic (volumetric) stress conditions this phenomenon can be observed, where under a fixed stress level, free volume gradually decreases over time, causing a gradual increase in stiffness. The Burger’s model is often used to model the creep behavior in asphalt:

$$\gamma = \frac{\tau}{G_0} + \frac{\tau}{G_1} \left(1 - e^{-\frac{t}{\eta_1}}\right) + \frac{\tau}{\eta_0} t \quad [4.1]$$

Where:

γ = strain resulting from the creep

τ = applied stress

t = loading time

G_0, G_1, η_0 and η_1 = elastic and viscous material constants.

Burger's model consists of a Maxwell and Kelvin models in series. At lower temperatures the effect of physical hardening can be described by the Kelvin model as there is no significant instantaneous change in volume after thermal equilibrium is achieved.

$$\gamma = \frac{\tau}{G_1} \left(1 - e^{-\frac{t}{\eta_1}}\right) \quad [4.2]$$

The creep behavior at the molecular level could be envisioned as similar to the behavior observed in physical hardening. The basic property that changes during physical hardening is segmental or molecular mobility; which is also claimed to be directly related to deformation under creep loading (6). The amount of free volume controls molecular mobility, which in turn controls the rate of volume change which is responsible for the rate of hardening. Thus, the controlling factor in the hardening rate would be the volume difference relative to the equilibrium state, as shown in Figure 4.7. This difference increases as temperature approaches the glass transition temperature in Figure 4.7 after which it starts to decrease. This concept explains the mechanism behind the observed trend in hardening rate as temperature decreases.

Thus, it is hypothesized that a modified creep model can be adjusted to fit physical hardening behavior. In such a model, strain or relative change in deflection (i.e., $\Delta l/l_0$), can be replaced by relative change in volume, $\Delta V/V_0$, which according to the free volume concept can be taken to be directly proportional to relative change in stiffness, or hardening rate ($\Delta S/S_0$). Hardening rate can be measured in the laboratory with the BBR and thus used as input in the model in place of $\Delta V/V_0$. The change in stiffness (ΔS) is calculated as the difference in $S(60)$ at time t_i and at time t_0 , which is the $S(60)$ at one hour conditioning.

Creep is usually driven by the stress of an applied load. In the physical hardening case, the "creep" behavior at isothermal conditions was considered to be induced by the excess internal energy due to the deviation of the material from thermo-dynamic equilibrium within the glass transition region, thus a "stress" parameter based on the glass transition temperature, relative position of the conditioning temperature from the glass transition temperature and the length of the glass transition region was envisioned for the model. In this case the loading time would be the length of time the material is in temperature at which the material is not at thermo-dynamic equilibrium, or in other words, the conditioning time (t_c).

As described previously, the rate of physical hardening ($\Delta S/S_0$), peaks at a certain temperature, hereby denoted as T_0 , and decreases toward zero as the temperature approaches the beginning and the end of the glass transition region, as is shown in Figure 4.10. This trend was taken into

account to formulate the “stress” term for the model. For the current study, the following empirical equation was shown to fit the observed behavior of physical hardening very well:

$$\tau_T = e^{-\frac{9(T-T_0)^2}{(2x)^2}} \quad [4.3]$$

In this equation τ_T is the “stress” term as a function of the temperature at which physical hardening peaks, T_0 , and the length of the glass transition region, $2x$.

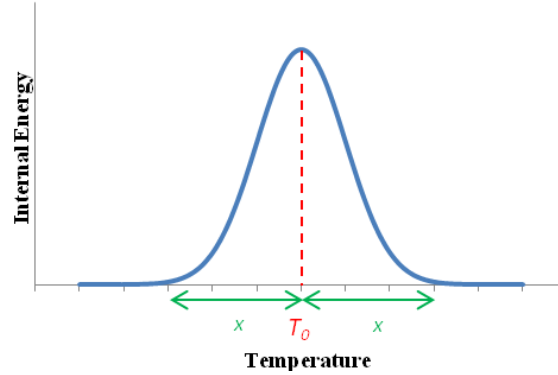


Figure 4.10: Empirical function used to account for glass transition temperature in prediction model. ($2*x$ is the length of the glass transition region)

From the experimental data it was recognized that the Internal energy variation around temperature T_0 is not completely symmetrical, but is in fact slightly skewed toward the lower temperatures, but for simplicity a symmetric formulation was used in [4.3]. Using [4.2] and [4.3], the model is rewritten as:

$$\gamma \approx \frac{\Delta V}{V_0} \approx \frac{\Delta S}{S_0} = \frac{e^{-\frac{9(T-T_0)^2}{(2x)^2}}}{G} \left(1 - e^{-t_c \frac{G}{\eta}} \right) \quad [4.4]$$

Where:

$\frac{\Delta S}{S_0}$ = change in hardening relative to the hardening after 1 hr of conditioning.

T_0 = peak temperature for hardening rate, assumed to be the T_g ($^{\circ}\text{C}$)

T = conditioning temperature ($^{\circ}\text{C}$)

t_c = conditioning time (hrs)

$2x$ = length of the temperature range of the glass transition region ($^{\circ}\text{C}$)

G and η = model constants, derived by fitting the model

This model was fitted to the experimental data using the least sum of squared errors method, replacing T_0 with the glass transition temperatures measured using the dilatometric method as reported by Bahia (2) and allowing the model to fit the length of the glass transition region to the data. As shown in Figures 4.11 and 4.12, the results accurately predict the experimental data. The model predicted the observed data for all test temperatures. Furthermore, the model predicted a

decrease in hardening rate as the temperature passed the glass transition temperature, as was evident in the experimental data from the samples conditioned at -35°C . A goodness of fit of 92% observed between measured and predicted hardening rates for the 8-core SHRP binders indicates the validity of assuming the glass transition temperature to be the peak temperature for the rate of physical hardening (Figure 4.12).

In a second set of runs instead of inputting the glass transition temperature as the peak temperature, the model was allowed to find the peak temperature based on the best fit to the experimental data. The resulting fitted peak temperatures were only within a few degrees of the measured glass transition temperatures. This indicates that if data from a few temperatures is available, the model can be used to estimate the T_g from the experimental hardening rate data. Figure 4.13 shows the goodness of fit of the model for fitted values.

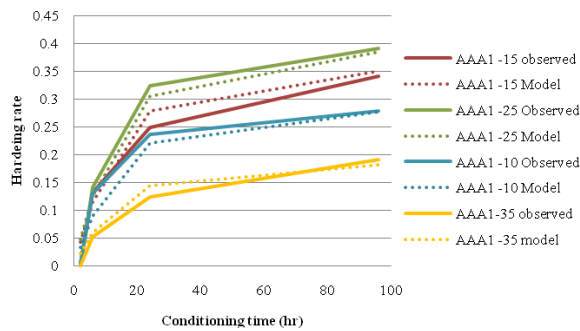


Figure 4.11: Comparison of model described by [4.4] with experimental data (hardening rate= $\Delta S/S_0$)

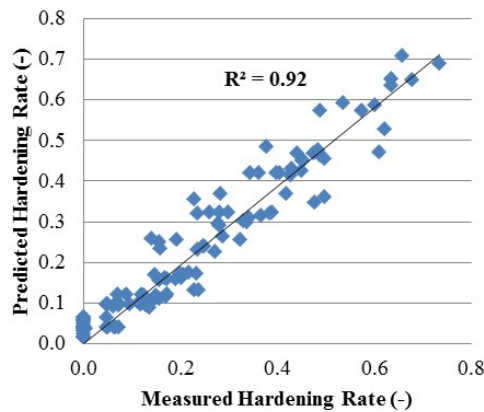


Figure 4.12: Goodness of fit between the predictions using Equation [4.4] using T_g for T_0 and the experimental data. (hardening rate= $\Delta S/S_0$)

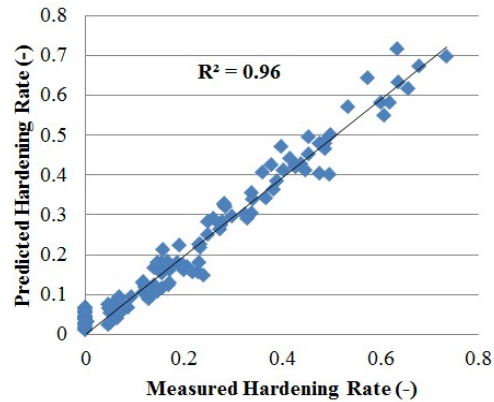


Figure 4.13: Goodness of fit between model described by [4.4] with fitted T_0 and experimental data (hardening rate= $\Delta S/S_0$)

It must be noted that for every binder, G and η are unique material parameters which are independent of temperature and conditioning time. Thus, by fitting the model to data from a single temperature, one may use the resulting G and η to predict the physical hardening at any other temperature or conditioning time.

The most important objective of developing this model is the ability to enable prediction with fewer tests or easily available data. For the proposed model, two possible prediction methods are considered. The first and simplest method would be to use 3 hardening rate data points from a BBR test carried out at a single temperature after relatively short conditioning times along with the glass transition temperature to fit the model and use the resulting G and η to predict the effect of much longer conditioning times or other conditioning temperatures. Although this is an improvement compared to the much longer conditioning times as well as other temperatures. It must be noted that as with any non-linear model, the closer the input data points are to each other (or in this case, the shorter the conditioning times used), the lower the accuracy of the extrapolation of the model to much longer conditioning times.

The second method is to find regression functions that can be used to relate BBR creep stiffness $S(60)$ or m -value at 1 hour conditioning, to predict the model parameters G and η . A promising relationship was observed between $S(60)$ and conditioning temperature from the SHRP binders and the model parameters. As shown in Figure 4.14, a power law was fitted to the curve for all binders and the A and B parameters were determined as described in [4.5].

$$S(60) = A|T|^B \quad [4.5]$$

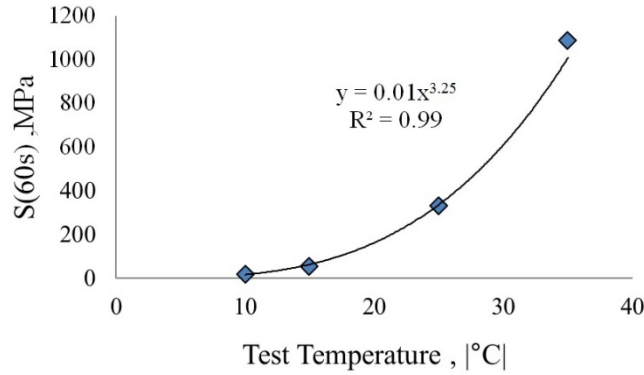


Figure 4.14: S(60) after 1hr conditioning for one of the SHRP binders plotted against test temperature

The A and B parameters were plotted against G and η . No apparent relationship existed with the A parameter. However, an interesting correlation was established using B from the SHRP binders. The relationships can be seen in Figure 4.15.

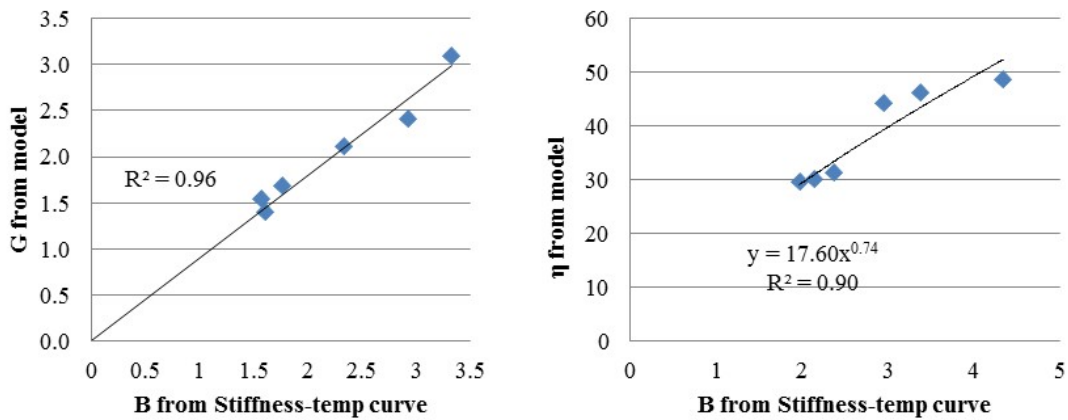


Figure 4.15: Correlation between G and η and B for the SHRP binders

The correlations showed that parameter G and parameter B are in equality. This equality is very intriguing and more investigation into this relationship may be warranted. Using the relationships shown in Figure 4.15, [4.4] can be rewritten as:

$$\frac{\Delta S}{S_0} = \frac{e^{-\frac{9(T-T_0)^2}{(2x)^2}}}{B} \left(1 - e^{-\frac{t_c B^{0.26}}{17.6}} \right) \quad [4.6]$$

Where:

$\frac{\Delta S}{S_0}$ = change in hardening relative to the hardening after 1 hr of conditioning.

T_0 = peak temperature for hardening rate, assumed to be the T_g (°C)

T = conditioning temperature (°C)

t_c = conditioning time (hrs)

$2x$ = length of the temperature range of the glass transition region ($^{\circ}\text{C}$)

B = derived from [4.5]

Equations such as [4.6] can be used to predict the hardening rate for other binders at any temperature and conditioning time, using only $S(60)$ at 1hr from BBR grading tests and the T_g . A comparison between this predicted model and the measured data is presented in Figure 4.16 for the tested binders. The applicability of using the proposed physical hardening model for different binders will increase as data from more binders are used to refine the observed relationship between the parameters. Although requiring measuring T_g may be inconvenient, this study has clearly shown that the glass transition behavior of a binder is one of the controlling factors in the physical hardening phenomenon and no model can accurately describe it without taking the glass transition into account.

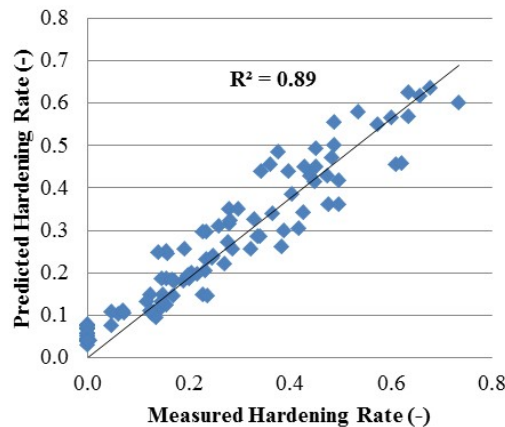


Figure 4.16: Goodness of fit between model described by [4.6] using T_g for T_0 and experimental data

Physical Hardening in MnROAD Binders

The asphalt binders described in Table 4.2 comprised of four neat binders (MnROAD 20, New York and Wisconsin) and four modified binders with the same base (MnROAD 33, 34, 35 and 77). The proposed physical hardening model was fit to experimental data from these binders by both inputting the dilatometric measurement of the glass transition temperature and by allowing the model to fit the model to the best glass transition temperature. As it can be seen in Figure 4.17, in both cases the goodness of fit was very good and the measured and predicted glass transition temperatures were within a few degrees of each other. Figures 4.18 and 4.19 compare the G , η and average hardening for all 8 binders.

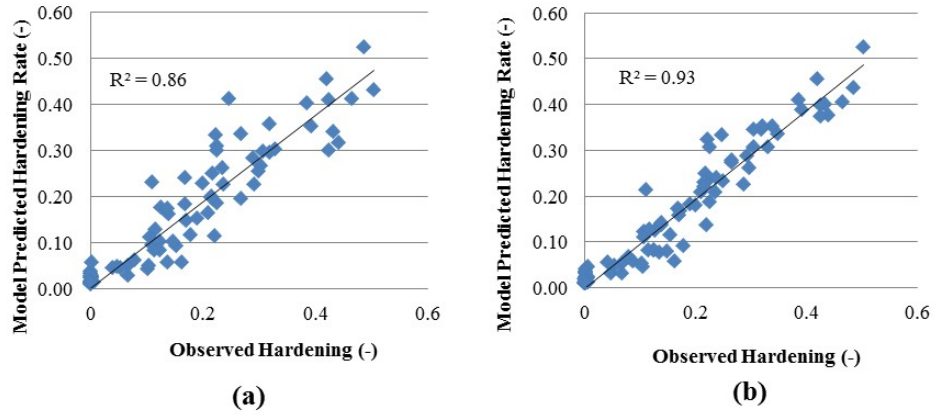


Figure 4.17: Goodness of fit of the physical hardening model for the MnROAD binders (a) using measured glass transition temperature values, (b) using values fitted by model

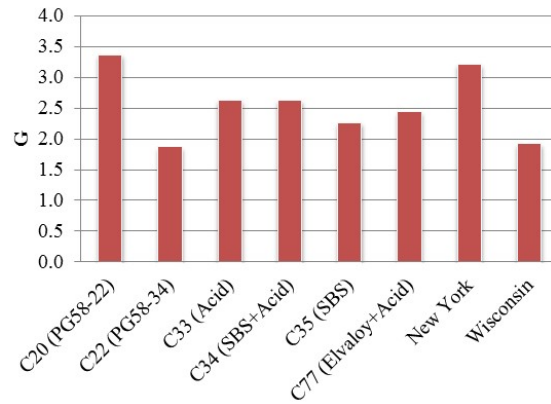


Figure 4.18: Comparison of the G parameter derived from the fitted physical hardening model

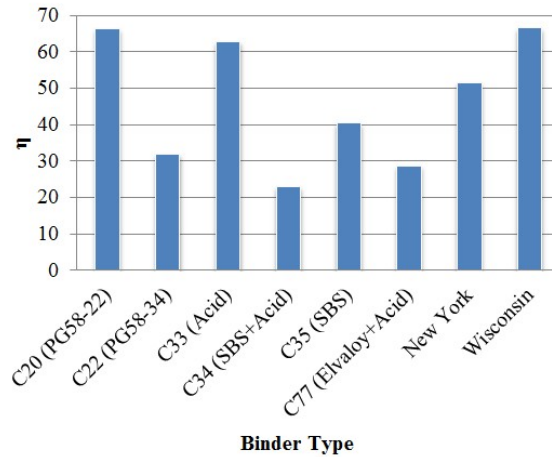


Figure 4.19: Comparison of the η parameter derived from the fitted physical hardening model

Ranking of the G parameter shows that MnROAD cell 22 and the Wisconsin binder are the most prone to physical hardening, while MnROAD cell 20 and New York binder are the least susceptible to hardening among the eight tested binders. Note that this is also reflected by the estimated average hardening obtained from the BBR tests as indicated in Figure 4.20.

It was observed that the polymer modified binders, MnROAD cells 34, 35, and 77, have very similar physical hardening susceptibility. This indicates that although the type of polymer modifier has changed, the amount of physical hardening remains almost constant. This trend was noted earlier through the review of existing test data from other studies. It was concluded that due to the predominant effect of the base binder phase in the two-phase polymer modified binder system, the polymer phase does not significantly alter the physical hardening behavior of the binder and thus polymer type becomes insignificant compared to the base binder type.

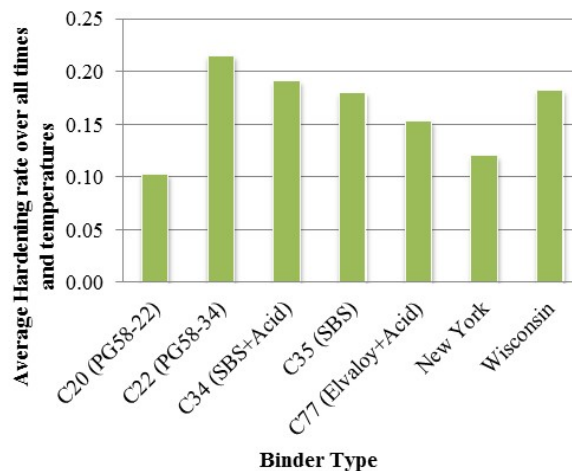


Figure 4.20: Comparison of the average hardening for each binder over all tested conditioning times and temperatures

Effect of Polyphosphoric Acid (PPA) and Warm Mix Additives (WMA)

The effect of Polyphosphoric Acid (PPA) and a Warm Mix Additive (WMA) on physical hardening was investigated by performing tests on a PG 64-22 binder modified with PPA and Sasobit (i.e., a wax commonly used as a warm mix additive in the pavement industry).

BBR beams were prepared for each binder and kept for isothermal conditioning at -12, -18 and -24°C for 72 hrs. The creep stiffness and m-value were measured after 1, 4, 24, and 72 hrs of conditioning. The proposed physical hardening model was fitted to the test results. As glass transition measurements were not done for these binders, the model was allowed to predict the glass transition temperature. It was noted that the predicted T_g decreased when PPA was added to the binder, but increased when Sasobit was added. This result indicates that binders containing Sasobit become brittle sooner than the binders modified with PPA. Consequently an inferior thermal cracking resistance will be expected in comparison to the neat and PPA modified binder.

The average hardening rate over all tested temperatures and conditioning times are shown in Figure 4.21. Figures 4.22 and 4.23 present a comparison of the model parameters for the tested binders. It can be seen that the binder containing PPA has a relatively smaller G , thus showing a higher hardening potential. The η parameter for the PPA modified binder is also lower, meaning that the hardening, although comparatively larger in magnitude, builds up at a relatively slower rate compared to the binder with Sasobit or the base binder. It was observed that the Sasobit decreased the magnitude of hardening; however it increased the rate at which this phenomenon develops. These trends are supported by the average hardening parameter presented in Figure 4.21. These experimental results indicate that PPA and WMA do indeed have a significant effect on the physical hardening of asphalt binders.

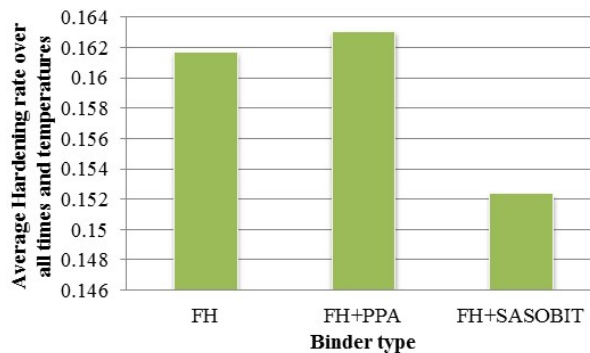


Figure 4.21: Comparison of the average hardening for each binder over all tested conditioning times and temperatures

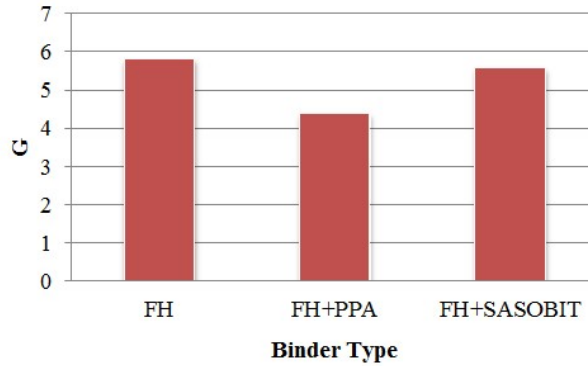


Figure 4.22: Comparison of G parameter derived from the fitted physical hardening model

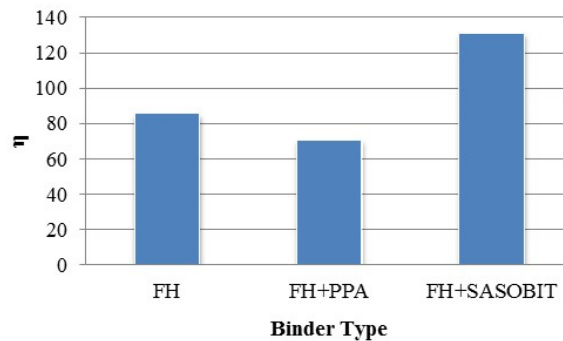


Figure 4.23: Comparison of the η parameter derived from the fitted physical hardening model

Dimensional Stability of Asphalt Mixtures during Isothermal Storage

The glass transition procedure for asphalt mixtures was modified to quantify effect of isothermal storage on dimensional stability of asphalt mixtures. Previously, glass transition measurements for asphalt mixtures were conducted using beam samples cut from slab compacted mixtures. However, since slab compactors are not readily available in many agencies and laboratories, the usefulness of a test requiring such machinery would be limited. Therefore, the new testing procedure focused on developing an adequate T_g sample geometry that is relatively easier to produce and prepare using equipment accessible in most laboratories.

Three possible preparation procedures, which use gyratory compacted samples, were investigated before selecting the optimal solution. The first two methods were based on coring the samples and gluing the cores which were 1" and 2.5" in diameter, respectively. The final specimen after gluing was approximately 12" long. This minimal length is required in glass transition temperature measurements of mixtures to allow measurable changes in length of the sample. Taking into account the usual height of a gyratory compacted sample, three cores are required for such a sample.

The first step was to confirm that the glue in the samples did not affect the glass transition measurements. Figure 4.24 shows the results for glass transition temperature obtained from a

mixture sample tested before and after cutting to 3 pieces and gluing back together using an epoxy resin. The results indicate that the glass transition behavior is unaffected by the gluing procedure.

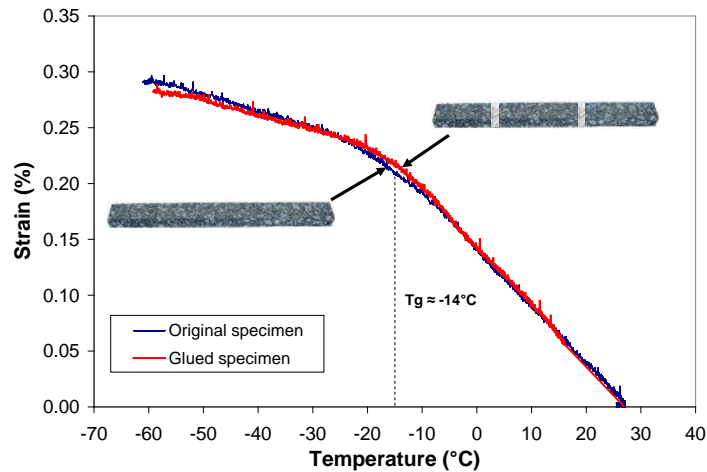


Figure 4.24: T_g mixture results for unglued and glued specimen

Then, glass transition tests were run on the samples with different diameters and the results showed that the core diameter did not significantly affect the glass transition measurements. It is observed in Figure 4.25 that both specimen sizes yielded similar glass transition temperatures. The main issue of the 2.5" specimen is the difficulty in extracting more than one core from each gyratory compacted sample. Furthermore, for the 1" specimen, concerns about size effects (e.g., specimen smaller than the representative volume element, RVE) prevented the research team to move forward with these geometries. Consequently, a third method which involves a prismatic geometry was considered. In the third method instead of coring, a few cuts were made in the gyratory compacted sample using a masonry saw, such that four prismatic beams of about 2 x 2" in cross section and about 4" long were produced. Three of these beams were glued to each other using epoxy resin to produce a 12" long prismatic beam (Figure 4.25). It was observed that this method was less time consuming than the coring methods and that the samples were easier to glue. Furthermore, positioning the sample on the rollers and between the two LVDTs was much easier as the sample geometry prevented it from moving laterally as it was in the case of the cylindrical samples produced from coring.

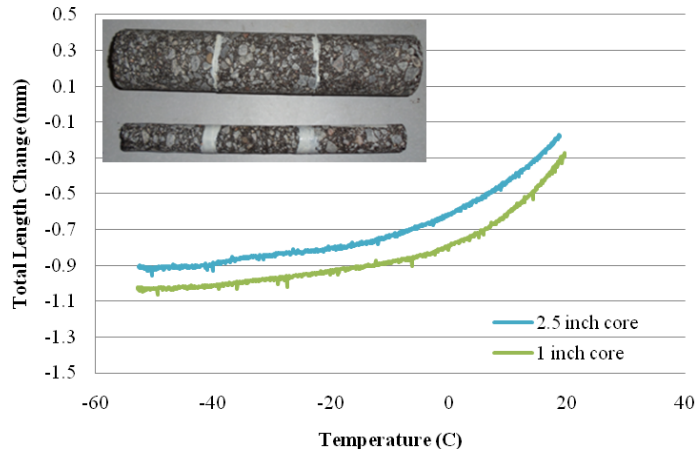


Figure 4.25: Comparison of T_g results from samples with $\phi = 1''$ and $2.5''$



Figure 4.26: Prismatic beams made from gluing blocks cut out of gyratory samples

Figure 4.27 shows the final setup used for the glass transition tests of asphalt mixtures. The LVDTs used in the T_g device were tested for linearity and accuracy using a micrometer. Furthermore, the setup was also checked by testing a Nickel rod with known coefficient of thermal contraction/expansion. The results of tests with cooling and heating cycles confirmed that the setup is not introducing any bias in the results.



Figure 4.27: Test setup used for the glass transition temperature of beams made from gyratory compacted samples

Preliminary tests to investigate the effect of isothermal storage on the dimensional stability of asphalt mixtures were conducted. The volumetric stability at isothermal conditions was tested with the T_g setup by decreasing the temperature to -25°C and then holding the temperature constant for conditioning. A decreasing length over time is visible over the course of the

isothermal conditioning. The isothermal reduction in length of the asphalt mixture measured after only 200 minutes (3.3 hours) was of a magnitude of about 7% of the total length change when the temperature is reduced from 30 to -25°C. Two independent replicates showed the same phenomenon. Further tests for longer times and more analysis of results are required to investigate the exact nature of the dimensional stability of asphalt mixtures due to isothermal storage.

Summary of Findings and Conclusions

Although researchers have been aware of physical hardening as a factor influencing low temperature properties of binders, the factors that affect this phenomenon are not well defined. The purpose of this task was to understand how physical hardening is affected by parameters such as temperature, conditioning time, modification, thermal history, and glass transition temperature, and to propose a comprehensive model in which the physical hardening of asphalt binders can be predicted for different conditions without lengthy tests. The tests performed in this study were combined with experimental data from previous studies to enable a broad analysis of the nature of physical hardening in asphalt binders and to propose a model. Based on the results, the following important conclusions were made:

- Physical hardening in asphalt binders results in significant changes in their creep response at temperatures below or near the glass transition. This phenomenon can be successfully characterized by a horizontal shift of the creep response along the loading time scale. The horizontal shifting indicates that the influence of physical hardening is similar to the influence of lowering temperature in thermo-rheological simple materials.
- The rate of physical hardening decreases rapidly with isothermal age and it is highly dependent on conditioning temperature and the source of the base binder. Different types of polymer modification did not significantly change the rate of physical hardening. This was explained as being the result of the two-phase nature of polymer modified binders, in which the hardening behavior of the base binder phase is dominant.
- The rate of physical hardening does not increase indefinitely as temperature decreases. Based on literature review and the experimental data collected, it is hypothesized that the rate of hardening peaks at a specific temperature, and approaches zero as the temperature increases or decrease toward the limits of the glass transition region. It was shown that the peak temperature corresponds to the glass transition temperature of the binder.
- The rate and magnitude of physical hardening is highly dependent on the thermal history applied to the asphalt binder. Creep tests performed over the course of a thermal cycle consisting of five consecutive isothermal conditioning periods of 26 hours at three different temperatures indicate that physical hardening occurs mostly during the first isothermal period. Both, the magnitude and rate of hardening is significantly reduced for the rest of the isothermal periods in the cooling phase. Moreover, insignificant hardening is observed during the isothermal periods in the heating phase of the thermal cycle. This results show the non-symmetric behavior of physical hardening during cooling and heating cycles.
- A modified creep model was shown to be able to reflect the change in physical hardening rate with conditioning time and temperature. The model parameters, G and η , were shown to be unique material parameters that remain constant at all conditioning times and temperatures. Thus, by fitting the model to three stiffness values at a single temperature,

and by having the T_g value, one may predict the physical hardening at any other temperature or conditioning time. The developed model can also be used to estimate T_g using physical hardening test results from 3 or more temperatures.

- The model was rewritten using correlations from existing PG grading data, making it possible to predict the hardening for any binder at any temperature and conditioning time using S(60) at 1 hr from BBR tests at multiple temperatures, the binder T_g , and the width of the glass transition region. Future work should focus on refining this relationship by increasing the pool of experimental data and binders used for developing the regression equations.
- The proposed physical hardening model can be used as a simple tool for the selection of asphalt binders that are less susceptible to extended isothermal conditions.

Chapter 5. Develop Low Temperature Specification for Asphalt Mixtures

Introduction

The main objective of this task is the development of low temperature performance specification for asphalt mixtures to control thermal cracking. This specification does not involve the use of a computer program as part of routine design. An optional, more rigorous specification, which requires running the ILLI-TC program, will be developed under Task 4. In order to accomplish this objective, the following subtasks were performed:

Subtask 1 – Develop Test Method

- Refine and possibly simplify the SCB and DCT fracture tests used in phase I.
- Propose a standard fracture test method based on SCB configuration for asphalt mixtures. Note that the DCT has been already approved as an ASTM standard.
- Develop standard fracture method. At the end of this task the research team will recommend only one fracture test but provide correlations between the results from the two methods.

Subtask 2 – Develop Specification

- Revisit the supporting field and experimental data that was used to develop the current PG system used to select asphalt binders. A similar approach, based on criteria providing limiting temperature values, will be used for the mixture specification
- Based on the experimental work performed in phase I and the work performed in task 2 and data available in previous research projects, develop limiting criteria for selecting asphalt mixtures resistant to low temperature cracking. The criteria will be based on fracture tests performed on specimens prepared from original loose mix.

Subtask 3 – Propose Simplified Method to Obtain Mixture Creep Compliance

- Since the IDT creep and strength data represent critical inputs in the MEPDG software it becomes important to revisit the IDT strength and creep test methods and analyses to find out if similar information can be obtained from other simpler tests.
 - Investigate if creep compliance can be obtained directly from tests performed in the SCB and DCT configuration
 - Investigate if BBR testing of thin asphalt mixture beams. This will be based on work in progress performed at University of Minnesota as part of recent NCHRP Idea project
 - Revisit work performed under previous MnDOT project to evaluate the feasibility of using Hirsch model
 - Investigate if strength can be obtained from BBR testing of thin asphalt mixture beams to failure; this work will be performed in conjunction with ARC work performed by University of Wisconsin.

Chapter 6. Subtask 1: Develop Test Method

Two fracture tests were used in this study to investigate the low temperature properties of asphalt mixtures. A summary of the two methods is provided next.

Summary of Fracture Testing Methods

Disc-Shaped Compact Tension DC(T) Test

The Disc-Shaped Compact Tension DC(T) test was developed as a practical method for the determination of low-temperature fracture properties of cylindrically-shaped asphalt concrete test specimens. The DCT's advantages include easy specimen fabrication, from both field and gyratory samples, and it is a standard fracture test configuration. The specimen configuration is shown in Figure 6.1. The DCT specimen are placed in a controlled chamber and conditioned for a minimum of 2 hours at the desired temperature. The test is performed under tensile loading and the crack mouth opening displacement (CMOD) is measured with a clip-on gage at the face of the crack mouth. After temperature conditioning, the specimens are inserted in loading fixtures, subjected to a preload, no greater than 0.2 kN, and then tested with a constant CMOD of 1mm/min (0.017 mm/s or 0.00067 in/s). The test is completed when the post peak level has reduced to 0.1 kN.

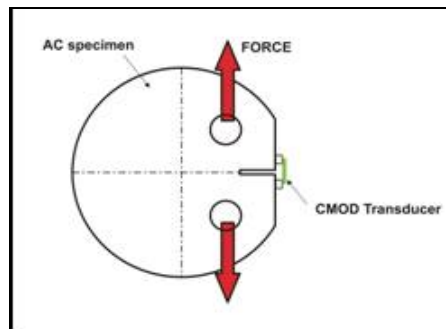


Figure 6.1: DC(T) testing scheme

Typical plots of Load vs. CMOD are shown in Figure 6.2. The fracture energy is calculated by determining the area under the Load-CMOD curve normalized by the initial ligament length and thickness.

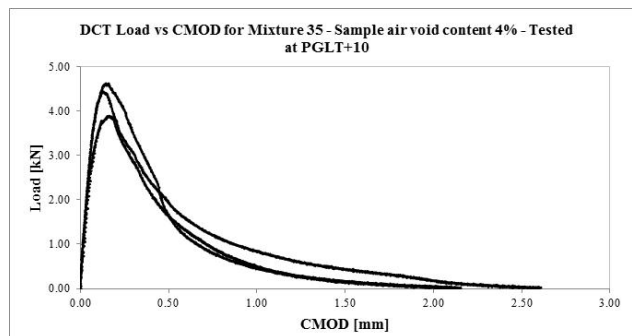


Figure 6.2: Typical load-CMOD plots from DCT tests of three replicates

Semi Circular Bend (SCB) Test

A schematic of the SCB specimen and loading is shown in Figure 6.3. Since loading is applied vertically to the specimen, the load line displacement (LLD), used to calculate fracture energy, is measured using vertically mounted extensometers on both faces of the specimen; one end of the extensometer is mounted on a button that is permanently fixed on a specially made frame, and the other end is attached to a metal button glued to the face of the specimen. The loading (cracking) is controlled by a crack mouth opening displacement (CMOD) attached at the bottom of the specimen. A constant CMOD rate of 0.0005mm/s is used for testing and the load and load line displacement are recorded and used to calculate Fracture toughness K_{IC} and fracture energy G_f .

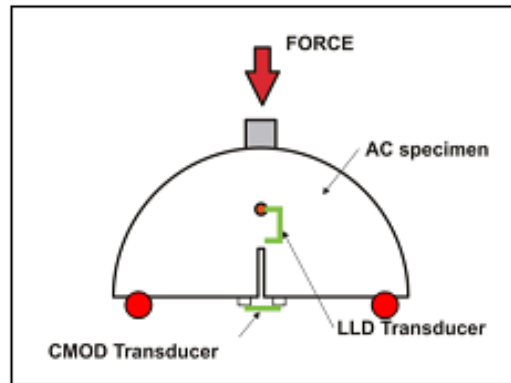


Figure 6.3: SCB testing scheme

A contact load with maximum load of 0.3 kN is applied before the actual loading to ensure uniform contact between the loading plate and the specimen. The testing is stopped when the load dropped to 0.5 kN in the post peak region. The tail part of the load-LLD curve can be reasonably obtained by fitting the data curve in post peak region following a method described elsewhere. Typical load versus LLD plots obtained from SCB tests are shown in Figure 6.4.

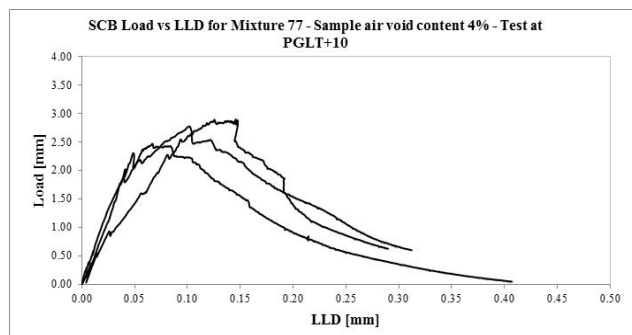


Figure 6.4: Typical load-LLD plots from SCB tests of three replicates

Proposed Standard Fracture Test Method

A simple comparison of the two fracture test method was performed to determine which method is less costly and time consuming and can be readily implemented as a standard fracture test for evaluating asphalt mixtures cracking resistance at low temperatures.

The Disk-Shaped Compact Tension Test, shown in Figure 6.5, is already specified in ASTM D7313.

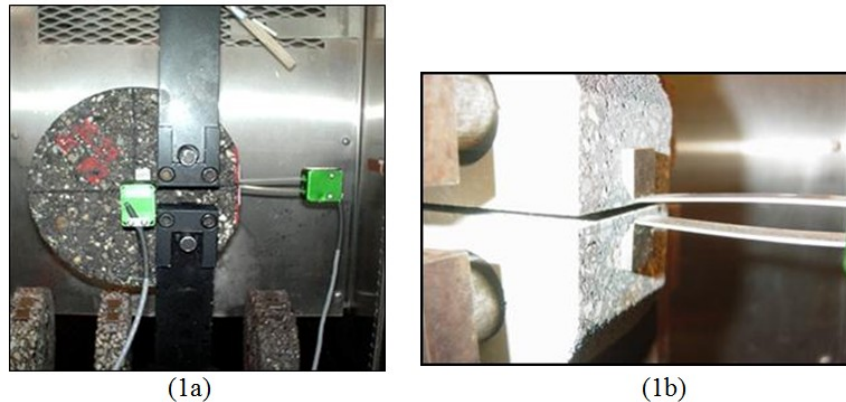


Figure 6.5: a) DC(T) test and b) CMOD gage attached to gage points

The test is used to obtain the fracture energy of asphalt mixture lab or field specimens, which can be used in performance-type specifications to control various forms of cracking, such as thermal, reflective, and block cracking of pavements surfaced with asphalt concrete. Standard testing is conducted at 10°C warmer than the PG low temperature limit. The DC(T) test is run in crack mouth opening displacement (CMOD) control mode at a rate of 1 mm/min. Typically, specimens are completely failed in the range of 1 to 6 mm of CMOD travel. Although the actual test takes only 1 to 6 minutes to perform, the actual amount of testing time per specimen is probably more akin to 15 minutes, accounting for stabilization of test temperature, loading samples into the test apparatus, etc.

Sample preparation involves sawing and coring operations. First, a water-cooled masonry saw (14 or 20 inch blade) is used to create the flat, circular faces, similar to the production of an indirect tension test specimen or simple performance test specimen. A single or dual saw system may be used. A dual saw system, while more costly, will produce more parallel faces and uniform thickness specimens, which may improve test repeatability. A marking template is used to indicate the location of the 1.0 inch loading holes to be drilled, see Figure 6.6.



Figure 6.6: DC(T) marking template

A water-cooled drilling device is then used to fabricate the loading holes, and a smaller masonry table saw is used to produce the final two cuts: a flattened face to facilitate the placement of the CMOD gage and a notch, which is a necessary feature of a true fracture mechanics based test.

Researchers at the University of Illinois have determined the average fabrication time per specimen to be in the 10 to 15 minute range for DC(T) testing, which includes the four saw cuts and two cored holes. This is based upon mass production of at least a dozen test specimens. The fabrication of fewer test specimens will obviously lead to a longer per-specimen preparation time. Thus, combined with testing time, each DC(T) test will take approximately 30 minutes of technician time for specimen preparation and testing when larger batches of specimens are tested. Material testing labs are currently charging in the neighborhood of \$200 per test specimen (replicate) for DC(T) testing, and somewhat less for larger quantities of specimens (\$150 per test). This is similar to the cost to perform other mixture and binder performance tests. The typical COV associated with DC(T) testing is around 10%; less for carefully controlled lab experiments with precisely fabricated specimens and uniform materials, and more for less carefully prepared and/or less homogeneous lab specimens and field cores. A COV level of 10% is excellent when compared to other fracture tests performed on infrastructure materials, which can have COV levels of 20 or even 30% or more.

- Estimated individual costs of the components required to build a DC(T) apparatus on an existing servo-hydraulic loading machine are shown in Table 6.1 below. For comparison purposes the estimated costs for the SCB test are also included in the table. Some equipment cost scenarios are shown below:
 - a. Lab with existing loading frame, existing cooling chamber, existing saws and coring rig, without optional dual saws: \$10,000.00 (\$13,000 if Labview programming costs are to be included).
 - b. Same as estimate #1, except cooling chamber purchase required: \$30,000.00. A lower estimate should be used if a simpler cooling chamber configuration is to be specified.
 - c. Purchase all components, including cooling chamber and both dual-saw systems: \$47,000.00.

At least two equipment manufacturers have recently developed or are in the process of developing DC(T) test apparatus, the most notable being James Cox and Sons, Inc. Although exact cost estimates should be pursued by contacting the equipment manufacturers directly, it is estimated that a future, simplified DC(T) test based upon a screw-type actuator system, would cost in the range of \$50k, not including dual-saw devices for sample prep. A more elaborate DC(T) test device, with a universal servo-hydraulic load frame capable of performing other tests, such as the simple performance test, IDT test, etc., would be expected to be in the \$140k range. Dual-saw sample preparation apparatus is currently being manufactured by Precision Machine Works (PMW) out of Salinas, KS. PMW also manufactures a version of the Hamburg Wheel track test.

Table 6.1: Estimated costs for DC(T) and SCB tests

Item	DC(T)	SCB
Loading fixtures	\$3,000	\$1,000
X-Y tables to facilitate coring and sawing	\$1,500	0
CMOD extensometer (Epsilon)	\$1,400	\$1,400
LLD extensometers (SCB only)	0	\$4,000
Environmental chamber*	\$20,000	\$20,000
Temperature modules and thermocouples	\$400	\$400
Coring barrels (five)	\$500	0
PC for data acquisition	\$1,000	\$1,000
Labview based interface board	\$700	\$700
Labview software for data acquisition	\$1,500	\$1,500
Labview programming**	\$3,000	\$3,000
Dual water cooled masonry saws***	\$10,000	\$10,000
Dual saw system for flat face and notching***	\$7,000	\$7,000

*A temperature chamber can be a major expense in low temperature performance testing of asphalt mixtures. The \$20,000 estimate is for a high-power, condenser-type cooling chamber, capable of testing down to -30C. A lower cooling chamber cost can result, if a less stringent cooling capacity is specified, or if a liquid-nitrogen based system is used.

** A simple Labview based data acquisition program can be provided to the participating states by the research team free of charge.

*** These items are optional, but recommended for labs conducting a high volume of testing

The Semi Circular Bend Test (SCB) is shown in Figure 6.7; a draft AASHTO specification was developed at the University of Minnesota.



Figure 6.7: The SCB test

SCB test is used to obtain the fracture energy of asphalt mixture lab or field specimens, which can be used in performance-type specifications to control various forms of cracking, such as thermal, reflective, and block cracking of pavements surfaced with asphalt concrete. Standard testing is conducted at 10°C warmer than the PG low temperature grade. Similar to DC(T) test, the SCB test is run in crack mouth opening displacement (CMOD) control mode. However, the rate is 0.03 mm/min, 33 times slower than the DCT loading rate, which increases the duration of the test to as much as 30 minutes. Another significant difference is in the thickness of the specimen: DC(T) is 2” thick, while SCB is 1” thick.

Sample preparation is similar to DCT except that no coring is required. The only additional operation is gluing one IDT-type button on each face of the specimen; the buttons are used for holding the extensometers used to measure load line displacement (the displacement in the direction of the applied force) required to calculate fracture energy.

Researchers at the University of Minnesota have determined the average fabrication time per specimen to be in the 10 to 15 minute range, similar to the time for DC(T) specimens preparation at University of Illinois. The typical coefficient of variation (COV) associated with SCB testing is around 20%; less for carefully controlled lab experiments with precisely fabricated specimens and uniform materials, and more for less carefully prepared and/or less homogeneous lab specimens and field cores. This is higher than the COV level of 10% reported for DCT.

Based on the existing information, it can be concluded that the two methods have similar costs associated with required equipment to perform the test and with specimen preparation and testing. **Since the DC(T) test for asphalt mixtures is already covered by an existing ASTM standard and follows a procedure that has been used for many years for other materials as part of the well accepted ASTM E399 fracture standard for testing metals, it is proposed to select the DC(T) as a fracture testing method for asphalt mixtures.** The SCB test can also be used as an alternative testing method, especially for situations in which only thinner specimens are available, such as testing for forensic studies. The research team will develop correlations between DC(T) fracture energy and SCB fracture energy based on the test data obtained as part of this research effort.

Chapter 7. Subtask 2: Develop Specification

Revisit Performance Grade (PG) Specification for Asphalt Binders

Asphalt binder is a highly temperature susceptible viscoelastic material. Prior to the introduction of the PG specifications, empirical test methods based on the measurements of viscosity, penetration, and ductility were largely adopted to characterize the binder properties. The current asphalt binder Performance Grade (PG) specification was developed during the Strategic Highway Research Program (SHRP). The new specification is based on fundamental rheological and failure parameters that can be related to pavement performance. The new parameters included complex shear modulus G^* , phase angle δ , creep stiffness $S(t)$, and logarithmic creep rate $m(t)$. New testing and aging methods were developed, such as Dynamic Shear Rheometer (DSR), Bending Beam Rheometer (BBR), Direct Tension Test (DTT), and Pressure Aging Vessel (PAV). In the next section, the development of the limiting criteria for low temperature cracking is summarized and discussed, since the development of these criteria was based on asphalt mixture field and laboratory data extrapolated to asphalt binder behavior.

Development of PG Low Temperature Cracking Criteria

In very cold climates, thermal cracking is the main distress that affects asphalt pavements. At these temperatures, asphalt binder becomes very stiff and reaches stress values higher than its strength, and cracks form and propagate. Cracking can occur due to a single critical low-temperature excursion or due to thermal cycling fatigue without necessarily reaching the critical low temperature. In the SHRP specification, only the former was considered.

The development of the SHRP asphalt binder criterion for low temperature cracking was based on the assumption that the 2-hour mixture stiffness correlated well with the severity of thermal cracking in the field. This assumption was extended to asphalt binder stiffness obtained in low-temperature creep tests. To expedite the testing process the time-temperature superposition principle was used to show that, for asphalt binders in general, the stiffness at 60 seconds at $T_1^\circ\text{C}$ is approximately equal to the stiffness at 2 hours at $T_1 - 10^\circ\text{C}$. To keep the PG binder specification to a reasonable level of simplicity the effects of physical hardening were not considered although one of the major findings during SHRP was the significant effect of physical hardening on binder physical properties.

The slope at 60 seconds of the stiffness vs. time curve on a double logarithmic scale, the m -value, was introduced as an additional parameter to control the rheological type of asphalt binders and to eliminate heavily blown asphalts, which in fact were associated with poor fatigue performance. This additional criterion was based on the idea that a low m -value corresponded to slower relaxation of the thermal stresses that build up at low temperatures, which was detrimental for performance.

A simple fracture test was also required as part of the original SHRP binder specification. A dog bone shaped specimen was pulled with a constant strain rate and the tensile fracture stress and strain were obtained. A second critical temperature was obtained as the temperature at which the failure strain was 1%. The 10°C shift was also applied to this temperature. Due to the low repeatability of the results, the direct tension test was made optional in the most recent version of

the specifications. However, fracture experiments are known to be less repeatable than other material characterization experiments that do not involve fracture; in addition test data indicates that the repeatability issue is significant only for certain types of binders, which indicates that the poor repeatability may be a material property or a specimen preparation problem and not a testing problem.

A review of the two papers used in the development of the BBR creep stiffness criterion, reveals some important information about mixture properties. Most of the results were obtained at the Ste. Anne Road Test, conducted by Shell Canada and the Manitoba Department of Highways in late 1960's. Twenty-nine sections were constructed with four different asphalts on clay and sand subgrades. Temperatures were measured at different levels in the pavement structures. Observations of cracking frequency and analysis of the rheological properties of the bitumens using the Van der Poel nomograph, the penetration-temperature relationships and Hills and Brien's method of calculating cracking temperatures showed reasonable agreement except that the calculated values were lower than the temperature at which significant cracking occurred in the field. Based on this research, it was concluded that the critical stiffness of the bitumen was 240MPa for a ½-hr. loading time, and that cracking would not occur if the binder did not reach this value of stiffness at the service temperatures encountered. In Ontario, Fromm and Phang, presented a method of specifying the grade of asphalt used for a given service temperature. They assumed a critical stiffness of 138MPa with a loading time of 2.8 hours. In a later paper, Readshaw concluded that transverse pavement cracking can be largely controlled by the use of binders which do not exceed a critical stiffness of about 200MPa at their lowest service temperature, as computed from Van der Poel diagram. This value was later used by researchers at Penn State to propose the existing 300MPa limit at 60s loading time.

In both papers, there is no mention about the mixture stiffness values used in the calculations. These values are found at the end of the Ste. Anne 1971 AAPT paper in the discussion prepared by N. W. McLeod. He mentions that, for a loading time of 20,000 seconds or 5.55 hours, the authors' critical pavement modulus of stiffness at which low temperature transverse pavement cracking is likely to occur, is 2,000,000 psi or 14GPa. However, based on his observations, he tentatively concluded that the critical low temperature pavement modulus of stiffness at which transverse pavement cracking is likely to occur is 1,000,000 psi or 7GPa, for a loading time of 20,000 seconds or 5.5 hours, a Cv value of 0.88, and 3 percent air voids. This limiting value was imposed on asphalt pavements at any time during its service life and "particularly as it nears the end of its service life." This information will be used in subtask 3 to propose a creep stiffness limiting value for low temperature cracking.

Develop Asphalt Mixture Low Temperature Specification

In this subtask, an approach similar to the one used to develop the current PG system is used to propose a low temperature mixture specification. The criterion is based on fracture tests performed on specimens prepared from original loose mix. This approach requires having both experimental fracture data as well as field performance for the same mixtures tested in the laboratory. Presently, the field sections constructed with the asphalt mixtures used in the experimental work performed in Task 2 have not cracked significantly to provide a wide range of values that can be used to develop a limiting criterion. This will be developed using the data

obtained in the first phase of this research effort and the data obtained in task 2 will be used to verify that the proposed threshold values work.

It should be however noted that the main obstacle in proposing critical values for asphalt mixtures is reasonably quantifying the effect of aging on mixture fracture parameters, since field performance when cracking most likely occurs represents a later stage in pavement life. At this point, there is no fully accepted long term aging method for asphalt mixtures. Therefore, for the time being and until a long term project will provide such critical information, it is proposed to use a fixed value to quantify the reduction in fracture energy with aging.

Asphalt Mixture Low Temperature Specification Based on DC(T) Fracture Energy

Using data collected in the initial phase of this study, field thermal cracking data was correlated to DC(T) fracture data. From these results, a minimum fracture energy of 400 J/m² is suggested for protection against thermal cracking (Figure 7.1), as determined at a test temperature equal to the binder Performance Grade low temperature (PGLT) limit plus 10 degrees Celsius (e.g., the test temperature that is used for verifying the Superpave PGLT grade). Fracture energy in the range of 350-400 J/m² is considered borderline, and may be permissible on projects of lower criticality, where a low to moderate degree of thermal cracking can be tolerated. For projects of high criticality, a factor of safety can be achieved by specifying a minimum fracture energy of 600 J/m². Mixtures with this level of fracture energy have been found to be resistant to both thermal cracking and reflective cracking. However, reflective cracking will only be avoided if the underlying pavement has high load transfer efficiency.

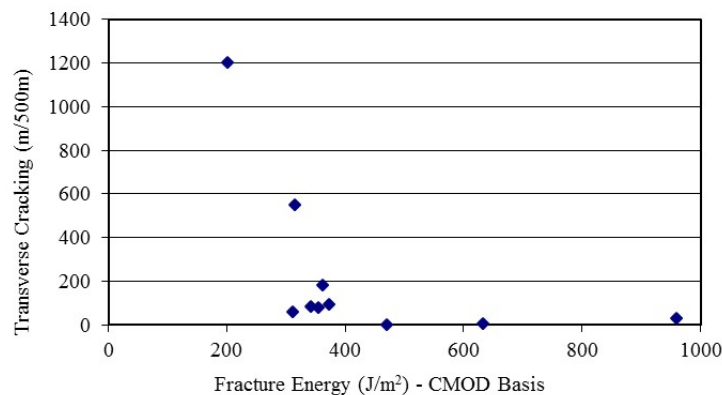


Figure 7.1: Field data suggesting a minimum fracture energy of 400 J/m² at PGLT + 10°C to prevent thermal cracking

The computer program ILLI-TC, which will be developed in Task 4 of this project, uses fracture energy and creep compliance data, along with pavement structure and climatic information to predict thermal cracking versus time. For projects with high or moderate criticality, this program provides extra assurance that thermal cracking will be controlled, since the combined effects of mixture fracture properties, creep/relaxation behavior, thermal coefficient, and site-specific diurnal temperature cycling are considered. For high criticality projects, only negligible amounts of thermal cracking can be tolerated. Due to the characteristics of the probabilistic model that converts the single predicted thermal crack to amount of cracking, the specification of exactly zero predicted cracking is likely to be overly conservative (a very shallow predicted crack will

yield a low amount of predicted cracking, but will not likely manifest itself as a visible crack in the field). Thus, a maximum predicted thermal cracking level of 4 m of cracking per 1 km of pavement (one crack per km) is specified. For projects of moderate criticality, a maximum predicted thermal cracking level of 64m/km is specified (assuming 4m wide pavement, this represents 16 cracks per km, or 1 lane-wide crack per 100 m). In addition, the use of ILLI-TC is specified as optional. For low criticality projects, the use of ILLI-TC is not required.

Based upon the results presented earlier, a thermal cracking specification is proposed. Since these results were based on cores taken out of older pavements, a 15% increase in fracture energy is proposed to take into account the fact that these requirements are specified for loose mixtures and short term aged laboratory mixtures (Braham et al., 2008). Specification limits for three levels of project criticality are provided. A higher fracture energy threshold is suggested in order to limit thermal cracking to lower levels on projects of high criticality. High criticality/high traffic pavement structures tend to involve thicker asphalt concrete layers, where the effects of thermal cracking on future maintenance and rehabilitation activities can be very significant. In addition, these pavements tend to have lower asphalt content, and higher in-place air voids, as a higher design gyration limit and stronger aggregate structure is required in order to mitigate rutting during summer months under heavy traffic. Thus, the potential for more rapid aging near the pavement surface exists, and can be addressed by specifying a higher fracture energy threshold. Finally, limiting thermal cracking on high traffic level facilities will serve to reduce the user costs associated with operating vehicles on rough pavement (Islam and Buttlar, TRB 2012).

Table 7.1: recommended low-temperature cracking specification for loose mix

Contents	Project Criticality/ Traffic Level		
	High >30M ESALS	Moderate 10-30M ESALS	Low <10M ESALS
Fracture Energy, minimum (J/m ²), PGLT + 10oC	690	460	400
Predicted Thermal Cracking using ILLI-TC(m/km)	< 4	< 64	Not required

Alternative Asphalt Mixture Low Temperature Specification Based on SCB Fracture Energy

The same approach used to propose the DC(T) based specification was used to propose alternative limits for the SCB fracture energy. Summaries of the data obtained in the first phase of the pooled fund study are provided in the next two tables. All parameters were correlated with the total length of transverse cracking. The comparisons were made at temperatures representative for each site to take into account local climate conditions.

Table 7.2: LTPP low pavement temperature at 50% reliability level

Section	Station	Temperature, [°C]
IL I74	Urbana, IL	-16.4
MN75 2	Collegeville, MN	-24.4
MN75 4	Collegeville, MN	-24.4
MnROAD 03	Buffalo, MN	-23.8
MnROAD 19	Buffalo, MN	-23.8
MnROAD 33	Buffalo, MN	-23.8
MnROAD 34	Buffalo, MN	-23.8
MnROAD 35	Buffalo, MN	-23.8
US20 6	Freeport, IL	-19.7
US20 7	Freeport, IL	-19.7
WI STH 73	Stanley, WI	-24.7

Table 7.3: Mixture parameter and total length of transverse cracking in the field

	SCB Fracture Energy [J/m ²]	IDT Creep Stiff. [GPa]	SCB, Fracture Tough. [MPa m ^{0.5}]	IDT Tensile Strength [MPa]	Transverse cracking [ft/500ft]
IL I74	161.7	-	0.591	-	1200
MN75 2	355.3	24.2	0.785	3.35	76
MN75 4	479.0	24.9	1.024	5.59	30
MnROAD 03	273.9	23.0	0.755	4.65	182
MnROAD 19	260.4	20.2	0.689	4.22	547
MnROAD 33	277.8	17.9	0.734	4.61	91
MnROAD 34	425.1	19.8	0.881	6.67	5.5
MnROAD 35	308.6	12.6	0.750	4.86	747
US20 6	341.0	-	0.711	-	84
US20 7	360.4	-	0.714	-	60
WI STH 73	295.0	22.2	0.881	5.68	0

Based on the results plotted in Figure 7.2, a limiting value of 350J/m² is proposed. This value is adjusted to a limit of 400J/m² to account for aging effects.

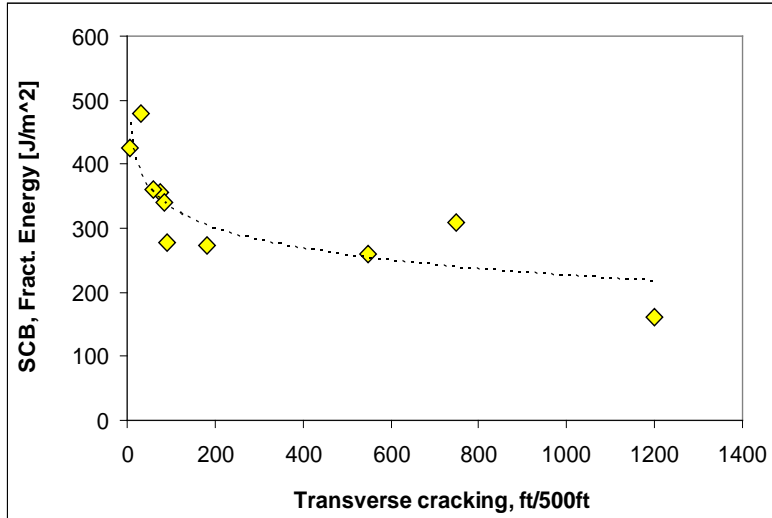


Figure 7.2: Field data suggesting a minimum SCB fracture energy of 350 J/m² at PGLT + 10°C to prevent thermal cracking

Since fracture toughness was also highly correlated to cracking occurrence, as seen in Figure 7.3, a value of 800 kPa*m^{0.5} is suggested as a possible limit that can be used in addition to fracture energy limit as an additional check for good fracture resistance. No age adjustment is proposed for fracture toughness.

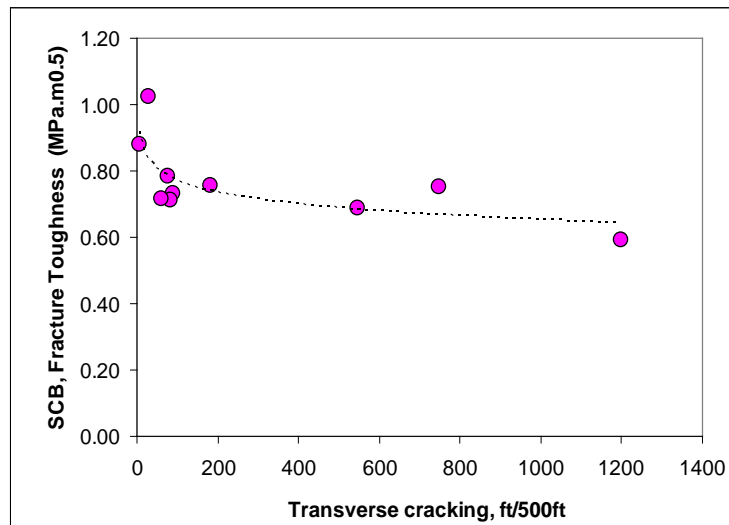


Figure 7.3: Field data suggesting a minimum fracture toughness of 800kPa×m^{0.5} at PGLT + 10°C to prevent thermal cracking

Chapter 8. Subtask 3: Proposed Simplified Method to Obtain Mixture Creep Compliance – Part 1

Since the IDT creep and strength data represent critical inputs in the ILLI-TC software it becomes important to revisit the IDT strength and creep test methods and analyses to find out if similar information can be obtained from other simpler tests.

Obtaining Creep Compliance from DC(T) Test

Since the IDT creep test may not be available in many labs due to its relatively high cost and complexity, a surrogate tests that can be run in conjunction with the DC(T) is under investigation (creep results obtained prior to running fracture test).

A key question that needed to be answered in order to assess the feasibility of such an approach was: “can a creep test be performed on a DC(T) specimen prior to fracture testing without compromising the integrity of subsequently obtained fracture data? It was also necessary to check whether or not the creep data obtained from the DC(T) test would be comparable to the data obtained from the IDT.

The IDT creep testing procedures are specified in AASHTO T322-07. In the combined creep/fracture test, a static tension load is applied on the DCT sample and extensometers are used to measure deflections at the notch tip on both faces of the sample. The extensometers are the same ones specified for creep testing in the Superpave Indirect Tension Test (IDT), specified AASHTO T322-07, which in the case of the Advanced Transportation Research and Engineering Laboratory (ATREL), involved the use of Epsilon 3910 series extensometers. By placing the extensometers slightly ahead of the crack tip, bulk material tensile straining can be measured during a creep test, which is in turn used to obtain creep compliance from the DC(T) testing arrangement. Once the creep test is completed, the DC(T) sample is allowed to recover. After recovery, the sample is tested for fracture energy using the ASTM D7313-07 standard. Figure 8.1 illustrates the concept of the combined creep/fracture test. Finite element modeling is being used to obtain a conversion factor to convert measured deformation and creep load to creep compliance, as explained in a later section. Figure 8.2 shows typical creep data obtained from the combined DCT-IDT test.

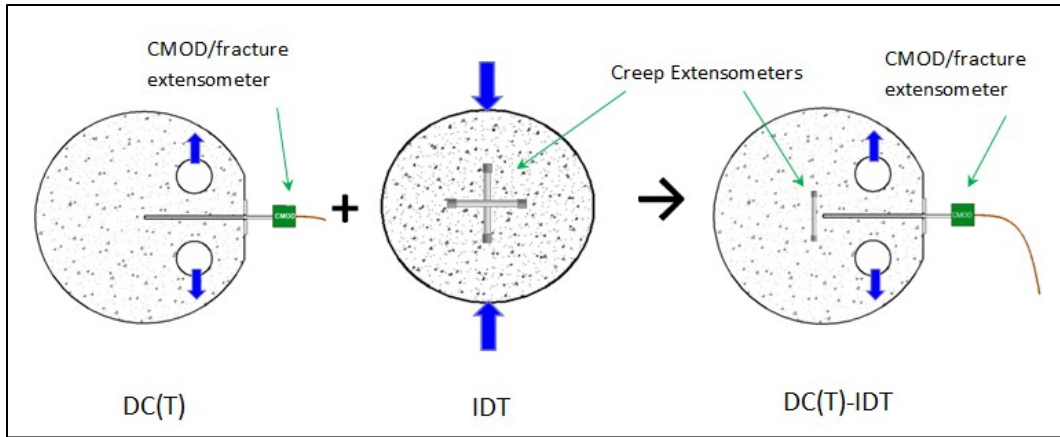


Figure 8.1: Comparison of disk-shaped compact tension [DC(T)] test, indirect tension test (IDT) and combined DC(T)-IDT test geometries.

Laboratory testing was conducted to evaluate whether or not conducting creep testing prior to fracture testing causes enough damage to significantly affect the measured fracture energy of the mix. This focused study involved testing 3 DC(T) samples for fracture energy and 3 DC(T) samples for both creep compliance and fracture energy. Preliminary tests were first conducted to determine the level of creep loading required obtaining strain responses in the extensometers that were within the allowable ranges specified in AASHTO T-322. Required creep loads were generally in the 1.5 kN range. After creep testing was completed, samples were allowed to recover for 24 hours and the fracture energy test was then conducted.

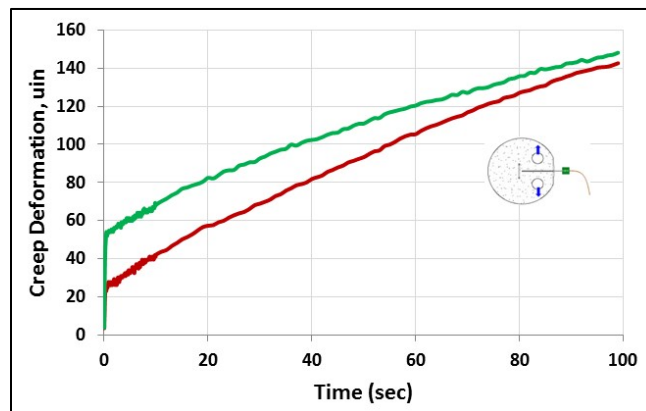


Figure 8.2: Typical creep deformation results in DC(T) - IDT test obtained from extensometers mounted on both sides of the specimen near the crack tip

The fracture energy test results suggest that there is no statistical difference between the fracture energy of the DC(T) samples tested only for fracture energy versus those tested for both creep compliance and fracture energy. Table 8.1 shows the comparison of the two fracture energies, with population means differing by around 1.5%. Since the typical coefficient of variance for the DC(T) test is around 9-10 percent, the difference obtained was statistically insignificant.

Table 8.1: Fracture energy for creep + fracture versus fracture only testing

Condition	Peak Load (kN)	Average Peak Load (kN)	Fracture Energy (J/m ²)		
			CMOD	CMOD average	CMOD CoV
Creep followed by fracture	3.3	3.4	346.0	371.7	9.3
	3.2		358.0		
	3.7		411.0		
Fracture testing only (control)	3.3	3.4	371.0	377.3	5.6
	3.5		360.0		
	3.3		401.0		

The above result suggests that conducting creep compliance testing followed by fracture testing on asphalt concrete samples in the DC(T) geometry may not compromise the traditional DC(T) fracture energy test results. Thus, for agencies wishing to control thermal cracking using both fracture and creep limits, such as in the case of mixtures containing significant amounts of RAP, it may be possible to conduct both tests with a single test apparatus (the DC(T) test apparatus). This could limit test device expense to under \$50k, as opposed to the need for >> \$100k of equipment, if both fracture and creep test apparatus was needed. Further work is needed to validate this result for a broader range of mixtures and to determine if a shorter rest period could be used; however, the preliminary results are very encouraging.

Finite Element Simulations

In the current study, an attempt was made to use finite element technique in conjunction with a cohesive zone model (CZM) to simulate the DCT-IDT test. Simulation of the new testing method is performed using the commercially available finite element software, ABAQUS, considering two-dimensional (2D) plane stress condition. Four-noded quadrilateral (Q4) elements were used to represent the asphalt mixture material. In addition to Q4-type elements, 2D bi-linear cohesive zone elements were embedded in the finite element model along pre-defined crack path. Various element sizes were used to develop the model. In critical region, along the horizontal diameter of DCT sample, element size reduced to 1mm×1mm. Special care was taken to keep the aspect ratio close to 1 and corner angles 90 for elements in and near the critical region. Prepared finite element model is shown in Figure 8.3.

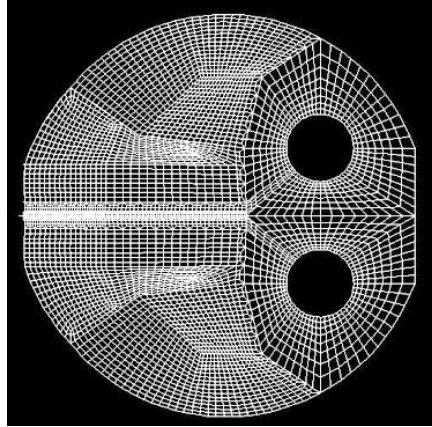


Figure 8.3: Finite element mesh of DCTIDT sample

To investigate the effects of notch on creep deformations, two different finite element models including DCTIDT sample with and without notch were prepared. Figure 8.4 schematically represents samples with and without notch.

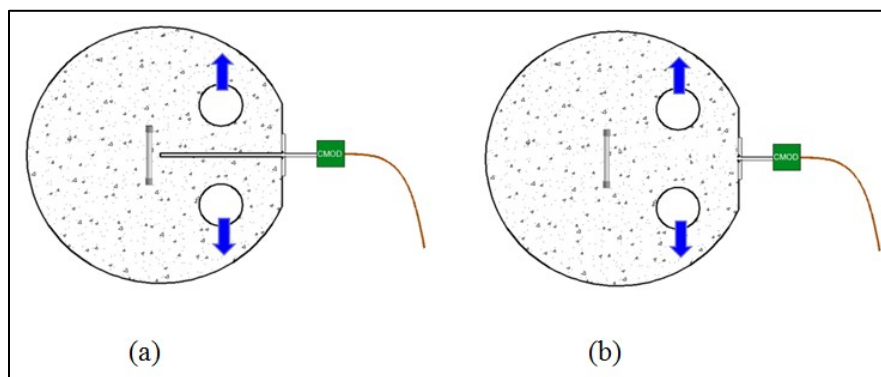


Figure 8.4: (a) DCTIDT sample with notch (b) DCTIDT sample without notch

The analyses were performed assuming modulus of 23 GPa and Poisson's ratio of 0.35 for asphalt materials. Static tensile creep load of 1kN was applied for 1000 seconds. Figures 8.5-8.7 and Figures 8.8-8.10 show the elastic simulation results of DCTIDT sample with and without notch, respectively.

The objectives were:

- To determine the area where the stress distribution along the Y axis is fairly uniform and the zone is relatively unaffected by the stress concentration near the notch tip.
- -To evaluate the distribution and magnitude of stresses built up inside the specimen during running creep test; making sure the induced stresses remain less than tensile strength of the material. This is done to assure there is no micro-damages that could possibly affect fracture test results, occurs during conducting creep test.

Since both models are symmetric, only the stress distribution and total deformation of half of sample (top half) are presented. The vertical stress (S_{yy}) distributions along the Y axis at different

locations along the X-axis are presented in Figures 8.7 and 8.10. Comparing the stress distribution of the area located fairly close to the notch tip (2mm) and the area located just a few millimeter farther from the notch tip (10mm) shows significant drop in the stress level. The high magnitude S_{yy} observed in the immediate vicinity of the notch tip can be attributed to the stress concentration effect due to presence of notch in the sample. It is observed that the S_{yy} stress distribution becomes fairly uniform when the area is located more than 10mm away from the notch tip. The S_{yy} distribution is shown in Figure 8.10. Comparison of the stress distribution of samples with and without notch clearly shows the effects of notch on S_{yy} stresses. There are significant drop in stress level is observed between samples with and without notch. The total relative deformation in Y direction followed the same trend; as U_2 of samples with notch were almost three times those of sample without notch.

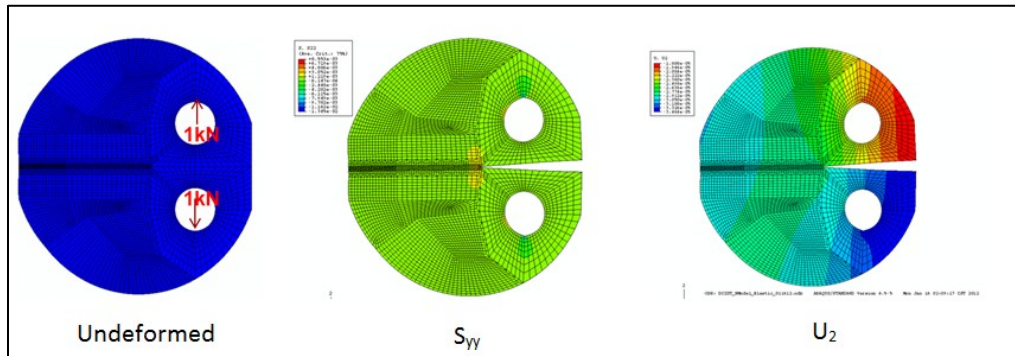


Figure 8.5: DCTIDT sample with notch elastic model simulation results

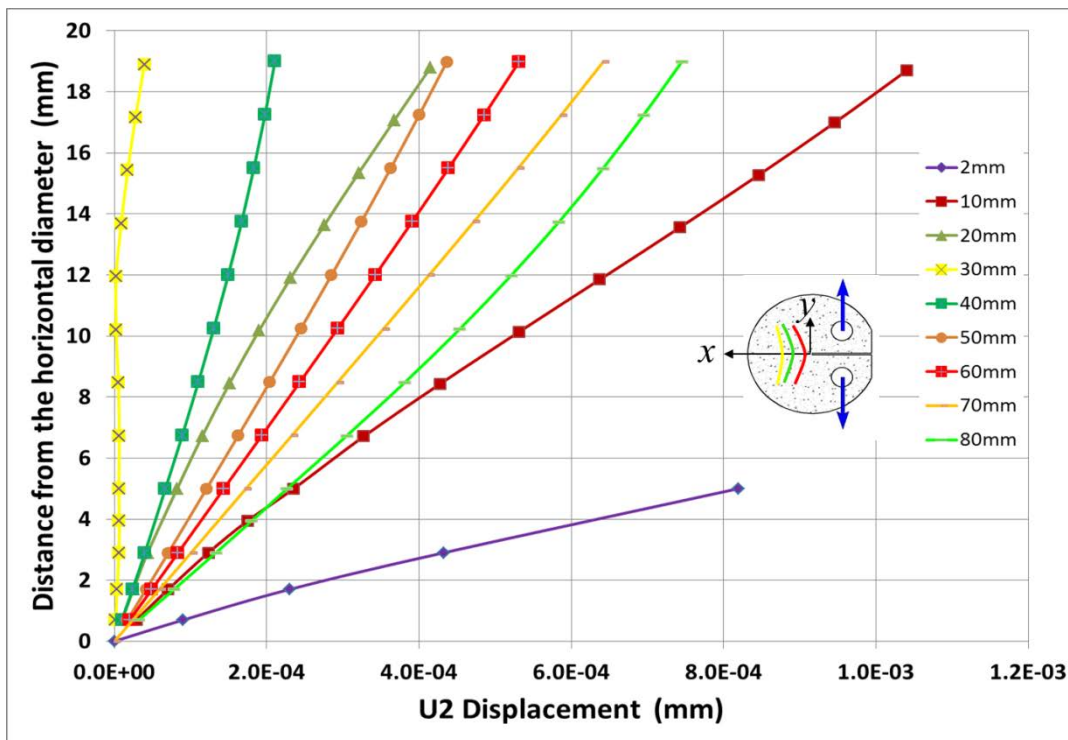


Figure 8.6: DCTIDT sample with notch elastic simulation results

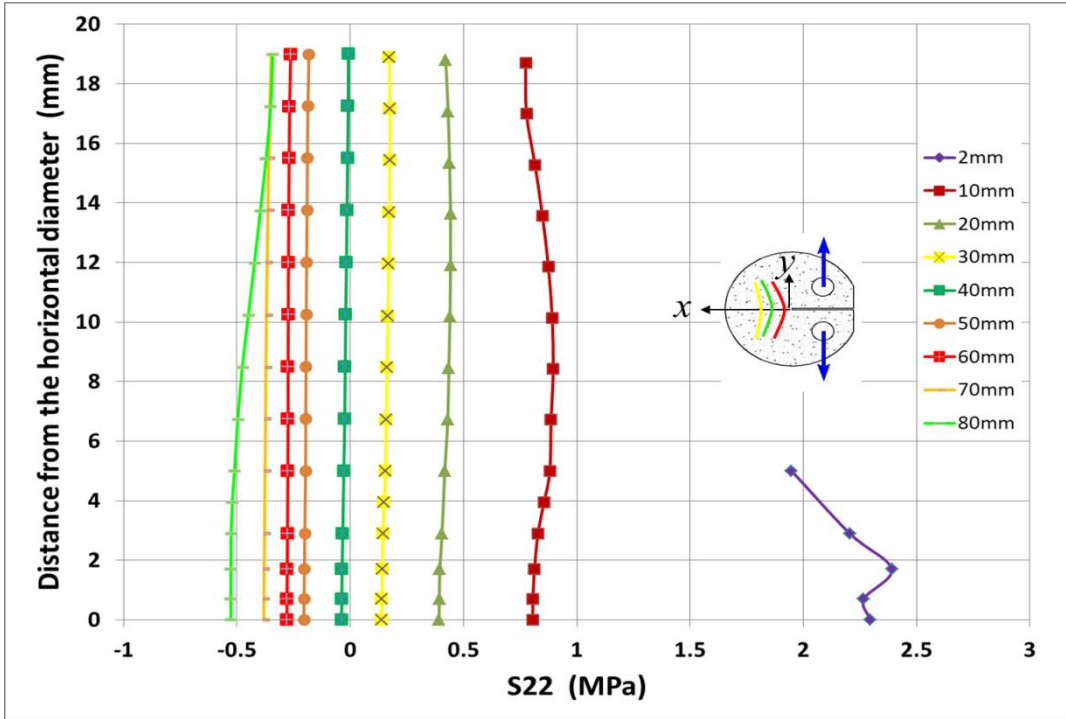


Figure 8.7: DCTIDT sample with notch elastic simulation results

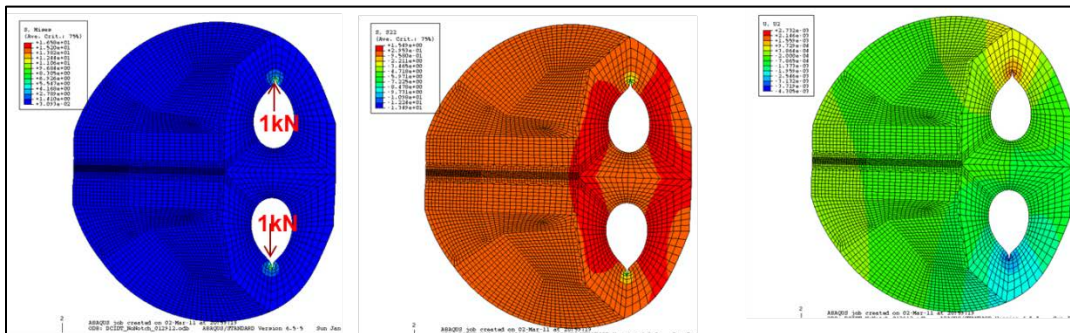


Figure 8.8: DCTIDT sample without notch elastic model simulation results

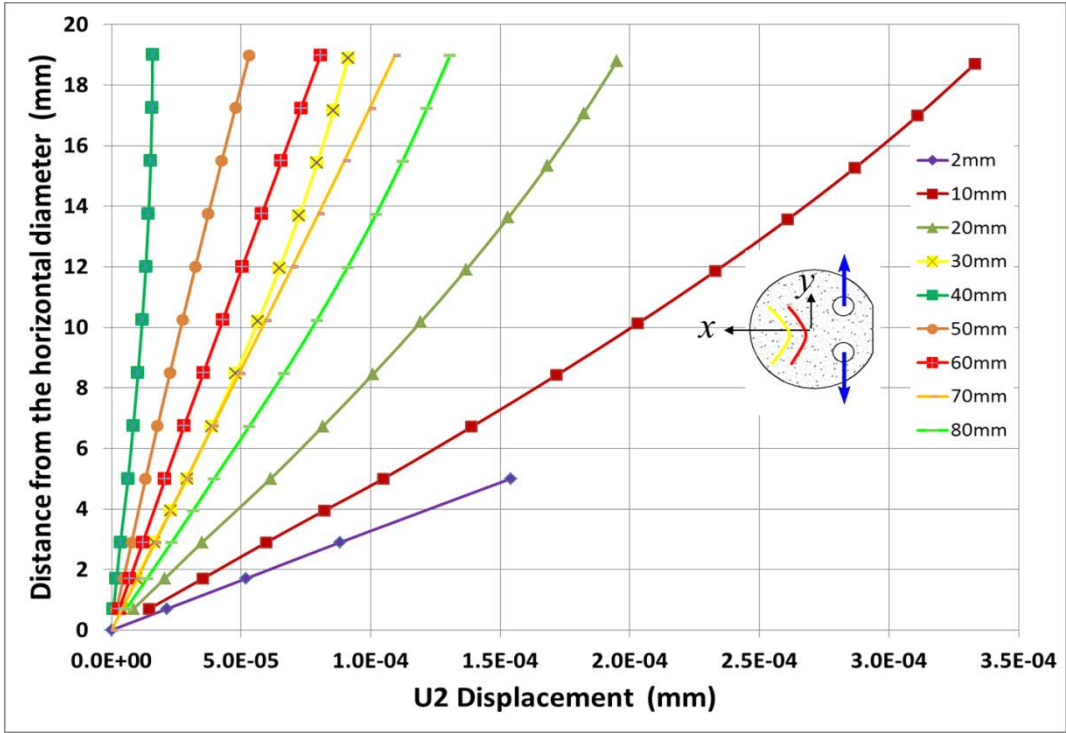


Figure 8.9: DCTIDT sample without notch elastic simulation results

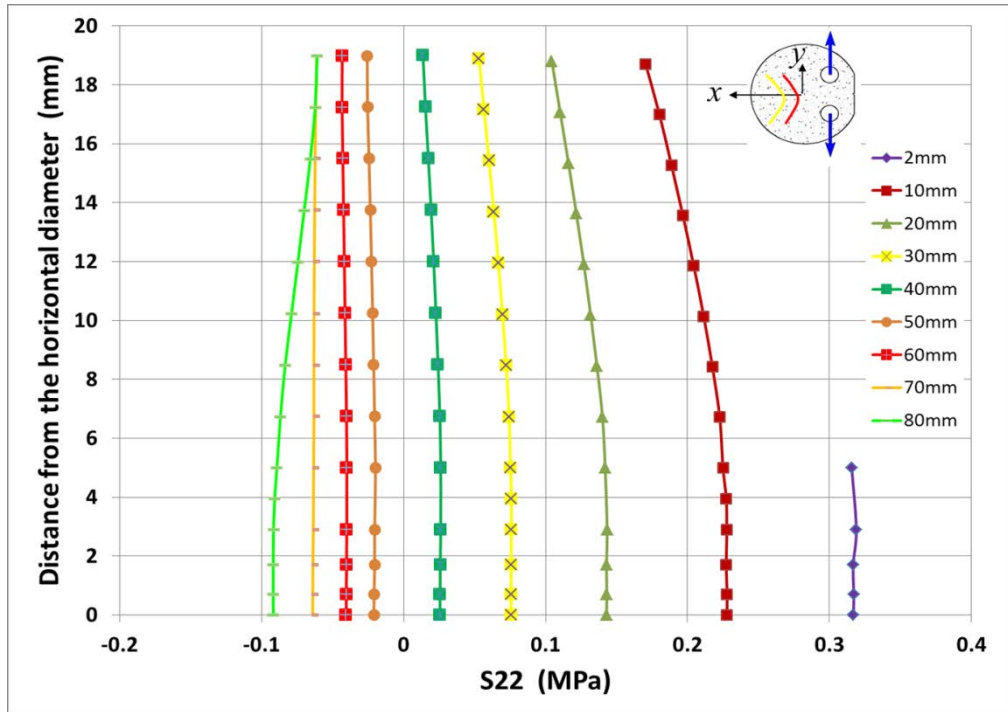


Figure 8.10: DCTIDT sample without notch elastic simulation results

Obtaining Creep Compliance from SCB Test

The test methodology proposed consists in using a standard notched SCB specimen to obtain both creep compliance and fracture parameters. In addition to the LLD and CMOD gauges used for fracture testing, a third gauge is employed for creep displacement measurement from a particular region of the specimen. The testing involves a mixed load and CMOD control approach. The specimen is conditioned at the desired test temperature for 2 hours and then subjected to a constant load for 1000 sec. At the completion of the creep test, the loading control is switched to a constant CMOD control to perform standard SCB fracture test. For the entire duration of creep and fracture testing, the specimen is kept in the environmental chamber. Determination of the best location for creep displacement measurement, as well as the optimal creep load, small enough to maintain the material in the linear viscoelastic region and yet produce appreciable displacements, are critical in this research investigation.

Linear Viscoelastic Conditions

Asphalt concrete is a composite material consisting of three phases: aggregate, binder and air (voids). The proportions of the components play a significant role in defining the mechanical properties of the mixture. In principle, the behavior of aggregate and asphalt binder can be idealized, as linear elastic and viscoelastic, respectively. The resulting composite material has a rather complicated behavior that is time, rate and temperature dependent (1). At low temperatures, it is fairly accurate to consider asphalt concrete as a linear viscoelastic material (2, 3), and a constitutive relationship between stresses σ and strains ε can be expressed in the form of convolution integrals by means of the Boltzman's superposition principle (4, 5):

$$\varepsilon_{ij}(t) = \int_0^t D_{ijkl}(t - \xi) \frac{\partial \sigma_{kl}(\xi)}{\partial \xi} d\xi \quad [8.1]$$

$$\sigma_{ij}(t) = \int_0^t E_{ijkl}(t - \xi) \frac{\partial \varepsilon_{kl}(\xi)}{\partial \xi} d\xi \quad [8.2]$$

D(t) and E(t) represent the creep compliance and relaxation modulus, respectively, and are related through a Voltera integral in equation [8.3):

$$t = \int_0^t E(t - \xi) D(\xi) d\xi \quad [8.3]$$

Several numerical methods (6, 7) are available to solve equation [8.3) for the relaxation modulus knowing the creep compliance since for many materials an analytical solution is not possible.

The estimation of a material parameter from stress and strain data involves an inverse problem solution. In theory, stresses and strains corresponding to sufficiently small loads and measured at a point far from the SCB specimen crack tip can be used to determine material's elastic parameters. For creep loading, the viscoelastic parameters are then easily derived through the elastic-viscoelastic correspondence principle. However, asphalt concrete is a non-homogeneous

material composed of aggregate, asphalt and air, and each component has different material properties. Thus material parameters derived from point measurements may not be accurate. To overcome this problem, the stress and strain are averaged along a sufficiently long segment. It is therefore important to identify and quantify accurately the regions of high stress concentration. By isolating the crack and boundary governed regions, the SCB elastic region is used for the determination of the elastic and viscoelastic parameters.

Analysis of Stress State in SCB Specimen

Due to the complex geometry, the stress state of notched SCB specimen in three-point bending was investigated through FE analyses. For this purpose the commercially available software ABAQUS was employed.

Numerical simulations were performed using the standard dimensions and loading configuration of a SCB specimen. A two dimensional plane stress model was developed using second-order quadrilateral elements. The material was assumed to be isotropic, homogeneous and linear elastic. Thus, the bulk of the model was described through the Young Modulus E and the Poisson’s ratio ν . The initial crack notch was modeled using a seam-crack, which is a crack modeling tool provided in ABAQUS. The crack tip was meshed using rings, centered at the crack tip, of collapsed quadratic quadrilateral elements. A “single node” degeneracy method was used for the elements in the first contour so that one edge of each element collapses to zero length allowing the nodes to locate at the crack tip. This type of settings allows the introduction of square root singularity for stress near the crack tip. Very fine meshes were used near singular points where high stress concentrations are expected to occur. For the rest of the specimen, relatively coarse mesh was applied.

The SCB finite element model was first used to compute the normalized stress intensity factor Y_I for varying initial notch lengths. The results were found to be in good agreement with the well-established normalized stress intensity factor equation for SCB specimen provided by Lim et al.,(8) as shown in Figure 8.11. This implies that the stress state, especially near the crack tip, is accurately captured by the adopted SCB finite element model. Hence, it can be used to isolate the regions of SCB specimen in which the stresses change rapidly over short distances.

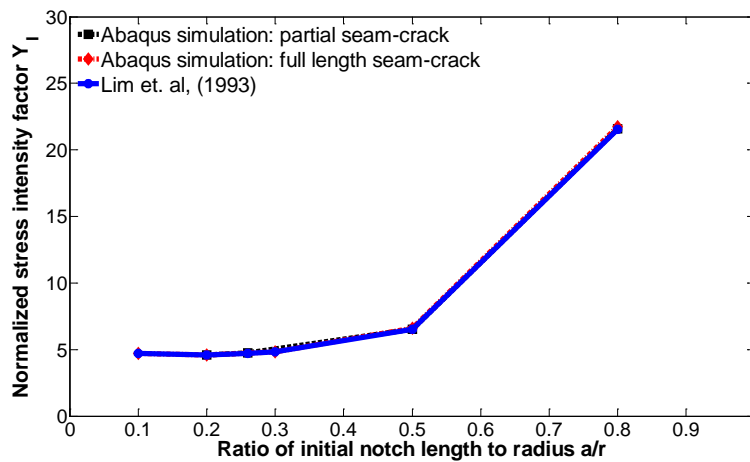


Figure 8.11: Verification of FE model

The stress state displayed in a SCB specimen under three-point loading is a very complex one. Figure 8.12 and Figure 8.13 show the Von Mises stress plots, respectively, for 1kN and 2 kN of load. The contour scale has been adjusted in order to identify the areas in the analysis that exceeded typical strength of asphalt mixtures. The strength value was set equal to 3MPa, very conservatively. The dark areas (colored in red in color print) represent high stress concentration, above the material strength. These areas correspond to the region near the crack tip, loading point, and vicinity of the support rollers. The sizes of these areas increase drastically with load.

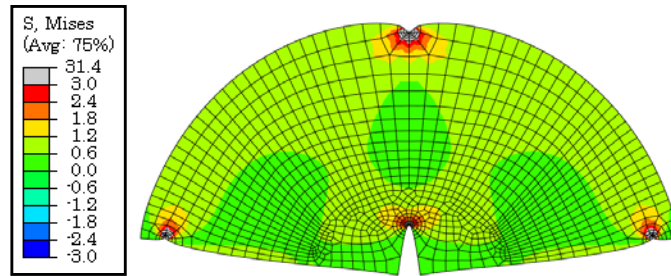


Figure 8.12: SCB stress state for a load of 1kN

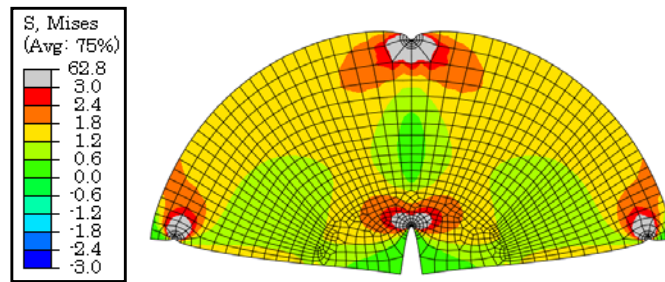


Figure 8.13: SCB stress state for a load of 2kN

The plot of principal stresses, illustrated in Figure 8.14, indicates that large tensile stresses are generated at the bottom of the specimen. The principal directions, of elements in the bottom region, are parallel to the longitudinal axis-x, hence the shear stress are practically close to null. While, in the upper region a compressive arch is developed. The inclined principal stresses, in the upper region, indicate the existence of shear stress.

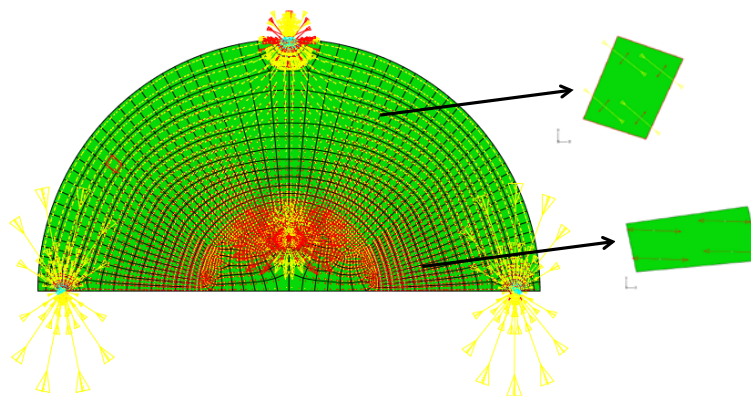


Figure 8.14: SCB stress state – plot of principal stress

Parametric analytical studies conducted by varying the material constants, E and ν , indicated that the stress state in a SCB specimen subjected to three-point loading is independent of the material constants. Thus, the stresses developed in an elastic SCB specimen subjected to a three-point bend test are similar to those in a viscoelastic SCB specimen tested at the same condition. This behavior is analogous to that observed in testing IDT specimens, in which the equations for the stresses along the central x and y axes are independent of material constants and remain unchanged when subjected to Laplace transforms. In addition, in order to apply the Laplace transforms, the stresses need to remain constant in time. The variation of stresses in time in a three point bending tests of a standard SCB specimen was analyzed through a viscoelastic FE model, and discussed in the next section.

The SCB elastic finite element model, with a notch of 15 mm, was used to analyze the stress distribution along several paths, on the SCB specimen surface, that could be used for displacement measurements. The transverse σ_{xx} and the vertical stresses σ_{yy} along the considered paths are shown in Figure 8.15. For the purpose of finding an approximated creep compliance equation, the shear stresses in the upper region of the SCB specimen were neglected. This assumption allows computing normal strains from displacement measurement obtained from a horizontal (parallel to the x-axis) trajectory. The stresses in the plot are normalized by the nominal stress σ_0 .

$$\sigma_0 = \frac{P}{bD} \quad [8.4]$$

Where b and D represent, respectively, the thickness and diameter of the specimen.

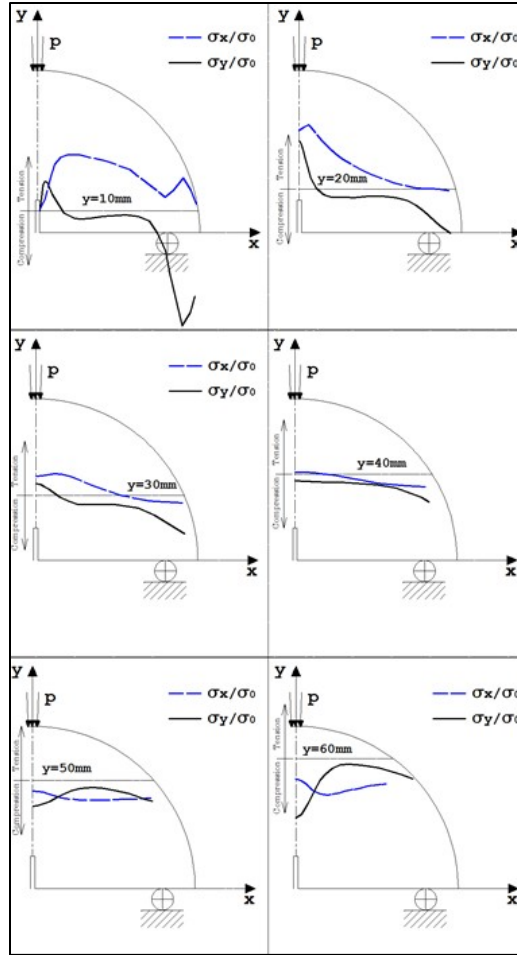


Figure 8.15: Stress distribution along several horizontal trajectories in SCB specimen

The trajectories that provide a sufficiently long segment in which the stresses have the same sign (tension or compression) and are almost uniform are favored. For $Y=10$ mm (10 mm from the x-axis) the stresses are almost uniform in the middle region but exhibit an abrupt change near the crack tip and the support rollers. It might be difficult to accurately identify a segment not affected by the boundary induced stresses. The stress distribution in the $Y=20$, $Y=30$, $Y=40$, and $Y=60$ trajectories exhibit one or all of the following: rapid change of slope, lack of sufficiently long segment with same sign of stresses. In contrast, a significant portion of the trajectory identified as $Y=50$ mm exhibits uniform distribution of the considered stresses. In addition, the stresses do not change drastically at both ends of this line. Based on the analyses of stress distributions, two strips (see Figure 8.16) having the central axis located, respectively, at 10 mm and 50 mm from the base of the specimen were selected for further investigation. The thickness of the strips was set to 5 mm in order to reflect the diameter of button gauge used in experiments.

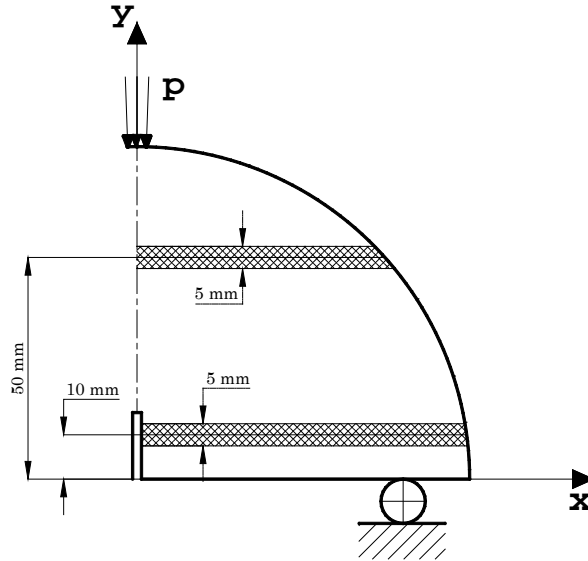


Figure 8.16: Potential SCB profiles for displacement measurements

The variations of the stresses along the thickness of the displacement measurement strips identified in Figure 8.16 were analyzed. The stresses along the lower and upper segments of the strips were obtained from FE analysis and the percent relative differences were computed through:

$$\text{var}[\%] = 100 \frac{|\sigma_i - \sigma_j|}{\max(|\sigma_i, \sigma_j|)} \quad [8.5]$$

The results are plotted in Figure 8.17 and Figure 8.18. The variation of transversal stresses along the thickness of the top strip is moderately significant. However, far from the central y-axis remains almost constant. While in the top strip, the variation fluctuates strongly throughout the length of the strip. The variation of the vertical stresses in the top strip is very small; the variation of vertical stresses in the bottom strip is considerably large.

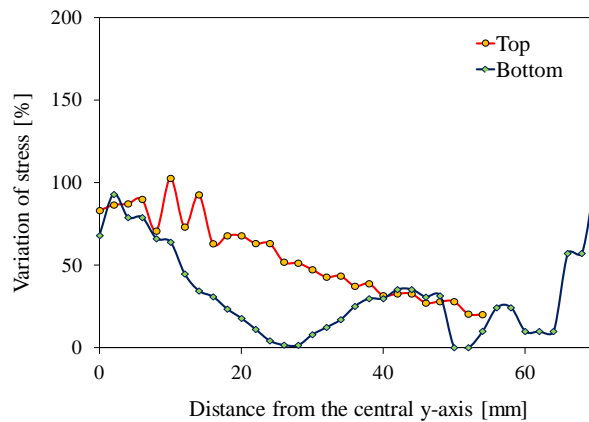


Figure 8.17: Variation of transversal stresses along the thickness of the measurement strip

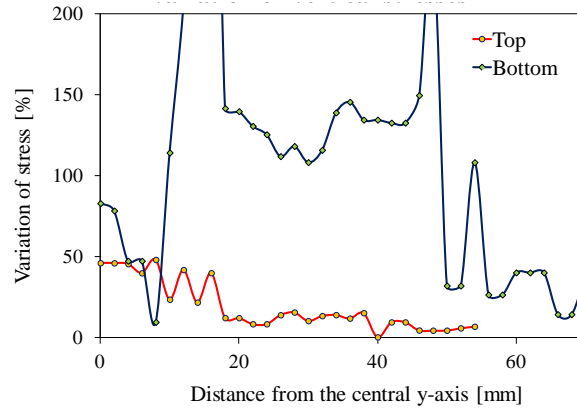


Figure 8.18: Variation of vertical stresses along the thickness of the measurement strip

Analysis of the Effect of Time on the Stresses in SCB Specimen

In order to investigate the variation of the stresses with time in a SCB specimen subjected to a three-point bend test, a 2D finite element viscoelastic model was developed. Asphalt concrete at low temperatures was modeled as homogeneous and linear viscoelastic material using the Generalized Maxwell Model (GMM) which is a built-in material model in ABAQUS. The viscoelastic model, presented in Figure 8.19, consisted of a single spring element representing instantaneous elasticity, and three spring-dashpot Maxwell elements to account for the relaxation that occurs in time.

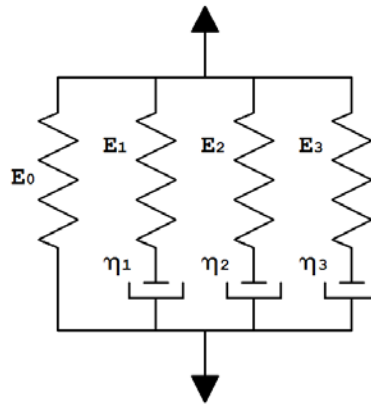


Figure 8.19: Generalized Maxwell Model (GMM)

The relaxation modulus for the GMM is written as:

$$E(t) = E_0 + \sum_0^n E_i e^{-\frac{t}{\rho_i}} \quad [8.6]$$

Where E_i and ρ_i represent, respectively, the modulus and the relaxation time for the i -th spring-dashpot element. The relaxation time is the ratio of viscosity and modulus:

$$\rho_i = \frac{\eta_i}{E_i} \quad [8.7]$$

The GMM model parameters can be determined from experimental creep data. The creep data is fitted in 3 term Prony series model through linear and non-linear optimization methods. The resulting creep model is then converted to a relaxation function through Laplace transform. ABAQUS requests that the modulus input parameters, for the spring-dashpot elements, are given in the form of normalized shear (g_i) and bulk (k_i) modulus. The work of obtaining these GMM parameters from experimental data was performed in a previous work by Zofka (9). Accordingly, the instantaneous modulus and Poisson's ration for the model were set equal to 8.44 GPa and 0.3, respectively. The normalized shear and bulk modulus, as well as the relaxation time values are reported in Table 8.2.

Table 8.2: Input parameters for GMM model in ABAQUS

g_i [-]	k_i [-]	ρ_i [sec]
0.3542	0.3542	2.8889
0.2114	0.2114	33.0071
0.2417	0.2417	334.0924

Using the viscoelastic model, the stresses along the axis $Y=10$ mm and $Y = 50$ mm, respectively, the central axis of the bottom and the top strip, were measured at 0.5 sec and 1000 sec. The variations computed using equation [8.5] are reported in Figure 8.20 and Figure 8.21. It can be observed that in the middle region of both top and bottom strips, the variations are negligible. However, in the bottom strip the vertical stresses exhibit a relatively strong variation in time.

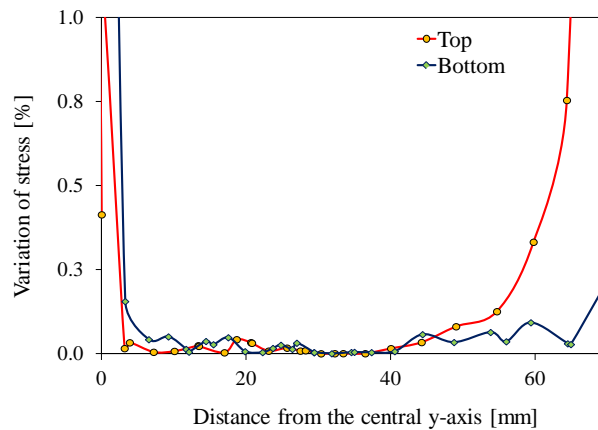


Figure 8.20: Variation of transversal stresses in time

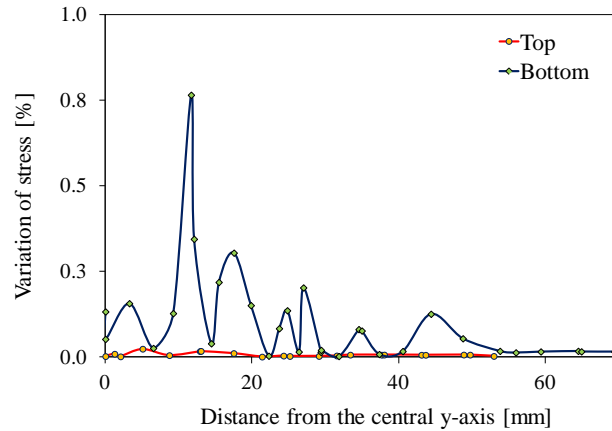


Figure 8.21: Variation of vertical stresses in time

Stress Equations

Based on the above considerations, two segments, within the $Y=10$ and $Y=50$ axis, shown in Figure 8.22, were selected for experimental investigation. The length of these segments was set to reflect the length of typical strain gauge l. The segment located at the bottom strip displays transverse tensile and vertical compressive stresses. In the second both stresses are compressive ones. As mentioned above, the extent by which the stresses in $Y=10$ are influenced by the boundary effects (crack tip and support) is difficult to accurately assess. This might cause certain degree of errors in experimental testing of materials.

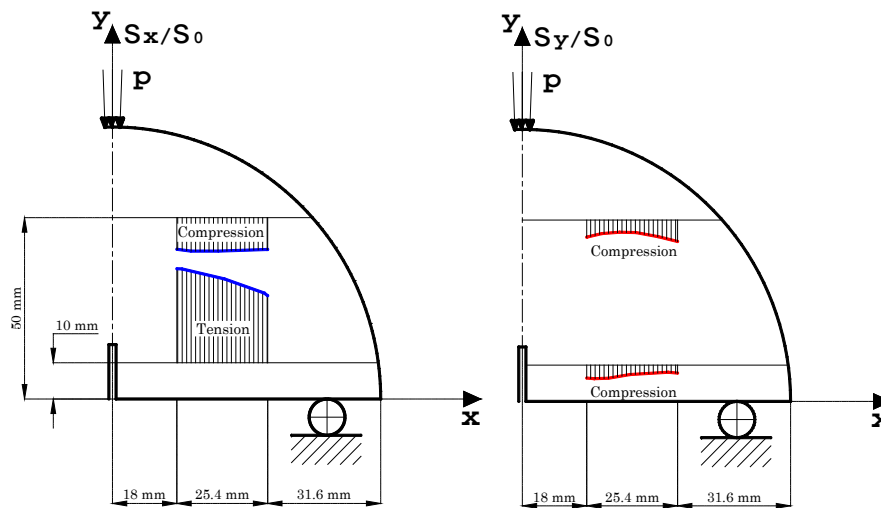


Figure 8.22: Segments selected for displacement measurements

The strain values for the creep function are to be obtained from displacement measurements in these segments. Whilst, the stress functions were determined numerically from the SCB finite element model and fitted into polynomial functions through the least square error (LSE) method, as shown in Equation 4.8 (Equations 4.8a and 4.8b):

$$\sigma_x = \frac{P}{bD} (a_x x^3 + b_x x^2 + c_x x + d_x) = \frac{P}{bD} s(x) \quad [8.8a]$$

$$\sigma_y = \frac{P}{bD} (a_y x^3 + b_y x^2 + c_y x + d_y) = \frac{P}{bD} v(x) \quad [8.8b]$$

The values for the fitting coefficients are reported in Table 8.3.

Table 8.3: Stress function fitting coefficients

Coeff.	segment in Y= 10 mm		segment in Y= 50 mm	
	X	y	x	y
a	-0.00002	-0.00005	-0.00003	0.00004
b	0.00011	0.00189	0.00171	-0.00384
c	-0.02081	-0.00719	-0.02292	0.06122
d	2.69094	-0.37243	-1.78151	-0.98555

Equation for SCB Creep Compliance

An extensometer of length l is used to measure the change in length, corresponding to load P , between two points located in the selected segments. Equation 4.9 provides an average strain over the measurement length:

$$\varepsilon_{x,ave} = \frac{1}{l} \int_0^l \varepsilon_x dx \quad [8.9]$$

Equations in 4.8 are used to compute the average stress values through:

$$\sigma_{x,ave} = \frac{P}{bD} \int_0^l s(x) dx \quad [8.10a]$$

$$\sigma_{y,ave} = \frac{P}{bD} \int_0^l v(x) dx \quad [8.10b]$$

In a creep test loading, the load P can be described using the Heaviside step function $H(t)$ as:

$$P = P(t) = P_0 H(t) \quad [8.11]$$

Noting that the change in time of the average stresses is negligible (specially for stresses in the top strip), equation 4.11 can be substituted in equations in 4.10 and taking the Laplace Transform the average stress values in the s variable are obtained:

$$\hat{\sigma}_{x,ave}(s) = \frac{\sigma_{x,0}}{s} \quad [8.12a]$$

$$\hat{\sigma}_{y,ave}(s) = \frac{\sigma_{y,0}}{s} \quad [8.12b]$$

Where $\sigma_{x,0}$ and $\sigma_{y,0}$ represent:

$$\hat{\sigma}_{x,0} = \frac{P_0}{bD} \frac{1}{l} \int_0^l s(x) dx \quad [8.13a]$$

$$\hat{\sigma}_{y,0} = \frac{P_0}{bD} \frac{1}{l} \int_0^l v(x) dx \quad [8.13a]$$

Equation 4.14 introduces Hooke's law for a linear elastic material in plane stress condition:

$$\varepsilon_x = \frac{1}{E} (\sigma_x - \nu \sigma_y) = D(\sigma_x - \nu \sigma_y) \quad [8.14]$$

At this point, the elastic-viscoelastic correspondence principle can be used to determine the viscoelastic solution. Assuming the Poisson ratio to be time and frequency independent, the plane stress constitutive equation for viscoelastic material is given by:

$$\hat{\varepsilon}_x(s) = s\hat{D}(s)(\hat{\sigma}_x(s) - \nu\hat{\sigma}_y(s)) \quad [8.15]$$

Note that the stress functions were found to be independent of material constants, hence they are not altered by either Laplace or Inverse Laplace Transforms. Then the creep compliance is determined by:

$$\hat{D}(s) = \frac{1}{s} \frac{\hat{\varepsilon}_x(s)}{(\hat{\sigma}_x(s) - \nu\hat{\sigma}_y(s))} \quad [8.16]$$

Substituting the average stress values in equation 4.16 yields:

$$\hat{D}(s) = \frac{1}{s} \frac{\hat{\varepsilon}_x(s)}{(\sigma_{x,0} - \nu\sigma_{y,0})} \quad [8.17]$$

The Inverse Laplace Transform of equation 4.17 yields the creep compliance function in time:

$$D(t) = \frac{\varepsilon_x(t)}{(\sigma_{x,0} - \nu\sigma_{y,0})} \quad [8.18]$$

Verification of the Proposed SCB Creep Model

The validity of the creep compliance equation proposed in this paper was checked through numerical simulation and experimental testing. The scheme outlined in Figure 8.23 summarizes the verification approach adopted. Accordingly, two different techniques are used to determine the creep function of a given viscoelastic material: The proposed SCB creep test method is compared to another well-established creep test methodology. If the SCB procedure is reasonable, the different tests should yield similar creep functions.

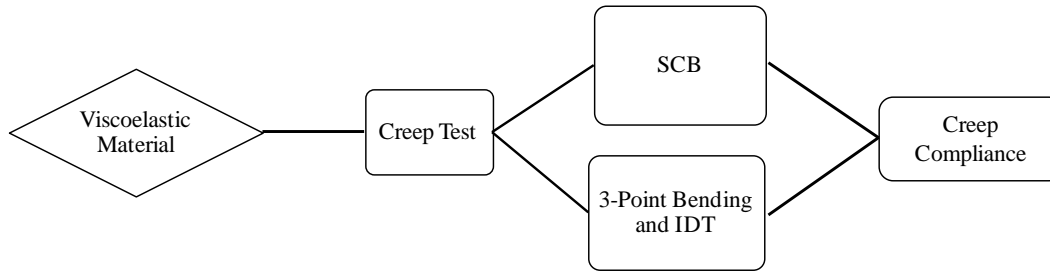


Figure 8.23: Validation of SCB creep model

Both numerical simulations and experimental testing were adopted. In the numerical simulation the SCB was compared to the Three-Point Bending Beam test. Whereas, in the experimental testing standard IDT test were first performed. The IDT specimens were then used to prepare notched SCB specimens on which SCB creep tests were performed. This way it was ensured that same specimens were tested by two different methods.

Numerical Validation

Creep test simulations in SCB and Three-Point Bending Beam loading configurations were performed in ABAQUS. Finite element simulation

Numerical simulations of SCB and 3-Point Bending creep tests were performed in ABAQUS. The GMM model parameters in Table 8.4 were used to define the material in both tests. Both models were modeled in 3D as simply supported structures without overhanging parts beyond the supports, see Figure 8.24.

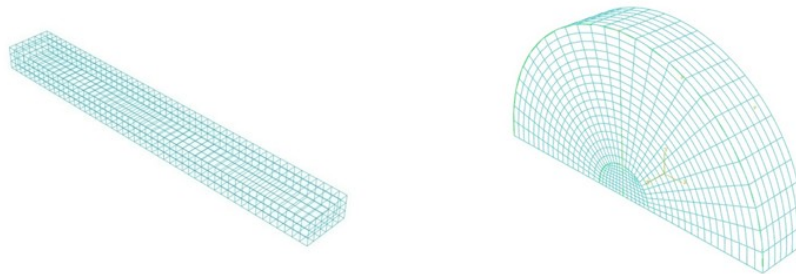


Figure 8.24: 3D model representations of 3-point bending and notched semi-circular beams

The dimensions of the specimens used in the numerical simulation are presented in Table 8.4. Geometry of model beams. The SCB model included an initial crack notch (surface) defined using a seam-crack surface with duplicate overlapping nodes in ABAQUS/CAE.

Table 8.4: Geometry of model beams

Beam Geometry			SCB Geometry		
Height	6.35	mm	Diameter	150	mm
Thickness	12.7	mm	Thickness	25	mm
Length	101.6	mm	Notch	15	mm

Concentrated vertical compressive forces were applied in creep mode, in the middle of the beams top surface. Therefore, an instantaneous force was applied at time =0 sec and hold for 10sec.

Different meshes were tried until convergence of results was achieved. For the BBR model convergence was obtained with a mesh of 6584 brick elements C3D20R. The SCB model required 7018 wedge elements of C3D20R.

Determination of Creep Compliance from Numerical Simulations

The bending beam theory states that in the three-point bending beam, depicted in Figure 8.25, the maximum elastic deflection δ_{\max} occurs at the midpoint of the span and can be computed using equation 4.19.

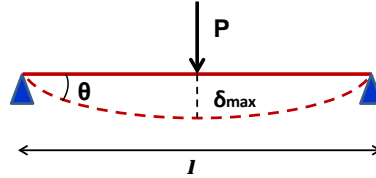


Figure 8.25: Schematization of 3-point bending beam

$$\delta_{\max} = \frac{Pl^3}{48EI} \quad [8.19]$$

Where l is the length of the span, P applied load, and I moment of inertia. The equation can be modified using the elastic-viscoelastic correspondence principle and applied using creep displacement history to determine the creep compliance $D(t)$:

$$D(t) = \frac{48EI\delta(t)}{Pl^3} \quad [8.20]$$

Equation 4.19 was used to check the accuracy of the 3-point bending beam creep model. The initial elastic deflection should equal δ_{\max} . The FE model used met this requirement as it is shown in Figure 8.26.

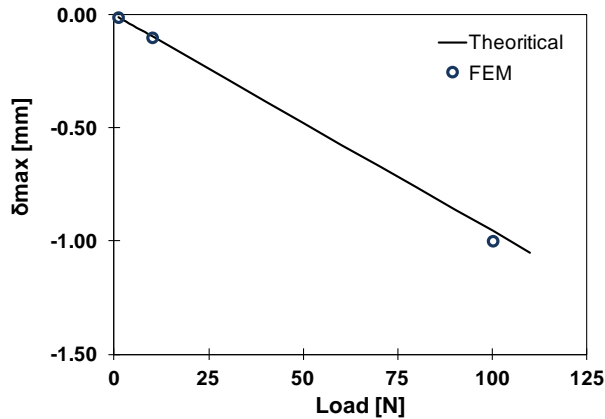


Figure 8.26: Calibration of the 3-point bending beam FE model

In the case of SCB creep simulation, the change in length between two model nodal points, located in the end points of the segments indicated in Figure 8.22, were used to determine the average strain values. Then using the stress equations proposed in equation in 4.8 and the creep function in equation 4.18, the SCB creep functions were computed.

Experimental Validation

A single reference asphalt concrete mixture was used to investigate the low temperature creep function through two different test procedures: IDT and SCB. The selected mixture is part of an ongoing research project at the University Minnesota and is identified as MIF 58-34 19mm Virgin. The nominal maximum aggregate size of the mixture is 19 mm and a plain PG58-34 asphalt binder was used for its mixing.

The loose mixture was gyratory compacted into cylindrical specimens with diameter 150 mm, height 171 mm and target air void content of 7%. Three cylinders were obtained as a result of this operation. The upper and lower 10 mm layers were cut and discarded.

From each cylinder a standard notched SCB specimen was obtained for preliminary tests, from which the optimal creep load was determined. This process consisted in cyclic creep loading and unloading with increasing load to determine the load magnitude that produces appreciable displacement measurements without damaging the specimen. In addition, the peak fracture load was determined to verify that the selected creep load remains within fraction of the peak load. The optimal creep load was found to be 0.8 kN.

Three IDT specimens were obtained from each gyratory cylinder and subjected to IDT creep test according to AASHTO T 322-07 (10). A constant load of 1.6 kN, double of that required for SCB, was found to be in agreement with the standard's specification.

After IDT testing, the IDT plates were cut into SCB slice with 15mm notch. The SCB slices were then creep tested. The testing setups for both test procedure are presented in Figure 8.27.

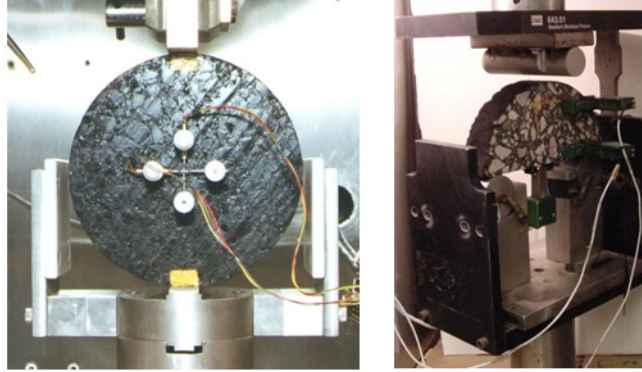


Figure 8.27: IDT and SCB experimental testing setup

All tests were performed in an environmental chamber at -12°C . Prior to testing the specimens were conditioned for 2 hours at the testing temperature. The load was kept for 1000 sec.

The displacement and load measured from IDT creep test are used to compute the creep compliance of the asphalt mixture according to AASHTO T 322-07. The expression for $D(t)$ is given as:

$$D(t) = \frac{\Delta X \cdot D_{avg} \cdot b_{avg}}{P_{avg} \cdot GL} \cdot C_{CMPL} \quad [8.21]$$

Where D , b , P , and GL indicate, respectively, diameter, thickness, load, and gauge length. ΔX is the trimmed horizontal deformation and $CCMPL$ creep compliance parameter computed as:

$$C_{CMPL} = 0.6354 \cdot \left(\frac{x}{y}\right)^{-1} - 0.332 \quad [8.22]$$

Where x and y represent, respectively the measured horizontal and vertical deformations.

The SCB creep compliance is determined according to the procedure proposed in this section. The creep compliance $D(t)$ functions obtained from different test set-ups, using both finite element numerical simulations and experimental laboratory tests are presented next. Additionally, the creep stiffness parameter $S(t)$ is computed as inverse of $D(t)$. The results are reported in Figure 8.28 and Figure 8.29.

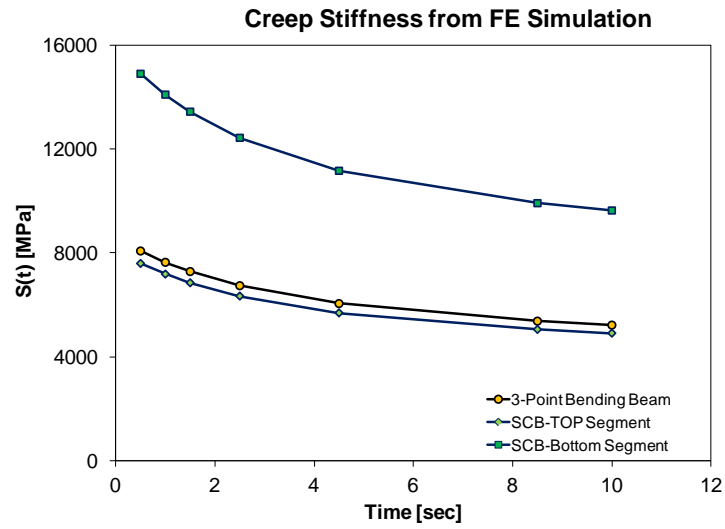
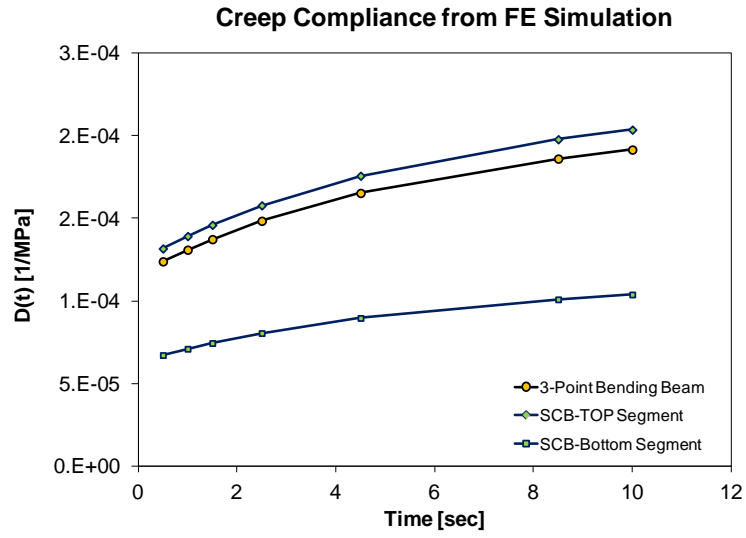


Figure 8.28: Results from numerical simulation

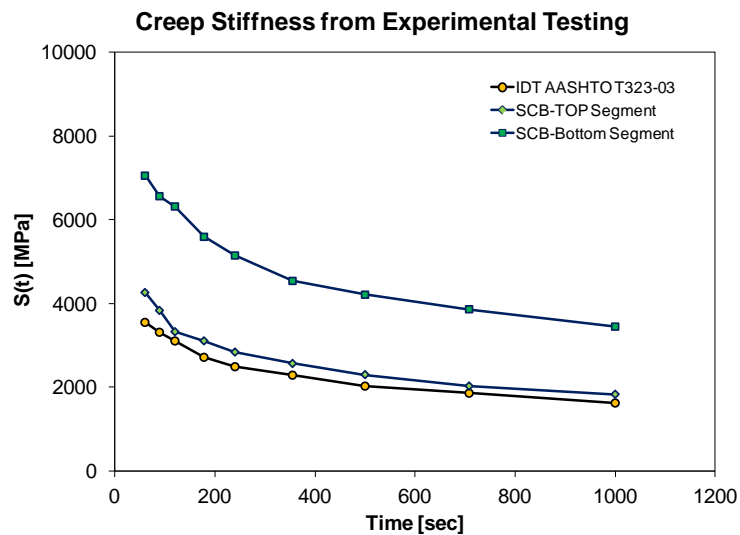
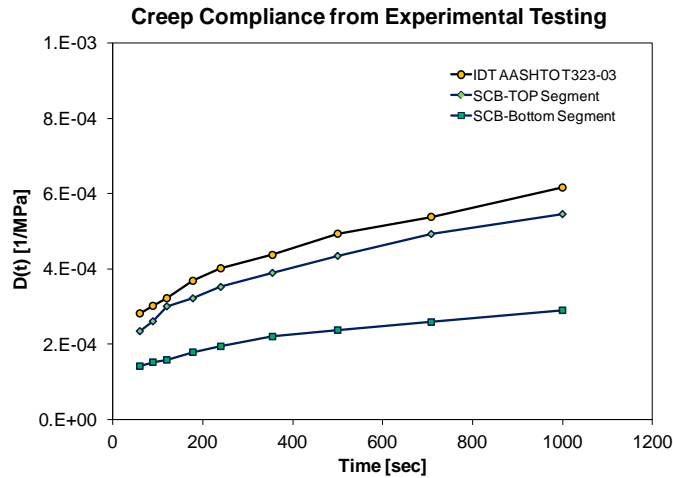


Figure 8.29: Results from experimental testing

The creep functions obtained from the SCB and the other two reference test configurations appear to have similar trends. However the creep compliance computed from the bottom region of the SCB is always smaller than the others. The vicinity to the crack tip and the support roller, as well as the relatively high variation of stress both in time and space observed in the bottom strip of the SCB specimen can be indicated as plausible reasons for this discrepancy. For these reasons, the average stress values used in the approximated SCB creep model described in equation 4.18, may not be suited for the determination of the creep function from the bottom segment. On the other hand, good agreement are obtained between the creep functions from the top segment of SCB specimen and those obtained from 3-point bending beam and IDT creep tests.

Conclusions

In this present work, the idea of determining asphalt concrete's creep compliance from the existing SCB fracture test is investigated. As a result, expressions that relate displacement measurement from particular region of the notched SCB specimen to the creep function of the asphalt concrete are derived. In particular two segments - one on the upper and another on the lower region of the SCB specimen - were identified for displacement measurement from which strains are to be computed.

The creep function computed from displacement measured at the upper segment of SCB specimen is in good agreement with creep functions from 3-point bending beam and IDT creep tests.

The findings of this research work indicate that the low temperature characterization of asphalt concrete can be entirely achieved from a single SCB test configuration. By eliminating the need for IDT creep testing, significant saving in material, time, and cost are achieved.

Chapter 9. Subtask 3 Proposed Simplified Method to Obtain Mixture Creep Compliance – Part 2

Obtaining Creep Compliance from BBR Tests on Mixture Beams

Previous research performed at the University of Minnesota (1) showed that the Bending Beam Rheometer (BBR), currently used for asphalt binder specifications, can be used to obtain creep properties of asphalt mixtures, see Figure 9.1.

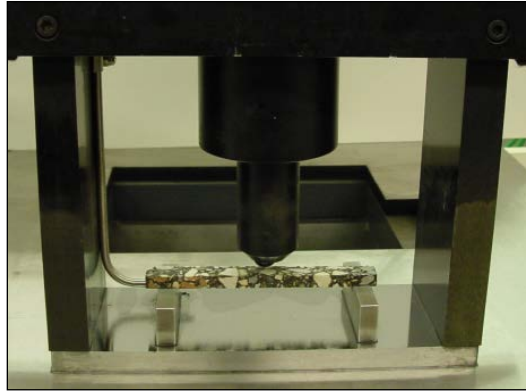


Figure 9.1: Bending beam rheometer with beam of asphalt mixture

The main difficulty in implementing this method into current practice is the use of small size specimens that may not capture the mechanical behavior of the actual asphalt pavement, see Figure 9.2. The volume of material tested may not be representative, especially when the asphalt mixtures contained aggregate sizes that are larger than the smallest dimension of the beam.



Figure 9.2: IDT and BBR test specimens

Work performed in a recent NCHRP Idea project investigated the feasibility of using the BBR for asphalt mixture characterization by means of creep tests, image analysis, microstructure characterization with spatial correlation functions, and finite element simulations of specimens of different sizes. A summary of the results is presented in the next paragraphs.

Experimental Work

A total of 360 three-point bending creep tests were performed on three beam sizes: $6.25 \times 12.5 \times 100$ mm (1x), $12.5 \times 25 \times 200$ mm (2x), and $18.75 \times 37.5 \times 300$ mm (3x). The bending creep test were performed at three temperatures: high temperature (HT) level (PG low limit + 22°C), intermediate temperature (IT) level (PG low limit + 10°C), and low temperature (LT) level (PG low limit - 2°C). The PG low limit is the low temperature performance grade limit of the asphalt binder. Three replicates were tested at high temperature level (HT) and low temperature level (LT) and six replicates were tested at intermediate temperature level (IT).

A total of ten laboratory prepared mixtures were tested. The mixtures were selected from the set of mixtures used in the first phase of the pooled fund study, and were prepared using four asphalt binder grades, and two types of aggregate: limestone and granite. They were compacted to 4% air voids using a linear kneading compactor. The mixing and compaction temperatures were 155°C and 135°C, respectively. Figure 9.3 shows the gradation curves of the granite and limestone aggregates used for asphalt mixture preparation. The particle size distribution curves for granite and limestone are very similar with a maximum aggregate size of 12.5 mm. The percent of material passing sieve #200 (i.e. 75 µm) is 5.1 and 5.4% for granite and limestone, respectively.

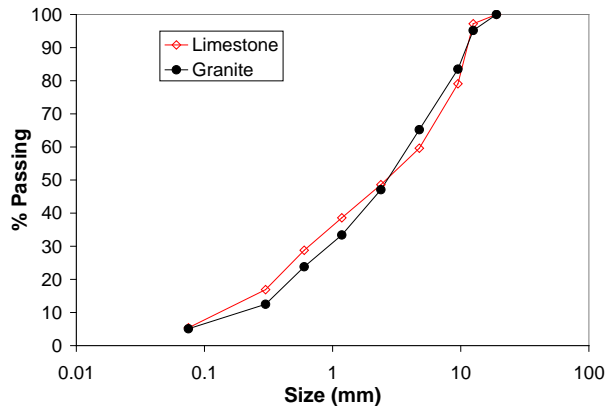


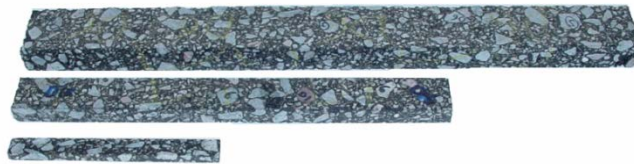
Figure 9.3: Gradation curves for granite and limestone aggregate

Table 9.1 contains a description of the ten asphalt mixtures tested, including the performance grade (PG) of the binder, modification, and type of aggregate.

Table 9.1: Description of asphalt mixtures

ID	PG binder	Modification	Aggregate
58-34:M2:4:GR	58-34	SBS	Granite
58-34:M2:4:LM	58-34	SBS	Limestone
58-28:U1:4:GR	58-28	Unmodified	Granite
58-28:U1:4:LM	58-28	Unmodified	Limestone
64-34:M1:4:GR	64-34	Elvaloy	Granite
64-34:M1:4:LM	64-34	Elvaloy	Limestone
64-28:U1:4:GR	64-28	Unmodified	Granite
64-28:U1:4:LM	64-28	Unmodified	Limestone
64-28:M1:4:GR	64-28	SBS	Granite
64-28:M1:4:LM	64-28	SBS	Limestone

The slab compacted mixtures were cut into 3x beams ($18.75 \times 37.5 \times 300$ mm) as shown in Figure 9.4. After testing was finished, the 3x beams were cut into 2x beams ($12.5 \times 25 \times 200$ mm) using a typical laboratory diamond saw. After completion of the testing of the 2x beams, specimens were cut into 1x beams ($6.25 \times 12.5 \times 100$ mm), which is the size of Bending Beam Rheometer (BBR) specimens.

**Figure 9.4: 1x, 2x, and 3x asphalt mixture beam specimens**

The thickness and width of the 3x, 2x, and 1x beams were measured at three locations along the length of the beam and average values were used in the calculation of the creep stiffness. A summary of basic statistical parameters of the measured dimensions, weight, and density is presented in Table 9.2. The coefficient of variation for width, thickness, length, and weight for the 3x, 2x and 1x beams indicate that specimens are uniform and very consistent. The 95% confidence intervals for the thickness, width, and density indicate that the variation of the dimensions of the 3x, 2x, and 1x beams are insignificant.

Table 9.2: Statistical summary for dimensions of 3x, 2x, and 1x beams

Contents	3x		2x		1x	
	μ	CV(%)	μ	CV(%)	μ	CV(%)
width (mm)	37.91	2.44	25.05	3.16	12.43	1.25
thickness (mm)	19.32	2.04	12.62	3.15	6.65	4.10
length (mm)	383.00	0.24	257.27	0.28	126.58	0.59
weight (gr)	622.96	5.26	183.41	4.87	23.43	5.12
\square (gr/cm ³)	2.22	4.16	2.26	4.45	2.24	5.11

The three-point bending tests for 3x and 2x beams were conducted using a MTS 810 servo hydraulic load frame. A special support manufactured in-house was used to hold the beam and to allow measurements of mid span deflection. The beam deflections were measured using Epsilon extensometers with 38 mm gage length and ± 1 mm range. The thin asphalt concrete beams (1x) were tested with the Bending Beam Rheometer (BBR) following the procedure described in detailed in (2).

The creep stiffness as a function of time was calculated using Euler- Bernoulli beam theory and the correspondence principle. For each mixture and temperature level, the average creep stiffness was calculated by:

$$S(t) = \frac{L^3}{48\delta(t)I} \left[P + \frac{5wL}{8} \right] \quad [9.1]$$

Where:

S = creep stiffness

P = constant load applied to the beam

L = span length

I = moment of inertia of the beam

t = deflection of the beam

w = uniformly distributed load due to weight of the beam

Due to the buoyancy forces in the BBR ethanol bath, the submerged weight for the 1x beams was negligible and not used in equation (9.1).

Figures 9.5 shows an example of the creep stiffness curves for the ten mixtures tested Visual inspection of the creep stiffness average curves indicates that, at intermediate and high temperature, the effect of the beam size is negligible.

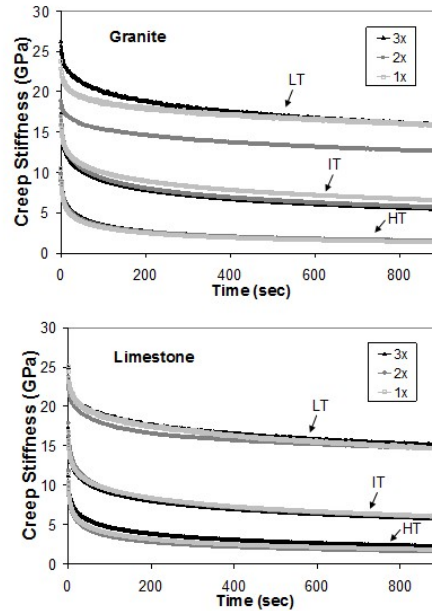


Figure 9.5: Test results for PG 58-34 mixtures

The experimental results at the high and intermediate temperature levels (HT and IT) indicate that the average information contained in the 1x beams ($6.25 \times 12.5 \times 100$ mm) is statistically representative of the material, even though the mixtures contain aggregate sizes (i.e. 12.5 mm) which are larger than the smallest dimension of the beam.

At low temperature, the size of the beam appears to influence the creep stiffness. However, it is important to note that, during testing of the 2x and 3x beams at the low temperature level (LT), the formation of layers of ice on the supports and around the extensometers was observed. This may have influenced the deflection readings, since the deflection values are very small at LT and the level of error in measurements is higher compared to the other temperature levels.

To investigate the influence of parameters such as the size of the specimen, performance grade (PG) of the binder, aggregate type, loading time, and temperature on the creep stiffness of asphalt mixtures, correlation matrices were calculated and analyses of variance (ANOVA) were performed using the creep stiffness as response variable and size, time, temperature, binder type, and aggregate as the independent parameters. A linear relation was assumed between response variable and the predictors. To reduce calculations, only the creep stiffness values at 8, 15, 30, 60, 120, and 240 seconds were used in the analysis. Table 9.3 shows how the variables were treated in the statistical analysis.

Table 9.3: Variables definition for statistical analysis

Variable	Type / Description
Binder PG	Factors (dummy): PG 58-34, PG 58-28, PG 64-34, PG 64-28
Binder modification	0 – unmodified; 1 – modified
Aggregate Type	0 – granite; 1 – limestone
Beam size	1 – 1x beams; 2 - 2x beams; 3 - 3x beams
Time	8, 15, 30, 60, 120 and 240 sec

The creep stiffness data from the low temperature level was not included in the statistical analysis due to the poor quality and high variability of the deflection measurements obtained. The formation of layers of ice between supports and the sample, the variability of the extensometers readings at this temperature, and the brittleness of the specimens are explanations on the level of error observed at this temperature level.

Correlation factors for the results obtained at intermediate and high temperatures are presented in Table 9.4. Correlation factors more than $2/n^{0.5}$ (3), where n is the number of sample points, indicates high linear correlation between the parameters. For the data set used in this analysis, correlations larger than 0.057 ($n = 1225$) are significant and presented in bold.

Table 9.4: Correlation factors for all temperatures

Variables	Creep Stiffness
Aggregate	0.128
Modification	-0.123
Size	-0.037
Size*Aggregate	0.095
Size*Time	-0.361
Temperature	-0.681
Time	-0.400

The only parameter that has no significant correlation with creep stiffness is size. This indicates that there are no statistically significant differences between the creep stiffness functions of the 3x, 2x, and 1x beams. From Table 9.4, mixtures containing limestone are stiffer than mixtures with granite aggregate. This observation can be explained by the higher binder absorption of the limestone aggregate in comparison to the granite aggregate. Also, asphalt concrete prepared with unmodified asphalt binder has higher creep stiffness than asphalt concrete mixed with modified binder. Significant correlation is observed between the interaction term of size and time and the creep stiffness: as time and size increases, the creep stiffness decreases. The correlation observed in the interaction terms is due to the highly statistical significance of the aggregate and time variables. As expected, significant correlation is observed between test temperature and creep stiffness.

The results of ANOVA are presented in Table 9.5. For a significance level of 5%, the variables with p-values smaller than 0.05 are significant and presented in bold.

Table 9.5: ANOVA for all temperatures

Variable	Estimate	Std. Error	t-value	p-value
Constant	3132.87	290.97	10.77	0
Size	-16.27	111.89	-0.15	0.884
Size*Aggregate	149.65	132.79	1.13	0.260
Size*Time	0.10	0.81	0.13	0.900
Binder[64-28]	1158.85	165.25	7.01	0
Binder[58-34]	288.82	240.86	1.20	0.231
Binder[64-34]	1934.80	249.58	7.75	0
Modified	-3601.87	165.05	-21.82	0
Aggregate	254.22	287.08	0.89	0.376
Temperature	-510.70	9.68	-52.75	0
Time	-19.73	1.74	-11.34	0

The parameters that are significant in the linear regression are: the factors from PG 64-34 and PG 64-28 binders, modification, temperature, and time. The positive coefficients for PG 64-34 and PG 64-28 indicate that mixtures prepared with these binders are stiffer than the mixtures prepared with PG 58-28. As indicated by the large t-values in Table 9.5, the variables that contain most of the information for the prediction of creep stiffness are modification, temperature, and time. As expected, when time and temperature increases, the creep stiffness of the mixture decreases.

The parameters in the regression that do not significantly contribute to the prediction of creep stiffness are size, aggregate type, and the interaction terms between size, aggregate and time. No significant difference is observed between the creep stiffness of mixtures prepared with PG 58-34 and with PG 58-28 (the reference level for binder PG in this analysis).

The results from this statistical analysis suggest that a representative creep stiffness of asphalt mixtures can be obtained from testing a minimum of three replicates of thin BBR asphalt mixture beams. Investigation of the microstructure of the thin beams, and finite element simulations of specimens of different sizes, not included in this summary, provided additional support to the feasibility of using BBR mixture beams to characterize asphalt mixtures.

Evaluate the Feasibility of Using Hirsch Model to Obtain Mixture Creep Stiffness from Binder Creep Stiffness

In this section, two models are investigated to obtain asphalt mixture properties from asphalt binder properties. The inverse problem is also analyzed since it can offer critical information related to the use of RAP in asphalt mixtures.

Hirsch Model

A semi-empirical model, based on Hirsch model (4), was proposed by Christensen et al. (5) to estimate the extensional and shear dynamic modulus of asphalt mixtures from asphalt binder

experimental data. This approach would avoid the need for performing mixture experimental work, which is significantly more expensive than testing asphalt binders. The effective response is obtained by assembling the elements of the mixture in parallel and in series, as shown in Figure 9.6.

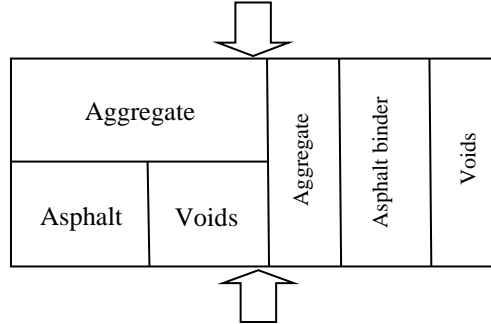


Figure 9.6: Semi-empirical model proposed by Christensen et al. (5)

The empirical factor P_c determines the amount of parallel or series elements in the mixtures. The general equation for this semi-empirical model is:

$$E_{mix} = P_c [E_{agg} V_{agg} + E_{binder} V_{binder}] + (1 - P_c) \left[\frac{V_{agg}}{E_{agg}} + \frac{(1 - V_{agg})^2}{E_{binder} V_{binder}} \right]^{-1} \quad [9.2]$$

Where:

E_{mix} = effective modulus of the mixture,

E_{agg} , V_{agg} = modulus and volume fraction of the aggregate,

E_{binder} , V_{binder} = modulus and volume fraction of binder, and

P_c = contact volume is an empirical factor defined as:

$$P_c = \frac{\left(P_0 + \frac{VFA \cdot E_{binder}}{VMA} \right)^{P_1}}{P_2 + \left(\frac{VFA \cdot E_{binder}}{VMA} \right)^{P_1}} \quad [9.3]$$

Where:

VFA = voids filled with asphalt binder (%),

VMA = voids between mineral aggregate (%), and

P_0 , P_1 and P_2 = fitting parameters.

Zofka et al. (6) used the above model to predict BBR mixture stiffness from BBR extracted binder stiffness. The predicted values were always higher than the measured stiffness values, and as a consequence, the aggregate modulus, E_{agg} , was changed from 4,200,000 psi (29 GPa), to 2,750,000 psi (19 GPa) based on these results and on numerical manipulation. Further modification of the model was proposed by Zofka (7) who proposed a new expression for P_c :

$$P_c = 0.11 \ln \left(\frac{E_{binder}}{a} \right) + 0.609 \quad [9.4]$$

Where:

E_{binder} = effective modulus of the binder in GPa, and

a = constant equal to 1 GPa.

This modified model was used by Velasquez (8, 9) to estimate the asphalt mixture relaxation modulus calculated from BBR experimental data. It was found that the model predicted well the relaxation modulus of the majority of the mixtures investigated.

Analogical Models

The application of micromechanical models to asphalt materials characterization remains a very challenging task due to the complex structure of asphalt mixture and the complex interaction between the aggregate particles and the binder or mastic phase. A simpler approach may be more appropriate in this case, such as using analogical models.

Different analogical models are available in literature. Dashpot and springs constitute the simplest analogical linear viscoelastic models (10, 11). When spring and dashpot are assembled in series and in parallel, Maxwell and Kelvin-Voigt models can be constructed, respectively (Figure 9.7).

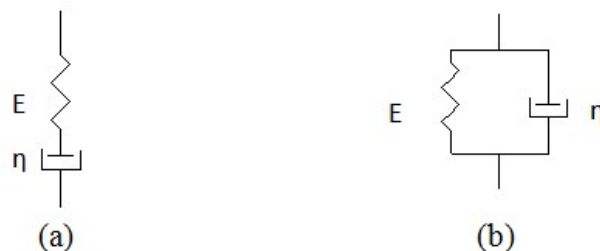


Figure 9.7: Maxwell Model (a) and Kelvin-Voigt Model (b)

These two models are not able to describe the complex properties of asphalt material but can be used as basic components of more sophisticated models. A satisfactory description of the behavior of asphalt binders and asphalt mixtures was obtained by Neifar and Di Benedetto (12) using a Generalized Maxwell Model and Generalized Kelvin-Voigt Model. Analogical models, with continuous rather than discrete spectra, were also applied to asphalt materials experimental data. The most important ones are presented next.

Huet Model

The Huet analogical model (13) is composed of two parabolic elements $J1(t)=a*t^h$ and $J2(t)=b*t^k$ plus a spring (stiffness E_∞) combined in series. (Figure 9.8)

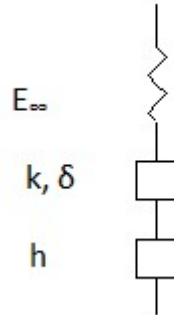


Figure 9.8: Huet Model

The Huet model was proposed for binders and mixtures and presents a continuous spectrum, which means it can be schematized by an infinite number of Kelvin-Voigt elements in series or Maxwell elements in parallel. The analytical expression of the Huet model for the creep compliance is:

$$D(t) = \frac{1}{E_\infty} \left(1 + \delta \frac{(t/\tau)^k}{\Gamma(k+1)} + \frac{(t/\tau)^h}{\Gamma(h+1)} \right) \quad [9.5]$$

Where:

$D(t)$ = creep compliance

E_∞ = glassy modulus,

h, k = exponents such that $0 < k < h < 1$,

δ = dimensionless constant,

t = time,

Γ = gamma function that can be expressed as:

$$\Gamma(n) = \int_0^\infty t^{n-1} e^{-t} dt$$

$$\Gamma(n+1) = n\Gamma(n)$$

$n > 0$ or $\text{Re}(n) > 0$

t = integration variable,

n = argument of the gamma function.

τ = characteristic time varying with temperature accounting for Time Temperature Superposition Principle (TTSP): $\tau = a_T(T)\tau_0(T_S)$

a_T = shift factor at temperature T that can be determined from Williams, Landel and Ferry (WLF) equation (14),

τ_0 = characteristic time determined at reference temperature T_S .

An expression of the complex modulus for this model is also available; however, there is no analytical formula for the relaxation function:

$$E^*(i\omega\tau) = \frac{E_\infty}{1 + \delta(i\omega\tau)^{-k} + (i\omega\tau)^{-h}} \quad [9.6]$$

Where:

i = complex number ($i^2 = -1$)

E_∞ = limit of the complex modulus for $\omega\tau \rightarrow \infty$ (Glassy modulus),

$\omega = 2\pi$ *frequency.

Huet-Sayegh Model

Huet model does not represent well mixture response at very low frequencies and high temperature, due to the inability to take into account the limiting value of the mixture modulus related to the aggregate skeleton. Sayegh (15) proposed a new expression for complex modulus introducing a spring in parallel in the Huet model (see Figure 9.9):

$$E^*(i\omega\tau) = E_0 + \frac{E_\infty - E_0}{1 + \delta(i\omega\tau)^{-k} + (i\omega\tau)^{-h}} \quad [9.7]$$

Where:

i = complex number ($i^2 = -1$)

E_∞ = limit of the complex modulus for $\omega\tau \rightarrow \infty$ (Glassy modulus),

E_0 = limit of the complex modulus for $\omega\tau \rightarrow 0$,

h, k = exponents such that $0 < k < h < 1$,

δ = dimensionless constant,

τ = characteristic time varying with temperature accounting for the Time Temperature Superposition Principle (TTSP),

$\omega = 2\pi$ *frequency.

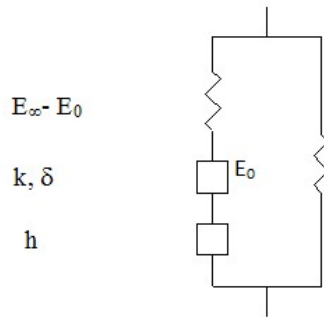


Figure 9.9: Huet-Sayegh Model (29)

Six constants are required in this model, δ , k , h , E_∞ , E_0 , and τ_0 , one more than the Huet model. The model was used by several authors (13, 16, 17, 18, 19, 20, 21) with good results in the small strain domain for any range of frequencies and temperatures. It should be mentioned that this model has some limitation when predicting binder modulus at very low frequencies where, instead of a parabolic element behavior, a linear dashpot would be more appropriate. The model was also used by Neifar (12) to calibrate a thermo-visco-plastic law named DBN law. This law allows describing with the same formalism different types of mixture behaviors according to the considered loading domain (22). A three dimensional extension of the DBN was also proposed by the same authors (23). It must be finally mentioned that there is no analytical expression for creep compliance in the time domain for this model.

2S2PID Model

An improved Huet-Sayegh model that takes into account the drawback for binder characterization was proposed by Di Benedetto & Olard (18, 24 and 25). This model is obtained from Huet-Sayegh model by adding a linear dashpot in series with the two parabolic elements and the spring of rigidity $E_\infty - E_0$ so that at low frequency it is equivalent to a linear dashpot in parallel with a spring of rigidity E_0 . The scheme of the model is shown in Figure 9.10 and the analytical expression of the complex modulus is given by equation 4.30.

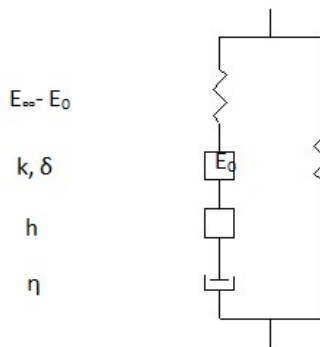


Figure 9.10: 2S2PID Model

$$E^*(i\omega\tau) = E_0 + \frac{E_\infty - E_0}{1 + \delta(i\omega\tau)^{-k} + (i\omega\tau)^{-h} + (i\omega\beta\tau)^{-1}} \quad (3.30)$$

Where:

β = dimensionless parameter introduced to take into account the Newtonian viscosity of the linear dashpot

The seven constants (δ , β , k , h , E_∞ , E_0 , and τ) are determined from the experimental data at a reference temperature using an error minimization process.

ENTPE Transformation

Di Benedetto et al. (25) applied 2S2P1D model to experimental data obtained at a reference temperature $T_S=10^\circ\text{C}$ for a series of binders and corresponding mixtures. The authors found that the model parameters δ , k , h and β , respectively, were the same for the binder and the corresponding mixture, and only the static and glassy modulus, E_0 and E_∞ , and τ were different. The values of E_0 and E_∞ for the mixtures were in the range of 0.250 to 1.050GPa and 40 to 45GPa, respectively. From the simple regression of the mixture characteristic time, τ_{mix} , on the corresponding binder characteristic time, τ_{binder} , at the reference temperature on log scale, the authors found following relationship:

$$\tau_{\text{mix}}(T) = 10^\alpha \tau_{\text{binder}}(T) \quad [9.8]$$

Where α is a regression coefficient depending on mixture and aging.

The value of α was determined in the range 2.66 to 2.82 according to the different mixtures and binders investigated.

Based on these findings, a relationship between the binder and the mixture complex moduli was proposed:

$$E_{\text{mix}}^*(\omega, T) = E_{0\text{mix}} + \left[E_{\text{binder}}^*(10^\alpha \omega, T) - E_{0\text{binder}} \right] \frac{E_{\infty\text{mix}} - E_{0\text{mix}}}{E_{\infty\text{binder}} - E_{0\text{binder}}} \quad [9.9a]$$

Where:

E_{mix}^* = complex modulus of the mixture,

E_{binder}^* = complex modulus of the binder,

$E_{\infty\text{mix}}$ = glassy modulus of the mixture,

$E_{0\text{mix}}$ = static modulus of the mixture,

$E_{\infty\text{binder}}$ = glassy modulus of the binder,

$E_{0\text{binder}}$ = static modulus of the binder,

T = temperature,

$\omega = 2\pi \cdot \text{frequency}$,

$\alpha = \text{regression coefficient depending on mixture and aging.}$

The expression (9.9a) is independent of any rheological model and can be interpreted as a combination of three transformations (Figure 9.11):

- a negative translation of value E_{0_binder} along the real axis,
- a homothetic expansion starting from the origin with a ratio of $(E_{\infty_mix} - E_{0_mix}) / (E_{\infty_binder} - E_{0_binder})$,
- a positive translation of value E_{0_mix} along the real axis.

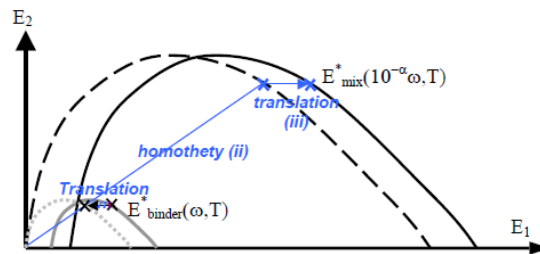


Figure 9.11: Binder to mixture transformation scheme

Expression (9.9a) was also validated by Di Benedetto et al. (25) for mixtures and binders other than those used to derive the transformation. Delaporte et al. (26) used the same approach to investigate the linear viscoelastic properties of asphalt binder and mastics, with and without aging. Equation (9.9a) can be simply rearranged to obtain E^*_{binder} from $E^*_{mixture}$:

$$E^*_{binder}(\omega, T) = E_{0binder} + \left[E^*_{mix}(10^{-\alpha} \omega, T) - E_{0mix} \right] \frac{E_{\infty binder} - E_{0binder}}{E_{\infty mix} - E_{0mix}} \quad [9.9b]$$

Expressions (9.9a) and (9.9b) are called ENTPE (École Nationale des Travaux Publics de l'État) transformation.

Since the conversion of E^* to creep compliance is not trivial, it was decided to use Huet model that has an expression for creep compliance. This model does not present the additional dashpot in series and the spring in parallel that are present in the 2S2P1D model, which is acceptable since the experimental data of interest was obtained at low temperature. Validation of the ENTPE transformation that offers a simple relation between binder and mixture is also investigated for low temperature creep data.

Material and Testing

Materials used in the previous phase of the pooled fund study representing eight different asphalt binders and sixteen different asphalt mixtures prepared with the eight binders and with two types of aggregates (granite and limestone) were used in the experimental work. The binders were RTOFT aged and the mixtures were short term aged according to current AASHTO specifications. To avoid any errors associated with time-temperature superposition shifting, experimental data obtained at the same test temperature was considered for the binder-mixture

analysis. Mixture testing was done with the BBR, following the procedure described in the previous section. Table 9.6 lists the eight binders, the sixteen corresponding mixtures investigated, and the test temperature considered. GR and LM stand for granite and for limestone, respectively. The volumetric properties of the mixtures are listed in Table 9.7, and the elastic modulus values for the two aggregates are listed in Table 9.8.

Table 9.6: Asphalt binders and mixtures

T(°C)	Binder	Mixtures	
		Granite (GR)	Limestone (LM)
-24	58-34:M1	58-34:M1:GR	58-34:M1:LM
-24	58-34:M2	58-34:M2:GR	58-34:M2:LM
-18	58-28:U1	58-28:U1:GR	58-28:U1:LM
-18	58-28:U2	58-28:U2:GR	58-28:U2:LM
-24	64-34:M1	64-34:M1:GR	64-34:M1:LM
-24	64-34:M2	64-34:M2:GR	64-34:M2:LM
-18	64-28:U1	64-28:U1:GR	64-28:U1:LM
-18	64-28:M1	64-28:M1:GR	64-28:M1:LM

Table 9.7: Mixture volumetric properties

	Granite mixtures	Limestone mixtures
Optimum asphalt content [%]	6.0	6.9
VMA [%]	16.3	16.2
VFA [%]	75.9	75.0

Table 9.8: Aggregate modulus

Parameter	Granite	Limestone
Elastic modulus, Eelastic[GPa]	30	25
([psi])	(4351131)	(3625942)

Data Analysis

Huet model expression in the time domain for the creep compliance is given by equation (9.4). The expressions for binder and for mixture, respectively, can be written as follows:

$$D_{binder}(t) = \frac{1}{E_{\infty_binder}} \left(1 + \delta \frac{(t/\tau_{binder})^k}{\Gamma(k+1)} + \frac{(t/\tau_{binder})^h}{\Gamma(h+1)} \right) \quad [9.10]$$

$$D_{mix}(t) = \frac{1}{E_{\infty_mix}} \left(1 + \delta \frac{(t/\tau_{mix})^k}{\Gamma(k+1)} + \frac{(t/\tau_{mix})^h}{\Gamma(h+1)} \right) \quad [9.11]$$

Where:

$D_{\text{binder}}(t), D_{\text{mix}}(t)$ = creep compliance of binder and mixture,

$E_{\infty_binder}, E_{\infty_mix}$ = glassy modulus of binder and mixture,

$\tau_{\text{binder}}, \tau_{\text{mix}}$ = characteristic time of binder and mixture.

The five constants required by the model, δ, k, h, E_{∞} , and τ , were determined through minimization of the sum of the distances between the experimental creep compliance and that Huet model at n time points:

$$\min \left(\sum_{i=1}^n [D^{\text{exp}}(t) - D^{\text{Huet}}(t)]^2 \right) \quad [9.12]$$

Where:

$D^{\text{exp}}(t)$ = experimental creep compliance,

$D^{\text{Huet}}(t)$ = model creep compliance.

Figures 9.12 and 9.13 provide examples on how the model fits the experimental data for PG 58-34 M2 modified asphalt binder and the corresponding asphalt mixture made with granite aggregate and tested at $T=-24^{\circ}\text{C}$, and for PG 58-28U2 plain asphalt binder and the corresponding limestone asphalt mixture tested at $T=-18^{\circ}\text{C}$, respectively.

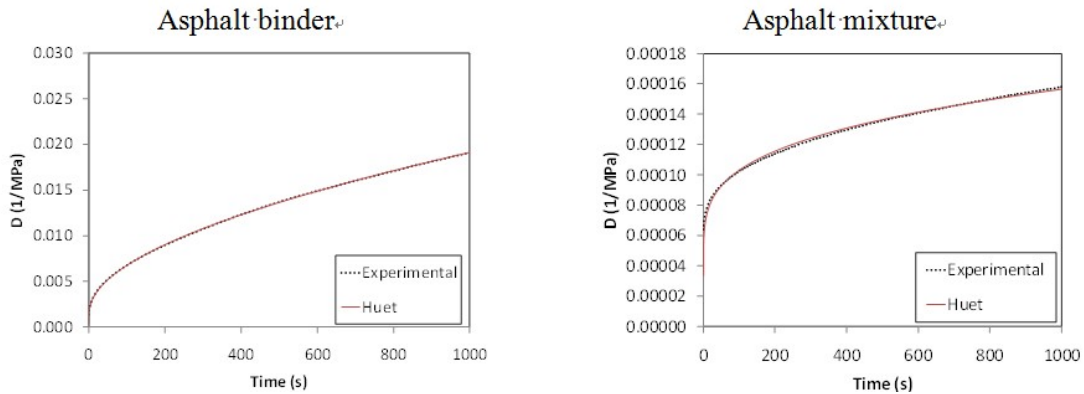


Figure 9.12: Huet Model for PG 58-34 M2 binder and granite mixture, $T=-24^{\circ}\text{C}$

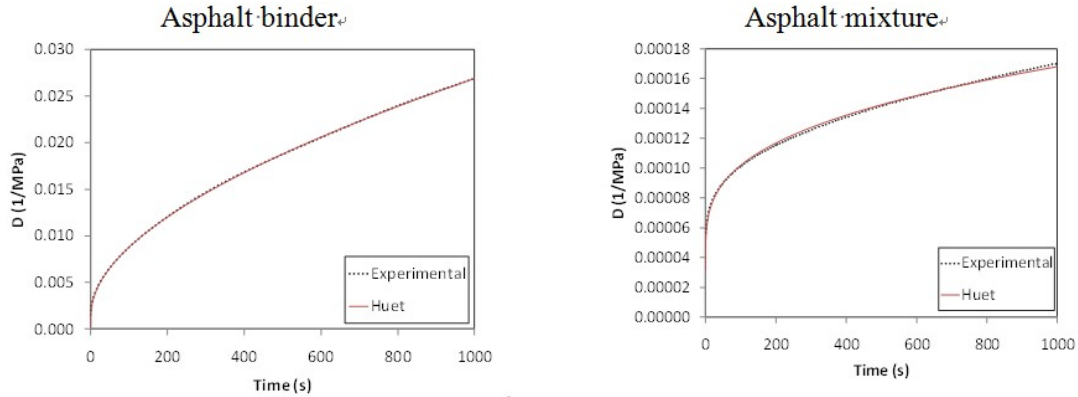


Figure 9.13: Huet Model for PG 58-34 M2 binder and limestone mixture, T=-24°C

Visual inspection indicates that Huet model fits asphalt binder and mixture experimental data very well. This is true for all binders and all mixtures evaluated. Table 9.9 lists the parameters of the model for four of the asphalt binders and the corresponding granite mixtures made with the same mix design and tested at T=-24°C.

Table 9.9: Huet Model parameters for binders and granite mixtures

Material	δ	k	h	E_{∞} (MPa)	Log(τ)	
Binder	58-34:M1	2.42	0.18	0.60	3000	0.251
	58-34:M2	4.18	0.22	0.62	3000	0.497
	64-34:M1	3.50	0.21	0.64	3000	0.387
	64-34:M2	3.99	0.23	0.64	3000	0.328
Mixtures	58-34:M1:GR	2.42	0.18	0.60	28000	3.420
	58-34:M2:GR	4.18	0.22	0.62	30000	3.675
	64-34:M1:GR	3.50	0.21	0.64	30000	3.547
	64-34:M2:GR	3.99	0.23	0.64	29001	3.523

It is observed that the values for δ , k, and h are the same for the binder and the corresponding mixture. It is also observed that the binders have similar values of δ , k, and h, identical glassy modulus E_{∞} (3000 MPa), and different characteristic time τ . The same is true for the mixtures; in this case glassy modulus is in the 28000-30000 MPa range. The values of the characteristic time of mixtures were compared with those found by Huet (13) and reasonable agreement was found.

In addition, by plotting $\log(\tau_{\text{binder}})$ vs. $\log(\tau_{\text{mix}})$, a linear correlation can be detected. Figures 9.14 and 9.15 contain the characteristic time plots for all binders and their corresponding granite and limestone mixtures at the reference temperatures (T=24°C for PG-34 and T=18°C for PG-28).

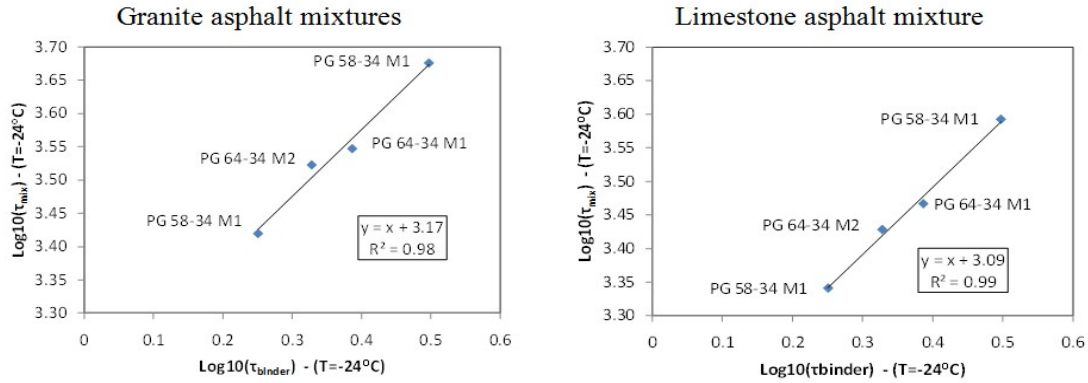


Figure 9.14: τ relationship for PG-34 binders and corresponding mixtures

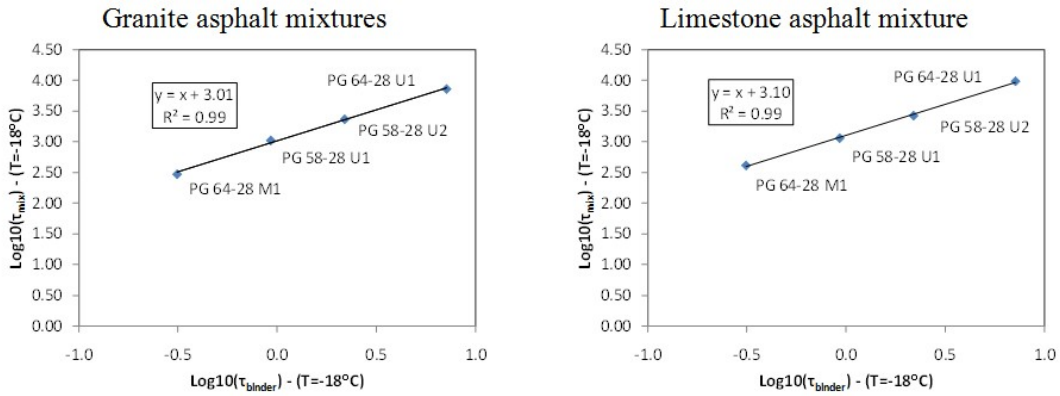


Figure 9.15: τ relationship for PG-28 binders and corresponding mixtures

Based on the strong linear correlation ($R^2=0.98-0.99$), the following expression can be written to relate the characteristic time of the binders and of the corresponding mixtures with similar mix designs:

$$\tau_{mix} = 10^{\alpha} \tau_{binder} \quad [9.13]$$

Where:

τ_{binder} =characteristic time of binder,

τ_{mix} = characteristic time of mixture,

α = regression parameter which may depend on mix design.

Table 9.10 lists the α values for all materials.

Table 9.10: α values for the four binders mixtures groups

Mixtures	PG -34 granite	PG -34 limestone	PG -28 granite	PG -28 Limestone
α	3.17	3.09	3.01	3.10
Difference	0.08		0.09	

The α values are very similar and range from 3.01 to 3.17, which reflects the fact that the mix designs were very similar even though the mixtures contain different type of aggregates. These values are also similar to the results reported by Olard and Di Benedetto for 2S2P1D model (18, 24, 25).

Combining (9.11), (9.12) and (9.13) the following expression can be written:

$$D_{mix}(t) = D_{binder}(t 10^{-\alpha}) \frac{E_{\infty_binder}}{E_{\infty_mix}} \quad [9.14]$$

Which can be also written in terms of the inverse of creep compliance, creep stiffness $S(t)$:

$$S_{mix}(t) = S_{binder}(t 10^{-\alpha}) \frac{E_{\infty_mix}}{E_{\infty_binder}} \quad [9.15a]$$

This expression can be simply rearranged to express S_{binder} as a function of S_{mix} as follows:

$$S_{binder}(t) = S_{mix}(t 10^{\alpha}) \frac{E_{\infty_binder}}{E_{\infty_mix}} \quad [9.15b]$$

Where:

$D_{mix}(t)$ = creep compliance of mixture,

$D_{binder}(t)$ = creep compliance of binder,

$S_{mix}(t)$ = creep stiffness of mixture,

$S_{binder}(t)$ = creep stiffness of binder,

E_{∞_mix} = glassy modulus of mixture,

E_{∞_binder} = glassy modulus of binder,

α = regression parameter which may depend on mix design,

t = time

These expressions are similar to expressions (9.15a) and (9.15b) and represent the ENTPE transformation for low temperature creep stiffness. They were used next to solve the forward and the inverse problem.

Forward Problem: Mixtures from Binders

Two approaches were used: Hirsch model and ENTPE transformation. For Hirsch model, equations (9.1), (9.2), and (9.3), were applied to the experimental data. Two formulations of the Hirsch model were used according to results obtained in previous work (6, 7, 8, 9, 27). In one study (6), a value of aggregate modulus different from the original formulation proposed by Christensen (5) was used ($E_{agg}=2750000\text{psi} - 19\text{GPa}$ instead of $E_{agg}=4200000\text{psi} - 29\text{GPa}$) with better fitting results. The alternative formulation of the P_c contact volume parameter (9.3) was applied in other studies (16, 17, 18 and 41) in which the aggregate modulus was set to 25GPa and 30GPa for limestone and granite respectively. Table 9.11 summarizes the parameters used for the models evaluation; G stands for granite and L for limestone.

Table 9.11: Parameters used in Hirsch Model

Granite	Limestone
Hirsch-2	Hirsch-2
$E_a=2750000\text{psi}$	$E_a=2750000\text{psi}$
Pc expression (9.2)	Pc expression (9.2)
Hirsch-3G	Hirsch-3L
$E_a=4351131\text{psi}$	$E_a=3625942\text{psi}$
Pc expression (9.3)	Pc expression (9.3)

Figures 9.16 to 9.19 contain plots of experimental data and creep stiffness predictions for granite and limestone mixtures.

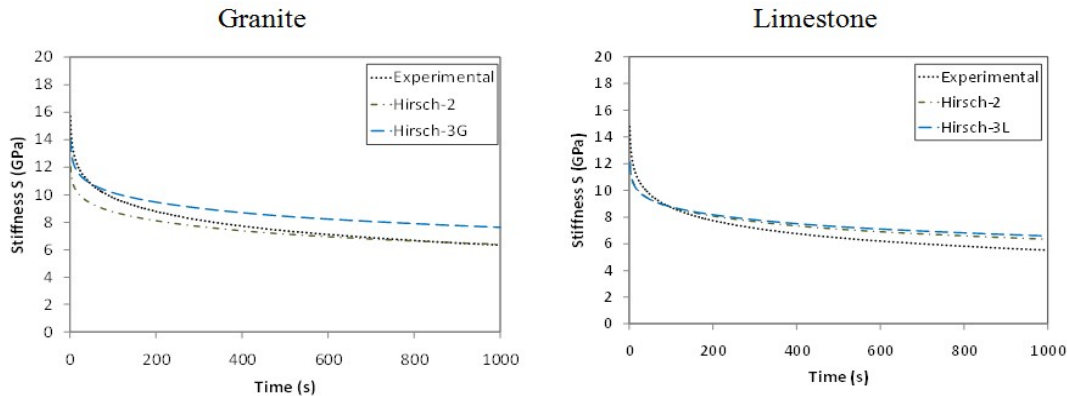


Figure 9.16: Hirsch Model predictions for PG 58-34 M2 mixture, T=-24°C

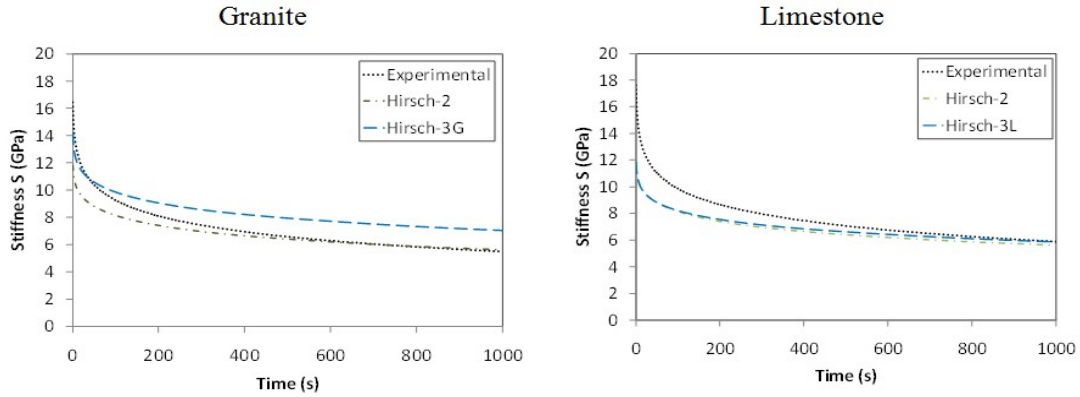


Figure 9.17: Hirsch Model predictions for PG 58-28 U2 mixtures, $T=-18^{\circ}\text{C}$

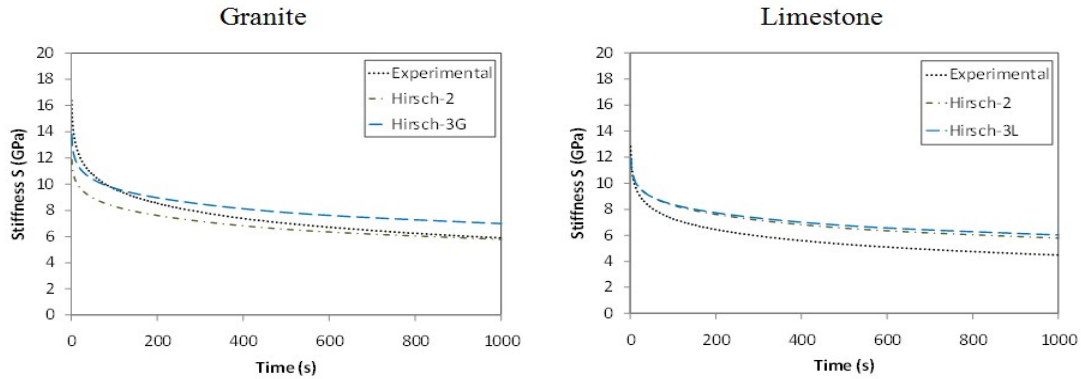


Figure 9.18: Hirsch Model predictions for PG 64-34 M2 mixture, $T=-24^{\circ}\text{C}$

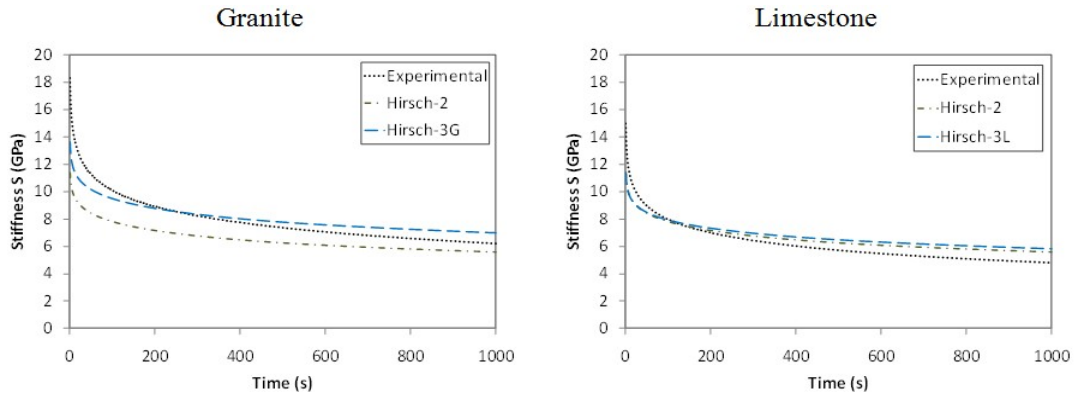


Figure 9.19: Hirsch Model predictions for PG 64-28 M1 mixtures, $T=-18^{\circ}\text{C}$

For the granite mixtures, the experimental curves are located between the two prediction curves: Hirsch-2 and Hirsch-3G. Different conclusions can be drawn for the limestone mixtures: Hirsch-2 and Hirsch-3L result in similar prediction curves and both overestimate the experimental data

except for the limestone mixture PG 58-28 U2 tested at $T=18^{\circ}\text{C}$. Overall, the Hirsch model seems to reasonably predict the creep stiffness of most mixtures investigated.

For the ENTPE transformation, equation (9.15a) was used to solve the forward problem for the asphalt binders and mixtures investigated. Figures 9.20 to 9.23 contain plots of the experimental data and transformation predictions for granite and limestone mixtures at $T=-24^{\circ}\text{C}$ and $T=-18^{\circ}\text{C}$.

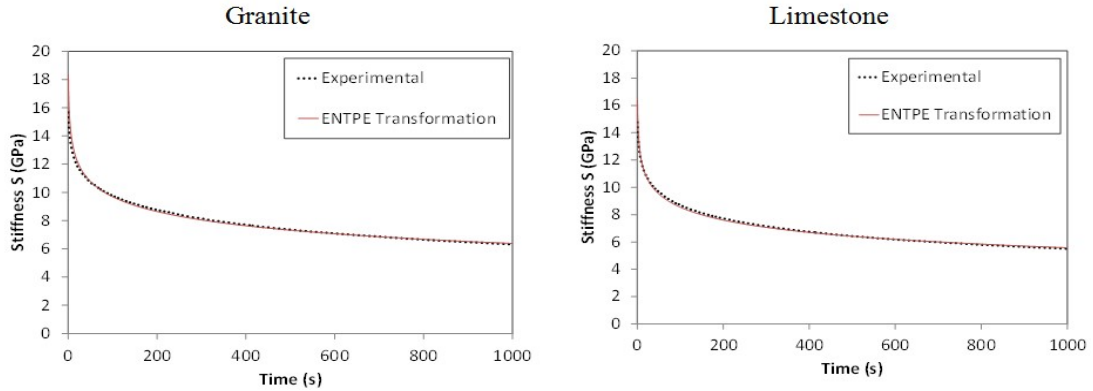


Figure 9.20: ENTPE transformation for PG 58-34 M2 mixtures, $T=-24^{\circ}\text{C}$

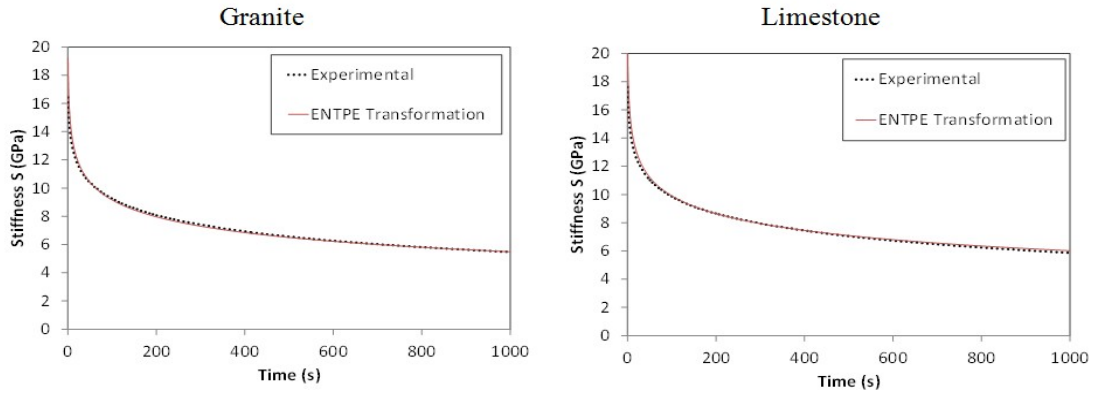


Figure 9.21: ENTPE transformation for PG 58-28 U2 mixtures, $T=-18^{\circ}\text{C}$

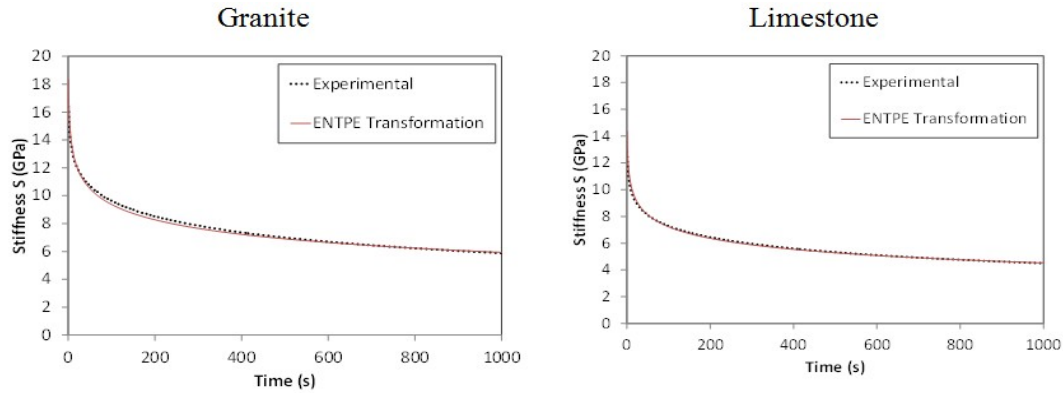


Figure 9.22: ENTPE transformation for PG 64-34 M2 mixture, T=-24°C

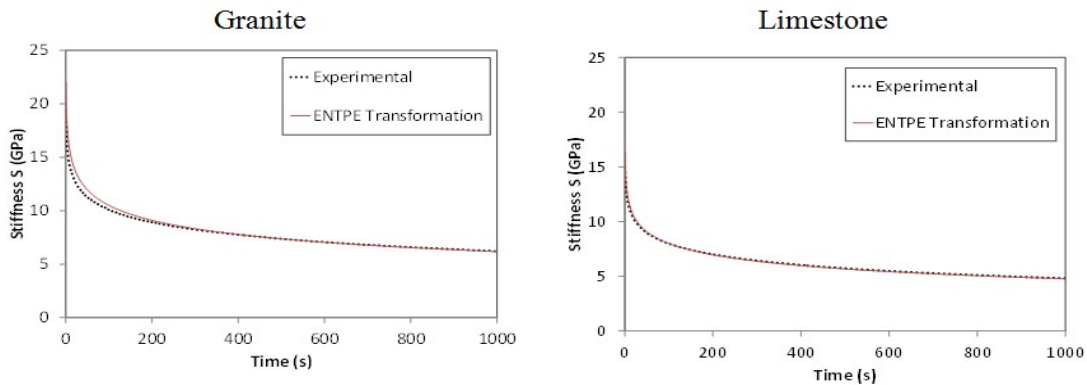


Figure 9.23: ENTPE transformation for PG 64-28 M1 mixtures, T=-18°C

The transformation fits very well the experimental creep stiffness $S(t)$ for all mixtures investigated and appears to predict the creep behavior of asphalt mixtures at low temperatures using asphalt binder data better than Hirsch model.

Inverse Problem: Binders from Mixtures

The prediction of a material property based on the measured (or observed) material response constitutes the objective of an inverse problem in mechanics. This process is called a parameter identification procedure. Two procedures for parameter identification for viscoelastic materials were proposed by Ohkami and Swoboda (28). Both methods contain boundary control concept introduced by Ichikawa and Ohkami (29). Amin et al (30) developed a similar approach by combining FEM simulations with inverse scheme. The viscoelastic behavior was modeled by the authors using a 3-parameter solid model. Kim and Kreider (31) used numerical inversion for 2D problem for linear viscoelastic homogenous material with three-seven parameters. Several potential problems with this scheme were detected. The solution might not be unique and might depend on the initial guess for optimization method and moreover there is no unique optimization approach that is suitable for all problem and material types.

Zofka et al. (6) used modified Hirsch (4) model proposed by Christensen (5) to “back-calculate” the asphalt binder stiffness and m-value from mixture creep stiffness at low temperatures. Since brute force was time consuming, the original equation (9.3) was combined with an alternative procedure to the numerical minimization based on the observation that a simple function could be fitted to the mix creep stiffness versus binder creep stiffness data. Based on these findings, Velasquez et al. (32) using additional experimental data developed two expressions for the Pc parameter: equations (9.2) and (9.3). Zofka (7) also used an inverse scheme based on the Zevin’s method of iterative functions (33). The asphalt mixture is treated as a 2-phase composite material consisting of elastic aggregate particles of arbitrary shape and viscoelastic asphalt mastic.

Hirsch Model

The method proposed by Zofka et al. (6) was used. First, based on the volumetric properties of the mixtures, plots of binder creep stiffness versus predicted mixture stiffness using modified equation (9.1) are generated for binder stiffness values between 50 to 1000MPa (Figures 9.25 and 9.26). Then, a very simple function is fitted to the mix log stiffness versus binder log stiffness data, as shown in Figure 9.24 and 9.25:

$$E_{mix} = a \cdot \ln(E_{binder}) + b \tag{9.16}$$

Where:

a and *b* are regression parameters.

Finally, the binder stiffness is simply calculated using equation (9.16) over the entire range of loading time.

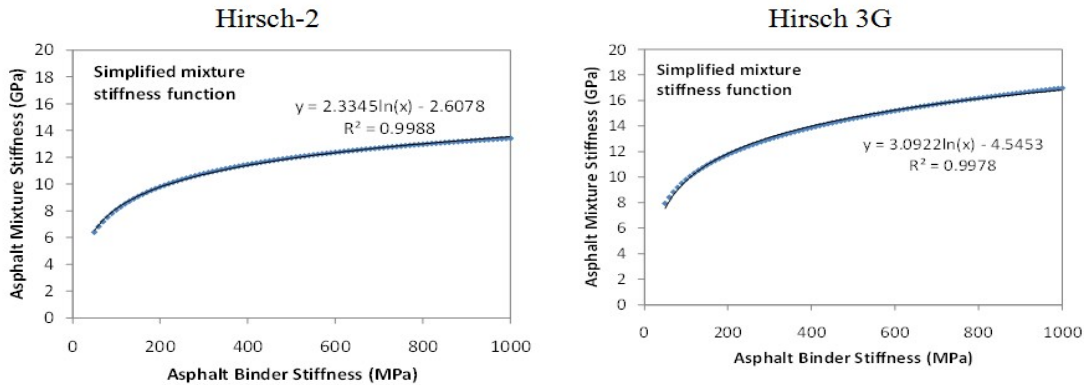


Figure 9.24: Simplified mixture function for granite mixture

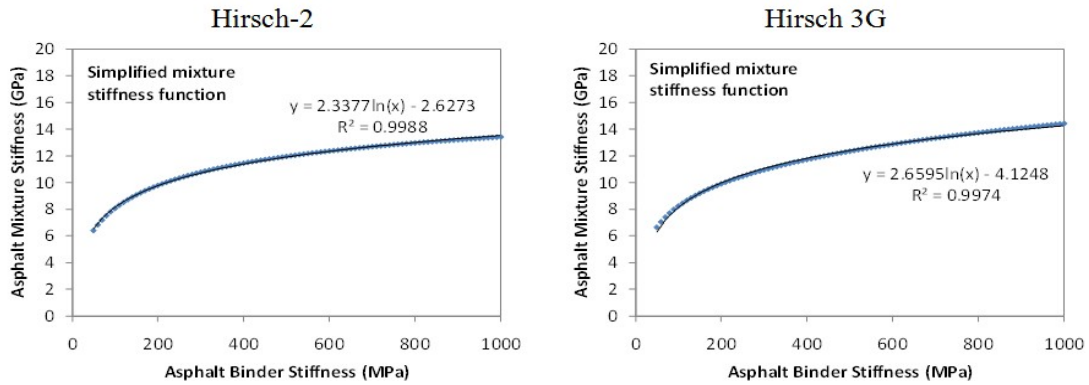


Figure 9.25: Simplified mixture function for limestone mixture

The parameters in Table 9.8 were introduced in the back calculation process along with the volumetric properties of the sixteen mixtures investigated. The back calculation algorithm was applied to the mixture data and binder creep stiffness was predicted and compared to the creep stiffness experimentally determined for the RTFOT binders used to prepare the corresponding mixtures. Figures 9.26 to 9.29 present examples for four of the binders investigated.

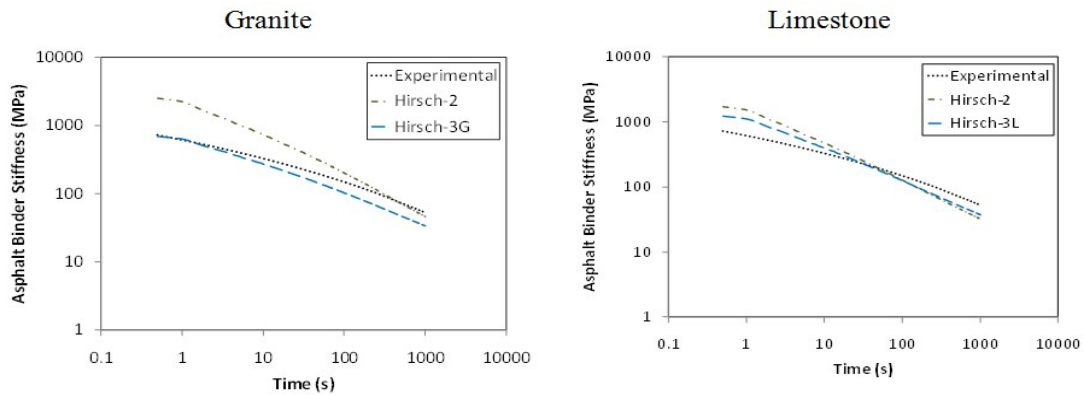


Figure 9.26: Predicted (Hirsch) binder creep stiffness for PG 58-34 M2 mixtures, T=-24°C

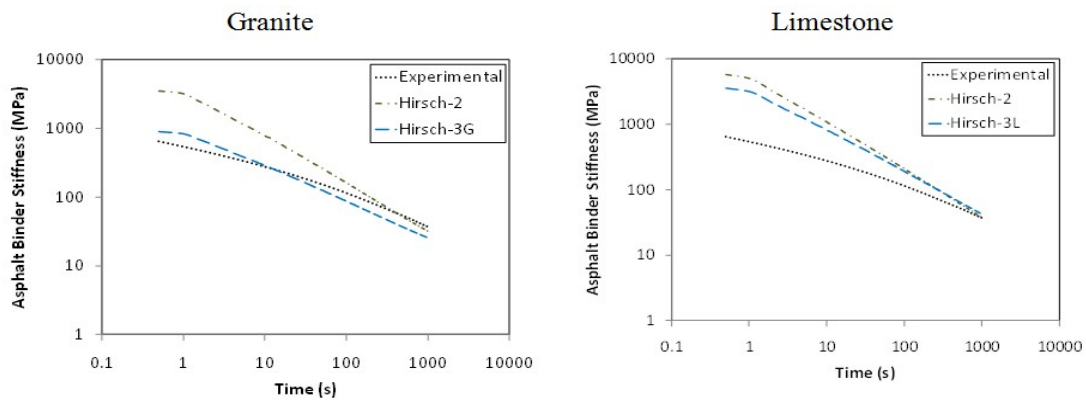


Figure 9.27: Predicted (Hirsch) binder creep stiffness for PG 58-28 U2 mixtures, T=-18°C

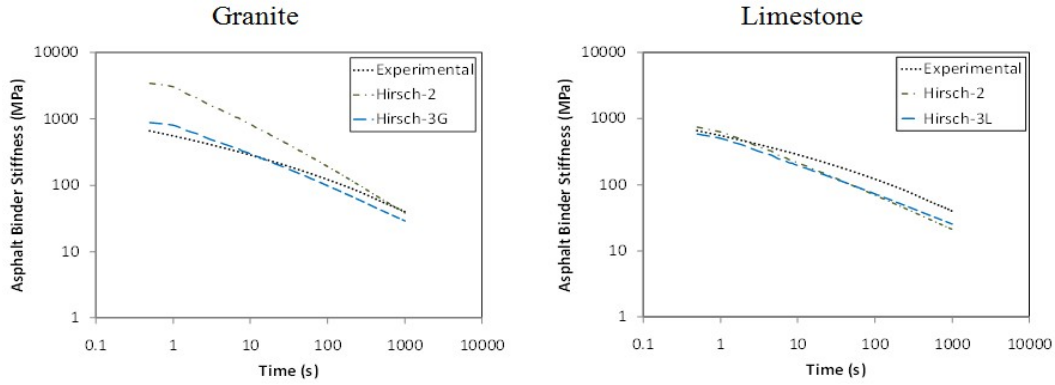


Figure 9.28: Predicted (Hirsch) binder creep stiffness for PG 64-34 M2 mixtures, T=-24°C

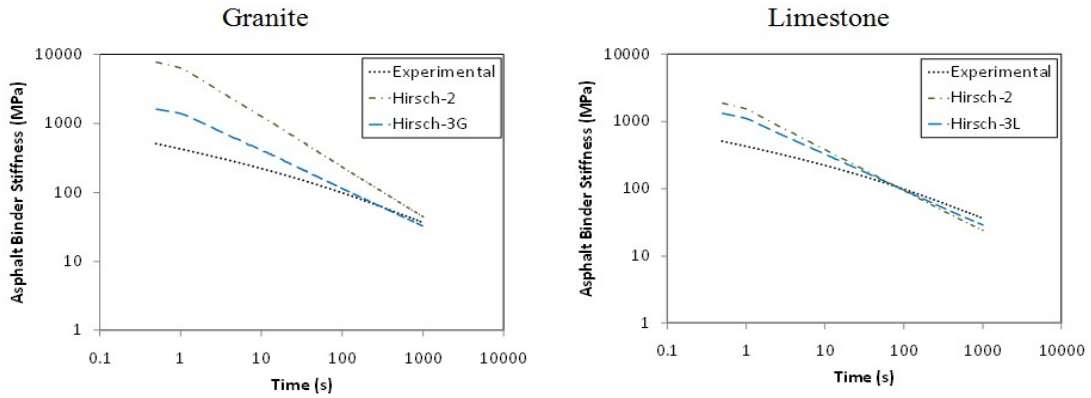


Figure 9.29: Predicted (Hirsch) binder creep stiffness for PG 64-28 M1 mixtures, T=-18°C

For granite and limestone mixtures, the back calculated binder stiffness fit the experimentally determined binder creep stiffness poorly with a few exceptions.

ENTPE Transformation

In this case, the approach is straight forward. First, from equation (9.13) the binder characteristic time is obtained from mixture characteristic time:

$$\tau_{binder} = 10^{-\alpha} \tau_{mix} \tag{9.17}$$

Then, asphalt binder creep stiffness S_{binder} can be easily predicted from asphalt mixture creep stiffness S_{mix} using equation (9.15b). Figures 9.30 to 9.33 contain plots of predicted binder creep stiffness $S(t)$ obtained using equation (9.15b) for granite and limestone mixtures at T = -24°C and T=-18°C.

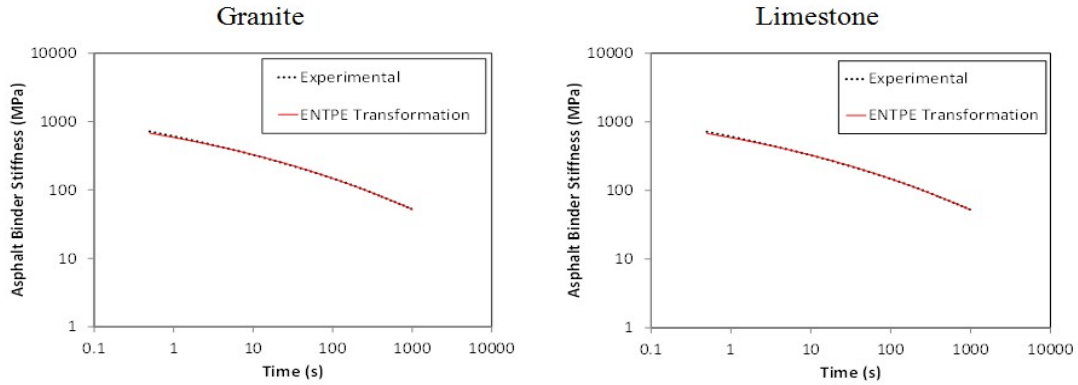


Figure 9.30: ENTPE transformation for PG 58-34 M2 mixtures, T=-24°C

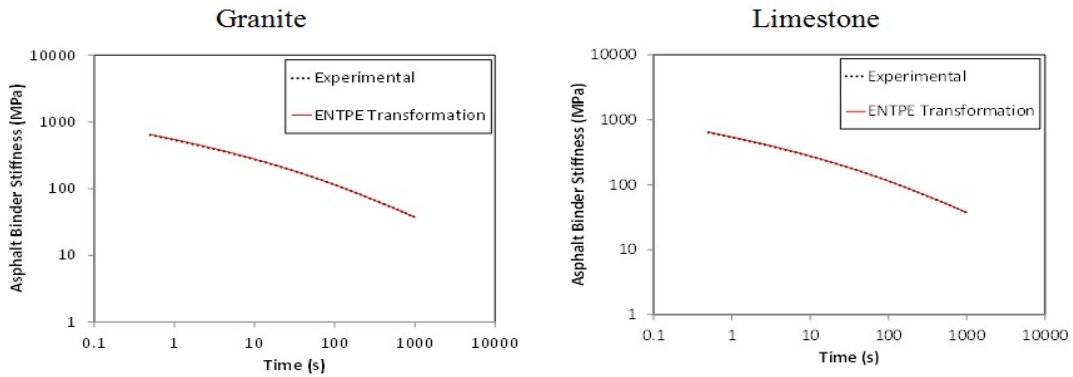


Figure 9.31: ENTPE transformation for PG 58-28 U2 mixtures, T=-18°C

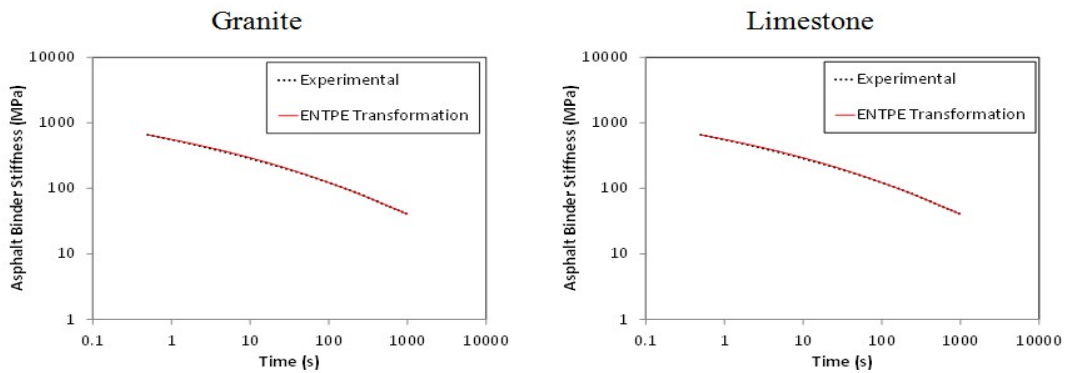


Figure 9.32: ENTPE transformation for PG 64-34 M2 mixtures, T=-24°C

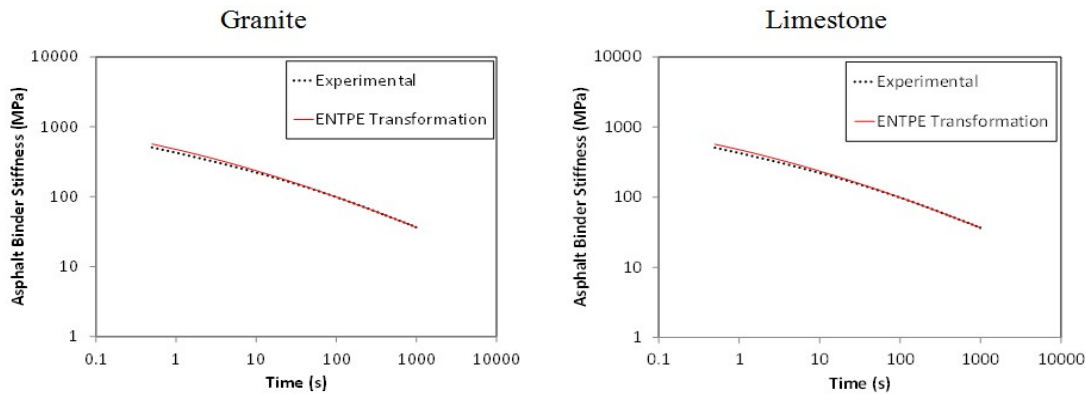


Figure 9.33: ENTPE transformation for PG 64-28 M1 mixtures, T=-18°C

It is obvious that expression (9.15b) predicts asphalt binder creep stiffness very well for all mixtures investigated.

Conclusions

Based on the results, the following conclusions are drawn:

Hirsch model predicted reasonably well the creep stiffness of the majority of mixtures investigated using binder creep stiffness and volumetric information. There was a small tendency to over predict the stiffness for the limestone mixtures.

For inverse problem, Hirsch model prediction of asphalt binder creep stiffness from asphalt mixture creep stiffness was poor. This may be due to the simplification used to fit the model expression.

ENTPE transformation performed very well for both forward and inverse problems. In particular, for the inverse problem of numerically “extracting” asphalt binder creep stiffness from experimental mixture data, the transformation performed much better than Hirsch model. However, the main obstacle is obtaining a reasonably accurate value for α parameter.

Using Binder Creep Stiffness to Obtain Mixture Creep Stiffness Threshold Value

As mentioned in subtask 2, the development of the SHRP asphalt binder criterion for low temperature cracking was based on the assumption that the 2-hour mixture stiffness correlated well with the severity of thermal cracking in the field (34). This assumption was extended to asphalt binder stiffness obtained in low-temperature creep tests. N. W. McLeod tentatively concluded that the critical low temperature pavement modulus of stiffness at which transverse pavement cracking is likely to occur is 1,000,000 psi or 7GPa. A value twice as high was proposed by Readshaw.

The research performed in the previous section demonstrated that mixture creep stiffness can be predicted using binder creep stiffness data. One interesting application is to predict what is the mixture creep stiffness value corresponding to a binder creep stiffness value of 300MPa, the current PG specification limit. The challenge is to reasonably match the aging condition of the

two materials. Since it is generally accepted that binder RTFOT matches the aging condition of the mixture after short term aging or as loose mix, it was decided to first determine the corresponding creep stiffness limit for binders in RTFOT condition and then use Hirsch model to predict mixture creep stiffness. The asphalt binders used in the first phase of the pooled fund study (see Table 9.6) were also used here because BBR data was obtained for both PAV and RTFOT conditions.

Binder PAV to Binder RTFOT

First, the BBR binder PAV data was used to calculate the critical temperature at which S(60s) is equal to 300MPa. This was done by assuming a linear relation between log S(60s) and test temperature and interpolating to obtain the critical temperature, as shown in Figure 9.34 (left side). Then, based on the same linearity assumption between the RTFOT log S(60s) and temperature, a corresponding stiffness value at the critical temperature is obtained, as shown in Figure 9.34 (right side).

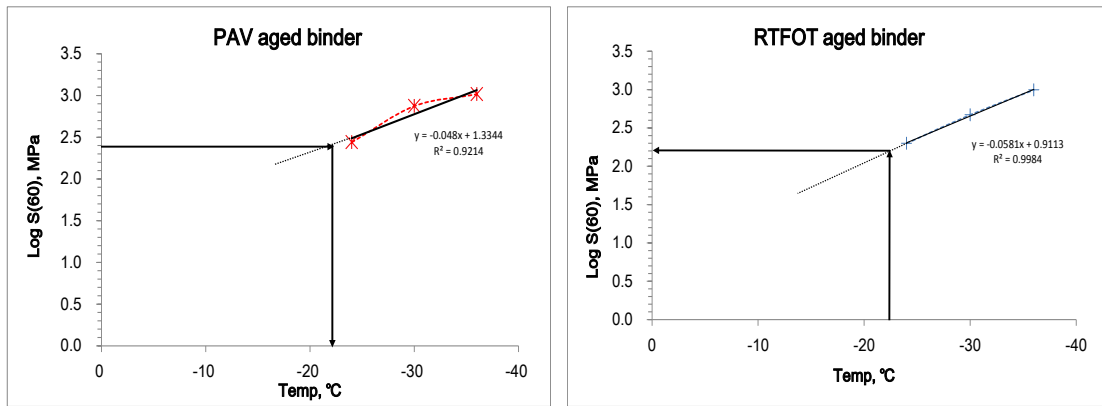


Figure 9.34: Predicting S(60)RTFOT corresponding to S(60)PAV = 300MPa

Since log creep stiffness for some of the binders did not follow a linear relation to temperature, another approach based on the CAM model was used. In this case, creep stiffness master curves were obtained using the model expression for stiffness:

$$S(t) = S(t)_g \cdot \left[1 + \left(\frac{t_c}{t} \right)^\nu \right]^{-w/\nu} \tag{9.18}$$

Where:

S(t)_g : glassy creep stiffness asymptote (3GPa);

t_c : cross over time, ν and w : fitting parameters

Table 9.12 summarizes the results of the two methods. No significant differences are observed between the simple regression method and CAM model fitting except for two binders.

Table 9.12: Binder PAV T_{cr} and corresponding S(60)RTFOT

Mix ID	PG Binder Grade	T _{cr} [PAV]	Simple Regression			CAM	Error [%]
			S(60s)T _{cr} [MPa]	R ² [PAV]	R ² [RTFOT]	S(60s)T _{cr} [MPa]	
B	58-34 M1	23.8	196	0.921	0.998	192	2.3
C	58-34 M2	26.5	255	0.992	0.994	289	11.6
D	58-28 U1	23.5	229	*	0.995	221	3.4
E	58-28 U2	20.5	180	0.996	*	178	0.9
F	64-34 M1	24.5	197	0.985	0.986	189	4.5
G	64-34 M2	27.0	238	0.985	0.994	294	19.0
H	64-28 U1	20.0	258	0.999	*	247	4.6
I	64-28 M1	23.7	261	0.999	0.999	263	0.9
J	64-22 U1	18.4	124	*	*	123	1.1

*: only two temperatures were considered.

Binder RTFOT to Mixture

Asphalt mixture creep stiffness was predicted from RTFOT binder creep stiffness by means of Hirsch model previously described. Table 9.13 and Figure 9.35 summarize the results.

Table 9.13: Predicted mixture S(60) at PAV binder critical temperature

Mix ID	S(60s)T _{cr} [MPa]	Mix ID	S(60s)T _{cr} [MPa]
B: G	10864	B: L	10873
C: G	12146	C: L	12156
D: G	11310	D: L	11319
E: G	10644	E: L	10654
F: G	10814	F: L	10823
G: G	12204	G: L	12214
H: G	11647	H: L	11657
I: G	11854	I: L	11864
J: G	9521	J: L	9530

*: G: Granite, L: Limestone

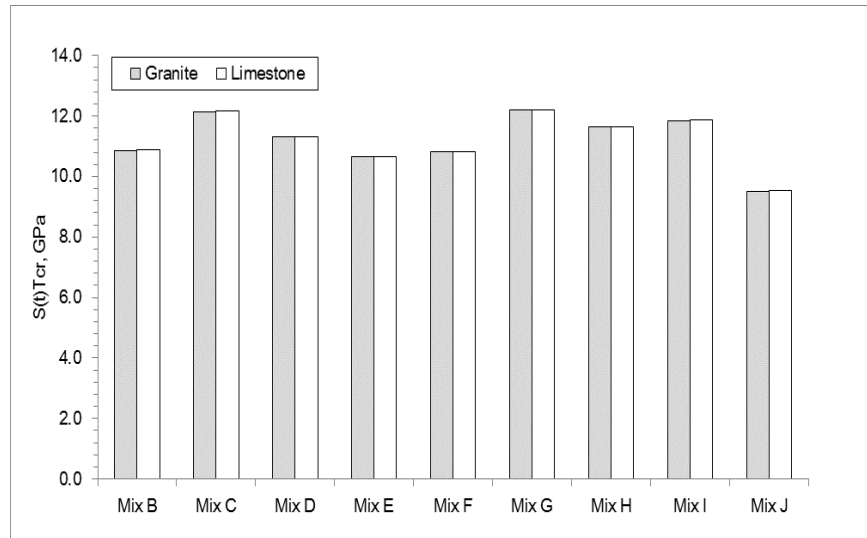


Figure 9.35: Predicted mixture $S(60s)$ at PAV binder critical temperature

It can be observed that the values range from 9.5GPa to approximately 12GPa. Since they represent the short term aging condition of the mixtures, it is expected that higher values would be obtained for long term aged mixtures, closer to the limit proposed by Readshaw.

Obtaining Strength from BBR Tests on Mixture Beams

As already mentioned, research performed at the University of Minnesota showed that the Bending Beam Rheometer (BBR), currently used for asphalt binders specifications, can be used to obtain creep properties of asphalt mixtures, (see Figure 9.1).

Work performed in an ongoing NCHRP Idea project investigates the feasibility of using BBR to obtain asphalt mixture bending strength. A summary of the results is presented in the next paragraphs.

Experimental Work

The TE-BBR Pro device provided by Canon Instrument Company was used to perform the strength tests. The new machine, shown in Figure 9.36, is equipped with a proportional valve that offers a much more complex control of the pressure in the air bearing system and is capable of providing constant loading rates to perform strength tests. The new load cell capacity is 44N.



Figure 9.36: TE-BBR pro device

Three asphalt binders used in phase I of the pooled fund study, for which DTT results were available, were investigated: PG 58-28 (unmodified), PG 58-34 (SBS modified) and PG 64-22 (unmodified). The first two asphalt binders were short and then long termed aged and bending strength tests were performed using the new BBR device for both aging conditions. DTT strength results were available for both aging conditions at which BBR strength tests were run.

Binder PG 64-22 was used in the second part of the experimental phase, in which BBR strength tests were run in ethanol and in potassium acetate. All tests results for this asphalt binder were obtained for RTFOT condition.

The loading procedure for the first two asphalt binder was selected such that DTT and BBR times to failure for PAV aged binder tested at lower PG+10°C were similar. This approach was selected based on the fact that the cohesive law, governing the fracture process zone (FPZ) propagation, is rate dependent and consequently time dependent. By selecting similar times to failure for the two tests, the FPZ propagation is imposed to occur with the same rate. This was done to obtain a procedure that facilitates the comparison of DTT and BBR strength since the two tests are performed using different loading procedures: displacement and load control, respectively.

The BBR nominal strength (maximum stress at peak load) σ_N and corresponding strain ϵ_N at the bottom of the thin beam (Figure 9.37a) can be estimated from the dimensions of the beam, the applied load, and the measurement of deflection.

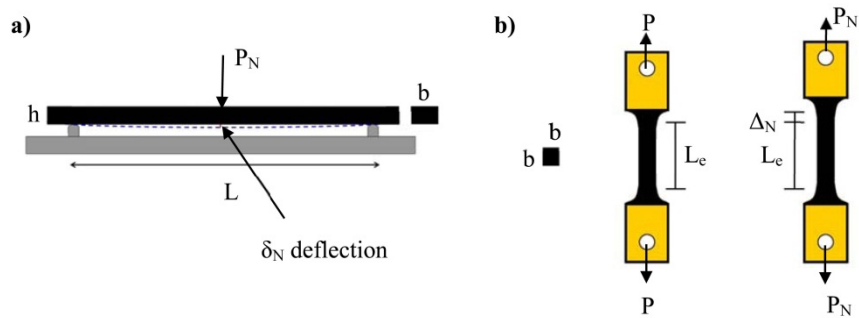


Figure 9.37: BBR (a) and DTT (b) strength tests

Table 9.14 summarizes the results obtained from BBR strength tests for the first two binders and Table 9.15 the results from DTT strength tests.

Table 9.14: BBR asphalt binder test results

Binder PG	Aging	Temperature (°C)	Rate N/min	Mean Strength (MPa)	CV (%)
58-28	RTFO	-18	1.4	1.4	39.9
			5.6	1.8	22.4
		-24	1.4	1.6	13.2
	PAV	-24	5.6	1.6	20.3
		-18	1.4	1.9	23.7
			5.6	2.1	17.1
58-34	RTFO	-24	1.4	1.8	42.6
			5.6	1.8	43.1
		-24	1.4	2.0	14.7
			5.6	2.1	19.9
	PAV	-30	1.4	2.2	15.8
			5.6	2.3	20.5
		-24	1.4	2.2	17.9
			5.6	1.9	20.5
PAV	-30	1.4	2.2	20.4	
		5.6	2.2	28.1	

Table 9.15: DTT asphalt binder experimental design and test results

Binder PG	Aging	Temperature (°C)	Mean Strength (MPa)	CV (%)
58-28	RTFOT	-18	4.4	8.6
		-24	4.8	12.6
	PAV	-18	4.2	13.9
		-24	4.2	30.8
58-34	RTFOT	-24	5.0	4.6
		-30	6.6	13.8
	PAV	-24	5.2	19.1
		-30	6.1	13.2

The results obtained on asphalt binder PG58-34 and PG58-28 clearly show that there is a significant difference between the values measured with BBR and DTT. However, the two tests are performed under different types of loading, three-point bending and direct tension, and the volumes of the specimens are significantly different: 9921.9mm³ and 1945.9mm³ for BBR and DTT, respectively. The dependence of structural strength on the structure size and geometry can be explained using the well-established size effect theory.

BBR and DTT specimens share the same failure mechanism, where the peak load is reached once a macro-crack initiates from one representative volume element (RVE). Therefore, the structure can be statistically represented by a chain of RVEs. The failure probability can be further calculated based on the joint probability theorem:

$$1 - P_f = \prod_{i=1}^n [1 - P_1(\sigma_i)] \quad [9.19]$$

or

$$\ln(1 - P_f) = \sum_{i=1}^n \ln[1 - P_1(\sigma_i)] \quad [9.20]$$

Where:

P_f = failure probability of the entire structure,

P_1 = failure probability of one RVE, and

σ_i = maximum principal stress at center of the i th RVE.

RVE plays a major role in the calculation. It has been shown that the RVE size is roughly equal to 2-3 times of the size of material inhomogeneity or grain size (Bažant and Pang, 2007). In the present study, the grain size of the binder is on the micro-scale. Therefore, we may assume that the RVE size is almost negligible compared to the specimen size. Based on equation (9.20), what matters for the failure probability of the structure is the tail part of the strength distribution of one RVE.

Recent studies (Bažant et al., 2009; Le et al., 2011) showed that, based on atomistic fracture mechanics and on statistical multi scale transition framework, the tail of the strength distribution of one RVE must follow a power-law, i.e. $P_1 = (\sigma_i / s_0)^m$ (Bažant and Pang, 2007). Furthermore, by using the approximation $\ln(1-x) = -x$ for small value of x , we can re-write equation (9.20) as:

$$P_f = 1 - \exp\left\{-\sum_{i=1}^n [s(x_i)]^m (\sigma_N / s_0)^m\right\} \quad [9.21]$$

Where:

$s(x_i)$ = dimensionless stress field such that $\sigma_i = s(x_i)\sigma_N$,

σ_N = nominal strength,

s_0 = material constant (scale parameter),

m = material constant called Weibull modulus (or shape parameter).

Since the structure size is much larger than the RVE size, the sum can be replaced by an integral over the volume V of the specimen:

$$P_f = 1 - \exp\left\{-\int_V [s(x)]^m dV(x)\right\} (\sigma_N / s_0)^m \quad [9.22]$$

Equation (9.22) indicates that the strength distribution would follow the classical two-parameter Weibull distribution (Rinne, 2009). By using simple elastic stress field for BBR and DTT, we can relate the mean strength of BBR specimen σ_N^B and the mean strength of DTT specimen σ_N^U

$$\frac{\sigma_N^B}{\sigma_N^U} = \left[4 \cdot (1+m)^2\right]^{1/m} \left(\frac{V_U}{V_B}\right)^{1/m} \quad [9.23]$$

where V_U and V_B are volume of DTT and BBR specimens, respectively. Using equation (9.23), we can predict the strength of DTT specimens from the strength of BBR specimens, where the Weibull modulus, m , is chosen to be about 10 based on the preliminary tests on strength histogram. Table 9.16 shows the comparison between predicted and measured DTT strengths.

Table 9.16: Comparison between DTT vs. BBR asphalt binder strength

Binder	Aging	T (°C)	Measured Mean Strength (MPa)		Ratio (%)	Corrected Mean Strength (MPa)		Ratio (%)
			BBR	DTT		BBR to DTT		
PG58-28	PAV	-18	2.1	4.2	51.3	1.4		32.6
PG58-34	PAV	-24	1.9	5.2	35.5	1.2		22.5

It is clear that the predicted DTT strength is three to four times lower than the measured one and other factor(s) are responsible for the significant difference. The other significant difference between DTT and BBR tests is the cooling medium: DTT specimens are cooled using potassium acetate and BBR specimens are cooled using ethanol. Based on previous research conducted by Dongre and D'Angelo (1998), in which the authors showed that DTT strength in ethanol is 3 to 5

times lower than DTT strength in potassium acetate or air, it was decided to investigate if cooling medium could cause such a significant effect on the structural strength.

Effect of Cooling Medium on BBR Strength

In order to determine whether cooling fluid affects the failure response of asphalt binder when tested in three-point bending with BBR, a new set of experiments was performed on PG64-22 binder in RTFOT condition. BBR strength tests were run in ethanol and then in potassium acetate at PG - 2°C. From the nominal stress strain curves in Figure 9.38, it is evident that BBR mean strength in potassium acetate is almost 4.5 times higher than BBR mean strength in ethanol. Also, a small decrease in the stiffness of the binder is observed for the specimens tested in ethanol.

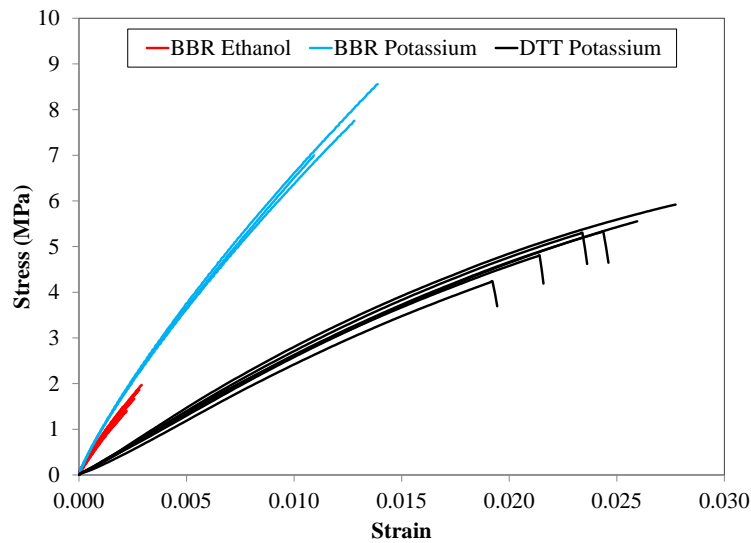


Figure 9.38: Cooling medium effect on BBR stress strain curves for binder PG64-22

Using the same Weibull approach it is possible to estimate of corrected strength for the new test results. Table 9.17 summarizes the test results as well as the corrected values for the BBR strength in ethanol (E) and in potassium acetate (PA).

Table 9.17: BBR and DTT results and comparison for different cooling media

Test	Rep.	Cooling Medium	Loading Rate	Mean Strength	Corrected BBR Mean Strength	Corrected BBR mean strength / DTT mean strength
Type	#		N/min	(MPa)	(MPa)	%
BBR-E	5	Ethanol	7.2	1.7	1.0	18.4
BBR-PA	3	Potassium Acetate	24	7.8	4.8	85.1
DTT	4	Potassium Acetate	-	5.7	-	

The corrected BBR strength in ethanol is almost five times smaller than DTT strength, while the corrected BBR strength in potassium acetate is fairly similar to DDT strength, since the 15% difference is less than testing variability.

The effect of cooling medium on BBR strength was further evaluated for binders PG58-28 and PG64-22, using the same loading rate (7.2N/min) and same testing temperature ($T = -24^{\circ}\text{C}$). The results in Table 9.18 provide further evidence of the strong effect of ethanol on the flexural strength, with a very similar impact on both asphalt binders (21-22% in ratio).

Table 9.18: Effect of cooling medium on BBR strength

Binder	Ethanol Mean Strength (MPa)	Potassium Acetate Mean Strength (MPa)	Ethanol - Potassium Acetate Mean Strength Ratio (%)
PG58-28	1.4	6.6	21.7
PG64-22	1.7	7.5	22.3

Many glassy polymers when exposed to organic solvents may fail at stresses and strains much lower than their normal values, if an adverse environment is present (Kambour, 1973; May, 1975). This is known in polymer literature as environmental stress cracking (ESC). Based on literature review, it can be hypothesized that both chemical interaction (with ethanol) and diffusion occurred in the asphalt binders specimens conditioned and tested in ethanol. This hypothesis needs to be further investigated and proved.

Conditioning and testing binder specimens in air appears to be a simple solution to this issue. However, asphalt binders are highly temperature susceptible materials and rigorous temperature control in air is much more difficult to achieve than in fluid. On-going research is addressing this challenge.

Chapter 10. Subtask 3: Proposed Simplified Method to Obtain Mixture Creep Compliance – Part 3

Introduction

It is recognized that a better approach for thermal cracking characterization of asphalt materials is to use fracture mechanics principles rather than to use continuum mechanics approach of linear viscoelastic materials. Current test methods to address low temperature cracking, such as the Bending Beam Rheometer (BBR) (1), characterize the material in the linear viscoelastic domain at small strain levels and, therefore, do not provide the complete picture for thermal cracking characterization.

Previous research by Hoare and Hesp (2), Hesp (3), Chailleux and Mouillet (4), Chailleux et al. (5) have used the Single-Edge Notched Bending (SENB) Test, which is a fracture mechanics-based test commonly used in metals and other materials, to obtain the fracture properties of asphalt binders at low temperatures. They succeeded in grading a broad range of materials with different levels of modification. The SENB test follows ASTM E399 standard (6) and assumes that linear elastic fracture mechanics (LEFM) conditions hold. Figure 10.1 shows a schematic of how the SENB test is performed and the parameters used for the calculation of fracture toughness (K_{IC}) and fracture energy (G_f).

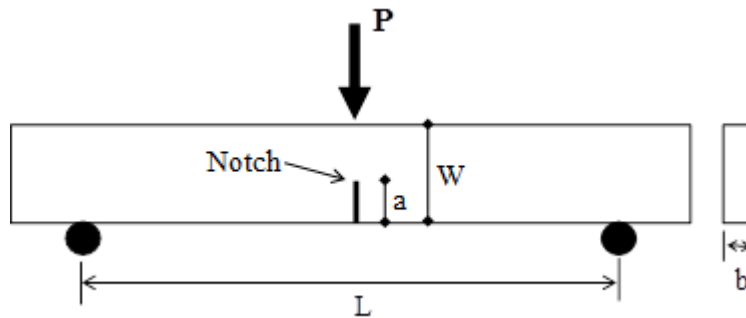


Figure 10.1: SENB test schematic

The following equation is used to calculate the fracture toughness, K_{IC} , of asphalt binders:

$$K_{IC} = \frac{PL}{bW^{3/2}} f\left(\frac{a}{W}\right) \quad [10.1]$$

with $f\left(\frac{a}{W}\right)$ defined for SENB geometry as:

$$f\left(\frac{a}{W}\right) = \frac{3\left(\frac{a}{W}\right)^{1/2} \left[1.99 - \frac{a}{W} \left(1 - \frac{a}{W}\right) \left(2.15 - 3.93\left(\frac{a}{W}\right) + 2.7\left(\frac{a}{W}\right)^2\right)\right]}{2\left(1 + 2\frac{a}{W}\right) \left(1 - \frac{a}{W}\right)^{3/2}} \quad [10.2]$$

The K_{IC} parameter denotes mode I fracture in which crack formation occurs in tensile mode due to bending.

The fracture energy, G_f is calculated as the total area under the entire load-deflection (P-u) curve, divided by the area of the ligament. This is shown in equation (10.3).

$$G_f = \frac{W_f}{A_{lig}} \quad [10.3]$$

Where:

$$W_f = \int P du$$

And A_{lig} is the area of the ligament.

The commonly used SENB specimen geometry proposed in recent studies (2-5) includes two metal bars to reduce the amount of asphalt binder used. However, when this geometry was used in testing, adhesion problems between the asphalt binder and the metal bars observed during sample preparation and handling of the specimen motivated the use of a new geometry based on the BBR specimens, without the need for the metal bars. The new proposed geometry can be used in the SENB system for low temperature characterization and ranking of a broad range of unmodified and modified asphalt binders.

The Single Edged Notched Beam Test

Proposed SENB Geometry

A new SENB geometry that adds a notch to the beams made using common BBR molds has been introduced. The new geometry resolves the adhesion problem encountered (Figure 10.2) by eliminating the need for metal bars and simplifying the specimen preparation procedure (7). It is noted that the sample preparation procedure is less time consuming and simpler when using the proposed BBR sample molds with minor modification to allow for inserting the notch.

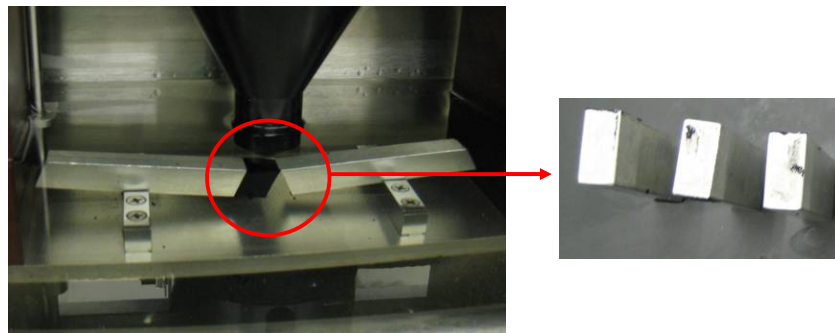


Figure 10.2: Adhesion problems observed in current SENB geometry

The proposed notched BBR beams can be prepared by making a notch of 3 mm (i.e., corresponding to 20-25% of beam depth, similar to previous geometry) in the wide side (i.e., 12.7 mm) of the BBR mold side-beams. The mold can still be used for regular BBR beam

fabrication as the notch is very thin and can be covered with the plastic sheets commonly used in BBR molding (Figure 10.3).

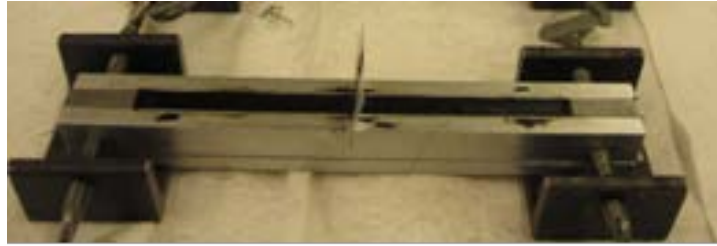


Figure 10.3: SENB specimen mold

Note that the height to width proportions of the existing SENB geometry and the BBR beams remain unchanged. The new geometry scales the dimensions by $\frac{1}{2}$. This geometry uses the same amount of asphalt binder (i.e., 10 g) required in the BBR standard and the current SENB composite beams, while resolving the adhesion problem between the binder and the metal bars.

Finite Element Simulations

Finite element (FE) simulations of both geometries were performed using the ABAQUS software package (8) to investigate differences between stress distributions around the notch from both geometries and to determine stress discontinuities in the current geometry.

For the FE simulations, the asphalt binder was considered as a linear viscoelastic material with $G_0 = 3$ GPa, $\nu = 0.3$, and the Prony series coefficients shown in Table 10.1. For the metal bars, an elastic material with $G_0 = 70$ GPa and $\nu = 0.3$ was used. The FE simulations were performed with standard 3D stress quadratic elements with reduced integration. The simulations were divided into two steps. First, the beam was loaded with a rate of 0.01 mm/sec for 1 sec, then a constant displacement of 0.01 mm was maintained for a period of 100 sec.

Table 10.1: Prony series coefficients for FE simulations

G_i	K_i	τ_i
0.12	0.12	2.89
0.07	0.07	33.01
0.08	0.08	334.09

Figure 10.4 shows the results from the FE simulations for both geometries. The finite element simulations indicate that the stress distributions around the notch for both geometries are very similar. Furthermore, the current SENB composite geometry shows stress discontinuity at the interface between the metal bars and the asphalt binder (Figure 10.4(b)), which may have a significant effect on the results of the test. Use of the standard BBR geometry results in uniform stress field outside of the loading and notch area, as showing in Figure 10.4(a).

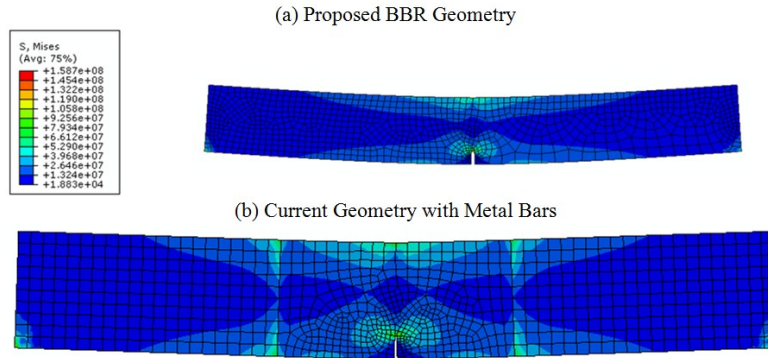


Figure 10.4: Stress distribution for (a) proposed and (b) current SENB geometry from finite element simulations

Single-Edge Notched Bending (SENB) Test Procedure

The BBR-SENB system which is very similar to current BBR is shown in Figure 10.5. The difference between the systems is in the addition of a loading motor that controls the displacement rate during testing and also in using a load cell with a higher load capacity than the regular BBR. Each test is run at a constant displacement rate of 0.01 mm/sec.

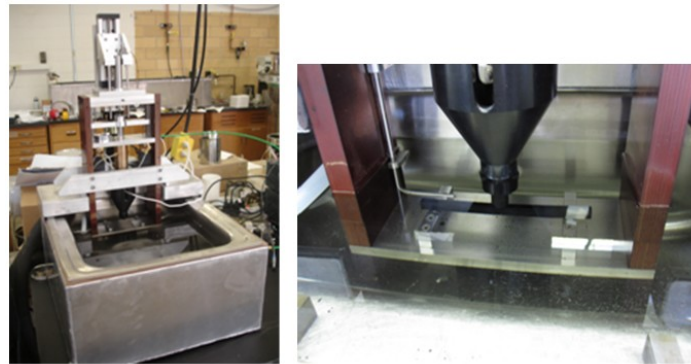


Figure 10.5: SENB system

Fracture properties of asphalt binders can be derived from failure tests on notched samples. These properties are of interest as they are measured at high strain values compared to the BBR, thus damage characterization is taken into account, which is especially important for modified asphalt binders.

The fracture parameters investigated included the load and displacement at fracture, the fracture toughness, K_{IC} , and the fracture energy (G_f). The fracture load was determined to be the peak load occurring during the test, and the fracture deformation was the corresponding deformation at the peak load. Depending on the binder type and test temperature, failure can occur at the peak load or at a lower load after the peak.

The European standard CEN/TS 15963:2010 “Bitumen and bituminous binders - Determination of the fracture toughness temperature by a three point bending test on a notched specimen,” specifies another fracture parameter referred to as the “Fracture Temperature” or TFT (9). This

parameter is the lowest temperature at which the displacement at the maximum load is 0.3 mm. It is speculated that this displacement value can be used as threshold to determine ductile to brittle transition of asphalt binders. To determine this point, the deflections at maximum load at different test temperatures are fitted with an exponential curve as shown in Figure 10.6.

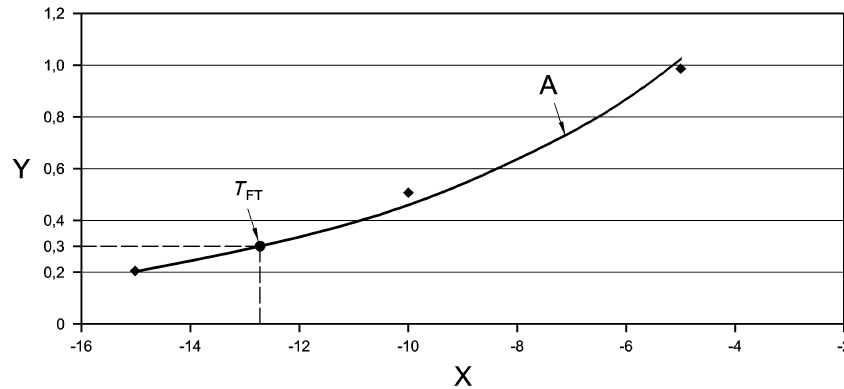


Figure 10.6: Temperature (X in °C) vs. deflection at maximum load curve (Y in mm) (9)

Sources of Variability in SENB

The sources of variability were identified and minimized. The repeatability of the test results was significantly improved after addressing the following issues:

- Damage to the sample notch during the de-molding process.
- Improper alignment of the loading shaft and the sample notch during loading.
- Variation in load calibration constants from test to test.

Although these factors varied in their relative effect on variability, all were deemed important. The following preventive actions were implemented in the SENB test procedure:

- Adding alignment pins to the aluminum mold setup (Figure 10.7) to prevent the movement of the mold end pieces relative to the notch position, which could potentially result in off center or angled notches on the sample beam.
- Recording the load calibration factor generated for every replicate and scaling all the results for a set of replicates to an average consistent calibration factor. This action is deemed a temporary solution. Efforts are being made to modify the test software to correct this issue.
- Specific control of the de-molding process to ensure minimal stress application to notch.
- Refrigeration of samples before de-molding to prevent excessive deformation during handling.

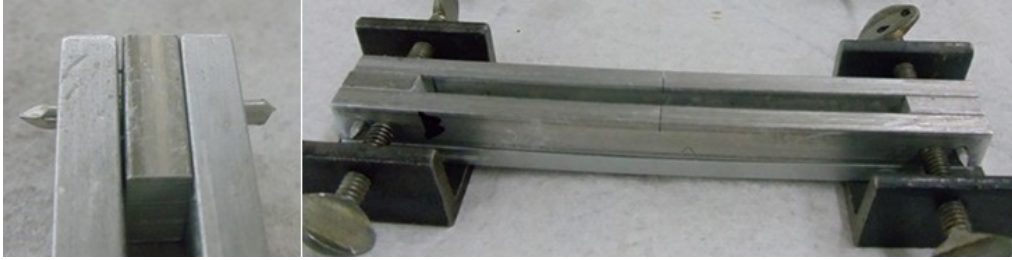


Figure 10.7: Modified SENB mold system with alignment pins

Figure 10.8 shows an example of SENB replicates after implementing aforementioned improvements to reduce variability. Test results showed the effectiveness of the mold alignment pins in limiting variability in fracture deflection, as well as the effect of the calibration factor correction in minimizing variability in the fracture load. Results of test sets ran after these changes show highly repeatable replicates with COV of fracture load and deformation generally under 10%.

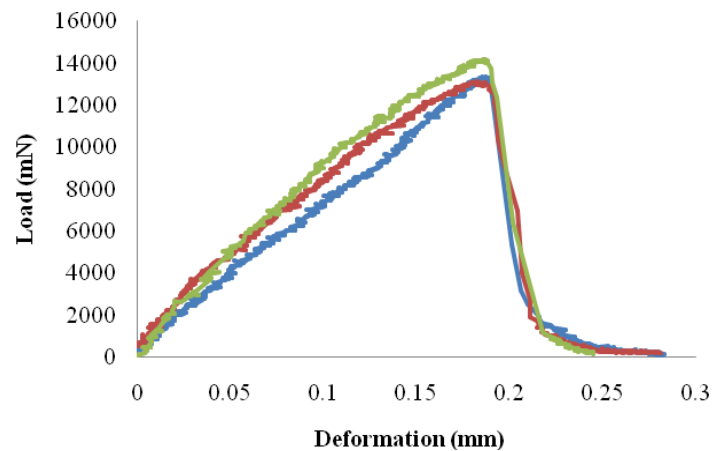


Figure 10.8: Results of SENB replicates after procedure improvement

Materials

The seven binders described in Task 2 were tested using the BBR-SENB, BBR, glass transition temperature test, and the Asphalt Binder Cracking Device (ABCD). Table 10.2 presents a description of these binders. All binders were subjected to short-term aging using the Rolling Thin Film Oven (RTFO). Furthermore, a large set of modified and unmodified binders from the Asphalt Research Consortium project, as well as binders from select LTPP validation sections were included in the test matrix. Details on how the glass transition temperature and ABCD tests were performed can be found in (7).

Table 10.2: Description of the asphalt binders tested in BBR-SENB

Binder	Location	Description
PG 58-34 PPA	MnROAD 33	Modified with Polyphosphoric Acid (PPA)
PG 58-34 SBS+PPA	MnROAD 34	Modified with Styrene-Butadiene Styrene (SBS) +PPA
PG 58-34 SBS	MnROAD 35	Modified with SBS
PG 58-34 Elvaloy +Acid	MnROAD 77	Modified with PPA + Elvaloy
PG 58-28	MnROAD 20	Neat
PG 58-34	MnROAD 22	Unknown Modification
PG 64-22	Wisconsin	Binder used in construction of SMA pavement in Wisconsin

Results and Discussion

SENB vs. BBR

BBR-SENB and BBR measurements were compared for an extensive set of binders which included materials in Table 10.2 and binders used in the Asphalt Research Consortium (ARC). In these tests the S(60) and m-value of the asphalt binders were measured after 1hr of conditioning at the same temperatures used for the BBR-SENB testing.

Although no specification for determining pavement performance based on low temperature fracture parameters exists, intuitively one would expect higher K_{IC} and G_f to indicate better performance.

The SENB parameters (i.e., G_f and K_{IC}) are plotted against the m-value and S(60) in Figures 10.9 and 10.10, respectively. It should be noted that all correlations made in subsequent sections are meant to compare the ranking capability of different low temperature performance indices and are not for the purpose of deriving direct relationships between the indices.

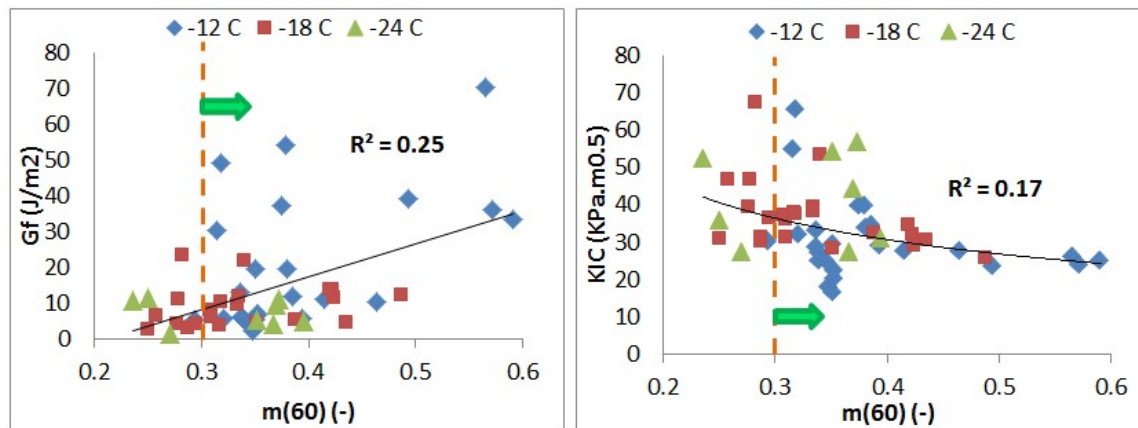


Figure 10.9: SENB G_f and K_{IC} plotted against BBR m-value at different temperatures (hatched line show Superpave BBR criteria limit; green arrow shows side passing this criterion)

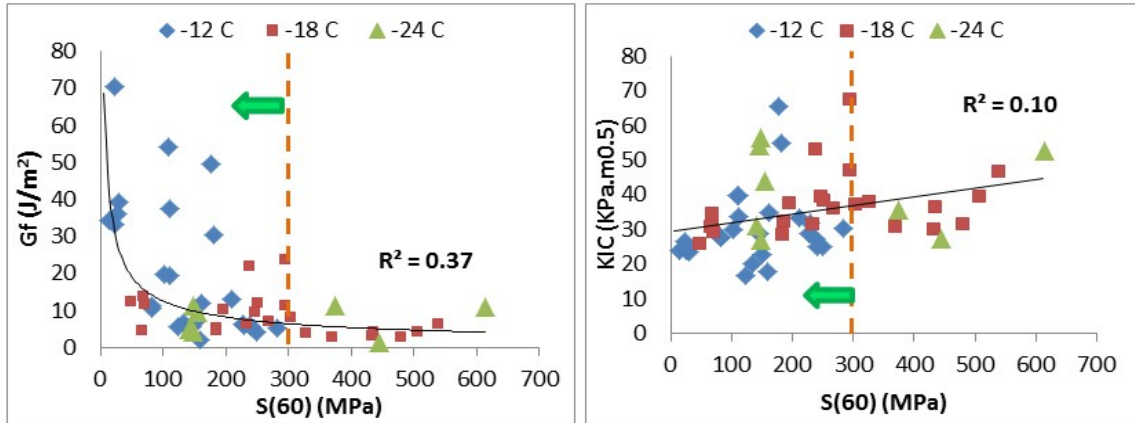


Figure 10.10: SENB G_f and KIC plotted against BBR creep stiffness at different temperatures (hatched line show Superpave BBR criteria limit; green arrow shows side passing this criterion)

The trends in Figures 10.9 and 10.10 show that the m -value, $m(60s)$, and creep stiffness, $S(60s)$, have very poor correlation with the fracture parameters obtained in the SENB test. It can also be seen that the BBR m -value and creep stiffness limits fail to account for many binders demonstrating poor fracture performance in terms of fracture energy. Furthermore, the SENB fracture energy (G_f) clearly discriminates between binders with similar stiffness and m -value, especially for the range passing the Superpave criteria ($S(60s) < 300$ MPa, and $m(60s) > 0.300$), indicating its potential as a performance index.

SENB vs. T_g

The glass transition temperature (T_g) is related to the asphalt binder performance at low temperatures. The transition to glassy behavior is known to increase the brittleness of the binder extensively, reducing the potential for stress relaxation, increasing stiffness, and thus resulting in higher cracking susceptibility.

The fracture energy from the SENB test at -12°C is compared to the glass transition temperature in Figure 10.11. It is observed that these parameters are closely related. The lower the glass transition temperature is, the lower the brittleness of the asphalt binder, and thus higher deformation to failure is expected. As the observed variation in peak fracture load was relatively low for different binders, the fracture deformation is usually the controlling parameter in the fracture energy. This leads to higher fracture energy for asphalt binders with lower glass transition temperatures and consequently higher ductility. Asphalt binders with low T_g are believed to have superior crack resistance in comparison to binders with higher T_g . This relationship is shown in Figure 10.11, using BBR-SENB data at -12°C .

The correlations between T_g and BBR parameters shown in Figure 10.12 are lower than the correlations observed between T_g and BBR-SENB fracture parameters. Note that the BBR measures properties in relatively small strains in the linear viscoelastic region in comparison to the BBR-SENB fracture parameters, which are measured at large strains.

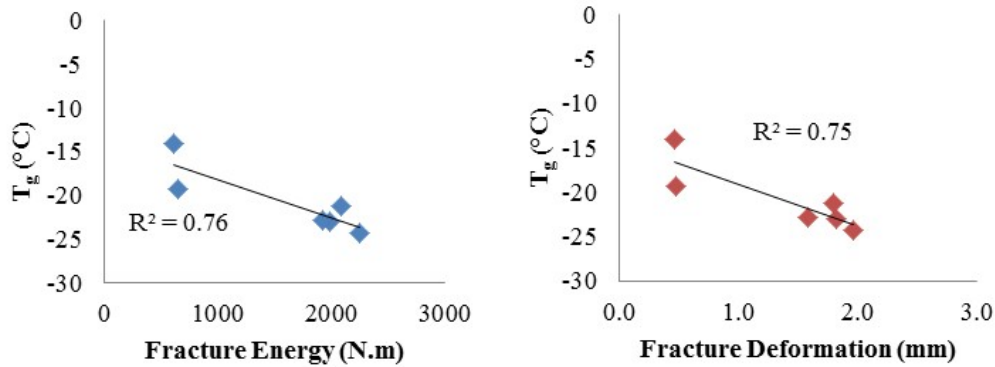


Figure 10.11: Glass transition temperature plotted against the BBR-SENB fracture energy and fracture deformation at -12°C

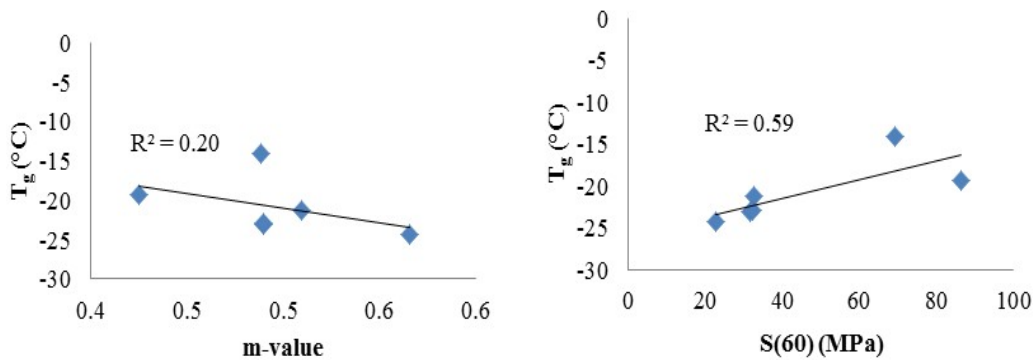


Figure 10.12: T_g plotted against BBR parameters at -12°C

SENB vs. ABCD

The Asphalt Binder Cracking Device (ABCD) has recently been introduced as another test method for determining the low temperature performance of binders (11). This test was used to investigate thermal cracking susceptibility of the asphalt binders. An important observation from the ABCD results was that the average critical cracking temperature determined from the tested binders (i.e., approximately -40°C) is about 20°C lower than the other low temperature indices measured (e.g., average T_g and average TFT are both approximately -20°C). The ABCD critical cracking temperatures were compared to parameters from the BBR, SENB and T_g tests. These correlations are presented in Figures 10.13, 10.14, and 10.15.

Figure 10.13 shows the TFT parameter from the SENB and the glass transition temperature (T_g) plotted against the ABCD cracking temperature. As expected the trend for both TFT and T_g are almost identical. This is not surprising considering the equivalency established between these two parameters. In either case, there is a poor correlation between the ABCD cracking temperature and the TFT and T_g .

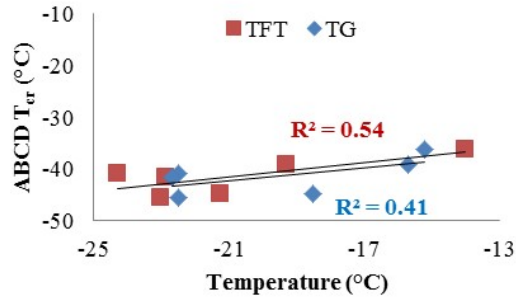


Figure 10.13: ABCD critical cracking temperature plotted against TFT and Tg

Figures 10.14 and 10.15 show that the SENB fracture load and deformation have a moderate correlation with the ABCD results. On the other hand, the correlation between the ABCD cracking temperature and the BBR parameters, especially the m-value, is relatively poor. It is recognized that the ABCD and the BBR-SENB are fundamentally different tests, since the first uses a thermally restrained sample with a circular hole while the second uses an unrestrained sample with a sharp notch to initiate crack propagation. It is not clear at this time which of these measures gives the best prediction of pavement cracking.

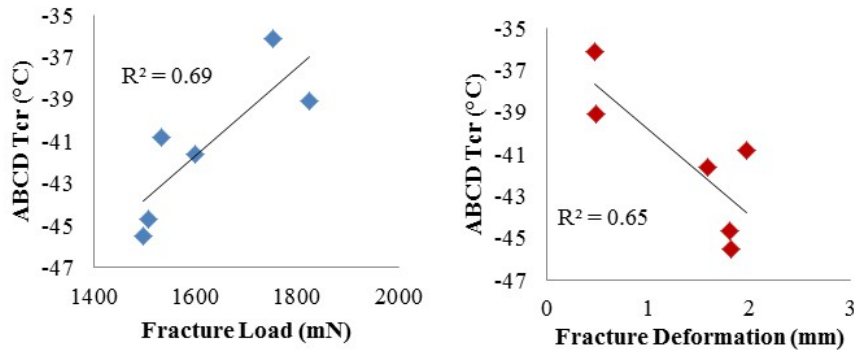


Figure 10.14: ABCD critical cracking temperature plotted against SENB fracture load and deformation

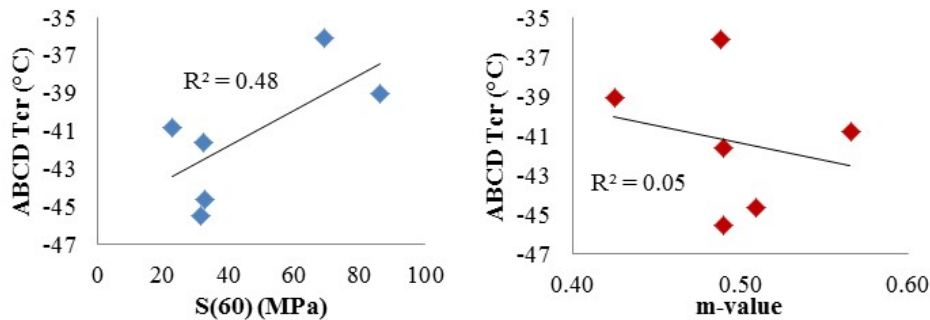


Figure 10.15: ABCD critical cracking temperature plotted against BBR parameters

Effect of Physical Hardening on SENB Fracture Properties

The effect of isothermal conditioning on binder fracture properties was also investigated. Figure 10.16 depicts results of testing five binders from Table 10.2 after 0.5 and 72hr of conditioning at their glass transition temperature (T_g). A 37% average increase in stiffness was observed, as indicated by the slope of the P-u curve after conditioning. The fracture toughness also increased for all binder tested after conditioning; however, the effect on fracture energy was not clear. Fracture energy increased for the 2 unmodified binders (i.e., MnROAD Cell 20 and NY), while decreasing for the 3 modified binders. This reduction is explained by the relative loss of strain tolerance with conditioning time. In other words, the increase in load at fracture is offset by reduction in deformation at break for the unmodified binders. The observed trend is more clearly shown for each parameter in Figure 10.17, in which results are normalized to their respective values measured after 0.5hr of isothermal conditioning.

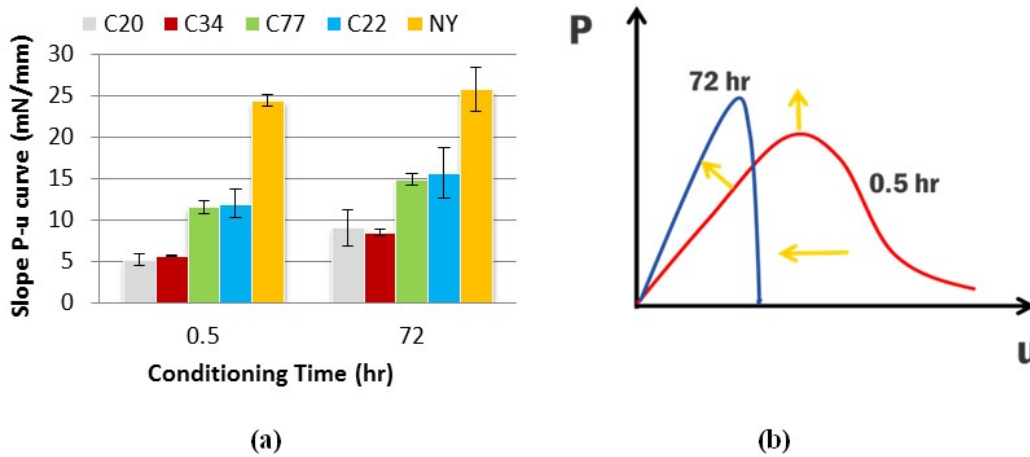


Figure 10.16: (a) Slope of P-u curve before and after isothermal conditioning at T_g (b) schematic of general trend observed after conditioning

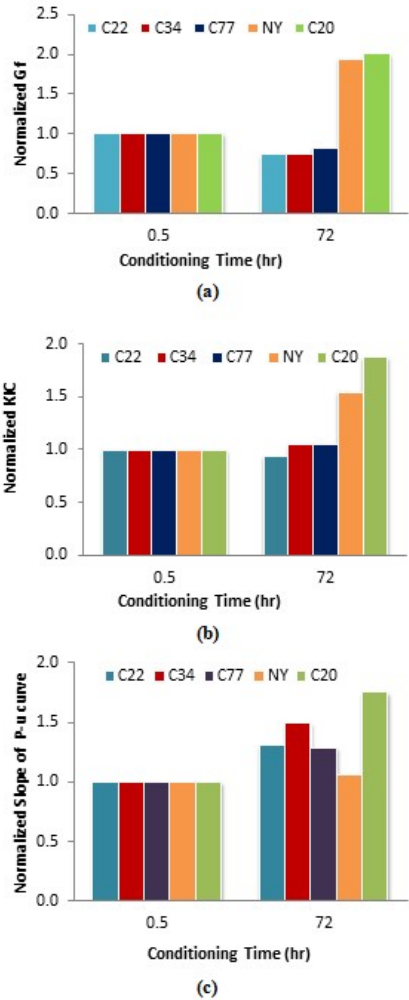


Figure 10.17: Normalized SENB parameters (a) Gf, (b) KIC, and (c) slope of P-u curve, after 0.5 and 72hrs of conditioning

SENB as a Low Temperature Performance Specification

As part of the SHRP research project, the Bending Beam Rheometer (BBR) and the Direct Tension Test (DTT) were introduced as methods to characterize the low temperature performance of asphalt binders.

The BBR used creep stiffness, $S(t)$, and a relaxation related parameter designated as the m-value, to characterize binders at low temperatures. These parameters were measured under a relatively small load and a short loading time, thus the experienced strain levels were relatively low, resulting in most binders performing in the linear viscoelastic range. Based on the nature of the thermal cracking distress, a fracture test method would seem to be the most direct method of simulating this phenomenon in a laboratory environment. Early studies have introduced the DTT test to measure brittleness and strain tolerance, but the test was shown to be hardly repeatable and very difficult to conduct. Early studies showed that the low temperature failure strain at break is highly correlated with the binder stiffness for unmodified binders (14, 15). However, these studies did not take into account the effect of modification. Non-linearity combined with

damage propagation in the binder can significantly complicate the behavior of modified asphalt binders at large strains. This has inspired some researchers to develop specifications that predict the binder's critical cracking temperature using calculations based on DTT and BBR results and fundamental mechanics modeling (14, 15).

The DTT applied a tensile load on the binder until failure occurred, reporting the failure stress and strain. As with many fracture tests, numerous complications in sample preparation and repeatability, have ultimately led to the exclusion of this test as part of the specification.

In this study the BBR-SENB test was evaluated as a possible alternative to the DTT test for estimation of strain tolerance, as well as providing valuable information on binder fracture resistance. The BBR-SENB is able to capture the ductile-brittle transition of binders and differentiate between fracture performances of binders of the same BBR low temperature performance grade. Figure 10.18 shows the difference in performance as measured by the SENB for binders of the same PG tested at -12°C , and -24°C . The binders tested correspond to a wide range of modified and unmodified binders presented in Table 10.2, binders obtained from WRI verification sections (Task 6), and LTPP sections.

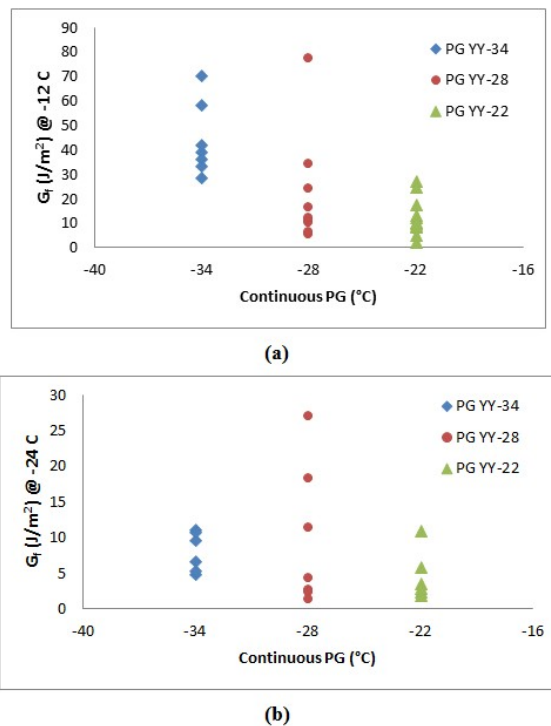


Figure 10.18: Difference in performance as measured by the SENB G_f for binders of the same PG, tested at (a) -12°C , and (b) -24°C

Figure 10.18 clearly shows a great difference in fracture energy for binders classified as the same performance grade using the Superpave BBR specification. It can be seen that binders that perform similarly based on the creep stiffness and m-value, can show up to 10 times difference in fracture energy. These results demonstrate the ability of the SENB fracture energy (G_f) to differentiate between different modified and unmodified binder systems in terms of low temperature performance.

Another important factor investigated in the BBR-SENB, was the ability to capture the brittle-ductile transition behavior of binders (assumed to be due to material undergoing glass transition) at low temperatures. SENB results in terms of fracture energy (G_f), fracture toughness (K_{IC}) and fracture deformation were plotted based on the relative distance of the test temperature to the respective binder's glass transition temperature (Figure 10.19). The T_g measurements were obtained using a dilatometric system described in (7) and included as part of the experimental plan in Task 5.

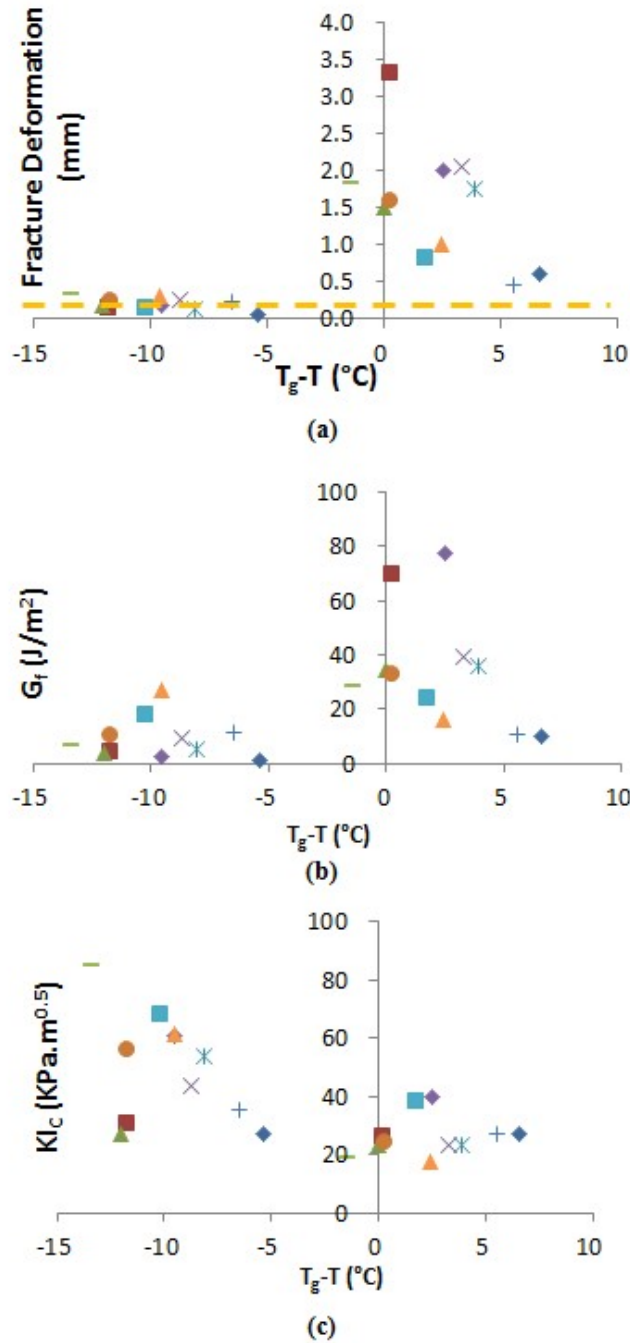


Figure 10.19: Brittle-ductile transition behavior using SENB parameters (a) fracture deflection, (b) fracture energy, and (c) fracture toughness

The results for fracture deformation shown in Figure 10.19(a) indicate that binders tested in the SENB at temperatures below their T_g show brittle behavior with fracture deformation/deflection consistently at or below 0.35 mm. The overall trend in the data show a clear differentiation between the brittle (below T_g) and ductile region (above the T_g) for all binders tested.

The ductile to brittle cut-off value is harder to discern when using fracture energy (G_f), which is influenced by both fracture load as well as the fracture deflection. Although 90% of the binders tested in the brittle temperatures fractured at energies at or below 10 J/m^2 , a few binders in the ductile zone also fractured at energies below this value.

Figure 10.19(c) shows an overall increase of the fracture toughness (i.e., increase of fracture load as measured by K_{IC}) as the binder enters the brittle temperature zone. However, K_{IC} does not show the clear differentiation of this parameter around this transition region. It is therefore not recommended for estimation of the ductile-brittle transition.

Assuming binders fracturing at deflections below 0.35 mm are in fact exhibiting brittle behavior, one may compare the ability of the SENB and BBR systems to capture the brittle-ductile transition (Figure 10.20). It can be seen in Figure 10.20 that a large number of binders performing within the 300MPa stiffness limit have fracture deflections well below the 0.35 mm limit discussed earlier, further highlighting the superior ability of using the SENB fracture deflection as an indication of the brittleness of the binder. It is envisioned that by controlling the binder SENB fracture energy and fracture deflection as performance and brittleness indicators respectively, one may better rank and discriminate wide ranges of binder sources and modification types, in comparison to current specifications.

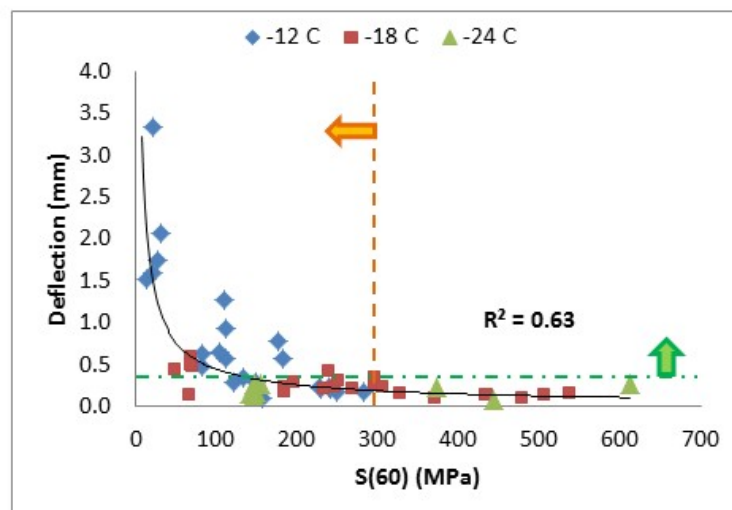


Figure 10.20: Comparison of SENB fracture deflection with BBR stiffness of modified and unmodified binders tested at -12, -18 and -24°C (orange line indicates BBR S(60) limit criteria and green line shows SENB deflection of 0.35mm)

The fracture deformation of 0.35 mm which appears to be a suitable ductile-brittle transition limit, as observed in Figure 10.19a) is interestingly very similar to the suggested 0.30 mm deformation value for the TFT parameter suggested by the CEN/TS 15963:2010 standard

specification. In SENB testing, as the test temperature decreases, the fracture deformation decreases exponentially. The TFT parameter is an indicator of the temperature at which the binder goes through a brittle to ductile transition. Figure 10.21(a) shows an example of how TFT is calculated based on deformation at fracture from three SENB tests. Figure 10.21(b) shows a good correlation between TFT and T_g . This finding also indicates that the SENB can be used as possible surrogate test to estimate the T_g of binders. Estimation of the TFT parameter based on fracture energy measurements instead of deformation at fracture was attempted and results are presented in Figure 10.22. It can be seen from Figures 10.21 and 10.22 that TFT, estimated based on deformation at fracture, provides a better indication of the glass transition of the binders.

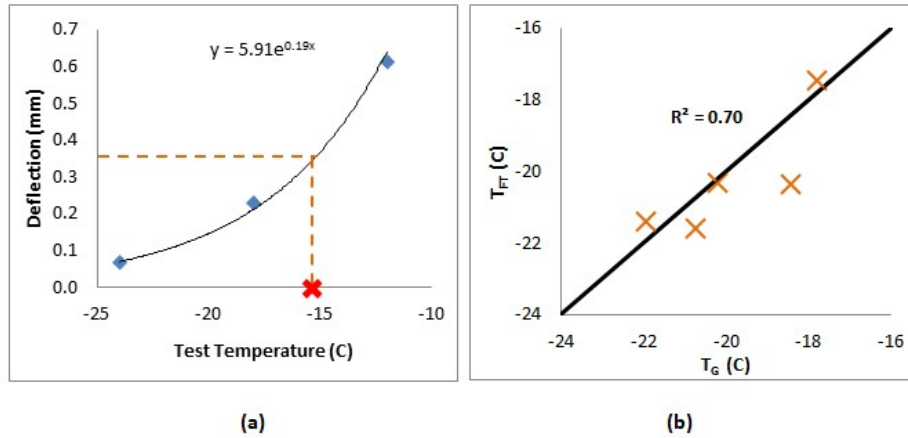


Figure 10.21: (a) Exponential curve fitting to fracture deflection at three test temperatures to use for calculation of TFT, and (b) the glass transition temperature (°C) plotted against the TFT (°C) parameter from the SENB

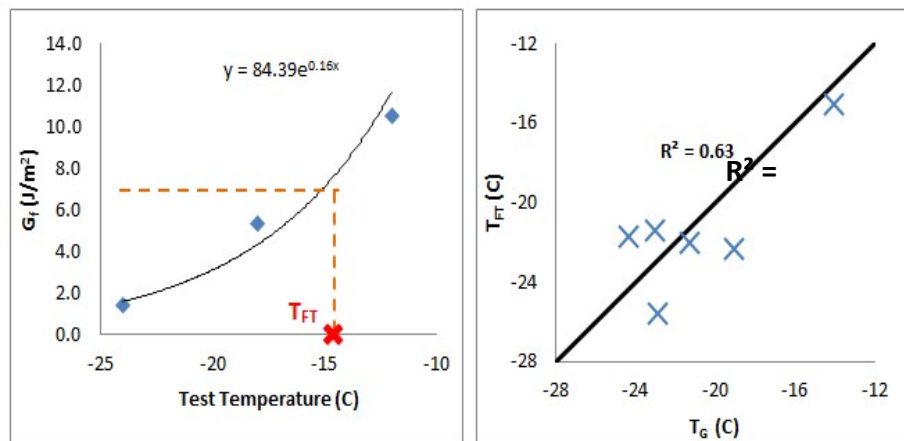


Figure 10.22: (a) Exponential curve fitting to fracture energy at three test temperatures to use for calculation of TFT, and (b) the glass transition temperature (°C) plotted against the TFT (°C) parameter from the SENB

Considering the relative ease of using the SENB compared to other binder fracture test procedures, it can be stated that the SENB fracture energy (G_f) and/or fracture deformation can be used to effectively differentiate binder low temperature performance and establish the binder brittle-ductile transition region. The test is a suitable alternative for the DTT to measure strain tolerance and to be used as a compliment to the current BBR specification.

Validation of SENB Measurements

Comparison of SENB Results to Mixture Fracture Tests

The relationship between binder and mixture fracture properties was also investigated by comparing results from SENB testing and mixture fracture properties obtained using the Semi Circular Bending (SCB) and the Disc Compact Tension (DCT) tests. Comparisons were made between the SENB tests done on binders from MnROAD cells and mixture SCB and DCT tests performed on samples from these cells by the University Minnesota and the University of Illinois at Urbana-Champaign. Figure 10.23 shows the correlations found for toughness (K_{IC}) and the fracture energy (G_f) of binders and mixes.

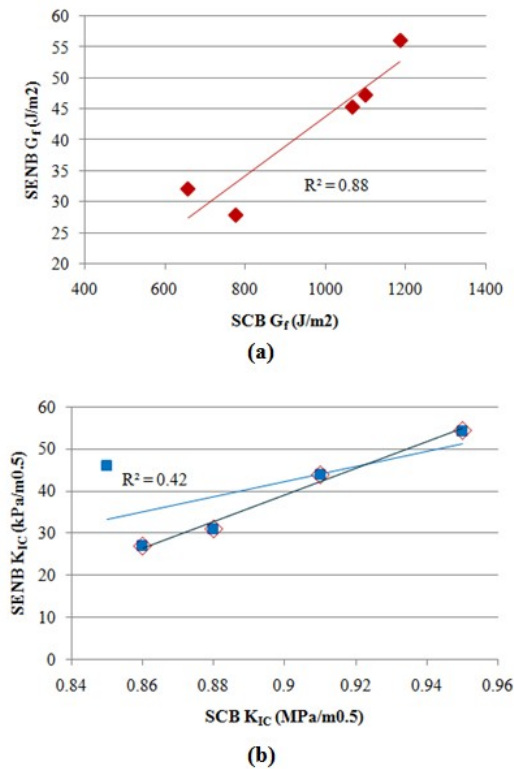


Figure 10.23: (a) SENB and SCB G_f compared (b) SENB and SCB K_{IC} compared

It was noted that one point in Figure 10.23(b) significantly decreased the correlation between binder and mixture data. It was later discovered that the mixture specimens for that specific cell had an unusually high deviation in air voids compared to the target air voids. Overall it is seen that a relatively good relationship between the SENB and the SCB results exists. Comparison of the test results between the SENB and the DCT did not yield any apparent correlation (plots not

shown). This is thought to be due to the significantly higher loading rates in the DCT compared to the SCB and SENB, both which use a similar loading rate.

Comparison of SENB Results to LTPP Field Data

The newly developed SENB testing results was validated by using field performance information from the Long Term Pavement Performance (LTPP) program. Selected LTPP binders were tested with the SENB procedure and results were compared to field thermal cracking performance recorded in the LTPP database. This work was conducted as part of collaboration with the Asphalt Research Consortium (ARC) project.

The materials tested include binders with SHRP ID numbers designated in Table 10.2. All binders were subject to RTFO aging. Table 10.3 shows fracture energy (G_f) and fracture toughness (K_{IC}) of the LTPP binders measured at -12°C . Due to the different climatic conditions in the LTPP sections, it was decided to normalize the amount of cracking in each section to its corresponding Freeze Index (degree days below 0°C). Also, the ranking of the binders based on normalized field performance, PG, fracture energy, and fracture toughness is presented in Table 10.3. Based on the rankings shown, there seems to be a good relationship between the low temperature pavement performance and binder fracture energy. Generally, similar ranking for binders is observed for field performance and G_f . As shown in the table, when the sum of differences in ranking is determined, G_f gives the lowest sum of differences indicating that it is the best indicator to field cracks count as compared to PG or K_{IC} .

Table 10.3: SENB results at -12°C for LTPP binders.

SHRP ID	PG Grade	RANK Based on PG grade	No. of Transverse cracks per section/ Freeze Index ($\times 10^{-3}$)	RANK Based on Cracks count	G_f (J/m^2) (total)	RANK Based on G_f	K_{IC} ($\text{kPa}\cdot\text{m}^{0.5}$)	RANK Based on K_{IC}
370901	64-22	4	702.58	7	5.45	7	26.83	6
370903	70-22	4	343.25	6	6.24	6	55.03	1
90961	58-34	2	9.26	4	44.2	2	31.98	5
90962	58-28	3	6.18	2	11.87	4	37.57	4
90903	64-22	4	24.71	5	10.98	5	38.54	3
89a902	52-40	1	7.01	3	103.82	1	23.12	7
350903	58-22	4	1	1	21.31	3	40.93	2
Sum of ranking difference= Sum of (Field Cracks – Other Rank)		14		0		8		16

Figure 10.24 show the relationship between fracture energy of the LTPP binders and normalized number of transverse cracks per section. The LTPP pavement sections with the highest

normalized number of transverse cracks had relatively low binder fracture energy. The shape and trend of this curve is very similar to the curves previously reported in Phase I in which fracture properties of asphalt mixtures obtained with the Semi-Circular Bending Test (SCB) were compared to field performance measured in MnROAD sections. These results indicate the potential of using G_f as thermal cracking performance index for asphalt binders.

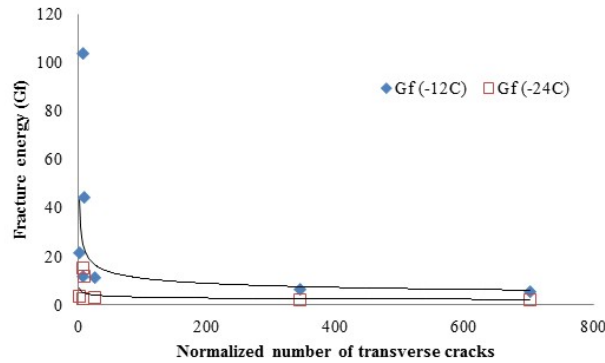


Figure 10.24: G_f vs. normalized number of transverse cracks at -12°C and -24°C

The ability of the SENB load-deflection curve to clearly estimate the low temperature performance of the binders can be seen in Figure 10.25. The section ID and respective LTPP performance index for each curve are presented on the plots. It can be seen that a very wide range of change in fracture deflection and consequently in G_f exists between binders. The SENB test clearly discriminates among the various binder types in terms of low temperature performance.

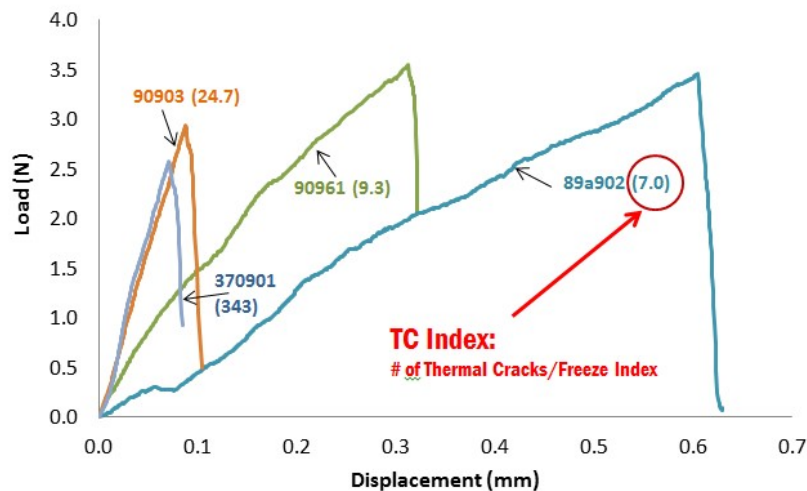


Figure 10.25: Comparison of SENB load-deflection curves for LTPP binders. Lower performance index shows better performance [Labels: LTPP code (performance index)]
summary of findings

The Single-Edge Notch Bending (SENB) test using beam samples made with the Bending Beam Rheometer (BBR) molds is a relatively simple test that can be carried out in a time frame similar to the current BBR test. The test was shown to be able to capture the ductile-brittle transition,

which is a good indicator of the glass transition of the binder. Furthermore, in contrast to the BBR, it is believed that the BBR-SENB test can capture the non-linear and damage resistance behavior of binders at low temperatures. These unique properties make the BBR-SENB test a potentially ideal performance characterization test, as it allows for the estimation of the relaxation modulus and the fracture resistance properties of binders. It is recognized that stress buildup in pavements and cracking is a complex phenomenon that requires knowledge of multiple factors such as moduli, shrinkage rates, and resistance to fracture. The following detailed findings can be drawn from the development of the BBR-SENB and corresponding experimental results:

- Results collected with the BBR-SENB test clearly show that binders of same low temperature grade can have significantly different fracture energy (G_f) measured at the grade temperature. For example, binders graded as PG (xx-28) showed a range of 5 to 80 J/m^2 measured at $-12^\circ C$.
- The results of the ABCD test do not correlate with the glass transition temperature nor with the fracture energy measured with the BBR-SENB.
- SENB experimental results showed that deformation at maximum load and fracture energy (G_f) are good indicators of the low temperature performance of asphalt binders in mixtures and pavements.
- The TFT parameter (i.e., temperature at which deformation at fracture = 0.35 mm), calculated from SENB tests at multiple temperatures, is well correlated to the glass transition temperature (T_g). These results indicate the potential of using the SENB test as an estimation method for the binder glass transition temperature.
- Fracture toughness (K_{IC}) cannot clearly differentiate the ductile to brittle transition binders. It is also not found to relate to performance of mixture in pavements, thus it is not recommended as performance indicator.
- Physical hardening can have significant effect on fracture behavior. The limited data collected with the SENB show that for some binders G_f values could decrease but for others it could increase by as much as 100% after 72 hours of isothermal conditioning.
- Validation efforts using LTPP materials indicate the potential of using SENB measurements to accurately estimate the role of binders in field thermal cracking performance. Results show that G_f can be used to rank binders according to field cracking significantly better than PG grade.

Chapter 11. Develop Improved TC Model

Background

This chapter presents a new thermal cracking model developed at the University of Illinois Urbana-Champaign, called “ILLI-TC.” The predecessor to ILLI-TC is TCMODEL, which is a mechanistic-empirical thermal cracking model developed under the Strategic Highway Research Program (SHRP). ILLI-TC improves the manner in which fracture is handled in the simulation scheme, namely; in the past TCMODEL used a 1D Paris-Law phenomenological modeling approach to simulate crack propagation, while ILLI-TC uses a 2D, cohesive zone fracture modeling approach implemented within a viscoelastic finite element modeling framework. The cohesive zone approach considers both material strength and fracture energy in computing crack initiation and propagation using fundamental fracture mechanics principles, while the Paris law approach used in TCMODEL used a phenomenological power-law type model to link change in stress intensity (which was calculated in an approximate manner) to crack growth, where the Paris law parameters were empirically linked to material strength and slope of the log mixture compliance vs. log time relationship at long loading times. In summary, the new approach used in ILLI-TC has the following improvements over TCMODEL:

- A 2D model is used instead of 1D.
- The physics of cracking in a quasi-brittle, heterogeneous particulate composite are more correctly captured by using a cohesive zone approach, where softening and fracture have a distinct length scale that is captured.
- Asphalt mixtures may have unique combinations of strength and ‘ductility’ (as characterized by mixture fracture energy). For instance, some polymer-modified mixes portray moderate tensile strength and high fracture energy; some have high strength and lower fracture energy, and some have both high strength and high fracture energy. Mixtures with higher recycled material content may have high strength, but low fracture energy. ILLI-TC can capture all of these combinations in a direct manner, while TCMODEL could only capture these effects in an indirect manner.
- A user-friendly graphical interface (GUI) has been provided for ILLI-TC. The GUI program module within ILLI-TC is referred to herein as Visual-LTC.

This chapter presents the ILLI-TC model components, model verification, and model calibration results.

Model Components

The software program (ILLI-TC) provides an intuitive and user-friendly graphical user interface (GUI), as a means to perform rigorous viscoelastic finite element analysis with cohesive zone modeling. The program can be divided into the GUI and analysis modules. The overall flow of program along with various inputs and outputs is graphically illustrated in Figure 11.1. The code consists of four main analysis modules, which are shown in blue boxes in Figure 11.1: the preprocessor, the input file generator, the preanalyzer, and the finite element analysis engine. In-depth descriptions and implementation details of the GUI and analysis modules are presented in the following subsections.

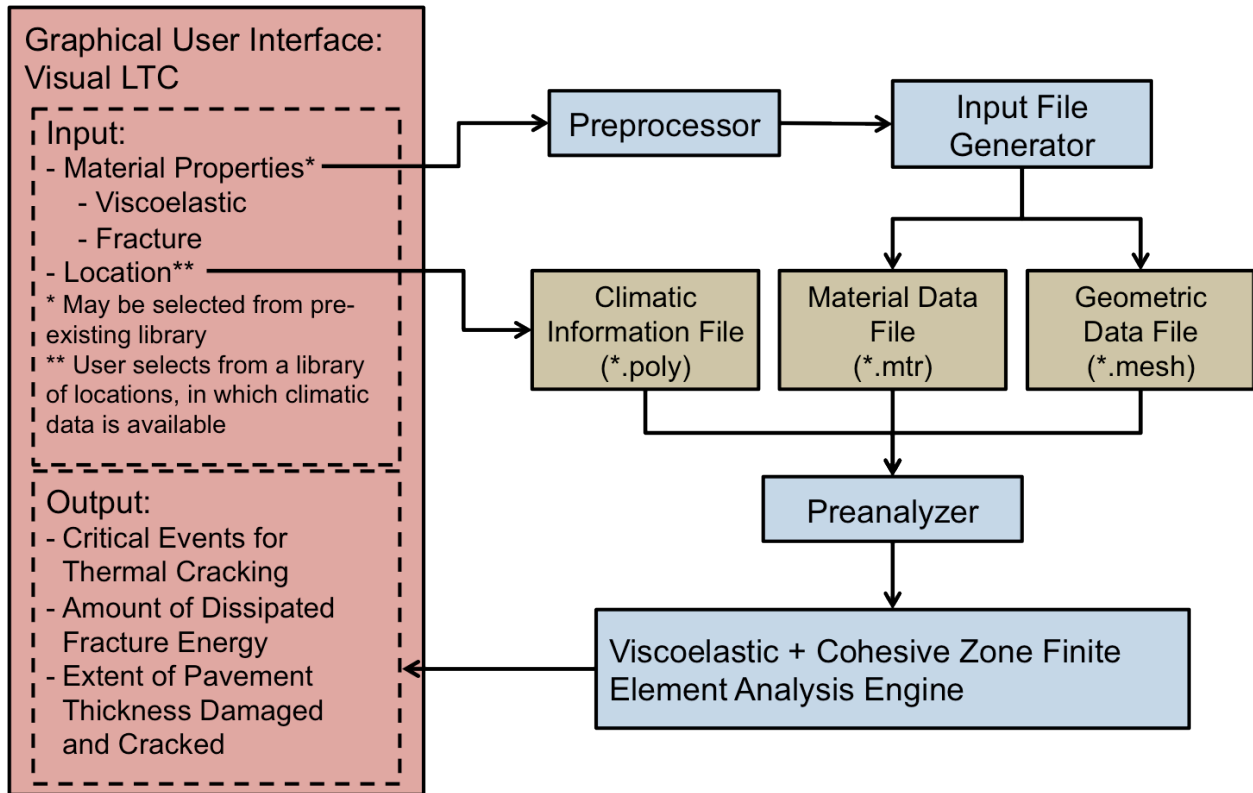


Figure 11.1: Flowchart of stand-alone low temperature cracking model, called ILLI-TC

Visual LTC

The GUI, called Visual LTC, collects and compiles the input conditions provided by the user, executes various analysis modules to conduct finite element analysis, and interprets and displays the results. Visual LTC was written with the object-oriented programming language C# (pronounced “see-sharp”) under Microsoft’s .NET framework, and which is intended for the development of robust, deployable software run on standard desktop or workstation personal computers.

Running Visual LTC

Visual LTC is organized into five sections: (1) Start, (2) Project Information, (3) Pavement Materials and Structure, (4) Run, (5) Results. For each section there are a number of inputs required from the user. The flow of the program is described below in the context of each of the five sections.

- (1). Start: The user either opens an existing project or starts a new project. When an existing project is opened, all inputs are pre-loaded into the GUI. However, the user still has the ability to alter or change any of the inputs. In the case of a new project, the user is required to provide all required inputs.
- (2). Project Information: The user inputs general information about the project, including project name, location, length of analysis, etc. The location of analysis is necessary to select the pavement temperature profiles.

- (3). Pavement Materials: The user provides the pavement material properties either by selecting an asphalt concrete mix from the pre-existing library, modifying an existing mix or by creating a new mix.
- (4). Run: Visual LTC executes the necessary analysis modules for pre-processing, finite element analysis and post-processing of the results. As the analysis runs, the GUI informs the user of the runtime progress by indicating which stages of the analysis are complete and which are in queue to be executed.
- (5). Results: The results from the finite element analysis is converted to a user-friendly format and displayed. Three sets of outputs are provided, namely: percent of fracture energy dissipated, extent of pavement thickness damaged and extent of pavement thickness cracked (c.f., Figure 11.8, appearing later in this chapter). The outputs are available to users in both graphical and tabular formats and data can be exported in a convenient comma-separated value (CSV) format.

Details of the use of Visual LTC, including screen shots, and user inputs are presented in the User Manual (Appendix B).

Communication with Analysis Modules

Data is passed between Visual LTC and the analysis modules via input/output files. Visual LTC reads the user input then performs the series of converting data, writing files, executing programs, and reading output shown in Table 11.1.

Table 11.1: Visual LTC steps

Read and store user input Extract and store climatic information for user specified analysis period Write input files for preprocessor Run preprocessor Read and convert preprocessor output Write input files for input file generator Run input file generator Run finite element analysis engine Read finite element analysis output Convert crack depth to amount of cracking Display results

During the analysis process, several files are written and stored in the user defined working directory. It is not necessary for the user to access the files at any point during or after analysis, however they are available for inspection by the advanced user.

User Types

Visual LTC is intended for use by practitioners and researchers alike. Therefore, two user types are supported: “Standard User,” and “Advanced User.” Both user types have access to all functionality previously described. However, advanced users also have the ability to add new asphalt mixes and to modify properties of existing asphalt mixes. The standard user is the preferred default user mode for most pavement designers, since existing properties are protected

from accidental user error when operating in this mode. The user can easily change from one user type to the other.

Visual LTC User Inputs

The main user inputs that are required for low temperature cracking analysis are the analysis location, analysis duration and the pavement material properties. In this section, the location and duration inputs are first discussed, followed by material properties.

A series of ICM (Integrated Climatic Model) simulations were conducted to create a library of pavement temperature profiles available to the user in Visual LTC. Sets of temperature profiles were generated for one cold, one intermediate and one warm location in each state participating in the Pooled Fund Study. The locations and the lowest air temperatures as well as pavement surface temperatures are shown in Table 11.2. The locations are also shown on the map in Figure 11.2. Temperature profiles at each location were generated for the following asphalt concrete thicknesses: 3”, 4”, 5”, 6”, 7”, 8”, 9”, 10”, 12”, 14”, and 16”. A full integration of the ICM and ILLI-TC models is possible, but was beyond the scope of this study.

In Visual LTC, the user selects a location that is the most climatically similar to the analysis location. The user also provides the length of analysis and depth of pavement. Visual LTC extracts the appropriate data from the temperature profiles associated with the location and pavement thickness. This data is passed to the finite element engine where nodal temperatures are computed.

Table 11.2: Climatic locations available to user in Visual LTC

State	Cold Climate			Intermediate Climate			Warm Climate		
	City	Air	PG	City	Air	PG	City	Air	PG
Connecticut	Norfolk	-29.5°C	-28°C	Hartford	-26°C	-22°C	New Haven	-20.5°C	-22°C
Illinois	Elizabeth	-37°C	-34°C	Urbana	-31.5°C	-28°C	Anna	-27°C	-22°C
Iowa	Decorah	-40.5°C	-34°C	Des Moines	-32°C	-28°C	Fort Madison	-30.5°C	-28°C
New York	Massena	-39°C	-34°C	Albany	-33.5°C	-28°C	New York City	-19.5°C	-16°C
North Dakota	Westthroe	-44°C	-40°C	Bismarck	-41.5°C	-40°C	Wahpeton	-38°C	-34°C
Minnesota	International Falls	-43.5°C	-40°C	St. Cloud	-41.5°C	-34°C	Worthington	-34.5°C	-34°C
Wisconsin	Minong	-46°C	-40°C	Steven’s Point	-36.5°C	-34°C	Milwaukee	-32°C	-28°C

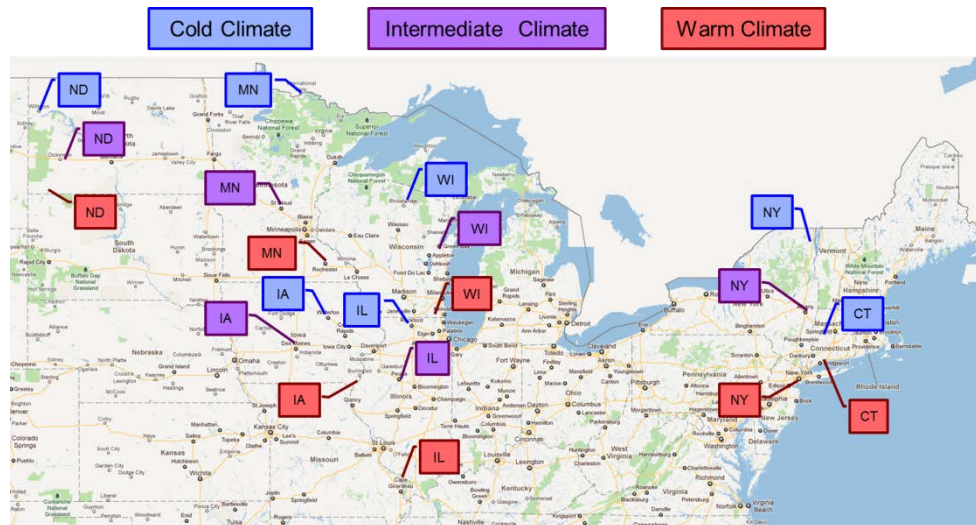


Figure 11.2: Locations in the library of pavement temperature profiles available to the user

The pavement material property user inputs are summarized in Table 11.3 and discussed below.

Table 11.3: Summary of pavement materials user inputs

Property	Units	Test
Tensile strength	MPa	AASHTO T-322
Fracture energy	J/m ²	ASTM D7313 1
Unit weight	g/cm ³	AASHTO M323
Thermal conductivity	BTU/lb-°F	No standardized test (default values provided)
Heat capacity	BTU/lb-°F	No standardized test (default values provided)
Mixture VMA ²	%	AASHTO M323
Aggregate coefficient of thermal expansion and contraction (CTEC) 2	mm/mm/°C	No standardized test
Mixture coefficient of thermal expansion and contraction (CTEC) 3	mm/mm/°C	See Task 5 Report (by University of Wisconsin)
Creep compliance test data (100 or 1000 seconds for 3 temperatures)	1/GPa	AASHTO T-322
Creep compliance test temperatures	°C	AASHTO T-322

1 Fracture energy may be obtained with a different test geometry, however the model is calibrated for the ASTM D7313 test procedure

2 Mixture VMA and aggregate CTEC do not need to be entered if Mixture CTEC is provided

3 Mixture CTEC will be calculated if mixture VMA and aggregate CTEC are provided

Tensile strength of asphalt concrete can be determined using the AASHTO T-322 test procedure. The fracture energy can be determined using a variety of test geometries, such as disk-shaped compact tension (DC[T]), semi-circular bend (SC[B]) and single-edge notched beam (SEN[B])

test. However, experimentally determined fracture energy is test-dependent (and specimen size dependent) and ILLI-TC has been calibrated and validated using the fracture energy obtained from the ASTM D7313 test procedure that utilizes DC[T] test geometry. According to ASTM D7313, the DC[T] test is performed at a crack mouth opening displacement (CMOD) rate of 0.0167 mm/s and at temperature of 10°C above the 98% reliability Superpave PG low temperature grade, as dictated by the project location.

The user can either directly input the coefficient of thermal expansion and contraction (CTEC) or provide asphalt mixture volumetric properties. If volumetric properties are provided, the CTEC is estimated using the approximation equation utilized by the AASHTO MEPDG software (ARA Inc., 2004). In the future, ILLI-TC can be modified to incorporate a non-linear thermal coefficient, as described in Task 5 report for this project. However, the use of a non-linear CTEC was beyond the scope of this project.

The user directly enters laboratory measured 100 or 1000 second creep test data from three temperatures following the AASHTO T-322 test procedure. This data is passed to the preprocessor, which converts the data into thermo-viscoelastic material properties in form of Prony series parameters (Generalized Maxwell model) and time temperature shift factors.

Data Storage

A simple and intuitive class structure is employed to store and maintain data required for low-temperature cracking analysis, i.e. material properties, climatic data, pavement structure, and project information. The data should be easily accessible by the user and should not require installation of additional software. A working directory containing input files stores all of the data necessary for Visual LTC to conduct analysis. Furthermore, the user is not required to directly access the files, as Visual LTC creates and modifies files automatically. The project input file stores general information (i.e. project name, description, date, etc.), climatic information, and the pavement structure. Asphalt concrete input files store all material properties associated with the mix. A working directory can contain many project files, thus giving the user the option of creating a new project by modifying an existing one. Similarly, the working directory can contain as many asphalt concrete input files as necessary, which creates a library of mix designs for the analyst or designer to investigate.

Preprocessor

The main task of the preprocessor is to convert raw creep compliance test data into thermo-viscoelastic material properties in form of Prony series parameters (Generalized Maxwell model) and time temperature shift factors. The master curve is constructed from the raw creep compliance data via Master (Buttlar et al. 1998). The Voigt-Kelvin model properties are then converted to Maxwell material model properties using TCMODEL (Lytton et al., 1993, Roque et al., 1995a, 1995b). Finally, the Maxwell model parameters are read from the TCMODEL output and passed to the input file generator.

Input File Generator

The first task of the Input File Generator is to develop a finite element mesh for the pavement geometry selected by user. The finite element mesh consists of coordinates of the nodal points, and an element connectivity table that links node numbers to their respective elements. During the first phase of low temperature pooled fund study preliminary version of mesh generator was developed (Marasteanu et al., 2007). In the present work, this mesh generation code was significantly revised and extended to develop full pavement models, perform checks for inconsistencies in the mesh, and automatically insert interfacial cohesive elements. Based on the recommendations and findings from previous studies (Paulino et al., 2006; Dave et al., 2007), the finite element domain size of 6 m was selected. The mesh generation code creates smaller elements near the potential crack path and gradually transitions them to larger size to reduce computational cost. The finite elements near the potential crack path are generated with 4 mm edge lengths, which are also based on the recommendations from previous studies (Paulino et al., 2006; Dave et al., 2007). The code generates a finite element mesh using four node quadrilateral elements (Q4) and it automatically increases the element side lengths in the longitudinal direction of pavement (x-direction) until the relative difference between the element side lengths reach 30%. At this point the mesh generator combines the smaller elements into one larger element using a three-to-one transition scheme.

Figure 11.3 shows a typical pavement mesh with a single asphalt concrete layer, including the three-to-one transition, which is all automatically generated by the software. The code supports multiple lifts of asphalt concrete, each with distinct material properties and thicknesses, however for the purposes of this study, the analysis was completed for a single layer only. To insert cohesive interface elements, the code traverses the mesh and generates duplicate nodes along the potential crack path. Next, cohesive zone elements are inserted and attached to the duplicate nodes. The location of cohesive elements is also illustrated in Figure 11.3.

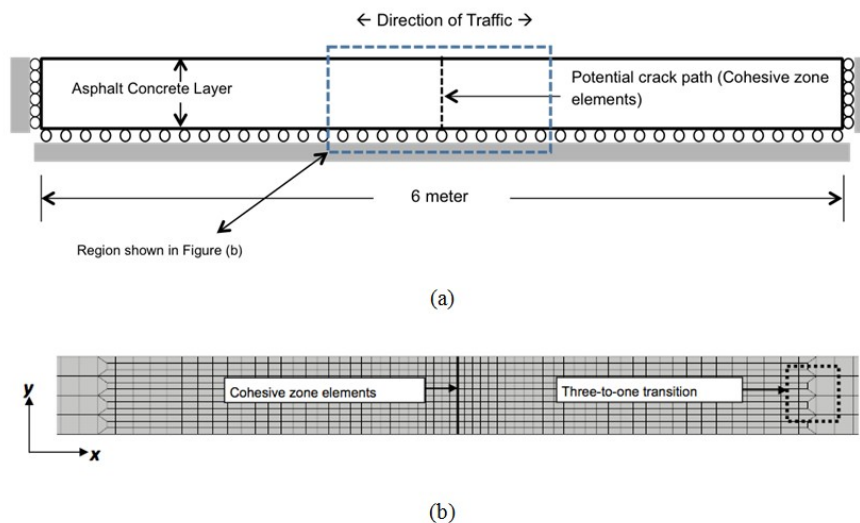


Figure 11.3: Finite element model from input file generator (a) model geometry and boundary conditions (domain size: 0.18 m by 6 m, four asphalt layers) (b) close-up of the mesh in vicinity of potential crack path

The second task of the Input File Generator is to create the material data file, which is primarily based on the information provided by the user. This file consists of viscoelastic (bulk) properties, the thermal expansion and contraction coefficient, and fracture properties. The list of properties utilized by the analysis code is shown in Table 11.4.

Table 11.4: Material properties required by the analysis model

Parameters for generalized Maxwell model (spring and dashpot coefficients) and reference temperature
Time-temperature shift factors for two temperatures other than reference temperature
Coefficient of thermal expansion and contraction
Fracture energy

The properties shown in Table 11.4 are calculated from the Visual LTC user inputs. Refer to the subsections on Visual LTC and the Preprocessor for information on the specific user inputs and calculations performed.

Preanalyzer

The preanalysis module was developed to optimize analysis times of the finite element engine. A simplified problem is solved to identify critical events that are then analyzed by the finite element analysis engine; hence only critical cooling events are analyzed with the full model. The preanalyzer modulus solves a one dimensional viscoelastic solution using thermo-viscoelastic properties of asphalt concrete and pavement surface temperatures to calculate the thermal stress on the surface of pavement. The one dimensional viscoelastic solution for thermal stress can be found in Apeagyei et al. (2008).

The results from the preanalyzer were verified with the analytical solution. The stresses obtained with the preanalyzer (VE1D) and the analytical solution is compared in Figure 11.4(a) for the thermal loading shown in Figure 11.4(b). Figure 11.4(a) shows the excellent agreement between the preanalyzer results and analytical solution, indicating that this portion of the ILLI-TC code has been verified.

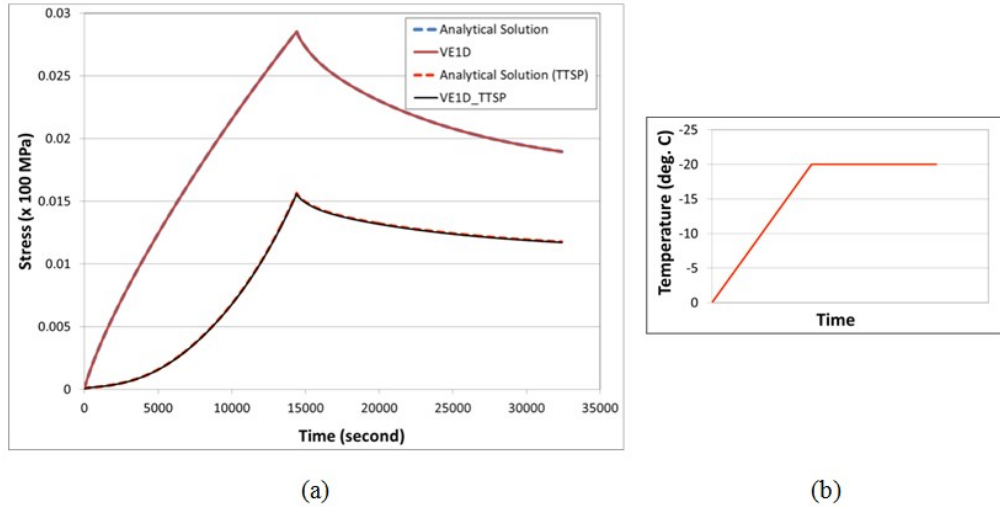


Figure 11.4: Verification of preanalyzer (a) comparison of stresses obtained with the preanalyzer (VE1D) and the analytical solution (b) Thermal loading

Critical events are identified when the surface stress exceeds 80% of the indirect tensile test (IDT) strength. This threshold was selected based on previous experience of researchers in determining the stress threshold corresponding to onset of damage. The full analysis with the finite element engine is performed for the 24 hours surrounding the critical event. Figure 11.5 shows an example of the results of the preanalyzer. The surface temperatures during the five-year analysis period are shown in Figure 11.5(a) and the resulting surfaces stresses are shown in Figure 11.5(b). Only the time duration between October 1st and March 31st are simulated. Four critical events were identified by this analysis; the full finite element simulation will be performed on these events accordingly.

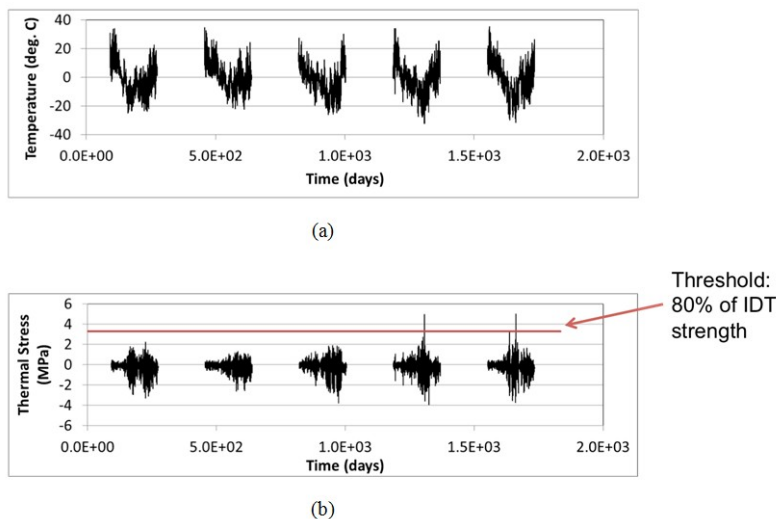


Figure 11.5: Results from preanalyzer (a) surface temperatures for five-year analysis period (b) resulting surface stresses where four critical events were identified

Finite Element Analysis Engine

Finite element analysis is becoming increasingly popular in the design and analysis of pavements. For example, the current AASHTO design guide (MEPDG) utilizes finite element analysis for determination of critical pavement responses. The ability to model complex geometries and boundary conditions make finite element analysis well suited for simulation of asphalt pavements. Material behavior of asphalt concrete is time and temperature dependent with hereditary response requiring the use of thermo-viscoelastic analysis.

In order to simulate the complex mechanisms underlying the thermal cracking phenomenon, a standard “strength of materials” type analysis is insufficient, due to: 1) the highly non-linear behavior in the vicinity of the crack tip, and 2) the importance of the crack in the overall structural response (i.e., the need to model thermal crack as a moving boundary value problem). The cohesive zone model provides a computationally efficient way to predict the damage occurring in a process zone located ahead of a crack tip in a material. In the present project a finite-element analysis program is being created that utilizes both, (1) bulk viscoelastic behavior and, (2) cohesive zone model. Descriptions and formulations for each of these components are described in following sub-sections.

Viscoelastic Finite Element Analysis

General viscoelastic theory can be found in several textbooks and articles, for example, Christensen (1982). A generalized Maxwell model is utilized in this study due to its flexibility in representing a wide variety of viscoelastic materials as well as the availability of established formulations in the literature. The constitutive relationship for generalized Maxwell model can be given as,

$$\boldsymbol{\sigma}(\xi) = \mathbf{E}_\infty \boldsymbol{\varepsilon}(\xi) + \int_0^t \mathbf{E}_t(\xi - \xi') \frac{d\boldsymbol{\varepsilon}(\xi')}{d\xi'} d\xi' \quad [11.1]$$

where $\boldsymbol{\sigma}$ is stress, $\boldsymbol{\varepsilon}$ is strain, ξ is reduced time and \mathbf{E}_∞ is fully relaxed modulus and \mathbf{E}_t is relaxation modulus for the Maxwell chains. The relaxation modulus for Maxwell units is given by,

$$\mathbf{E}_t = \sum_{m=1}^M \mathbf{E}_m e^{-(\xi - \xi')/\tau_m}; \tau_m = \frac{\eta_m}{\mathbf{E}_m} \quad [11.2]$$

The material parameters \mathbf{E}_m, η_m are spring coefficients and viscosities for the m^{th} Maxwell unit. The spring coefficients and viscosities are related through relaxation times τ_m and the total number of Maxwell units in the model is given by M . The effect of temperature on the material properties is accounted for through use of time-temperature superposition principle. The superposition is governed time-temperature shift factor a_T which is a material property. The real time t is related to the reduced time ξ and temperature T as,

$$\xi = \int_0^t \frac{dt'}{a_T(T, t')} \quad [11.3]$$

For isotropic conditions the above shown constitutive relationships can be re-written in form of deviatoric and volumetric stress-strain relationships as,

$$\begin{aligned} \sigma_{kk}(\xi) &= 3K_\infty \varepsilon_{kk}(\xi) + \int_0^\xi 3K_t(\xi - \xi') \frac{d\varepsilon_{kk}(\xi')}{d\xi'} d\xi' \\ s_{ij}(\xi) &= 2G_\infty \varepsilon_{ij}^s(\xi) + \int_0^\xi 2G_t(\xi - \xi') \frac{d\varepsilon_{ij}^s(\xi')}{d\xi'} d\xi' \end{aligned} \quad [11.4]$$

where, $K_\infty, K_t, G_\infty, G_t$ are shear and bulk relaxation modulus components following the similar descriptions as shown before. The deviatoric strain components are shown by ε_{ij}^s and the corresponding stress components by s_{ij} , these are evaluated as,

$$s_{ij} = \sigma_{ij} - \frac{1}{3} \sigma_{kk} \delta_{ij}; \quad \varepsilon_{ij}^s = \varepsilon_{ij} - \frac{1}{3} \varepsilon_{kk} \delta_{ij} \quad [11.5]$$

where, δ_{ij} is Kronecker's delta.

The time-integration approach used in this study is based on the recursive-incremental scheme developed by Yi and Hilton (1994). Similar schemes have been utilized for solving viscoelastic finite element problems by several researchers (for example, Muliana and Khan 2008). In field of asphalt concrete, Dai and You (2009) have utilized an incremental-recursive scheme for analysis of asphalt mixtures undergoing damage in lab sized specimens.

The incremental-recursive formulations (Zocher et al. 1997) rely on determination of incremental stress components ($d\sigma$) in response to the strain increment ($d\varepsilon$) given by,

$$d\sigma(\xi) = \mathbf{K}(\mathbf{x}, \xi) \times d\varepsilon(\xi) + d\sigma^R(\xi) \quad [11.6]$$

where, the stiffness is given by \mathbf{K} and the viscoelastic history effect is accounted through residual stress term $d\sigma^R$. Using the constitutive relationships shown in equation (11.4) and recursive-incremental formulation in equation (11.6), the volumetric and deviatoric stress increments can be evaluated as,

$$\begin{aligned} ds_{ij}(\xi) &= 2 \left[G_\infty + \sum_{m=1}^M \frac{G_m \tau_m}{d\xi} (1 - e^{-d\xi/\tau_m}) \right] d\varepsilon_{ij}^s(\xi) + ds_{ij}^R(\xi) \\ d\sigma_{kk}(\xi) &= 3 \left[K_\infty + \sum_{m=1}^M \frac{K_m \tau_m}{d\xi} (1 - e^{-d\xi/\tau_m}) \right] d\varepsilon_{kk}(\xi) + d\sigma_{kk}^R(\xi) \end{aligned} \quad [11.7]$$

At any reduced time ξ_n the increment in reduced time ($d\xi$) and the corresponding strain rates (\mathbf{R}) can be approximated as,

$$d\xi \approx \Delta\xi = \xi_n - \xi_{n-1}; \mathbf{R} = \frac{d\boldsymbol{\varepsilon}}{d\xi} \approx \frac{\Delta\boldsymbol{\varepsilon}}{\Delta\xi}. \quad [11.8]$$

The residual stress can be evaluated for deviatoric and volumetric components using the approximations shown in equation (11.8) as,

$$ds_{ij}^R(\xi_n) = \sum_{m=1}^M -(1 - e^{-\Delta\xi/\tau_m}) S_m(\xi_n); d\sigma_{kk}^R(\xi_n) = \sum_{m=1}^M -(1 - e^{-\Delta\xi/\tau_m}) V_m(\xi_n) \quad [11.9]$$

Where, symbols S_m and V_m represent viscoelastic (history) stress contributions at any given reduced time. These effects account for hereditary contributions should be tracked for each stress component throughout the entire range of time-steps used in a given simulation. Also notice that these terms are independent for each Maxwell unit in the material constitutive properties. The viscoelastic stress contributions are updated for each time increment. Using the approximate strain rate (equation (11.8)) and the expansion of equations (11.4) and (11.7) the viscoelastic stress contributions can be evaluated as,

$$\begin{aligned} S_m(\xi_n) &= 2G_m \tau_m (1 - e^{-\Delta\xi/\tau_m}) R_{ij}^s + S_m(\xi_{n-1}) e^{-\Delta\xi/\tau_m} \\ V_m(\xi_n) &= 3K_m \tau_m (1 - e^{-\Delta\xi/\tau_m}) R_{kk} + V_m(\xi_{n-1}) e^{-\Delta\xi/\tau_m} \end{aligned} \quad [11.10]$$

Dave et al. (2010) conducted thermo-viscoelastic verifications to verify the accuracy of the recursive-incremental viscoelastic finite element formulations in the context of time dependent temperature conditions and temperature dependent viscoelastic properties. The boundary value problem simulated in this case is similar to the thermal stress restrained specimen test (TSRST), which is sometimes used for the evaluation of thermal cracking performance of asphalt concrete (AASHTO TP-10). In order to ensure good accuracy for thermal cooling and warming conditions, the temperature boundary conditions were chosen to impose both warming and cooling events. The results from the finite element formulations used in this study were compared with the results obtained from the commercial software ABAQUS. Figure 11.6 shows the variation of temperature with time as well as the corresponding thermal stresses generated in the restrained viscoelastic body. The stress response is shown for the formulations and implementation from the present study as well as those obtained using ABAQUS, showing excellent agreement. This provides verification for this portion of the ILLI-TC code.

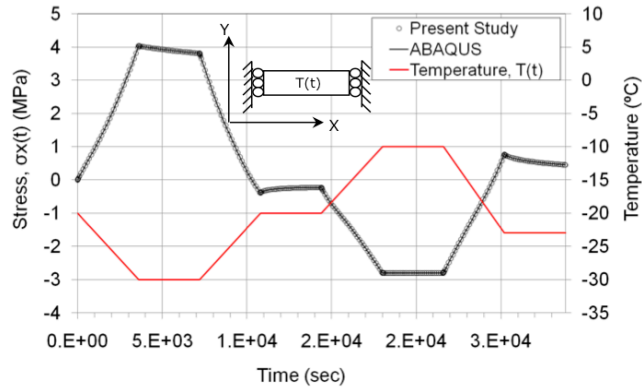


Figure 11.6: Comparisons for thermo-viscoelastic analysis conducted using recursive-incremental viscoelastic finite element formulations and commercial software ABAQUS (from Dave et al., 2010)

Fracture Modeling of Asphalt Concrete

Asphalt concrete is classified as a quasi-brittle material because of the large nonlinear fracture process zone resulting from crack overlapping and branching, and from the weak interface between aggregates and asphalt binder. Such nonlinear fracture process zone is approximated by the cohesive zone model (Baranblatt 1959; Dugdale 1960). The cohesive zone model has been widely utilized to investigate a range of civil engineering materials such as Portland cement concrete (Hillerborg et al. 1976), reinforced concrete (Ingraffea et al. 1984), asphalt concrete (Song et al. 2006), and fiber reinforced concrete (Park et al. 2010), etc.

In the cohesive zone model, nonlinear cohesive traction is defined as a function of separation (or crack opening width) ahead of a macroscopic crack tip. A crack is initiated when the cohesive traction reaches the cohesive strength of the material. Note that further investigation is needed for crack initiation criteria. Then, as the separation increases the cohesive traction decreases. Finally, when the separation is greater than a critical value, the material no longer has load carrying capacity and the cohesive traction is zero. In this study, the bi-linear CZM described by Song et al. (2006) is being employed. This model has been successfully employed for simulation of thermal and reflective cracking in asphalt pavements and overlays, for example by Dave et al. (2007, 2008). Additionally, an intrinsic cohesive zone modeling approach is used; hence a penalty stiffness (i.e. initial ascending slope) is introduced in the computational implementation. The initial penalty stiffness is determined on the basis of the numerical stability associated with the finite element implementation (Roesler et al. 2007).

The material parameters used in the cohesive fracture model are: material strength (σ_f) and fracture energy (G_f). Figure 11.7 shows schematically illustration of the bi-linear cohesive model. The horizontal axis represents the displacement-jump across the cohesive zone and vertical axis represents the traction. The area under the plot is the fracture energy (G_f) and the peak traction is limited to material strength (σ_f). The unloading and loading during the course of softening are also shown in the model. The displacement jump at the complete separation is indicated by critical displacement jump (δ_c). The bi-linear cohesive zone model was implemented in the program using a modified Newton-Raphson solution scheme.

The implementation of the cohesive zone model with recursive incremental viscoelastic finite element formulations is verified by comparing the results of the finite element analysis engine with the results of the commercial software ABAQUS. Figure 11.8 illustrates the stress variation with respect to time and shows excellent agreement. The stress reaches a given cohesive strength (e.g. 2MPa), and decrease to zero while temperature decreases from 0°C to -10°C during 600 sec. This provides verification for this portion of the ILLI-TC code.

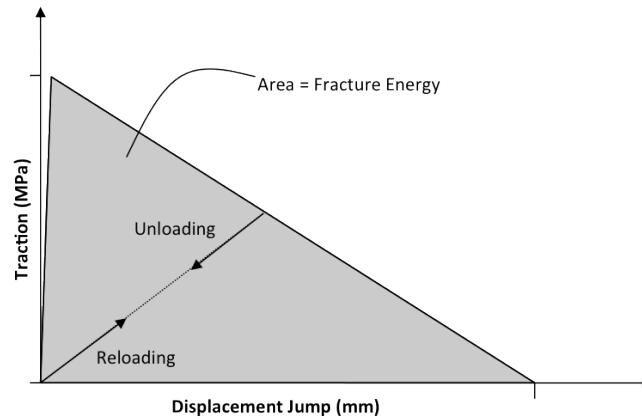


Figure 11.7: Bi-linear cohesive zone model

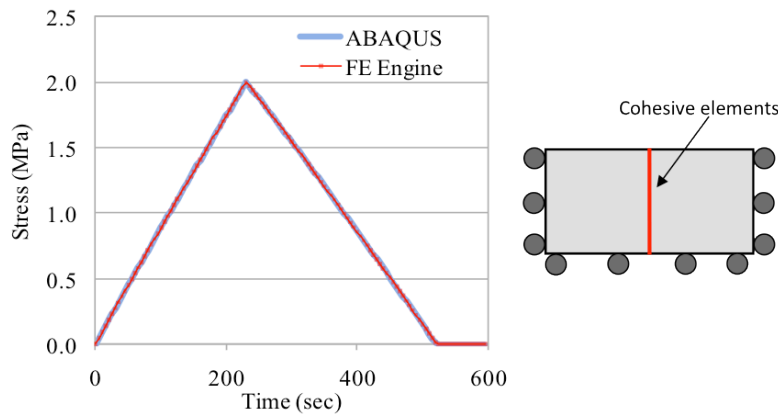


Figure 11.8: Finite element (FE) engine results of the cohesive zone model with recursive incremental viscoelastic finite element formulations. Temperature linearly decreases from 0°C to -10°C during 600 sec

Probabilistic Crack Distribution Model

To avoid the modeling complexities and computation expense needed to simulate multiple thermal cracks, the scheme used in the original TCMODEL to translate a single thermal crack depth prediction to thermal crack density (spacing) was adopted in the current version of ILLI-TC (ILLI-TC v1.0). The modeling of multiple thermal cracks, while more exact, was not deemed as being worth the added computational expense, since the point at which crack interaction

occurs is well within the range of severe cracking. Since it is unlikely that a designer would use a high cracking level as a design target, it was decided that multiple cracks would not be considered in this version of ILLI-TC. Rather, the model completes its execution once a high level of cracking reached (200 m of transverse cracking per 500 m of pavement, which corresponds to a crack spacing of 10 m).

This probabilistic crack distribution model converts the computed crack depth of a single modeled crack (viewed as a representative thermal crack, having a crack depth representing an average crack depth) to an amount of thermal cracking (crack frequency) with the following expression:

$$C_f = \beta_I * P_R (\log C > \log h_{ac}) \quad [11.11]$$

$$C_f = \beta_I * N \left(\frac{\log C / h_{ac}}{\sigma} \right) \quad [11.12]$$

Where:

C_f = Predicted amount of thermal cracking (m/500m) at a given simulation time

β_I = Multiplier representing maximum thermal cracking level

$N(x)$ = Standard normal distribution evaluated at x

σ = Standard deviation of the log of the depth of cracks in the pavement

C = Depth of crack predicted by ILLI-TC at a given simulation time

h_{ac} = Thickness of asphalt layer being simulated (generally taken as the thickness of all asphalt layers)

Crack amount (m/500m) can be converted to thermal crack spacing by dividing predicted crack amount, C_f , by lane width (typically assumed to be 4 m), and taking the inverse of this quotient and multiplying by the unit section length (500 m). Citing the example provided earlier in this section, a crack amount of 200 m corresponds to: $(1/(200/4))*500$ or 10 meters. This corresponds to 1000/10 or 100 full-lane-width cracks per km, which corresponds to approximately 161 thermal cracks per mile. This corresponds to the maximum thermal cracking level predicted by ILLI-TC in the current version. Note, similar to the approach taken in the development of TCMODEL, the parameters β_I and σ were taken as model calibration parameters. Since thermal cracks are difficult to detect until they propagate completely through the pavement, it would be extremely difficult to directly measure and assess the σ parameter. Thus, its selection as a model calibration parameter is a practical means to circumvent the need to directly measure σ .

Calibration of ILLI-TC Model

As described in the project proposal, MN/Road sections from Phase I of this pooled funds study were used to calibrate ILLI-TC, namely; sections 03, 19, 33 and 34. Details about these sections can be found in the Phase I final report (Marasteanu et al., 2007). A decision needed to be made with regards to the climatic files used in model calibration, since two approaches were possible:

(1) use the actual time ranges corresponding to the field thermal cracking data for each section simulated, or; (2) use the climatic files provided in ILLI-TC. The argument for using the actual time ranges that correspond with the field data is that predicted critical cooling events would match actual critical events in the crack history data files, leading to more accurate thermal cracking predictions for model calibration. The argument for using the climatic files included in ILLI-TC is that future pavement simulations conducted using ILLI-TC would be expected to utilize these climatic files (unless the user takes the effort to modify ILLI-TC to utilize alternate climatic files, which is a cumbersome process in the current version of the software). Considering that most users will likely utilize the climatic files provided in ILLI-TC, and also considering that the model should be re-calibrated to local conditions rather than rely on the calibration provided herein, it was decided to conduct model calibration using the climatic files provided in the current version of ILLI-TC.

Pre-Analyzer Runs

Selected outputs from ILLI-TC's preprocessor are provided in Figures 11.9 through 11.13, and summarized in Table 11.5. By comparing Figure 11.9 with Figure 11.10 through 11.13, it is clear that the days with the coldest temperatures correspond to the events with the highest surface tensile stress. Table 11.5 shows that 1 critical cooling event was computed for MnROAD section 03 during the simulated 5-year analysis period, while 4, 1, and 0 critical cooling events were predicted for sections 19, 33, and 34 respectively. Comparing the number of computed critical cooling events with field cracking behavior indicates the correlation between mixture viscoelastic behavior (as captured by the creep compliance master curves) and cracking behavior. The correlation between mix creep compliance and fracture behavior was also demonstrated via a statistical analysis in Phase I of this study (Marasteanu et al., 2007).

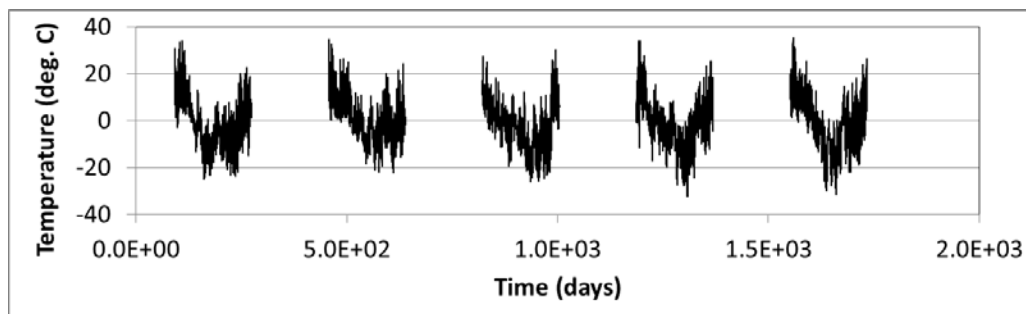


Figure 11.9: Pavement surface temperature using default climatic files in ILLI-TC for MnROAD site (in the category of moderate climate within the state of Minnesota)

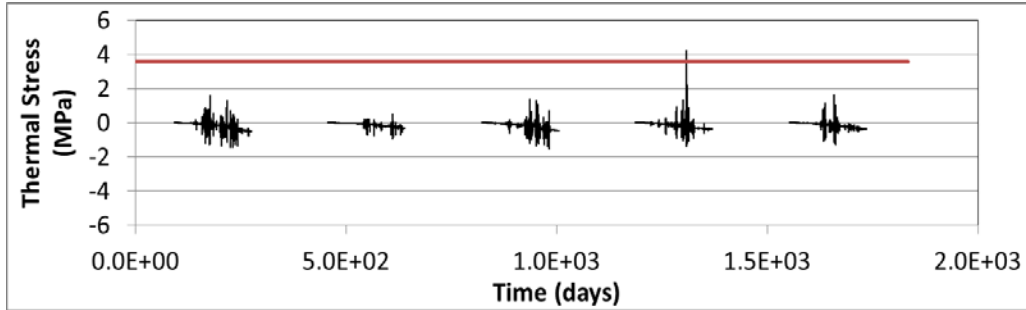


Figure 11.10: Thermal stress on pavement surface for MnROAD03 from pre-analyzer (red line indicated 80% of IDT tensile strength)

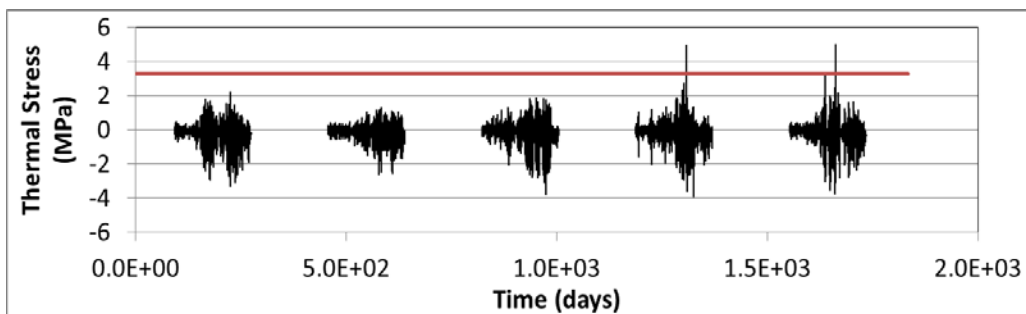


Figure 11.11: Thermal stress on pavement surface for MnROAD19 from pre-analyzer (red line indicated 80% of IDT tensile strength)

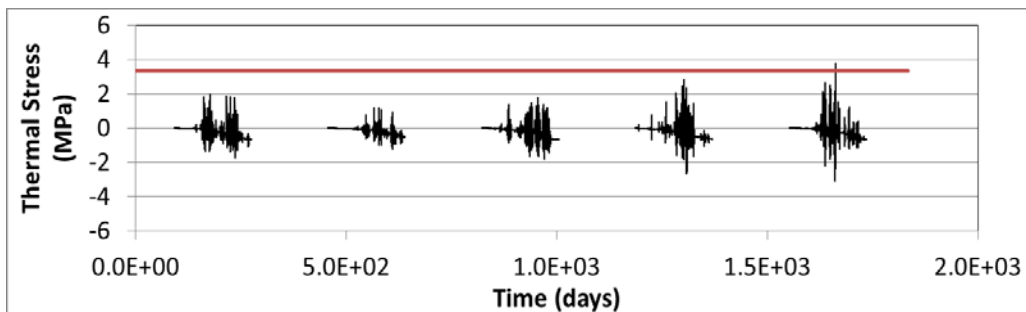


Figure 11.5: Thermal stress on pavement surface for MnROAD33 from pre-analyzer (red line indicated 80% of IDT tensile strength)

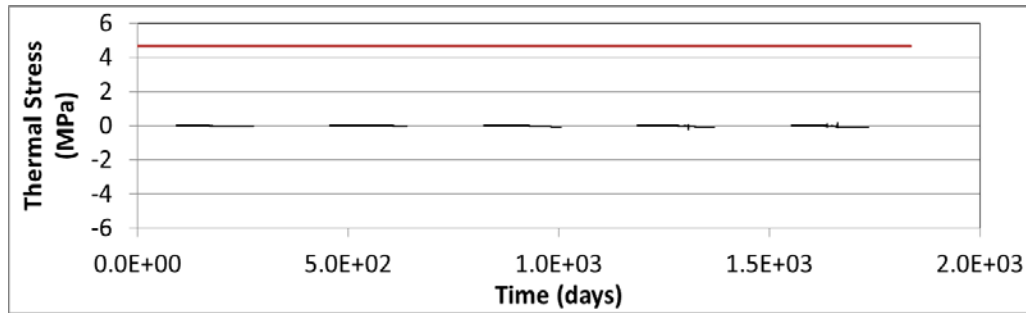


Figure 11.13: Thermal stress on pavement surface for MnROAD34 from pre-analyzer (red line indicated 80% of IDT tensile strength)

Table 11.5: Preanalyzer results (number of critical events) compared to field cracking

MnROAD Cell	Number of Critical Events (as predicted by Pre-Analyzer)	Binder Grade	Field Cracking (m/500 m)
03	1	PEN 120/150 (PG58-28)	182
19	4	AC20 (PG64-22)	547
33	1	PG 58-28	91
34	0	PG 58-34	6

Finite Element Runs

Sample finite element modeling results from the calibration phase of the study for MnROAD section 19 are provided in Figures 11.14 through 11.17. The various aspects of the cohesive zone based finite element modeling approach can be seen in these stress and (exaggerated) deformed structure plots, which show the elevation view of the asphalt layers in the vicinity of the modeled crack. The progression of stress build-up, crack initiation, and crack propagation can be tracked as follows:

- Figure 11.14 shows high surface tensile stress (as indicated by the red color contours), and a slight disruption in the contours at the crack interface caused by the early stages of damage (post-peak softening when tensile stress exceeded material strength at the surface of the pavement) at -23.3 C surface temperature. Mild compression is still present in the lower regions of the pavement, due to time-lag effects of heat flow.
- Figure 11.15 shows that a thermal crack has propagated partially downward through the pavement at a temperature of -24.3 C, and that a fracture process zone of about 15% of the pavement thickness exists ahead of the current crack tip location, illustrating one of the features of the cohesive zone modeling approach (length scale of fracture is directly

considered). A compression zone still exists near the bottom of the asphalt layer.

- Figure 11.16 shows a later stage of crack propagation, and that the fracture process zone has grown in size, and that a compression zone no longer exists (which may partially explain the expansion of the fracture process zone) at a temperature of -25.4 C.
- Figure 11.17 shows a fully formed crack, occurring around -29.6 C. In reality, ILLI-TC considers the pavement section as fully cracked prior to this analysis step, as described below.

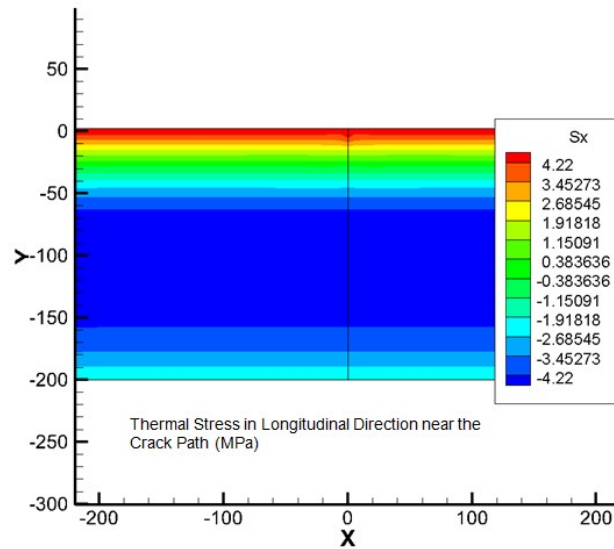


Figure 11.6: Thermal stress built-up along longitudinal direction for MnROAD19 (tensile strength = 4.22 MPa, surface temperature = -23.3°C)

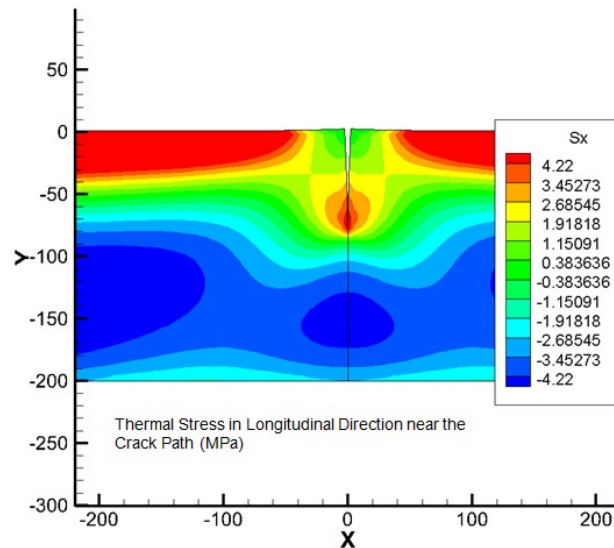


Figure 11.15: Partial depth softening damage for MnROAD19 (tensile strength = 4.22 MPa, surface temperature = -24.3°C)

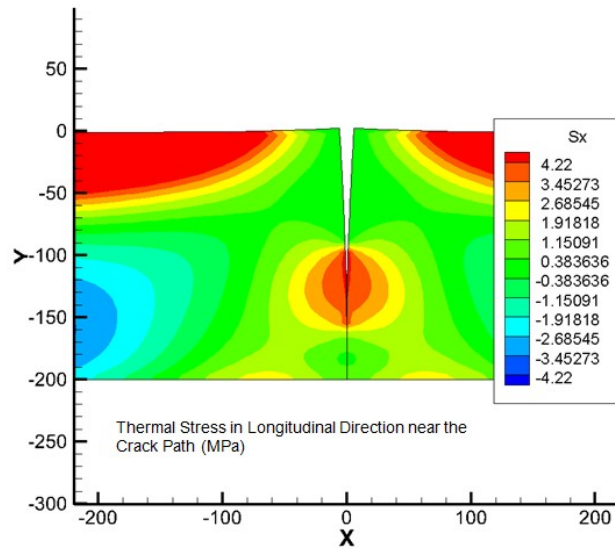


Figure 11.16: Partial crack for MnROAD19 (tensile strength = 4.22 MPa, surface temperature = -25.4°C)

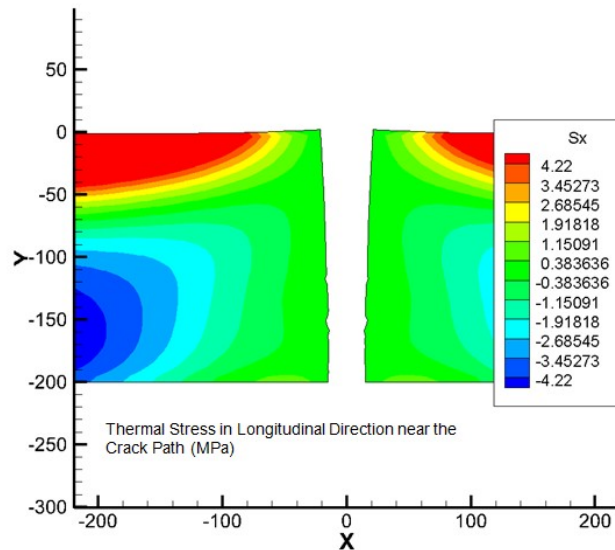


Figure 11.17: Fully-formed crack for MnROAD19 (tensile strength = 4.22 MPa, surface temperature = -29.6°C)

Model Calibration Discussion

Model calibration in pavement studies acknowledges the significant complexities associated with pavement materials, construction, climatic effects, traffic loading and performance. Pavement performance model calibration is almost always needed as a result. In the case of thermal cracking, factors such as construction variability, inability to model aging and aging gradients with accuracy, approximate nature of tests and material models, approximate nature of climatic

records and pavement temperature predictions, presence of load-associated effects and damage on pavement, etc., exist and result in the need for model calibration.

A number of factors were available to be used for model calibration, including: fracture energy multiplier, tensile strength multiplier, thermal coefficient multiplier, crack tip definition, and beta and sigma parameters from the probabilistic crack distribution model were readily available for use in model calibration. As a preliminary approach, it was decided to leave the material property factors as uncalibrated, and focus on the following three factors for model calibration: crack tip definition, beta parameter, sigma parameter. Crack tip definition refers to the fact that more than one material state can be considered as the point of crack initiation in the cohesive zone modeling technique. For instance, in Figure 11.7, any point along the post-peak softening curve (declining linear function in the case of the bi-linear cohesive zone model, which represents the gradual accumulation of material damage and loss of load carrying capacity across the forming crack as the material separates) could be selected as the arbitrarily chosen location of the crack tip. The point at where the softening curve reaches zero traction (the right hand limit of the plot shown in Figure 11.7) is arguably the point where the material no longer possesses the ability to heal. However, it can also be argued that an intermediate point along the softening curve may be a realistic choice for the crack tip, and a threshold where little to no healing may be possible. After examining the finite element results from the Mn/ROAD calibration finite element runs, it was decided that the crack tip would be defined as the point in the pavement along the line of cohesive zone elements where a softening threshold of 75% post-peak decay of material strength (25% traction remaining) is reached. In addition, an identical beta factor ($\beta = 400$ m of cracking per 500 m of pavement section) as used in the original TCMODEL as calibrated in the MEPDG would be used. Finally, the sigma parameter in the probabilistic crack distribution model was calibrated to a value of $\sigma = 1.1$.

As per the project work plan, only MnROAD sections were used in model calibration. The results of the calibrated ILLI-TC model, using MnROAD pavement sections, are presented in Table 11.6. As can be seen, good modeling prediction were achieved for three out of the four sections evaluated. For instance, MnROAD section 19, which experienced very high pavement cracking due to the use of an AC-20 binder (PG 64-22) in a PG XX-34 climate, was predicted to have a maximum level of cracking. Recall that when the maximum predicted crack depth is reached (crack depth = thickness of pavement), this implies that the average crack is equal to the pavement thickness. Thus, half of the other pavement cracks will be shorter than the thickness of the pavement, and therefore, not yet counted as thermal cracks. Stated otherwise, the probabilistic crack distribution model has a maximum cracking level of 200 m of cracking per 500 m section, when $\beta = 400$.

MnROAD section 33 was found to have a cracking level of 94 m of cracking, as compared to a measured level of 91 m (this was the section that weighed heavily on the calibration of the parameter σ), and MnROAD section 34 was found to have a cracking amount of 0 m as compared to a measured cracking level of 6 m. The only poor prediction that resulted was for MnROAD section 03, where zero cracking was predicted as compared to 182 m of measured cracking. It should be noted, however, that ILLI-TC did indicate that softening damage had begun to occur in this section (although not enough to reach the 75% softened threshold). It is also acknowledged that the time period for the ILLI-TC simulation was shorter than the period of field performance reported for Section 03. In addition, the master curve data used in the

calibration was less-than-optimal, with data from only two test temperatures being available (three is preferred). Rather than add additional calibration factors to ILLI-TC, it was decided that the aforementioned calibration parameters were sufficient for the calibration of ILLI-TC. However, it is recommended that ILLI-TC be recalibrated to local conditions to arrive at better model accuracy. Model validation using an independent data set is provided through Task 6 for the project.

Table 11.6: ILLI-TC model calibration results

MnROAD Cell	Binder Grade	Measured Field Cracking (m/500 m)	Predicted Field Cracking (using non-synchronized climate files)
03	PEN 120/150 (PG58-28)	182	0
19	AC20 (PG64-22)	>200 (547)	>=200 (max cracking)
33	PG 58-28	91	94
34	PG 58-34	6	0

Summary

This chapter presented a new thermal cracking model developed at the University of Illinois Urbana-Champaign, called “ILLI-TC.” This chapter presents the ILLI-TC model components, model verification, and model calibration results. ILLI-TC improves the manner in which fracture is handled in the simulation scheme, namely; in the past TCMODEL used a 1D Paris-Law phenomenological modeling approach to simulate crack propagation, while ILLI-TC uses a 2D, cohesive zone fracture modeling approach implemented within a viscoelastic finite element modeling framework. A user-friendly graphical interface (GUI) has been provided for ILLI-TC. The GUI program module within ILLI-TC is referred to herein as Visual-LTC. A detailed account of the finite element modeling approach used herein was also provided. Intermediate results, including stress contours and deformed pavement structure were presented and discussed. A probabilistic crack distribution model, identical to the one used in the original TCMODEL program, was also presented. Model calibration strategies, including a discussion on the arbitrary selection of the definition of a crack tip in the cohesive zone modeling scheme was also presented.

As per the project work plan, only MnROAD sections were used in model calibration. MnROAD sections 19, 33, and 34 were found to have very good model predictions after model calibration. The only poor prediction that resulted was for MnROAD section 03, where zero cracking was predicted as compared to 182 m of measured cracking. It should be noted, however, that ILLI-TC did indicate that softening damage had begun to occur in this section (although not enough to reach the 75% softened threshold). It is also acknowledged that the time period for the ILLI-TC simulation was shorter than the period of field performance reported for Section 03. In addition, the master curve data used in the calibration was less-than-optimal, with data from only two test temperatures being available (three is preferred). Rather than add additional calibration factors to

ILLI-TC, it was decided that the aforementioned calibration parameters were sufficient for the calibration of ILLI-TC. However, it is recommended that ILLI-TC be recalibrated to local conditions to arrive at better model accuracy. Model validation using an independent data set is provided in the Task 6 report for this project.

ILLI-TC is a modular finite element code, and can be upgraded in the future to include additional 'physics' which could include: multiple HMA lifts; non-linear thermal coefficient; non-linear softening curve shape for cohesive zone model; integrated ICM climatic model; a year-round modeling option, combined with a multi-processor code option to handle the extra computing requirements; aging gradient effects on bulk and fracture mixture properties, and; 3-D code to allow combined block/thermal cracking analysis to be performed. Although beyond of this study, these modeling improvements will serve to improve the accuracy and the breadth of capabilities of the ILLI-TC modeling program. From a practitioner standpoint, the current ILLI-TC program has the benefit of relatively fast run times and relatively few material property testing requirement and inputs. From a research standpoint, the proposed future updates to ILLI-TC will provide more insight into the mechanisms behind thermal cracking, but will require more testing and modeling effort.

Chapter 12. Modeling of Asphalt Mixtures Contraction and Expansion Due to Thermal Cycling

Introduction

This report summarizes a comprehensive experimental and modeling investigation on the contraction and expansion of asphalt mixtures due to thermal cycles. As part of this study, a model was developed for thermal stress analysis during cooling/heating cycles using different cooling rates and isothermal conditioning periods. The model accounts for the asphalt mixture glass transition and physical hardening, and it can be used to investigate which thermo-volumetric parameters (e.g, coefficients of thermal expansion/contraction, glass transition temperature, etc) significantly affect the asphalt mixture response during cooling and heating cycles. The thermal stress model uses relaxation modulus master curves, the William-Landel-Ferry equation, Boltzmann superposition principle, and a sub-model describing the isothermal contraction of asphalt materials as a continuous function of conditioning time and temperature. Using the model predictions it is shown that thermal stress relaxation and stress build-up induced by physical hardening can continuously affect thermal stress throughout the cooling process. Cooling rate also affected the amount of delayed stress buildup occurring after the temperature has stabilized at isothermal condition due to physical hardening.

The thermal stress model was validated with experimental thermal cyclic results using the recently introduced Asphalt Thermal Cracking Analyzer (ATCA). Mixture testing performed in the ATCA at different cooling rates and isothermal conditions supported the theoretical predictions. The findings show clearly that the effect of physical hardening on stress build-up in mixtures is measurable and important.

A semi-empirical micromechanical model for the estimation of mixture coefficient of thermal contraction/expansion above and below the glass transition temperature (T_g) based on the commonly used Hirsch model and Finite Element Modeling (FEM) is also introduced in this report. Almost all the published models, including those used in the Mechanistic Empirical Pavement Design Guide (MEPDG), consider a single value for the coefficient of thermal expansion/contraction. Many models use a default coefficient value or a formula that was introduced in the 1960s derived empirically based on testing a relatively small set of mixtures. The only justification for this over-simplification is the difficulty of measuring the coefficient of contraction and expansion and the lack of sufficient knowledge about effects of various mixture variables on these coefficients. Results in this study show the importance of the proper estimation of the thermo-volumetric properties of asphalt mixtures in the prediction of thermal cracking of pavements and proposes a method for estimating the coefficient based on the thermo-volumetric properties of the asphalt binder and the internal structure of the mixture.

Finally, as part of the Task 5 objectives, the aforementioned thermal cycling model for representing the contraction/expansion of mixtures was used to study the statistical importance of the material thermo-volumetric properties on the thermal stress response of the mixture.

Objectives

According to the project work plan the main objectives to be addressed in Task 5 are:

- Expand the database for thermo-volumetric properties of asphalt binders and mixtures to a wider range of modified asphalts and types of mixtures to fully quantify the effects of binders and aggregates in the asymmetrical thermo-volumetric behavior (i.e., glass transitions and contraction/expansion coefficients).
- Develop a micromechanical numerical model that can be used to estimate the glass transition temperatures and coefficients from mixture variables commonly measured for binder grading and for mixture design.
- Conduct thermal cracking sensitivity analysis to determine which of the glass transition parameters are statistically important for cracking, which ones need to be measured, and the effect of using estimated values rather than measured values.

In this report these objectives are investigated and results discussed in the stated order.

Background

Low temperature cracking is a major distress in many regions with cold climates. It is believed that the excessive brittleness due to the increase in stiffness and decrease in the ability to relax stress leads to the buildup of thermally induced stress and ultimately cracking of mixtures in pavements.

Visco-elastic materials such as asphalt mixtures can relax stress by viscous flow. Asphalt pavements are restrained from significant movement, thus thermally induced contraction can lead to significant stress buildup in the pavement. Due to the time dependent behavior of visco-elastic materials, the higher the capability of the material to relax stress, the lower the thermal stress buildup will be at a given temperature, and consequently the pavement can withstand lower temperatures before fracture (1, 2). Thus, stress relaxation has been considered an important factor in the thermal cracking resistance of asphalt pavements (3). Researchers also consider factors such as the rate of cooling, coefficients of expansion/contraction, glass transition temperature, shape of master curve at low temperatures and the tensile strength to affect the critical cracking temperature (2). Measuring all these factors in a controlled laboratory environment has been exceedingly difficult; therefore theoretical calculations of thermal stress have often utilized simplifying assumptions in place of many of the aforementioned factors. Furthermore, current methods have not consider thermal cycling in the analysis as it is assumed that thermal cracking occurs in a single cold temperature event.

Monismith et al. (4) developed a theoretical calculation method for the thermally induced stress in asphalt pavements. This method is currently used for the estimation of critical cracking temperature by researchers and designers in many procedures. However, this method does not take into account the glass transition behavior and physical hardening observed in asphalt binders, instead utilizing a constant coefficient of thermal expansion/contraction (CTE).

The change in behavior near or below the glass transition temperature and physical hardening in asphalt materials has been noted by many researchers in recent years (5-16); the increase in brittleness as well as the time dependent behavior of the material in this temperature range can

have a detrimental effect on actual performance. Bouldin et al. (2) reported that the midpoint of the binder’s glass transition, typically referred to as the “glass transition temperature”, is in the vicinity of the pavement critical cracking temperature. Kriz et al. (10) showed that physical hardening can affect the position of the glass transition temperature in asphalt binders. Furthermore, change in relaxation properties has been noted in asphalt and many polymers during physical hardening (9, 10, and 12).

Researchers have noted the effect of isothermal conditioning, typically referred to as “physical hardening” or “physical aging”, in amorphous material for many years. Struik described physical hardening in polymers as a type of thermo-reversible relaxation process, taking place in the glass transition region of amorphous materials (12). The first comprehensive study on physical hardening in asphalt binders was reported during SHRP (5, 6). Physical hardening is usually explained by the free volume theory proposed by Struik (12) and Ferry (13). However, some researchers have also associated physical hardening with the crystalline domain and wax fraction of the asphalt binder (7, 8, and 10).

Researchers such as Shenoy (17) have claimed that stress relaxation in the binder can cancel out any effect of physical hardening in mixtures, thus believing the phenomenon to be of no practical importance. Recent studies by others such as Falchetto et al. (18), Falchetto and Marasteanu (19) and Evans and Hesp (16) have concluded otherwise. Falchetto and his co-workers measured the increase in stiffness in both binder and mixture BBR beams, showing that the semi-empirical Hirsch model can be used to predict the hardening of the mixture beams based on the binder beam hardening (18, 19). Evan and Hesp (16) showed that binders that had higher BBR grade loss after 72hrs of conditioning retained more residual stress after relaxation.

Materials and Experimental Methods

Asphalt Binders and Mixtures

For this task, the seven binders and the corresponding loose mixes described in Task 2 and shown in Table 12.1 were tested using the binder and mixture glass transition temperature tests. All binders were subjected to short-term aging using the Rolling Thin Film Oven (RTFO) in an attempt to match the short term aging of the asphalt loose mixture.

Table 12.1: Asphalt binders selected for Task 2

Binder	Location	Description
PG 58-34 PPA	MnROAD 33	Modified with Poly-phosphoric Acid (PPA)
PG 58-34 SBS+Acid	MnROAD 34	Modified with Styrene-Butadiene Styrene (SBS) +PPA
PG 58-34 SBS	MnROAD35	Modified with SBS
PG 58-34 Elvaloy +Acid	MnROAD 77	Modified with PPA + Elvaloy
PG 58-28	MnROAD 20	Neat
PG 58-34	MnROAD 22	Unknown Modification
Wisconsin	Wisconsin	Binder used in construction of SMA pavement
PG 64-22 – New York	New York	Typical binder used in New York

Asphalt mixtures prepared with the asphalt binders presented in Table 12.1 as well as samples used as part of the NCHRP 9-10 project (21) were tested in the Asphalt Thermal Cracking Analyzer (ATCA) to obtain thermal stress as a function of core temperature and testing time for different thermal loading history. Mixture testing in ATCA included single cooling events, extended isothermal conditioning, and thermal cycling.

Test Methods

Glass Transition (T_g) Test Procedure for Asphalt Binders

A dilatometric system was used to measure the glass transition temperature and the coefficients of thermal contraction/expansion of the asphalt binders. Currently, no formal standard for this device is available and therefore the test was performed following the procedure developed by Bahia and Anderson (22) and later modified by Nam and Bahia (23). The concept behind the procedure is based on precise measurements of volume change in time for an asphalt binder specimen, as temperature is decreased at a constant rate. The binder sample is prepared by pouring 10 g of hot asphalt into a circular silicone rubber mold with a diameter of 40 mm and a height of 8.0 mm.

The dilatometric cell is connected to a vertical capillary tube with $\phi = 1$ mm and its top end open. The volume changes in the sample are calculated by estimating the change in the height of the ethyl alcohol column inside the capillary tube. The system uses a very precise pressure transducer (Figure 12.1) to measure the changes in ethyl alcohol column height.

Calculation of the glass transition temperature (T_g) is based on a non-linear model proposed originally by Bahia (22) and later used by Nam and Bahia (23). Figures 12.1 and 12.2 show the dilatometric system and typical results for T_g measurements, respectively.

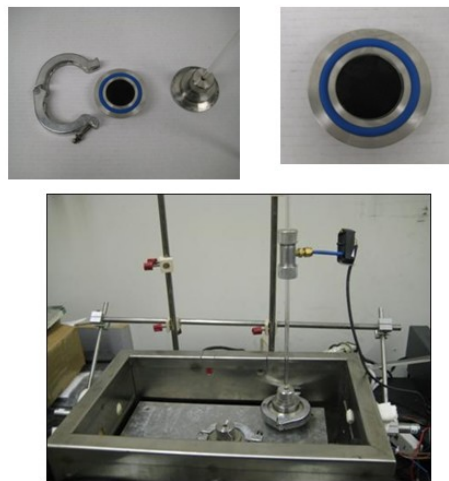


Figure 12.1: Dilatometric system used to measure glass transition temperature (T_g) of asphalt binders

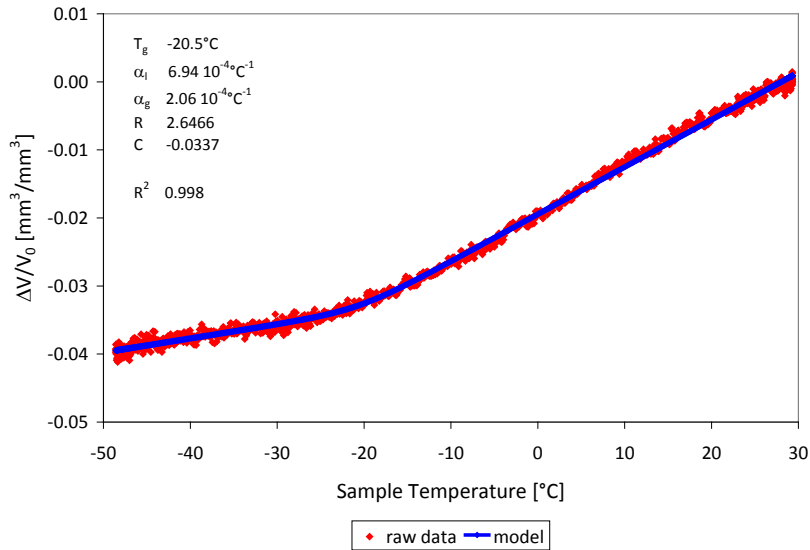


Figure 12.2: Typical results from glass transition temperature (T_g) test of asphalt binders

Asphalt Thermal Cracking Analyzer (ATCA)

In an effort to address issues in existing thermal cracking testing setups, a device was developed that simultaneously tests two asphalt mixture beams; one unrestrained, and the other with restrained ends. The unrestrained beam is used to measure the change in volumetric properties with temperature, and consequently the glass transition temperature (T_g) and coefficients of expansion/contraction above (α_l) and below (α_g) glass transition temperature. The restrained beam is used to capture the induced thermal stress buildup due to prevented contraction. This device is currently being referred to as the Asphalt Thermal Cracking Analyzer (ATCA).

In this device both tested beams are obtained from the same asphalt mixture gyratory compacted sample or core, and both are exposed to the same temperature regime. The system is schematically shown in Figure 12.3.

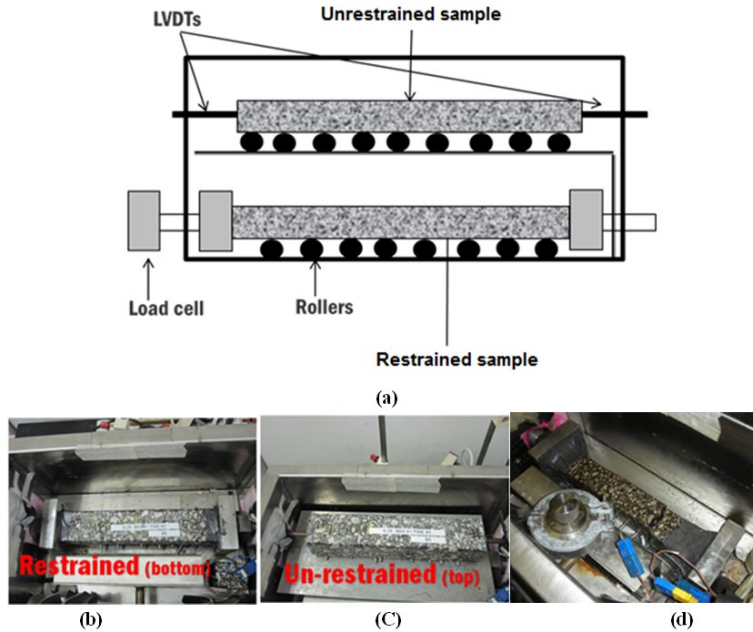


Figure 12.3: (a) Illustration of the Asphalt Thermal Cracking Analyzer (ATCA) system; (b) restrained beam setup, (c) unrestrained beam setup, and (d) restrained beam after failure

Figure 12.4 shows typical output results obtained from the ATCA system when temperature is decreased at the rate of 1°C/min from 30 to -70°C.

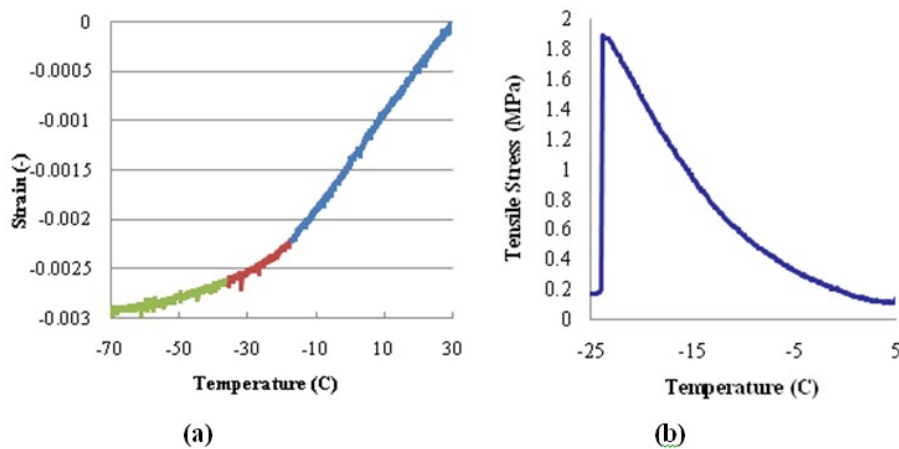


Figure 12.4: (a) Typical Tg result for asphalt mixtures, (b) typical result of the stress buildup

The unrestrained and restrained samples are produced from one Superpave gyratory compacted sample using a masonry saw. Four prismatic beams of 5 by 5-cm in cross section and 15 cm long are cut from 17 cm gyratory samples. Two of these beams are sawed in half to produce four 7.5 cm blocks. By gluing a 7.5 cm block to each end of the two 15 cm blocks, two 30 cm beams are produced (Figure 12.5). As both beams are produced from the same sample and both are exposed to the same thermal history, the stress buildup, glass transition temperature, α_l and α_g can be used to get a comprehensive picture of the low temperature performance of the asphalt mixture.

Due to the temperature control flexibility possible with the ATCA system, many complex experiments, such as thermal cycling with isothermal steps and measurement of thermal stress relaxation are possible. Using the ATCA, a thermal stress relaxation experiment was designed in which the chamber temperature was reduced to a predefined low temperature at a controlled cooling rate (e.g., 0.1 to 1 °C/min), continuously monitored using temperature probes within the chamber and the core of the asphalt beams. The temperature was then kept at the predefined temperature for prolonged periods, between 1 to 10 hours, and the stress buildup in the restrained specimen, as well as thermal strain in the unrestrained sample were measured continuously. The results were used to plot curves of thermal stress as a function of core temperature and testing time, both during cooling and heating and during the extended isothermal conditioning.

Results from the ATCA can also be used to calculate relevant low temperature material properties, most notably, the relaxation modulus. The relaxation modulus convolution integral can be solved numerically by directly measuring both thermal stress (i.e., restrained beam) and strain (i.e., unrestrained beam) as function of time and temperature. An example of ATCA results and the calculated relaxation modulus curve are shown in Figure 12.6.

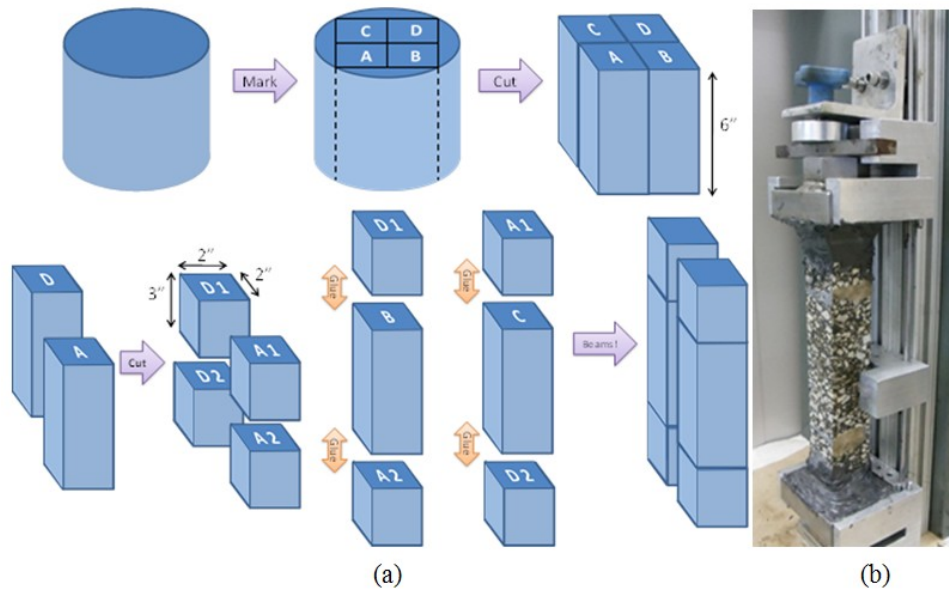


Figure 12.5: (a) Cutting of SGC sample for thermal cycling testing of mixtures in ATCA (b) sample gluing setup

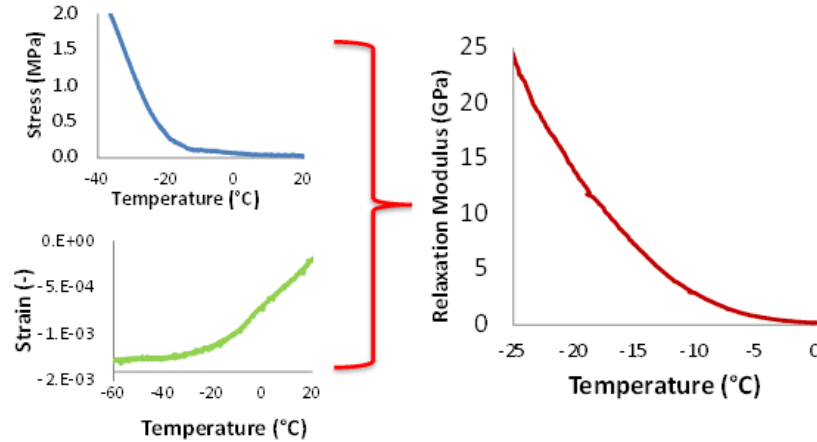


Figure 12.6: ATCA results and calculated relaxation modulus curve

Experimental Evaluation of Thermal Response of Asphalt Binders and Mixtures during Cooling and Heating (Objective 1)

Thermo-Volumetric Response of Asphalt Binders and Mixtures during Thermal Cycles

The main objective of Task 5 was to expand the database of thermo-volumetric properties of asphalt binders and mixtures in both cooling and heating. Toward achieving this objective, the research team performed glass transition temperature tests in cooling and heating on the binders listed in Table 12.1 and their corresponding mixtures, as well as the binders and mixtures used in the validation sections of Task 6 (i.e., MN County Road 112). The results were fitted using the non-linear model proposed by Bahia and Anderson (22) and the resulting parameters are reported in Tables 12.2 and 12.3.

Table 12.2: Asphalt binder and mixture thermal strain model parameters during cooling

Cell	Binder					Mixture				
	Cv (-)	Tg (°C)	R (-)	α_l (1/°C)	α_g (1/°C)	Cv (-)	Tg (°C)	R (-)	α_l (1/°C)	α_g (1/°C)
20	0.003	-17.4	6.9	7.9E-04	1.8E-04	-0.002	-20.5	4.9	5.0E-05	1.4E-05
22	-0.023	-20.2	2.7	7.7E-04	3.3E-04	-0.003	-28.7	2.6	4.9E-05	9.4E-06
33	-0.032	-18.4	3.1	6.9E-04	3.4E-04	-0.002	-26.8	6.0	5.1E-05	6.9E-06
34	0.007	-20.7	13.1	9.6E-04	4.9E-04	-0.002	-22.2	6.2	5.1E-05	1.3E-05
35	-0.030	-17.8	4.5	6.9E-04	2.6E-04	-0.003	-25.6	3.5	5.0E-05	1.4E-05
77	-0.030	-21.9	6.6	7.6E-04	5.7E-05	-0.003	-19.5	6.9	5.4E-05	1.5E-05
WI	-0.033	-19.1	2.8	7.1E-04	3.8E-04	-0.002	-21.1	4.7	4.8E-05	1.4E-05
NY	-0.031	-18.3	4.7	6.8E-04	2.7E-04	N/A	N/A	N/A	N/A	N/A
MTN CR112	-0.017	-17.6	5.3	6.3E-04	2.3E-04	N/A	N/A	N/A	N/A	N/A
VAL CR112	-0.036	-22.9	6.8	8.4E-04	2.0E-05	-0.002	-22.3	7.0	4.3E-05	6.9E-06
CAN CR112	-0.013	-17.4	3.0	7.0E-04	2.9E-04	N/A	N/A	N/A	N/A	N/A
CIT CR112	-0.025	-16.5	5.8	7.3E-04	6.8E-05	-0.002	-19.3	4.0	4.3E-05	1.3E-05

Table 12.3: Asphalt binder and mixture thermal strain model parameters during heating

Cell	Binder					Mixture				
	Cv (-)	T _g (°C)	R (-)	α _l (1/°C)	α _g (1/°C)	Cv (-)	T _g (°C)	R (-)	α _l (1/°C)	α _g (1/°C)
20	0.003	-17.4	6.9	7.9E-04	1.8E-04	N/A	-21.2	N/A	4.5E-05	6.5E-07
22	0.004	-20.4	5.4	8.6E-04	2.7E-04	N/A	-19.5	N/A	4.9E-05	5.4E-06
33	0.006	-24.1	6.3	8.9E-04	2.9E-04	N/A	-13.5	N/A	5.0E-05	1.1E-05
34	0.007	-14.6	1.0	7.4E-04	4.1E-04	N/A	-16.2	N/A	5.0E-05	9.3E-06
35	0.005	-21.3	6.0	8.0E-04	2.2E-04	N/A	-13.3	N/A	5.4E-05	8.6E-06
77	0.007	-17.2	5.8	8.3E-04	3.2E-04	N/A	-11.5	N/A	5.1E-05	1.5E-05
WI	0.008	-18.9	3.5	8.9E-04	4.8E-04	N/A	-14.3	N/A	4.7E-05	9.2E-06
NY	0.004	-20.7	6.6	8.3E-04	2.4E-04	N/A	N/A	N/A	N/A	N/A

Although direct comparison of the T_g results from the binders and mixtures is difficult due to variation in the volumetrics of the mix, aggregate properties, and gradation from sample to sample, it was generally noted that the asphalt mixture have glass transition temperatures up to 8°C lower than the T_g of the binder, with an average difference of 3.5°C (Figure 12.7).

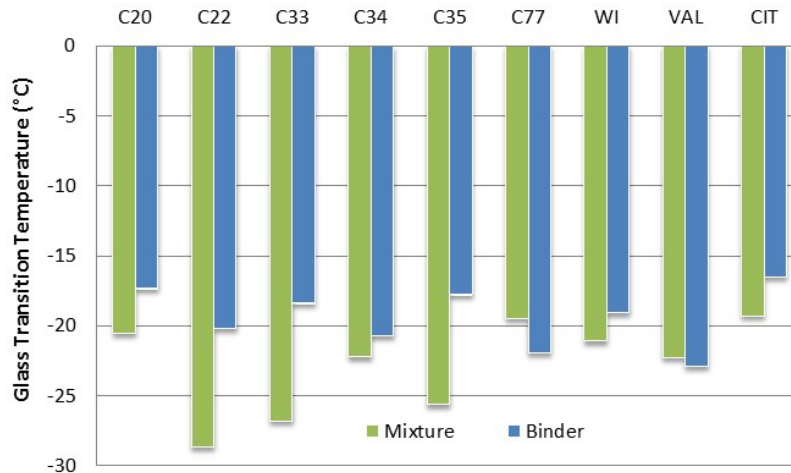


Figure 12.7: Glass transition temperature of binders and mixtures

The research team conducted a detailed study on the effect of aggregate internal structure and mixture volumetric properties on the glass transition temperature of mixtures (Objective 2). The study showed that although these factors significantly affect the coefficients of thermal contraction and expansion both above and below the glass transition temperature, the actual position of the glass transition temperature is not changed by variation in these factors. The observed reduction in the glass transition temperature was attributed to the chemical interaction between the binder and the mineral filler, based on a recent study conducted by Clopotel et al. (24), as shown in Figures 12.8 and 12.9.

Figures 12.8 and 12.9 show that as filler content increased the glass transition of the mastic decreased. The extent of this reduction could not be explained using mechanical theories, but was shown to be dependent on filler mineralogy.

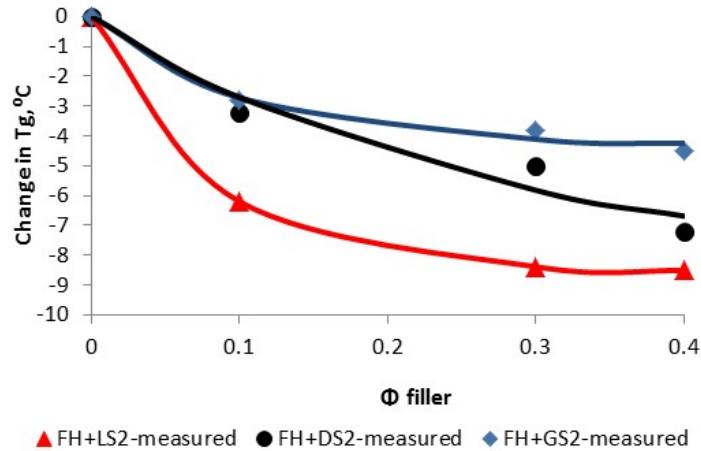


Figure 12.8: Change in glass transition temperature of base binder FH PG 64-22 with volume fraction (ϕ) for different fillers (LS2-limestone, DS2-dolomite, GS2-granite) (24)

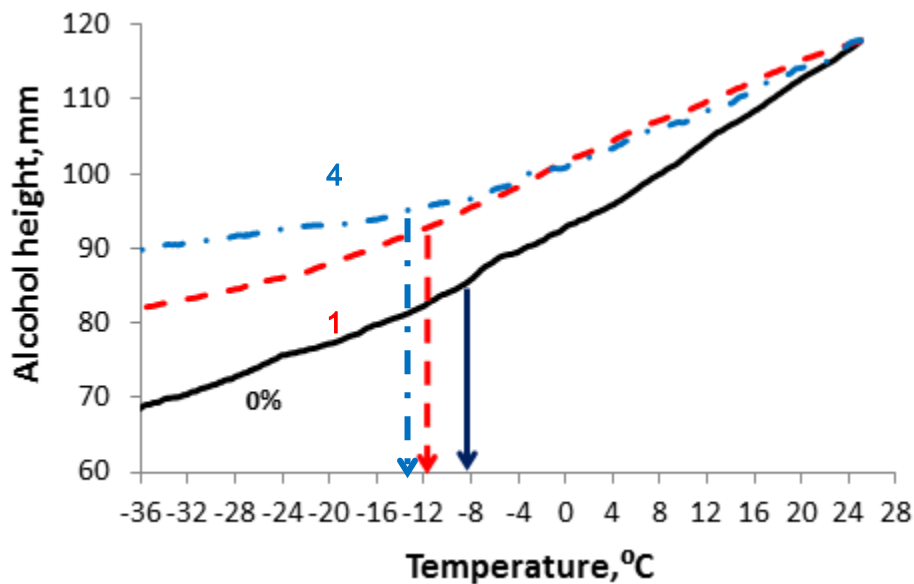


Figure 12.9: Change in glass transition temperature with volume fraction, PG 64-22 mixed with granite filler at (ϕ)=0, 10, 40% (24)

The evolution of the mixture thermal response during a full cooling and heating cycle was investigated by subjecting beam samples to full thermal cycles using the ATCA. During such thermal cycles the behavior shown in Figure 12.10 was typically observed for all tested material. The asymmetric stress behavior during cooling and heating is believed to be due to the asymmetry in the rate at which the time-dependent strain (i.e., physical hardening) builds up and decreases in the glass transition region. During heating the time-dependent strain is minimal and thus is not different from the strain due to temperature. This behavior results in the trend seen in Figure 12.10. This concept is used to develop the model proposed in this study to calculate thermal strain and stress during cooling and differentiated from that during heating cycles.

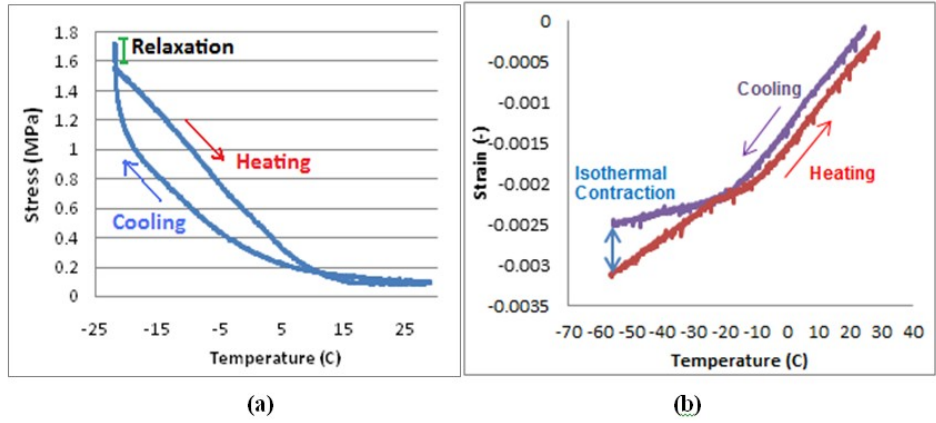


Figure 12.10: Stress buildup vs. temperature for full thermal cycle (a) Experimental, and (b) modeled

The thermo-volumetric response of the MnROAD mixtures was investigated using the ATCA. The unrestrained samples did not significantly change from cycle to cycle, as indicated in Figures 12.11 and 6.12. However, heating and cooling curves in each cycle are slightly different as shown in Figure 12.12.

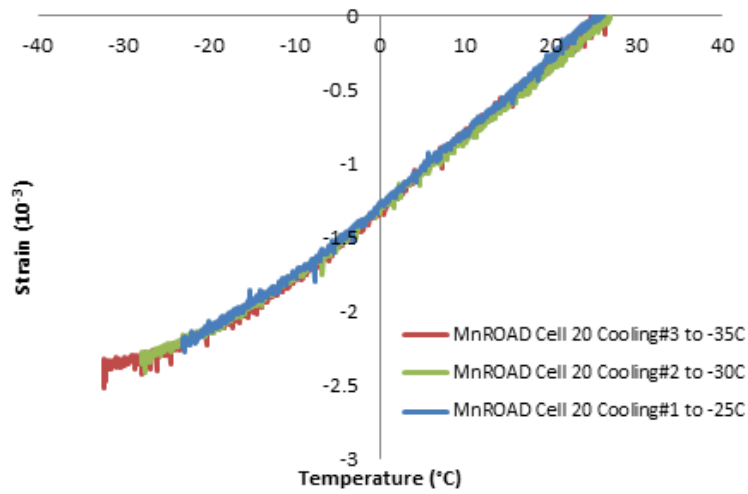


Figure 12.11: Thermal strain in MnROAD Cell 20 in the cooling cycles

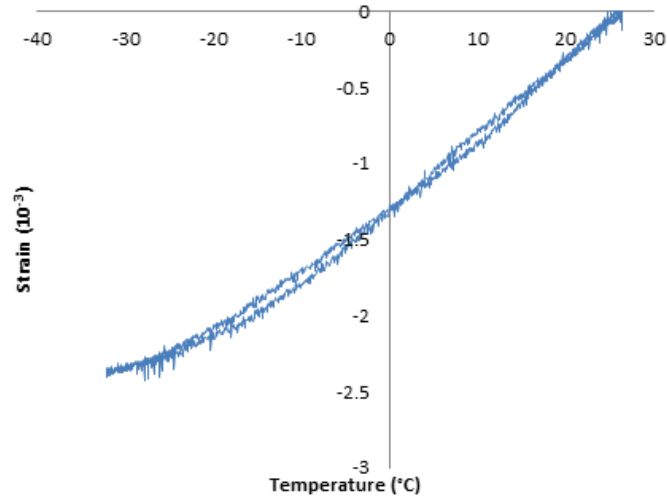


Figure 12.12: Thermal strain for MnROAD Cell 20 sample during one cooling and heating cycle

Figure 12.13 shows the thermal strain in an asphalt beam prepared with the WI binder. The temperature was cycled between +30°C and -70°C three times. No significant change in coefficients of thermal contraction/expansion and the glass transition temperature was observed between one cycle and the next. However, the coefficient of contraction below T_g is significantly different than the coefficient of expansion.

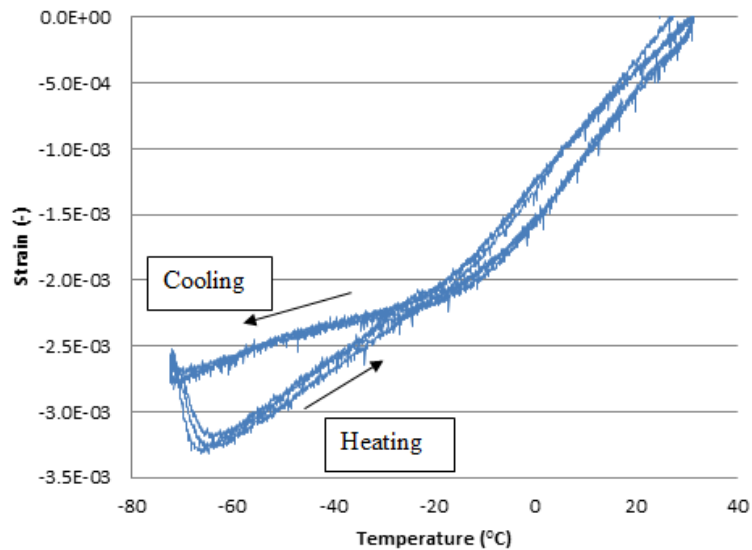


Figure 12.13: Thermal strain in asphalt mixture beam (WI) in 3 consecutive cycles

Thermal Stress Response of Asphalt Binders and Mixtures during Thermal Cycles

To better understand the thermal stress response of asphalt mixtures during a thermal cycle, the research team conducted an additional study on a number of thermal cycling tests on restrained specimens, measuring thermal stress in the process.

Figure 12.14 shows the results of stress buildup measured for MnROAD Cell 20. The sample was cycled between 30 and -20°C three times before progressively decreasing the lower limit by 5°C increments to -35°C. The trend in the stress buildup shows a very sudden drop in thermal stress when the sample was cooled toward -25°C in the 4th cycle, while subsequent cycles failed to buildup significant stress. Visual inspection of the sample after cyclic testing showed no visible crack or failure in the sample, thus it was concluded that significant damage had occurred during the first 4 cycles, leading to an internal structural failure in the sample.

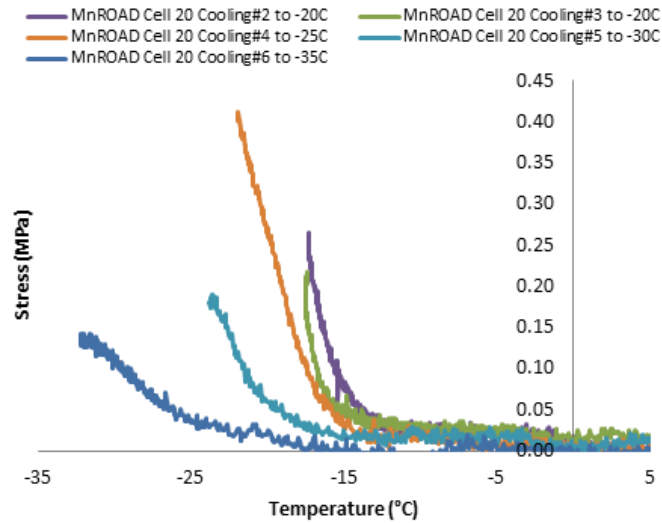


Figure 12.14: Stress buildup curves under thermal cycling for MnROAD Cell 20

Figure 12.15 shows thermal cycles for MnROAD Cell 33 with isothermal conditioning in last cycle. It can be seen that the area of the loop (i.e., hysteresis) decreases after each cycle. Furthermore, the area of the loop significantly decreases when the specimen is subjected to isothermal conditioning at the end of the cooling step. These results indicate the importance of taking into account isothermal conditioning (i.e., physical hardening) when estimating thermal cracking susceptibility of asphalt mixtures subjected to cooling and heating cycles.

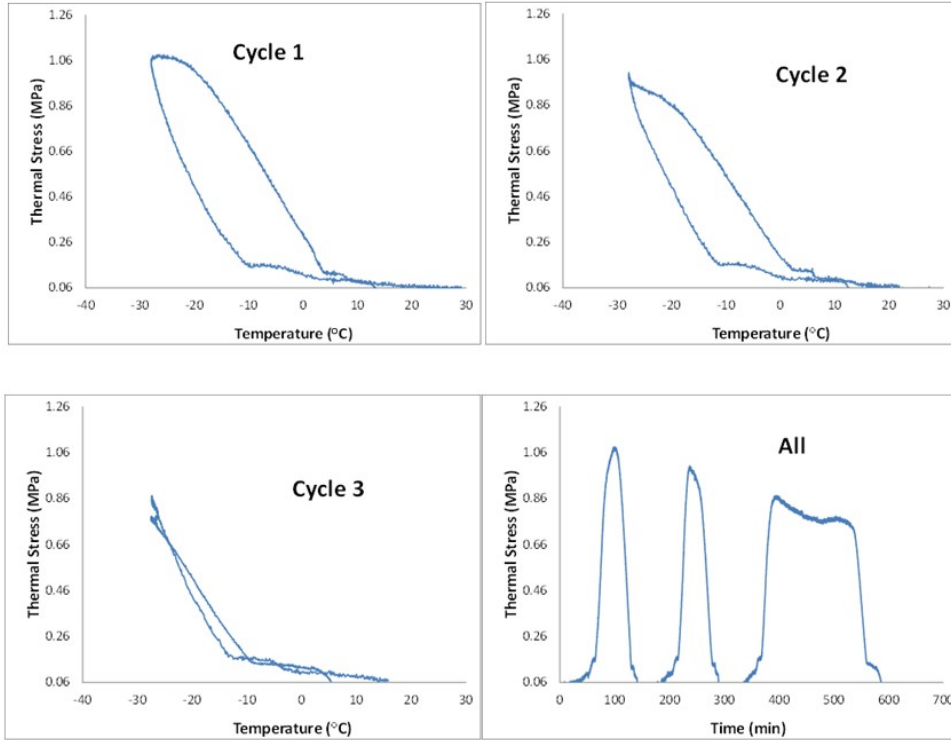


Figure 12.15: Stress buildup curves under thermal cycling and isothermal conditioning for MnROAD Cell 33

Figure 12.16 shows a fourth cycle of thermal loading applied to the restrained beam to bring it to complete failure. It can be seen that the trend of stress buildup for cycle 4 in which the temperature was decreased at a constant rate down to the point of cracking varies from the cycles including an isothermal conditioning step. It can be seen that the maximum thermal stress observed in cycle 2 with isothermal conditioning was reached 12°C earlier in comparison to the cooling cycle 4 with no isothermal conditioning. This observation is extremely important if one considers that the common Thermal Stress Restrained Specimen Test (TSRST) measures the cracking temperature by cooling at a constant rate without taking isothermal conditioning or thermal cycles into account.

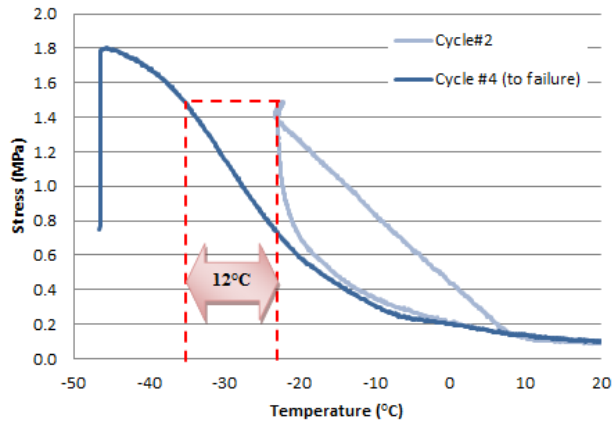


Figure 12.16: Stress buildup in restrained MnROAD Cell 33 beam using the ATCA, with and without the isothermal conditioning step

Thermal Stress Buildup and Relaxation

This study also investigated thermal stress relaxation of asphalt mixtures based on a limited number of asphalt samples tested. Using the ATCA, cooling and relaxation experiments were carried out at different rates, isothermal temperatures, and isothermal relaxation times. For all experiments thermal stress was observed to build up as the temperature decreased in the restrained beam. Temperature reduction was stopped at a predefined temperature to start the isothermal stage. Although the temperature measured at the core of the asphalt sample was kept constant, the sample stress continued to build up even after the core temperature had stabilized. Isothermal contraction was also observed simultaneously in the unrestrained beam. As the isothermal conditioning continued, the stress gradually started to relax. This trend was observed for all asphalt mixture samples tested, as shown in Figure 12.17 in which two identical samples were cooled to -20°C and then held isothermally for 5 and 10 hours, respectively. It is observed that after the initial isothermal stress buildup, the rate of build-up gradually decreases, followed by a relaxation of stress until stabilizing at a constant value over time.

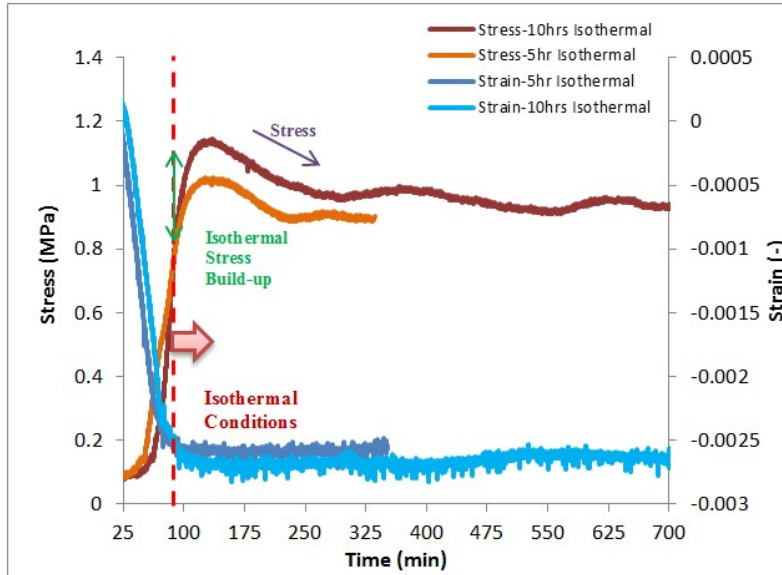


Figure 12.17: Thermal stress in asphalt mixtures after 5 and 10hrs of isothermal conditioning

Furthermore, it is noted that the amount of isothermal stress (Figure 12.18b) and strain (Figure 12.18a) buildup is dependent on the rate of cooling. When a rate of $0.1^{\circ}\text{C}/\text{min}$ ($6^{\circ}\text{C}/\text{hr}$) was used as much as 10% of the ultimate stress continued to build up after achieving a stable core temperature (Figure 12.18b). When rate was increased to an extremely fast cooling rate of $1^{\circ}\text{C}/\text{min}$, most of the ultimate stress is reached after achieving a stable core temperature, although the specimen ultimately reached the same stress levels as with the slower rate as indicated in Figure 12.18. Tests performed at an intermediate rate of $0.5^{\circ}\text{C}/\text{min}$ resulted in isothermal stress buildup in between the two extreme cooling rates.

Researchers in earlier studies have used many cooling rates to test and model field conditions. Bouldin et al. (2) used $3^{\circ}\text{C}/\text{hr}$ to match studied field sections, while suggesting that resulting cracking temperature may be “bumped” up or down for faster and slower rates, respectively. Modeling by Bahia et al. (8) for rates lower than $10^{\circ}\text{C}/\text{hr}$ showed that reducing cooling rate corresponded to a shift in thermal stress buildup toward lower temperatures. SHRP researchers reported that although typical field cooling rates seldom exceed $2.7^{\circ}\text{C}/\text{hr}$, most TSRST tests are done at cooling rates of $10^{\circ}\text{C}/\text{hr}$ or higher to reduce testing time (1). Tests conducted during SHRP showed a decrease in fracture temperature as the cooling rate varied between 1 to $5^{\circ}\text{C}/\text{hr}$, while the effect on tensile strength varied for different samples. They noted that previous researchers reported little or no effect on fracture temperature and tensile strength for cooling rates higher than $5^{\circ}\text{C}/\text{hr}$. They concluded that although these cooling rates do not necessarily match typical field conditions, they are sufficient to assess relative performance of specimens.

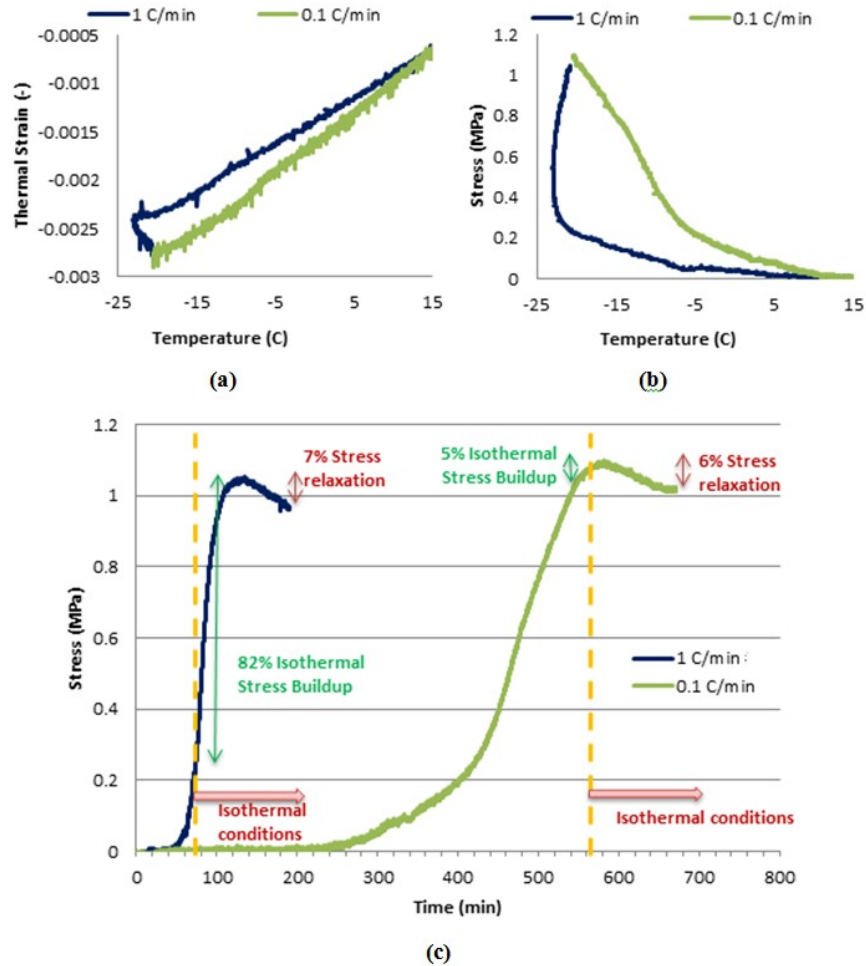


Figure 12.18: Comparison of thermal stress and strain during cooling and isothermal conditions at 0.1 and 1°C/min cooling rates

In this study, it is hypothesized that the observed isothermal behavior is due to the time-dependent nature of thermal contraction as temperature approaches the glass transition region. The complete explanation of the mechanism of glass transition and physical hardening is beyond the scope of this report and can be found in Bahia and Anderson (22), Tabatabaee et al. (25) and Bahia and Velasquez (11).

If cooling rate is sufficiently slow, the specimen has ample time to fully contract; but as the cooling rate increases, although core of samples can reach conditioning temperature, the amount of delayed contraction increases. The delayed contraction takes place over time after sample core reaches isothermal contraction, hence causing the specimen to buildup thermal stress while at a constant temperature. After sufficient time has passed, all samples will achieve full contraction, thus ultimately building up the same amount of thermal stress. This behavior is shown in Figures 12.18(a) and 12.18(b).

An important consequence of the observed behavior is that thermal stress will build up at slower rate during cooling if the cooling rate is high enough to not allow for complete contraction during the cooling period, as shown in Figure 12.18(c). Although at first glance this seems

counter intuitive, it must be pointed out that for sufficiently slow cooling rates in which full contraction is taking place during cooling, the trend will be opposite, as the slower cooling rates will allow for more thermal stress relaxation and consequently a lower rate of stress build up during cooling. It is important to note that relaxation and time-dependent strain happen continuously and simultaneously during thermal loading. Depending on the relative rate of these two competing phenomenon at any given time, temperature, and cooling rate, one or the other will be dominant. Thus, an increase in thermal stress will result when time-dependent strain is accumulating at a rate higher than the decreasing effect of modulus relaxation, and vice versa.

Another important observation made during isothermal conditioning of various mixtures is shown in Figures 12.19 and 12.20. It is observed that during isothermal conditions, mixture samples can reach a critical value of thermal stress that result in sample fracture. The importance of this observation becomes more apparent when considering that under continuous constant cooling these samples would not have built up this level of stress until temperatures well below the current fracture temperature. This experimental observation can explain discrepancy between predicted low temperature cracking temperatures and observed under- performance in the field, underscoring the importance of considering the potential of isothermal contraction and time-dependent strain in asphalt mixtures when selecting appropriate material for specific climatic conditions.

The possible effect of different levels of isothermal physical hardening of asphalt binders in mixtures was observed when comparing the performance of field sections constructed for the validation effort in Task 6. Mixtures prepared using asphalt binders of identical Superpave performance grades (i.e., PG 58-28) were used in the construction of Task 6 validation sections. After being exposed to identical climatic conditions, one of the sections was observed to have cracked two times more than the others. Although various performance tests failed to differentiate the asphalt binders significantly, physical hardening tests using both the Bending Beam Rheometer (BBR) for the asphalt binders and the ATCA for the mixture showed that one of the asphalt binders has considerably higher susceptibility to isothermal contraction than the others. This asphalt corresponds to the worse field performance, as indicated in Figure 12.21.

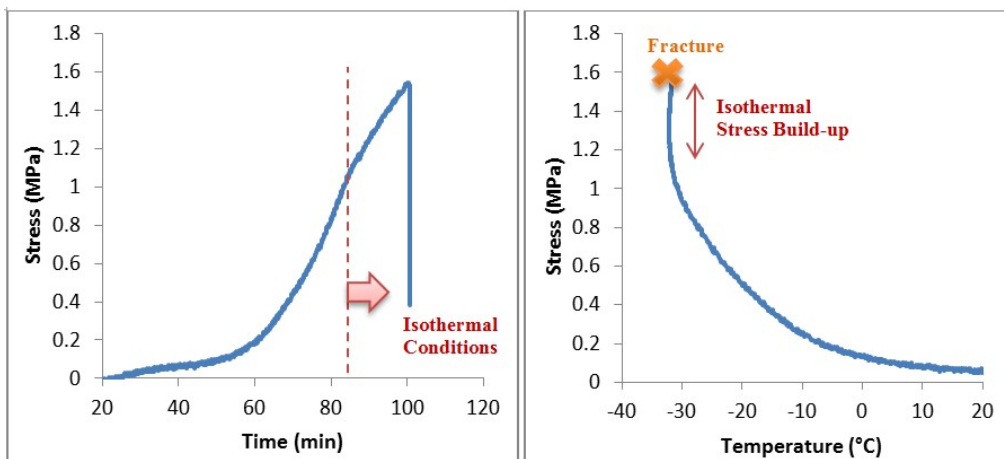


Figure 12.19: ATCA restrained beam fracture during isothermal conditions (MN County Road 112-Valero)

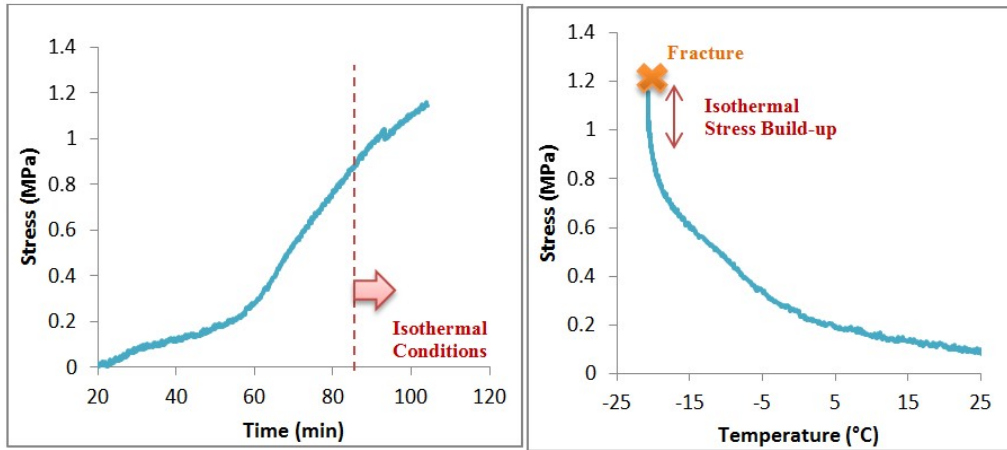


Figure 12.20: ATCA restrained beam fracture under isothermal conditions (MN County Road 112-CITGO)

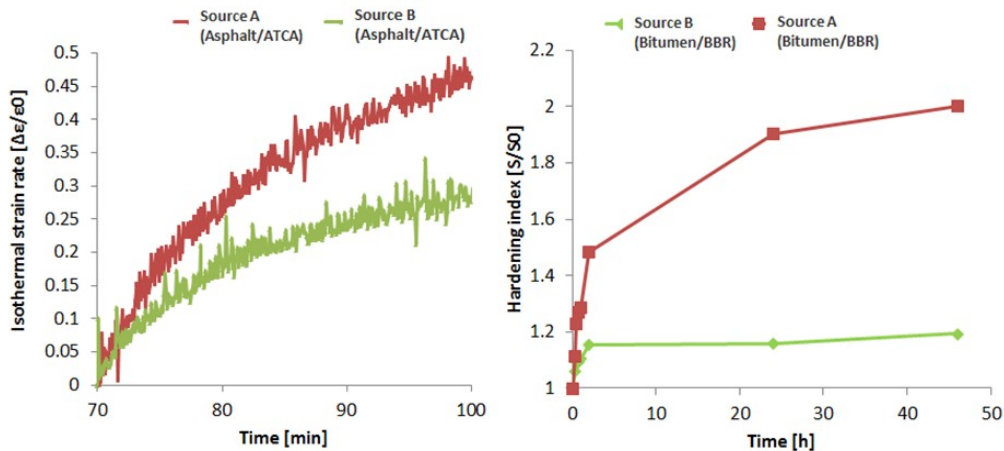


Figure 12.21: Comparison of physical hardening susceptibility of two asphalt binders of identical Superpave performance grades. The field section using mixture of source “A” cracked two times more than mixture of source “B”

The importance of the observed behavior in this section is its implications for the validity of the current method for thermal stress calculations. Currently, the prevalent method for thermal stress calculation is to use a restrained beam geometry for which the rate of potential thermal strain is calculated using appropriate coefficients of thermal contraction; and coupling this input with the calculated change of the relaxation modulus, to ultimately estimate the resulting stress in the specimen. The relaxation modulus in this method is a function of both loading time and temperature, thus accounting for stress relaxation in the viscoelastic material. On the other hand, thermal strain is assumed as only a function of temperature, thus the time dependency of the strain, especially when approaching the glass transition temperature is ignored. This assumption leads to a deviation from the true thermal stress build up as the temperature approaches the glass transition region. Such discrepancies have been noted by previous research when comparing experimental and calculated thermal stress, but have usually been attributed solely to the

unreliability of the relaxation modulus master curves or the coefficients of thermal contraction in this temperature range.

Micromechanical Simulation of Thermo-Volumetric Properties in Asphalt Mixtures – Objective 2

Introduction

Finite element modeling was used to develop a semi-empirical model to better estimate the coefficients of thermal contraction/expansion (CTEs) of asphalt mixtures. Also, modeling was used to investigate how the thermo-volumetric properties (i.e., CTEs and T_g) of the mastic (i.e., asphalt binder+ filler) is changed by the addition of large aggregate particles.

Dilatometric testing is used to obtain the glass transition behavior of the mastic and digital images of mixture specimens are used to represent the internal aggregate structure of the asphalt mixture. The finite element model developed in ABAQUS considers the mixture as a two-phase heterogeneous material (e.g., asphalt mastic and large aggregate). The simulations were used to assess the effect of volumetric fraction and microstructural properties of asphalt mixture (e.g., aggregate to aggregate contact length and number of contact zones) on the glass transition of the mixture. The results indicate that the aggregate structure plays an important role in controlling the coefficient of expansion/contraction above the transition (i.e., α_1). However, the coefficient of expansion/ contraction below T_g (i.e., α_g) was less affected by internal aggregate structure. The FE simulations indicated that it is possible to estimate the transition behavior measured with the ATCA from mastic glass transition and specific aggregate structure characteristics.

Background

As discussed in the previous section, one of the most important pavement material properties considered for the estimation of thermal cracking susceptibility is the coefficient of thermal expansion/contraction (CTE). Limited research has been conducted to accurately determine this property for both asphalt binders and mixtures (22, 26-30, 31-34). However, a considerable portion of thermal cracking behavior can be explained by studying the change in thermal coefficients of contraction for asphalt binders below, within, and above their glass transition temperature (35, 36).

Thermo-volumetric properties of the mixture are dependent on the thermal contraction coefficients of its main constituents: aggregate and asphalt binder (or more appropriately, the binder-filler mastic). It is important to note that the linear contraction coefficient of an asphalt binder may be up to 10 times that of the asphalt mix (26). The CTE of the asphalt binder is significantly different than the CTE of the asphalt mixture due to the volumetric fraction of its constituents, the very low CTE of the aggregates, and the internal structure of the mix.

Recently, research has shown that the properties of the aggregate skeleton may affect various aspects of the asphalt mixture performance, although this effect has not been studied with regards to the thermo-volumetric properties (37, 38). Thus, the main objective of this portion of the study was to determine the relationship between the thermal-volumetric properties of asphalt mixtures and the properties of its components such as the mastic's thermo-volumetric

parameters, mastic-mixture stiffness ratio, and the internal aggregate structure (e.g., number of aggregate to aggregate contact zones and contact length) (39).

Thermal Expansion/Contraction Coefficient of Composites

Asphalt mixtures can be treated as two phase composite materials consisting of a mastic (binder plus filler) and aggregate phase. There are several micromechanical methods associated with calculating the mean properties of a composite. Depending on the spatial configuration and phase interface condition, two extreme cases can be considered as the upper (Figure 12.22) and lower (Figure 12.23) bounds of the composite properties. All non-ideal composites, such as asphalt mixtures, will fall somewhere in between these two extremes cases.

Figures 12.22 and 12.23 can be used to deduce the equations for the coefficient of thermal expansion/contraction for the two ideal configurations (i.e., parallel and series) of a two-phase composite material. Figures 12.22 and 12.23 represent the composite material for the arithmetic and harmonic model, respectively.

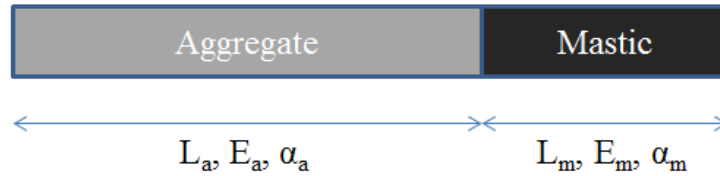


Figure 12.22: Composite under temperature shrinkage in x-direction (Case 1)

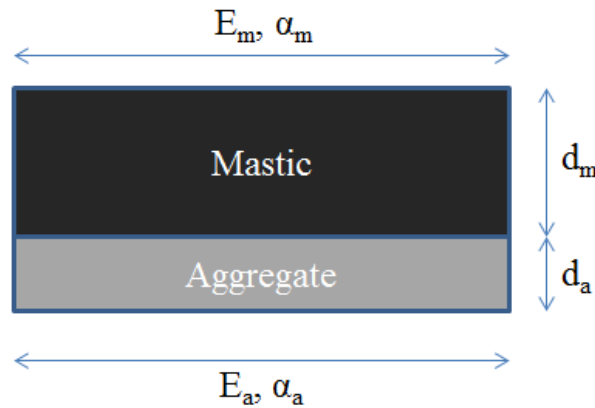


Figure 12.23: Composite under temperature shrinkage in x-direction (Case 2)

In Figures 12.22-12.23, the parameters L , d , E , and α are length, width, elastic modulus, and thermal coefficient of expansion, respectively. The effective thermal coefficient of expansion (CTE) of the composite material in these two extreme situations can be calculated using equilibrium and kinematic equations as follow:

Case 1:

$$\Delta l_c = \Delta l_a + \Delta l_m \rightarrow l_c \alpha_c \Delta T = l_a \alpha_a \Delta T + l_m \alpha_m \Delta T \rightarrow \alpha_c = \alpha_a \left(\frac{l_a}{l_c} \right) + \alpha_m \left(\frac{l_m}{l_c} \right) \quad [12.1]$$

It is defined that

$$\Phi_a = \frac{l_a}{l_c}, \Phi_m = \frac{l_m}{l_c} \quad [12.2]$$

Thus, the equivalent coefficient of thermal expansion in this case can be calculated with:

$$\alpha_c = \alpha_a \Phi_a + \alpha_m \Phi_m \quad [12.3]$$

Case 2:

$$\Delta l_c = \Delta l_a = \Delta l_m \rightarrow l \alpha_c \Delta T = l \alpha_a \Delta T + \frac{Fl}{d_a \cdot 1 E_a} = l \alpha_m \Delta T - \frac{Fl}{d_m \cdot 1 E_m} \quad [12.4]$$

By simplifying the above equation, the equivalent thermal coefficient of expansion of the composite can be calculated as

$$\alpha_c = \frac{d_a \alpha_a E_a + d_m \alpha_m E_m}{d_a E_a + d_m E_m} \quad [12.5]$$

By defining the following parameters we can rewrite the expression for the equivalent coefficient of expansion as follows:

$$\Phi_a = \frac{d_a}{d_c}, \Phi_m = \frac{d_m}{d_c} \quad [12.6]$$

Thus:

$$\alpha_c = \frac{\Phi_a \alpha_a E_a + \Phi_m \alpha_m E_m}{\Phi_a E_a + \Phi_m E_m} \quad [12.7]$$

It can be seen that in case 1, the mastic has the maximum contribution to the thermal contraction coefficient of the total mixture; on the other hand in case 2 its contribution is minimum.

Therefore, it can be said that Equation [12.3] is an upper bound and equation [12.7] is the lower bound for the thermal expansion/contraction coefficient of a two-phase composite material. The two calculated bounds can be used to check the results from the FE thermal analysis of the asphalt mixtures and to develop semi-empirical models for the estimation of CTE of mixtures.

General Description of FEM Simulation

The Finite Element (FE) analysis software ABAQUS was used to model asphalt mixtures undergoing thermal contraction and glass transition. A 4-node bilinear plane stress quadrilateral

and reduced integration element (i.e., CPS4R) was used in the simulations. Colored images of asphalt mixtures obtained using a flatbed scanner were converted to binary images using digital imaging processing techniques. The pixels in the binary image were mapped into CPS4R elements in the FE model using MATLAB.

The modulus of elasticity and Poisson's ratio for the aggregates used in the model were assumed to be 40 GPa and 0.3, respectively. The Poisson's ratio of the mastic is assumed to be constant with a value of 0.5. The imaging techniques and filters cannot accurately capture aggregate particles smaller than 1.18 mm, and therefore the mastic phase is considered to be a homogenous mixture of the fine aggregate particles dispersed in the binder phase.

The boundary conditions considered in the modeling are shown in Figure 12.24. The coefficient of expansion for the mastic was entered in 2°C increments of temperature starting from 0° and decreasing to -60°C. As the mastic reached the glass transition zone the coefficient of expansion/contraction was gradually decreased incrementally until settling at a lower constant "glassy" value. Thermo-volumetric properties for mastics used in the simulations were measured with the dilatometric system described earlier in this report. Adjustments were made for the effect of varying fine content in the mastics by assuming that an arithmetic model can be applied to the homogeneously dispersed fine particles in the binder matrix. A typical constant temperature-independent coefficient of expansion was used for the aggregate phase.

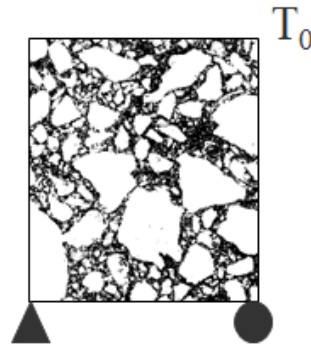


Figure 12.24: 2D asphalt mixture model showing the boundary conditions

More than 50 simulations were conducted to investigate the effect of the microstructure on the glass transition of the mixture. These simulations consisted of a number of idealized models with circular aggregates using different configurations and volume fractions, as well as many FE simulations using binary images of actual asphalt mixtures with various gradations and volume fractions.

Importance of Aggregate Structure on Thermal Properties of the Mixture

As the first step in developing the micromechanical models for thermo-volumetric properties of asphalt mixtures, it was decided to perform an initial investigation using an idealized mixture consisting of uniform round aggregates. The idealized geometry was used to isolate the effect of aggregate shape on the simulations.

Three mixtures with circular aggregate particles and the same volumetric fraction (i.e., 10 percent) but different internal structures were considered as shown in Figure 12.25.

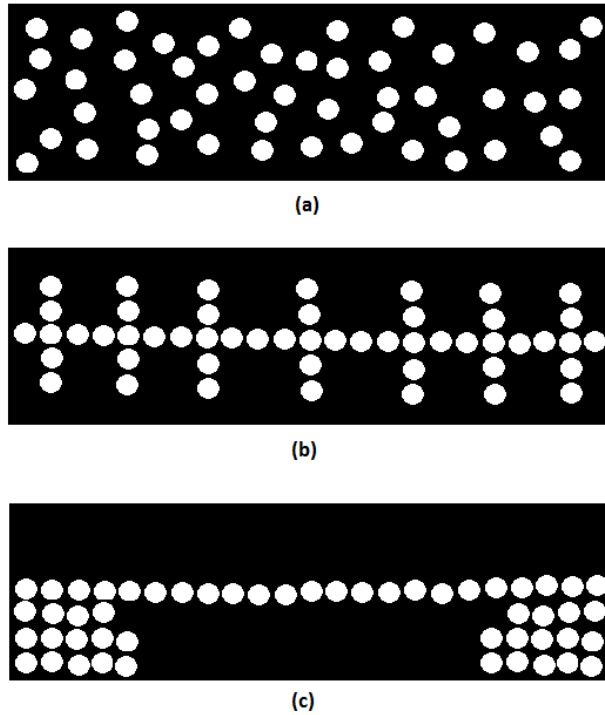


Figure 12.25: (a) Random structure (b) first structure (c) second structure

These artificial mixes were subjected to a reduction in temperature in ABAQUS using the boundary conditions in Figure 12.24. The results from these simulations are presented in Figure 12.26. As it can be seen, the thermal contraction coefficient (CTE) of the mixture decreased as the connectivity of the aggregates increased. This is thought to be due to the increase in aggregate connectivity interfering with the contraction of the mastic (i.e., continuous phase), causing a reduction in the overall thermal strain rate.

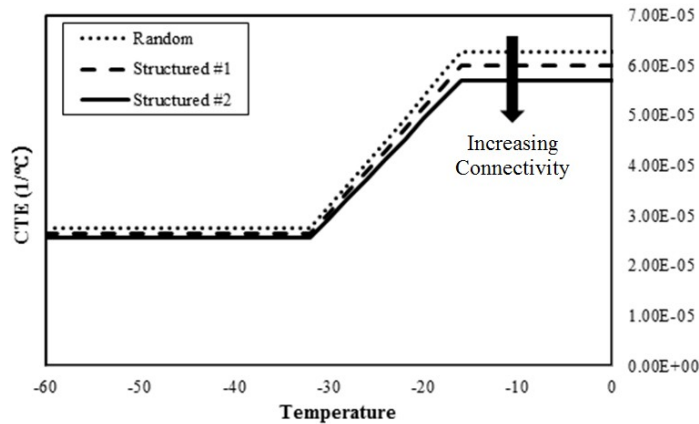


Figure 12.26: CTE versus temperature

Finite Element Modeling of Asphalt Mixture Binary Images

The simple model discussed in the previous section highlighted how the internal aggregate structure can be an important factor in the determination of the thermo-volumetric properties of the mixture. Different parameters which provide a good characterization of the internal aggregate structure of the mixture have been discussed in detail in the literature (39). For this research, the number of aggregate to aggregate contact zones, and the overall length of the aggregate to aggregate contact were selected as the representative parameters for the effect of microstructure on thermo-volumetric properties of the asphalt mixture. These parameters were calculated using iPas, a 2-D image analysis software under development by the University of Wisconsin-Madison and Michigan State University.

Different mixtures with different aggregate structures as shown in Table 12.4, and over a range of gradations covering most of the allowable range of gradations for a 12.5 mm nominal maximum aggregate size (NMAS) were used (Figures 12.27 and 12.28). Mastic properties were calculated based on dilatometric tests run on the binders shown in Table 12.1 (Figure 12.29).

Table 12.4: Microstructural analysis of mixtures

Mixture	No of Contact Zones	Volumetric Fraction of Large Aggregates (%)
Mix 1	886	58.8
Mix 2	831	60.2
Mix 3	914	60.3
Mix 4	770	59.5
Mix 5	975	59.7

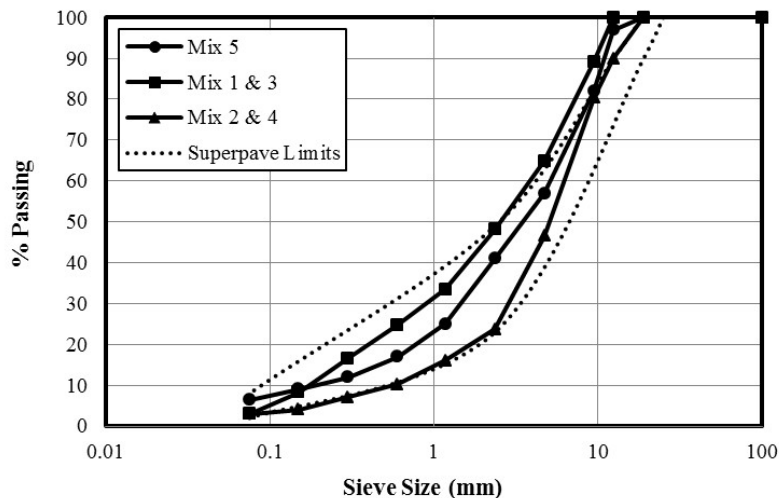


Figure 12.27: Gradation of mixtures for FEM

Figure 12.28 shows the binary images obtained from iPas for two of the analyzed mixtures having the highest and lowest number of aggregate contact zones, (i.e., connectivity).

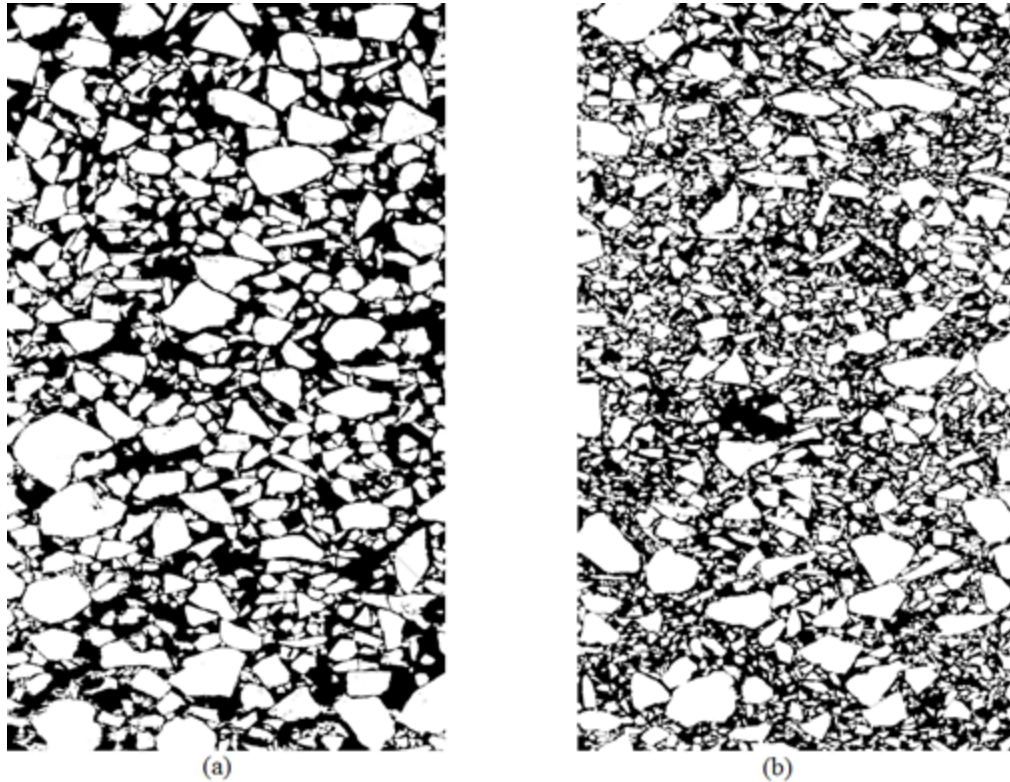


Figure 12.28: Binary representation of asphalt mixtures (a) lowest number of contact zones (b) highest number of contact zones

It is observed that the number of contact zones for a fine gradation is higher than that of a coarse gradation. Three different asphalt mastics with highly different CTE values and temperature dependency were used. The variation of the thermal contraction coefficients of these mastics as function of temperature is shown in Figure 12.29.

The stiffness vs. temperature curve was generated by using the assumption that a viscoelastic material follows a sigmoidal trend, with the main change in modulus happening during the glass transition zone, after which the modulus levels off to a constant glassy value. Thus, having the glass transition behavior for each mastic from the dilatometric test, a sigmoidal curve was fitted to BBR creep stiffness measurements at three temperatures, -12, -18, and -24°C, allowing for a good coverage of the modulus transition zone. Figure 12.30 shows the resulting curves.

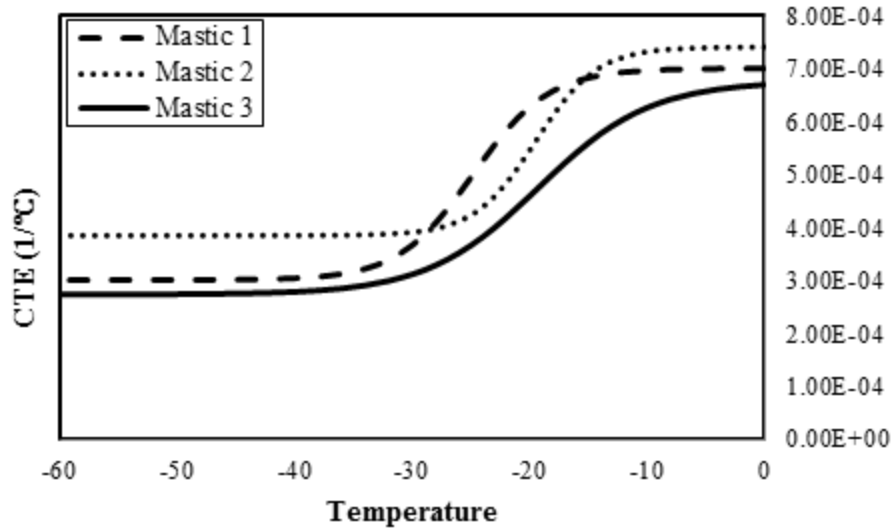


Figure 12.29: CTE of three different mastics

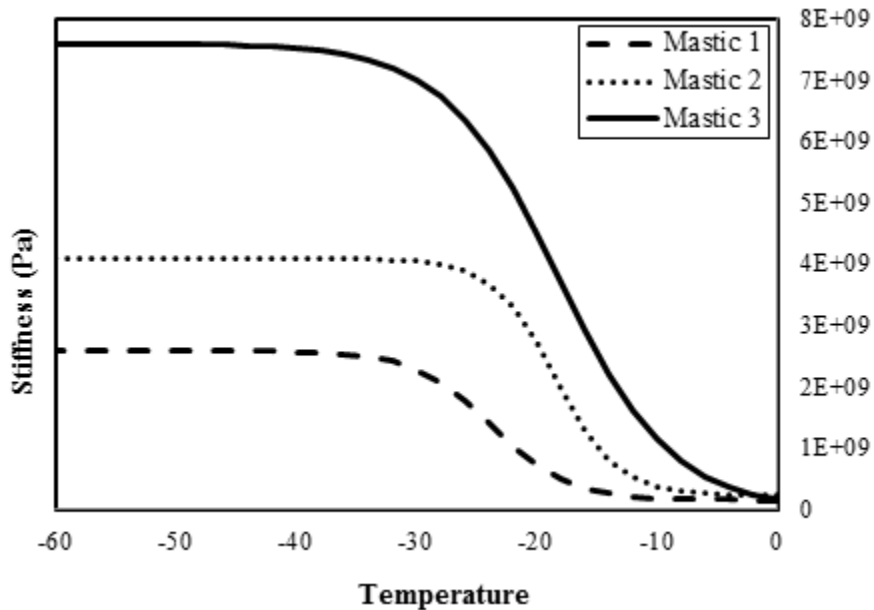


Figure 12.30: Stiffness of three different mastics

Using the CTE and modulus of mastics from Figures 12.29 and 12.30 as input, and knowing the volume fraction for the mastic and aggregate phases for each mixture, the ABAQUS model was used to estimate the thermal strain and to calculate the CTE for each mixture as temperature decreased.

Based on the number of aggregate to aggregate contact zones presented in Table 12.4, it can be concluded that increasing the number of contact zones generally will cause a reduction in the thermal contraction coefficient (CTE). Figures 12.31, 12.32, and 12.33 show the relation between contact points/zones and CTE below and above T_g . In these figures, α_1 and α_g have been

shown versus the number of contact zones for the three different mastics and five different mixtures considered. It is observed that there is a good correlation between the number of contact zones and α_l , and a fair correlation with α_g .

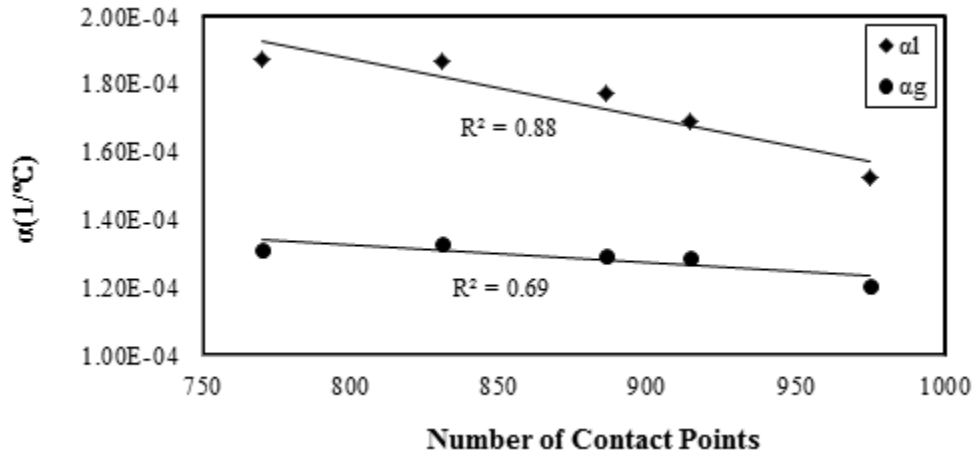


Figure 12.31: CTE vs. number of contact zones/points for mixtures with Mastic 1

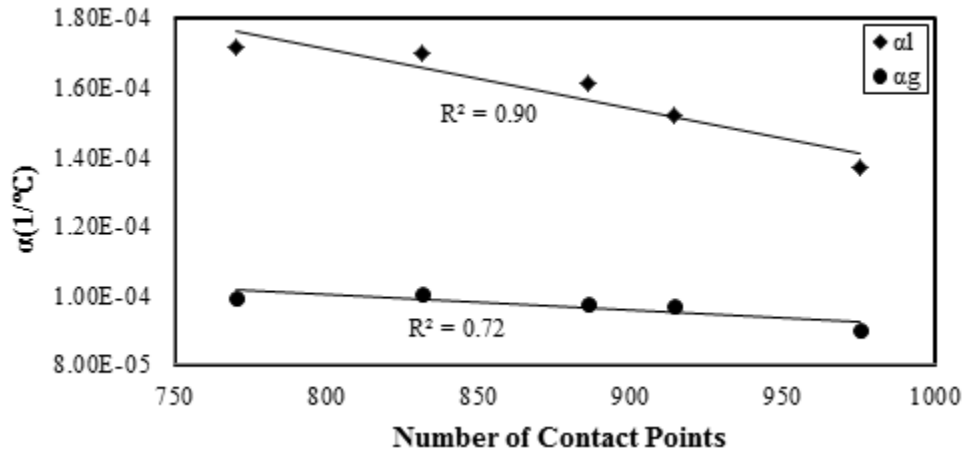


Figure 12.32: CTE vs. number of contact zones/points for mixtures with Mastic 2

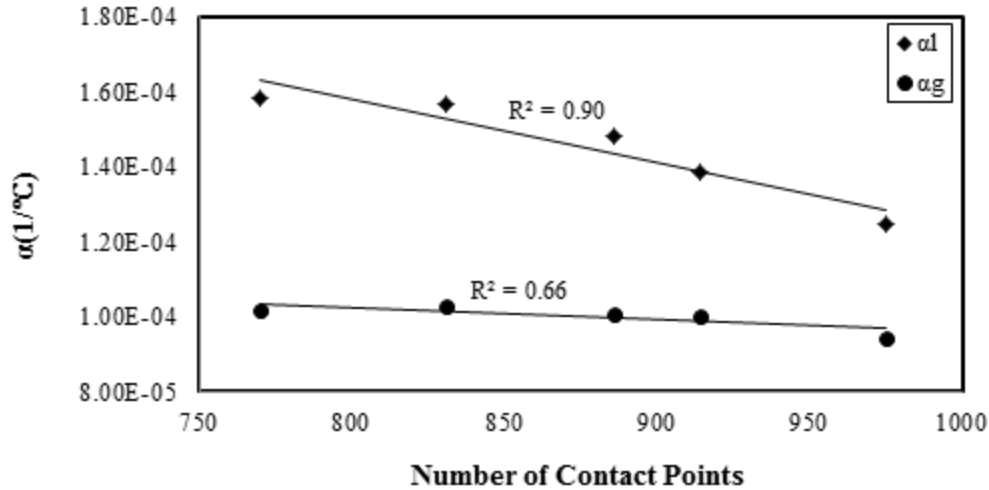


Figure 12.33: CTE vs. number of contact zones/points for mixtures with Mastic 3

Based on the simulations performed, it was observed that a decrease in the number of aggregate contact zones, which may implies a less effective aggregate skeleton structure, and an increase in the elastic modulus of the mastic phase will result in an overall increase in the level of contribution of the mastic phase in the total thermal contraction coefficient of the composite mixture.

Models for Estimation of α_l and α_g of Asphalt Mixtures

It has been observed based on the FE simulations, that other than the thermo-volumetric properties of the mastic phase and the volume fractions of each phase, the total coefficient thermal expansion/contraction of the mixture is also dependent on the internal structure of the aggregate skeleton.

In this section based on the aforementioned results, and relatively large number of additional FE simulations, a model is proposed for the approximation of the asphalt mixture α_l and α_g . The general structure of the model is based on the Hirsch model, which is commonly used for estimation of modulus of asphalt mixes. The proposed model assumes that the mixture CTE is a weighted average of the upper and lower theoretical bounds of the CTE. The theoretical bounds are calculated based on the volume fractions and moduli of each phase. An empirical weighting factor is used to show the contribution of each of the bounds to the total CTE as temperature changes. This empirical factor is dependent on the number of aggregate to aggregate contact zones in the mixture aggregate skeleton and on the mastic to aggregate stiffness ratio, which in turn is a function of temperature. The general form of the model is shown in Equation [12.8] and Equation [12.13] for the thermal contraction/expansion coefficient of the mixture above and below T_g , respectively.

$$\alpha_{mix}^L = \alpha_{up}^L F + \alpha_{low}^L (1 - F) \quad [12.8]$$

Where F is a function of internal aggregate structure, mastic stiffness, and α_l of the mastic.

$$F = (0.7 - 0.31\beta) * E_l^{100\alpha_l} \quad [12.9]$$

Where:

$$\beta = \frac{\text{Number of Contact Zones of the Mixture}}{770} \quad [12.10]$$

Where, β is a function that adjust the number of contact zones based on aggregate volume fraction and E_1 is the stiffness of the mastic before glass transition.

$$\alpha_{low}^L = \frac{\Phi_a \alpha_a E_a + \Phi_m \alpha_m E_m}{\Phi_a E_a + \Phi_m E_m} \quad [12.11]$$

Φ_a and Φ_m are the volumetric fraction of the aggregate and mastic, respectively.

$$\alpha_{up}^L = \alpha_a \Phi_a + \alpha_m \Phi_m \quad [12.12]$$

$$\alpha_{mix}^G = \alpha_{up}^G F + \alpha_{low}^{LG} (1 - F) \quad [12.13]$$

$$F = (0.98 - 0.29\beta) * E_g^{20\alpha_g} \quad [12.14]$$

Where, E_g and α_g are the stiffness and CTE of the mastic below glass transition, respectively.

Fifteen different mixtures were used to obtain the constants of the proposed semi-empirical model. Figures 12.34 and 12.35 showed the α_1 and α_g calculated using the optimized model constants versus the results obtained from the simulation in ABAQUS.

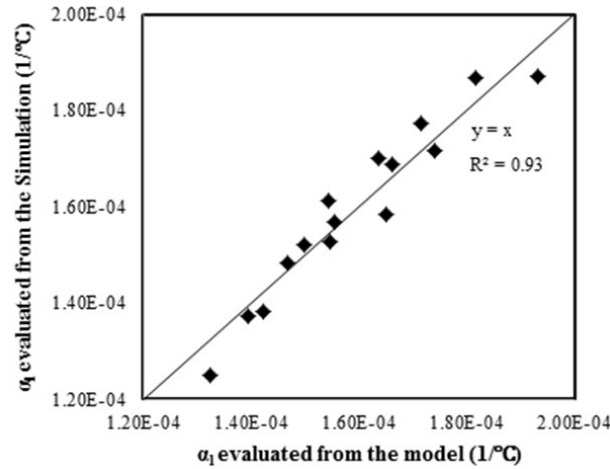


Figure 12.34: α_1 from FEM vs. prediction using proposed model

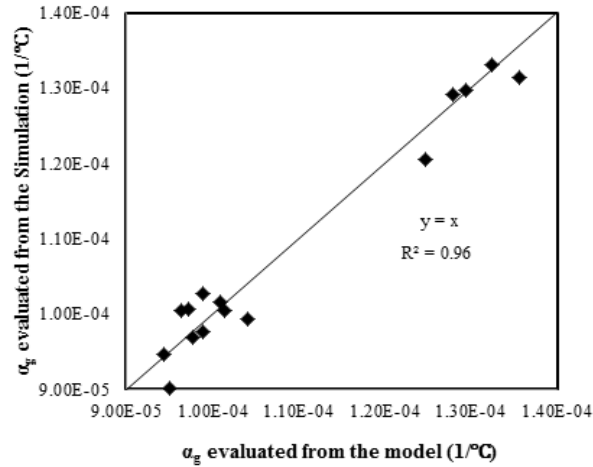


Figure 12.35: α_g from FEM vs. prediction using proposed model

To validate the proposed semi-empirical model, nine different mixtures with different aggregate structures and mastic properties were used. Note that these mixtures were not used in the calibration of the constants of the models. The calculated α_l and α_g for these nine different mixtures from the proposed model have been shown versus the results of simulations by ABAQUS (Figures 12.36 and 12.37).

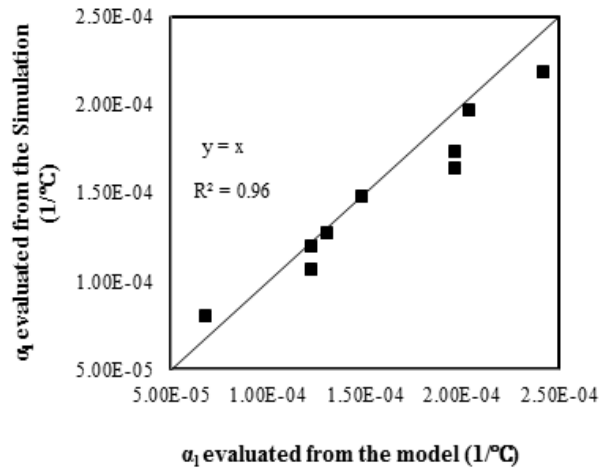


Figure 12.36: Comparison of α_l from FE simulations and using proposed model

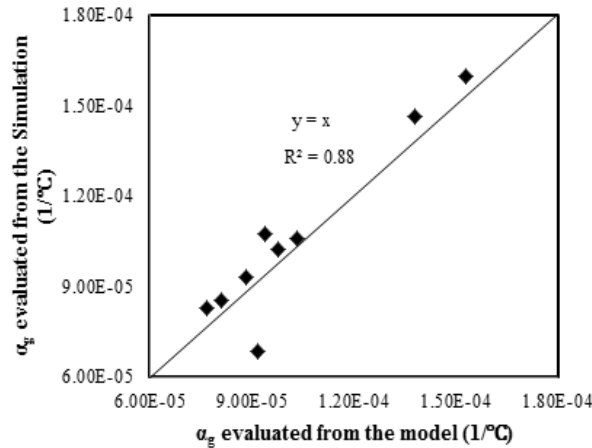


Figure 12.37: Comparison of α_g from FE simulations and using proposed model

Based on the results observed in Figures 12.36 and 12.37, it can be seen that the model performs relatively well for the estimation of the CTE of the mixtures in both the liquid and glassy phase. It must be noted that this model can only serve as an approximation of the mixture thermo-volumetric properties. The true value of such a model is its ability to take into account the mixture aggregate skeleton microstructure properties, the glass transition, and the stiffness ratios of the phases, for the estimation of the total CTE, rather than simply relying on the volume fractions of each phase, as it is commonly done in most applications such as the MEPDG.

Sensitivity Analysis of Thermo-Volumetric Parameters through Modeling (Objective 3)

Sensitivity analysis of thermo-volumetric properties was performed for eight parameters during cooling and heating. The width of glass transition region during cooling and heating was also considered as a potentially important parameter, thus it was added to the original 6 parameters considered in the work plan (T_g , α_l and α_g in cooling and heating).

The sensitivity analysis was performed using a thermal stress calculation framework recently developed at the University of Wisconsin-Madison (40). A theoretical approach for the calculation of thermal stress build-up in mixtures subjected to varying cooling and isothermal conditions was derived. The approach combines relaxation modulus master curves, the WLF equation for time-temperature superposition of thermo-rheological simple material, Boltzmann's superposition principle, and a sub-model describing the isothermal contraction of asphalt mixture as a continuous function of conditioning time and temperature.

The model uses a nonlinear thermo-volumetric curve with different T_g , α_l and α_g in cooling and heating. The model also includes the effect of time dependent strain on the thermal stress during cooling, isothermal conditioning, and heating. The model inputs are described in the following sections.

Model Input and Assumptions

Many methods exist to determine the relaxation modulus of asphalt material. Relaxation modulus master curves acquired from different methods may be used as required input for the thermal stress prediction model.

Thermo-Volumetric Behavior and Glass Transition of Asphalt Mixtures

Thermal stress calculations are based on the potential thermal strain of the mixture due to temperature differential. Thermal strain is measured directly for asphalt mixture beams using the ATCA device. The resulting strain may be plotted as a function of temperature and fitted using the formulation proposed by (5). The relationship is shown in equation [12.15].

$$\epsilon_{th} = \frac{\Delta l}{l_0} = C + \alpha_l(T - T_g) + \ln \left\{ \left[1 + e^{\frac{T-T_g}{R}} \right]^{R(\alpha_l - \alpha_g)} \right\} \quad [12.15]$$

Where:

- $\frac{\Delta l}{l_0}$ is the relative change of length, or thermal strain,
- C is an intercept with no physical meaning,
- α_l and α_g are the liquid and glassy coefficients of thermal contraction/expansion, and
- R is a parameter representing the curvature between the two linear asymptotes

The formulation fits two linear portions to the curves above a below the non-linear “glass transition” region, the slopes of which are defined as the liquid and glassy coefficients of thermal contraction/expansion (α_l and α_g). The temperature at the intersection of the two linear sections is defined as the glass transition temperature (T_g). The “R” parameter represents the “strength” of the transition, which is a measure of the difference of slopes before and after the transition as well as the length and curvature of the transition region. Equation [12.15] was used to predict thermal strain at any given temperature.

Physical Hardening in Asphalt Binders and Mixtures

A prediction model for the rate of physical hardening at different temperatures and conditioning times based on a creep viscoelastic model was used to account for the physical hardening strain in the thermal stress buildup. This model is described in great detail in (24) and presented in Task 2.

The model is based on concepts of rheological response of viscoelastic materials, postulating that the creep behavior at the molecular level is similar to the volume relaxation behavior observed in physical hardening. Thus, it is hypothesized that a modified creep expression, the Kelvin-voigt model, can be adjusted to explain physical hardening behavior. In such a model, strain or relative change in deflection (i.e., $\Delta l/l_0$), is replaced by relative change in volume, $\Delta V/V_0$, which according to the free volume concept is taken to be directly proportional to relative change in stiffness, or hardening rate ($\Delta S/S_0$). The change in stiffness (ΔS) is the difference in stiffness after conditioning time t_c and the initial stiffness, S_0 .

The “creep” behavior at isothermal conditions was considered to be induced by the excess of internal energy due to the deviation of the material from thermo-dynamic equilibrium within the glass transition region. Experimental data from the authors shows that the rate of physical hardening ($\Delta S/S_0$) peaks at the glass transition temperature, hereby denoted as T_g , and decreases toward zero as the temperature approaches the beginning and the end of the glass transition region. This is also supported by experimental data reported by Planche et al. (7). Thus a “stress” parameter based on the glass transition temperature, the relative position of the conditioning temperature from the glass transition temperature, and the length of the glass transition region was envisioned for the model. The loading time is the length of time the material is in not at thermo-dynamic equilibrium, or in other words, the conditioning time (t_c).

By implementing these changes into the Kelvin-Voigt creep model, Equation [12.16] is derived, and it is shown to fit the observed physical hardening behavior of a number of asphalt binders very well. A three-dimensional representation of the physical hardening as a function of conditioning time and temperature, is shown in Figure 12.38.

$$\epsilon_{PH} = \frac{e^{\frac{-9(T-T_0)^2}{(2x)^2}}}{G} \left(1 - e^{-t_c \frac{G}{\eta}}\right) \propto \frac{\Delta V}{V_0} \propto \frac{\Delta S}{S_0} \quad [12.16]$$

Where:

- $\frac{\Delta S}{S_0}$ is the hardening rate,
- T_0 is the peak temperature for hardening rate, assumed to be the T_g ($^{\circ}\text{C}$),
- T is the conditioning temperature ($^{\circ}\text{C}$),
- t_c is the conditioning time (hrs),
- $2x$ is the length of the temperature range of the glass transition region ($^{\circ}\text{C}$),
- G and η are model constants, derived by fitting the model.

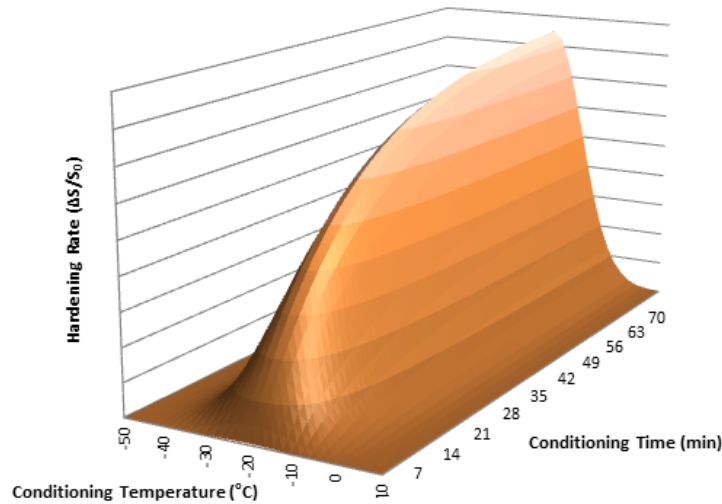


Figure 12.38: 3-D representation of the physical hardening model for a glass transition temperature of -20°C

The model parameters, G and η , are shown to be unique material parameters that remain constant at all conditioning times and temperatures. Thus, by fitting the model to data from a single conditioning temperature and having the T_g , one may predict the binder physical hardening at any other temperature or conditioning time.

Equation [12.16] is developed and verified using asphalt binder stiffness measurements with the BBR. Assuming that isothermal shrinkage is proportional to hardening, it is expected that the trend of physical hardening strain buildup in asphalt mixtures be similar to that of binders, but of a much smaller magnitude due to the relatively small volume of binder in the entire asphalt mixture. The trend of isothermal strain in an asphalt mixture measured with the ATCA is shown in Figure 12.39, in which Equation [12.16] was successfully fitted to the curve (Figure 12.39a). Since the measurements can only show the total response, the exact nature of the transformation between binder and mixture hardening is still under investigation, however initial tests measuring isothermal shrinkage and stiffness of asphalt mixture beams using the ATCA and BBR respectively, support the aforementioned assumptions.

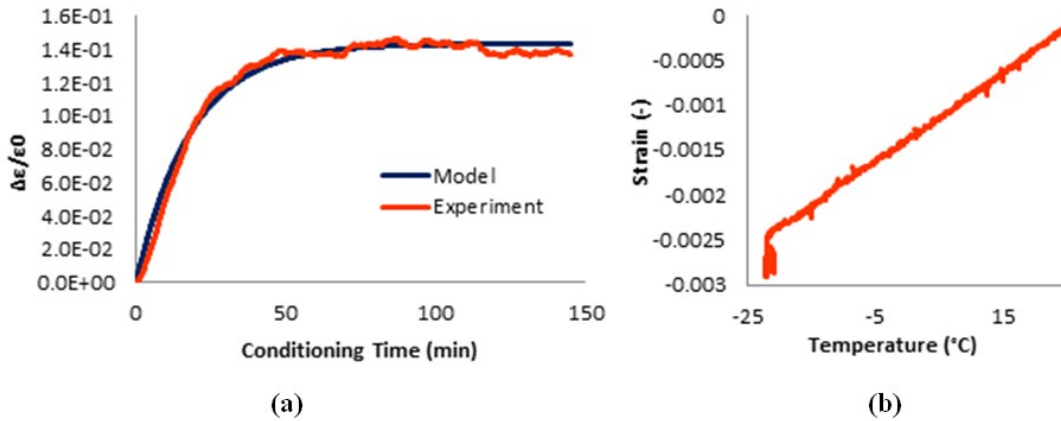


Figure 12.39: (a) Isothermal strain rate in asphalt mixture beam plotted against conditioning time, and (b) strain in the same asphalt mixture beam plotted against specimen temperature

Prediction of Thermal Stress Buildup and Relaxation

Thermal stress in a restrained beam of visco-elastic material is calculated using the following convolution integral (2, 9, and 40):

$$\sigma(t) = \int_0^t E(t - \xi) \frac{\partial \varepsilon(\xi)}{\partial \xi} d\xi \quad [12.17]$$

Where,

$\sigma(t)$ is stress as a function of time,

E is the relaxation modulus,

ε is thermal strain,

and ξ is reduced time.

The true nature of this integral is better understood if its broken down to a finite number of increments. The input thermal strain can be divided into small step increments for which the relaxation response can be easily computed and added in time to obtain the total thermal stress, according to Boltzmann's superposition principle. This concept is depicted in Figure 12.40.

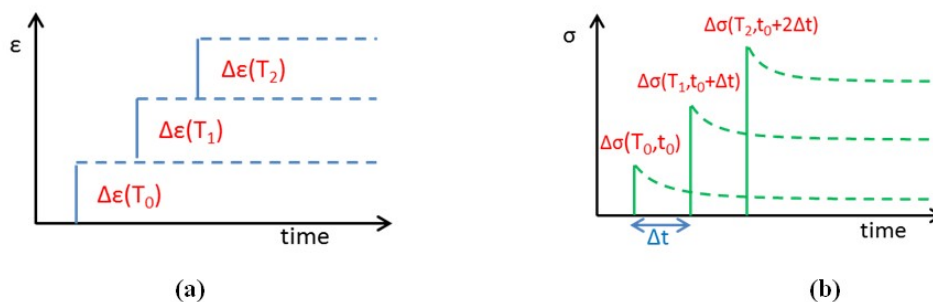


Figure 12.40: Concept of incremental stress buildup and relaxation in viscoelastic material

Following this logic, if at any point the temperature is held constant, stress in subsequent steps will only be the sum of the relaxing stresses in previous steps, thus will continue to decrease over time, since no additional stress can build up once temperature is held constant, the total stress will begin to decrease immediately due to relaxation. This expected behavior, however, is not observed in the ATCA experiments due to physical hardening and continued shrinkage at constant temperature. In the proposed model, the addition of a time-dependent strain to the temperature-dependent strain is shown to be able to describe stress buildup trends very similar to observations. This time-dependent strain term is applied to the aforementioned procedure by multiplying this term by the relaxed modulus at the corresponding loading time. The initially high rate of isothermal strain will result in a gradual isothermal stress buildup.

The rate of buildup will gradually decrease as the modulus further relaxes, ultimately resulting in a gradual stress relaxation. Figure 12.41 shows the effect of using a time-dependent strain term in the thermal stress build-up and relaxation.

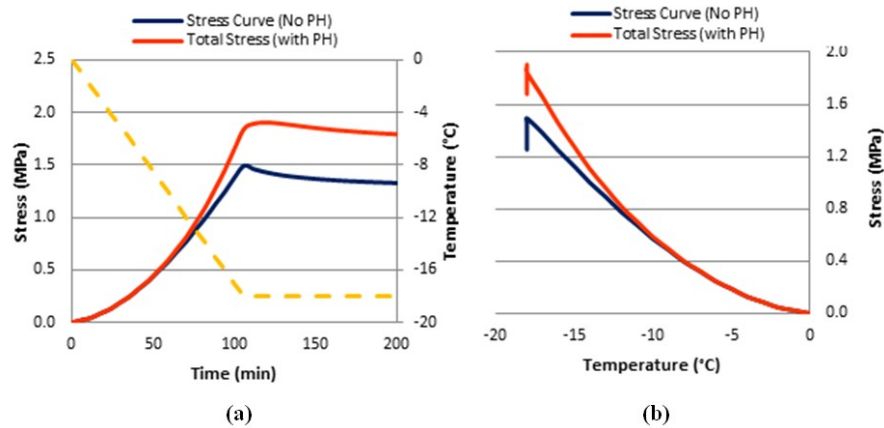


Figure 12.41: Thermal stress calculation with and without using time-dependent strain and accounting for physical hardening (PH) as a function of time (a), and temperature (b)

It can be seen in Figure 12.41 that the addition of the time dependent strain causes the stress buildup to deviate from the common calculation method as the temperature approaches the glass transition temperature. Furthermore, the stress does not immediately relax once temperature is held constant, but initially builds up and peaks isothermally, before gradually relaxing. Considering the time-dependent physical hardening improved the prediction of stress build up with time significantly.

In summary, the model for the calculation of thermal stress buildup in mixtures was derived using relaxation modulus master curves, the WLF equation for time-temperature superposition of thermo-rheological simple material, Boltzmann’s superposition principle, and a model describing the isothermal contraction of asphalt mixtures as a continuous function of conditioning time and temperature. The key idea behind this model is that the input thermal strain can be divided into small increments for which the relaxation response can be easily computed and added in time to obtain the total thermal stress.

Thermal stress buildup and relaxation tests were performed on selected asphalt mixtures to verify the accuracy of the proposed calculation scheme, and to show the influence of binder physical

hardening on mixtures stress history. The tests were done at 0.1 and 1 °C/min cooling rates and held isothermally for periods ranging from 1 to 10 hours, during which the stress and strain in the beams were continuously monitored. Figure 12.42 show experimental results of beams cooled to the temperature of -20°C, at which they were kept isothermally.

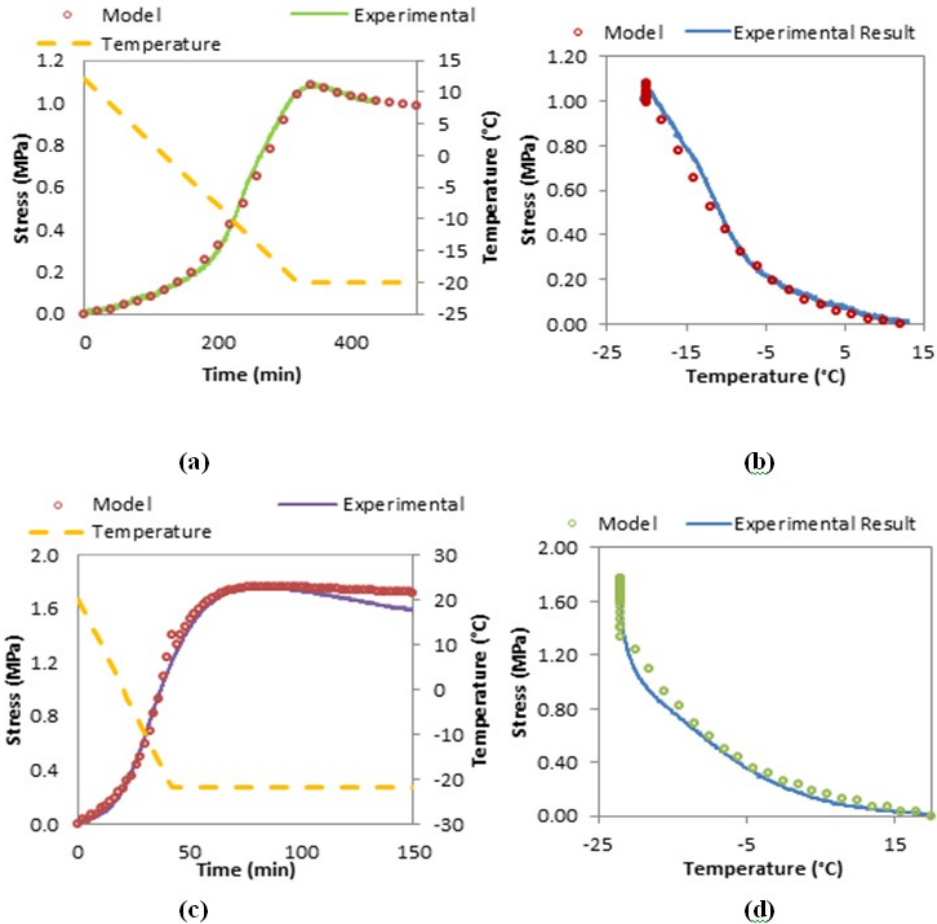


Figure 12.42: Calculated and measured thermal stress buildup plotted against time and temperature at cooling rates of 0.1°C/min (a, b) and 1°C/min (c, d)

In Figures 12.42(a) and 12.42(b) at the cooling rate of 0.1°C/min no sudden isothermal stress buildup is observed. On the other hand, when the rate was increased to 1°C/min (Figures 12.42(c) and 12.42(d)), it can be seen that a significant amount of stress buildup occurs during isothermal conditions due to delayed time-dependent strain. This behavior is reflected in the analytical calculation. It is seen that a very good agreement between experimental and calculated results exists.

Sensitivity Analysis

A sensitivity analysis of thermal stress to eight thermo-volumetric parameters during cooling and heating was performed. The width of glass transition region during cooling and heating was also considered as a potentially important parameter, thus a parameter describing the transition width

(R) was added to the six parameters originally considered (T_g , α_l and α_g in cooling and heating). These parameters were defined earlier, following Equation [12.15].

Parameter values for a typical mixture were used as a baseline. The parameters were then systematically varied by $\pm 20\%$ to capture the sensitivity of the parameters on thermal stress buildup in the mixture. The 20% variation was selected as the maximum percentage of change allowable to keep all parameters in a realistic and practical range. Tables 12.5 and 12.6 show the analysis matrix and the values used in this study.

Table 12.5: Analysis matrix used for the sensitivity analysis

		Run 1	Run 2	Run 3	Run 4	Run 5	Run 6	Run 7	Run 8	Run 9	Run 10	Run 11	Run 12	Run 13	Run 14	Run 15	Run 16	Run 17
Cooling	Tg	1	1.2	0.8	1	1	1	1	1	1	1	1	1	1	1	1	1	1
	R	1	1	1	1.2	0.8	1	1	1	1	1	1	1	1	1	1	1	1
	α_l	1	1	1	1	1	1.2	0.8	1	1	1	1	1	1	1	1	1	1
	α_g	1	1	1	1	1	1	1	1.2	0.8	1	1	1	1	1	1	1	1
Heating	Tg	1	1	1	1	1	1	1	1	1	1.2	0.8	1	1	1	1	1	1
	R	1	1	1	1	1	1	1	1	1	1	1	1.2	0.8	1	1	1	1
	α_l	1	1	1	1	1	1	1	1	1	1	1	1	1	1.2	0.8	1	1
	α_g	1	1	1	1	1	1	1	1	1	1	1	1	1	1	1	1	1.2

Table 12.6: Parameter values used for the sensitivity analysis

		Run 1	Run 2	Run 3	Run 4	Run 5	Run 6	Run 7	Run 8	Run 9	Run 10	Run 11	Run 12	Run 13	Run 14	Run 15	Run 16	Run 17
Cooling	Tg	-17	-20	-13	-17	-17	-17	-17	-17	-17	-17	-17	-17	-17	-17	-17	-17	-17
	R	6	6	6	7	5	6	6	6	6	6	6	6	6	6	6	6	6
	α_l	5E-5	5E-5	5E-5	5E-5	5E-5	6E-5	4E-5	5E-5	5E-5	5E-5	5E-5	5E-5	5E-5	5E-5	5E-5	5E-5	5E-5
	α_g	1E-5	1.3E-5	9E-6	1E-5													
Heating	Tg	-17	-17	-17	-17	-17	-17	-17	-17	-17	-20	-13	-17	-17	-17	-17	-17	-17
	R	6	6	6	6	6	6	6	6	6	6	6	7	5	6	6	6	6
	α_l	5E-5	5E-5	5E-5	5E-5	5E-5	5E-5	6E-5	4E-5	5E-5	5E-5							
	α_g	1E-5	1E-5	1E-5	1E-5	1E-5	1E-5	1E-5	1E-5	1E-5	1.3E-5							

Figures 12.43(a-d) show the results of thermal stress calculations for a mixture cooled at $1^\circ\text{C}/\text{min}$ from 10 to -22°C and then held isothermally for 180 minutes before being heated back up to 10°C at the same rate. The stress calculations were made both with and without taking time-dependent strain into account (i.e., solid and dotted lines respectively).

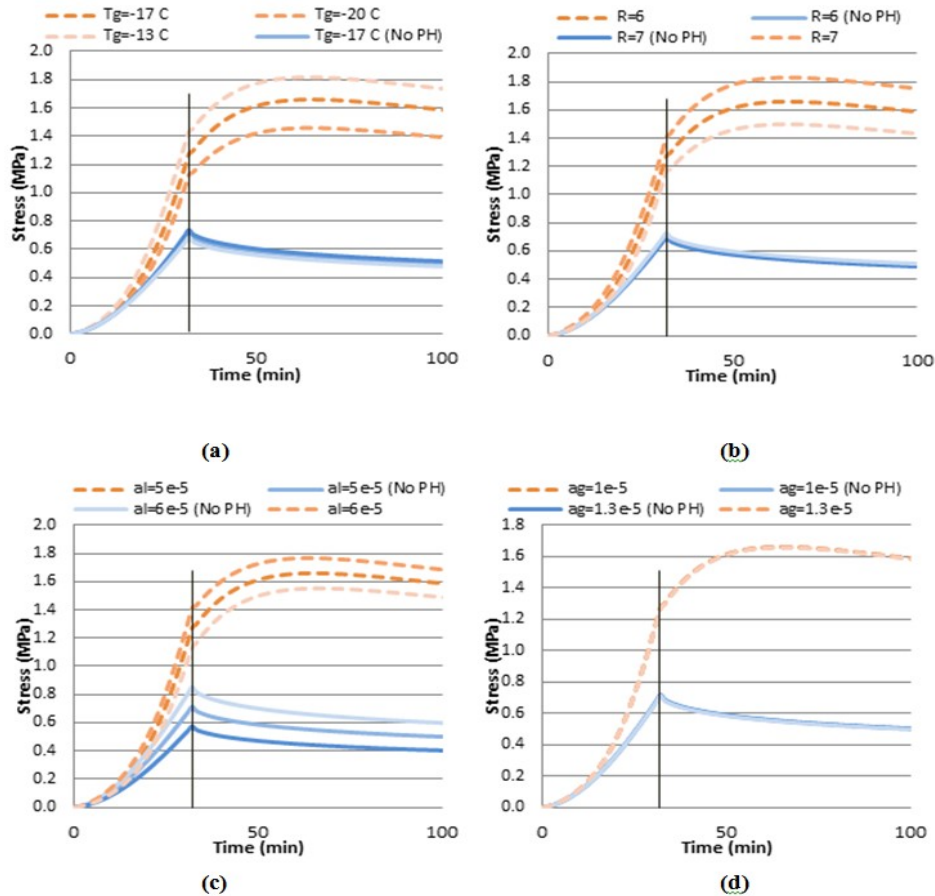


Figure 12.43: Sensitivity analysis of calculated mixture stress buildup with and without accounting for physical hardening, by changing (a) T_g , (b) R , (c) α_l , and (d) α_g

A qualitative analysis of Figure 12.43 shows that changing α_l has the most effect on the thermal stress buildup during cooling, when not accounting for physical hardening, while changing the glass transition temperature and the related parameters (α_l and R) did not show significant effects. On the other hand, the stress sensitivity to T_g and R increased significantly when accounting for the physical hardening. These variations are shown in Figure 12.44 by plotting the thermal stress buildup for every condition, normalized to the initial unchanged state of the parameters.

A noteworthy trend in Figure 12.44 can be seen when comparing the T_{g+} and T_{g-} conditions to the base condition. If no time-dependent strain (physical hardening) is considered in the stress calculations, a higher T_g would simply lead to the CTE value reducing from α_l to α_g at higher temperatures, thus less subsequent stress buildup will be calculated for any given temperature below the T_g . As mentioned earlier, for the calculation of physical hardening it is assumed that the rate of time dependent strain increases as the temperature approaches the T_g , from both sides. Thus, if physical hardening is considered in the stress calculation, increasing the T_g would also mean that time dependent strain accumulate at a higher rate at higher temperatures, potentially resulting in a higher stress buildup in the sample, as seen in Figure 12.44.

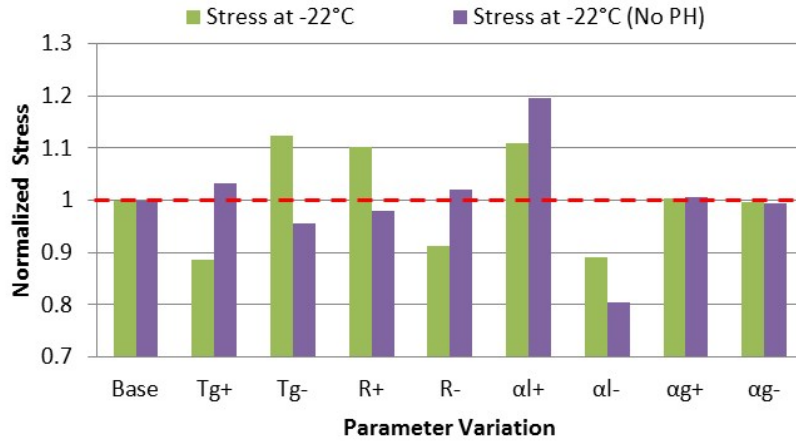


Figure 12.44: Variation of thermal stress at -20°C, by changing thermal parameters by ±20% (X± shown in the chart indicates that parameter X has been changed by ±20%)

The glassy coefficient of expansion/contraction (α_g) did not significantly affect thermal stress calculations. Subsequent tests at -30, -40, and -45°C did not show any significant effect from changing α_g . This observation does not indicate the unimportance of considering α_g . This fact is highlighted in Figures 12.45(a, b), in which the thermal stress is calculated in three methods: a. using full strain-temperature curve considering glass transition, b. using a constant CTE equal to α_l , and c. using a constant CTE equal to the average of α_l and α_g for all temperatures. It can be seen that the simplifying assumptions made for the CTE lead to more than 25% difference in the total accumulated thermal stress at -30°C. On the other hand, the thermal stress insensitivity to changes in α_g observed in Figure 12.43(d) would indicate that using a typical value for α_g may be sufficient for thermal stress calculation, and measurement of an exact α_g may not be necessary.

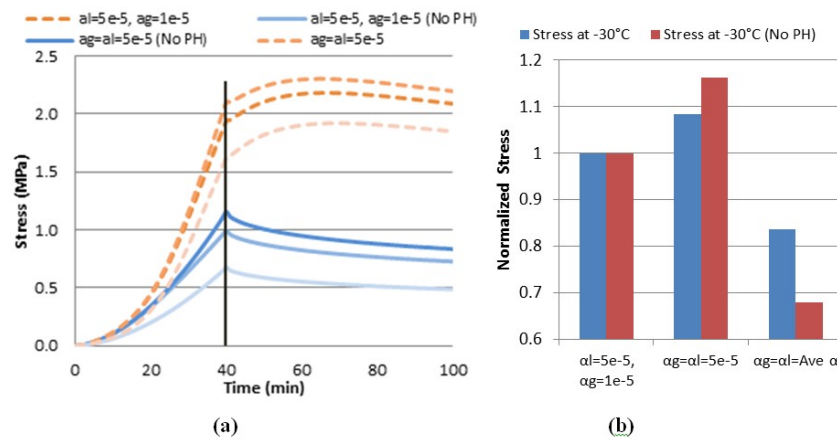


Figure 12.45: Comparison of effect of different assumptions for CTE on (a) thermal stress curves, and (b) stress at -30°C normalized to stress at when both α_l and α_g are considered

Using the model, the CTEs and Tg in the heating phase were also varied by ±20% and compared in Figure 12.46. It can be seen that the variation of the α_l , followed by the variation of Tg, had the highest effect on the rate of thermal stress reduction as the sample is heated back up to the initial temperature, while little sensitivity was observed to the R and α_g parameters. As indicated

by the overall small level of change for thermal stress for all parameters during heating, the importance of experimentally measuring actual parameter values for this range seems to be minimal, indicating the possibility of using typical average values for this range.

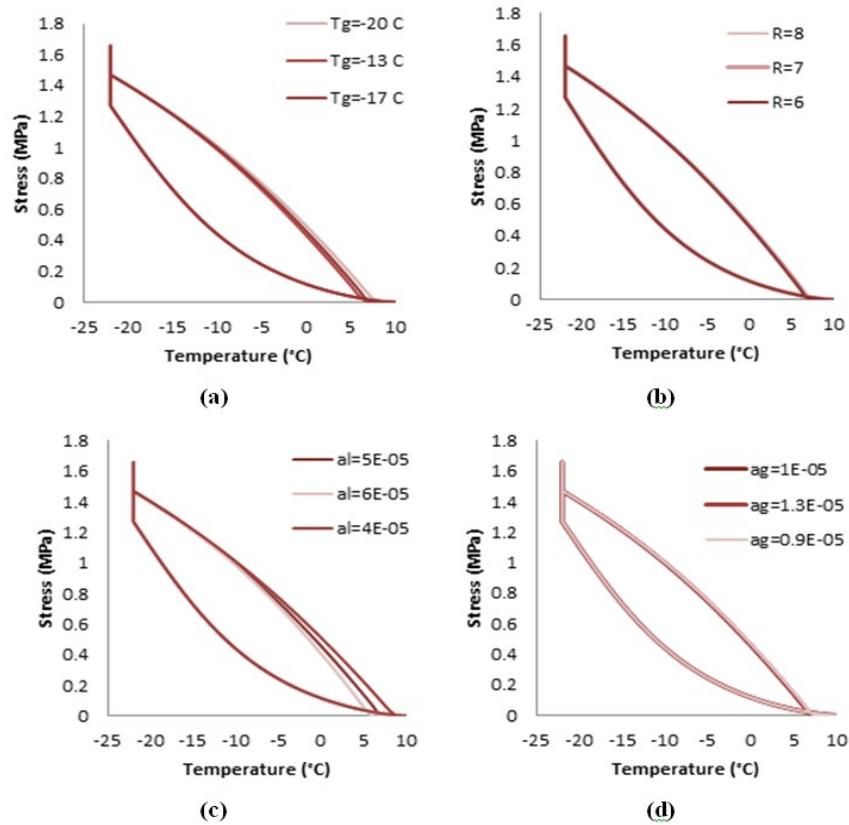


Figure 12.46: Sensitivity analysis of calculated mixture stress reduction during heating with and without accounting for physical hardening, by changing (a) T_g , (b) R , (c) a_l , and (d) a_g

Summary of Findings and Conclusions

Conclusions

The primary objectives of Task 5 were to: (1) expand the database developed in Phase I for thermo-volumetric properties of asphalt binders and mixtures to a wider range of modified asphalts and types of mixtures, (2) develop a micromechanical numerical model that can be used to estimate coefficients of thermal contraction/expansion of mixtures from variables commonly measured for binder grading and for mixture design, and (3) conduct thermal cracking sensitivity analysis to determine which of the glass transition parameters are statistically important for cracking, which ones need to be measured, and the effect of using estimated values rather than measured values. To address these objectives a comprehensive experimental and modeling investigation on the contraction and expansion of asphalt mixtures due to thermal cycles was completed. The experimental effort used the recently developed Asphalt Thermal Cracking Analyzer (ATCA) to investigate thermal stress buildup during cooling and the subsequent reduction during heating of MnROAD mixes. The thermal cracking sensitivity analysis of the glass transition parameters was conducted based on a calculation model experimentally validated

to account for temperature and time-dependent strain (i.e., physical hardening) effects. Based on the analysis of results the following notable conclusions are derived:

- The liquid phase CTE (α_l) and the glass transition temperature (T_g) showed the most influence on the rate and trend of thermal stress buildup; the later becoming more prominent when accounting for the time dependency of strains in the glass transition region. Generally, an asphalt mixture with lower liquid CTE and T_g is expected to accumulate less thermal stress during a cooling cycle, and thus has the potential to be less susceptible to thermal cracking.
- Almost all published thermal cracking models, including those used in the Mechanistic Empirical Pavement Design Guide (MEPDG), use a default value for CTE or a formula derived empirically based on testing a relatively small set of mixtures. The only justification for this over-simplification is the lack of a proper experimental device to measure CTE of asphalt mixes as a function of temperature. In this Task, results indicate that using the assumption of a constant value for CTE estimated from the MEPDG model can lead to significant error (up to 25%) in calculation of thermal stress and strain in asphalt mix exposed to a cooling cycle between 10 and -30°C .
- The limited sensitivity of thermal stress to changes in magnitude of α_g indicates the possibility of using a typical value for α_g in place of experimental measurements. Therefore, thermal cracking modeling can include a simplified glass transition model.
- Overall, it is concluded that accurate calculation of thermal stress during cooling is not possible without reliable measures of the α_l , T_g , and the transition rate near the T_g . A database of these parameters for typical mixtures used in Minnesota is available to designers and DOT personal for proper estimation of thermal cracking. It is recommended that these values be used in place of the estimated values in MEPDG.
- Thermal expansion coefficient of the asphalt mixture is strongly dependent on the elastic modulus of its constituents and the variation of the mastic-aggregate stiffness ratio as temperature varies.
- In this study it was shown that the CTE has a notable dependency on the internal aggregate structure. It is observed that there is a good correlation between number of contacts zones and α_l of the mixture and a model has been proposed to evaluate this term based on micromechanical properties of the mixture. Also it has been shown that for temperatures below T_g the effect of the microstructure on the thermal expansion/contraction coefficient is not significant. Generally, asphalt mixtures with high connectivity (i.e., high number of contact zones) have lower liquid CTE and consequently their thermal stress and deformation potential is lower.
- A semi-empirical model based on the Hirsch model has been proposed to estimate CTE of asphalt mixtures below and above T_g . The model takes into account the aggregate skeleton microstructure, the glass transition, and the stiffness ratios of the phases, for the estimation of the total CTE, rather than simply relying on the volume fractions of each phase.

Recommendations and Potential Applications for DOTs

Most of the thermal cracking models/tools (e.g., MEPDG) available to transportation agencies and contractors consider Relaxation Modulus/Creep Compliance and Fracture Properties (i.e., K_{IC} and G_f) as the most important properties driven thermal cracking performance and

consistently assume simple linear CTE for asphalt materials while ignoring glass transition change. However, CTE of asphalt materials are non-linear function of temperature and its impact on low temperature performance can be as important as the aforementioned properties. These assumptions are believed to cause serious errors in estimating thermal stresses. The findings from this Task can be used to:

- Modify thermal stress estimation model in ILLI-TC by using more realistic values for CTE above glass transition and inclusion of T_g .
- Select proper CTE values either from typical experimental results obtained in this Task with the Asphalt Thermal Cracking Analyzer (ATCA) or from the micromechanical model proposed (i.e., CTE of mix is function of aggregate skeleton microstructure, the glass transition, and the stiffness ratios of the phases). Use these values in MEPDG or current version of ILLI-TC for better prediction of thermal cracking.
- Conduct testing of a wider range of mixtures for thermo-volumetric properties using the recently developed ATCA to enhance the CTE and T_g database.

Chapter 13. Validation of New Specification

Introduction

Based on the work performed in Task 3, the Disc-Shaped Compact Tension (DC(T)) was selected for further validation. Eleven mixtures used in pavement sections constructed in Olmsted County (Minnesota) during the 2006 construction season, were selected for the analysis part of the validation process, see Table 13.1.

Table 13.1: Asphalt mixtures used in Task 6

Location	Construction date	Binder Grade	Description
Olmsted Co Rd 104	July 2007	PG 58-28 RAP	Warm Mix (w/RAP & antistrip)
Olmsted Co Rd 112	August 2006	PG 58-28	WRI-Mathy Study (Citgo, 12.5 mm)
Olmsted Co Rd 112	August 2006	PG 58-28	WRI-Mathy Study (Citgo, 19 mm)
Olmsted Co Rd 112	August 2006	PG 58-28	WRI-Mathy Study (Marathon, 12.5 mm)
Olmsted Co Rd 112	August 2006	PG 58-28	WRI-Mathy Study (Marathon, 19 mm)
Olmsted Co Rd 112	August 2006	PG 58-34 RAP	WRI-Mathy Study (MIF, 12.5 mm)
Olmsted Co Rd 112	August 2006	PG 58-34	WRI-Mathy Study (MIF, 12.5 mm)
Olmsted Co Rd 112	August 2006	PG 58-34 RAP	WRI-Mathy Study (MIF, 19 mm)
Olmsted Co Rd 112	August 2006	PG 58-34	WRI-Mathy Study (MIF, 19 mm)
Olmsted Co Rd 112	August 2006	PG 58-28	WRI-Mathy Study (Valero, 12.5 mm)
Olmsted Co Rd 112	August 2006	PG 58-28	WRI-Mathy Study (Valero, 19 mm)

Three mixtures (Warm Mix, MIF 12.5 mm, and MIF 19 mm) contained RAP. Asphalt binder PG 58-28 was used in the majority of the mixtures except in the mixtures denominated MIF. For these latter mixtures, asphalt binder PG 58-34 was used. For all mixtures except Warm Mix, two different aggregate sizes, Nominal Maximum Aggregate Size (NMAS) 12.5 mm and 19 mm, were considered.

Due to difficulties in compacting 4% mixtures, only specimens with 7% air voids were prepared and tested. To make up for the reduction in testing effort, Semi-Circular Bend (SCB) specimens were also prepared and tested. Testing of the samples was performed at two different test temperatures corresponding to the asphalt binders' PG low temperature limit (PGLT) and 10°C above the PG low temperature limit (PGLT+ 10°C).

Considering three test replicates for each test configuration and condition, a total of 132 samples were tested in this study. The SCB and DC(T) tests were conducted, respectively, at the University of Minnesota (UMN) and University of Illinois Urbana-Champaign (UIUC).

Test results

A summary of the DC(T) results is presented in Table 13.2 and Table 13.3. The G_f values ranged from 174 J/m² to 375 J/m². The COV values were generally lower than 30%, except in two cases.

Table 13.2: DC(T) fracture energy for mixtures tested at PGLT+10°C

Mixture	Binder PG	Temp °C	G_f [J/m ²]		
			Rep.	Mean	COV
Warm Mix	58-28	-18	340.00	288.00	26%
			236.00		
			N/A		
Citgo_ 12.5mm	58-28	-18	311.00	313.50	1%
			316.00		
			N/A		
Citgo_ 19mm	58-28	-18	316.00	308.00	4%
			300.00		
			N/A		
Marathon_12.5mm	58-28	-18	406.00	333.00	21%
			329.00		
			264.00		
Marathon_ 19mm	58-28	-18	327.00	315.67	12%
			348.00		
			272.00		
MIF_ RAP_12.5mm	58-34	-24	288.00	297.67	3%
			299.00		
			306.00		
MIF_12.5mm	58-34	-24	349.00	367.67	8%
			354.00		
			400.00		
MIF_RAP_19mm	58-34	-24	281.00	290.33	9%
			271.00		
			319.00		
MIF_19mm	58-34	-24	358.00	365.67	2%
			364.00		
			375.00		
Valero_12.5mm	58-28	-18	327.00	376.67	21%
			468.00		
			335.00		
Valero_19mm	58-28	-18	261.00	278.00	25%
			354.00		
			219.00		

Table 13.3: DC(T) fracture energy for mixtures tested at PGLT

Mixture	Binder PG	Temp °C	G _f [J/m ²]		
			Rep.	Mean	COV
Warm Mix	58-28	-28	208.00	224.50	10%
			241.00		
			N/A		
Citgo_ 12.5mm	58-28	-28	238.00	234.33	2%
			229.00		
			236.00		
Citgo_ 19mm	58-28	-28	152.00	233.33	39%
			333.00		
			215.00		
Marathon_ 12.5mm	58-28	-28	240.00	249.00	24%
			314.00		
			193.00		
Marathon_ 19mm	58-28	-28	237.00	210.00	11%
			193.00		
			200.00		
MIF_ RAP_ 12.5mm	58-34	-34	206.00	201.00	14%
			170.00		
			227.00		
MIF_ 12.5mm	58-34	-34	262.00	251.67	9%
			267.00		
			226.00		
MIF_ RAP_ 19mm	58-34	-34	183.00	178.00	12%
			154.00		
			197.00		
MIF_ 19mm	58-34	-34	230.00	209.67	41%
			115.00		
			284.00		
Valero_ 12.5mm	58-28	-28	338.00	284.33	16%
			253.00		
			262.00		
Valero_ 19mm	58-28	-28	123.00	174.00	30%
			173.00		
			226.00		

The SCB fracture energy (G_f) results are presented in Table 13.4 and Table 13.5. The SCB fracture toughness (K_{IC}) are reported in Table 13.6 and Table 13.7. The responses ranged approximately from 172 J/m² to 320 J/m² and from 0.57 MPa·m^{0.5} to 0.86 MPa·m^{0.5}, respectively,

for G_f and K_{IC} . The repeatability of the tests was reasonably good as indicated by the small COV values.

Table 13.4: SCB fracture energy for mixtures tested at PGLT+10°C

Mixture	Binder PG	Temp °C	G_f [J/m ²]		
			Rep.	Mean	COV
Warm Mix	58-28	-18	243.45	229.33	8%
			236.89		
			207.64		
Citgo_ 12.5mm	58-28	-18	330.87	234.94	35%
			185.38		
			188.59		
Citgo_ 19mm	58-28	-18	343.73	313.77	12%
			272.60		
			324.99		
Marathon_12.5mm	58-28	-18	268.26	229.98	16%
			227.11		
			194.57		
Marathon_ 19mm	58-28	-18	290.33	239.22	19%
			206.07		
			221.28		
MIF_ RAP_12.5mm	58-34	-24	240.61	216.76	13%
			225.06		
			184.62		
MIF_12.5mm	58-34	-24	334.42	305.93	12%
			266.11		
			317.26		
MIF_ RAP_19mm	58-34	-24	223.65	246.87	9%
			248.65		
			268.31		
MIF_19mm	58-34	-24	241.65	257.23	12%
			292.49		
			237.54		
Valero_12.5mm	58-28	-18	349.44	319.05	12%
			277.54		
			330.18		
Valero_19mm	58-28	-18	257.68	288.92	25%
			370.99		
			238.08		

Table 13.5: SCB fracture energy for mixtures tested at PGLT

Mixture	Binder PG	Temp °C	G _f [J/m ²]		
			Rep.	Mean	COV
Warm Mix	58-28	-28	186.29	189.28	6%
			202.73		
			178.82		
Citgo_ 12.5mm	58-28	-28	212.77	208.84	8%
			190.87		
			222.89		
Citgo_ 19mm	58-28	-28	N/A	190.35	35%
			237.72		
			142.97		
Marathon_12.5mm	58-28	-28	197.72	212.57	11%
			239.82		
			200.16		
Marathon_ 19mm	58-28	-28	201.88	199.33	2%
			200.59		
			195.51		
MIF_ RAP_12.5mm	58-34	-34	N/A	244.05	17%
			272.83		
			215.26		
MIF_12.5mm	58-34	-34	170.98	189.32	24%
			240.98		
			156.01		
MIF_ RAP_19mm	58-34	-34	164.75	172.73	9%
			162.00		
			191.44		
MIF_19mm	58-34	-34	N/A	186.28	14%
			167.38		
			205.19		
Valero_12.5mm	58-28	-28	214.08	184.19	15%
			176.17		
			162.32		
Valero_19mm	58-28	-28	203.14	185.90	9%
			185.44		
			169.10		

Table 13.6: SCB fracture toughness for mixtures tested at PGLT+10°C

Mixture	Binder PG	Temp °C	K _{IC} [MPa*m ^{0.5}]		
			Rep.	Mean	COV
Warm Mix	58-28	-18	0.69	0.64	8%
			0.63		
			0.59		
Citgo_ 12.5mm	58-28	-18	0.75	0.73	4%
			0.73		
			0.70		
Citgo_ 19mm	58-28	-18	0.60	0.60	7%
			0.55		
			0.64		
Marathon_12.5mm	58-28	-18	0.61	0.62	7%
			0.67		
			0.58		
Marathon_ 19mm	58-28	-18	0.71	0.63	12%
			0.60		
			0.57		
MIF_ RAP_12.5mm	58-34	-24	0.76	0.72	5%
			0.68		
			0.71		
MIF_12.5mm	58-34	-24	0.82	0.80	8%
			0.73		
			0.86		
MIF_RAP_19mm	58-34	-24	0.78	0.77	3%
			0.78		
			0.74		
MIF_19mm	58-34	-24	0.59	0.65	14%
			0.76		
			0.61		
Valero_12.5mm	58-28	-18	0.63	0.71	15%
			0.68		
			0.83		
Valero_19mm	58-28	-18	0.55	0.57	10%
			0.63		
			0.53		

Table 13.7: SCB fracture toughness for mixtures tested at PGLT

Mixture	Binder PG	Temp °C	K _{IC} [MPa*m ^{0.5}]		
			Rep.	Mean	COV
Warm Mix	58-28	-28	0.70	0.72	14%
			0.64		
			0.83		
Citgo_ 12.5mm	58-28	-28	0.81	0.86	7%
			0.83		
			0.93		
Citgo_ 19mm	58-28	-28	N/A	0.71	1%
			0.71		
			0.71		
Marathon_ 12.5mm	58-28	-28	0.80	0.71	12%
			0.68		
			0.64		
Marathon_ 19mm	58-28	-28	0.61	0.64	8%
			0.70		
			0.62		
MIF_ RAP_ 12.5mm	58-34	-34	N/A	0.81	7%
			0.85		
			0.77		
MIF_ 12.5mm	58-34	-34	0.78	0.80	14%
			0.92		
			0.70		
MIF_ RAP_ 19mm	58-34	-34	0.80	0.78	5%
			0.73		
			0.81		
MIF_ 19mm	58-34	-34	N/A	0.72	8%
			0.68		
			0.76		
Valero_ 12.5mm	58-28	-28	0.69	0.69	2%
			0.69		
			0.67		
Valero_ 19mm	58-28	-28	0.62	0.66	5%
			0.68		
			0.69		

Both SCB and DC(T) yielded a similar range of values for G_f, between approximately 170 J/m² and 380 J/m². The average G_f values, computed from the results of three replicates, are summarized in Figure 13.1 and Figure 13.2, respectively, for the SCB and DC(T) tests. It can be observed that the fracture energy values obtained at PGLT+10°C are always higher than those

obtained at PGLT, except for SCB MIF_RAP_12.5. This confirms the typical behavior of asphalt mixtures: as temperature drops, the mixtures behave in an increasingly brittle manner and absorb relatively little energy prior to fracture. This important aspect, ductile-to-brittle transition, is well captured by the fracture energy parameter of both DC(T) and SCB tests.

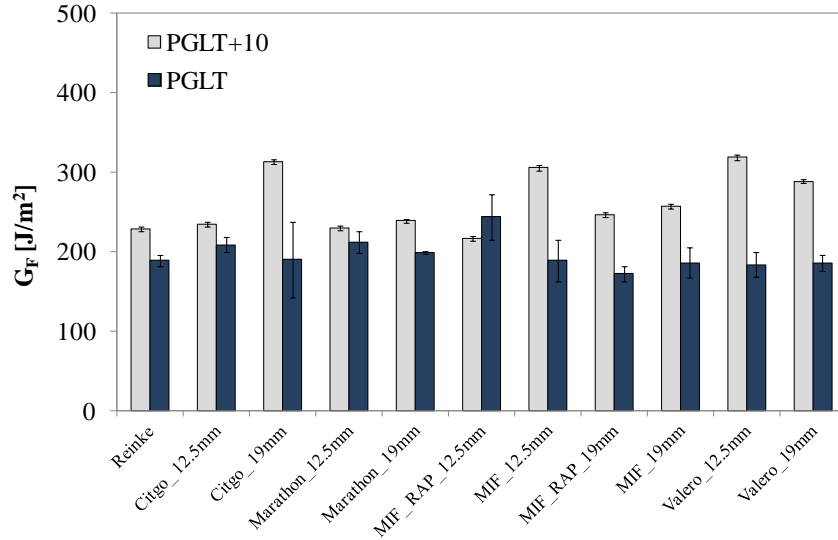


Figure 13.1: Final validation: SCB fracture energy

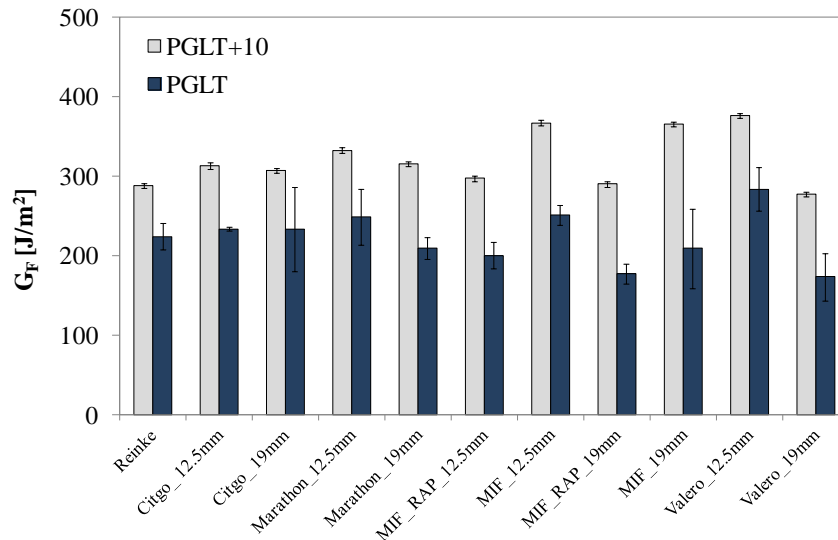


Figure 13.2: Final validation: DC(T) fracture energy

The average K_{IC} values, computed from the results of three test replicates, are summarized in Figure 13.3. It can be observed that generally the toughness of the material is higher at the lowest test temperature. However, two mixtures, MIF_12.5 mm and Valero_12.5 mm, appeared to be indifferent to change in temperature.

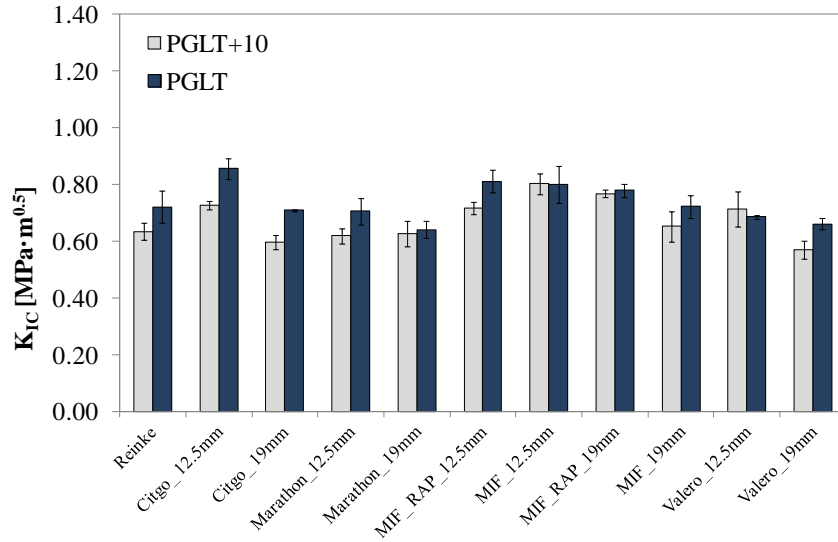


Figure 13.3: Final validation: SCB fracture toughness

Table 13.8 and Table 13.9 contain a ranking of the mixtures, from the largest response to the smallest, according to each test parameter. The mixtures with the highest response are indicated in the shaded cells. Overall, SCB and DC(T) yielded very similar fracture energy values.

Table 13.8: Summary of results for mixtures tested at PGLT+10°C

Mixture	DC(T)		SCB		SCB	
	rank	G_f [J/m ²]	rank	G_f [J/m ²]	rank	K_{IC} [MPa·m ^{0.5}]
Reinke	10	288.00	10	229.33	7	0.64
Citgo_12.5mm	6	313.50	8	234.94	3	0.73
Citgo_19mm	7	308.00	2	313.77	10	0.60
Marathon_12.5mm	4	333.00	9	229.98	9	0.62
Marathon_19mm	5	315.67	7	239.22	8	0.63
MIF_RAP_12.5mm	8	297.67	11	216.76	4	0.72
MIF_12.5mm	2	367.67	3	305.93	1	0.80
MIF_RAP_19mm	9	290.33	6	246.87	2	0.77
MIF_19mm	3	365.67	5	257.23	6	0.65
Valero_12.5mm	1	376.67	1	319.05	5	0.71
Valero_19mm	11	278.00	4	288.92	11	0.57

Table 13.9: Summary of results for mixtures tested at PGLT

Mixture	DC(T)		SCB		SCB	
	rank	G_f [J/m ²]	rank	G_f [J/m ²]	rank	K_{IC} [MPa·m ^{0.5}]
Reinke	6	224.50	7	189.28	6	0.72
Citgo_ 12.5mm	4	234.33	3	208.84	1	0.86
Citgo_ 19mm	5	233.33	5	190.35	7	0.71
Marathon_ 12.5mm	3	249.00	2	212.57	8	0.71
Marathon_ 19mm	7	210.00	4	199.33	11	0.64
MIF_RAP_ 12.5mm	9	201.00	1	244.05	2	0.81
MIF_ 12.5mm	2	251.67	6	189.32	3	0.80
MIF_RAP_ 19mm	10	178.00	11	172.73	4	0.78
MIF_ 19mm	8	209.67	8	186.28	5	0.72
Valero_ 12.5mm	1	284.33	10	184.19	9	0.69
Valero_ 19mm	11	174.00	9	185.90	10	0.66

In general, the ranking of the mixtures according to the DC(T) and SCB fracture energy were in good agreement. Figure 13.4 and Figure 13.5 include plots of mixture’s rankings according to SCB and DC(T) test parameters. At the highest test temperature, the mixtures Valero and MIF, with NMAS 12.5 mm, have the highest fracture energy values. The mixture MIF with NMAS 12.5 mm has also the highest SCB fracture toughness.

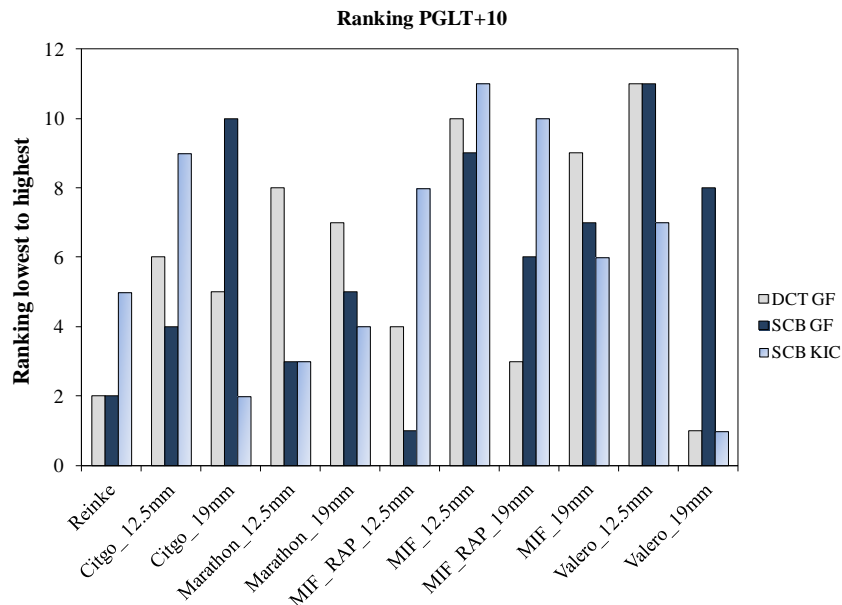


Figure 13.4: Ranking of mixtures tested at PGLT+10°C

At the lowest test temperature, the mixtures Marathon and Citgo, with NMAS 12.5 mm, have the highest fracture energy values (considering both SCB and DC(T) responses). The highest fracture toughness values are observed in mixtures Citgo and MIF with NMAS 12.5 mm.

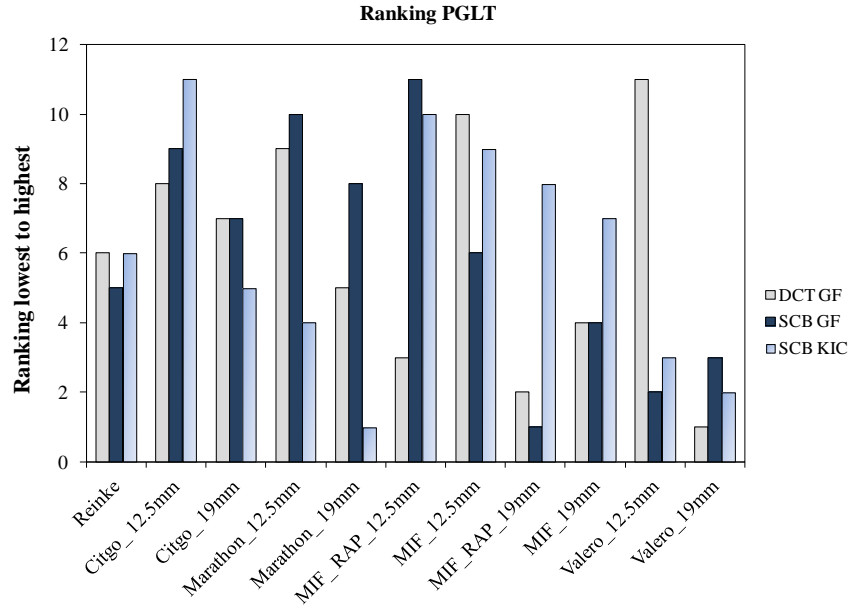


Figure 13.5: Ranking of mixtures tested at PGLT

The effects of aggregate size and RAP on the fracture properties of the different set mixtures (see Table 13.1) were also analyzed.

Effect of Aggregate Size

The effects of aggregate size on the fracture response of the material are multiple and can be observed by looking at the example provided in Figure 13.6.

The curves in the figure represent the average Load – Load Line Displacement (LLD) obtained from SCB testing of mixture Citgo. It can be observed that the slopes of the initial linear parts of the curves are less affected by the size of the aggregates (especially at the lowest test temperature), indicating not significant change in stiffness of the mixture. The peak loads, at both testing temperatures, have increased as the result of using smaller size of aggregates (NMAS 12.5 mm). However, the post-peak softening curves of the mixture with the smallest NMAS appear to be steeper.

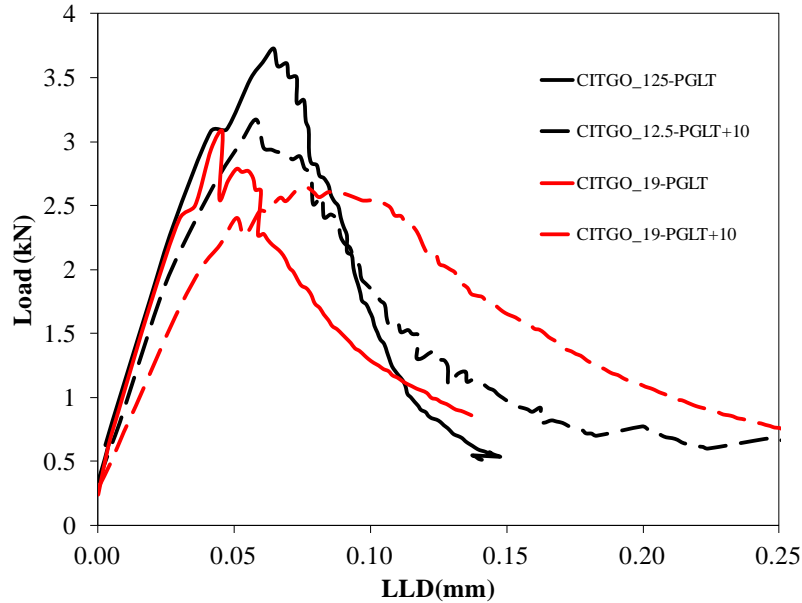


Figure 13.6: Example of SCB test data

According to the DC(T) fracture energy results (see Table 13.4 and Table 13.5), the mixtures with smallest aggregate size (NMAAS 12.5 mm) yielded always significantly higher fracture energy than the ones with large aggregates size (NMAAS 19 mm).

The SCB test results showed a mixed behavior: at the lowest test temperature (PGLT) the trend observed in DC(T) fracture energy was confirmed. Whilst at the highest test temperature the contrary was observed: the mixtures with largest aggregate size (NMAAS 19 mm) yielded higher fracture energy. In addition, the SCB fracture toughness was always higher for mixtures with small aggregate size (NMAAS 12.5 mm) in all cases except for mixtures Marathon and MIF w/RAP tested at the highest test temperature.

Effect of RAP

The effect of RAP on the fracture properties of the mixtures was investigated using the mixtures denominated MIF with PG 58-34. The DC(T) result showed that the fracture energy of the mixtures decreases significantly when RAP is used regardless of the test temperature.

The SCB fracture energy showed similar behavior to that observed for DC(T), except for one case: MIF with NMAAS 12.5 mm tested at the lowest test temperature. On the contrary, the SCB fracture toughness results of mixtures containing RAP were considerably higher than that of mixtures without RAP (except MIF with NMAAS 12.5 mm tested at the lowest test temperature). This indicates that adding RAP increases the strength and toughness of the material but reduces the energy required for crack propagation.

Field Validation

Based upon the outcomes of the testing preliminary validation experimental plan (Task 2), the DC(T) test method was selected for evaluation in the final field validation. In this section, DC(T)

fracture energy values measured on field-cored specimens are compared to the recommended fracture energy threshold for the thermal cracking specification developed in this study, which is in turn compared to measured field thermal cracking as a means to validate the recommended threshold. Instead of using the fracture energy threshold for lab-compacted mixtures as a means of comparison (460 J/m²), a fracture energy threshold of 400 J/m² was used. This value represents the long-term fracture energy that has been associated with very low to zero thermal cracking, while the 460 J/m² threshold is recommended to evaluate lab-compacted mix design specimens, where a higher fracture energy is required to account for the eventual drop in fracture energy that is expected to occur as a result of field aging.

As shown in Table 13.10, the recommended long-term fracture energy level appears to correlate well with the limited field performance data available for the Olmsted field sections investigated (5 years of performance data available at the time of this report). Although all of the field sections have experienced only minor thermal cracking to date, it is clear that the four sections with a fracture energy level below the recommended threshold have begun to exhibit thermal cracking, while the section with a fracture energy in excess of 400 J/m² (section WRI1-2), has very minimal thermal cracking. Although the number of sections and amount of field performance data is fairly limited, the results provide an early validation of the proposed thermal cracking specification.

Table 13.10: Fracture energy and field cracking for validation sections

Pavement Section	Surface Mix	DC(T) Fracture Energy @ -18°C (J/m ²)	Meet DC(T) Fracture Energy Threshold (> 400 J/m ²)	Field Performance (Transverse cracking m/500m)
WRI1-1	MIF_RAP_12.5mm	355.7	No	23
WRI1-2	MIF_12.5mm	437.3	Yes	2
WRI1-3	Marathon_12.5mm	333.0	No	29
WRI1-4	Valero_12.5mm	376.7	No	53
WRI1-5	Citgo_12.5mm	313.5	No	25

Please note that for some of the mixes, the fracture energies in the above table were extrapolated to -18 °C. This was due to a lack of test results at -18 °C for mixes produced with PG 58-34 binder. As discussed in previous sections and other task reports the recommended threshold for the DC(T) fracture energy is to be evaluated at PGLT + 10 °C, where PGLT is the recommended 98% reliability PG low temperature grade at the location of the roadway and not the actual PGLT of virgin binder used in the manufacture of the mix. Since the Olmsted test sections are in a climate where a PG XX-28 binder is specified, the analysis above required fracture energy values to be determined at -18 C. Figure 13.7 demonstrates the linear extrapolation technique

used. The two sections requiring extrapolation were the MIF sections (WRI1-1 and WRI1-2), which utilized a PG XX-34 base binder.

Figures 13.8 through 13.12 graphically illustrate the output from the ILLI-TC preanalyzer routine. As can be seen, only the WRI1-4 section experienced a critical tensile stress level in the five years analyzed. Since this was the worst section in terms of field cracking, this indicates that the ILLI-TC program has correctly ranked the five field sections. In addition, softening was activated along the cohesive zone fracture elements, as shown in Figure 13.13. However, under the current calibration parameters established in Chapter 11, zero cracking was predicted for all sections. Given the fact that the sections have only experienced low cracking to date, it can be concluded that ILLI-TC is slightly under-predicting the cracking behavior for these sections. Again, it should be noted that only a limited amount of creep compliance data was available for these sections (testing at two temperatures instead of the preferred three), so errors caused by incomplete compliance data could also have contributed to the under prediction. Given the fact that one of the five sections in the calibration data set was also under-predicted, the validation trials here may suggest that ILLI-TC should be recalibrated to produce higher levels of cracking. However, since local calibration is recommended before implementing ILLI-TC in a given region, further calibration of ILLI-TC was not pursued herein.

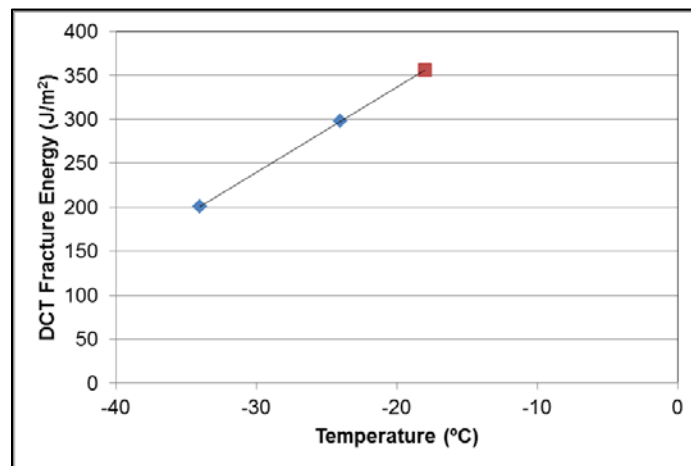


Figure 13.7: Example of linear extrapolation to obtain DC(T) Gf at PGLT+10 °C (MIF_RAP_12.5mm)

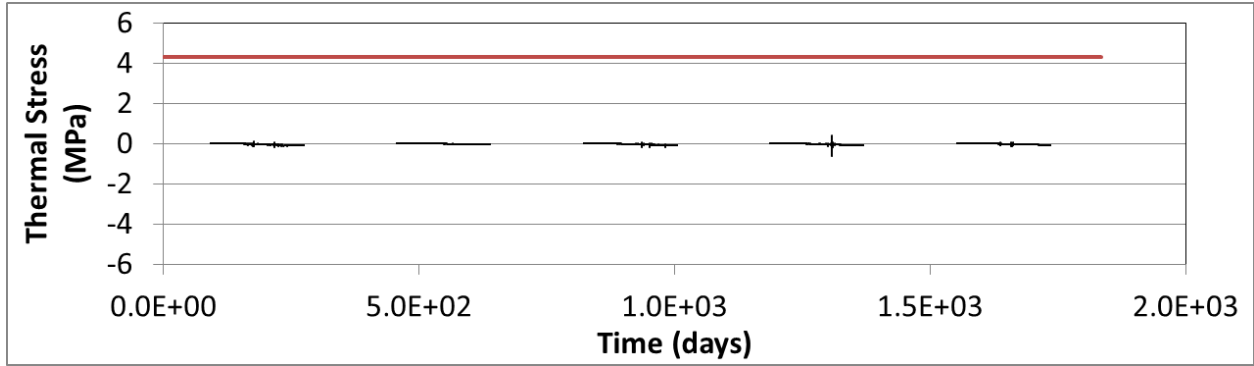


Figure 13.8: Preanalyzer results for WRI1-1 section (MIF_RAP_12.5mm)

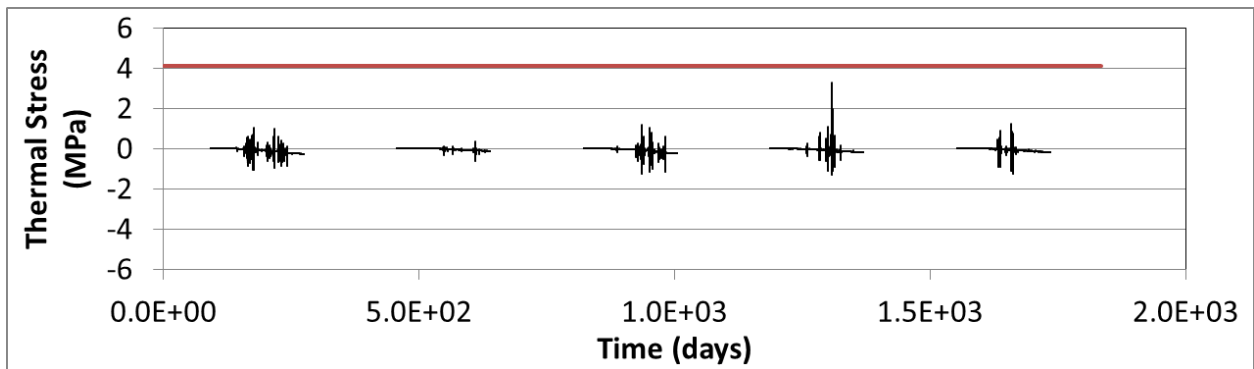


Figure 13.9: Preanalyzer results for WRI1-2 section (MIF_12.5mm)

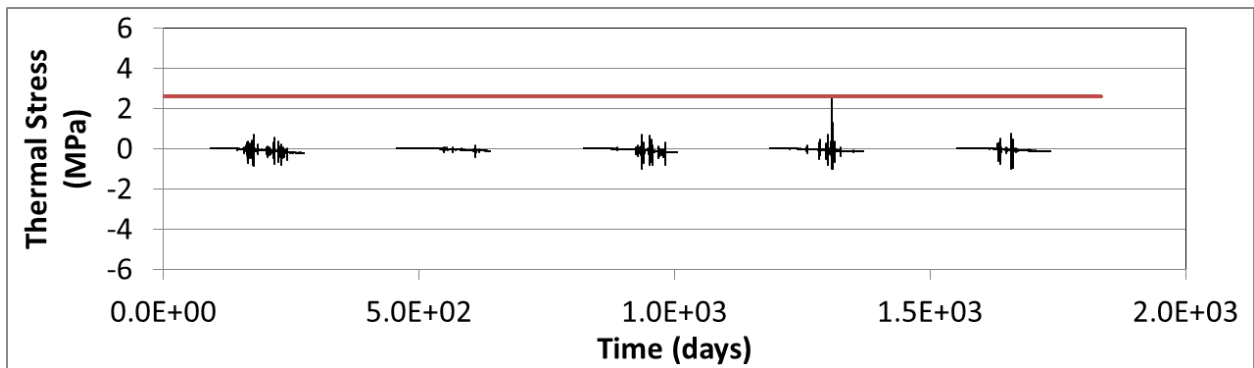


Figure 13.10: Preanalyzer results for WRI1-3 section (Marathon_12.5mm)

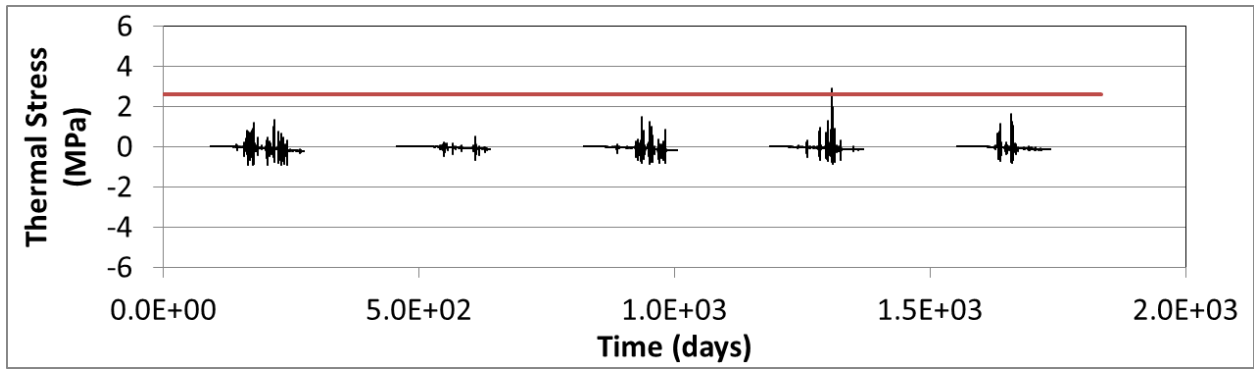


Figure 13.11: Preanalyzer results for WRI1-4 section (Valero_12.5mm)

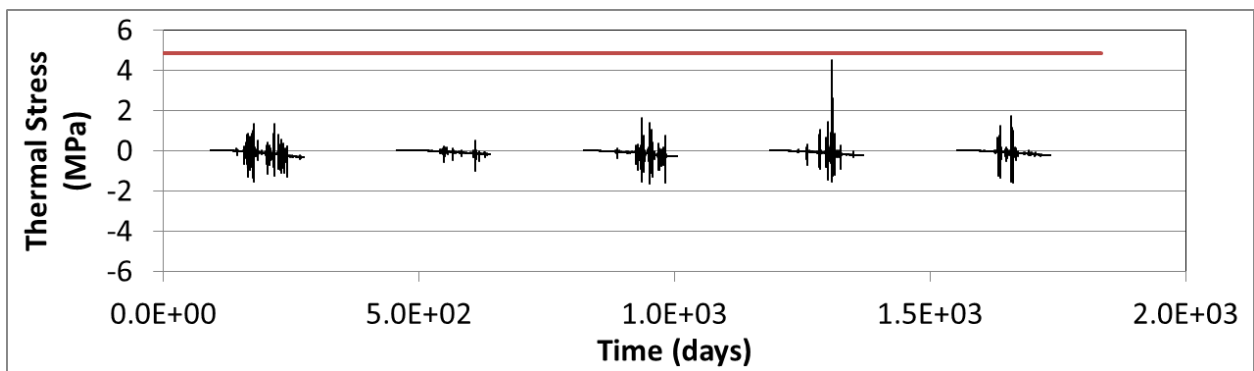


Figure 13.12: Preanalyzer results for WRI1-5 section (Citgo_12.5mm)

Table 13.11: Preanalyzer results and field cracking for validation sections

Pavement Section	Surface Mix	Number of Critical Events (Predicted by Preanalyzer)	Field Performance (Transverse cracking m/500m)
WRI1-1	MIF_ RAP_12.5mm	0	23
WRI1-2	MIF_12.5mm	0	2
WRI1-3	Marathon_12.5mm	0	29
WRI1-4	Valero_12.5mm	1	53
WRI1-5	Citgo_12.5mm	0	25

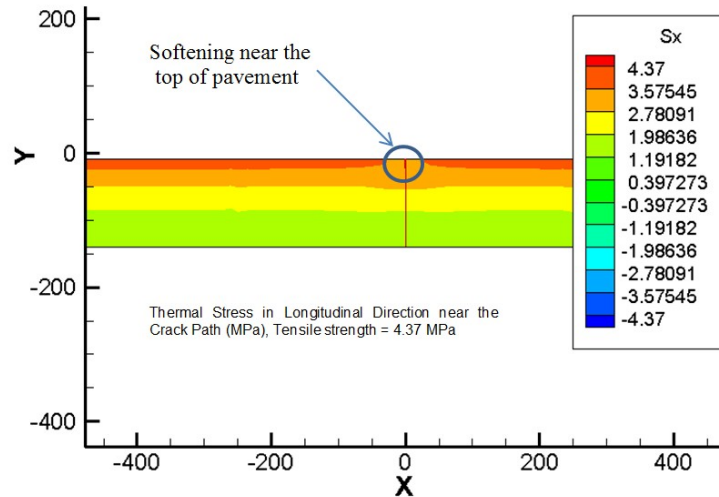


Figure 13.13: Thermal stresses at the end of the critical event for WRI1-4 section (Valero 12.5mm)

Table 13.12: ILLI-TC predictions and field cracking for validation sections using calibrations from Task 4

Pavement Section	Surface Mix	Predicted Crack Depth (mm)	Predicted Field Cracking (m/500m)	Actual Transverse Field Cracking (m/500m)
WRI1-1	MIF_RAP_12.5mm	0	0	23
WRI1-2	MIF_12.5mm	0	0	2
WRI1-3	Marathon_12.5mm	0	0	29
WRI1-4	Valero_12.5mm	0	0*	53
WRI1-5	Citgo_12.5mm	0	0	25

*softening was predicted, indicating that thermal cracking would likely results if a longer analysis period was used.

It can be concluded that the recommended long-term fracture energy level in the table-type thermal cracking specification appears to correlate well with the limited field performance data available for the Olmsted field sections investigated (5 years of performance data available at the time of this report). Although all of the field sections have experienced only minor thermal cracking to date, it is clear that the four sections with a fracture energy level below the recommended threshold have begun to exhibit thermal cracking, while the section with a fracture energy in excess of 400 J/m² (section WRI1-2), has very minimal thermal cracking. Although the

number of sections and amount of field performance data is fairly limited, the results provide an early validation of the proposed thermal cracking specification.

The ILLI-TC program was found to correctly rank the five field validation sections. In addition, softening was activated along the cohesive zone fracture elements in the section with the most field cracking (WRI1-4). However, under the current calibration parameters established in Chapter 11, zero cracking was predicted for all sections. Given the fact that the sections have only experienced a relatively low amount of cracking to date, it can be concluded that ILLI-TC is slightly under predicting the cracking behavior for these sections. Incomplete compliance data could have contributed to the slight under prediction observed. Given the fact that one of the five sections in the calibration data set was also under predicted, the validation trials here may suggest that ILLI-TC calibration parameters should be tuned to produce higher levels of cracking. However, since local calibration is recommended before implementing ILLI-TC in a given region, further calibration of ILLI-TC was not pursued herein.

Predicting Mixture Creep Stiffness from Binder Creep Stiffness

In this section, Bending Beam Rheometer (BBR) binder creep test (AASHTO Designation: T 313-06, 2006) and Indirect Tensile (IDT) mixture creep test (AASHTO Designation: T 322-07, 2009) were performed on the materials described in Table 13.1 (except for the warm mix and the corresponding binder) to determine if mixture creep stiffness can be reasonably predicted from asphalt binder experimental data using two models recently published: Hirsch model and ENTPE transformation.

The four asphalt binders, Citgo (PG 58-28), Marathon (PG 58-28), MIF (PG 58-34), and Valero (PG 58-28) were short term aged (RTFOT) to match the binder condition in the loose mix used to prepare the IDT specimens. All BBR and IDT creep tests were performed at PG+10°C. Binder creep stiffness and m-value results at 60 seconds from BBR testing are presented in Table 13.13 and Figure 13.14. Note that two replicates were tested at each testing temperature.

Table 13.13: Summary of RTFOT binder S(60s) and m(60s) from BBR creep testing

Binder type	Temp, °C	S(60s), MPa	m(60s)
Citgo PG 58-28	-18	171	0.420
Marathon PG 58-28	-18	142	0.413
MIF PG 58-34	-24	222	0.388
Valero PG 58-28	-18	78	0.400

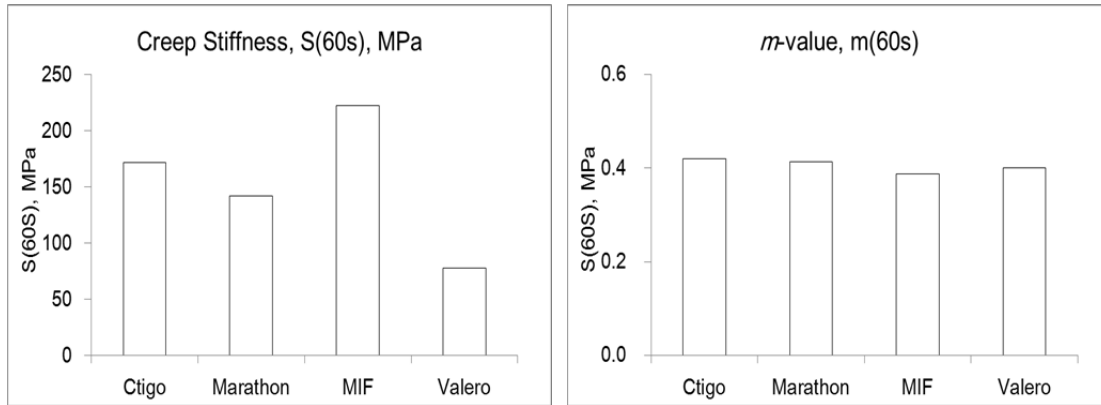


Figure 13.14: RTFOT binder S(60s) and m(60s) results from BBR creep testing

Mixture creep stiffness results at 60 and 500 seconds from IDT creep testing are presented in Table 13.14 and Figure 13.15. Three replicates were tested at each test temperature. In Figure 13.15, Citgo is labeled as C, Marathon as M, MIF as MI, Valero as V, and for the mixtures prepared with RAP, R is used as identifier.

Table 13.14: Summary of S(60s) and S(500s) from IDT mixture creep testing

Mixture type	Temp, °C	S(60s), GPa	S(60s), C.V.%	S(500s), GPa	S(500s), C.V.%
Citgo 12.5mm	-18	16.4	3.9	11.8	2.9
Citgo 19.0mm	-18	13.6	1.2	8.7	3.8
Marathon 12.5mm	-18	11.0	3.2	8.0	11.4
Marathon 19.0mm	-18	12.8	10.2	7.7	8.1
MIF w/R 12.5mm	-24	15.3	15.8	11.3	13.4
MIF 12.5mm	-24	15.6	11.2	11.3	13.4
MIF w/R 19.0mm	-24	15.4	6.1	11.5	1.9
MIF 19.0mm	-24	15.3	1.0	11.1	1.2
Valero 12.5mm	-18	9.4	7.7	6.3	6.2
Valero 19.0mm	-18	6.8	18.6	3.5	23.9

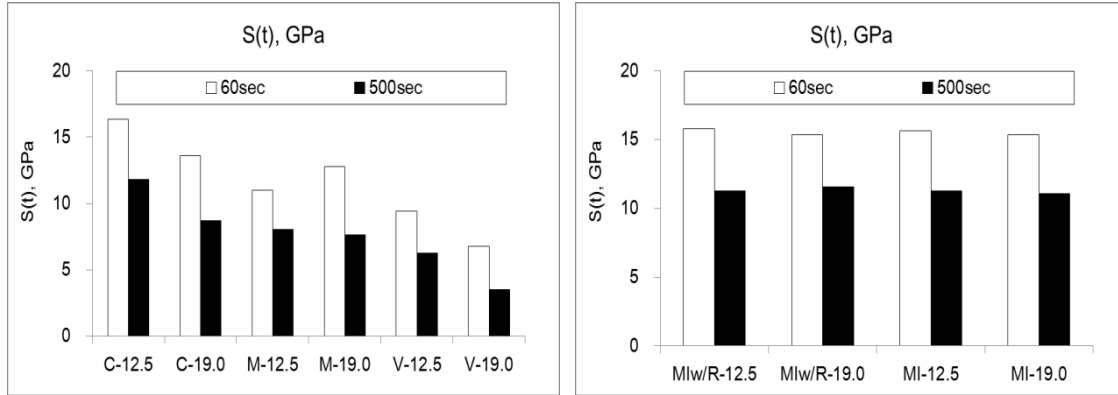


Figure 13.15: Results of S(60s) and S(500s) from IDT mixture creep testing

Most of the 12.5mm mixtures had higher creep stiffness values than the 19.0mm mixtures except for the mixtures prepared with Marathon binder. It was also observed that the mixtures with RAP had slightly higher stiffness values than the standard mixtures.

Hirsch Model

A semi-empirical model, based on Hirsch model (1962) was proposed by Christensen et al. (2003) to estimate the extensional and shear dynamic modulus of asphalt mixture. The effective model was generated by combining aggregate, asphalt binder and air void in parallel and perpendicular direction as follows (see Figure 13.16):

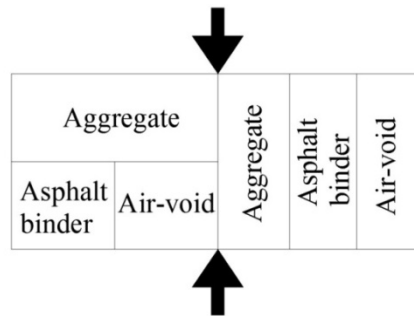


Figure 13.16: Semi-empirical model proposed by (Christensen et al., 2003)

Based on Figure 13.16, the effective modulus of asphalt mixture can be expressed as follows:

$$E_{mixture} = Pc \left[E_{agg} V_{agg} + E_{binder} V_{binder} \right] + (1 - Pc) \left[\frac{V_{agg}}{E_{agg}} + \frac{(1 - V_{agg})^2}{E_{binder} V_{binder}} \right]^{-1} \quad [13.1]$$

Where:

$E_{mixture}$ = effective modulus of the mixture,

E_{agg}, V_{agg} = modulus and volume fraction of the aggregate, respectively,

E_{binder}, V_{binder} = modulus and volume fraction of binder, respectively,

Pc = contact volume as an empirical factor defined as:

$$P_c = \frac{\left(P_0 + \frac{VFA \cdot E_{binder}}{VMA} \right)^{P_1}}{P_2 + \left(\frac{VFA \cdot E_{binder}}{VMA} \right)^{P_1}} \quad [13.2]$$

Where:

VFA = voids filled with asphalt binder (%),

VMA = voids between mineral aggregate (%),

P_0, P_1, P_2 = fitting parameters.

Equation [13.1] can be changed in terms of stiffness as follows:

$$S_{mixture} = P_c [S_{agg} V_{agg} + S_{binder} V_{binder}] + (1 - P_c) \left[\frac{V_{agg}}{S_{agg}} + \frac{(1 - V_{agg})^2}{S_{binder} V_{binder}} \right]^{-1} \quad [13.3]$$

Based on mixture creep tests performed on small beams, Zofka et al. (2005) changed the aggregate modulus, E_{agg} from 4,200,000 psi (29GPa) to 2,750,000 psi (19GPa) and later on (2007) proposed a new expression for the parameter P_c :

$$P_c = 0.1 \cdot \ln \left(\frac{E_{binder}}{a} \right) + 0.609 \quad [13.4]$$

Where:

E_{binder} = relaxation modulus of the binder, GPa,

a = constant equal to 1 GPa.

Huet Model and ENTPE Transformation

The Huet model is composed of two parabolic elements $J_1(t) = a * t^h$ and $J_2(t) = b * t^k$ plus a spring element (stiffness E_∞) combined in series (Figure 13.17) as follows:

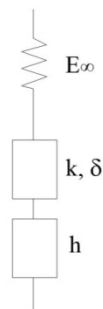


Figure 13.17: Huet Model (Huet, 1963)

The creep compliance function, $D(t)$, in Huet model can be expressed as follows:

$$D(t) = \frac{1}{E_\infty} \left(1 + \delta \frac{(t/\tau)^k}{\Gamma(k+1)} + \frac{(t/\tau)^h}{\Gamma(h+1)} \right) \quad [13.5]$$

Where:

E_∞ = glassy modulus,

δ = dimensionless constant,

h, k = exponents, $0 < k < h < 1$,

τ = characteristic time varying with temperature accounting for

the Time Temperature Superposition Principle (TTSP), $\tau = a_T(T) \cdot \tau_0(T_S)$,

a_T = shift factor at temperature T ,

τ_0 = characteristic time determined at reference temperature T_S ,

Γ = gamma function which can be expressed as follows:

$$\Gamma(n) = \int_0^\infty t^{n-1} e^{-t} dt \quad [13.6]$$

$$\Gamma(n+1) = n \cdot \Gamma(n) \quad [13.7]$$

$n > 0$ or Real (n) > 0 ,

t = integration variable,

n = argument of the gamma function.

For bituminous materials $\delta \approx 2$, $k \approx 0.3$, and h is between 0.3 and 0.8, with lower values characteristic of aged, oxidized binders obtained by air blowing or aging during production and service life (Huet, 1999).

Based on previous work performed by Di Benedetto et al. (2004) and on Huet model, Cannone Falchetto et al. (2011) developed an expression relating asphalt mixture and asphalt binder creep stiffness:

$$D_{mixture}(t) = D_{binder}(t \cdot 10^{-\alpha}) \cdot \frac{E_{\infty binder}}{E_{\infty mixture}} \quad [13.8]$$

Equation [13.8] can also be written for creep stiffness $S(t)$:

$$S_{mixture}(t) = S_{binder}(t \cdot 10^{-\alpha}) \cdot \frac{E_{\infty mixture}}{E_{\infty binder}} \quad [13.9]$$

An inverse relation can be easily written to obtain binder creep stiffness from mixture experimental data:

$$S_{binder}(t) = S_{mixture}(t \cdot 10^\alpha) \cdot \frac{E_{\infty binder}}{E_{\infty mixture}} \quad [13.10]$$

The authors found that the relationship between characteristic time of the binder, τ_{binder} , and the corresponding characteristic time of the mixture, $\tau_{mixture}$, developed by Di Benedetto et al. (2004) also holds at low temperature:

$$\tau_{mixture}(T) = 10^\alpha \tau_{binder}(T) \quad [13.11]$$

Where:

α = a regression coefficient depending on mixture type and binder aging.

Equation [13.9] represents ENTPE (École Nationale des Travaux Publics de l'État) transformation at low temperature.

Predicting Mixture Creep Stiffness from Binder Experimental Data

The binder experimental data was used as input in the two models models to predict mixture creep stiffness and compare the results with the experimentally determined IDT creep stiffness.

For Hirsch model, based on preliminary trials, the original aggregate modulus $E_{agg} = 4200000$ psi was used in the calculations. Using equations [13.3] and [13.4], the creep stiffness of corresponding mixtures were calculated based on asphalt binder creep stiffness. However, the predicted values correspond to creep stiffness of mixtures obtained using BBR small mixture beams. To obtain IDT creep stiffness, the equation proposed by Zofka (2005) was used:

$$S(t)_{IDT \text{ creep test}} = \frac{1}{0.865} \times S(t)_{BBR \text{ creep test}} \quad [13.12]$$

Figures 13.18 to 13.22 contain the plots of experimental data from IDT mixture creep test and predicted creep stiffness from BBR binder creep test.

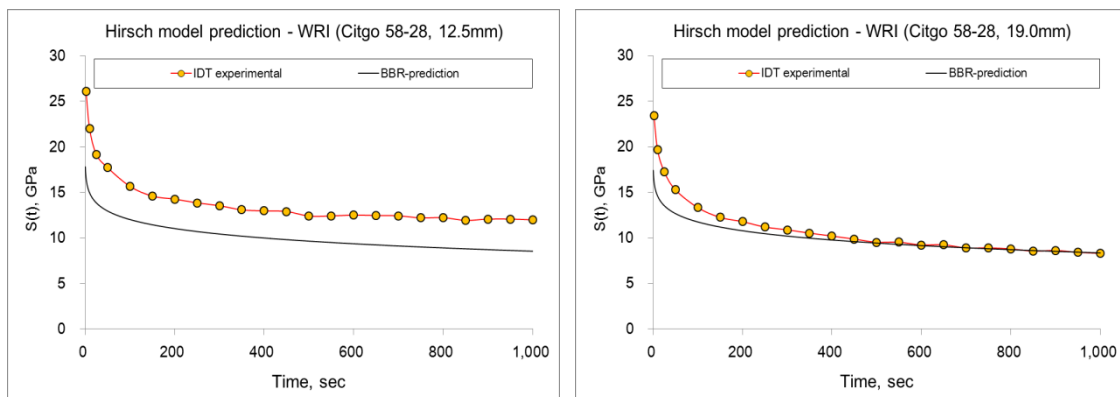


Figure 13.18: Hirsch Model predictions for Citgo mixtures

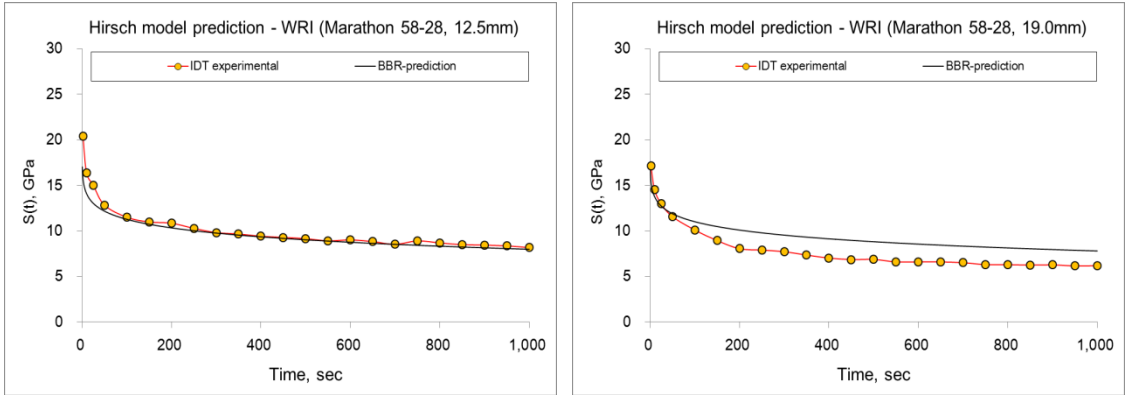


Figure 13.19: Hirsch Model predictions for Marathon mixtures

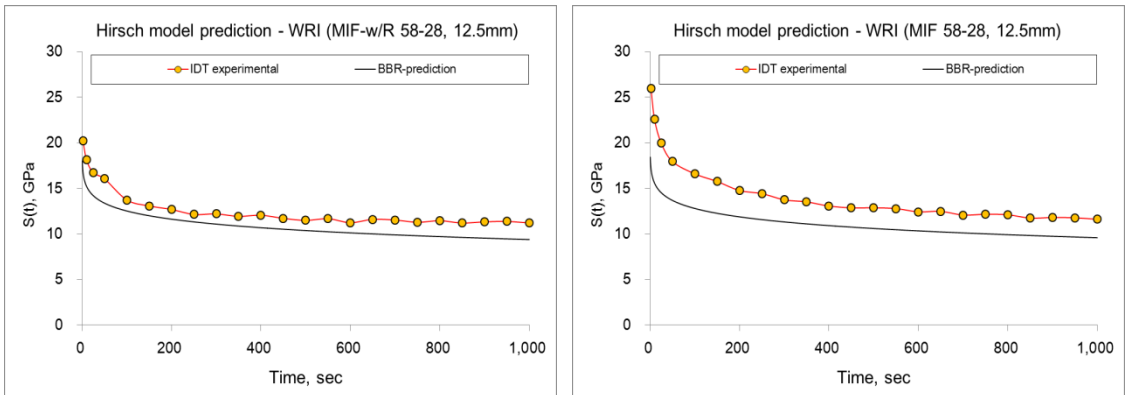


Figure 13.20: Hirsch Model predictions for MIF 12.5mm mixtures

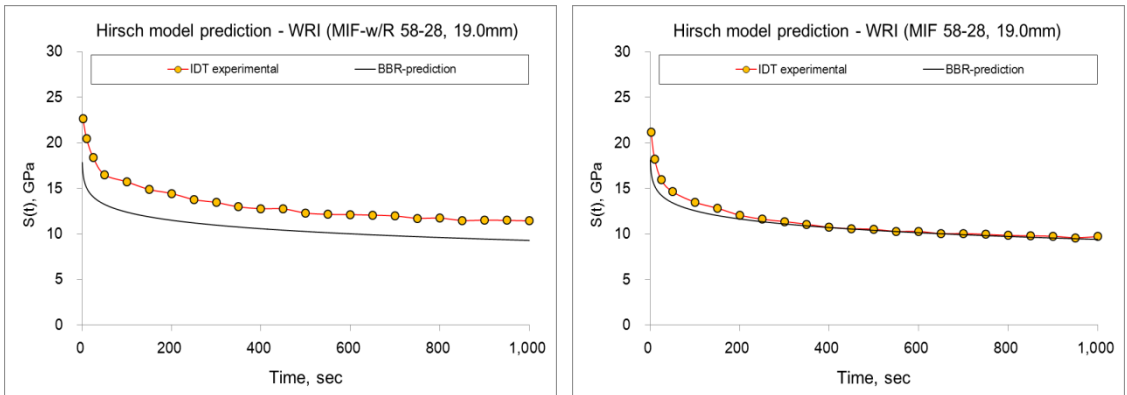


Figure 13.21: Hirsch Model predictions for MIF 19.0mm mixtures

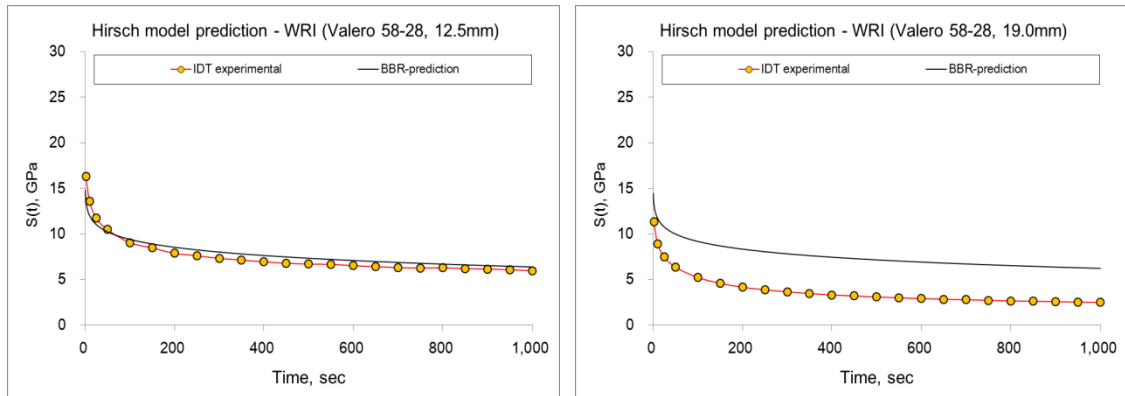


Figure 13.22: Hirsch Model predictions for Valero mixtures

It can be observed that the Hirsch model predictions are reasonable for most mixtures. However, for some mixtures, the predicted results were significantly higher (Valero 19.0mm mixture) or lower (Citgo 12.5mm mixture) compared to the experimental results.

For ENTPE transformation, equation [13.5] was first used to fit the creep compliance results of asphalt binder and five parameters were determined through minimization of sum of the distances between the experimental creep compliance results from BBR test and predicted results from Huet model fitting at 1250 time points:

$$\min \left(\sum_{i=1}^{1250} \left[D(t)_{\text{experimental}} - D(t)_{\text{Huet model}} \right]^2 \right) \quad [13.13]$$

Table 13.15 lists the computed parameters of the Huet model for four different types of asphalt binder which were tested at PG+10°C.

Table 13.15: Huet Model parameters for tested binders

Binder Type	δ	k	h	$E_{\infty b}$, MPa	τ_{binder}
Citgo PG 58-28	1.5294	0.1113	0.5419	2500	0.9331
Marathon PG 58-28	2.8959	0.2044	0.5966	2500	1.5363
MIF PG 58-34	1.0362	0.1161	0.4912	2586	0.8779
Valero PG 58-28	2.4469	0.1069	0.4823	2500	0.0895

From the plots in Figures 13.23 to 13.24 it can be seen that Huet model fits the binder creep compliance experimental results very well.

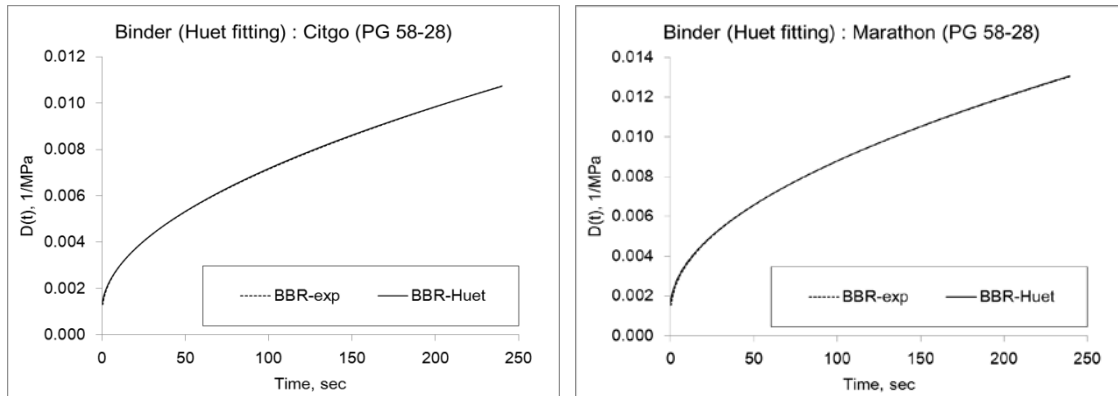


Figure 13.23: Huet Model predictions for binders Citgo (PG 58-28) and Marathon (PG 58-28)

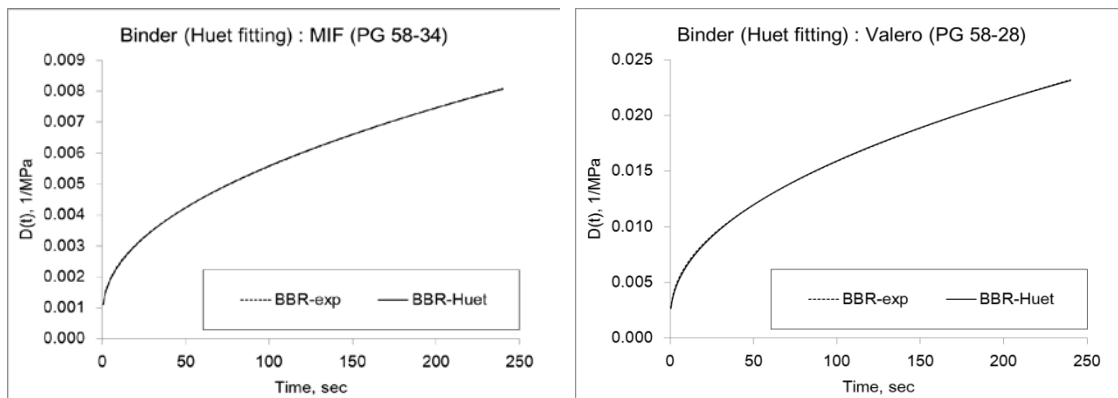


Figure 13.24: Huet Model predictions for binders MIF (PG 58-28) and Valero (PG 58-28)

Knowing that the same model parameters can be used to fit the asphalt mixture creep data, except for the characteristic time τ , and that the binder characteristic time and mixture characteristic time are related through parameter α , the following α values were obtained and tabulated in Table 13.16.

Table 13.16: α parameter values for mixtures for ENTPE transformation

Binder type	Citgo PG 58-28		Marathon PG 58-28		MIF PG 58-34			Valero PG 58-28		
	NMAS, mm	12.5	19.0	12.5	19.0	12.5 w/R	12.5	19.0 w/R	19.0	12.5
\square	3.343	3.039	3.510	3.191	3.599	3.460	3.273	3.146	3.677	3.343

The creep stiffness of corresponding mixtures can be then easily predicted using Equation [13.9]. Figures 13.25 to 13.29 contain plots of predicted mixture creep stiffness using ENTPE transformation.

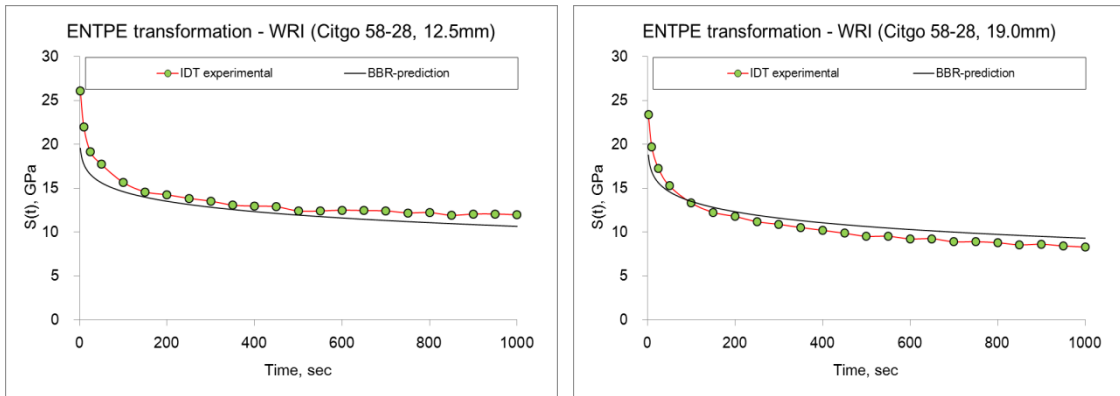


Figure 13.25: ENTPE transformation predictions for Citgo mixtures

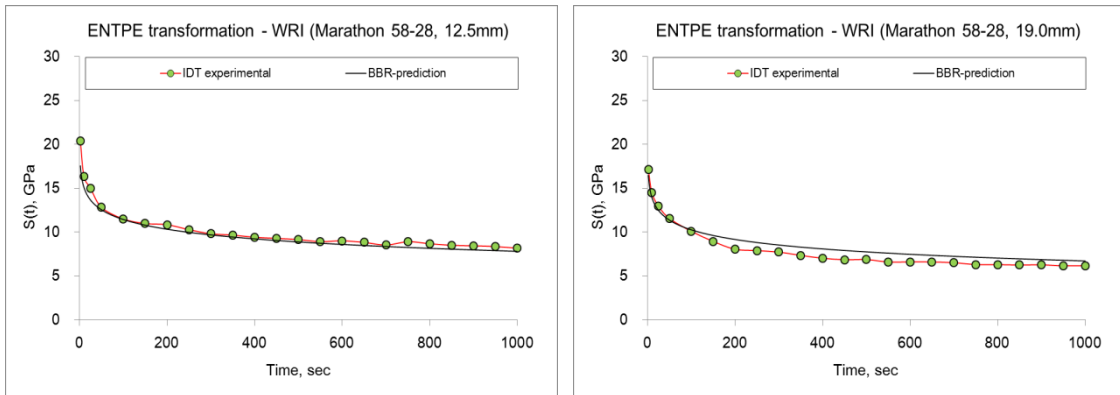


Figure 13.26: ENTPE transformation predictions for Marathon mixtures

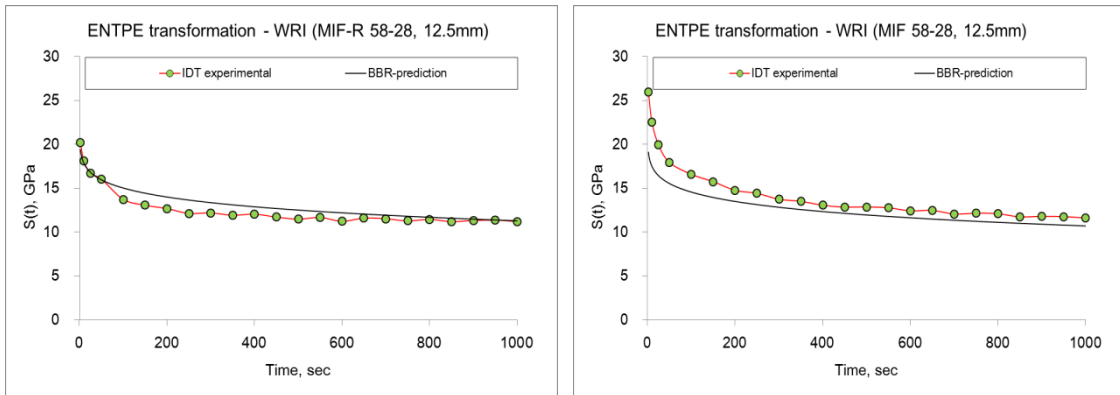


Figure 13.27: ENTPE transformation predictions for MIF 12.5mm mixtures

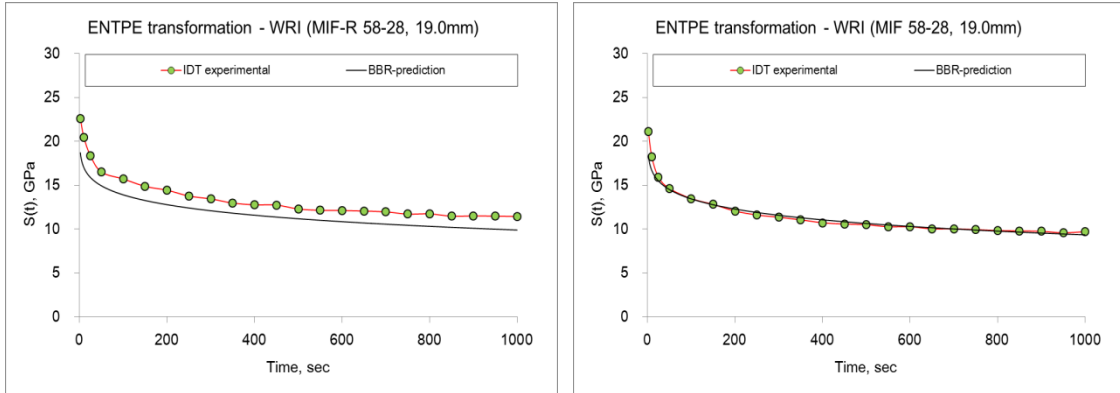


Figure 13.28: ENTPE transformation predictions for MIF 19.0mm mixtures

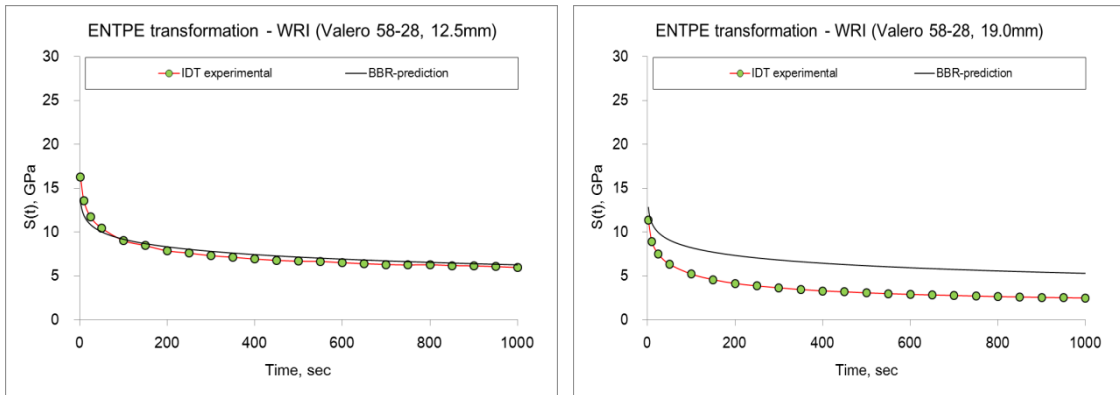


Figure 13.29: ENTPE transformation predictions for Valero mixtures

Except for Valero 19.0mm mixture, the ENTPE transformation predicted the creep stiffness of corresponding mixtures very well. It should be mentioned that this is not unexpected since the same set of mixtures were used to obtain α parameter and to validate the model prediction.

Chapter 14. Summary and Conclusions

The work performed in phase II built upon the findings and recommendations of phase I. Each of the four main recommendations were addressed, however, the main thrust was the development of test methods and specification criteria for selecting fracture resistant asphalt mixtures and binders at low temperatures.

In Chapter 1, a comprehensive literature review was performed addressing various aspects of low temperature asphalt materials characterization and bring up to date the review performed in Phase I of this research.

In Chapter 2, a set of asphalt mixtures, included Recycled Asphalt Pavement (RAP) mixtures, Poly-Phosphoric Acid (PPA) modified mixtures, and polymer modified mixtures (SBS, and Elvaloy), were evaluated using Indirect Tensile (IDT), Semi-Circular Bend (SCB), and Disc-Shaped Compact Tension (DCT) test protocols. The effect of aging was also investigated by conditioning the mixtures for 5 days at 85°C. In addition, field specimens cored from MnROAD test cells, were tested and compared to the laboratory asphalt mixtures. The experimental results were analyzed using a range of statistical tools and it was concluded that the fracture tests could discriminate between the different mixtures used in the experimental matrix. The two fracture testing methods provided similar results and rankings except for a few cases.

Also in Chapter 2, research was performed to understand how physical hardening is affected by parameters such as temperature, conditioning time, modification, thermal history, and glass transition temperature, and to propose a comprehensive model in which the physical hardening of asphalt binders can be predicted for different conditions without lengthy tests. The tests performed in this study were combined with experimental data from previous studies to enable a broad analysis of the nature of physical hardening in asphalt binders and to propose a model. It was found that physical hardening in asphalt binders results in significant changes in their creep response at temperatures below or near the glass transition. Also the rate of physical hardening decreases rapidly with isothermal age and it is highly dependent on conditioning temperature and the source of the base binder. Different types of polymer modification did not significantly change the rate of physical hardening. This was explained as being the result of the two-phase nature of polymer modified binders, in which the hardening behavior of the base binder phase is dominant.

In Chapter 3, a thermal cracking specification for asphalt mixtures was proposed based on DCT results. A 15% increase in fracture energy was proposed to take into account the fact that the criterion was specified for loose mixtures and short term aged laboratory mixtures. Specification limits for three levels of project criticality are provided. A higher fracture energy threshold was suggested in order to limit thermal cracking to lower levels on projects of high criticality. An alternative specification based on SCB fracture energy was also proposed.

Also in Chapter 3, testing methods to obtain mixture creep compliance from DC(T) and SCB testing configurations were proposed and validated with limited experimental data. In addition, a method to obtain mixture creep compliance from BBR tests on thin mixture beams was presented, and the feasibility of predicting mixture creep compliance from asphalt binder creep

compliance experimental testing was discussed and used to calculate a threshold asphalt mixture creep stiffness limiting value equivalent to the current binder creep stiffness criterion. Chapter 3 ended with summaries of two research efforts to develop a new test method to obtain relevant asphalt binder fracture and strength properties at low temperatures.

In Chapter 6, the research performed at the University of Illinois Urbana-Champaign to develop a new thermal cracking model, called “ILLI-TC,” was presented. The predecessor to ILLI-TC is TCMODEL, which is a mechanistic-empirical thermal cracking model developed under the Strategic Highway Research Program (SHRP). ILLI-TC improves the manner in which fracture is handled in the simulation scheme, namely; in the past TCMODEL used a 1D Paris-Law phenomenological modeling approach to simulate crack propagation, while ILLI-TC uses 2D, cohesive zone fracture modeling approach implemented within a viscoelastic finite element modeling framework. The cohesive zone approach considers both material strength and fracture energy in computing crack initiation and propagation using fundamental fracture mechanics principles, while the Paris law approach used in TCMODEL used a phenomenological power-law type model to link change in stress intensity (which was calculated in an approximate manner) to crack growth, where the Paris law parameters were empirically linked to material strength and slope of the log mixture compliance vs. log time relationship at long loading times. It is expected that in some instances the predictions from ILLI-TC will be different from TCMODEL predictions, because for instance, some high fracture energy mixes receive more credit for crack resistance in ILLI-TC, but might not be portrayed well in the older TCMODEL (since fracture energy was not considered).

Chapter 11 contains a comprehensive experimental and modeling investigation on the contraction and expansion of asphalt mixtures due to thermal cycles. As part of this study, a model was developed for thermal stress analysis during cooling/heating cycles using different cooling rates and isothermal conditioning periods. The model accounts for the asphalt mixture glass transition and physical hardening, and it can be used to investigate which thermo-volumetric parameters (e.g, coefficients of thermal expansion/contraction, glass transition temperature, etc) significantly affect the asphalt mixture response during cooling and heating cycles. The thermal stress model uses relaxation modulus master curves, the William-Landel-Ferry equation, Boltzmann superposition principle, and a sub-model describing the isothermal contraction of asphalt materials as a continuous function of conditioning time and temperature. Using the model predictions it is shown that thermal stress relaxation and stress build-up induced by physical hardening can continuously affect thermal stress throughout the cooling process. Cooling rate also affected the amount of delayed stress buildup occurring after the temperature has stabilized at isothermal condition due to physical hardening.

In Chapter 12, the specification proposed in Chapter 3 based on the Disc-Shaped Compact Tension (DC(T)) was validated using eleven mixtures used in pavement sections constructed in Olmsted County (Minnesota) during the 2006 construction season. The preliminary results (very few cracks have developed at the time of writing this report) indicate that the proposed method and the new thermal cracking program do a reasonable job predicting field performance. A validation of the proposed method to predict mixture creep stiffness from binder experimental data was also performed at the end of this chapter.

The work performed in this research effort has resulted in a number of significant contributions. Two fracture testing methods were proposed and specifications were developed for selecting mixtures based on fracture energy criteria. For the DC(T), an ASTM standard has already been published, and the published version is in the process of being updated and reformatted and will be submitted to AASHTO. A draft SCB specification has received approval by the ETG and has been taken to AASHTO committee of materials.

In addition, alternative methods were proposed to obtain mixture creep compliance needed to calculate thermal stresses. Dilatometric measurements performed on asphalt mixtures has resulted in a set of coefficients of thermal contraction that can be used to more accurately predict thermal stresses and physical hardening effects were further evaluated and an improved model was proposed to take these effects into account. Also, two methods for obtaining asphalt binder fracture properties were summarized and discussed.

A new thermal cracking model, called "ILLI-TC," was developed and validated. This model represents a significant step forward in accurately quantifying the cracking mechanism in pavements. The work performed in Chapter 11 opened the discussion on the cyclic behavior of asphalt mixtures that may hold the key to developing cracking resistant mixtures under multiple cycles of temperature.

References

Chapter 2. Literature Review

1. American Association of State Highway and Transportation Officials (AASHTO) Standard T 313-08 (2008), "Standard Method of Test for Determining the Flexural Creep Stiffness of Asphalt Binder Using the Bending Beam Rheometer (BBR) ", *Standard Specifications for Transportation Materials and Methods of Sampling and Testing, 29th Edition*, Washington, D.C.
2. American Association of State Highway and Transportation Officials (AASHTO) Designation T314-07 (2007), "Standard Method of Test for Determining the Fracture Properties of Asphalt Binder in Direct Tension (DT) ", *Standard Specifications for Transportation Materials and Methods of Sampling and Testing "29nd Edition*, Washington, D.C.
3. American Association of State Highway and Transportation Officials (AASHTO) Designation M320-05 (2002), "Standard Specification for Performance Graded Asphalt Binder", *Standard Specifications for Transportation Materials and Methods of Sampling and Testing, 29nd Edition*, Washington, D.C.
4. American Association of State Highway and Transportation Officials (AASHTO) Standard R28-06, "Standard practice for accelerated aging of asphalt binder using a Pressurized Aging Vessel (PAV)", *Standard Specifications for Transportation Materials and Methods of Sampling and Testing, 26th Edition*, 2006.
5. American Association of State Highway and Transportation Officials (AASHTO) Designation T322-07 (2009), "Standard Method of Test for Determining the Creep Compliance and Strength of Hot-Mix Asphalt (HMA) Using the Indirect Tensile Test Device", *Standard Specifications for Transportation Materials and Methods of Sampling and Testing, 29nd Edition*, Washington, D.C.
6. Hallin J., (2004), *Development of the 2002 Guide for the Design of New and Rehabilitated Pavement Structures: Phase II, National Cooperative Highway Research Program*, NCHRP 1-37A, Washington, D.C.
7. Hase M., Oelkers C., (2009) "Influence of low temperature behaviour of PmB on life cycle", Proceeding of the 7th International RILEM Symposium ATCBM09 on Advanced Testing and Characterization of Bituminous Materials, 23-32.
8. Deutsches Institut für Normung DIN EN 14771 (2005): "Bitumen und bitumenhaltige Bindemittel—Bestimmung der Biegesteifigkeit— Biegebalkenrheometer (BBR)" according EN 14771 (2005): "Bitumen and bituminous binders— Determination of the flexural creep stiffness—Bending Beam Rheometer (BBR)".
9. Khedoe R., Molenaar A., & v.d. Ven M., (2008), "Low temperature behavior of very hard bituminous binder material for road applications" Proceeding of the 6th RILEM conference on Cracking in Pavement, 481-490, Chicago, IL.
10. Yee P., Aida N., Hesp S.A.M., Marks P. and Tam K. K., (2006), "Analysis of Premature Low-Temperature Cracking in Three Ontario, Canada, Pavements", *Transportation Research Record*, 1962, 44–51.
11. Struik L. C. E., (1978), *Physical Ageing in Amorphous Polymers and Other Materials*, Elsevier Scientific Publishing Co., Amsterdam, Netherlands.

12. Bahia, H.U. “Low-Temperature Isothermal Physical Hardening of Asphalt Cements. Ph.D.” Thesis, Pennsylvania State University, December 1991.
13. Al-Qadi I. L., HseinYang S., Dessouky S. and Masson J. F., (2007), “Development of Crack Sealant Bending Beam Rheometer (CSBBR) Testing to Characterize Hot-Poured Bituminous Crack Sealant at Low Temperature”, *Journal of the Association of Asphalt Paving Technologists*, Vol. 76, 85-122
14. Zanzotto L., (1996), *Laboratory Testing of Crack Sealing Materials for Flexible Pavements*, Transportation Association of Canada, Ottawa, ON, 171 pp.
15. Zofka A., Marasteanu M, Li X., Clyne T., Jim McGraw J., (2005), “Simple Method to Obtain Asphalt Binders Low Temperature Properties from Asphalt Mixtures Properties”, *Journal of the Association of Asphalt Paving Technologists*, Vol. 74, 255-282.
16. Elseifi M., Dessouky S., Al-Qadi I. L. and Yang S-H., (2006), “Viscoelastic Model to Describe the Mechanical Response of Bituminous Sealants at Low Temperature”, *Transportation Research Record*, 1958, 82-89.
17. Velásquez R., Marasteanu M., Turos M., Labuz J., (2009), “Effect of beam size on the creep stiffness of asphalt mixtures at low temperatures”, Proceeding of the 7th International RILEM Symposium ATCBM09 on Advanced Testing and Characterization of Bituminous Materials, 313-322, Rhodes, Greece.
18. Apeageyi A. K., Buttlar W. G. and Dempsey B. J., (2008), “Investigation of Cracking Behavior of Antioxidant-Modified Asphalt Mixtures”, *Journal of the Association of Asphalt Paving Technologists*, Vol. 77, 519-545
19. Kim Y. R., King Y. and Momen M., (2004), “Dynamic Modulus Testing of Asphalt Concrete in Indirect Tension Mode”, *Transportation Research Record*, 1891, 163–173.
20. Katicha S., Flintsch G., (2009), “Theoretical investigation of the stress distribution in a Bimodular IDT specimen”, Proceeding of the 7th International RILEM Symposium ATCBM09 on Advanced Testing and Characterization of Bituminous Materials, 453-462, Rhodes, Greece
21. Ambartsumyan S., (1965), “The axisymmetric problem of circular cylindrical shell made of materials with different stiffness in tension and compression”, *Izv. Akad. Nauk. SSR Mekh.* 4, 77–85.
22. Ambartsumyan S., and Khachartryan A., (1969), “Basic equations and relations of the different modulus theory of elasticity of an anisotropic body”, *Mechanics of Solids*, 4, 48-56.
23. Birgisson B., Montepara A., Romeo E., Roque l R. and Tebaldi G., (2007), “The displacement discontinuity method for predicting HMA fracture energy in the bending beam test”, Proceeding of the International Conference on Advanced Characterization of Pavement and Soil Engineering Materials, 69-77, Athens, Greece.
24. Sauzéat C., Di Benedetto H., Chaverot P. and Gauthier G., (2007), “Low temperature behavior of bituminous mixes: TSRS tests and acoustic emission”, Proceeding of the International Conference on Advanced Characterization of Pavement and Soil Engineering Materials, 1263-1272, Athens, Greece.
25. Hase M., Oelkers C., (2009), “Influence of low temperature behaviour of PmB on life cycle”, Proceeding of the 7th International RILEM Symposium ATCBM09 on Advanced Testing and Characterization of Bituminous Materials, 23-32, Rhodes, Greece.
26. Janoo V., (1989), Performances of ‘Soft’ Asphalt Pavements in Cold Regions USA CRREL Special Report.

27. Koh C., Lopp G. and Roque R., (2009), “Development of a Dog-Bone Direct Tension Test (DBDT) for asphalt concrete”, Proceeding of the 7th International RILEM Symposium ATCBM09 on Advanced Testing and Characterization of Bituminous Materials, 585-596, Rhodes, Greece.
28. ASTM Method E399-90, “Plane-Strain Fracture Toughness for Metallic Materials”, Annual book of ASTM Standards, Vol. 03.01. (2002) American Society for Testing and Materials, Philadelphia, PA
29. Portillo O. and Cebon D., (2008), “An experimental investigation of the fracture mechanics of bitumen and asphalt”, Proceeding of the 6th RILEM conference on Cracking in Pavement, 627-636, Chicago, IL.
30. Harvey J.A.F. & Cebon D., (2003), “Failure Mechanism in Viscoelastic Films”, *Journal of Materials Science*, 38, 1021–1032.
31. Genin G.M. and Cebon D., (2000), “Fracture Mechanics in Asphalt Concrete”, *Road Materials and Pavement Design*, 1(4): 419–450.
32. Harvey J. A. F. and Cebon D., (2005), “Fracture Tests on Bitumen Films”, *Journal of Material in Civil Engineering*, Vol. 17, Issue 1, 99-106.
33. Wagoner M.P. and Buttlar W.G., (2007), “Influence of specimen size in fracture energy of asphalt concrete”, *Journal of the Association of Asphalt Paving Technologists*, Vol. 76, 391-426
34. Bazant Z.P. (1984), “Size effect in blunt fracture: concrete, rock, metal”, *Journal of Engineering Mechanics*, Vol.110, No 4, 518-535.
35. Marasteanu M., Li X., Labuz J., (2006), “Observation of Crack Propagation in Asphalt Mixtures Using Acoustic Emission”, presented at Transportation Research Board 85th Annual Meeting, January 2006.
36. Kim H., Partl M. N., Wagoner M.P., Buttlar W. G., (2009), “Size effect investigation on fracturing of asphalt concrete using the cohesive softening Discrete Element Model”, Proceeding of the 7th International RILEM Symposium ATCBM09 on Advanced Testing and Characterization of Bituminous Materials, 827-836, Rhodes, Greece.
37. Kim H., Wagoner M. P. and Buttlar W. G., (2007), “Fracture modeling considered rate – dependency of asphalt concrete using discrete element method”, Proceeding of the International Conference on Advanced Characterization of Pavement and Soil Engineering Materials, 79-92, Athens, Greece.
38. Hu X., Wittmann F., (2002), “Size Effect on Toughness Induced by Crack Close to Free Surface”, *Engineering Fracture Mechanics*, Vol. 69,555-562.
39. Chong K. and Kuruppu M., (1984), "New Specimen for Fracture Toughness Determination for Rock and Other Materials", *International Journal of Fracture*, Vol. 26, R59-R62.
40. Van Rooijen R. C. and de Bondt A. H., (2008), “Crack propagation performance evaluation of asphaltic mixtures using a new procedure based on cyclic Semi-Circular Bending test (SCB)”, Proceeding of the 6th RILEM conference on Cracking in Pavement, 437-446, Chicago, IL.
41. European Committee for Standardization (CEN), EN 13589, CEN/TC 336 - Bituminous binders, EN 13589:2008, Bitumen and bituminous binders - Determination of the tensile properties of modified bitumen by the force ductility method.
42. European Committee for Standardization (CEN), EN 13589, CEN/TC 336 - Bituminous binders, EN 13703:2003, Bitumen and bituminous binders - Determination of deformation energy.

43. Perez F., Botella R., Valdes G., (2009), "Experimental study on resistance to cracking of bituminous mixtures using the Fenix test", Proceeding of the 7th International RILEM Symposium ATCBM09 on Advanced Testing and Characterization of Bituminous Materials, 707-714, Rhodes, Greece.
44. Zbrowski A. and Kaloush K. E., (2007), "Predictive equation to Evaluate Thermal Fracture of Asphalt Rubber Mixtures", *Road materials and pavement design*, Vol.8, no4, pp. 819-833.
45. Kim J., Roque R. and Birgisson B., (2008), "Integration of thermal fracture in the HMA fracture model", *Journal of the Association of Asphalt Paving Technologists*, Vol. 77, 631-661.
46. Roque R., Birgisson B., Zhang Z., Sangpetngam B., and Grant T., (2002), *Implementation of SHRP Indirect Tension Tester to Mitigate Cracking in Asphalt Pavements and Overlays*, Final Report, FDOT BA-546, University of Florida, Gainesville, FL.
47. Roque R., Birgisson B., Drakos C., and Dietrich B., (2004), "Development and Field Evaluation of Energy-Based Criteria for Topdown Cracking Performance of Hot Mix Asphalt," *Journal of the Association of Asphalt Paving Technologists*, Vol. 73, pp. 229-260.
48. Zhang Z., Roque R., Birgisson B. and Sangpetngam B., (2001), "Identification and Verification of a Suitable Crack Growth Law", *Journal of the Association of Asphalt Paving Technologists*, Vol. 70, 206-241.
49. Apeageyi A. K., Dave E. V. and Buttlar W. G., (2008), "Effect of cooling rate on thermal cracking of asphalt", *Journal of the Association of Asphalt Paving Technologist*, Vol. 77, 709-738.
50. Marasteanu M., Zofka A., Turos M., Li X., Velasquez R., Buttlar W., Paulino G., Braham A., Dave E., Ojo J., Bahia H., Williams C., Bausano J., Kvasnak A., Gallistel A., McGraw J., (2007), *Investigation of Low Temperature Cracking in Asphalt Pavements National Pooled Fund Study 776*, Final Report prepared for Minnesota Department of Transportation Research Services MS 330, University of Minnesota, Minneapolis, MN.
51. Dave E. V., Braham A. F., Buttlar W. G., Paulino G. H. and Zofka A., (2008), "Integration of laboratory testing, field performance data and numerical simulations for the study of low-temperature cracking", Proceeding of the 6th RILEM conference on Cracking in Pavement, 369-378, Chicago, IL.
52. Wistuba M, and Spiegl M., (2007), "Asphalt Pavement in Cold Climates – A Systematic Approach for the Assessment of Cracking Resistance", Proceeding of the International Conference on Advanced Characterization of Pavement and Soil Engineering Materials, 1199-1208, Athens, Greece.
53. Bae A., Stoffels S., Chehab G, Clyne T. and Worel B., (2007) , "Direct effects of thermal cracks on pavement roughness", *Journal of the Association of Asphalt Paving Technologists*, Vol. 76, 59-84.
54. Cundall, P. A. and Strack, O. D. L., (1979), "A discrete numerical model for granular assemblies", *Géotechnique*, 29, 47–65.
55. Wu J., A. Collop A. and McDowell G., (2008), "Discrete element modeling of low temperature monotonic compression tests in an idealized asphalt mixture", Proceeding of the 6th RILEM conference on Cracking in Pavement, 395-403.
56. Feng Z, Zhang P., Guddati M. N., Kim Y. R. and Little D. N., (2008), "Virtual testing procedure for cracking performance prediction of HMA", Proceeding of the 6th RILEM conference on Cracking in Pavement, 575-585, Chicago, IL.

57. Marasteanu M., Labuz J. and Li X., (2008), "Acoustic emission in asphalt mixture IDT creep and strength tests", Proceeding of the 7th International RILEM Symposium ATCBM09 on Advanced Testing and Characterization of Bituminous Materials, 501-508, Rhodes, Greece.
58. Marasteanu M., Li X. and Turos M., (2007), "Study of low temperature cracking in asphalt mixtures using mechanical testing and acoustic emission", *Journal of the Association of Asphalt Paving Technologists*, Vol. 76, 427-453.
59. Lim I. L., Johnston I. W., and Choi S. K., (1993), "Stress Intensity Factor for Semi Circular Specimen under Three-Point Bending", *Engineering Fracture Mechanics*, Vol. 44, No.3, 363-382.
60. Asphalt Research Consortium, Annual Work Plan for Year 2 – Revised, April 1, 2008 – March 31, 2009 December 2008 (Western Research Institute, Texas A&M University, University of Wisconsin-Madison, University of Nevada-Reno, Advanced Asphalt Technologies)
61. Johnson, A., Clyne, T. R., Worel, B. J., 2008 *MnROAD Phase II Construction Report*, Minnesota Department of Transportation, June 2009, St. Paul, MN.
62. Clyne T. R., Johnson E. N., James McGraw J. and Reinke G., (2009), *Field Investigation of Polyphosphoric Acid Modified Binders at MnROAD*, Minnesota Department of Transportation Office of Materials.
63. Marasteanu M., Moon, K. H., Turos M. I., *Asphalt Mixture and Binder Fracture Testing for 2008 MnROAD Construction*, Minnesota Department of Transportation, December 2009, St. Paul, MN.

Chapter 3. Expand Phase I Test Matrix

1. AASHTO. (2002). *Mixture Conditioning of Hot Mix Asphalt. Standard Specification for Transportation Materials and Methods of Sampling and Testing*. American Association of State Highway and Transportation Officials, Washington, D.C..
2. Mugurel Turos, Ki Hoon Moon, Mihai Marasteanu. (2010). *Air Voids Testing for MnROAD Cells*. St. Paul Minnesota: Minnesota Departement of Transportation.
3. ASTM D7313-06. (2006). *Standard Test Method for Determining Fracture Energy of Asphalt-Aggregate Mixtures Using the Disk-Shaped Tension Geometry*. American Society for Testing and Materials, Philadelphia .
4. Wagoner, M., Buttlar, W., & Paulino, G. (2005). "Disk-shaped compact tension test for asphalt concrete fracture," *Experimental Mechanics*, Vol. 45, No. 3 , 270-277.
5. Li, X., & Marasteanu, M. (2004). Evaluation of the Low Temperature Fracture Resistance of Asphalt Mixtures Using the Semi Circular Bend Test. *Association of Asphalt Paving Technologists*, No. 73 , 401-426.
6. Marasteanu, M., Zofka, A., Turos, M., Li, X., Velasquez, R., Li, X., et al. (2007). *National Pooled Fund Study 776 - Investigations of Low Temperature Cracking in Asphalt Pavements*. St. Paul, MN: Mn/DOT.
7. AASHTO T322-03. (2003). *Standard Method of Test for Determining the Creep Compliance and Strength of Hot-Mix Asphalt (HMA) Using Indirect Tensile Test Device*. American Association of State Highway and Transportation Officials, Washington, D.C..

Chapter 4. Subtask on Physical Hardening

1. Anderson, D., Christensen, D., Bahia, H.U., Dongre, R., Sharma, M., Antle, C., and Button J. "Binder Characterization and Evaluation Vol. 3: Physical Characterization. SHRPA-369", Strategic Highway Research Program, National Research Council, Washington, D.C. (1994).
2. Bahia H.U., "Low-Temperature Isothermal Physical Hardening of Asphalt Cements." Ph.D. Thesis. Pennsylvania State University, (1991), University Park, Pennsylvania.
3. American Association of State Highway and Transportation Officials (AASHTO) M320, "Standard Specification for Performance-Graded Asphalt Binder", AASHTO Provisional Standards, Washington, D.C. (2002).
4. Hesp, SAM and Subramani, S. "Another Look at the Bending Beam Rheometer for Specification Grading of Asphalt Cements", Proceedings of 6th MAIREPAV Conference, Torino, Italy, (2009).
5. Lu, X., and Isacson, U., "Laboratory Study on the Low Temperature Physical Hardening of Conventional and Polymer Modified Bitumens," *Construction and Building Materials*, Vol. 14, pp. 79-88, (2000).
6. Struik, LCE., *Physical Hardening in Amorphous Polymers and Other Materials*, Elsevier, (1978).
7. Ferry, J.D., *Viscoelastic Properties of Polymers*, 3rd Edition, Wiley, New York, NY, (1980).
8. Doolittle, A.K., "Studies in Newtonian Flow. II The Dependence of Viscosity of Liquids on Free-Space", *Journal of Applied Physics* 22 (12), pp. 1471, (1951).
9. Doolittle, A.K., and Doolittle, D.B., "Studies in Newtonian Flow. V Further Verification of the Free Space Viscosity Equation", *Journal of Applied Physics* 28 (8), pp. 901, (1957).
10. Williams, M.L., Landel, R.F., Ferry, J.D., "The Temperature Dependence of Relaxation Mechanisms in Amorphous Polymers and Other Glass-forming Liquids", *Journal of the American Chemical Society* 77, pp. 3701-3706, (1955).
11. Brandrup, J., Immergut, E.H., Grulke, E.A., *Polymer Handbook*, 4th Edition, Wiley-Interscience, New York, NY, (2003).
12. Claudy, P., Planche, J.P., King, G., Letoffe, J.M., "Characterization of Asphalt Cements by Thermomicroscopy and Differential Scanning Calorimetry: Correlation to Classic Physical Properties", Proceedings of the 204th American Chemical Society National Meeting, Division of Fuel Chemistry 37 (3), (1992), Washington, D.C..
13. Kriz, P., Stastna, J., Zanzotto, L., "Physical Aging in Semi-Crystalline Asphalt Binders", *Journal of the Association of Asphalt Paving Technologists* 77 pp.795-825, (2008).
14. Anderson, D.A., and Marasteanu, M.O., "Physical Hardening of Asphalt Binders Relative to Their Glass Transition Temperatures", *Transportation Research Record*. Journal, pp. 27-34, (1999).
15. Marasteanu, M.O., "Low-Temperature Inter-Conversions of the Linear Viscoelastic Functions for the Rheological Characterization of Asphalt Binders." Ph.D. Thesis. Pennsylvania State University, (1999), University Park, Pennsylvania.
16. Romero, P., Youtcheff, J., Stuart, K., "Low-Temperature Physical Hardening of Hot-Mix Asphalt", *Transportation Research Record*, pp. 22-26, (1999).
17. American Association of State Highway and Transportation Officials (AASHTO) Standard T313-05, "Standard method of test for determining the flexural creep stiffness of asphalt binder using the Bending Beam Rheometer (BBR)", *Standard Specifications for Transportation Materials and Methods of Sampling and Testing*, 25th Edition, (2005).

18. Bahia, H. and Anderson, D., "Glass Transition Behavior and Physical Hardening of Asphalt Binders," *Journal of the Association of Asphalt Paving Technologists*, Vol. 62, pp. 93-129, (1993).
19. Nam, K. and Bahia, H., "Effect of Binder and Mixture Variables on Glass Transition Behavior of Asphalt Mixtures", *Journal of the Association of Asphalt Paving Technologists*, Vol. 73, pp. 89, (2004).
20. Johansson, L. and Isacson, U., Effect of filler on low temperature physical hardening of bitumen, *Construction and Building Materials*, Vol. 12, pp. 463-470, (1998).
21. Lakes, R., *Viscoelastic Materials*, Cambridge University Press, New York, (2009).

Chapter 6. Subtask Part 1: Develop Test Method

1. Monsmith, C. L. and Secor, K. E., Viscoelastic Behaviour of Asphalt Concrete Pavements, *Journal of the Association of Asphalt Paving Technologist*, Vol.34, pp. 248-285, 1962.
2. SHRP-A-357, Development and Validation of Prediction Models and Specifications for Asphalt Binder and Paving Mixes, 1993.
3. Buttlar, W.G. and Roque, R., Development and Evaluation of the Strategic Highway Research Program Measurements and Analysis for Indirect Tensile Testing at Low Temperature, *Transportation Research Record No. 1454*, pp. 163-171, 1994.
4. Christensen, R.M. *Theory of Viscoelasticity, an introduction*. s.l. : Academic Press, 1982.
5. Findley, William N., Lai, James S. and Kasif, Onaran. *Creep and Relaxation of Nonlinear Viscoelastic Mateals*. New York : Dover Publications, 1998.
6. Hopkins, I.L. and Hamming, R.W., On Creep and Relaxation, *Applied Physics*, Vol. 28, pp. 906-909, 1957.
7. Secor, K.E. and Monsmith, C.L., Analysis and Interrelation of Stress-Strain-Time Data for Asphalt Concrete, *Transaction of the Society of Rheology*, Vol. 8, pp. 19-32, 1964.
8. Lim, I.L. and Johnston, Stress Intensity Factors for Semi-Circular Specimens Under Three-Point Bending, I.W. 3, *Engineering Fracture Mechanics*, Vol. 44, pp. 363-382, 1993.
9. Zofka, A., Investigation of Asphalt Concrete Creep Behavior Using 3-Point Bending Test, PhD Thesis, University of Minnesota, 2007.
10. AASHTO T 322-07, Standard Method of Test for Determining the Creep Compliance and Strength of Hot-Mix Asphalt (HMA) Using the Indirect Tensile Test Device, American Association of State Highway and Transportation Officials, 2007.

Chapter 7. Subtask Part 2: Develop Specification

1. M. O. Marasteanu, R. A. Velasquez, A. Zofka, A. Cannone Falchetto, *Development of a simple test to determine the low temperature creep compliance of asphalt mixture*. IDEA Program, 2009, *Transportation Research Board of the National Academies*.
2. American Association of State Highway and Transportation Officials (AASHTO) Standard T313-08, "Standard method of test for determining the flexural creep stiffness of asphalt binder using the Bending Beam Rheometer (BBR)", *Standard Specifications for Transportation Materials and Methods of Sampling and Testing*, 2009 Edition.
3. Krehbiel, T., "Correlation Coefficient Rule of Thumb". *The Decision Science Journal of Innovative Education*. Vol. 2(1), pp. 97-100, 2004.

4. T. J. Hirsch, "Modulus of elasticity of concrete affected by elastic moduli of cement paste matrix and aggregate". *Journal of the American Concrete Institute*, Vol. 59(3), 1962, pp. 427-452
5. D. Christensen, T. Pellinen, R. F. Bonaquist, "Hirsch model for estimating the modulus of asphalt concrete". *Journal of Association of Asphalt Paving Technologists*, Vol. 72, 2003, pp 97-121
6. A. Zofka, M. O. Marasteanu, X. Li, T. Clyne, J. McGraw, "Simple method to obtain asphalt binders low temperature properties from asphalt mixtures properties". *Journal of the Association of Asphalt Paving Technologists*, Vol. 74, 2005, pp255-282
7. A. Zofka, "Investigation of Asphalt Concrete Creep Behavior Using 3-Point Bending Test". PhD thesis, University of Minnesota, Minneapolis, July 2007
8. R. A. Velasquez, "On the Representative Volume Element of Asphalt Concrete with Application to Low Temperature". PhD thesis, University of Minnesota, Minneapolis, July 2009
9. R. A. Velasquez, A. CannoneFalchetto, M. O. Marasteanu, "From Mixtures to Binder. Can the Inverse Problem be Solved?". *Road Material and Pavement Design*, Vol. 11 – Special Issue, 2010, pp.225-250
10. J. D. Ferry, *Viscoelastic properties of polymers*. 3rd ed., Wiley and Sons, New York, 1980
11. W. N. Findley, J. S. Lai, K. Onaran, *Creep and relaxation of nonlinear viscoelastic materials*. Dover Publications, INC., New York, 1989
12. M. Neifar, H. Di Benedetto, "Thermo-viscoplastic law for bituminous mixes". *Road Material and Pavement Design*, Vol. 2, Issue 1, 2001
13. C. Huet, "Etude par une méthode d'impédance du comportement viscoélastique des matériaux hydrocarbonés". Thèse de doctorat d'ingénieur, Faculté des Sciences de l'Université de Paris, October 1963, pp 69, [In French].
14. M. L. Williams, R. F. Landel, J. D. Ferry, "The temperature dependence of relaxation mechanism in amorphous polymers and other glass-forming liquids". *Journal of the American Chemical Society*, Vol. 77(14), 1955, pp 3701-3707
15. G. Sayegh, "Variation des modules de quelques bitumes purs et enrobés bitumineux". Thèse de doctorat d'ingénieur, Faculté des Sciences de l'Université de Paris, June 1965. 74p. [In French]
16. C. De La Roche, "Module de rigidité et comportement en fatigue des enrobés bitumineux. Expérimentations et nouvelles perspectives d'analyse". Thèse de Doctorat : Ecole Centrale Paris, Décembre 1996. 189 p. [In French]
17. M. Neifar, "Comportement thermomécanique des enrobés bitumineux : expérimentation et modélisation". Thèse de Doctorat ENTPE-INSA Lyon, 1997. 289 p. [In French]
18. F. Olard, H. Di Benedetto, "General "2S2P1D" model and relation between the linear viscoelastic behaviors of bituminous binders and mixes". *Road Material and Pavement Design*, Vol. 4/2 – Special Issue, 2003, pp185-224
19. D. Bodin, G. Pijaudier-Cabot, C. De La Roche, J. Piau, C. Chabot, "Continuum Damage Approach to Asphalt Concrete Fatigue, Modeling". *Journal of Engineering Mechanics*, ASCE, June 2004
20. W. N. Findley, J. S. Lai, K. Onaran, *Creep and relaxation of nonlinear viscoelastic materials*. Dover Publications, INC., New York, 1989
21. M. Neifar, H. Di Benedetto, "Thermo-viscoplastic law for bituminous mixes". *Road Material and Pavement Design*, Vol. 2, Issue 1, 2001

22. F. Olard, H. Di Benedetto, “The DBN model: a thermo-visco-elasto-plastic approach for pavement behavior modeling”. *Journal of the Association of Asphalt Paving Technologists*, Vol. 74, 2005
23. H. Di Benedetto, M. Neifar, C. Sauzéat, F. Olard, “Three-dimensional thermo-viscoplastic behavior of bituminous materials. The DBN law”. *Road Material and Pavement Design*, Vol. 8, 2007, pp.285-315
24. F. Olard, “Comportement thermomécanique des enrobes bitumineux a basses températures – relation entre les propriétés du liant et de l’enrobe”. Thèse de Doctorat : Ecole Nationale des Travaux Publics de l’Etat, Octobre 2003. 226 p. [In French]
25. H. Di Benedetto, F. Olard, C. Sauzéat, B. Delaporte, “Linear viscoelastic behaviour of bituminous materials: from binders to mixes”, *Road Material and Pavement Design*, Vol. 5 – Special Issue, 2004, pp163-202
26. B. Delaporte, H. Di Benedetto, P. Chaverot, G. Gauthier, “Linear viscoelastic properties of bituminous materials: from binders to mastics”. *Journal of the Association of Asphalt Paving Technologists*, Vol. 76, 2007, pp 455-494
27. M. O. Marasteanu, R. A. Velasquez, A. Zofka, A. Cannone Falchetto, *Development of a simple test to determine the low temperature creep compliance of asphalt mixture*. IDEA Program Final Report NCHRP 133, 2009, Transportation Research Board of the National Academies.
28. T. Ohkami, G. Swoboda, “Parameter identification of viscoelastic materials”. *Computers and Geotechnics*, Vol. 24, 1999, pp 279-295
29. Y. Ichikawa, T. Ohkami, “A parameter identification procedure as a dual boundary control problem for linear elastic materials”. *Soils and Foundations*, Vol. 32(2), 1992, pp 35-44
30. A. F. M. S. Amin, M. S. Alam, Y. Okui, “An improved hyperelasticity relation in modeling viscoelasticity response of natural and high damping rubbers in compression: experiments, parameter identification and numerical verification”. *Mechanics of Materials*, Vol. 34, 2002, pp 75-95
31. S Kim, K. L. Kreider, “Parameter identification for nonlinear elastic and viscoelastic plates”. *Applied Numerical Mathematics*, Vol. 56(12), 2006, pp 1538-1554
32. A. T. Papagiannakis, A. Abbas, E. Masad, “Micromechanical analysis of viscoelastic properties of asphalt concretes”. *Transportation Research Board*, Vol. 1789, 2002, pp 113-120
33. A. A. Zevin, “Approximation of functions of Volterra operators in Boundary Value Problems for aging materials”. *Ivestiya Vuzov AN SSSR MTT (Proceedings of Universities of the Academy of Science of USSR, Mechanics of Solid Bodies)*, no. 3, pp. 127-134, 1979 (in Russian)
34. Anderson, D.A., and Kennedy T., “Development of SHRP Binder Specification”, *Proceedings of the Association of Asphalt Paving Technologies*, Vol. 62, pp. 481-507, 1993, Austin, TX.

Chapter 8, 9, & 10. Subtask Part 3: Proposed Simplified Method to Obtain Mixture Creep Compliance

1. American Association of State Highway and Transportation Officials (AASHTO) Standard T313-05, "Standard method of test for determining the flexural creep stiffness of asphalt binder using the Bending Beam Rheometer (BBR)," *Standard Specifications for Transportation Materials and Methods of Sampling and Testing*, 25th Edition, 2005.

2. T. Hoare and S. Hesp, "Low-Temperature Fracture Testing of Asphalt Binders: Regular and Modified Systems." *Transportation Research Record* 1728, pp. 36-42, 2000.
3. S. Hesp, *An improved low-temperature asphalt binder specification method*. Ministry of Transportation Ontario Contract 9015-A-000190, 2003.
4. E. Chailleux, and V. Mouillet, "Determination of the low temperature bitumen cracking properties: fracture mechanics principle applied to a three points bending test using a non-homogeneous geometry," ICAP Proceedings, Quebec, 2006.
5. E. Chailleux, V. Mouillet, L. Gaillet, D. Hamon, *Towards a Better Understanding of the Three Point Bending Test Performed on Bituminous Binders. Advanced Characterization of Pavement and Soil Engineering Materials*. Taylor & Francis Group, London, 2007.
6. ASTM Standard E399, *Standard Test Method for Linear-Elastic Plane-Strain Fracture Toughness K_{IC} of Metallic Materials*, West Conshohocken, PA, 2006.
7. Velasquez R., Tabatabaee, H.A. and Bahia, H.U., Low Temperature Cracking Characterization of Asphalt Binders by Means of the Single-Edge Notch Bending (SENB) Test. *Journal of the Association of Asphalt Pavement Technologists*, 2011.
8. ABAQUS, help documentation, ver. 6.6-1, 2006.
9. European Standard CEN/TS 15963:2010, "Bitumen and bituminous binders - Determination of the fracture toughness temperature by a three point bending test on a notched specimen," 2010.
10. Swiertz, D. Mahmoud, E., Bahia, H.U., "Estimating the Effect of RAP and RAS on Fresh Binder Low Temperature Properties without Extraction & Recovery." Proceedings of the 90th Annual Meeting of the Transportation Research Board, Washington D.C, 2011.
11. S.S. Kim, "Direct Measurement of Asphalt Binder Thermal Cracking," *Journal of Material in Civil Engineering*. Volume 17, Issue 6, pp. 632-639, 2005.
12. Copeland, *Reclaimed Asphalt Pavement in Asphalt Mixtures: State-of-the-Practice*. FHWA Office of Infrastructure Research, 2009.
13. McDaniel, R. S., Soleymani, H., Anderson, R. M., Turner, P. and Peterson, R., Recommended use of Reclaimed Asphalt Pavement in the Superpave Mix Design Method. Web Document 30 (Project 9-12), NCHRP, 2000.
14. Bouldin, M., Dongre, R., Rowe, G., Sharrock, M.J., Anderson, D. "Predicting Thermal Cracking of Pavements from Binder Properties-Theoretical Basis and Field Validation." *Journal of the Association of Asphalt Pavement Technologists*, 69 (2000): 455.
15. Sushanta, R. and Hesp, S. "Low-Temperature Binder Specification Development: Thermal Stress Restrained Specimen Testing of Asphalt Binders and Mixtures." *Transportation Research Record*, (2001): 7-14.

Chapter 11. Develop Improved TC Model

1. ARA, Inc. (2004). *Guide for Mechanistic-Empirical Design of New and Rehabilitated Pavement Structures*, National Cooperative Highway Research Program,
2. A. K. Apeageyi, E. V. Dave, and W. G. Buttlar (2008). "Effect of Cooling Rate on Thermal Cracking of Asphalt Concrete Pavements," *Journal of Association of the Asphalt Paving Technologists*, Volume 77, pp. 709-738.
3. G. I. Barenblatt (1959). "The formation of equilibrium cracks during brittle fracture: general ideas and hypotheses, axially symmetric cracks," *Applied Mathematics and Mechanics*, Volume 23(3), pp. 622-636.

4. Buttlar, W. G., Roque, R., & Reid, B. (1998). Automated Procedure for Generation of Creep Compliance Master Curve for Asphalt Mixtures. *Transportation Research Record*, Volume 1630, pp. 28–36.
5. R. M. Christensen (1982). *Theory of Viscoelasticity*. Dover Publications, Inc., Mineola, NY.
6. Q. Dai, and Z. You (2009). “Micromechanical Finite Element Framework for Predicting Viscoelastic Properties of Heterogeneous Asphalt Mixtures,” *Materials and Structures*, Volume 41(6), pp. 1025-1037.
7. E. V. Dave, S. H. Song, W. G. Buttlar, and G. H. Paulino (2007). "Reflective and Thermal Cracking Modeling of Asphalt Concrete Overlays," Proceedings of the International Conference on Advanced Characterization of Pavement and Soil Engineering Materials, Taylor and Francis, Athens, Greece.
8. E. V. Dave, A. F. Braham, W. G. Buttlar, G. H. Paulino, and A. Zofka (2008). “Integration of Laboratory Testing, Field Performance Data, and Numerical Simulations for the Study of Low-Temperature Cracking,” Proceedings of the 6th RILEM International Conference on Cracking in Pavements, Chicago, pp. 369-378.
9. D. S. Dugdale (1960). “Yielding of steel sheets containing slits,” *Journal of the Mechanics and Physics of Solids*, Volume 8(2), pp. 100–104.
10. A. Hillerborg, M. Modeer, and P. E. Petersson (1976). “Analysis of crack formation and crack growth in concrete by means of fracture mechanics and finite elements,” *Cement and Concrete Research*, Volume 6(6), pp. 773–781.
11. A. R. Ingraffea, W. H. Gerstle, P. Gergely, V. Saouma (1984). “Fracture mechanics of bond in reinforced concrete,” *Journal of Structural Engineering*, Volume 110 (4), pp. 871–890.
12. R. L. Lytton, J. Uzan, E. G. Femando, R. Roque, D. Hiltunen, and S. M. Stoffels (1993). *Development and Validation of Performance Prediction Models and Specifications for Asphalt Binders and Paving Mixes*, Final Report, Strategic Highway Research Program, Project SHRP-A357, Washington DC.
13. M. Marasteanu, A. Zofka, M. Turos, X. Li, R. Velasquez, X. Li, C. Williams, J. Bausano, W. Buttlar, G. Paulino, A. Braham, E. Dave, J. Ojo, H. Bahia, A. Gallistel, and J. McGraw (2007). *Investigation of Low Temperature Cracking in Asphalt Pavements*, Minnesota Department of Transportation, St. Paul, MN.
14. A. Muliana, and K. A. Khan (2008). “A Time-Integration Algorithm for Thermo-Rheologically Complex Polymers,” *Computational Materials Science*, Volume 41, pp. 576-589.
15. K. Park, G. H. Paulino, J. R. Roesler (2010). “Cohesive fracture model for functionally graded fiber reinforced concrete”, *Cement and Concrete Research*, Volume 40 (6), pp. 956-965.
16. G. H. Paulino, W. G. Buttlar, P. B. Blankenship, M. P. Wagoner, S. H. Song, and E. V. Dave (2006). *Final Report for NSF-GOALI Project - CMS:0219566*, National Science Foundation, Washington, DC, 2006.
17. R. Roque, D. R. Hiltunen, W. G. Buttlar. (1995a) “Thermal Cracking Performance and Design of Mixtures Using Superpave(TM),” *Journal of the Association of Asphalt Paving Technologists*, Volume 64, pp. 718-735.
18. R. Roque, D. Hiltunen, W. Buttlar, T. Farwana. (1995b) “Engineering Properties of Asphalt Mixtures and the Relationship to their Performance,” STP1265 Engineering Properties of Asphalt Mixtures and the Relationship to their Performance, ASTM International.

19. Roseler, J., G. H. Paulino, K. Park, C. Gaedicke. (2007). "Concrete fracture prediction using bilinear softening," *Cement and Concrete Composites*, Volume 29 (4), pp. 300-312.
20. S. H. Song, G. H. Paulino, and W. G. Buttlar. (2006) "A Bilinear Cohesive Zone Model Tailored for Fracture of Asphalt Concrete considering Rate Effects in Bulk Materials," *Engineering Fracture Mechanics*, Volume 73, Number 18, pp. 2829-2848.
21. S. Yi and H. H. Hilton (1994). "Dynamic Finite Element Analysis of Viscoelastic Composite Plates in the Time Domain." *International Journal of Numerical Methods in Engineering*, Volume 37(12), pp. 4081-4096.
22. M. A. Zocher, S. E. Groves, and D. H. Allen (1997). "A Three-Dimensional Finite Element Formulation for Thermoviscoelastic Orthotropic Media." *International Journal of Numerical Methods in Engineering*, Volume 40(12), pp. 2267-2288.

Chapter 12. Modeling of Asphalt Mixtures Contraction and Expansion Due to Thermal Cycling

1. Jung, D.H., Vinson, T.S., "SHRP-A-400: Low-Temperature Cracking: Test Selection." *Strategic Highway Research Program, National Research Council*. Washington D.C., 1994.
2. Bouldin, M., Dongre, R., Rowe, G., Sharrock, M.J., Anderson, D. "Predicting Thermal Cracking of Pavements from Binder Properties-Theoretical Basis and Field Validation." *Journal of the Association of Asphalt Pavement Technologists*, Vol. 69, 2000, pp. 455.
3. Bahia, H.U., and Anderson, D.A., "The Development of the Bending Beam Rheometer: Basics and Critical Evaluation of the Rheometer." Edited by J.C. Hardin. *Physical Properties of Asphalt Cement Binders: ASTM STP 1241*, American Society for Testing Materials, 1995.
4. Monismith, C.L, Secor, G.A. and Secor, K.E., "Temperature Induced Stresses and Deformations in Asphalt Concrete." *Journal of the Association of Asphalt Pavement Technologists*, Vol. 34, 1965, pp. 245-285.
5. Bahia H.U., "Low-Temperature Isothermal Physical Hardening of Asphalt Cements." *Ph.D. Thesis*. Pennsylvania State University, 1991, University Park, Pennsylvania.
6. Anderson, D., Christensen, D., Bahia, H.U., Dongre, R., Sharma, M., Antle, C., and Button J. "Binder Characterization and Evaluation Vol. 3: Physical Characterization. SHRPA-369", Strategic Highway Research Program, National Research Council, Washington, D.C., 1994.
7. Planche, J.P., Claudy, P.M., Létoffé, J.M., Martin, D., "Using Thermal Analysis Methods to Better Understand Asphalt Rheology," *ThermochimicaActa*, Vol. 324, 1998, pp. 223-227.
8. Anderson, D.A., and Marasteanu, M.O., "Physical Hardening of Asphalt Binders Relative to Their Glass Transition Temperatures", *Transportation Research Record*, No. 1661, Transportation Research Board of the National Academies, Washington, D.C., 1999, pp. 27-34.
9. Bahia, H., Zeng, M., Nam, K., "Consideration of Strain at Failure and Strength in Prediction of Pavement Thermal Cracking." *Journal of the Association of Asphalt Pavement Technologists*, Vol. 69, 2000, pp. 497-540.
10. Kriz, P., Stastna, J. and Zanzotto, L., "Temperature Dependence and Thermo-reversibility of Physical Hardening of Asphalt Binders," submitted to 4th Eurasphalt & Eurobitume Congress, Copenhagen, Denmark, 2008.
11. Bahia, H.U., and Velasquez, R., "Understanding the Mechanism of Low Temperature Physical Hardening of Asphalt Binders." Proceedings of the 55th Annual Meeting of the Canadian Technical Asphalt Association, 2010.

12. Struik, LCE., *Physical Hardening in Amorphous Polymers and Other Materials*, Elsevier, 1978.
13. Ferry, J.D., *Viscoelastic Properties of Polymers*, 3rd Edition, Wiley, New York, NY, 1980.
14. Hesp, SAM and Subramani, S. "Another Look at the Bending Beam Rheometer for Specification Grading of Asphalt Cements", Proceedings of 6th MAIREPAV Conference, Torino, Italy, 2009.
15. Romero, P., Youtcheff, J., Stuart, K., "Low-Temperature Physical Hardening of Hot-Mix Asphalt", In *Transportation Research Record*, No. 1661, Washington, D.C., 1999, pp. 22-26.
16. Evans, M. and Hesp, S.A.M., "Physical Hardening Effects on Stress Relaxation in Asphalt Cements and Implications for Pavement performance," Presented at the 90th Annual Meeting of the Transportation Research Board, Washington D.C., 2011.
17. Shenoy, A., "Stress Relaxation can Perturb and Prevent Physical Hardening in a Constrained Binder at Low Temperatures," *Road Materials and Pavement Design*, Vol.3, Issue 1, 2002, pp. 87-94.
18. Cannone-Falchetto, A., Marasteanu, M.O., Di Benedetto, H.V., "Analogical Based Approach to Forward and Inverse Problems for Asphalt Materials Characterization at Low Temperatures," *Preprints of the Association of Asphalt Pavement Technologists*, 2011.
19. Cannone-Falchetto, A., Mugurel, T., Ki Hoon, M., Marasteanu, M.O., Dongre, R.N., "Physical Hardening: from Binders to Mixtures," Presented at the 90th Annual Meeting of the Transportation Research Board, Washington D.C., 2011.
20. Marasteanu, M., Zofka, A., Turos, M., Li, X., Velasquez, R., Li, X., Buttler, W., Paulino, G., Braham, A., Dave, E., Ojo, J., Bahia, H., Williams, C., Bausano, J., Gallistel, A., McGraw, J., *Investigation of Low Temperature Cracking in Asphalt: Pavements National pooled Fund Study*, Minnesota Department of Transportation, MN/RC 2007-43 (2007), St. Paul, MN.
21. Bahia, H.U., Hanson, D.H., Zeng, M., Zhai, H., Khatri, M.A. & Anderson, R.M., *Characterization of Modified Asphalt Binders in Superpave Mix Design, NCHRP Report 459*. Washington DC: National Academy Press (2001).
22. Bahia, H.U., and Anderson, D.A., "Glass Transition Behavior and Physical Hardening of Asphalt Binders," *Journal of the Association of Asphalt Pavement Technologists*, Vol. 62, 1993, pp. 93-129.
23. Nam, K., and Bahia, H.U., "Effect of Binder and Mixture Variables on Glass Transition Behavior of Asphalt Mixtures," *Journal of the Association of Asphalt Paving Technologists*, Vol. 73, pp. 89, 2004.
24. Clopotel, C., Velasquez, R., Bahia, H.U., "Measuring Physico-Chemical Interaction in Mastics Using Glass Transition," Accepted for publication in the *Journal of the Association of Asphalt Pavement Technologists*, 2012.
25. Tabatabaee, H.A., Velasquez R., Bahia, H.U., "Predicting Low Temperature Physical Hardening in Asphalt Binders." Submitted for publication in *the Journal of Construction and Building Materials*, Elsevier, 2011.
26. Hass, R.G.G., and Phang, W.A., "Relationships between mix characteristics and low temperature pavement cracking", paper presented to AAPT, 1998.
27. Domaschuk, L., Skasgard, P.S., and Christianson, R.H., "Cracking of asphalt pavement due to thermal contraction", Proceedings of the Golden Jubilee Convention, Canadian good roads association, October, Montreal, Que., pp. 395-407, 1964.

28. Gaw, W. J., Burgess, R. A., and Yoong, F. D., "Road performance after five years and laboratory predictions of low temperature performance", proceeding of the Canadian technical asphalt association, Vol. 19, 1974.
29. Janoo, V., Bayer, J., and Walsh, M., "Thermal stress measurements in asphalt concrete", CRREL Report 93-10. July 1993.
30. Stoffels, S. M. and Kwanda, F. D., "Determination of the Coefficient of thermal contraction of asphalt concrete using the resistance strain gage technique", Proceeding of the association of asphalt paving technologists, Vol. 65, pp. 73-98, 1996.
31. Wada, Y., and Hirose, H., "Glass transition phenomena and rheological properties of petroleum asphalt", *Journal of the Physical Society of Japan*, Vol. 15, No.10 ,p. 1885, 1960.
32. Schimidt, R.J. and Sntucci, L.E., "A practical method for determining the glass transition temperature of asphalt and calculation of their low temperature viscosities", *Proceeding of the Association of asphalt paving technologists*, Vol. 35, p. 61, 1966.
33. Jongepier, R. and Kuilman, B., "The dynamic shear modulus of bitumens as a function of frequency and temperature", *Rheological Acta*, Band 7, Heft 1, p.102, 1970.
34. Nam, K., "Effect of asphalt modification on low-temperature cracking", M.S. dissertation, University of Wisconsin-Madison, 2001.
35. Bahia, H.U., Zeng, M., and Nam, K., "Consideration of strain at failure and strength in prediction of pavement thermal cracking", *Proceedings of the association of asphalt paving technologists*, Vol. 69, pp. 445-498, 2000.
36. Nam, K., "Effect of thermo-volumetric properties of modified asphalt mixtures on low-temperature cracking", Ph.D. dissertation, University of Wisconsin-Madison, 2005.
37. Abu Al-Rub, R. K., You T., Masad, E. A., and Little, D. N., *Mesomechanical modeling of the thermo-viscoelastic, thermo-viscoplastic, and thermo-viscodamage response of asphalt concrete*, 2011.
38. Sadd, M.H. and Dai, Q., "Simulation of asphalt materials using Finite Element Micromechanical model with damage mechanics", 2010.
39. Roohi, N., Tashman, L., and Bahia, H. U., "Internal structure characterization of asphalt mixtures for rutting performance using imaging analysis", Accepted for publication in the *Journal of the Association of Asphalt Pavement Technologists*, 2012.
40. Tabatabaee, H.A., Velasquez, R., and Bahia, H.U., "Modeling Thermal Stress in Asphalt Mixtures Undergoing Glass Transition and Physical Hardening," Submitted to 91st Annual Meeting of Transportation Research Board, Washington. D.C., 2012.
41. Marasteanu, M. "Role of Bending Beam Rheometer Parameters in Thermal Stress Calculations." *Transportation Research Record* 1875, pp.9-13, 2004.

Chapter 13. Validation of New Specification

1. American Association of State Highway and Transportation Officials (AASHTO) Standard T313-08, "Standard method of test for determining the flexural creep stiffness of asphalt binder using the Bending Beam Rheometer (BBR)," *Standard Specifications for Transportation Materials and Methods of Sampling and Testing*, 2009 Edition.
2. American Association of State Highway and Transportation Officials (AASHTO) "Standard T 322-07. Determining the Creep Compliance and Strength of Hot-Mix Asphalt (HMA) Using the Indirect Tensile Test Device." *Standard Specifications for Transportation and Methods of Sampling and Testing*, 2009 Edition.

3. Cannone Falchetto A., Marasteanu M. O., and Di Benedetto H., "Analogical Based Approach to Forward and Inverse Problems for Asphalt Materials Characterization at Low Temperatures," *Journal the Association of Asphalt Paving Technologists*, (AAPT), Vol. 80, 2011.
4. Christensen D., Pellinen T., Bonaquist R. F. "Hirsch model for estimating the modulus of asphalt concrete," *Journal of the Association of Asphalt Paving Technologists*, (AAPT), Vol. 72, pp. 97-121, 2003.
5. Di Benedetto H., Olard F., Sauzéat C., Delaporte B., "Linear viscoelastic behavior of bituminous materials: from binders to mixes," *Road Material and Pavement Design*, Vol. 5, Special Issue, pp.163-202, 2004.
6. Hirsch T. J., "Modulus of elasticity of concrete affected by elastic moduli of cement paste matrix and aggregate," *Journal of the American Concrete Institute*, Vol. 59(3), pp. 427-452, 1962.
7. Huet, C., "Coupled size and boundary-condition effects in viscoelastic heterogeneous and composite bodies," *Mechanics of Materials*, pp. 787-829, 1999.
8. Marasteanu M., Velasquez R., Cannone Falchetto A., Zofka A., "Development of a simple test to determine the low temperature creep compliance of asphalt mixture," IDEA Program Final Report NCHRP 133, *Transportation Research Board*, 2009.
9. Zofka A., Marasteanu M., Li X., Clyne T., McGraw J., "Simple method to obtain asphalt binders low temperature properties from asphalt mixtures properties," *Journal of the Association of Asphalt Paving Technologists*, Vol. 74, pp.255-282, 2005.
10. Zofka A., "Investigation of Asphalt Concrete Creep Behavior using 3-Point Bending Test," Ph.D. thesis, University of Minnesota, Minneapolis, July 2007

Appendix A: Air Void and Temperature Analysis

DCT Air Void and Temperature Analysis

Response Gf [J/m2]

Summary of Fit

RSquare	0.768015
RSquare Adj	0.715158
Root Mean Square Error	73.41386
Mean of Response	466.4486
Observations (or Sum Wgts)	98

Analysis of Variance

Source	DF	Sum of Squares	Mean Square	F Ratio
Model	18	1409592.3	78310.7	14.5300
Error	79	425778.0	5389.6	Prob > F
C. Total	97	1835370.4		≤.0001

Lack Of Fit

Source	DF	Sum of Squares	Mean Square	F Ratio
Lack Of Fit	15	134981.62	8998.77	Prob > F
Pure Error	64	290796.41	4543.69	0.0308
Total Error	79	425778.03		Max RSq
				0.8416

Tests wrt Random Effects

Source	SS	MS Num	DF Num	F Ratio	Prob > F
Air Voids (%)	66430	66430	1	1.2346	0.2840
Mix[Air Voids (%)]&Random	810437	54029.1	15	10.0247	≤.0001
Relative Temp	585141	585141	1	108.5685	≤.0001
Relative Temp*Air Voids (%)	1018.81	1018.81	1	0.1890	0.6649

Effect Details

Air Voids (%)

Effect Test

Sum of Squares	F Ratio	DF	Prob > F
66430.040	1.23461		0.2840

Denominator MS Synthesis: 0.9955*Mix[Air Voids (%)]&Random+0.0045*Residual

Least Squares Means Table

Level	Sq Mean	Std Error	Mean
4	488.04105	33.907867	489.504
7	435.71991	32.674438	445.201

LSMeans Differences Student's t

α=	0.050	2.13128
----	-------	---------

Level	Sq Mean
4 A	488.04105
7 A	435.71991

Levels not connected by same letter are significantly different.

Mix[Air Voids (%)]&Random

Effect Test

Sum of Squares	F Ratio	DF	Prob > F
810436.84	10.02475		≤.0001

Denominator MS Synthesis: Residual

LSMeans Differences Tukey HSD

α=	0.050	3.57397
----	-------	---------

Level	Sq Mean
[4]DCT-34 A	593.70833
[4]DCT-35 A	589.08333
[7]DCT-34 A B	573.54833
[7]DCT-35 A B	560.18833
[4]DCT-77 A B C	506.40500
[4]DCT-33 A B C D	500.15171
[4]DCT-21 A B C D	477.22167
[7]DCT-77 A B C D	472.30561
[4]DCT-22 A B C D	470.52667
[7]DCT-21 A B C D	468.35333
[7]DCT-33 A B C D	467.59833
[4]DCT-20 B C D	423.39833
[7]DCT-20 B C D	423.35500
[7]DCT-22 C D	381.61500
[7]DCT-NY C D E	367.79561
[4]DCT-W D E	343.83333
[7]DCT-W E	206.71961

Levels not connected by same letter are significantly different.

Relative Temp

Effect Test

Sum of Squares	F Ratio	DF	Prob > F
585140.52	108.5685		<.0001

Denominator MS Synthesis: Residual

Least Squares Means Table

Level	Sq Mean	Std Error	Mean
PG	384.23678	10.772610	389.033
PG+10	539.52218	10.297829	537.793

LSMeans Differences Student's t

q*	0.960	1.99045
----	-------	---------

Least Squares Means Table

Level	Sq Mean	Std Error	Mean
PG+10 A	539.52218		
PG B	384.23678		

Levels not connected by same letter are significantly different.

Relative Temp*Air Voids (%)

Effect Test

Sum of Squares	F Ratio	DF	Prob > F
1018.8125	0.18901		0.6649

Denominator MS Synthesis: Residual

Least Squares Means Table

Level	Sq Mean	Std Error	Mean
PG,4	407.15959	15.364983	
PG,7	361.31796	15.104007	
PG+10,4	568.92250	14.985542	
PG+10,7	510.12185	14.128505	

LSMeans Differences Tukey HSD

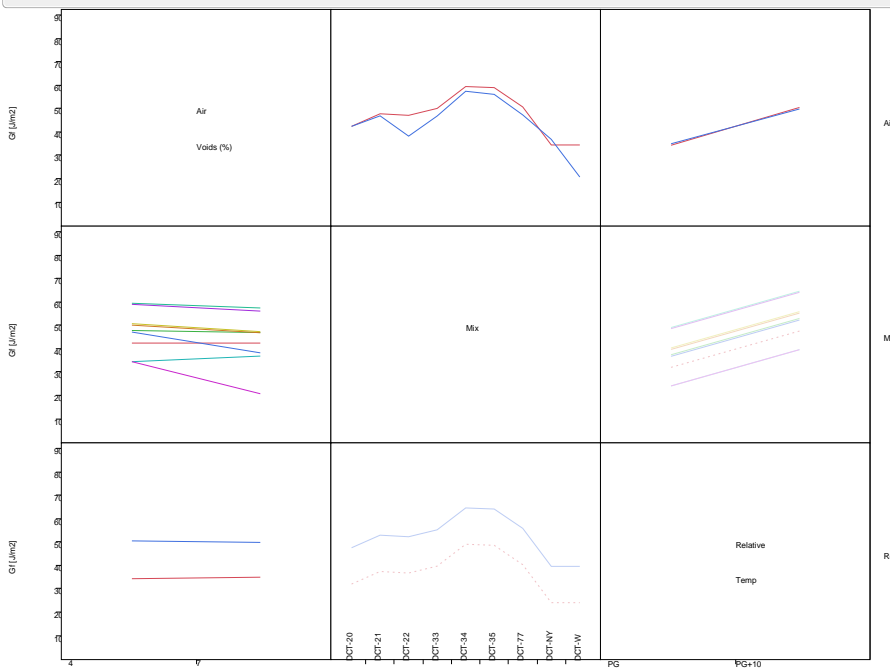
q*	0.099	2.62457
----	-------	---------

Least Squares Means Table

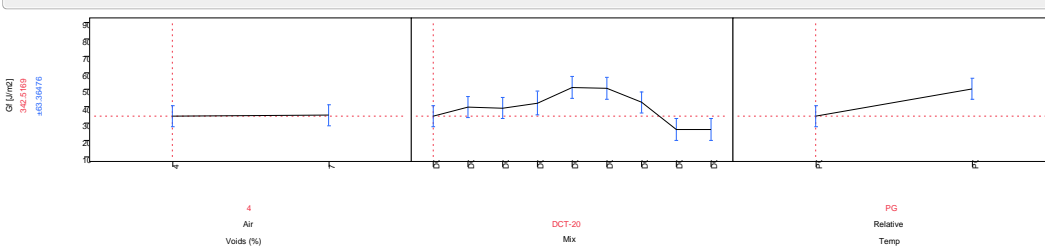
Level	Sq Mean	Std Error	Mean
PG+10,4 A	568.92250		
PG+10,7 B	510.12185		
PG,4 C	407.15959		
PG,7 C	361.31796		

Levels not connected by same letter are significantly different.

Interaction Profiles



Prediction Profiler



SCB Air Void and Temperature Analysis K_{IC}

Response K_{IC}

Summary of Fit

RSquare	0.536383
RSquare Adj	0.430749
Root Mean Square Error	0.095019
Mean of Response	0.841224
Observations (or Sum Wgts)	98

Analysis of Variance

Source	DF	Sum of Squares	Mean Square	F Ratio	Prob > F
Model	18	0.8252002	0.045844	5.0777	
Error	79	0.7132528	0.009029		Prob > F
C. Total	97	1.5384531			≤.0001

Lack Of Fit

Source	DF	Sum of Squares	Mean Square	F Ratio	Prob > F
Lack Of Fit	15	0.05095284	0.003397	0.3282	Prob > F
Pure Error	64	0.66230000	0.010348	0.9902	
Total Error	79	0.71325284		Max RSq	0.5695

Tests wrt Random Effects

Source	SS	MS Num	DF Num	F Ratio	Prob > F
Air Voids	0.52602	0.52602	1	34.2528	≤.0001
Mix[Air Voids]&Random	0.23195	0.01546	15	1.7127	0.0651
Relative Temp	0.04693	0.04693	1	5.1982	0.0253
Relative Temp*Air Voids	0.03585	0.03585	1	3.9712	0.0497

Effect Details

Air Voids

Effect Test

Sum of Squares	F Ratio	DF	Prob > F
0.52602160	34.2528	1	≤.0001

Denominator MS Synthesis: 0.9835*Mix[Air Voids]&Random+0.0165*Residual

Least Squares Means Table

Level	Sq Mean	Std Error	Mean
4	0.92420833	0.01886615	0.921136
7	0.77611111	0.01686386	0.776111

LSMeans Differences Student's t

α= 0.050 2.12788

Level	A	B	Sq Mean
4	A		0.92420833
7	B		0.77611111

Levels not connected by same letter are significantly different.

Mix[Air Voids]&Random

Effect Test

Sum of Squares	F Ratio	DF	Prob > F
0.23194564	1.7127	15	0.0651

Denominator MS Synthesis: Residual

LSMeans Differences Tukey HSD

α= 0.050 3.57397

Level	A	B	Sq Mean
[4]SCB-20	A B		0.99000000
[4]SCB-34	A		0.98333333
[4]SCB-35	A B C		0.97173394
[4]SCB-22	A B C D		0.92666667
[4]SCB-21	A B C D E		0.88833333
[4]SCB-77	A B C D E F		0.88026606
[4]SCB-33	A B C D E F		0.88000000
[4]SCB-W	A B C D E F		0.87333333
[7]SCB-35	A B C D E F		0.86500000
[7]SCB-NY	A B C D E F		0.83333333
[7]SCB-34	A B C D E F		0.80000000
[7]SCB-22	B C D E F		0.77666667
[7]SCB-W	B C D E F		0.77666667
[7]SCB-20	C D E F		0.77000000
[7]SCB-77	D E F		0.75000000
[7]SCB-33	E F		0.72833333
[7]SCB-21	F		0.68500000

Levels not connected by same letter are significantly different.

Relative Temp

Effect Test

Sum of Squares	F Ratio	DF	Prob > F
0.04693169	5.1982	1	0.0253

Denominator MS Synthesis: Residual

Least Squares Means Table

Level	Sq Mean	Std Error	Mean
PG	0.87221375	0.01369964	0.862245
PG+10	0.62810570	0.01369964	0.620204

LSMeans Differences Student's t

alpha	0.050	1.99045
-------	-------	---------

Level	Least Sq Mean
PG	A 0.87221375
PG+10	B 0.62810570

Levels not connected by same letter are significantly different.

Relative Temp*Air Voids

Effect Test

Sum of Squares	F Ratio	DF	Prob > F
0.05853362	3.9712	1	0.0497

Denominator MS Synthesis: Residual

Least Squares Means Table

Level	Sq Mean	Std Error
PG,4	0.96553861	0.02040419
PG,7	0.77888889	0.01628632
PG+10,4	0.88287806	0.02040419
PG+10,7	0.77333333	0.01628632

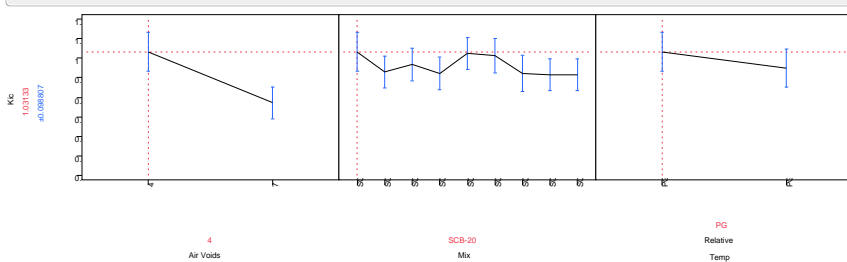
LSMeans Differences Tukey HSD

alpha	0.000	2.62457
-------	-------	---------

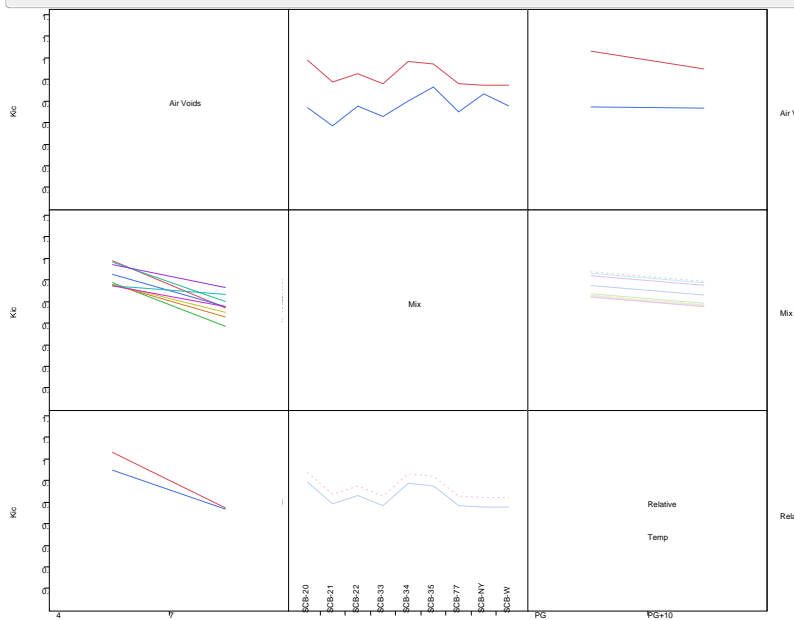
Level	Least Sq Mean
PG,4	A 0.96553861
PG+10,4	B 0.88287806
PG,7	C 0.77888889
PG+10,7	C 0.77333333

Levels not connected by same letter are significantly different.

Prediction Profiler



Interaction Profiles



SCB Air Void and Temperature Analysis G_f

Response G_f

Summary of Fit

RSquare	0.515482
RSquare Adj	0.40367
Root Mean Square Error	108.3136
Mean of Response	365.2812
Observations (or Sum Wgts)	97

Analysis of Variance

Source	DF	Sum of Squares	Mean Square	F Ratio	Prob > F
Model	18	973561.7	54086.8	4.6103	
Error	78	915083.4	11731.8		Prob > F
C. Total	96	1888645.1			≤.0001

Variance Component Estimates

Component	Var	Percent
Mix[Air Voids]&Random	2596.486	18.121
Residual	11731.84	81.879
Total	14328.32	100.000

These estimates based on equating Mean Squares to Expected Value.

Tests wrt Random Effects

Source	SS	MS Num	DF Num	F Ratio	Prob > F
Air Voids	117712	117712	1	4.4778	0.0512
Mix[Air Voids]&Random	397823	26521.5	15	2.2606	0.0106
Relative Temp	466915	466915	1	39.7990	≤.0001
Relative Temp*Air Voids	9.84146	9.84146	1	0.0008	0.9770

Effect Details

Air Voids

Effect Test

Sum of Squares	F Ratio	DF	Prob > F
117712.23	4.4778	1	0.0512

Denominator MS Synthesis: 0.9842*Mix[Air Voids]&Random+0.0158*Residual

Least Squares Means Table

Level	Sq Mean	Std Error	Mean
4	405.60417	24.683636	400.361
7	335.19377	22.313247	336.158

LSMeans Differences Student's t

α=	0.050	2.12885
----	-------	---------

Level	Sq Mean
4 A	405.60417
7 A	335.19377

Levels not connected by same letter are significantly different.

Mix[Air Voids]&Random

Effect Test

Sum of Squares	F Ratio	DF	Prob > F
397822.78	2.2606	15	0.0106

Denominator MS Synthesis: Residual

LSMeans Differences Tukey HSD

α=	0.050	3.57546
----	-------	---------

Level	Sq Mean
[4]SCB-34 A	503.20333
[4]SCB-35 A B	465.82271
[4]SCB-20 A B	462.75500
[4]SCB-77 A B	461.77729
[7]SCB-35 A B C	390.29000
[7]SCB-77 A B C	374.53167
[7]SCB-34 A B C	368.80167
[4]SCB-33 A B C	367.01667
[4]SCB-21 A B C	361.73000
[4]SCB-22 A B C	359.36000
[7]SCB-NY A B C	358.14833
[7]SCB-21 A B C	354.30890
[7]SCB-22 A B C	335.09333
[7]SCB-20 A B C	328.49667
[7]SCB-33 A B C	294.69667
[4]SCB-W B C	263.16833
[7]SCB-W C	212.37667

Levels not connected by same letter are significantly different.

Levels not connected by same letter are significantly different.

Relative Temp

Effect Test

Sum of Squares	F Ratio	DF	Prob > F
466915.22	39.7993		<.0001

Denominator MS Synthesis: Residual

Least Squares Means Table

Level	Sq Mean	Std Error	Mean
PG	300.48445	15.773806	294.765
PG+10	440.31348	15.616507	434.359

LSMeans Differences Student's t

o*	0.9650	1.99085
----	--------	---------

Level	Least Sq Mean	Std Error	Mean
PG+10 A	440.31348		
PG B	300.48445		

Levels not connected by same letter are significantly different.

Relative Temp*Air Voids

Effect Test

Sum of Squares	F Ratio	DF	Prob > F
9.8414647	0.00081		0.9770

Denominator MS Synthesis: Residual

Least Squares Means Table

Level	Sq Mean	Std Error	Mean
PG,4	336.01063	23.259163	
PG,7	284.95927	21.313449	
PG+10,4	475.19770	23.259163	
PG+10,7	405.42928	20.844964	

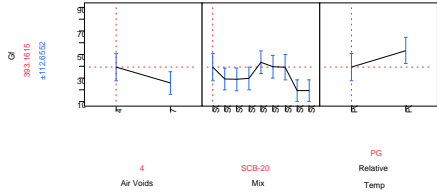
LSMeans Differences Tukey HSD

o*	0.096	2.62529
----	-------	---------

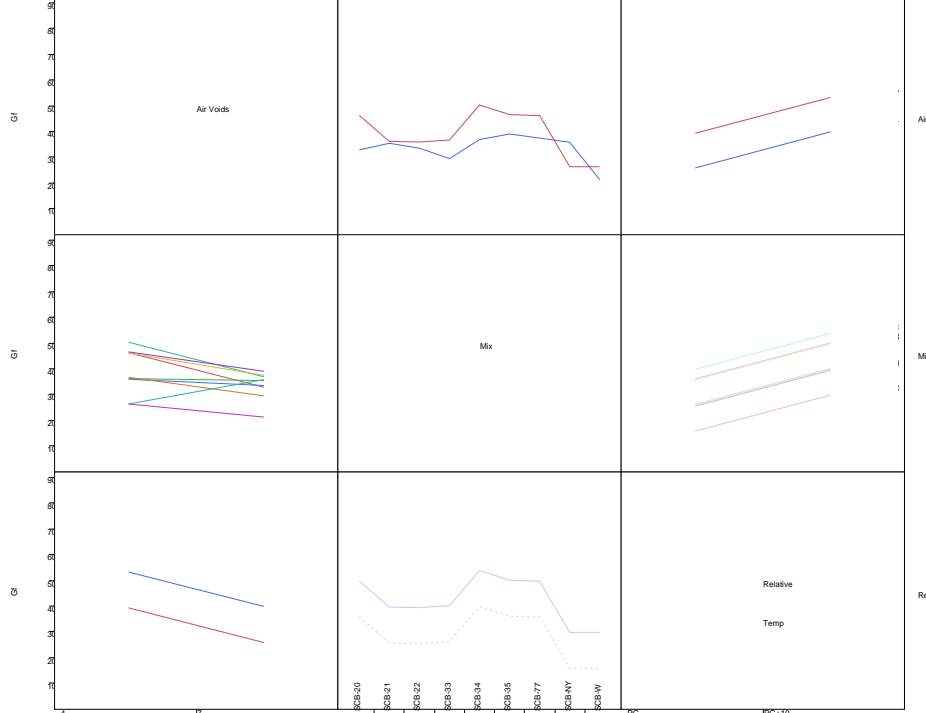
Level	Least Sq Mean	Mean
PG+10,4 A	475.19770	
PG+10,7 A B	405.42928	
PG,4 B C	336.01063	
PG,7 C	284.95927	

Levels not connected by same letter are significantly different.

Prediction Profiler



Interaction Profiles



IDT Air Void and Temperature Analysis Stiffness at 500s

Response Creep Stiffness @ 500

Summary of Fit

RSquare	0.722412
RSquare Adj	0.660725
Root Mean Square Error	3.409656
Mean of Response	13.8413
Observations (or Sum Wgts)	100

Analysis of Variance

Source	DF	Sum of Squares	Mean Square	F Ratio
Model	18	2450.6983	136.150	11.7111
Error	81	941.6860	11.626	Prob > F
C. Total	99	3392.3843		≤ 0.001

Tests wrt Random Effects

Source	SS	MS Num	DF Num	F Ratio	Prob > F
Air Voids	152.546	152.546	1	3.9566	0.0652
Mix[Air Voids]&Random	581.186	38.7457	15	3.3327	0.0002
Relative Temp	1690.47	1690.47	1	145.4070	≤ 0.001
Relative Temp*Air Voids	16.9607	16.9607	1	1.4589	0.2306

Effect Details

Air Voids

Effect Test

Sum of Squares	F Ratio	DF	Prob > F
152.54639	3.9566	1	0.0652

Denominator MS Synthesis: 0.993*Mix[Air Voids]&Random+0.007*Residual

Least Squares Means Table

Level	Sq Mean	Std Error	Mean
4	15.081776	0.91950761	15.3011
7	12.597778	0.84496918	12.5978

LSMeans Differences Student's t

α= 0.050 2.13066

Level	Sq Mean
4 A	15.081776
7 A	12.597778

Levels not connected by same letter are significantly different.

Mix[Air Voids]&Random

Effect Test

Sum of Squares	F Ratio	DF	Prob > F
581.18551	3.3327	15	0.0002

Denominator MS Synthesis: Residual

LSMeans Differences Tukey HSD

α= 0.050 3.57109

Level	Sq Mean
[7]IDT-22 A	18.225000
[4]IDT-W A	17.998333
[4]IDT-22 A B	16.402272
[7]IDT-W A B	16.326667
[4]IDT-35 A B	15.856667
[4]IDT-77 A B C	15.256667
[4]IDT-34 A B C	14.936667
[4]IDT-21 A B C	14.151667
[7]IDT-34 A B C	13.381667
[4]IDT-33 A B C	13.281667
[7]IDT-77 A B C	13.158333
[4]IDT-20 A B C	12.770272
[7]IDT-35 A B C	12.051667
[7]IDT-20 A B C	11.203333
[7]IDT-33 B C	10.883333
[7]IDT-21 B C	9.850000
[7]IDT-NY C	8.300000

Relative Temp

Effect Test

Sum of Squares	F Ratio	DF	Prob > F
1690.4657	145.4030		0.0001
Denominator MS Synthesis:		Residual	

Least Squares Means Table

Level	Sq Mean	Std Error	Mean
PG	17.974282	0.47827551	17.8769
PG+10	9.705272	0.49142141	9.6410

LSMeans Differences Student's t

σ² = 0.9650 1.98969

Level	Least Sq Mean
PG	A 17.974282
PG+10	B 9.705272

Levels not connected by same letter are significantly different.

Relative Temp*Air Voids

Effect Test

Sum of Squares	F Ratio	DF	Prob > F
16.960674	1.4589 1		0.2306
Denominator MS Synthesis:		Residual	

Least Squares Means Table

Level	Sq Mean	Std Error
PG,4	19.630417	0.69599310
PG,7	16.318148	0.65618859
PG+10,4	10.533136	0.73170796
PG+10,7	8.877407	0.65618859

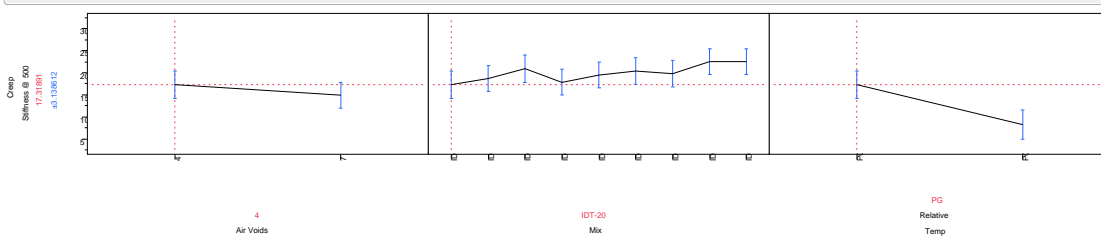
LSMeans Differences Tukey HSD

σ² = 0.039 2.62318

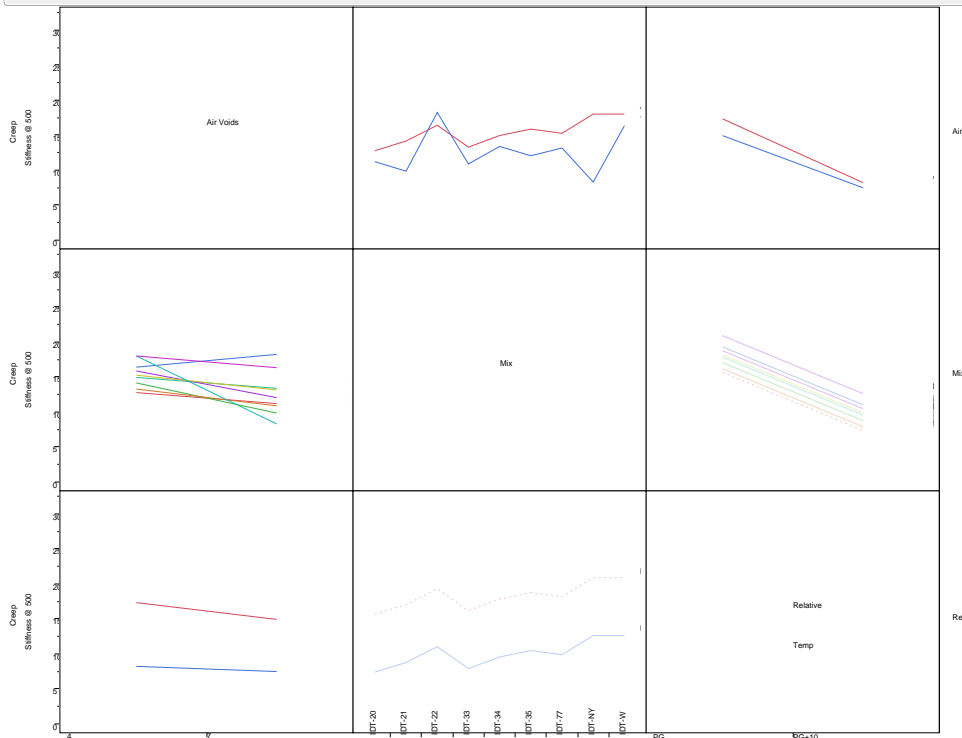
Level	Least Sq Mean
PG,4	A 19.630417
PG,7	B 16.318148
PG+10,4	C 10.533136
PG+10,7	C 8.877407

Levels not connected by same letter are significantly different.

Prediction Profiler



Interaction Profiles



IDT Air Void and Temperature Analysis Peak Strength

Response Strength

Summary of Fit

RSquare	0.845389
RSquare Adj	0.80971
Root Mean Square Error	0.486717
Mean of Response	5.001134
Observations (or Sum Wgts)	97

Analysis of Variance

Source	DF	Sum of Squares	Mean Square	F Ratio
Model	18	101.03312	5.61295	23.6940
Error	78	18.47766	0.23689	Prob > F
C. Total	96	119.51078		≤.0001

Tests wrt Random Effects

Source	SS	MS Num	DF Num	F Ratio	Prob > F
Air Voids	8.96788	8.96788	1	1.5016	0.2393
Mix[Air Voids]&Random	90.4405	6.02937	15	25.4518	≤.0001
Relative Temp	2.04034	2.04034	1	8.6129	0.0044
Relative Temp*Air Voids	0.04088	0.04088	1	0.1726	0.6790

Effect Details

Air Voids

Effect Test

Sum of Squares	F Ratio	DF	Prob > F
8.9678824	1.5016	1	0.2393

Denominator MS Synthesis: 0.9902*Mix[Air Voids]&Random+0.0098*Residual

Least Squares Means Table

Level	Sq Mean	Std Error	Mean
4	5.3160586	0.36676055	5.31444
7	4.7033333	0.33987552	4.73000

LSMeans Differences Student's t

α= 0.050 2.1313

Level	Sq Mean
4 A	5.3160586
7 A	4.7033333

Levels not connected by same letter are significantly different.

Mix[Air Voids]&Random

Effect Test

Sum of Squares	F Ratio	DF	Prob > F
90.440492	25.4518	15	≤.0001

Denominator MS Synthesis: Residual

Denominator MS Synthesis: Residual

LSMeans Differences Tukey HSD

$\alpha = 0.050$ 3.57546

Level	Least Sq Mean
[4]DT-W A	7.3116667
[7]DT-NY A	6.7050000
[7]DT-W A B	6.3733333
[4]DT-35 B C	5.5450000
[4]DT-22 C D	5.2713784
[4]DT-20 C D	5.1873784
[4]DT-34 C D	5.0733333
[4]DT-21 C D E	5.0613784
[7]DT-22 C D E F	4.6816667
[4]DT-33 C D E F	4.5550000
[4]DT-77 D E F	4.5233333
[7]DT-35 D E F	4.5233333
[7]DT-21 D E F	4.4966667
[7]DT-20 D E F G	4.2568992
[7]DT-34 E F G	4.0616667
[7]DT-77 F G	3.7631008
[7]DT-33 G	3.4683333

Levels not connected by same letter are significantly different.

Relative Temp

Effect Test

Sum of Squares	F Ratio	DF	Prob > F
2.0403450	8.6129	1	0.0044

Denominator MS Synthesis: Residual

Least Squares Means Table

Level	Sq Mean	Std Error	Mean
PG	4.8634981	0.06899887	4.86100
PG+10	5.1558938	0.07184011	5.15021

LSMeans Differences Student's t

$\alpha = 0.950$ 1.99085

Level	Least Sq Mean
PG+10 A	5.1558938
PG B	4.8634981

Levels not connected by same letter are significantly different.

Relative Temp*Air Voids

Effect Test

Sum of Squares	F Ratio	DF	Prob > F
0.04087998	0.1726	1	0.6790

Denominator MS Synthesis: Residual

Least Squares Means Table

Level	Sq Mean	Std Error
PG,4	5.1491667	0.09935061
PG,7	4.5778295	0.09577491
PG+10,4	5.4829505	0.10710356
PG+10,7	4.8288372	0.09577491

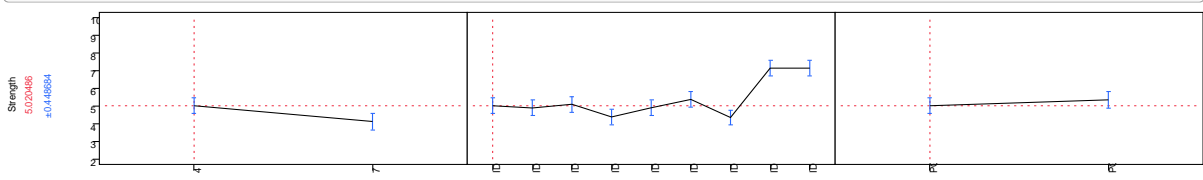
LSMeans Differences Tukey HSD

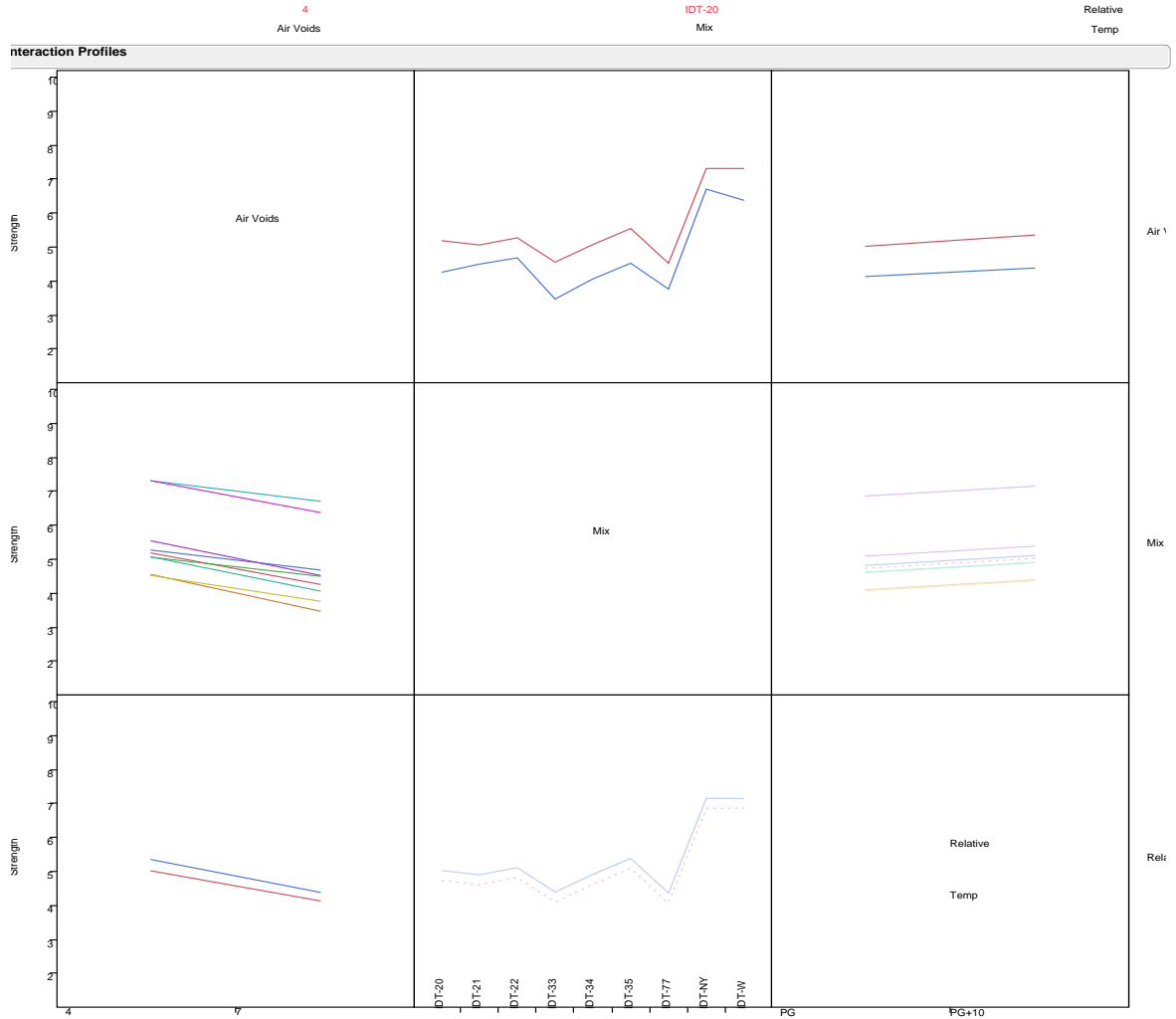
$\alpha = 0.050$ 2.62529

Level	Least Sq Mean
PG+10,4 A	5.4829505
PG,4 A B	5.1491667
PG+10,7 B C	4.8288372
PG,7 C	4.5778295

Levels not connected by same letter are significantly different.

Prediction Profiler





Comparison of Laboratories JMP analysis

Response DCT Gf

Summary of Fit

RSquare	0.561868
RSquare Adj	0.432052
Root Mean Square Error	88.14443
Mean of Response	493.7494
Observations (or Sum Wgts)	36

Analysis of Variance

Source	DF	Sum of Squares	Mean Square	F Ratio
Model	8	269019.40	33627.4	4.3282
Error	27	209774.91	7769.4	Prob > F
C. Total	35	478794.31		0.0019

Tests wrt Random Effects

Source	SS	MS Num	DF Num	F Ratio	Prob > F
Mix-AV	7244.42	3622.21	2	0.0598	0.9431
University[Mix-AV]&Random	181828	60609.4	3	7.8010	0.0007
Relative Temp	76196.2	76196.2	1	9.8072	0.0042
Mix-AV*Relative Temp	3750.57	1875.29	2	0.2414	0.7872

Effect Details

Mix-AV

Effect Test

Sum of Squares	F Ratio	DF	Prob > F
7244.4199	0.05982		0.9431

Denominator MS Synthesis: University[Mix-AV]&Random

Least Squares Means Table

Level	Sq Mean	Std Error	Mean
DCT-20-7%AV	488.04167	71.068856	488.042
DCT-21-4%AV	513.25917	71.068856	513.259
DCT-22-7%AV	479.94750	71.068856	479.948

University[Mix-AV]&Random

Effect Test

Sum of Squares	F Ratio	DF	Prob > F
181828.16	7.80103		0.0007

Denominator MS Synthesis: Residual

LSMeans Differences Tukey HSD

$\alpha = 0.050$ 3.06385

Level	Least Sq Mean
[DCT-22-7%AV]UMN A	578.28000
[DCT-20-7%AV]UMN A	552.72833
[DCT-21-4%AV]UMN A	549.29667
[DCT-21-4%AV]UIUC A B	477.22167
[DCT-20-7%AV]UIUC A B	423.35500
[DCT-22-7%AV]UIUC B	381.61500

Levels not connected by same letter are significantly different.

Relative Temp

Effect Test

Sum of Squares	F Ratio	DF	Prob > F
76196.241	9.8072	1	0.0042

Denominator MS Synthesis: Residual

Least Squares Means Table

Level	Sq Mean	Std Error	Mean
PG	447.74333	20.775842	447.743
PG+10	539.75556	20.775842	539.756

LSMeans Differences Student's t

alpha = 0.0500 2.05183

Level	Least Sq Mean
PG+10 A	539.75556
PG B	447.74333

Levels not connected by same letter are significantly different.

Mix-AV*Relative Temp

Effect Test

Sum of Squares	F Ratio	DF	Prob > F
3750.5744	0.24142		0.7872

Denominator MS Synthesis: Residual

Least Squares Means Table

Level	Least Sq Mean	Std Error
DCT-20-7%AV,PG	447.72000	35.984814
DCT-20-7%AV,PG+10	528.36333	35.984814
DCT-21-4%AV,PG	452.92000	35.984814
DCT-21-4%AV,PG+10	573.59833	35.984814
DCT-22-7%AV,PG	442.59000	35.984814
DCT-22-7%AV,PG+10	517.30500	35.984814

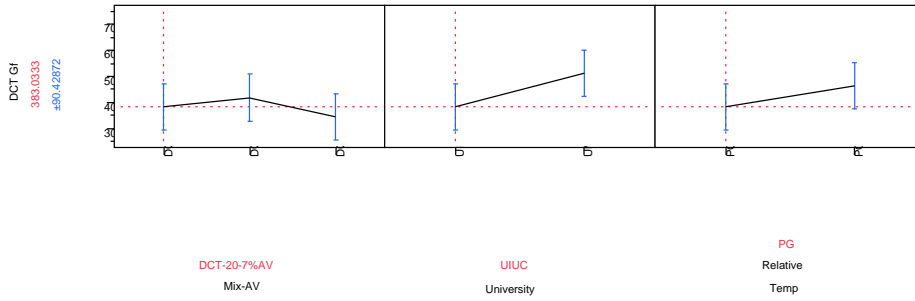
LSMeans Differences Tukey HSD

alpha = 0.0500 3.06385

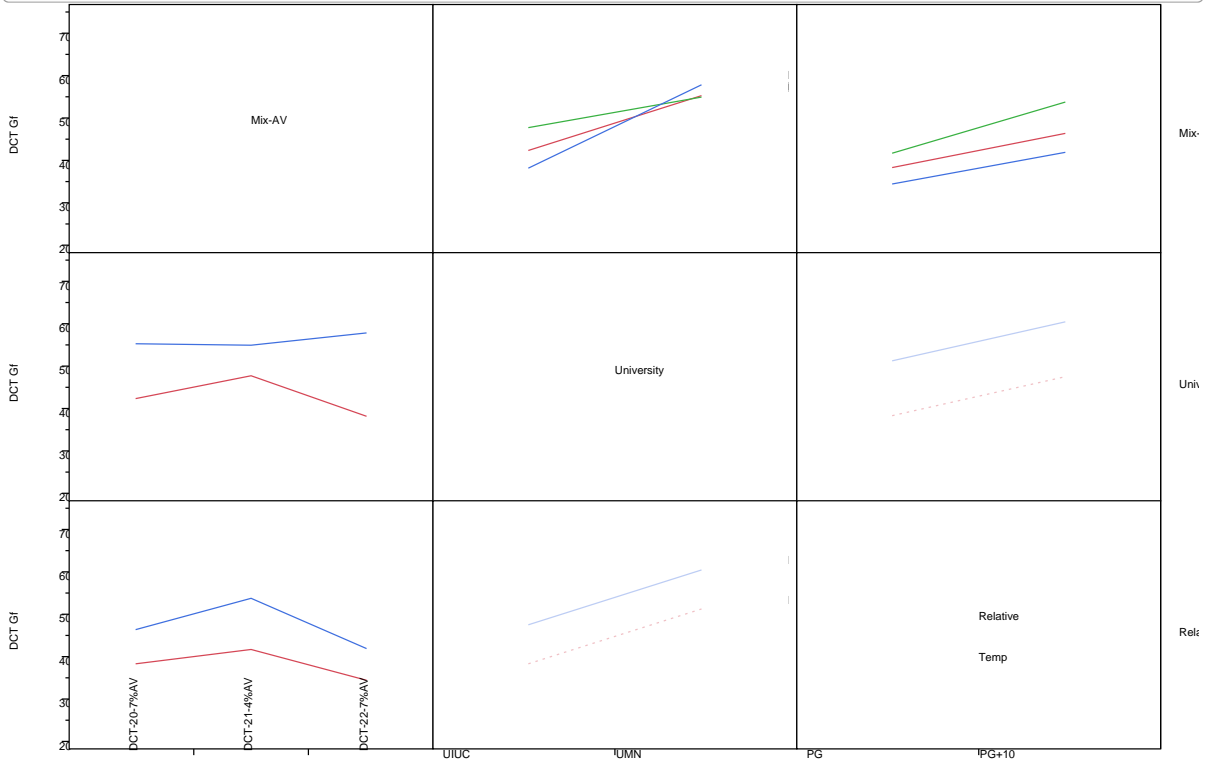
Level	Least Sq Mean
DCT-21-4%AV,PG+10 A	573.59833
DCT-20-7%AV,PG+10 A	528.36333
DCT-22-7%AV,PG+10 A	517.30500
DCT-21-4%AV,PG A	452.92000
DCT-20-7%AV,PG A	447.72000
DCT-22-7%AV,PG A	442.59000

Levels not connected by same letter are significantly different.

Prediction Profiler



Interaction Profiles



Appendix C: User's Manual for ILLI-TC using Visual-LTC GUI

Visual LTC User Manual

ILLI-TC is comprised of several analysis modules (preprocessor, input file generator, preanalyzer, and finite element analysis engine), which are unified through a graphical user interface (GUI), called Visual LTC. The following user manual provides detailed explanations for how to run ILLI-TC through its user interface, Visual LTC.

Download

ILLI-TC is available for download, and the contents of the program are zipped into a single folder containing the items listed in Table B1.

Table C1. Contents of zipped ILLI-TC distribution folder

VisualLTC.exe	Graphical user interface
analysis_modules\	Folder of executable analysis modules
Master.exe	Constructs master curve
TCModel.exe	Extracts Maxwell model parameters
VE1D.exe	Preanalyzer
FEengine.exe	Finite element analysis engine
ac_mixes\	Folder of existing asphalt concrete mixes
MnRoad33.acinp	Existing asphalt concrete mixes
MnRoad34.acinp	
MnRoad35.acinp	
climatic\	Folder of temperature profiles
CT_int_3.poly	Text files of temperature profiles for intermediate, cold, and warm climates in participating states for various pavement depths
CT_int_4.poly	
CT_int_5.poly	
...	
WI_warm_14.poly	
WI_warm_16.poly	

Setup Working Directory

Communication between Visual LTC and the various analysis modules is achieved through reading and writing text files stored in the working directory. The first step in running Visual LTC is to select a working directory. This directory must contain certain folder and files organized in such a way that Visual LTC can find them. The organization of the working directory is shown Table B2.

Table C2. Contents and organization of working directory (folders shown in bold)

Working Directory\ VisualLTC.exe
Existing_mix1.acinp (optional)
Existing_mix2.acinp (optional)
...
Existing_mix.acinp (optional)
analysis_modules\ Master.exe
TCModel.exe
VE1D.exe
FEEngine.exe
climatic\ CT_int_3.poly
CT_int_4.poly
CT_int_5.poly
...
WI_warm_14.poly

Existing asphalt concrete files (*.acinp) may be included in the root of the home directory, although they are not required. Existing mixes present in the working directory will be available to the user. If no mixes are in the working directory root, then the user will either have to enter all of the material properties by hand, or he/she can import *.acinp files located in a different folder on his/her machine.

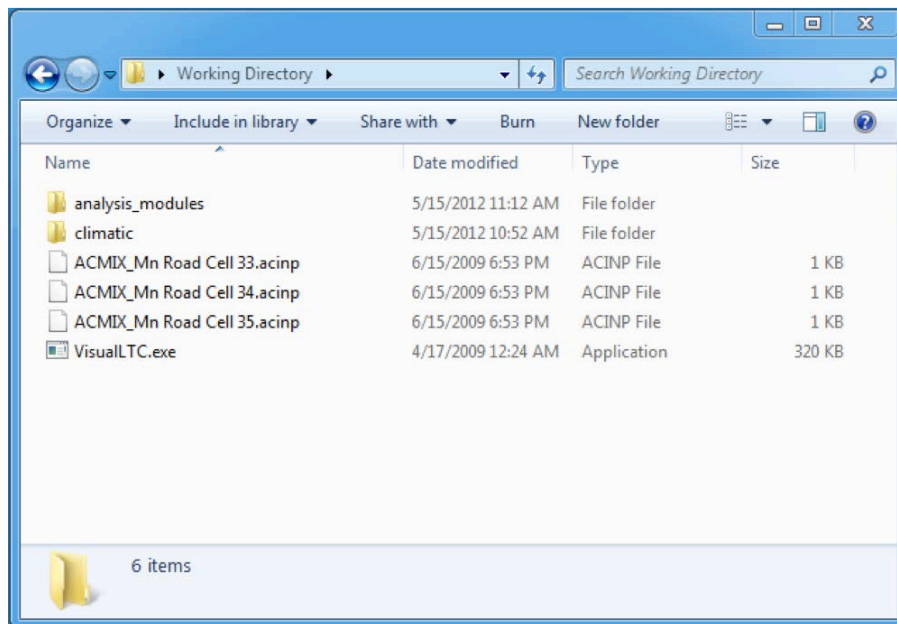


Figure C1. Screenshot of working directory with optional *.acinp files

Several files are created and moved inside the working directory during analysis. After the analysis completed, the intermediate files are stored in a directory called “intermediate_files” inside the working directory. The advanced user may access and inspect these files, however this is not necessary as they are internal to the overall analysis process.

Supported Platforms

Visual LTC and the analysis modules are only supported on Windows XP and Windows 7 operating systems. Both 64 bit and 32 bit versions are available.

Use of Visual LTC

The key features of Visual LTC are described next. This section is organized as follows: first the typical usage of ILLI-TC through Visual LTC is described, additional features including saving mixes and projects, importing new mixes, and changing the user type for advanced capabilities are discussed next, finally, typical errors and warnings the user may encounter are explained.

Typical Usage

The first step in Visual LTC is to create a new project or open an existing one, as shown in Figure B2. If the user chooses to create a new project, he/she will be prompted for the location of the working directory, which must be formatted properly, as discussed in the previous section and shown in Figure B1. If the user chooses to open an existing project, he/she will be prompted to select a *.prj file, which would have been saved from a previous Visual LTC run. More information on saving projects will be provided in the next section.

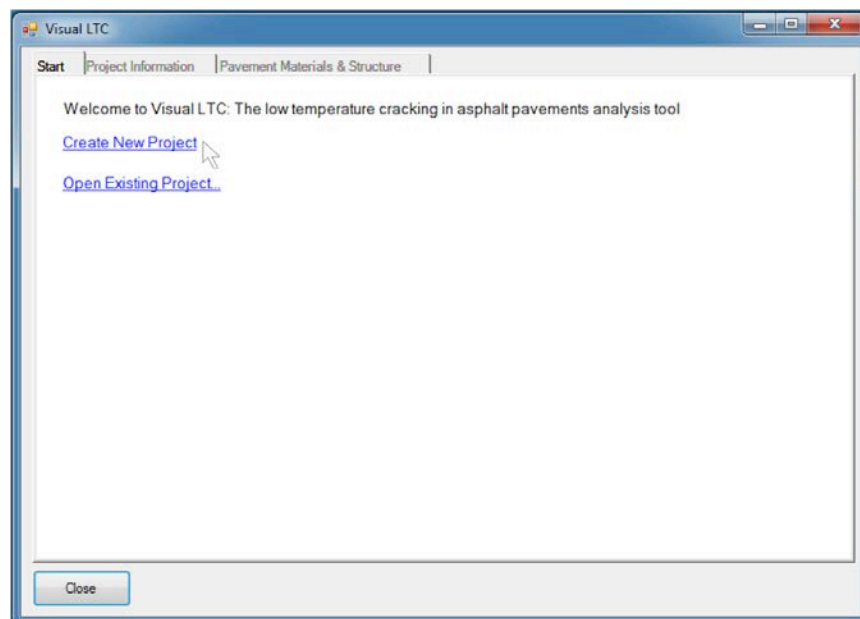


Figure C2. Start project: the user may either create and new project or open an existing project

In the following descriptions it is assumed that the user started a new project, so required fields are initially blank. If the user chose to start from an existing project, fields may be fully or partially completed. The next step is for the user to enter project information, as shown in Figure B3. The general information includes the project name, project description, analyzer, and date, all of which will be saved if the user chooses to save the project. The project location and analysis period are important pieces of information that will be fed to the finite element analysis engine. The project location is organized by state, then by zone. The locations are populated by the *.poly files in the climatic\ folder shown in Table B2. The user may plot the air temperatures of the selected location, shown in Figure B4. The analysis period can be entered either in number of years or specific dates. Hourly data for a five-year period is available for the provided locations. If the user chooses an analysis period of longer than five years the data is spliced together appropriately.

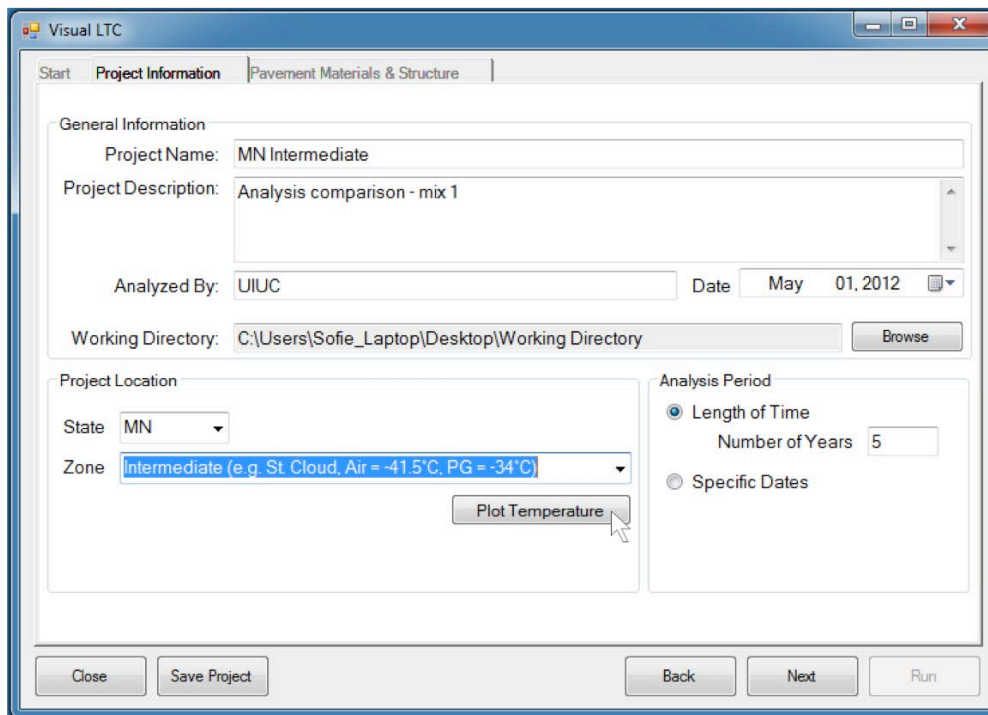


Figure C3. Project information

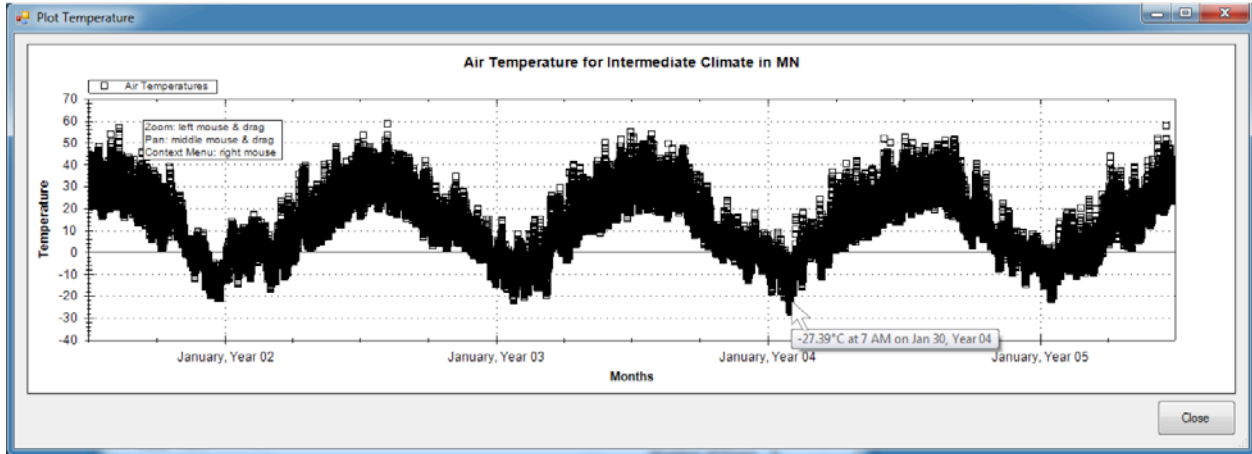


Figure C4. Plot of air temperatures

- Standard user features, reference to advanced user section
- Information shown during analysis run
- Plotted preanalyzer results
- Final result

The next set of user inputs describes the properties of the asphalt concrete layer. On the “Pavement Materials & Structure” tab, the user inserts the asphalt layer by clicking the button shown in Figure B5.

The figure shows the "Visual LTC" software interface with the "Pavement Materials & Structure" tab selected. The "Asphalt Layer Properties" section is active, featuring three buttons: "Insert Asphalt Layer" (highlighted with a mouse cursor), "Edit Asphalt Layer", and "Clear Asphalt Layer". Below these buttons are several input fields: "Mixture Name" (None selected), "Description" (empty text area), "Thickness" (input field), "Unit Weight" (input field), "Thermal Conductivity" (input field), "Heat Capacity" (input field), "Creep Compliance" (input field with a "View Data" button), "Mixture VMA" (input field), "Aggregate alpha" (input field), "Mixture alpha" (input field), "Fracture Energy" (input field), and "Tensile Strength" (input field). Below the "Asphalt Layer Properties" section are two sub-sections: "Base Layer Properties" with fields for "Base Type" (Granular), "Base Material" (Crushed gravel), and "Base Thickness" (12 in); and "Subgrade Properties" with fields for "Subgrade Material" (A-7-5) and "Last Layer?" (yes). At the bottom of the window are buttons for "Close", "Save Project", "Back", "Next", and "Run".

Figure C5. Pavement materials and structure: inserting the layer

One the “Add Asphalt Layer” screen the user may select from existing mixes that are present in the working directory, as shown in Figure B6, or he/she may import a mix (*.acinp file) if it is not located in the working directory. If no mixes are in the working directory the user may import a mix or add a new mix and enter the data manually. In order to create a new mix the user must select “Advanced User”. This option will be discussed in more detail in a later section.

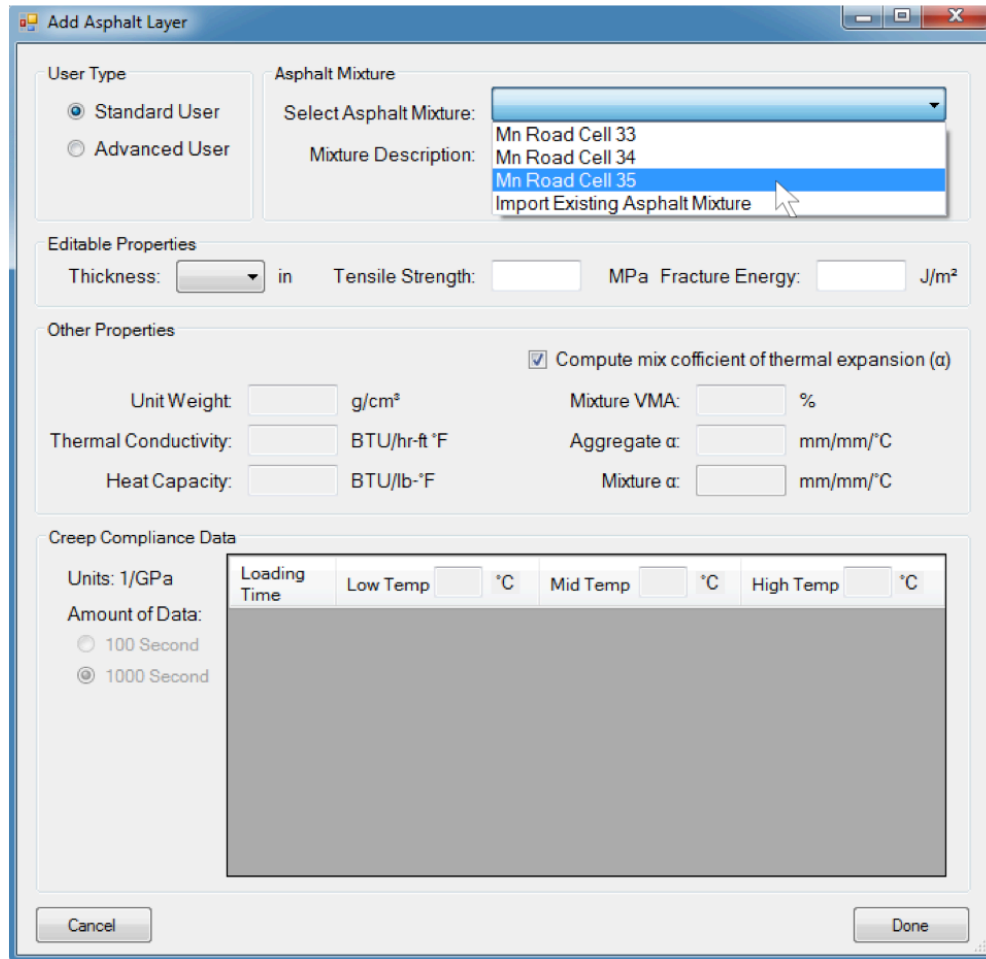


Figure C6. Add asphalt layer: selection of existing asphalt mix

When an existing mix is selected the material properties are populated. There are three editable properties available for the standard user: pavement thickness, tensile strength and fracture energy. All material properties are editable for the advanced user; see subsequent section for more information. The user selects the pavement thickness from a list of available thicknesses, as shown in Figure B7. The available thicknesses are determined by the *.poly files, because each file contains the temperature profile for a specific depth at a specific location.

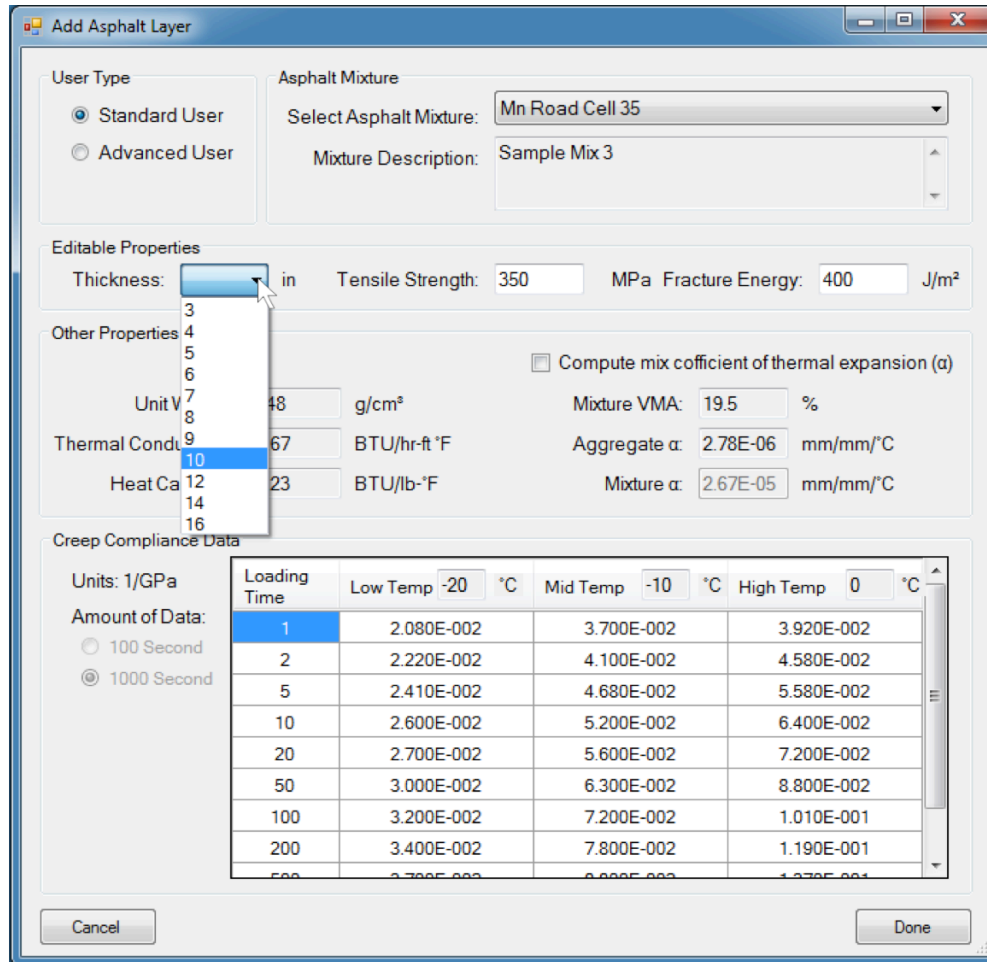


Figure C7. Add asphalt layer: selecting layer thickness

Once the asphalt properties are inserted, they summarized on the Pavement Materials & Structure page. The user can view the creep compliance data if needed, as shown in Figure B8. The user also has the option of editing or clearing the layer properties.

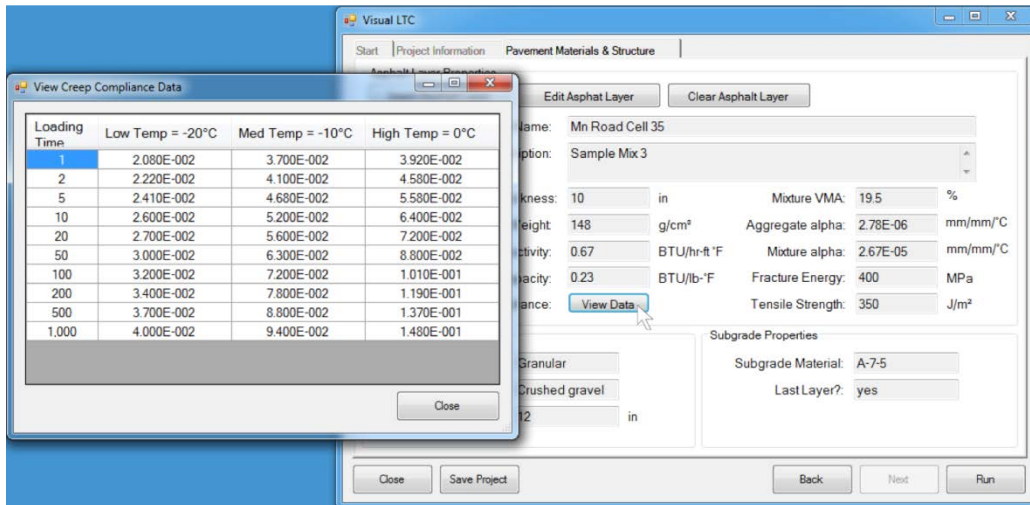


Figure C8. Summary of asphalt layer material properties

Now, the analysis is ready to be executed, and the user selected the “Run” button. The analysis modules run in the background and the user sees an update of the processes that are completed and in progress, as shown in Figure B9.

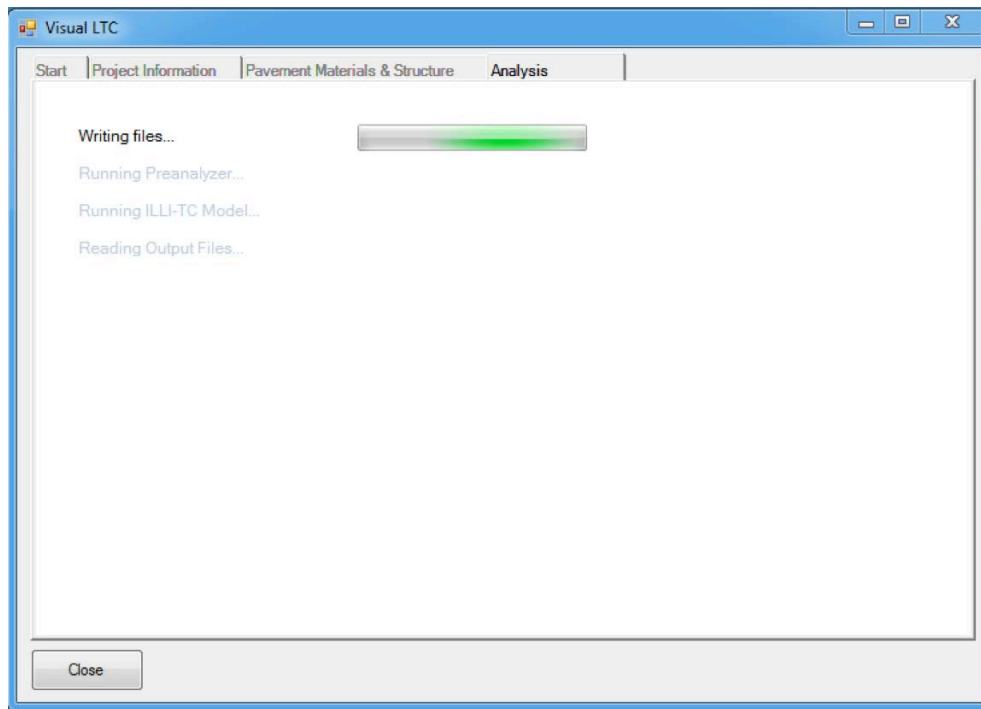


Figure C9. Analysis running

After the preanalyzer runs, the results appear on the screen for the user to view, as shown in Figure B10. The preanalyzer identifies critical events that then get analyzed by the finite element analysis engine. The user can choose to stop or continue with the analysis. If no selection is made within 30 seconds the analysis continues.

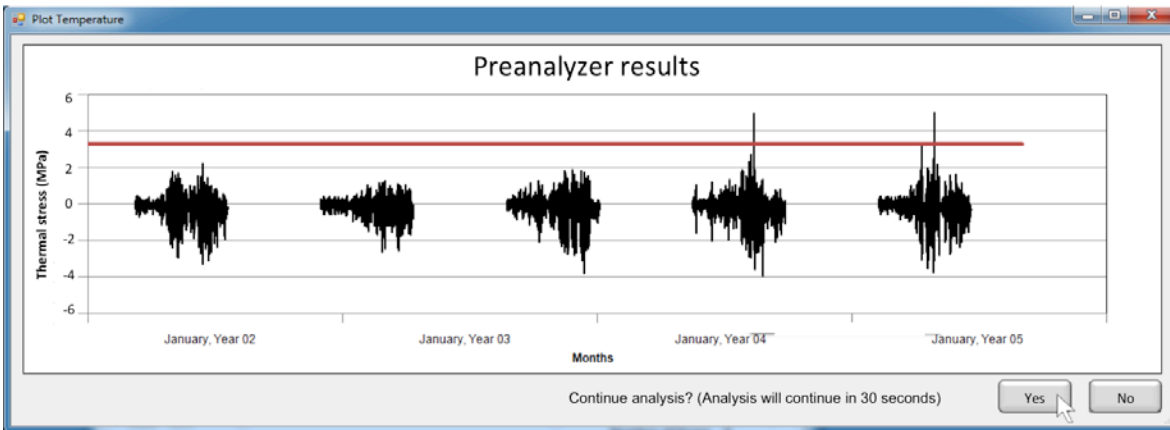


Figure C10. Preanalyzer results

The results of the full analysis are shown to the user in a simple window, containing the number of months simulated, the number of months completed, and the amount of cracking at the end of the simulation. As sample result screen is shown in Figure B11. The user has the option of saving the results to a text file.

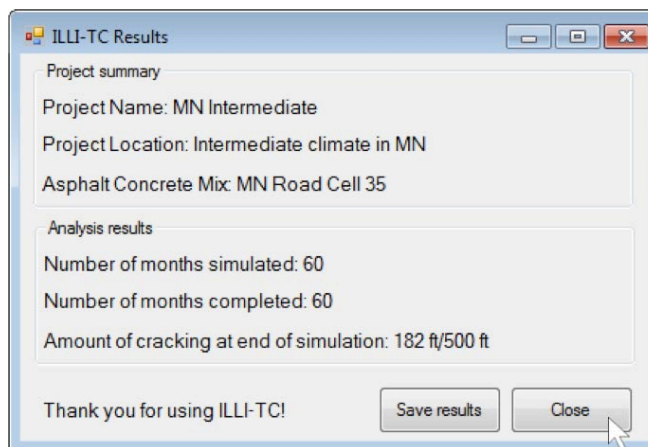


Figure C11. ILLI-TC results

Changing User Type

Advanced Users have the additional capability of adding new asphalt mixes and modifying properties of existing asphalt mixes. The user can easily change from one user type to the other, and assumes the responsibility of entering consistent data. Figure B12 the option for the user to toggle between type “Standard User” and “Advanced User”. Notice that all of the material properties are editable for the advanced. If the advanced user modifies a mix, he/she will be prompted to save the mix for future Visual LTC runs. As advanced user, the “Select Asphalt Mixture” dropdown box also has the option to create a new mix. The new mix can also be saved for future runs.

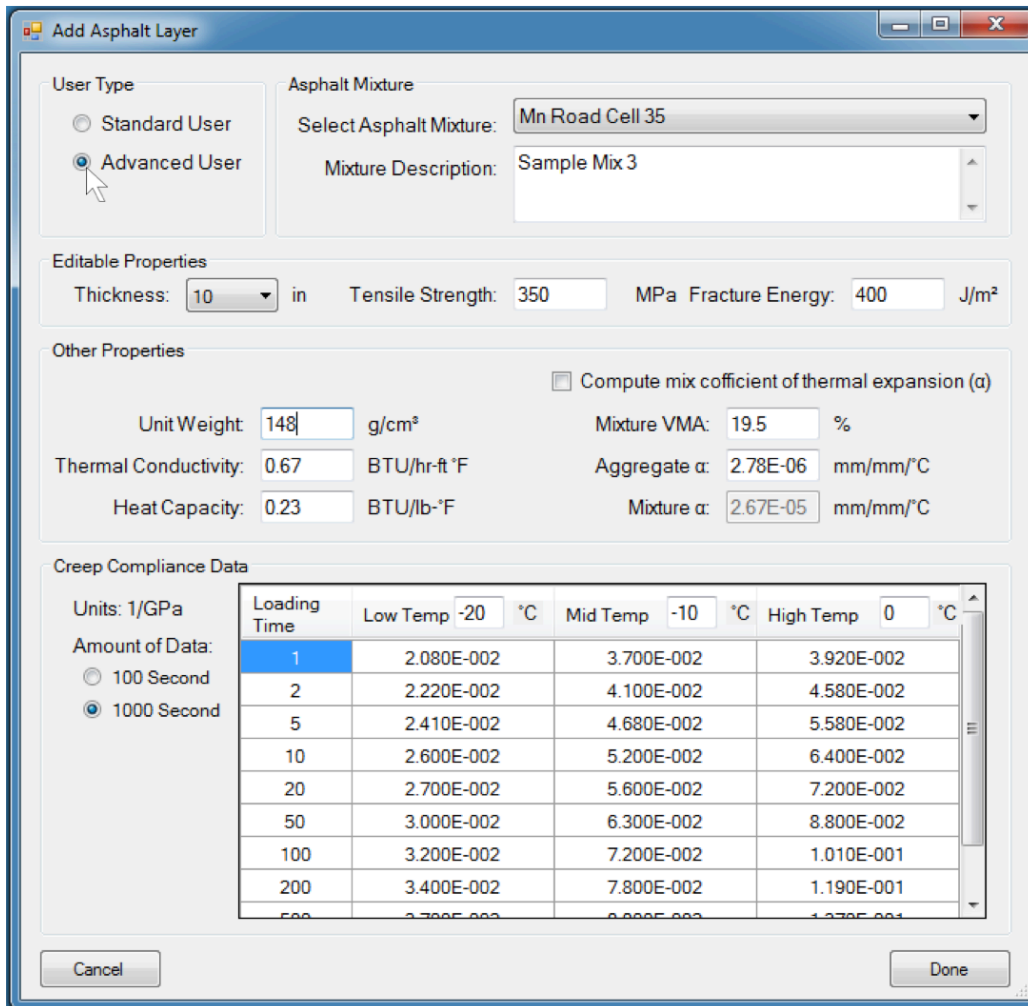


Figure C12. Advanced user type. As an advanced user, all material properties become editable and there is the option to create a new mix.

Saving Visual LTC Projects and Mixes

The user may save the current project, as shown in Figure B13. The project will be written to a text file with the *.prj extension. During a new Visual LTC run, the user may open this project instead of creating a new one.

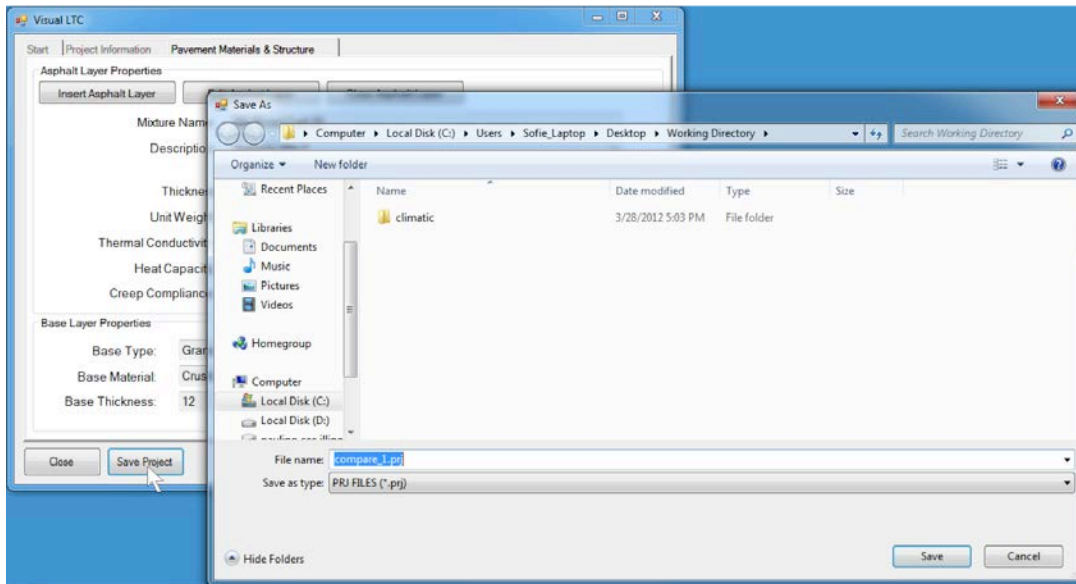


Figure C13. Save project

If the user adds a new mix or modifies an existing mix as an Advanced User (see previous section), he/she may save that mix for use in future Visual LTC runs. The user is automatically prompted to save a new or modified mix by Visual LTC. The mix is saved as a text file with the *.acinp extension.

Warnings and Errors during Analysis

Visual LTC is equipped with several error checks and warns the user appropriately for potential problems. Warnings may occur during analysis, in which case Visual LTC collects the information from the appropriate analysis module, reports the error to the user, and allows the user to decide how to proceed. One such example is shown in Figure B14. In this case, the Master analysis module is going to override an existing file. Visual LTC alerts the user and allows him/her to handle the problem accordingly.

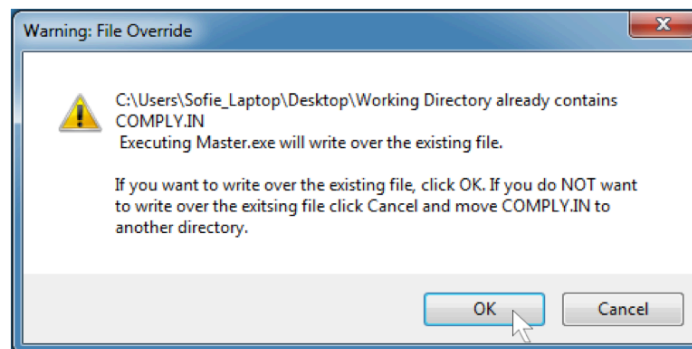


Figure C14. Typical warning screen for writing over existing files